Springer Proceedings in Energy

Ion Visa *Editor*

Sustainable Energy in the Built Environment - Steps Towards nZEB

Proceedings of the Conference for Sustainable Energy (CSE) 2014

Springer

Springer Proceedings in Energy

More information about this series at http://www.springer.com/series/13370

Ion Visa
Editor

Sustainable Energy in the Built Environment - Steps Towards nZEB

Proceedings of the Conference for Sustainable Energy (CSE) 2014

Springer

Editor
Ion Visa
Department of Product Design,
Mechatronics and Environment
Transilvania University of Braşov
Braşov
Romania

ISSN 2352-2534 ISSN 2352-2542 (electronic)
ISBN 978-3-319-09706-0 ISBN 978-3-319-09707-7 (eBook)
DOI 10.1007/978-3-319-09707-7

Library of Congress Control Number: 2014946738

Springer Cham Heidelberg New York Dordrecht London

Printed on acid-free paper

Springer is part of Springer Science+Business Media (www.springer.com)

Foreword

Beginning with the second half of the twentieth century, serious and well-substantiated concerns were formulated considering humanity development, as accelerated economic progress was the main focus without considering the medium- and long-term effects on the environment and on the natural resources. The economy progress supported the population increase, raising the demand for new resources, for food, for working places, supporting further technological progress. This spiral, launched by the Industrial Revolution in the nineteenth century could function as long as the Earth's resources were in large amounts and the environmental quality was not endangered.

Development scenarios firstly formulated in the '70s, and further refined and updated, outline that accelerated consumption depletes raw materials, but mainly shows that nature is no longer able to balance the resources and to mitigate the effect of end-products; pollution became thus one of the major threats affecting humanity.

Energy is the key to economic development; for over 150 years, fossil fuels (coal, oil, gas) represented the main raw materials in thermal and electric energy production, releasing large amounts of wastes; among these, greenhouse gases (GHG) were found responsible for severe consequences that are now at the border of irreversibility: climate change and global heating. Thus, concerted actions are required to mitigate GHG and their effects, by following two major paths: increasing the efficient use of traditional energy fuels (thus getting more output for the same input), but mainly by replacing fossil fuels with inexhaustible sources—renewable energies.

New concepts are therefore expected to be found, designed, and implemented in all areas where energy is used: industry, agriculture, transportation, etc.

A significant part of energy is used in the built environment for covering thermal and electric needs; additionally, other common utilities (particularly water and wastes) require energy for being produced, delivered, or disposed. This makes the built environment one of the most important components that need to be specifically addressed and changed in the future sustainable energy model.

The development of a sustainable built environment requires reductions in energy consumption (by cutting the losses and implementing energy efficient consumers), for reaching the *Low Energy Building* status. By implementing renewable energy systems, the much lower energy demand could be totally or partially met based on sustainable, non-polluting systems in the *Nearly Zero Energy Buildings* (nZEB). Conceptually, this stepwise development is logical but its implementation needs novel solutions for making buildings not only efficient and green but also affordable. To speed up this process, a legal frame was proposed and will be implemented by 2018 all over EU, requiring for all public buildings to meet the nZEB standards, and by 2020 imposing the same thresholds for each new building. Therefore intensive research is under development all over the world, for developing novel concepts, equipment, systems to be implemented in the built environment. For reaching a feasible output, an interdisciplinary approach is required to develop optimized energy mixes, considering the available on-site renewable energy resources and able to meet the energy demand in the building.

Sensing this need, the R&D Centre Renewable Energy Systems and Recycling (RES-REC) in the Transilvania University of Braşov, activated in the past 10 years for developing complex interdisciplinary systems for promoting advanced concepts, products, and processes supporting the implementation of sustainable energy solutions from "material to prototype". In the past years, special focus was set on finding novel, feasible, and acceptable solutions for the built environment. Many of these are now implemented, monitored, and optimized in the R&D Institute of the university, designed as a sustainable community and opened in 2013.

As an instrument to support the R&D international effort, the RES-REC center launched in 2005 the Conference for Sustainable Energy, CSE. A trend was set for each edition by proposing subjects of high interest in promoting sustainable solutions for the future energy patterns: the second edition (2008) was dedicated to Solar Energy, while the third edition (2011) allowed formulating major problems and possible solutions for the transition toward Sustainable Communities.

Considering the actuality of the topic, the fourth edition of the Conference for Sustainable Energy was dedicated to various aspects that support the transition toward nZEB. Gathering attendees from nine countries the conference represents an opportunity for ideas and experience exchange, and for networking in joint cooperation. This volume gathered papers that were presented during CSE 2014 and proved that promoting nZEB requires an interdisciplinary effort that implies almost all engineering topics, along with social acceptance and specific education and training.

The conference is developed under the patronage of the International Federation for the Promotion of Mechanism and Machine Science (IFToMM), through the Technical Committee Sustainable Energy Systems.

We are convinced that the papers in this volume represent an input for further research and for speeding up the implementation of nZEB as a main component of Sustainable Development.

Brasov, November 2014 Ion Visa

Scientific Committee

Adrian Badea, University Politehnica of Bucharest, Romania
Viorel Bădescu, Romanian Academy of Science, Romania
Bogdan Burduhos, Transilvania University of Braşov, Romania
Marco Ceccarelli, University of Cassino, Italy
Shuo Hung Chang, National Taiwan University, Taipei, Taiwan
Anca Duţă, Transilvania University of Braşov, Romania
Istvan Farkas, Szent István University, Gödöllő, Hungary
Maria Gavrilescu, "Gheorghe Asachi" Technical University, Iaşi, Romania
Andreas Haeberle, Fraunhofer PSE, Germany
Yuh-Shan Ho, Asia University, Taichung, Taiwan
Florin Iordache, University of Civil Engineering, Bucharest, Romania
Codruta Jaliu, Transilvania University of Braşov, Romania
Harald Kainz, Graz University of Technology, Austria
Yoram Krozer, University of Twente, The Netherlands
Joseph Choi Lam, City University of Hong Kong, China
Macedon Moldovan, Transilvania University of Braşov, Romania
Paola Mazzucchelli, EUREC, Belgium
Aurelia Meghea, University Politehnica of Bucharest, Romania
Nikolai Mihailov, University of Russe, Bulgaria
Richard Morris, University of Brighton, UK
Mircea Neagoe, Transilvania University of Braşov, Romania
Brian Norton, Dublin Institute of Technology, Dublin, Ireland
Nicolae Olariu, The Romanian PV Industry Association, SUNE, Bucharest, Romania
Victor Petuya, University of the Basque Country, Bilbao, Spain
Teresa Ponce De Leao, LNEG, Portugal

Mathias Rommel, Institut für Solartechnik SPF, Switzerland
Elias Stathatos, University of Patras, Greece
Gintaras Stauskis, Vilnius Gediminas Technical University, Lithuania
Florin Tănăsescu, Romanian Academy of Technical Sciences, Romania
Ion Vişa, Transilvania University of Braşov, Romania
Maria Zaharescu, Romanian Academy of Science, Bucharest, Romania
Teresa Zielinska, Warsaw University of Technology, Poland

Contents

Part I
Towards Nearly Zero Energy Buildings

The Built Environment in Sustainable Communities

Ion Visa and Anca Duta

Abstract The built environment is one the major contributors to the global increase of greenhouse gases emissions, thus novel solutions supporting sustainability are developed, considering both energy efficiency—targeting the Low Energy Buildings (LEB) status, and renewable energy systems, aiming at implementing Nearly Zero Energy Buildings (nZEB). The large scale can be well satisfied when developing assemblies of highly efficient buildings, in sustainable communities, when synergy can occur if well planning the balance between common and individual utilities for heating, cooling, powering the buildings along with water supply and discharge unit(s) and sustainable transportation. The paper presents the stepwise design for developing a sustainable community and proves the concept for a new research community: the R&D Institute of the Transilvania University of Brasov, Romania. The design and development of 11 LEBs is presented and it is outline the need for valorizing the available natural resources in the passive solar design along with the use of tailored construction materials, selected based on the climatic profile. Further on, the implementation of sustainable energy mixes renewable based is discussed for reaching the nZEB status. Combined solutions are analyzed, considering the individual energy mixes installed on each building *and* the centralized production of thermal and electrical energy. Tailored solutions for insuring the water supply and discharge are further presented, based on ground-water resources and a combination of conventional biologic treatment with advanced wastewater treatment processes, able to remove the wide range of pollutants that are expected from a multi-disciplinary R&D facility.

Keywords Sustainable community · Low energy building · Nearly zero energy building · Sustainable design

I. Visa (✉) · A. Duta
Renewable Energy Systems and Recycling R&D Centre, RES-REC, Transilvania University of Brasov, Eroilor 29, 500036 Brasov, Romania
e-mail: visaion@unitbv.ro

I. Visa (ed.), *Sustainable Energy in the Built Environment - Steps Towards nZEB*,
Springer Proceedings in Energy, DOI 10.1007/978-3-319-09707-7_1

1 Introduction

Starting with the industrial revolution in the XVIIIth century, the economy progress and quality of life experienced a continuous increasing trend, followed by the increase of the world population and of the resources used to further support the development. This ascending spiral led to an accelerated depletion of the natural resources and brought an un-foreseen side-effect: pollution. The combined effect of population growth, resources depletion and pollution imposes major threats on the global development; these were for the first time coherently formulated, modelled and presented in the well-known report "The Limits of Growth", [1], commissioned by The Club of Rome in 1972. Although highly contested, the conclusions of this report raised an alarm signal on the future development pattern that further supported the coagulation of a novel concept: *Sustainable Development*. Introduced by the Brundtland Report [2], this concept is simply formulated as "*the development that meets the needs of the present without compromising the ability of future generations to meet their own needs*". Implementing this concept proved to be a hard and ongoing task, as there are many different—yet complementary aspects involved in sustainability. Additionally, climate change and global warming were further depicted as major consequences of the un-sustainable development, requiring more concrete actions towards sustainability. Thus, United Nations launched a series of high-level events, starting with the conference from Rio de Janeiro which launched (in 1992) the Agenda 21 Programme [3, 4]. Agenda 21 promotes the global thinking for concrete local actions ("*Think global, act local*") and empowers communities to identify and implement the specific paths that lead them to sustainability by efficient and affordable solutions.

Three pillars are mainly used to define sustainable development: economy, environment and society, and congruent actions need to be developed, by considering the requirements imposed by each of these pillars. Thus, a fourth pillar was recently proposed [5], the institutional sustainability, insuring the coherent and cohesive approach. This means that the major problems need to be addressed simultaneously considering all three/four pillars.

The No. 1 problem recognized at global level is Energy [6]. Energy consumption represented for over a century a measure of the economic (mainly industrial) development, with the highest values per capita registered in the developed countries; recently, the World Bank and International Energy Agency (IEA) delivered reports that estimate a doubling in the energy capacity over the next 40 years to meet the demands of developing countries, evaluated based on the past 10 years trends [7]. This demand can no longer be covered following the current energy pattern, heavily based on fossil (and nuclear) fuels, as these are mainly responsible for the environmental pollution and rely on resources that are fast depleting, thus supporting social insecurity and the risk of worldwide conflagrations. This is why a huge effort was and is worldwide devoted to identify sustainable solutions for energy production and consumption, able to meet the progress needs without

reducing the economy development and the personal comfort. The *Sustainable Energy* term covers the energy production from clean and secure sources (*Renewable Energy Sources*) and the efficient energy consumption, including cutting the losses (*Energy Efficiency, EE*) [8].

The development of novel energy production/consumption models, matching Sustainable Energy, needs to be done in a very short term and the implementation of these solutions needs to be acceptable thus should meet at least three objectives:

1. competitive costs (as compared to the current production/consumption paths);
2. security of supply (relying on rather non-limited sources), and
3. environmental friendly (for reducing global pollution and climate change) [9].

Energy for sustainable development represents thus a clear technological challenge, with direct effect on environment protection and on social development.

The past two decades experienced a broad range of actions towards Sustainable Energy, with specific solutions for different sectors of the economy: industry, agriculture, tourism, built environment. The built environment accounts now-a-days for 20–40 % of the total energy consumption, with the highest values in developed regions (US and EU [10, 11]). Therefore, a complex frame is developed for fastening the transition towards a sustainable built environment: this frame includes incentives (e.g. for implementing *Renewable Energy Systems*, RES, or for reducing the CO_2 emissions) and regulations, as the Energy Performance in Buildings Directive [10] or the well-known 20-20-20 EU directive stating that by 2020 an average of 20 % from the total EU energy consumption will be covered by RES, simultaneously with a 20 % increase in the EE and a 20 % decrease in the CO_2 emissions [12]. To meet these targets, ***The European Strategic Energy Technology Plan* (SET Plan)** formulates the energy technology policy, aiming at accelerating the development and deployment of cost-effective low carbon technologies.

Following this frame, RES were largely implemented and EE measures were applied in the built environment, but this parallel approach led to results that were not meeting the milestones set for 2020. Therefore, in 2013, the targets set for each EU country were revised and the measures in the SET Plan were more specifically formulated for planning, implementation, resources and international cooperation in the field of energy technologies. Particularly, it was outlined the need for combined measures of RES implementation *and* EE.

Considering the energy consumption in buildings, this represents the re-focus from solutions aiming at Low Energy Buildings (LEB) towards Nearly Zero Energy Buildings (nZEB). On the other hand, considering the built environment, this is translated into a shift of interest from one building towards a community.

The paper reviews the current knowledge and practical results obtained in the development of sustainable communities and analyses the steps that need to be followed for identifying specific sustainable and affordable solutions.

2 Sustainable Communities

There are many definitions describing a "community", most of them dealing with the territory and the population density. Considering the paths for solving the energy problem as the main feature of a sustainable community, it should also be noticed that technological development cannot be seen as independent from people, thus technological development and humans are influencing each other and are developing in cooperation [13]. This means that the technological and environmental challenges must be solved based on solutions that gain social and societal acceptance and, on the other hand, the community education level is permanently improving, for being able to understand and accept the new solutions.

Additionally, a community is far from being a sum of buildings; thus, planning a sustainable community should make use of the knowledge developed at buildings' level and should further aim at synergy when finding and implementing solutions that are targeting:

- *Sustainable energy production and consumption*: thermal and electric energy, produced mainly by RES as part of optimized energy mixes; alternatives could complementary cover the on-site energy systems (thus RES-based mixes installed on the buildings), and the community energy production/consumption using larger scale RES mixes interconnected in micro-community grids.
- *Sustainable built environment*: for efficiently implementing RES-based energy mixes, the energy consumption needs to be significantly lowered, reaching the LEB status. This status is unevenly defined all over the world (also at EU level) and it is not likely to get a set of unique values as the energy consumed in a building significantly depends on the geographical location (especially latitude and altitude). Once reached the LEB status, the coverage of at least 50 % of the energy need by using renewable sources will meet the nZEB status. Along with technical solutions, this also implies life-cycle and environmental impact assessment, climate change and social policy issues [14] in a joint approach, that so far allowed the development of nZEBs only at demo/pilot scale.
- *Sustainable water use*: treatment, delivery, reuse and recycling represent a cycle that should be developed by protecting the natural water resources. On the other hand, these processes are energy-consuming, thus should be included in the overall energy balance at community level [15].
- *Wastes management*: household waste and the wastes resulted from energy production and/or wastewater treatment need to be processed in a large extent (as for example as energy source) and the rest should be subject of disposal respecting the environmental regulations.
- *Sustainable transportation*: that requires minimizing the emissions and the use of clean fuels.

Considering these aspects, energy production and consumption needs to be approached in an integrate manner, giving specific solutions for each of the components. Communities fully independent from the energy point of view are called

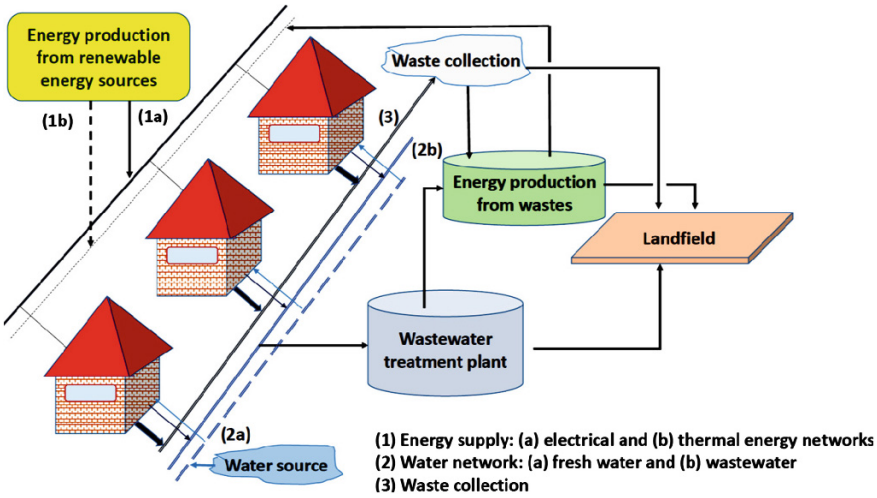

Fig. 1 Energy and utilities jointly used at community level

"energy autarkic" [16] or energy independent. The advantage of sustainable communities (towards energy independence) over a sum of sustainable buildings (e.g. nZEB) relies in the micro-grids and networks that can be developed for electric and thermal energy, for fresh water supply, and for wastes and wastewater collection and use, as Fig. 1 shows.

This allows using the already existent infrastructure and brings less changes in the inhabitants' behavior, thus increasing the acceptance. The integrate system should be able to [17]:

- Provide enough energy for meeting the demands of all inhabitants and joint facilities at community level;
- Have a storage system that mitigates the risks associated with the variability of the renewable energy sources;
- Operate off-grid; if accessible, the power grid can be used as storage system but the system should be able also to operate as "stand alone".

It is obvious that an optimum number of inhabitants/households can be identified when developing a sustainable community. The optimum mainly depends on the main feature that differentiates a sustainable community from a regular one: the energy produced from clean sources, using RES. Many studies are therefore focusing on the degree of "energy autonomy" and the availability of the renewable energy sources.

The first communities aiming at sustainability were developed as an answer to specific needs and less under environmental constraints or civic attitude. Thus, many reports are related to sustainable communities developed on islands, that were the first to experience the effects of the oil embargo(s), during time, as: Pulau Ubin near Singapore [18], Karpathos Island in Greece [19], Norfolk Island in UK [20],

and many others. Most of the reports show that energy autonomy 100 % insured by RES is not cost-effective yet, particularly for larger communities (e.g. Madeira and the Azores) [17].

Other applications reported are the rural remote communities, mainly focusing on the electricity generation using stand-alone hybrids systems. The main issue hereby identified is related to the lack of optimized systems chosen for implementation; these communities are not fully exploiting their potential as, most of the time, RES implementation was done without the involvement of the inhabitants and based on pre-set designs, without considering the specifics of the implementation locations [21].

As the CO_2 emissions are steadily increasing and the fossil fuel resources are depleted at the same rate, the option towards a sustainable built environment is no longer left for remote areas but has to be also considered in rural and urban regions that have centralized power and thermal energy supply (grid connected). Transforming these regions into sustainable communities, with an increased degree of energy autonomy mainly satisfied by renewables, represents the path that has to be followed. To assess the sustainability at community level represents another difficult task. Ecological Footprint, Barometer of Sustainability, Environmental Sustainability Index, are only several sustainability indicators that can be completed by the urban environmental indicators formulated through the "EEA Environmental Indicators" initiative [22, 23]. The main issue here is related to the extent of the community considered as reference: most of these indicators have meaning for communities larger than 100,000 inhabitants. Therefore, the development of sustainable communities should simultaneously be done with the formulation of a set of clear and straightforward indicators that could give a realistic view on the community status and would allow the dissemination and replication of the design solutions that lead to true sustainability. Eventually, on long term, sustainable cities can be developed being cleaner, greener and smarter [24].

3 Renewable Energy Systems in Sustainable Communities

Based on the lessons learned from previous attempts, the development of urban sustainable communities needs to be based on careful planning, optimized design, giving value to the local resources without imposing a depletion threat and without interfering with the highly sensitive ecological equilibrium.

Solving the energy problem requires, in the Sustainable Development concept, the large scale use of renewable energy sources to meet the needs of the built environment.

The solar, wind, hydro and geo-thermal energies can be converted into electric or thermal energy; the use of biomass is also included in this approach, although biomass conversion leads to CO_2 emissions, equal to the CO_2 processed during the biomass growth. Additionally, a deficient planning of a biomass-based energy pattern has the risk of deforestation and ecological unbalance [7]; on the other hand,

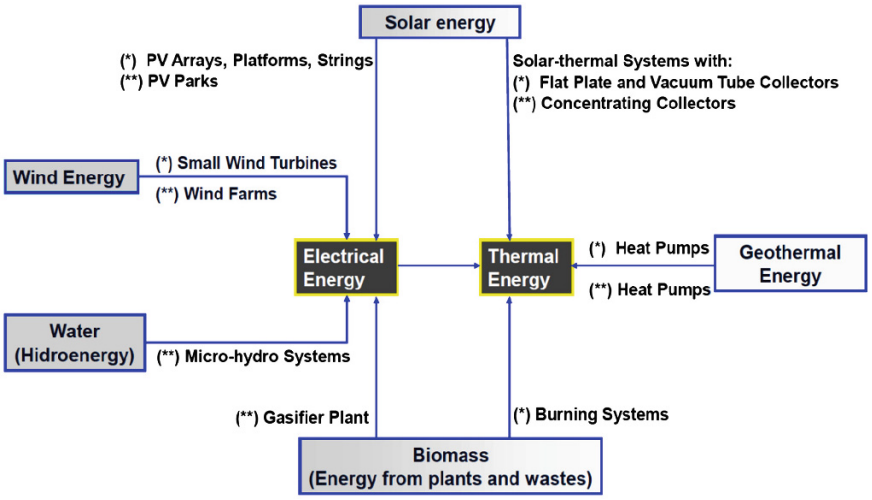

Fig. 2 Renewable energy conversion technologies implementable in (*) buildings and (**) at community levels

biomass is traditionally used in many world areas, thus including biomass in the transition towards sustainable built environment will increase the acceptance towards the other RES.

The main conversion processes involving renewable energy sources that can be implemented in buildings and at community level are presented in Fig. 2.

Despite the obvious environmental benefit, various barriers could be identified when implementing RES, Table 1. As the comparative analysis shows, objective constraints are linked to the technical and functional aspects [25]; thus plenty of effort is dedicated to R&D for identifying novel solutions able to surpass these limitations. This involves fundamental knowledge as in the case of photovoltaics for which novel materials/assemblies are intensively investigated to reach significantly higher efficiency values as compared to the physical limit of the single junction cells (33 %, under 1sun irradiation [26]). This also involves applied research as most of the expected solutions are a combination of novel materials and improved systems.

The subjective limitations are mainly the result of RES novelty: it is hard to believe that the sight of a tower in a coal-based CHP in the city outskirts is more attractive than a PV park, but people are less used with the later, while the first one is so common as most of the time it is not actually "seen". This type of barriers could and should be overcame by education.

A common technical constraint in RES implementation is the variability and limited predictability of the renewable resources potential. This has two main consequences:

Table 1 Barriers in implementing RES in the built environment

Renewable energy system	Objective constraints	Subjective limitations
Photovoltaic systems	Variability in the solar energy potential	Landscape distortion
		Possible electromagnetic emissions
	Limited efficiency	
	High initial investment	
Solar-thermal systems	Variability in the solar energy potential	Limited architectural acceptance
	Risk of overheating	
Wind turbines	Variability in the wind energy potential	The NIMBY syndrome
	Noise and vibrations	
	High initial investment	
Geothermal systems (ground coupled heat pumps)	Land availability	
	Ecological balance	
	High initial investment	
Micro-hydro systems	Point-type resource	Highly difficult to integrate inside a community
	Consistent additional works and systems	
	Environmental distortion	
Biomass systems	Needs additional systems (storage, ash disposal)	

- *On-site potential estimation*: there are well-recognized tools that estimate the solar and wind energy potential in different locations (METEONORM, TRNSYS, etc.) but these are—for most of the locations—calculated by interpolating the data provided by a limited number of weather stations. Thus, they provide approximate values, while the accurate design requires on-site weather data, gathered over at least 1 year (but preferably over more years, to sense the trends). This is particularly necessary for implemented RES in the built environment, when significant distortions are likely, as result of buildings (shading, wind barriers and turbulences, etc.).
- *Developing energy mixes*: able to continuously provide the required energy, by complementary using two or more renewable energy sources.

Another common barrier is the initial investment cost. The solar and wind energy—based RES are well recognized as having low operation costs and this represents an asset but the initial investment is high, thus their affordability in buildings implementation is quite low; community implementation, covering the needs of more households and jointly using the auxiliary equipment represents a path in costs reduction.

As the cost and the systems output represent important issues in the development of sustainable communities, the accurate design represents a must and should follow a well-defined algorithm.

4 Steps in Developing Sustainable Communities

There are common and specific features in the steps to be followed for developing sustainable communities and, respectively, nZEBs. The fundamental principle is the same: the optimized solutions should match the needs with the available energy, by giving a high share to renewables. Additionally, the solution should be technically and economically feasible, affordable and environmental-friendly.

Step1: Identifying the energy demand
The specific features in designing a sustainable community as compared to a nZEB mainly rely on defining the needs, Table 2.

As Table 2 shows, the thermal and the electric energy demand need to be evaluated, separately in a preliminary step and complementary in an integrated approach.

Electric energy demand in buildings:

1. The needs for lighting and household appliances can be evaluated based on national or international regulations.
2. Depending on the RES-based energy mix chosen for thermal energy production, electricity can be needed for powering the heat pumps or for forced circulation in the solar-thermal systems, installed on the buildings.

Additional electric energy demand in communities:

1. The electricity needed for community lighting (streets, monuments, etc.) and other appliances (e.g. traffic lamps) can be simply calculated based on the power of the specific consumer, their number and the average functioning hours per unit.

Table 2 Common and specific energy demand in nZEB sustainable communities

	Common needs in nZEB and in communities	Specific needs in sustainable community
Electric energy	Lighting the household	Street lighting
	Household appliances	Wastewater treatment
	Powering the auxiliary equipment of the RES integrated in the building	Powering the auxiliary equipment of community RES
Thermal energy	Domestic hot water	Wastes processing
	Building heating	Wastewater treatment
	Building cooling	Additional heating and drying processes

2. Fresh water supply: the power needed for fresh water extraction (underground sources) and/or for water treatment should be added to the energy demand. Water management can be developed following two schemes: (i) for drinking water, a common/community freshwater source is recommendable, instead of using deep fountains for each building. The advantages are both in terms of costs and of potable water quality, since centralized water treatment is more effective and safe as compared to tap-treatment, (ii) for non-potable use (toilet, laundry, and gardening) the ground water needs no treatment, thus reducing the electricity consumption [27].
3. Wastewater treatment: on-site treatment uses traditional lime and soda systems that need to be periodically revised and are highly unsuitable in communities. Centralized wastewater treatment facilities involve at least two steps: mechanical treatment (which in the final steps removes the large organic parts, further used in biogas production) and biological treatment (with aerobic bacteria). The power consumption depends on the water flow. Additional treatment is required for specific pollutants (heavy metals, toxic organics, surfactants, dyes) and the small-scale facilities should include additional steps, with quite large energy consumption when involving ion exchange or advanced oxidation processes. Large wastewater treatment facilities are more (cost) effective as compared to the small ones, therefore, whenever possible, collecting the sewer from more small communities to a larger plant represents a more advantageous solution [28].
4. The additional equipment for community RES depends on the systems implemented at community level (e.g. large solar-thermal facilities) and is mainly related to pumping systems, thus, these RES should be positioned close to the community.

Thermal energy demand in buildings:

In developing sustainable communities one compulsory step is to reduce the thermal energy demand of the buildings, targeting the LEB status. The following components are considered:

1. *Domestic hot water* that has an almost constant daily consumption and represents about 20 % of the total thermal energy demand in a building. The values are fluctuating depending on the building destination (residential, office, hospital, hotel, etc.).
2. *Heating* represents in the temperate climate the largest share of the total thermal energy used in buildings (over 60 %). Thus many efforts are concentrated on reducing the heating demand, mainly by energy saving measures. Reducing the heat loss requires a well-insulated building envelope and an optimize opaque/transparent ratio in this envelope (opaque surfaces have a thermal resistance almost five time higher than the transparent ones, but large glazed surfaces support natural lighting and increase the indoor comfort). For new buildings these optimized solutions can be easily implemented, making use of the novel

construction materials and technologies. But new buildings accounts for less than 5 % of the entire building stock; thus building retrofit represents actually the important part that has to be solved by each household, and this is one of the most difficult barrier to surpass. Retrofitting at the performance level of a LEB raises not only cost challenges but is also usually limited by the architectural and structural specific features of the building. Additionally, for heritage buildings, preserving the historical aspect makes highly difficult (and costly) the retrofitting process. Specific solutions, adapted to each building (considering the initial materials, their wearing) should be designed and integrated into a distinct architectural community concept.

3. *Cooling* (in temperate climate) requires a thermal energy demand estimated at maximum 20 % from the total thermal energy need. Combined solutions of natural cooling (e.g. night cooling) and shading can significantly reduce the cooling demand in well-insulated buildings.

Additional thermal energy demand in communities: can be the results of different auxiliary facilities (e.g. greenhouses, swimming pools) with continuous or seasonal functioning. Additionally, the biological wastewater treatment and the waste processing (biomass to biogas) require a certain amount of thermal energy, depending on the scale of each facility/plant.

Step 2: Evaluating the renewable energies potential
Depending on the renewable energy source, the potential is site-dependent or site-independent:

- *Site-dependent potential* characterizes the solar energy (and its components: direct and diffuse radiation), the wind energy (speed, direction) and, in some extent, the water flow on small rivers. According to the geographical coordinates, these have a seasonal variation, although the overall yearly amount is quite constant. For designing renewable-based energy mixes, the monthly (or weekly) variations are needed; the periods with very low potential of every renewable need to be outlined, for identifying the amount of energy that must be covered by back-up sources, along with the periods when excess energy production is expected, for an accurate design of the storage systems and contingency measures. Thus, monthly/weekly variations need to be available, covering at least 1 year, but preferably 2 up to 5 years.
- *Site-independent potential* is expected for geothermal sources (when using ground coupled heat pumps) as the earth temperature at the depth of interest is quite constant. The main limitation here is the availability of a certain surface for implementing the ground heat exchanger, and the deep drill heat exchangers are, in this view, preferable. The biomass potential is also site-independent in terms of weather data, but depends on the supply and logistics, with specific features for various types of biomass: wood, manure, straw, etc.

As RES implementation should/could be done both at building and at community levels, the side-dependent potentials should be monitored in more available implementation sites, for identifying the optimal ones. This is compulsory for the

small wind turbines (mounted at rather low height), as the buildings geometry can strongly influence the height distribution, on edges, corners and the rooftop [29]. This is also necessary when implementing solar energy convertors (PVs, flat plate solar-thermal collectors), as the smog that usually characterizes the urban agglomerations can modify the ratio direct/diffuse solar radiation, lowering the overall potential and output.

At community level, an additional restriction is imposed by the available sites, and optimal planning must balance the land used in agriculture with those used for energy production (including the energy crops) [30]. Ideally, the land used for installing RES (PV parks, wind farms, solar-thermal large arrays) should be of limited/no use in agriculture (degraded or polluted areas), and one option is to plan and implement soil remediation during the expected lifetime of the renewable system (20–30 years) [31].

Step 3. Designing the energy mix
Analyzing the development of various RES, the barriers and physical limitations, the European SET plan differentiates between the RES recommended to be installed at low scale and those that allow large scale production. A simplified conclusion states that electricity production is recommended to run in large facilities (PV parks, wind farms with average or large wind turbines), while thermal energy production (solar-thermal, heat pumps, biomass) should run on-site, on or near the buildings, allowing thus to cut the losses during transporting the heating agent [32]. These recommendations should be further tailored according to the community's needs, dimensions, location, available renewable resources, grid availability, etc. Additional non-technical criteria should also be considered: economy profile (rural, industrial, etc.), welfare, cultural background, average level of education, supporting legal frame. Therefore, more than one mix scenarios should be developed and the optimal one need to gain large acceptance (and commitment) in the community.

Scenario 1. Renewable based energy mixes implemented in buildings (Fig. 3)
Considering the technical design, functional efficiency, environmental impact and cost-affordability represent the main optimizing criteria. Basically, three scenarios could be considered in designing the energy mix, as Figs. 3, 4 and 5 show.

Renewables-based energy mixes can be cost-effective and affordable only if implemented in performant buildings. Once reaching the LEB status in a building (new or retrofitted), the design algorithm for the energy mix follows identical steps.

As previously presented [33, 34], besides the mix design for meeting the energy demand, the steps to be followed for implementing renewables in the built environment should additionally consider the passive energy gain (greenhouse effect of large glazing during cold seasons or night cooling during hot periods).

Autonomous energy houses or nZEBs are therefore developed in two steps:

1. Design the energy mix for meeting the thermal energy need (heating, cooling, domestic hot water);

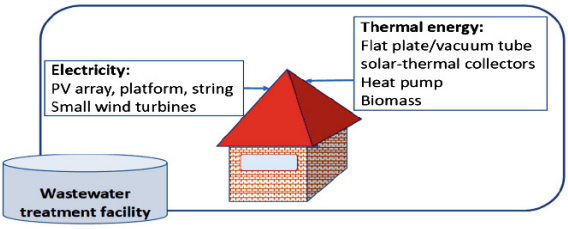

Fig. 3 Renewables-based scheme energy mixes implemented in sustainable buildings

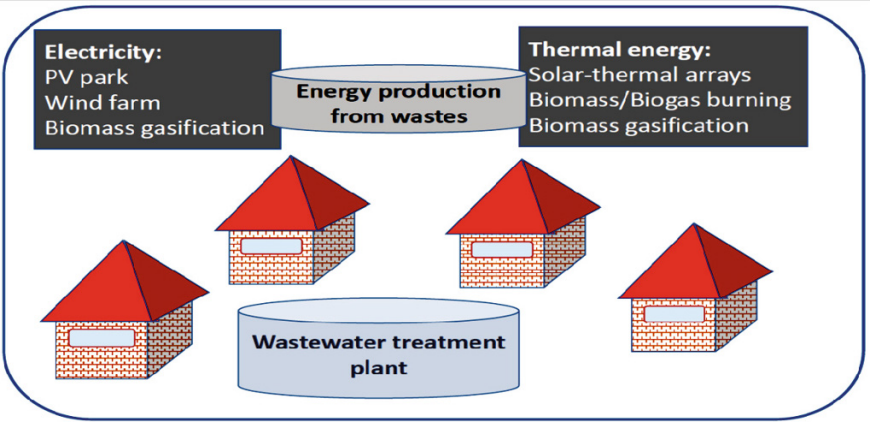

Fig. 4 Renewables-based energy mixes implemented at community level

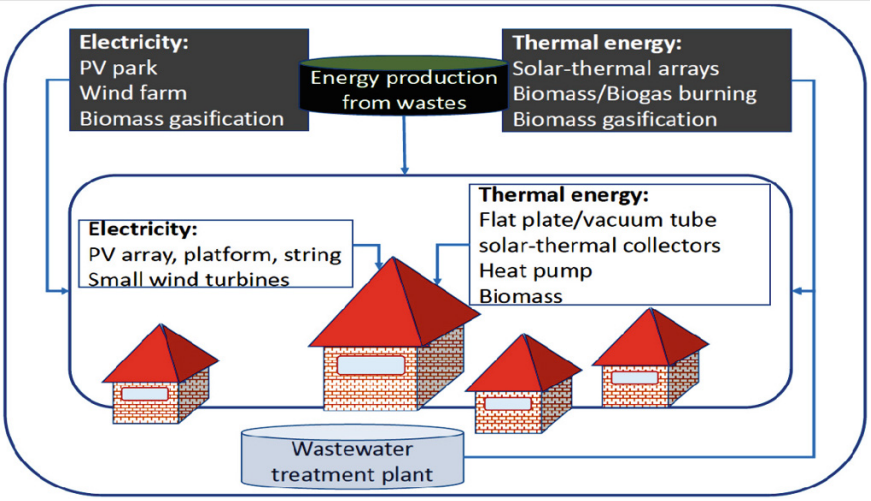

Fig. 5 Renewables-based scenario integrating building and community energy mixes

2. The mix for electricity production will be further designed, at least for powering the thermal RES (heat pumps, equipment for forced circulation in solar-thermal arrays).

Scenario 2. Renewable based energy mixes at community level (Fig. 4)
For a LEB office building implemented in a temperate climatic area in a mountain location, one feasible mix could consider a heat pump covering 70–90 % of the thermal energy need, a solar-thermal system covering the rest and an additional PV array, for covering the lighting demand and for powering the heat pump and the pumps in the solar-thermal system.

Following the SET plan guidelines, these energy mixes should mainly meet the electric energy demand. Thus the design will follow two steps, starting with:

1. The design of the renewable-based energy mix for electric energy production. The community needs should be primarily targeted. It is also recommended to consider the entire energy need (including those of the individual buildings) and the use of the community micro-grid for all powered appliances. This also has the advantage of leaving enough available surface on the building, for implementing the thermal energy sources.
2. Optionally, the design of thermal energy mixes, based on renewables should follow. If this is a viable option, the implementation site should be close to the users, for avoiding thermal losses (or increasing costs due to long, insulated pipe systems). The community thermal energy mix represents a viable option when choosing biomass from wastes for direct burning or bio-gas production. It also is recommended when various local industries are using the energy, as greenhouses, crops drying, food industries, etc.

Scenario 3. Integrated built and community sustainable energy mixes (Fig. 5)
After a preliminary design of the two types of energy mixes, one key issue is to match them. For being effective, this should be not a simple addition operation; the complementary, integrated implementation of both schemes must also target balancing the energy production with the energy needs, especially in the upper and lower production peaks.

Integrated approach of Scheme 1 and 2 allows the optimal design of the storage systems and of the back-up sources. Several examples are given bellow:

- It was outlined that solar-thermal systems are associated with the risks of overheating (during hot summer days), with negative consequences on the collectors durability and overall system's efficiency [35]. Thus a buffer storage system at community level could gather the exceeding heat agent and use it in community applications (swimming pool, local industries). Oppositely, for peak consumption, the design of the back-up source (gas, biogas, biomass) can include the thermal energy stored in the buffer (either a tank or other alternative heat storage systems, e.g. based on phase transitions);

- If power grid is available, then this should be used for delivering the excess electricity produced during summer, and for additional injection when needed (days with low renewable energy potential). In this situation, the overall energy balance (toward the grid) will give the electric energy autonomy. For stand-alone systems, the balance is usually closed by using a back-up source that can be operated "on demand", e.g. by a Diesel generator.

Thus, when integrating the building and community renewable-based scenarios, a re-optimizing step is necessary, considering:

- The renewable energies potential in the implementation locations;
- The specific thermal and electric energy demands;
- The preliminary renewable-based energy scenarios (Scheme 1 and Scheme 2);
- The common facilities that can be extended from building to community level.

Once defining these, the following will be calculated:

- The ratio of building-implemented/community implemented energy mixes;
- The type and capacity of the backup sources;
- The type and capacity of the storage systems.

5 Case Study: The R&D Institute of the Transilvania University, Romania

For a faster transition of today's communities towards sustainability, examples of good practice are needed along with optimized technical solutions, able to be easily replicated. This was the core concept in developing the R&D Institute of the Transilvania University as a sustainable community, the first one of this kind in Romania.

Several examples from Europe (Gussing, Austria; Freiburg Solar City and Kaiserslautern University, in Germany) were studied and the lessons learned allowed to develop the project *RTD Institute: High-Tech Products for Sustainable Development, PRO-DD* that was financed (2009–2013) by structural funds and by own university founds. The PRO-DD project developed the new location of the Institute and completed the infrastructure of the R&D Centers in the University, supporting research on various and complementary aspects of sustainable development. Developing the Institute as a sustainable micro-community had therefore the advantage of getting a 1:1 testing rig for the novel/innovative results, allowing their optimization and supporting the transfer/replication in sustainable communities. The R&D Institute is developed as a sustainable community on a surface of about 10 ha, and the Master Plan is presented in Fig. 6.

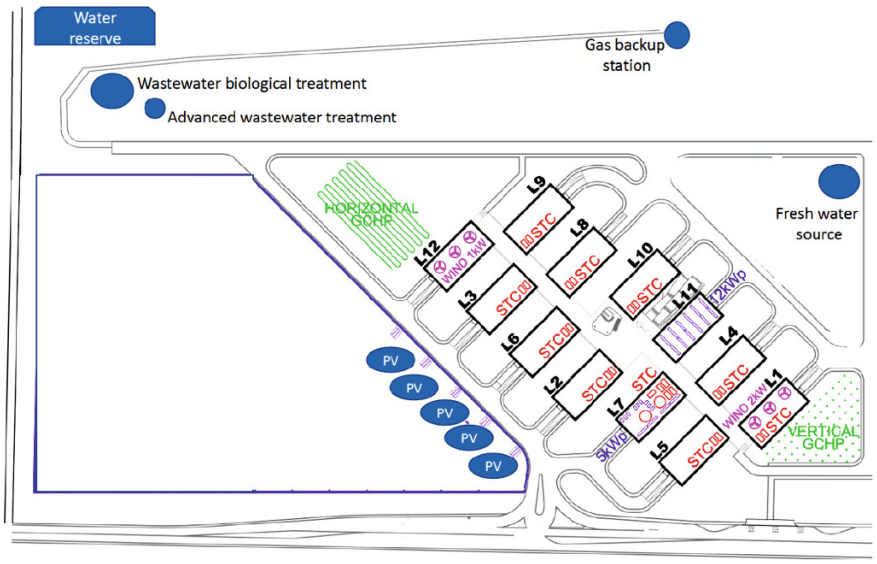

Fig. 6 Master plan of the R&D Institute and installed RES: solar-thermal collectors (STC), PV platforms and string, small wind turbines, ground coupled heat pumps (GCHP)

Step 1. Identify the energy demand in the micro-community

The steps defined for developing a sustainable community were followed in the design of the R&D Institute:

1.1. *Energy demand in the buildings*: the R&D Institute consists of 11 buildings with three stores (basement, ground floor and 1st level); an additional building inside the community is occupied by the Technology Transfer Centre (CTIB) and by the Business Incubator. All the buildings have identical structure (large open spaces, covering half of each floor, 4 rooms and 2 toilets at each level), and an overall surface of 1,350 m^2. The basement and the ground floor are hosting the research laboratories while the first floor is dedicated to the researchers' desks and offices. Light walls were used to generate spaces specific to the R&D facilities at the basement and ground floor, as Fig. 7 shows.

The Institute was developed in the outskirts of the Brasov City (45.65°N, 25.59°E, 600 m above the sea level) and was designed from the very beginning to reach the LEB status. Therefore, the buildings are interconnected with a glazed buffer space: two spines and a high atrium that also represents the main entrance.

In the design step, subject of optimization were: the ratio transparent/opaque surfaces (larger on South and lower in North); the insulation of the entire envelope (triple glazed, double Low*E* windows, insulated walls of metal/polymer/ceramic multilayers, well insulated foundation and rooftop, etc.); the thermal utilities, allowing differential flow control of the heating agent; the electrical appliances (low energy consuming lighting). A detailed description of the steps followed in the

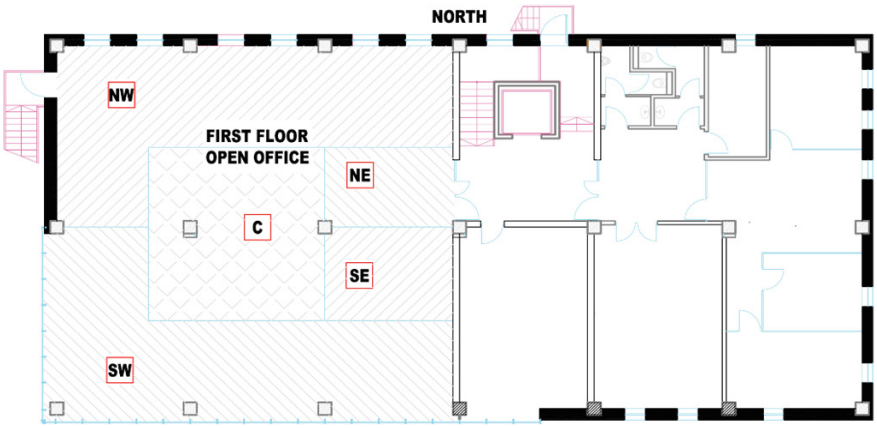

Fig. 7 Common structure of each floor, preserved at the first floor of each building

design, development and implementation of the LEB solutions was previously done [33].

The monitored data showed an average thermal energy demand of 66.69 kWh/m^2/year, consisting of: 57.8 kWh/m^2/year for heating, 5.75 kWh/m^2/year for cooling and 3.14 kWh/m^2/year for DHW. The electric energy demand for lighting and other powered appliances (except the specific laboratory equipment) is 13,224 kWh, representing 12.6 % from the total energy demand.

According to the optimal mix design, the electricity need could increase when using powered renewable energy systems (as heat pumps).

1.2. *Fresh water supply* is insured for the entire micro-community by using ground water (132 m depth), with a pump of 2.2 kW. Two reasons supported the choice of this depth: (i) the water quality (monthly monitoring showed that there is no need for treatment, the water has a mild hardness, no micro-organisms and is free of toxic or polluting compounds); (ii) the other major fresh water users in the neighborhood —several companies are also using their own freshwater sources, thus going deeper avoided the depletion of the underground water layers.

1.3. *Wastewater treatment* is done in a centralized biological treatment installation, of 6 kW. The Institute is likely to provide wastewaters that, without being in large amounts, can have a highly variable flow and difficult pollutants load. For these types of wastewaters, a separate collection system is implemented and their treatment is done using a flexible research facility: a small pilot plant operating based on advanced oxidation processes and/or adsorption. The use of these specific installations is linked to regular consumers (pumps) but also to irradiation sources (UV and VIS lamps with controlled power) with max. 1 kW power.

Step 2. Identifying the renewable energy potential in the micro-community
The solar radiation (total, direct and diffuse), temperature, humidity and the wind potential were and are monitored using a Kipp & Zonen SOLYS 2 sun tracker system and a Delta-T Automatic Weather Station. Comparative data are provided by a weather station installed in the city and by using the reference data provided by the station of the National Institute for Meteorology (for validation).

2.1 *The overall solar energy potential* is on average 1,200 kWh/m^2/year with large variations between the winter months (20–45 kWh/m^2/month in November–February) and the summer months (150–250 kWh/m^2/month in May–August).

2.2 *Wind energy*: Being surrounded by mountains, the wind potential is low on average, with wind speeds less than 2.5 m/s during more than 75 % of the year and peak values reaching 9 m/s at 15 m height.

2.3 *Micro-hydros*: There is no surface water flow in the micro-community, thus implementing micro-hydros does not represent an option.

2.4 *Geothermal energy*: As Fig. 6 shows, the location allows implementing geothermal systems of ground coupled heat pumps.

2.5 *Biomass*: The use of biomass is restricted by the need for quite large storage systems for the raw wood/pellets and for the ash. In the future, the alternative of using part of the available land for fast growing wooden biomass (energy willow) could be considered. Another alternative is the joint use of biomass for biogas production, in partnership with the neighboring Institute for Potato and Sugar Beat.

Step 3. Designing the energy mix
Based on the available renewable energies potential and on the restrictions imposed by the location and activity profile, the selection of RES to be implemented in the micro-community as energy mixes was:

- Electricity production: photovoltaic systems and small wind turbines with very low cut-in speed. As the Institute is grid-connected, the grid is use as backup and storage source.
- Thermal energy production: solar-thermal systems and ground coupled heat pumps. The backup source is natural gas.

Assessing the infield output of the RES
The research in our group focused in the past years on increasing the efficiency of renewable energy systems implemented in the built environment. By comparing the results of outdoor and indoor (standard) tests, one common conclusion could be formulated: obviously the standard indoor tests show a higher conversion efficiency (close to the nominal one) and the outdoor output was lower but the interesting aspect was that the relative efficiency loss was very different, depending on many factors. This is particularly significant for solar energy conversion systems, PVs and

solar-thermal flat plate collectors. Therefore, parallel outdoor tests are run on the roof top of the laboratory building belonging to the R&D Centre Renewable Energy Systems and Recycling (RES-REC), Fig. 8a and on a PV platform installed on the ground, Fig. 8b. This infrastructure consists of:

- L7: tracked PV modules (mono- and poly-crystalline Si, amorphous/flexible Si, CdTe, total installed power 7 kWp); trough solar-thermal collectors and tracked solar-thermal collectors; PVT (mono-crystalline Si)
- Ground PV platform: containing mono- and poly-crystalline Si, CIS, CIGS and CdTe (2kWp), the latest in Fig. 8b.

The results obtained on these testing rigs and on the additional infrastructure installed in the city (Colina Campus) outlined that the PV response is highly different in terms of efficiency loss as result of variable intensity in the direct solar radiation but especially as result of the heating under sun irradiation. The relative efficiency loss was defined as $\Delta\eta_{PV} = [(\eta_{PV}s - \eta_{ref})/\eta_{ref}] \times 100$, where η_{PV} represents the outdoor efficiency and η_{ref} is the nominal efficiency (in standard conditions) [36]. For two transient month (April and September) the peak values corresponding to $\Delta\eta_{PV}$ are presented in Table 3.

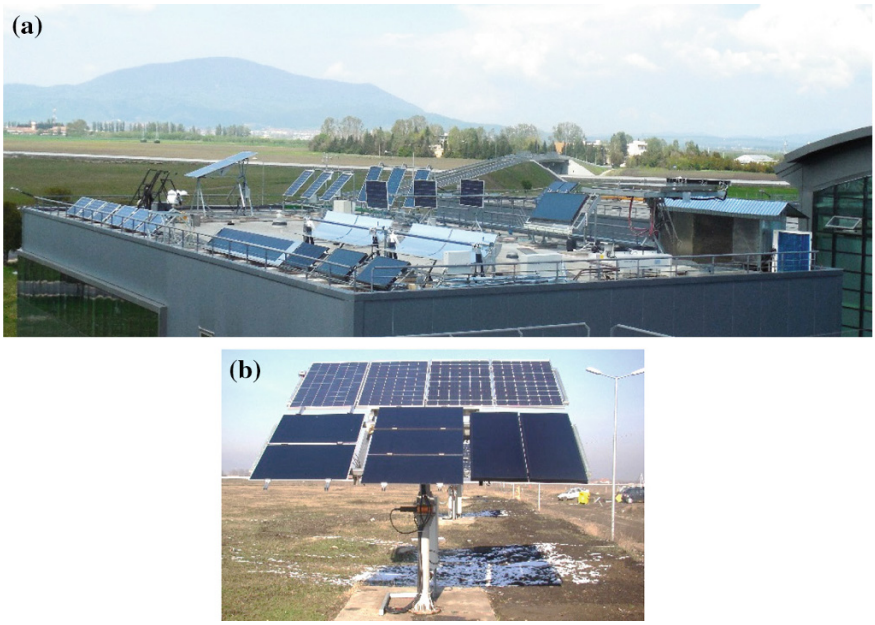

Fig. 8 Outdoor testing rigs in the RES-REC center: **a** on the roof top of the laboratory L7; **b** on the ground

Table 3 Relative efficiency loss ($\Delta\eta_{PV}$) for different fixed tilt PV modules

PV module	Si-mon (%)	Si-poly (%)	Si-amorphous (%)	CIS (%)
$\Delta\eta_{PV}$ in April	−40	−35	−60	−20
$\Delta\eta_{PV}$ in September	−70	−45	−60	−33

These type of information is important when selecting the modules for a given implementation location, with given temperature and direct solar radiation profiles. It shows that, for fixed tilt modules, one would recommend (from the four type of investigated modules) the thin film CIS PVs, as being the closest to their nominal output.

For the solar-thermal flat plate collectors the output is less differentiated among various commercial spectrally selective coatings but differences can be registered in their durability. Outdoor accelerated aging tests were developed and proved that saline aerosols may lead to degrading the absorber plate within several weeks under solar irradiation [37].

Increasing the energy output of solar energy convertors

Another feature that can have a significant and positive effect on the energy output is the implementation of tracking systems. These aim at orienting the solar energy convertor (PV or flat plate solar thermal collector), allowing optimal incidence angle of the solar beam onto the convertor's surface.

Literature mentions an increase in the energy output that can amount an average of 30 %, thus implementing tracking systems represents a viable path for community implementation of solar energy convertors. For being affordable, the tracking systems should be low cost (thus are recommended for tracking strings or platforms and not individual modules), should have a low energy consumption (experiments proved that for driving the tracking systems less than 1 % of the power produced is consumed) and should need little maintenance, thus being simple from a mechanical point of view [38].

Tracking increases the amount of the total solar radiation, including the IR part, thus is followed by a temperature increase on the module's surface. This has different consequences on the solar energy convertors:

- *PV modules* get heated and the efficiency drop could be higher for silicon-based modules. Unexpectedly, tracking did actually limit the relative efficiency loss, and had a leveling effect on the power output; similarly to the fixed tilt modules, the minimum efficiency loss was registered for CIS modules (about 10 %) [36], recommending them for implementation in tracked platforms or strings.
- *Solar-thermal flat plate collectors* will benefit by an increased amount of heat (transferred by convection to the absorber plate). On the other hand, when reaching the maximum temperature threshold, back-tracking could be used for protecting the collector again accelerated thermal aging [35].

Based on infield monitoring and optimization, the optimal types of solar energy convertors can be further selected and used in tracked assemblies. In terms of mechanisms, tracking systems can be designed considering the ability to meet the performances imposed by the tracking algorithms (the angular stroke, the pressure angles in extreme positions, etc.) and optimization can be done on single modules. For practical applications, tracking is meaningful when associated to platforms and strings, especially for PVs. A broad variety of tracking mechanisms were developed in our group targeting the increase in the green energy output on RES implemented in the built environment.

In the built environment, implementation restrictions are linked to the available mounting space (on the roof top or in close vicinity to the building). One option is represented by a tracked PV string of 12 kWp (mono- and poly-crystalline Si), installed on the 450 m^2 roof top of one laboratory building, Fig. 9. All eight strings are driven by a single tracking mechanism with N-S horizontal axis (patent application no. A/00467/2012). This solution is scalable to any flat configuration, giving full use to roof tops or terraces.

When the roof is inclined, providing limited space, one option is represented by the implementation of small platforms or strings that could bring added value as architectural objects. Several tracking solutions were developed and are investigated in terms of modules, tracking algorithms and tracking mechanisms as presented in Fig. 10.

PV modules have low weight thus small platforms and strings require light structures and low power for driving the tracking systems.

Solar-thermal collectors are heavier as such and is increased by the weight of the thermal agent. Additionally, the associated infrastructure (pipes, tubes) imposes several limitations. Still tracking could significantly increase the thermal energy output and may solve the difficult problem of overheating and stagnation. A tracked platform for two solar-thermal flat plate collectors is presented in Fig. 11 and is associated to an outdoor testing rig.

Designing the energy mix for a laboratory building

As outlined in the general methodology (Chap. 4) the thermal energy need should be covered by on-site (on-building) RES.

The domestic hot water is produced, for each laboratory building, by systems consisting of two flat plate or vacuum tube collectors. A comparative monitoring is ongoing, aiming at optimizing the tilt angle for fully covering the needs and at avoiding overheating.

A full energy mix was designed and optimized for the Laboratory building L7. The RES mix consists of a heat pump and a solar thermal array with flat plate collectors. In the design the following pre-requisites were considered:

- Covering the thermal energy demand (heating cooling and domestic hot water);
- Minimizing the electric energy needed for powering the heat pump;
- Minimizing overheating the flat plate collectors.

Fig. 9 Tracked PV string installed on the rooftop of a laboratory building. **a** General view and **b** tracking mechanism

The results show that the optimal mix consists of a heat pump (21.2 kW, COP = 4.5) covering 80 % of the energy demand while the rest (20 %) is covered by the solar-thermal system. In this configuration, the heat pump functions in direct mode for heating and in reverse mode for cooling.

The electric energy demand for lighting, office appliances and for powering the heat pump and solar-thermal system is 31,825 kWh/year and, could be covered by a mono-axial tracked PV array of 35.8 kW_p, representing on average a PV surface of about 238 m^2, thus an implementation surface of about 1,000 m^2 (much larger than the PV actual surface, for avoiding shading). This surface is not available on the building (the rooftop has 450 m^2) and does not represent a feasible alternative when replicating the energy mix towards other micro-communities.

Design the energy mix for the micro-community

The electric energy demand is designed to be covered by community RES mix, consisting of PV arrays and of small wind turbine farms.

The total electric energy demand for the 12 buildings is 381,900 kWh/year. Additionally, at the micro-community level, the following consumers were added: the wastewater treatment micro-plant, the fresh water pump, lighting the street and

Fig. 10 Tracked PV platforms for implementation close to the buildings: general view and tracking systems: **a** and **b** azimuthal biaxial tracking systems with actuators; **c** azimuthal, biaxial tracking system with universal joint; **d** monoaxial tracking system with driven elevation control, and **e** monoaxial tracking system with manual system for elevation control

Fig. 11 Tracked platform with solar—thermal flat plate collectors: **a** general view and **b** biaxial, azimuthal tracking mechanism

common areas (spines, atrium). This adds a maximum of 65,000 kWh/year and the total is thus 445,550 kWh/year.

If covering this need only by PVs, a PV surface of 1,081 m^2 would be needed (thus about 4,000 m^2). So far, the monitoring data of the small wind turbine farms (1.6 and 2 kW respectively) shows that their output could cover about 12 % of the power need.

On-going monitoring will allow to develop the accurate design for the micro-community represented by the Institute. This monitoring step is compulsory, as the electric energy need was estimated based on the nominal powers of the appliances; still a coefficient of simultaneity (less than 1) could be applied, as not all the consumers are functioning at the same time. Peak values could be thus identified and used in the accurate calculation of the energy need. It is expected a reduction thus a lowering in the RES dimensions. Afterwards, a combined solutions involving small wind farms, PVs on the buildings' roof top and a community PV park is under consideration. After at least 1 year of monitoring, the systems will be designed. Then, the integrated approach of the building and micro-community energy mixes will follow, for getting an optimized, efficient and affordable solution.

6 Conclusions

The development of sustainable communities should be step-wise done, based on optimized solutions that are using accurate input data (energy demand, renewable energy potential), evaluated based on the specific features of the community and on the on-site climatic conditions.

Renewables—based energy mixes should be preliminary designed following two schemes: (i) to be installed on the buildings and (ii) to be installed at community level. Afterwards, the two schemes need to be integrated, aiming at synergy in the detailed design of the energy mix for the community.

Pilot solutions should be developed and tested before large scale replication.

A case study, following the proposed design steps is represented by the R&D Institute of the Transilvania University of Brasov. This micro-community can reach full energy autonomy by using RES mixes based on heat pumps, solar-thermal arrays, PV tracked platforms and small wind turbine farms, for covering the energy needs for: the 12 buildings, community lighting, fresh water supply and wastewater treatment.

Acknowledgments We hereby acknowledge the structural founds project PRO-DD (POS-CCE, O.2.2.1., ID 123, SMIS 2637, No 11/2009) for providing the infrastructure used in this work and the PNII-Cooperation project EST IN URBA, contract no. 28/2012 financed by UEFISCDI which supported the latest research hereby presented.

References

1. Meadows, D., Meadows, D., Randers, J., & Behrens, W. (1972). *The Limits to Growth*. New York: Universe Books. ISBN 0-87663-165-0.
2. World Commission on Environment and Development (1987). *Our Common Future*. Oxford: Oxford University Press. p. 27. ISBN 019282080X.
3. United Nations General Assembly. (1992). The Rio declaration on environment and development. In *United Nations Conference on Environment and Development* (UNCED), Rio de Janeiro.
4. United Nations General Assembly. (1992). In *Agenda 21, United Nations Conference on Environment and Development* (UNCED), Rio de Janeiro.
5. Hosseini, H. M., & Kaneko, S. (2012). Causality between pillars of sustainable development: Global stylized facts or regional phenomena? *Ecological Indicators, 14*, 197–201.
6. Smalley, R. (2003). Top ten problems of humanity for next 50 years. Energy and NanoTechnology Conference, Rice University, May 3, 2003.
7. Yanine, F. F., & Sauma, E. E. (2013). Review of grid-tie micro-generation systems without energy storage: Towards a new approach to sustainable hybrid energy systems linked to energy efficiency. Renewable and Sustainable Energy Reviews, *26*, 60–95.
8. Mansoor, M., Mariun, N., Ismail, N., & Wahab, N. I. A. (2013). A guidance chart for most probable solution directions in sustainable energy developments. *Renewable and Sustainable Energy Reviews, 24*, 306–313.
9. Martinez-Val, J. M. (2013). Energy for sustainable development: A systematic approach for a badly defined challenge. *Energy Conversion and Management, 72*, 3–11.
10. The Directive 2010/31/EU of the European Parliament and of the Council on the energy performance of buildings. *Official Journal of the European Union*, *53* (2010).
11. US Department of Energy's Office of Energy Efficiency and Renewable Energy (2011). *Buildings Energy Data Book*. Silver Spring, MD: PE D&R International Ltd. 2012.
12. The Directive 2009/28/EC of the European Parliament, on the promotion of the use of energy from renewable sources and amending and subsequently repealing Directives 2001/77/EC and 2003/30/EC.

13. Schweizer-Ries, P. (2008). Energy sustainable communities: Environmental psychological investigations. *Energy Policy, 36*, 4126–4135.
14. Li, D. H. W., Yang, L., & Lam, J. C. (2013). Zero energy buildings and sustainable development implications—a review. *Energy, 54*, 1–10.
15. Varbanov, S. P. (2014). Energy and water interactions: Implications for industry. *Current Opinion in Chemical Engineering, 5*, 15–21.
16. Müller, M. O., Stämpfli, A., Dold, U., & Hammer, T. (2011). Energy autarky: A conceptual framework for sustainable regional development. *Energy Policy, 39*, 5800–5810.
17. Rae, C., & Bradley, F. (2012). Energy autonomy in sustainable communities—a review of key issues. *Renewable and Sustainable Energy Reviews, 16*, 6497–6506.
18. Chua, K. J., Yang, W. M., Er, S. S., & Ho, C. A. (2014). Sustainable energy systems for a remote island community. *Applied Energy, 113*, 1752–1763.
19. Giatrakos, G. P., Tsoutsos, T. D., Mouchtaropoulos, P. G., Naxakis, G. D., & Stavrakakis, G. (2009). Sustainable energy planning based on a stand-alone hybrid renewable energy/hydrogen power system: Application in Karpathos island, Greece. *Renewable Energy, 34*, 2562–2570.
20. Lenzen, M. (2008). Sustainable island businesses: A case study of Norfolk Island. *Journal of Cleaner Production, 16*, 2018–2035.
21. Doukas, H., Papadopoulou, A., Savvakis, N., Tsoutsos, T., & Psarras, J. (2012). Assessing energy sustainability of rural communities using Principal Component Analysis. *Renewable and Sustainable Energy Reviews, 16*, 1949–1957.
22. Moreno, P. S., Fidélis, T., & Ramos, T. B. (2014). Measuring and comparing local sustainable development through common indicators: Constraints and achievements in practice. *Cities, 39*, 1–9.
23. Doukas, H., Papadopoulou, A., Savvakis, N., Tsoutsos, T., & Psarras, J. (2012). Assessing energy sustainability of rural communities using Principal Component Analysis. *Renewable and Sustainable Energy Reviews, 16*, 1949–1957.
24. Ghaffarian Hoseini, A. H., Dahlan, N. D., Berardi, U., Ghaffarian Hoseini, A., Makaremi, N., & Ghaffarian Hoseini, M. (2013). Sustainable energy performances of green buildings: A review of current theories, implementations and challenges. *Renewable and Sustainable Energy Reviews, 25*, 1–17.
25. Zyadin, A., Halder, P., Kähkönen, T., & Puhakka, A. (2014). Challenges to renewable energy: A bulletin of perceptions from international academic arena. *Renewable Energy, 69*, 82–88.
26. Green, M. (2006). Energy, entropy and efficiency. In T. Kamiya, B. Monemar, & H. Venghaus (Eds.), *Third Generation Photovoltaics* (p. 21). Berlin, Heidelberg: Springer.
27. Dzidic, P., & Green, M. (2012). Outdoing the Joneses: Understanding community acceptance of an alternative water supply scheme and sustainable urban design. *Landscape and Urban Planning, 105*, 266–273.
28. Engin, G. O., & Demir, I. (2006). Cost analysis of alternative methods for wastewater handling in small communities. *Journal of Environmental Management, 79*, 357–363.
29. Balduzzi, F., Bianchini, A., & Ferrari, L. (2012). Microeolic turbines in the built environment: Influence of the installation site on the potential energy yield. *Renewable Energy, 45*, 163–174.
30. Rahman, M. M., Mostafiz, S. B., Paatero, J. V., & Lahdelma, R. (2014). Extension of energy crops on surplus agricultural lands: A potentially viable option in developing countries while fossil fuel reserves are diminishing. *Renewable and Sustainable Energy Reviews, 29*, 108–119.
31. Adelaja, S., Shaw, J., Beyea, W., & McKeown, J. D. C. (2010). Renewable energy potential on brownfield sites: A case study of Michigan. *Energy Policy, 38*, 7021–7030.
32. Communication from the Commission to the Council, the European Parliament, the European Economic and Social Committee and the Committee of the Regions. A European strategic energy technology plan (SET Plan)—Towards a low carbon future, [COM(2007) 723 final]. http://europa.eu/legislation_summaries/energy/european_energy_policy/l27079 _en.htm.

33. Moldovan, M. D., Visa, I., Neagoe, M., & Burduhos, B. G. (2014). Solar heating and cooling energy mixes to transform low energy buildings in nearly zero energy buildings. *Energy Procedia, 48*, 924–937.
34. Visa, I., Moldovan, M. D., Comsit, M., & Duta, A. (2014). Improving the renewable energy mix in a building toward the nearly zero energy status. *Energy and Buildings, 68*, 72–78.
35. Neagoe, M., Visa, I., Burduhos, B. G., & Moldovan, M. D. (2014). Thermal load based adaptive tracking for flat plate solar collectors. *Energy Procedia, 48*, 1401–1411.
36. Visa, I., Comsit, M., Moldovan, M. D., & Duta A. (2014). Outdoor simultaneous testing of four types of PV tracked modules. *Journal of Renewable and Sustainable Energy*, *6*, 033142.
37. Ciobanu, D., Visa, I., & Duta, A. (2014). Solar thermal collectors outdoor testing in saline environment. *Energy Procedia, 48*, 707–714.
38. Burduhos, B.G., Visa, I., Neagoe, M., & Badea, M. (2014). Modeling and optimization of the global solar irradiance collecting efficiency. *International Journal of Green Energy* (accepted for publication).

Use of Thermo-Vision for Early Detection of Heat Losses, Inside and Outside Buildings with Mixed Heating

Mihaela Baritz, Diana Cotoros and Daniela Barbu

Abstract Buildings of private residences with one or two levels are very different from one area to another, on the entire surface of our country, regarding architecture, chromatic or construction materials. Instead, the insulation manners and accomplishing the inside thermal comfort are generally applicable requirements regardless of the construction complexity, of the used materials or geographic area. Thus, we find that there are however essential differences determined by the energy sources, their recovery capacity and offered volume. In this paper, two cases of private residences are presented and analyzed from thermal point of view, with about the same habitable surface but different from the room distribution point of view, located in different geographic areas (lowlands, highlands) and use mixed energy sources (methane gas + wooden material, respectively methane gas + electricity). In the second part of the paper the analysis by thermo-vision of the performances of the heating equipment existing in the two residences are presented as well as the thermal comfort degree versus the shape, size and structure of the thermal insulation system. In the final part of the paper we presented the results and conclusions of these thermo-graphic analyses on walls insulation, windows/doors insulations, foundations and roofs.

Keywords Thermo-vision · Heat loss · Insulation

1 Introduction

At this moment, the energy which is essential in developing all activities, either inside or outside the buildings is assured mostly by using some fossil fuels but also renewable sources. Energy sustainability is determined by the manner we are able to use renewable energy which is the most efficient and less aggressive to the

M. Baritz (✉) · D. Cotoros · D. Barbu
Product Design, Mechatronics and Environment Department, University Transilvania Brasov, Brasov, Romania
e-mail: mbaritz@unitbv.ro

I. Visa (ed.), *Sustainable Energy in the Built Environment - Steps Towards nZEB*, Springer Proceedings in Energy, DOI 10.1007/978-3-319-09707-7_2

environment. The benefits of sustainable energy from the point of view of the use inside buildings are highlighted by reducing costs of the heating and electricity invoices, by increasing comfort and maybe not last in a significant contribution to avoiding climate changes [1].

Generally a residential building is defined as a complex system and the factors affecting the energetic performances are the following: structural loads, external temperature, solar exposure, precipitations/wind (in quantity and content). From these points of view, any limitation or extreme values of these factors may affect the building performances and quality. An example in this respect is given by the building insulation which may change the level of energy consumption required for internal heating in relation to assuring a comfortable level of humidity and air circulation. The building insulation is essential and efficient for any residential building both newly built and from the category of renovated/rehabilitated buildings. Thus, the insulation process involves the development of insulation at walls level, roof/attic, foundation, floor, doors and windows. In correlation with these general requirements and in order to assure protection to the external elements aggression, the insulations should allow the access of natural light, to allow the entrance and exit of the building occupants, to separate the internal environment from the outside environment conditions and also to assure the air, heat and humidity management, between inside and outside. The external and internal walls insulation was manufactured during time from different materials, with technologies correlated to the used materials and considering the basic material (stone, brick, wood, concrete etc.) of the walls. In this respect we find presently a fast evolution in the use of light, synthetic materials, with low costs but high efficiency in that what means a growth of the buildings thermal comfort. From the analysis of requirements regarding the constructive elements of a building, we place on the first position the requirements imposed on the external walls, requirements that should be met already during the design phase. These requirements such as: control of rain penetration, control of natural light access, resistance structure and load on each direction, fire protection, control of noise and vibrations, control of heat losses, control of water vapours diffusion, and control of air circulation are responsible of obtaining thermal performances of the walls system [2]. This is why the optimal thermal performance must be obtained on the entire surface of the wall, as a follow it does not matter how much insulation is applied but how it is applied on the surface. The results of the insulations effect on the walls can be quantified by increasing the inhabitable comfort, increase of building durability, increase of real estate and aesthetic value and of course significant reduction of energy costs. The other areas (foundation, roof, floor and attics) from a residential building, requiring insulation represent a set of structures which complete and in their turn influence the level of thermal comfort, respectively by lowering the energy costs. Another important aspect that should be analyzed in case of establishing the comfort level is represented by the influence exerted by the doors-windows-skylights assembly on the internal environment parameters, supplemented by the aesthetic, photometric and safety parameters. The shape, size and disposition of windows and access doors presents a high importance from the point of view of air circulation but also of the

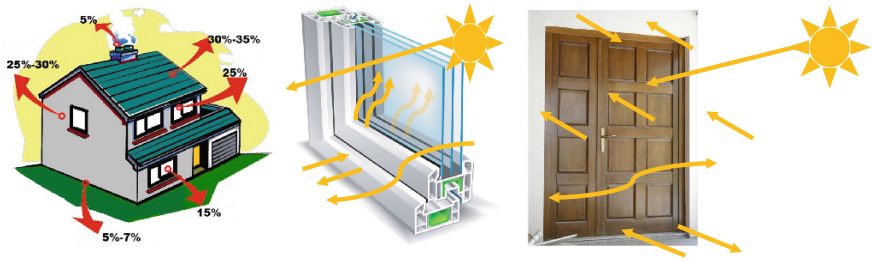

Fig. 1 Heat losses estimation in house, air circulation around a window and an external door [3]

process of reducing air infiltrations because these phenomena are responsible of approx. 25 % of the energy losses recorded at a building level (Fig. 1).

On the other hand the ventilation and air cooling systems inside the residence represent another analysis structure when we look for an optimized thermal comfort. Ventilation system should provide a balance between temperature, noise, odour removal and material particles in suspension removal in order to obtain a high quality of the air. Energy sources and drinkable water supplying a residence represent an important module in designing and constructing a building because according to its size, design, geographic and administrative location, specific combinations meant to optimize consumption can be accomplished. The selected fuels as well as the equipment required for water heating and transportation depend mostly on the local sources and respectively on the level of technologies implemented in the residence construction. As a follow, in order to establish the performances of living in a residential building we need to analyze all these aspects, correlated to the aesthetic, administrative or social-economic ones [4].

2 Problem Formulation

A complex process of heat transfer involves concurrently proceeding processes of conduction, convection, and thermal radiation. In practical applications heat is usually transferred from one fluid to another through a partition or separating wall. Three stages can be distinguished here, during which heat is transferred: from a fluid with a higher temperature t_{f1} to a separating wall which is at a lower temperature t_{p1}, by thermal radiation and/or **convection**; in the wall, by **conduction** at a temperature difference ($t_{p1} - t_{p2}$); from the surface with the temperature t_{p2} to a fluid with a lower temperature t_{f2}, by thermal radiation and/or **convection.**

In the present situation we are not dealing with a homogeneous wall, as insulation means in fact a multilayer composite wall that requires a different approach [5].

The heat transfer equation for the composite wall becomes:

$$\dot{Q} = k_{pn} \cdot \left(t_{f1} - t_{f2}\right) \cdot A \tag{1}$$

where

$$k_{pn} = \frac{1}{\frac{1}{\alpha_{f1}} + \sum_i \frac{\delta_i}{\lambda_i} + \frac{1}{\alpha_{f2}}} \tag{2}$$

is the global heat transfer coefficient, including α_{f1}, α_{f2}—local heat transfer coefficients, δ_i—thickness of layer "i", λ_i—thermal conductivity of layer "i".

In driving the heat transfer equation we used the concept of thermal resistance, as the reciprocal of thermal conductivity.

$$R_{cond} = \frac{\delta}{\lambda} \tag{3}$$

This allows us to sum up the individual thermal resistances in the direction of flow and the quantity of heat per unit time through unit of isothermal area will be:

$$\frac{t_1 - t'}{\frac{\delta_1}{\lambda_1}} = \frac{t' - t''}{\frac{\delta_2}{\lambda_2}} = \frac{t'' - t_2}{\frac{\delta_3}{\lambda_3}} = \frac{t_1 - t_2}{\frac{\delta_1}{\lambda_1} + \frac{\delta_2}{\lambda_2} + \frac{\delta_3}{\lambda_3}} = q \tag{4}$$

In order to highlight the heat losses in residential buildings, we developed within this research a recording system for the thermal behaviour of the building structures (walls, doors, windows) by thermo-vision procedure.

Two residential buildings were selected, one in Brasov area and the other in Bucharest, for which the external insulation was build in the same conditions on the fundamental brick structure.

The recorded data by capturing thermo-graphic images of different areas (walls, windows, doors) from the finalized insulated construction were analyzed at two different moments (November and April) in order to emphasize the process of exterior/interior heat transfer (average ratio between the sunny days in the two selected months is 1/3). Still, geographic orientation is different for the two residences, house H1 (Brasov) being oriented with an access way towards S–E/N–W while the house H2 (Bucharest) has the main access way towards E/W (Fig. 2).

The two private residences have about the same inhabitable surface (H1 = 106 m^2 and H2 = 120 m^2) but different located (house in Brasov just ground floor, while the one in Bucharest has two floors) and are made of the same basic material-brick and were insulated with the same type of material (thickness 12 cm), according to the same technology.

Fig. 2 The two residential buildings H1 (Brasov) (*left*) and H2 (Bucharest) (*right*) [6]

3 Results and Discussions

In order to observe the influence of insulation upon the quantity of heat transferred through buildings walls, we used a non-contact modern method based on the use of a thermo-vision camera from FLIR systems with dedicated software.

The images were captured from the outside and also from the inside of the building (mirror-like). Of course the phenomenon of heat transfer goes from inside towards outside in November and becomes reversed in April. By help of FLIR software we were able to extract from the captured images the entire set of temperature values, for each 1 cm^2 and select a certain surface for study. In the following images (Figs. 3 and 4) we present some of the captures for different situations from houses H1 and H2.

Starting from the thermo-graphic images we were able to sequentially analyze some construction areas and make evaluations of the temperature variation on one direction or another (e.g. in Fig. 5 the wall area exposed to the West and the direct access door exposed to the East). Thermo-graphic analysis highlights the balance between the external and internal temperatures allowing the determination of heat losses.

These values, determined according the theory are for H1 during November of 34.4 W/m^2 and respectively 21.3 W/m^2 for April, while for H2 the values for November are 23.5 W/m^2 and respectively for April 14.6 W/m^2. Also

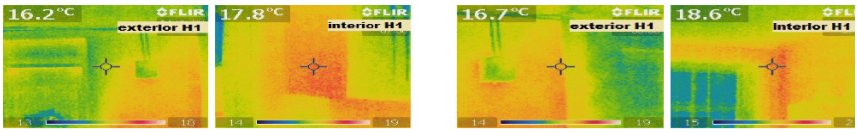

Fig. 3 Analysis of temperature, at wall level in building H1, in November (*left*), April (*right*) [6]

Fig. 4 Analysis of temperature, at wall level in building H2, in November (*left*), April (*right*) [6]

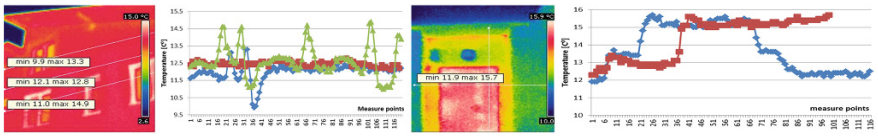

Fig. 5 Analysis of temperature exterior areas, walls/windows (*left*), entrance door (*right*) in H2

Fig. 6 Checking the routes of heating equipment in the ceiling and floor for building H2 [6]

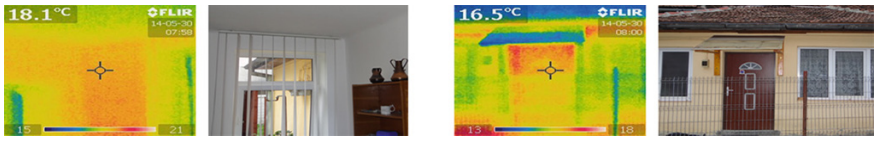

Fig. 7 Checking the joints insulation at walls/roof and entrance door at H1 [6]

thermographic images were able to highlight the transport routes of heating agent from the house heating equipment's in order to analyze the losses or heat dissipation in the floor, walls or ceiling (egg. Fig. 6 building H2 central heating using methane gas with floor routes and Fig. 7 building H1, insulation joints). Based on the above can be done a number of specific determinations which can highlight the insulation behavior, structure and mode of heating system or high heat loss areas.

Interior heating circuit analysis revealed the temperature gradient in the floor and ceiling, from H2 (Fig. 6) and heat loss through the window and door, from H1 (Fig. 7). It can therefore be concluded that although both buildings have achieved the same insulation losses are higher in H1 versus H2 due to the structure on one level, due to its heating (gas stove H1 and H2 gas central soaking) and not least the compass orientation and climatic conditions in the areas in which they are.

4 Conclusions

From the analysis of thermo-graphic images and the determination of heat loss values were found following issues: using the simple methodology of a thermo-vision camera associated with the dedicated software allows the determination of heat flow through various types of walls or around openings (doors, windows). This determination will not only pinpoint the problem areas but also provide the optimal

possibilities concerning the insulation (thickness, type of material, number of layers etc.) in a very accurate way. Finally we may be able to indicate the best material to use, also considering the price-quality ratio and the optimal thickness.

References

1. Sustainable Energy Ireland—the National Development Plan (2000–2006). www.sei.ie
2. da Cunha, I. (2009). *Energy efficient housing. Reference Guide*. Ontario: CEATI International.
3. Magyar, Z. (2011). *Applicability of the thermal manikin for thermal comfort investigations*. PhD thesis, Szent István University, Gödöllő, Hungary.
4. Petrasincu, N., & Fara, L. (2006). Bioclimatic elements for traditional romanian houses. In *Conference PLEA2006, Geneva, Switzerland*. September, 6–8, 2006.
5. Cotoros, D., et al. (2011) Correlative analysis of energy efficiency in urban buildings (pp. 111–114). In *Proceeding of the 2nd International conference USCUDAR*, Praga.
6. Personal archive of photographs.

Criteria Analysis for Optimal Choice of Efficient Energy Use in Residential Buildings

Mihaela Baritz, Diana Cotoros and Daniela Barbu

Abstract Around 11 % of the total energy consumption in the world goes to the residential and commercial sector, most of it being covered by petroleum, gas and coal. Not only they are not sustainable energy sources, but they also enhance the carbon footprint and increase the damage upon climate changes and environmental pollution. Financial burden and poor insulation issues are also to be considered especially at individual level. The present paper proposes some statistical processing of various data obtained in previous researches that will allow an educated choice of methods designed to increase the efficient use of energy in residential buildings, as people and also local authorities are reluctant of using expensive and revolutionary methods without a thorough documentation. The performed study will be based upon multi-criteria analysis and analysis of variance with several factors. The tools come from Excel data analysis, taking into consideration all factors and data that might influence an individual strategy of saving energy and money at the same time.

Keywords Energy efficiency · Multi-criteria analysis · Insulation

1 Introduction

One of the main objectives of the national and world energy policies is represented by the gradual diminishing of the fossil fuel consumption. This is why, using renewable energy sources for residences heating can be the first step in the context of sustainable development, increasing safety of energy sources, actions for protecting and preserving the environment and respectively in an efficient development at commercial level of viable energy producing technologies [1].

M. Baritz (✉) · D. Cotoros · D. Barbu
Product Design, Mechatronics and Environment Department, University Transilvania Brasov, Brasov, Romania
e-mail: mbaritz@unitbv.ro

I. Visa (ed.), *Sustainable Energy in the Built Environment - Steps Towards nZEB*, Springer Proceedings in Energy, DOI 10.1007/978-3-319-09707-7_3

The use at large scale of energy sources provided by fossil fuels leads unfortunately to an average growth of CO_2 emissions up to 2 % yearly. Thus, it is estimated that following the massive growth of CO_2 emissions, at the end of the century the greenhouse emissions should be reduced 10 times, providing the fact that the population will reach around 10 billion people and carbon emissions to 0.3 tons C/person [2].

Therefore it is imperative that sustainable development and a profound evolution of lifestyle, accompanied by the evolution of techniques and technologies, should accelerate the development rate of the new clean technologies and of those providing low energy consumption. Thus, nowadays we still use fossil fuels for heating in private buildings or assemblies of residential buildings but there are many attempts of diversifying the energy sources by combining classic sources with renewable ones [3].

An extremely important issue in analyzing the residential heating sources is represented by the correlation between the temperature of the thermal agent and the climate factors.

In the functioning of such system, the correlation mechanism is based upon the buildings heating process (walls, roof, foundation) and criteria analysis highlights the quality-quantity adjustment of the primary thermal agent related to the external temperature, as well as accomplishing interior comfort conditions by a rational selection of the insulation material and thickness [4].

2 Problem Formulation

Multi-criteria analysis can be successfully used in various situations in order to perform rankings or to evaluate several options in order to highlight the optimal one according to some proposed criteria. The benefit of this analysis is the fact that its results offer us an objective choice in a very high proportion, providing a scientific basis for our decisions.

Our goal is to identify the best choice of heating for residential buildings from the point of view of its efficiency. We are going to compare the most used types of heating provided in our country such as: methane gas heating (G), electric based heating (radiant panels) (E), solar power based heating (S), combined heating (solar + methane gas) (SG) [5, 6].

The most important part of the analysis is the criteria selection, as this is the condition in obtaining objective and solid results. According to the studies performed at global level, we decided to select the following criteria: type of fuel used for heating (FT); type of insulation (materials) (IM); insulation thickness (IT); costs (CO); geographic area (GA); type of residence (RT); inhabitants' opinion (IO). We establish the weight of each criterion by awarding a value chosen from 3 possible values: 0; 0.5; 1, in comparing each criterion with the other one. Table 1 allows us to determine the weight of each criterion (γ_i) based upon FRISCO formula:

$$\gamma_i = \frac{p + \Delta p + m + 0.5}{-\Delta p' + \frac{N_{crt}}{2}} \quad (1)$$

where

p—sum of the points obtained by the considered element;
Δp—difference between the score obtained by the considered element and the last level element;
m—number of surpassed criteria;
N_{crt}—number of considered criteria;
Δp′—difference between the score of the considered element and the first level element (negative value).

3 Results and Discussions

For each heating option we considered that a certain grade will be given according to each criterion, as shown in Table 1 and consequently the grade is multiplied to the weight determined for the studied criterion, finally obtaining the score for each type of heating, helping us to make the optimal choice (Table 2) (Fig. 1).

By analyzing the results we find that for the time being and existing records, the combined type of heating, using both solar energy and methane gas is the optimal choice for residential buildings heating. There is though a very small difference between this and solar power heating, proving the fact that the future tendencies are towards sustainable and renewable sources of energy.

The linear correlation coefficient "**r**" is showing us the strength of the linear correlation between two variables. In order to find out if there is any correlation between the heat flow through the walls of the residence and other factors such as the thickness of the insulation or the values of the external temperatures we use the Data Analysis tool in Excel. The results are presented in the Table 3 (Figs. 2 and 3).

The linear correlation coefficient proves to be close enough to (−1) when we analyze the correlation between the heat flow and the external temperatures (−0.77),

Table 1 Criteria analysis

	FT	IM	IT	CO	GA	RT	IO	Score	Level	Weight
FT	0.5	1	1	1	1	1	1	6.5	1	5.428
IM	0	0.5	1	0	1	1	1	4.5	3	2.363
IT	0	0	0.5	0	0	0	0	0.5	7	0.105
CO	0	1	1	0.5	1	1	1	5.5	2	3.555
GA	0	0	1	0	0.5	1	0	2.5	5	0.933
RT	0	0	1	0	0	0.5	0	1.5	6	0.470
IO	0	0	1	0	1	1	0.5	3.5	4	1.538

Type of fuel used for heating (FT); type of insulation (materials) (IM); insulation thickness (IT); costs (CO); geographic area (GA); type of residence (RT); inhabitants' opinion (IO)

Table 2 Optimal choice of heating systems

	G		E		S		SG	
Criterion	Ni	Niγi	Ni	Niγi	Ni	Niγi	Ni	Niγi
FT	7	38.00	8	43.43	10	54.29	9	48.86
IM	6	14.18	6	14.18	7	16.55	7	16.55
IT	5	0.53	5	0.53	8	0.84	8	0.84
CO	4	14.22	3	10.67	7	24.89	8	28.44
GA	5	4.67	7	6.53	9	8.40	8	7.47
RT	5	2.35	4	1.88	6	2.82	6	2.82
IO	8	12.31	7	10.77	5	7.69	8	12.31
Final scores		**86.26**		**87.99**		**115.48**		**117.29**
Ranking	**4**		**3**		**2**		**1**	

Type of fuel used for heating (FT); type of insulation (materials) (IM); insulation thickness (IT); costs (CO); geographic area (GA); type of residence (RT); inhabitants' opinion (IO)

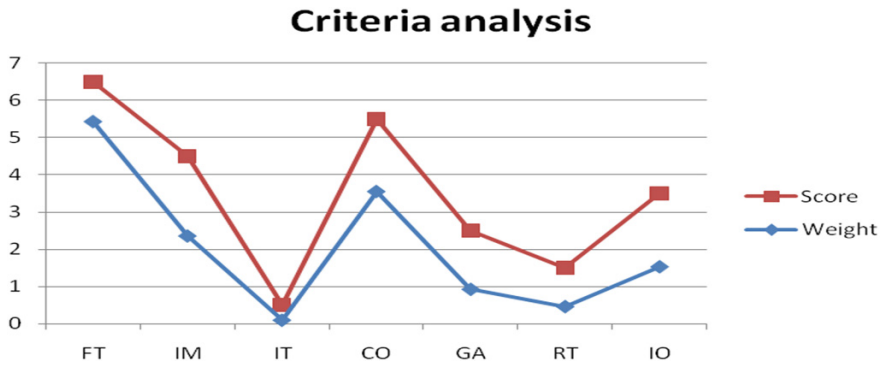

Fig. 1 Criteria analysis for heating systems

Table 3 Data Analysis

	Heat flow	Thickness	Ext. temp
Heat flow	1		
Thickness	−0.59049	1	
Ext. temp	−0.77037	0.014226	1

while the correlation is obviously weaker when concerning the variation of heat flow with the insulation thickness (−0.59). There is obviously no correlation between the external temperatures and the insulation thickness as expected (0.01). As the correlation is given by negative values it means that there is a negative strong correlation between the heat flow and the external temperature [7].

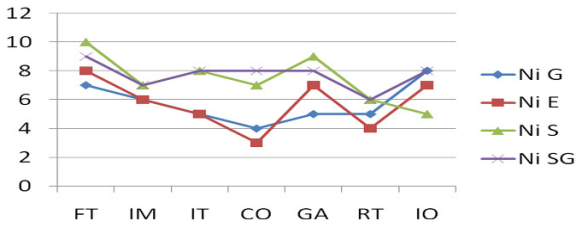

Fig. 2 Optimal choice of heating systems

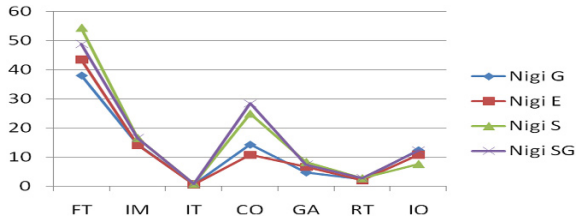

Fig. 3 Variation of criteria values according to the heating type

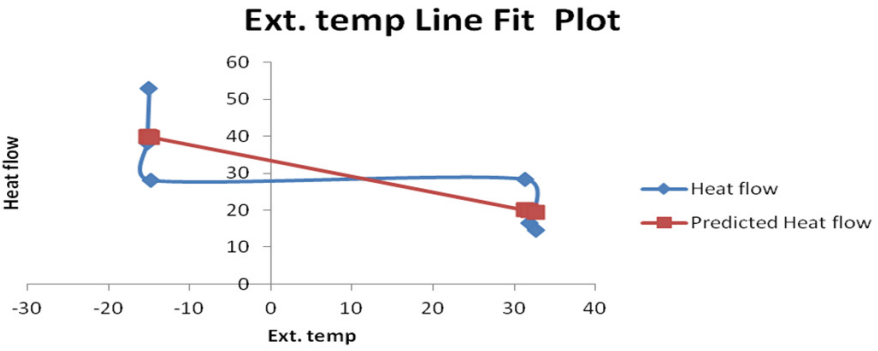

Fig. 4 Prediction of the heat flow values for different external temperatures

Regression is used to predict the value of certain variables which are correlated. If we consider the stronger correlation between the external temperatures for example and the heat flow we are able to predict the values of the heat flow according to the diagram below (Fig. 4).

The predicted heat flow is decreasing with the growth of external temperatures because obviously the heat losses are diminishing, but the methodology can be applied also to other measurable parameters that may influence the heating efficiency in residential buildings.

Thus, according to the factors considered to be a priority, we are able to perform analysis and predictions in order to create the scientific grounds of selecting the best heating type for an individual assembly of residential or even industrial buildings.

4 Conclusions

The activities of energy conservation, including the optimal use of primary and secondary energy resources, represent the most urgent and efficient objectives for the development of a healthy social and economical life. These activities require correct and reliable information upon the energy losses of different structures. Based upon these information's, specialists are able to perform energy balances or analyzes with scientific support. This way, according to the new regulations, the studied buildings may obtain an energy certificate stating the insulation efficiency [8].

The method based upon thermo-graphics offers reliable information related to the temperature distribution, both outside and inside the building walls, highlights the problem areas, processes the results, avoiding complicated calculus and errors.

By providing the exact positions of the problem areas, contractors will know exactly where to apply the insulation materials. By applying the correct insulation materials, the thermal resistance increases according to the insulation thickness and physical properties, leading to a decrease of the heat transfer coefficient and thus of the heat losses.

Therefore, validation requires a complex decision evaluation of the chosen solution behavior throughout the lifetime of the system using the appropriate criteria cost-global methodology to assess the relation heating system—thermal insulation.

Also the method can be used to compare several buildings that where renovated and insulated with different types of materials in order to identify the optimal choice of material, also considering the best quality-cost ratio. In the same context we can analyze the effects of climate change on buildings respectively on the state of environmental comfort in buildings [9, 10].

References

1. da Cunha, I. (2009). *Energy efficient housing, Reference Guide*. Ontario: CEATI International.
2. http://www.worldbank.org/. Accessed March 2013.
3. Roger, C., & Petch, J. (1999). *Uncertainty and Risk Analysis*. London: Business Dynamics, Pricewaterhouse.
4. http://www.r-project.org/doc/bib/R-books.html. Accessed February 2013.
5. Cotoros, D., Bacanu, G., Baritz, M. (2011) Advanced Methodology of Heat Losses Assessment in Buildings. *International Journal of Arts and Sciences*, *4*(19). ISSN 1944-6934.
6. Cotoros, D., Băcanu, G., Baritz, M. (2011). Correlative Analysis of Energy Efficiency in Urban Buildings. In *Proceeding of the 2nd International conference on Urban Sustainability, Cultural Sustainability, Green Development, Green Structures and Clean Cars (USCUDAR'11), Praga*.

7. Băcanu, Gh., Cotoros, D., Dumitrescu, L., Baritz, M., & Ulea, M. (2009). An energy policy for Europe. In *Proceedings of Workshop on Effect of Energy Use on Environment and Ecosystems, Brasov*.
8. Bacanu, Gh. (2008). Thermal rehabilitation of multi-flats buildings. In *Proceedings of the 1st WSEAS International Conference on Urban Rehabilitation and Sustainability* (*URES'08*), *Bucharest, Romania*.
9. Summary Report—Energy Efficiency in Buildings. Available at http://www.wbcsd.org/web/eeb
10. Păun, V. (2011). *Analiza comportamentului termo-hidraulic variabil al sistemelor centralizate de alimentare cu căldură*. PhD thesis.

Architecturally Integrated Multifunctional Solar-Thermal Façades

Mihai Comsit, Ion Visa, Macedon Dumitru Moldovan and Luminita Isac

Abstract This paper discusses relevant issue related to the architectural integration of active solar technologies (e.g. solar collectors) in the facades. In respect with the criteria which defines an optimal integration of solar technologies at the buildings level, the paper proposes a multifunctional solar facade concept that has the flexibility to be implemented in very different situations that can be met within the built environment. The results embed concepts of interest for architects, engineers and designers working on the implementation and integration of solar energy conversion systems in the built environment, towards sustainable communities.

Keywords Solar-thermal façades · Solar-thermal collector shape · Solar-thermal collector colour · Solar-thermal arrays

1 Introduction

A broad variety of solar technologies are still struggling to play the key role they deserve in the fossil fuel based energy reduction. One option recently more and more outlined is represented by the renewables' integration in the built environment, particularly of the solar energy conversion systems. Even though competitive technologies and innovative cost effective solutions raised on the market, this is not sufficient for increasing the spread of built integrated systems worldwide [1]. The most cited references in literature and the most recent developments are showing that multifunctionality is required for the building integrated solar facades, focusing on shape and aesthetics, on energy conversion efficiency and operation, correlated with multiple functionality as shadowing and insulation [2], and on modularity in obtaining innovative configurations; one emergent trend is related to the

M. Comsit (✉) · I. Visa · M.D. Moldovan · L. Isac
R&D Center of Renewable Energy Systems and Recycling, Transilvania University of Brasov, Eroilor 29, 500036 Brasov, Romania
e-mail: comsit@unitbv.ro

I. Visa (ed.), *Sustainable Energy in the Built Environment - Steps Towards nZEB*, Springer Proceedings in Energy, DOI 10.1007/978-3-319-09707-7_4

possibility/feasibility of sun tracking or reversed tracking (to avoid overheating or efficiency losses) [3, 4].

Both photovoltaics and solar-thermal flat plate collectors started to adapt to the aesthetics criteria required to increase the acceptance of solar building facades by developing coloured surfaces (reported at laboratory/pilot scale), but the flat rectangular traditional geometry of the solar energy convertors has to be carefully treated when it comes to the development of more appealing solar energy conversion systems [5]. This is particularly important, because the chromatic aspects are of average interest in terms of architectural quality as, the solar energy convertors are still considered as a technical component of the system [6–8]. Thus shape and colour could increase the acceptance of the solar facades.

The combined approach of novel shapes and novel colours is—to the best of our knowledge, not reported for flat plate solar-thermal collectors. Therefore, this paper fills the gap and describes the work developed for formulating a novel concept legotype that integrates new shapes and various colors of flat plate solar thermal collectors, aiming at increasing the social/architectural acceptance of renewables in the built environment towards Nearly Zero Energy Buildings. Further on, the energy efficiency can be controlled, by limited tracking; various tilt/tracking angles could be used for inverse tracking (decreasing the amount of solar radiation on the solar thermal flat plate collectors, thus avoiding overheating) [3]. The study is developed and the results are under implementation on an existing infrastructure that allows comparative monitoring and testing of the novel collectors and of the commercial ones.

2 Problem Formulation

As solar energy is available in its active or passive forms, the problem of integration is expected to provide a response to the energy needs of the building, in terms of thermal energy for domestic hot water (DHW) space heating and/or cooling, [9] and electric energy for lighting and powering the common appliances (Fig. 1).

Considering the architectural integration as a “form follows function” matter, the problem of solar technologies integration into the buildings it’s not to be approached only as a shape (aesthetic) issue but should simultaneously fulfil the functional demand. The building integration of current solar energy conversion systems is generally characterised by a low level of architectural quality. In the built environment, the photovoltaic technology usually has the advantage of the grid as a transport and “storage” system. This brings an added freedom related to mounting the conversion system at given distance from the consumer’s place. The concept developed for the next decade actually states that PV technologies should be concentrated in large facilities, in the outskirts of the communities or on degraded grounds. This is not possible/recommendable for solar-thermal systems, due to significant losses that may occur when the convertor is mounted far from the boiler/user [10]. Thus, large spread of solar-thermal collectors requires specific and novel

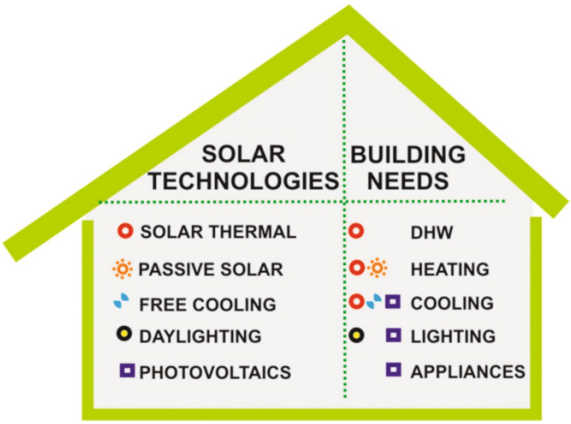

Fig. 1 Different energy needs covered by solar technologies

solutions for installing solar flat plate collectors on/near the building, for providing thermal energy, mainly for DHW and heating [11, 12]. Most often solar collectors are considered only as technical elements, being installed on the roof top, on flat or tilted surfaces. This type of installation, with low integration features, is less visible and makes the architectural impact minor. Unfortunately the solar thermal collectors are heavy structures that introduce a supplementary load on the roof structures. Even though the annual yield of the roof integrated systems is increased, the seasonal heat production and consumption variations may cause overheating and so the dimensioning of such systems becomes difficult and the durability can be affected.

Literature shows that for the mid-latitudes the installation of collectors on vertical surfaces is a viable option as it brings the advantages of an increased surface available for mounting and a better distribution of the heat production. The vertical implementation of solar collectors implies the integration in the facades which imposes a more elaborate approach when it comes to the design of the whole system as the facades represents the expression of the building [13]. The facades are mirror the functional structures of the interior and are influenced by proportion, size of openings (doors and windows), and material. The complexity of the facades design is imposed by the multitude of pre-requisites to be met: (1) functional (shading, insulation), aesthetic (proportion, rhythm of a structural matrix), constructive (respecting the principles of building construction), etc [14]. Thus, the quality of architectural integration of solar energy conversion systems has to be a controlled and coherent process, approaching simultaneously the functional, constructive, and aesthetic aspects (Fig. 2).

Integration of solar-thermal systems represents the insertion a technical element (solar collector) in a new or existing exterior wall system. Different buildings, with different facades will therefore have specific and personalized demand for integrating the solar-thermal systems in the architectural concepts.

Lately, three different concepts were formulated on how solar energy conversion systems should be integrated into the buildings:

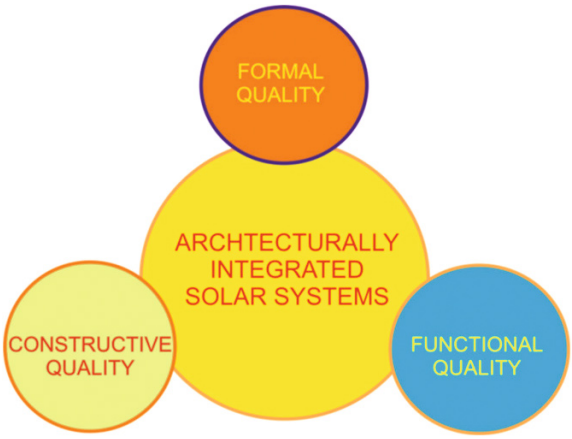

Fig. 2 Architectural integration quality

- *Hiding the components in the facade* [15];
- *Mounting the components on the facade, without drawing the attention*;
- *Outlining the solar components in the building design*.

Design aspects such as dimensions, proportions, the structure of the surface and colour have to be also considered in these strategies. Also the surfaces of roof and façade are essential as usually most of the roofing-materials and the materials used for facades show rough surfaces and warm colours while solar energy conversion systems are usually flat with shining faces made from metal and glass.

The energy demand in the building represents the key technical data that imposes the size of the systems that have to be installed. But, the optimal functional size has a significant impact on the building aspect and implicitly on the façade. This leads to a methodical approach focusing on the coherency of form, function and design. Previous studies highlight several guidelines [14, 16] that are to be considered for a qualitative architectural integrated solution:

- *Utilisation of the solar energy conversion system as a construction element* (facilitates the integration as the conversion system becomes a part of the building);
- *Optimal dimensioning and positioning of the conversion system* (in order to fulfil this goal, shape requirements, the conversion technology and energy production issues have to be simultaneously solved);
- *Balance of colors and textures;* for the selected solar technology this depends on the availability of a various range of colors and textures for the elements installed on visible surfaces; by considering the building as a whole entity, the "visible" elements (e.g. the solar-thermal collectors) need to comply with the aesthetic context of the building;
- *Sizing and shaping* considering the composition grid and stereotomy of the building.

The criteria imposed for a qualitative architectural integration are difficult to fulfil when using commercial collectors, therefore there is a need for novel, more "building oriented" solutions for solar thermal systems integrated in facades.

For state-of-the art collectors, development mainly focuses on sizing for optimisation of heat production, manufacturability, handling and installation [16]. Without compromising any of these features, the new generation of solar collectors/facades must be developed as multifunctional structures, able to additionally meet several criteria:

- Broad range of implementation alternatives in various building/architectural functions: balconies, fences, roofs, curtain walls, brick walls, etc.;
- Modularity of the system, allowing to extend the collecting area;
- Flexibility in assembling, able to: (1) generate different geometries, particularly in the highly exposed places of the building, (2) allow various configuration connections (serial/parallel, unit-unit/grid piping) without major interventions in the building structure (mounting on adjacent light structure).
- Easy maintenance;
- Durability;

These criteria make possible the implementation of the novel solar-thermal facades in already existing or in new buildings.

To fulfil these criteria, novel concepts are required in the design of the solar-thermal collector in terms of: (1) shape and size, and (2) surface texture, finishing and colour [17]. Further on, integrated collectors into solar-thermal arrays represents another novel design concept that will be discussed.

3 Results and Discussions

3.1 The Solar Collector and the Array Units

Development of novel multifunctional solar thermal arrays/facades, able to have an optimal coverage degree of the available area, calls for a variety of shapes other than the regularly used rectangular geometry [13, 17].

In order to develop a multifunctional solar array/façade a requirements list was developed for the main unit (the collector):

- Type of collector: flat plate solar collector;
- Shape: different polygonal shapes;
- Colour: variety of colors for the absorber plate and/or for the glazing;
- Performance: efficiency meeting the market threshold;
- Durability: corrosion protected system;
- Manufacturing: using already existing technologies;
- System: common equipment for piping, pumping and storage;
- Mounting: easy coupling;
- Maintenance: accessible maintenance.

Considering the requirement list, the innovative multifunctional concept is based on colored flat solar-thermal collectors with various polygonal geometries as triangle, trapeze, and hexagon [17].

The modularity of the conversion unit (collector) imposes regular polygonal shapes (equilateral triangle, regular hexagon, isosceles trapeze) to get high flexibility in covering various facades.

Studies on the optimal size of the new collectors have to consider two different aspects: functionality and aesthetics.

Large dimensions collectors are efficient but aesthetically restrictive, as increasing size the coverage of medium and small facades becomes restricted. For the flexibility of the designs and configurations, the aesthetic aspect would impose small areas that allow a high degree of freedom in creating appealing structures of shapes and colours on the building facades, but the functional aspect imposes a minimum limit for small sizes considering the hydraulic balance of the assembly and the heat transfer capacity of the tubing [17]. Previous studies showed that polygonal geometries within a range of 700–1,200 mm are able to satisfy a good flexibility in filling different facades configurations (I. Visa et al., patent proposal no. A/00156/18.02.2013).

There were identified polygonal units as equilateral triangle Fig. 3a and isosceles trapeze that are able to satisfy the requirements above formulated; the triangular equilateral shape has a great flexibility in development of various patterns with

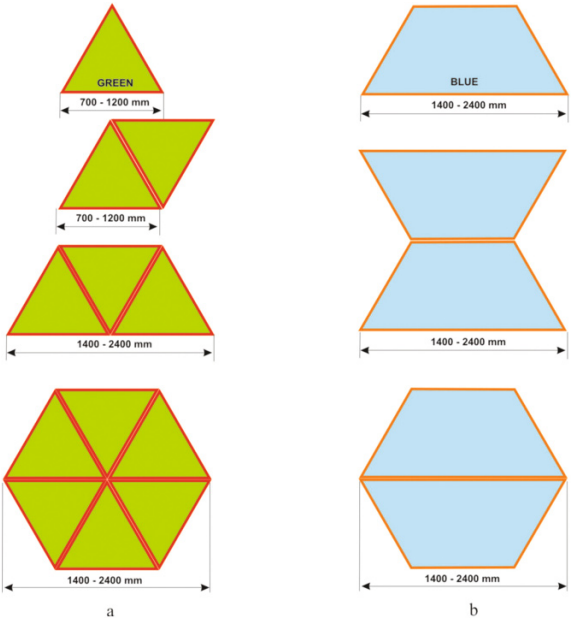

Fig. 3 Novel geometric configurations for solar thermal collectors and examples of derived geometries for **a** equilateral triangle basic unit and **b** isosceles trapeze

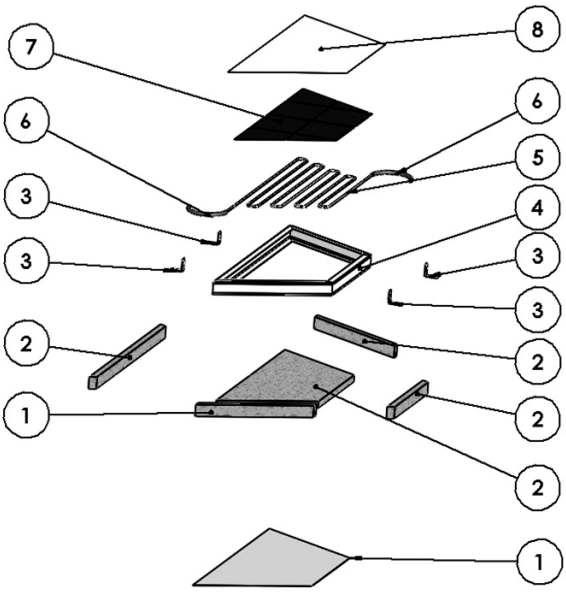

Fig. 4 The design of the collector (the trapeze configuration): *1* back aluminium plate, *2* basaltic foam insulation, *3* aluminium flanges, *4* aluminium frame, *5* copper tube serpentine, *6* rubber quick connections, *7* absorber plate, *8* glazing

direct applications for small and medium facades, with various openings and volumetric structures. The requirements for cost effective larger arrays are better met by the isosceles trapeze unit which facilitates an easier connection and mounting. Both solutions may be used in combined structures and can also include rectangular collectors.

These novel shapes impose new solutions for the internal tubing; this has to be designed to provide a maximum collection of heat from the absorber plate. In the design of the internal piping one has also to consider the interconnectivity between the collector units, to form an array with a given configuration.

The structure of the novel type of the solar thermal collector is mounted inside an aluminum frame profile, giving the triangular or trapeze (element 4 Fig. 4.) shape and is backwards closed with a 1.2 mm sheet of aluminum plate (element 1 Fig. 4). A copper tube serpentine Ø10 × 1 mm (element 5 Fig. 4) is integrated within the frame, on a 50 mm thick basaltic foam insulation (elements 2 Fig. 4). The absorber plate (element 7 Fig. 4) is an aluminum or copper thin plate covered with the selective absorber coating and is attached on the tube by using tin welding. A single or double glazing layer (element 8 Fig. 4) ensures the enclosing of the collector being attached with a silicon gasket on the frame. Flexible rubber quick connections (element 6 Fig. 4) provide the high flexibility degree of mounting while aluminum flanges 3 mm thick (element 3 Fig. 4) support the entire collector assembly on the mounting structure attached to the façade.

Considering the previous investigations on the optimum ratio between the collector's shape and area (*I. Visa et al., Patent proposal no. A/00156/18.02.2013*), several possibilities were explored. The obvious possibilities for the inlet/outlet

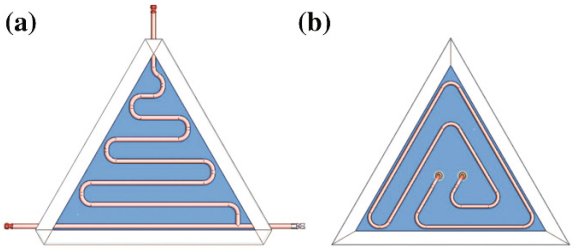

Fig. 5 The design of internal tubes for the triangular unit: **a** traditional design; **b** novel design

tubes in a triangulated geometry were identified on the corners, Fig. 5a, or in the center, Fig. 5b. These solutions are considered for a further step of implementation and testing in order to determine basic units able to provide the optimal solution in terms of flexibility, functionality and aesthetic.

The corner inlet/outlet allows left or right mounting depending on the array design by closing one of the fittings while the other one is used for the water circuit. The design allows serial or parallel connection of multiple triangular collectors. For the serial connection the number of collectors is limited but considering the reduced size of the unit preliminary estimations show that is higher than in the case of the serially connected regular collectors. Various geometries of the tube design are available considering that sizing calculations. The preliminary optimization of heat transfer developed by using "the wing method" led to an optimal distance of 60–90 mm between the tubes if the tube diameter is Ø10 mm with a thickness of 1 mm.

The center inlet/outlet supports a hidden mounting of the coupling system if flexible tubes with fast fitting are used for the interconnection of the collector. The tubing scheme also allows serial or parallel connection in between the collectors or to a central pipeline of the building.

For the isosceles trapeze units, the geometry of internal tubing may have a wide variety of solutions. One conceptual solution follows the classic serpentine with two inlet/outlet connection (Fig. 6). As a novel collector has to be approached also from the technology aspects an optimized serpentine in two stages is proposed in Fig. 7, combining 2 regularly used serpentines having two different sizes for the straight lines of the tubes. This reduces the production costs of the inner tubing by 9 %.

By assembling the basic units on the opaque areas of the buildings/facades (preferably South, acceptable SE or SW), the novel solar thermal collectors may provide a wide range of solutions for building rehabilitation or for efficiency increasing of the building.

Having a large spectrum of implementation the design imposes adaptability to parallel and serial interconnection (i.e Fig. 8). Flexible tubes and fast fittings are able to provide the modularity of the system while the installation on the facades is recommended on light frames/structures to support the array.

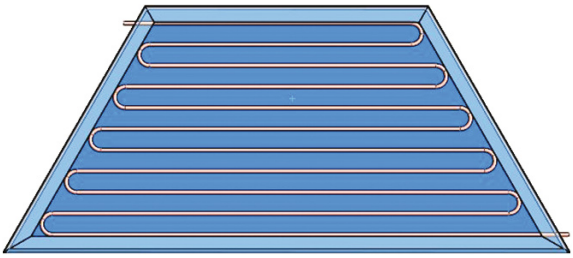

Fig. 6 The design of internal tubes for the isosceles trapeze unit

Fig. 7 Technologically optimized design of internal tubes for the isosceles trapeze unit

Such approach ensures the protection of the façade, hiding the adjacent water circuit, ensuring an additional insulation. Tracking is possible for limited angles for the entire array or for specific strings within the configuration. This may provide an increase in energy gain (direct tracking) or allows to avoid overheating during the warm seasons, by back-tracking.

Another aspect that contributes to increasing the acceptance and architectural integration is represented by the possibility to provide a variety of coloring options. As already mentioned, aesthetics imposes various colours of the absorber plate, while preserving the threshold spectral selectivity, S, accepted for quality commercial collectors (S = 9). So far there were obtained red absorbers plates, with shades varying from bright to dark red, with the composition $Al/Al_2O_3/Fe_2O_3/Au/TiO_2$ (S = 9, 7), [18, 19]. Colour can be obtained also through the glazing, by covering the solar glass with multiple layers having various porosity of TiO_2 [6], TiO_2/Fe_2O_3 or TiO_2/Co_2O_3.

The modularity of the geometrical structure allows the possibility to deliver array units readily made. Several variants of array units are proposed for the triangular collector unit (Fig. 9), for the trapeze based array unit (Fig. 10) and for the hexagonal based array unit (Fig. 11).

The main advantage of the modular array units is the wide range of possibilities to develop aesthetical and architectural complex facades. These units already equipped and connected may be lego-like configured in combined structures in order to respond to the customers and architects requirements. By combining

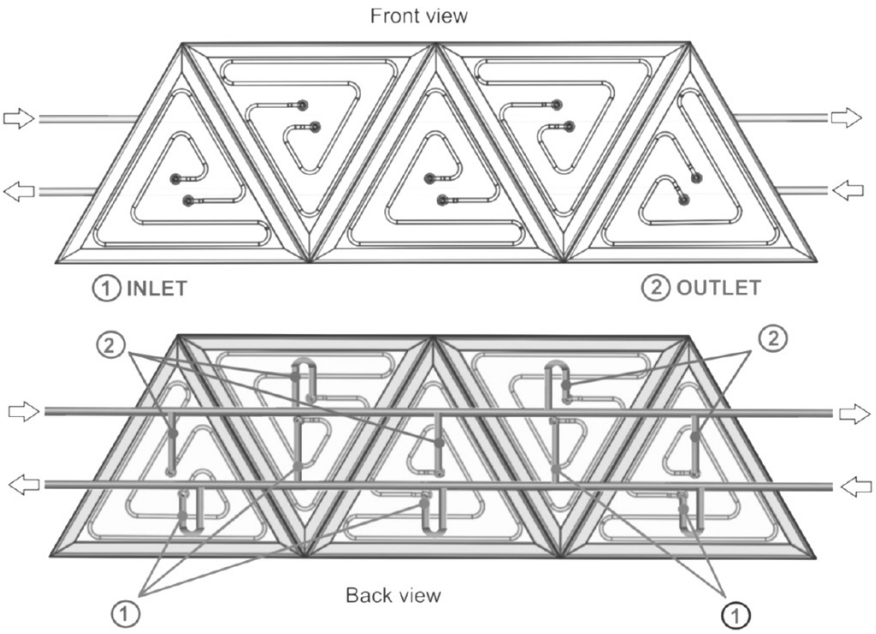

Fig. 8 Example of serially connected triangular solar collectors units

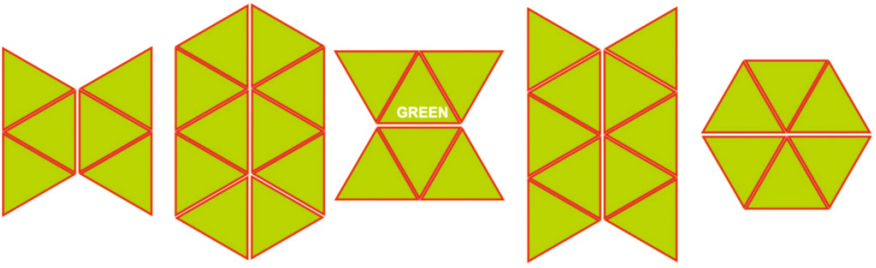

Fig. 9 Various configurations of triangle based array units

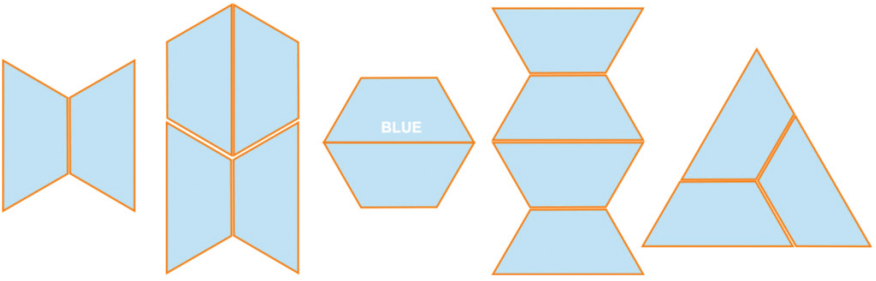

Fig. 10 Various configurations of trapeze based array units

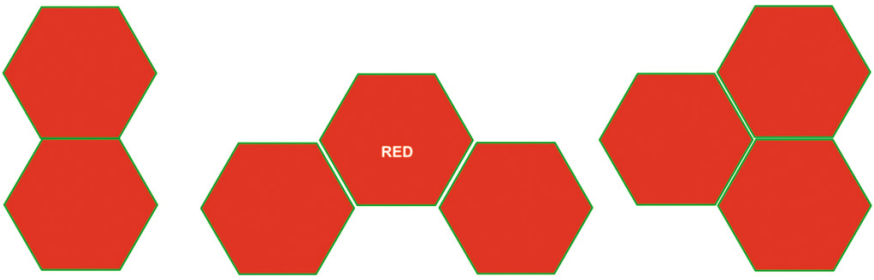

Fig. 11 Various configurations of hexagonal based array units

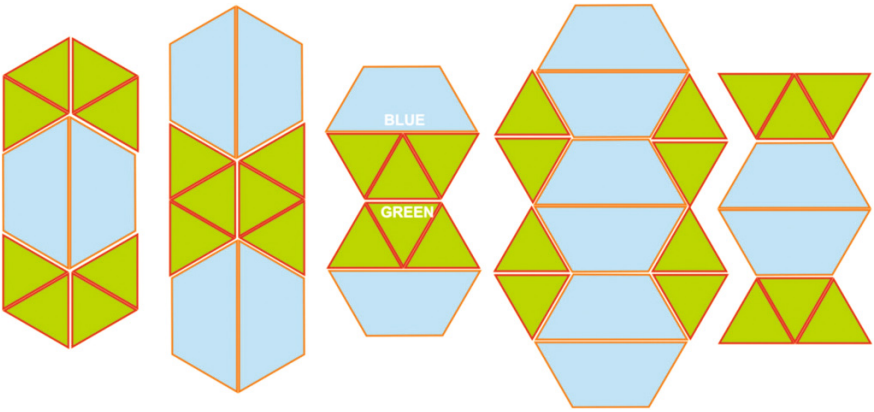

Fig. 12 Combinations between triangle and trapeze based array units

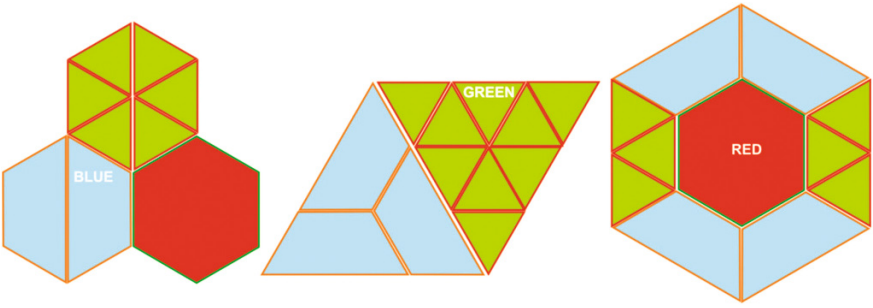

Fig. 13 Combinations between triangle, trapeze and hexagonal based array units

different array units of different geometries and/or colors, spectacular effects to improve the appearance of the buildings may be obtained. A series o combined solutions of array units are provided in the Figs. 12 and 13.

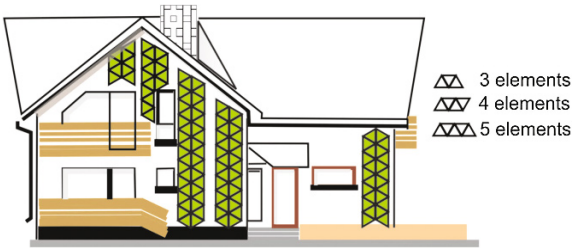

Fig. 14 Vertically disposed array units with triangular elements on the façade of a residential house

This array units, associating solar-thermal collectors give a certain flexibility in dimensioning and designing reliable circuits for the heating agent and for the hydraulic balance of the thermal system.

While these configurations outline the capability of the collector units to adapt to a large variety of combinations between shapes and color, the functionality of the array unit it's yet to be discussed, considering sizing and connections between the collector units within the array. This significantly depends on the type of the building and the available surfaces for implementing the solar-thermal façade. The geometrical modularity makes the units suitable for residential homes, public buildings, blocks of flats, offices, etc. Avoiding monotony, is possible as the collector/array units allow to cover a given area in different combinations or mountings, forming different structures.

To identify the optimal array units requires a closer study on the typology of certain types of facades. For residential houses an example is presented in Fig. 14; starting from the triangular basic collector unit and considering the stereotomy of the south façade, different configurations were developed on the same areas available on the façade.

Using only the triangular collector unit, several unit arrays were developed that can be vertically or horizontally mounted on the same available areas of the facade. The development of the array units becomes very useful when avoiding the problems of wrong mounting. For the same available area the vertical and horizontal disposure of the triangular based arrays allows an approximately equivalent degree of coverage but the connections and hydraulic circuit of the façade is completely different. The vertical configuration has the disadvantage of pressure losses on the collecting water columns which would involve higher energy consumption for pumps circulation while the horizontal disposure is allowing a parallel connection between the rows (Fig. 15).

The triangular units can evolve in a multitude of configurations, diversely disposed on the same available areas of the façade, but they have the disadvantage of a large numbers of units necessary to cover the façade.

Considering the cost involved because of the large number of units, configurations based on trapeze units and trapeze based array units were proposed for horizontal and vertical mounting as shown in Figs. 16 and 17. Similarly to the case

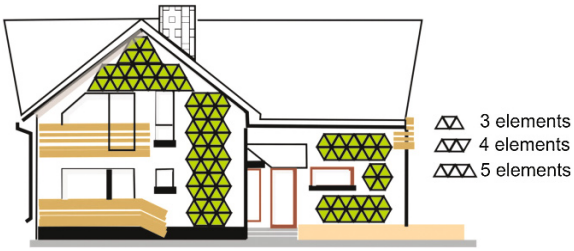

Fig. 15 Horizontally disposed array units with triangular elements on the façade of a residential house

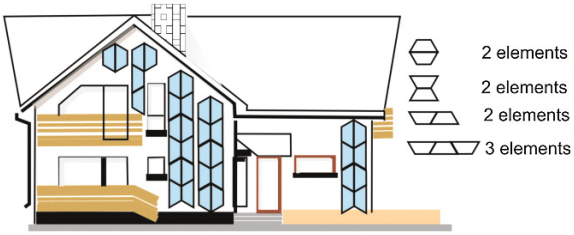

Fig. 16 Vertically disposed array units with trapeze elements on the façade of a residential house

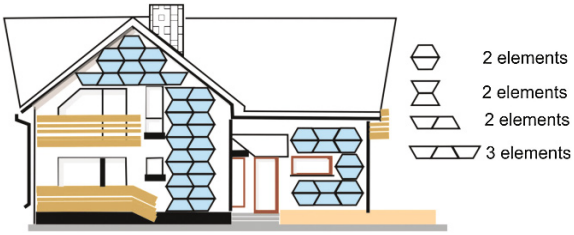

Fig. 17 Horizontally disposed array units with trapeze elements on the façade of a residential house

of the triangle based array units, the horizontal disposure of the trapeze based array units support a better functional solution.

The disadvantage of the horizontal mounting consists in a lower aesthetical quality of the façade than in the case of vertical ones. As the block of flats are not even nowadays architecturally and structurally different of the old ones which need rehabilitation, several facades proposals developed from array units are presented in Figs. 18 and 19.

These configurations prove the utility and the flexibility and support the development of a personalized signature within the community.

Fig. 18 Horizontally and vertically disposed triangular array units on the façade of a block of flats

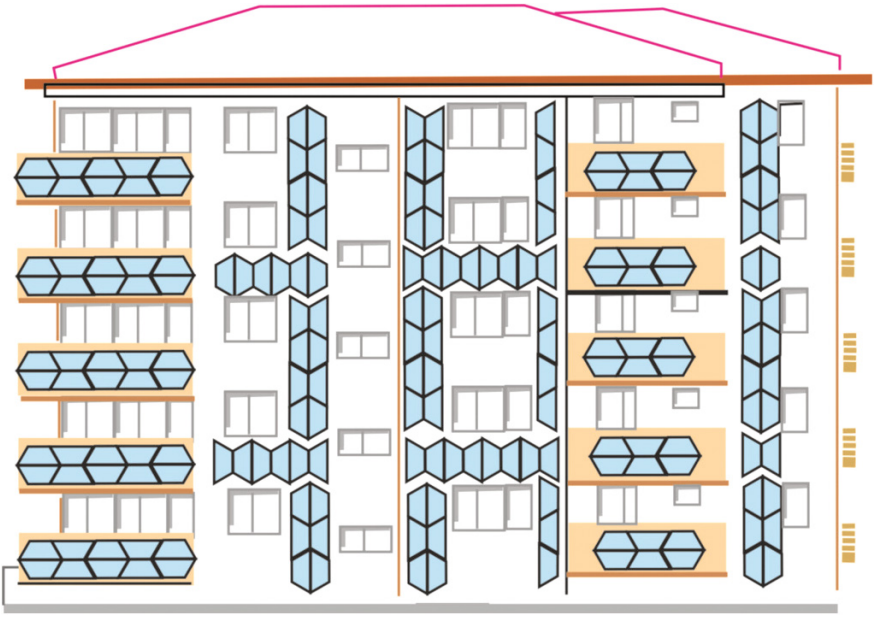

Fig. 19 Horizontally and vertically disposed triangular array units on the façade of a block of flats

3.2 Multifunctional Solar-Thermal Facades

The implementation of solar thermal systems integrated in the building facades may significantly contribute to the acceptance of the implemented renewable solar conversion systems by improving the aspects of the block of flats built in the last three decades of the 20th century which, were characterized by monotonous parallelepipedic grey concrete structures.

The aspect improvement may contribute to the rehabilitation of these edifices not only from aesthetical perspective but also considering the reduction of the thermal energy losses, providing insulation on the concrete walls *and* domestic hot water for the residents. As the Romanian architectural environment has a large distribution of such structures in the urban areas, a preliminary design study was developed considering the geometrical features of a wide range of blocks and conceptual designs were proposed as solutions for implementation, Fig. 20:

The studies developed within the EST IN URBA project proved a high versatility of the modular solar thermal arrays. The geometry and the variety of colours allow installation on residential buildings or public edifices, on the facades or on the roof tops, improving the appearance of the building as shown in Fig. 21.

One of the project outcomes involves the implementation of a modular solar thermal façade within the R&D Institute of the Transilvania University in Brasov. The institute consist in eleven low energy buildings with three floors. As the buildings aims to the Zero Energy Building status they integrate different solutions for energy mixes. These mixes will include solar thermal systems to meet the domestic hot water need, while the excess of thermal energy may be used for cooling [20]. Thus, solutions for façade integration of solar-thermal arrays were proposed, Fig. 22.

The implementation of these innovative solutions are subject to further calculation, to identify the optimal configuration able to provide domestic hot water yield and a low energy consumption for the forced circulation. The calculation will be validated on a pilot installation in the Institute, allowing testing and optimizing the

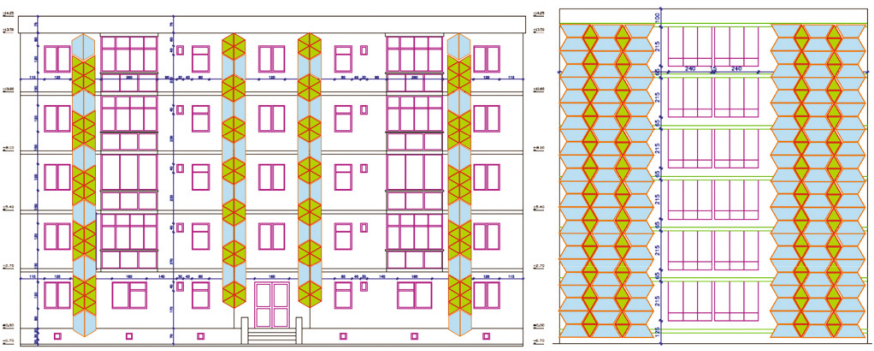

Fig. 20 Solar thermal facades obtained by combining unit arrays of triangular and trapeze STC

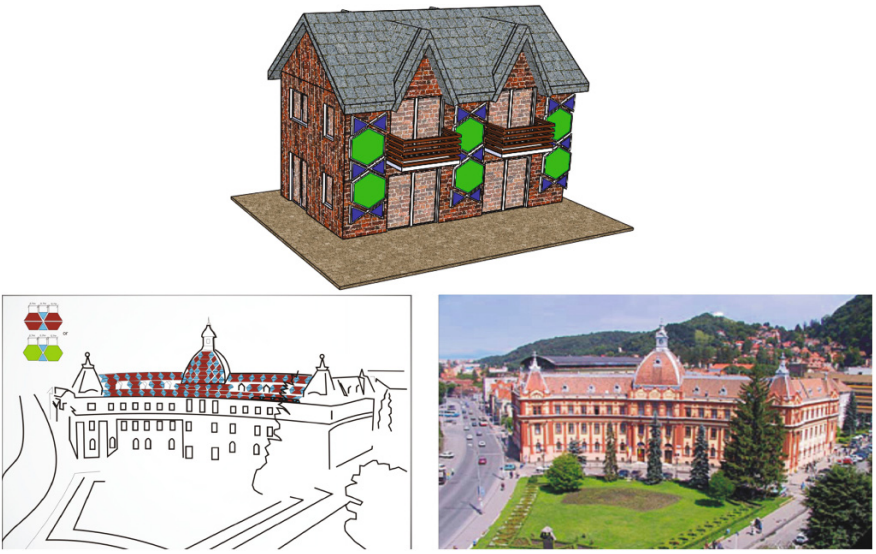

Fig. 21 Solar thermal arrays on community buildings

collector/array units. This is under development on the façade of a parallelepiped structure and will be equipped with all the necessary features for outdoor testing (sensors, piping, mounting structure, boilers, storage etc.). This testing facility is designed for simultaneously testing: (1) one trapeze collector with red absorber plate; (2) one trapeze collector with black absorber plate; one commercial flat plate solar thermal collector and one commercial vacuum tube collector, the last allowing benchmarking the novel collectors. Each collector is connected to an individual storage tank by individual pumping group and solar controller for the automation of each solar circuit. Two Identical commercial collectors are installed at an optimized tilt angle on the rooftop.

The monitoring testing system of the facility consists of: thermal probes to the inlet/outlet of each collector, storage tank and energy meters installed on each solar circuit.

The testing rig has the following components:

1. Red absorber plate (S > 9)
2. Black absorber plate (S > 13)

B. Reference: commercial ST collectors

3. Flat plate ST—vertical
4. Flat plate ST tilted (30°)
5. Vacuum tube ST—vertical
6. Vacuum tube ST tilted (30°)

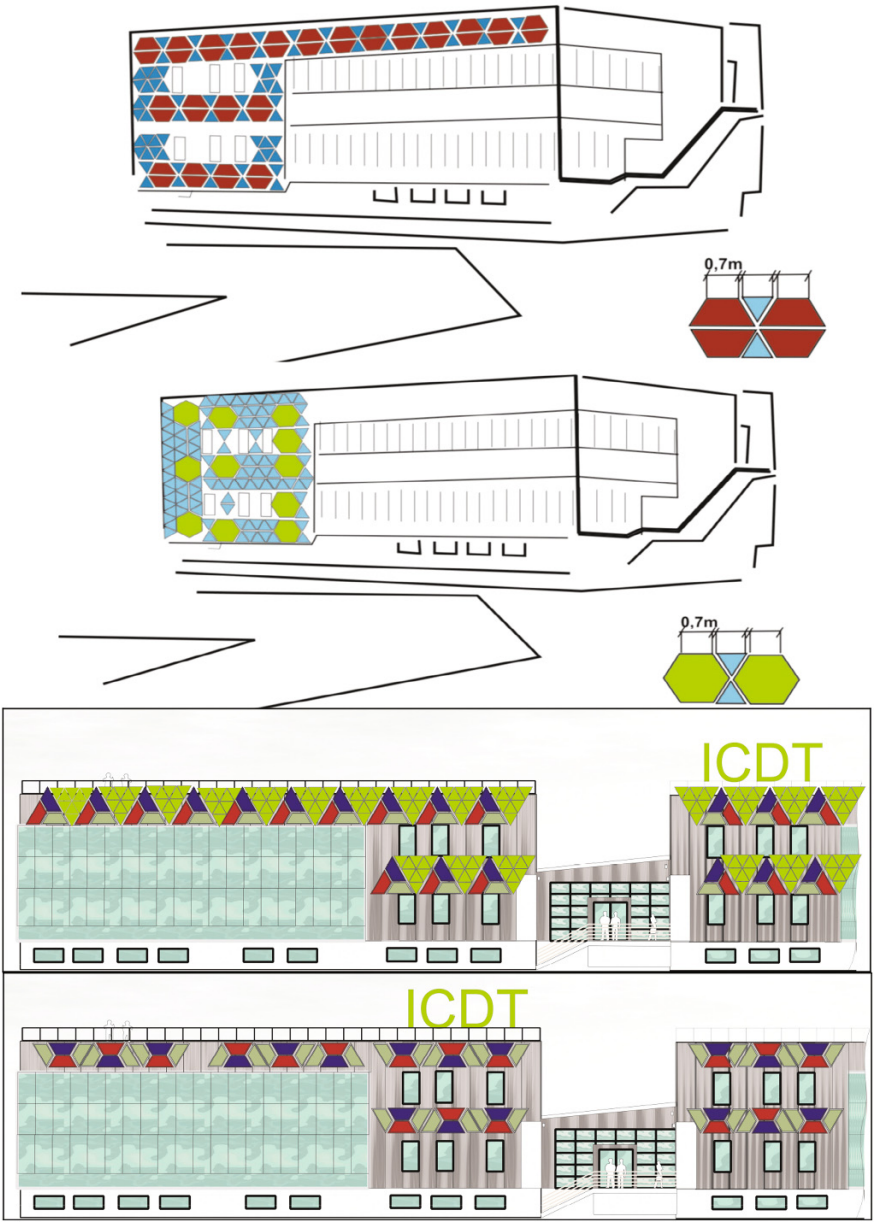

Fig. 22 Solar-thermal façades on a laboratory building of the R&D Institute of the Transilvania University of Brasov, Romania—conceptual design solutions

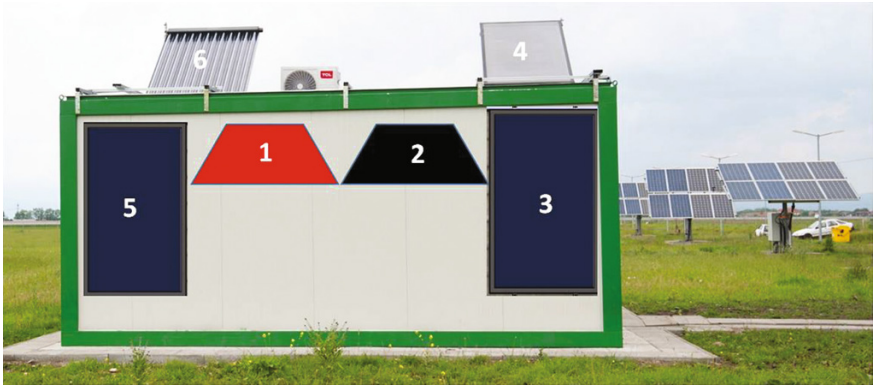

Fig. 23 The concept of the testing facility for the novel shaped solar thermal collectors

The outdoor parameters (ambient temperature, relative humidity, wind speed and direction, solar radiation) are monitored by a Delta T weather station and a Solys 2 Sun Tracker available on site. The testing facility is presented in Fig. 23.

The outdoor testing rig will allow characterizing the novel collectors, outlining the differences brought by shape, colour and mounting. After optimizing the prototype, a 10 m^2 façade is designed to be installed in the Institute.

4 Conclusions

Novel active multifunctional solar thermal systems impose the development of efficient convertors with increased architectural acceptance. The novel concept of solar thermal collectors units and solar thermal units arrays based on triangular, trapeze and/or hexagonal geometry represents a possible response to this need.

The paper presents solutions also for the internal structure of the collector: case, insulation, pipes, inter-connecting solutions. These solutions ensure large heat coverage and allow serial and parallel connections in various positions and assemblies.

Additionally, novel coloured absorber plates and/or glazing will increase the aesthetic component and can impose the solar-thermal facades as the representative features describing a community.

The novel type of solar collector and array units in different geometrical configurations or colour combinations will be tested on the outdoor testing rig available in the Institute.

Acknowledgments This work was done in the frame of the Program: Cooperation in Priority Fields—PNII, developed with the support of ANCS, CNDI-UEFISCDI, Romania in the project EST IN URBA, PN-II-PT-PCCA-2011-3.2-051.

References

1. Kalogirou, S. A. (2004). Solar thermal collectors and applications. *Progress in Energy and Combustion Science, 30*, 231–295.
2. Aste, N., Adhikari, R. S., & Tagliabue, L. C. (2012). Solar integrated roof: Electrical and thermal production for a building renovation. *Energy Procedia, 30*, 1042–1051.
3. Visa, I., Comsit, M., & Duta, A. (2014). Urban acceptance of facade integrated novel solar thermal collectors. *Energy Procedia, 48*, 1429–1435.
4. Neagoe, M., Visa, I., Burduhos, B. G., & Moldovan, M. D. (2014). Thermal load based adaptive tracking for flat plate solar collectors. *Energy Procedia, 48*, 1401–1411.
5. D'Antoni, M., & Saro, O. (2012). Massive solar-thermal collectors: A critical literature review. *Renewable and Sustainable Energy Reviews, 16*, 3666–3679.
6. Anderson, T. N., Duke, M., & Carson, J. K. (2010). The effect of colour on the thermal performance of building integrated solar collectors. *Solar Energy Materials and Solar Cells, 94*, 350–354.
7. Bonhote, P., Eperon, Y., & Renaud, P. (2009). Unglazed coloured solar absorbers on faccade: Modelling and performance evaluation. *Solar Energy, 83*, 799–811.
8. Krippner, R., & Herzog, T. (2000). Architectural aspects of solar techniques. Studies on the integration of solar energy systems into the building skin.
9. Maurer, C., Pflug, T., Di Lauro, P., Hafner, J., Knez, F., Jordan, S., et al. (2012). Solar heating and cooling with transparent façade collectors in a demonstration building. *Energy Procedia, 30*, 1035–1041.
10. Motte, F., Notton, G., Cristofari, C., & Canaletti, J.-L. (2013). A building integrated solar collector: Performances characterization and first stage of numerical calculation. *Renewable Energy, 49*, 1–5.
11. Yin, H. M., Yang, D. J., Kelly, G., & Garant, J. (2013). Design and performance of a novel building integrated PV/thermal system for energy efficiency of buildings. *Solar Energy, 87*, 184–195.
12. Matuska, T., & Sourek, B. (2006). Façade solar collectors. *Solar Energy, 80*, 1443–1452.
13. Quesada, G., Rousse, D., Dutil, Y., Badache, M., & Hallé, S. (2012). A comprehensive review of solar facades. Transparent and translucent solar facades. *Renewable and Sustainable Energy Reviews, 16*, 2643–2651.
14. Munari Probst, M., & Roecker, C. (2007). Towards an improved architectural quality of building integrated solar thermal systems (BIST). *Solar Energy, 81*, 1104–1116.
15. Motte, F., Notton, G., Cristofari, C., & Canaletti, J.-L. (2013). Design and modelling of a new patented thermal solar collector with high building integration. *Applied Energy, 102*, 631–639.
16. Munari Probst, M., & Roecker, C. (2012). Criteria for architectural integration of active solar systems IEA Task 41, Subtask A. *Energy Procedia, 30*, 1195–1204.
17. Visa, I., Comsit, M., & Duta, A. (2014). Urban acceptance of facade integrated novel solar thermal col-lectors. *Energy Procedia, 48*, 1429–1435.
18. Duta, A., Isac, L., Milea, A., Ienei, E., & Perniu, D. (2014). Coloured solar-thermal absorbers —A comparative analysis of cermet structures. *Energy Procedia*, *48*, 543–553. ISSN 1876-6102.
19. Dudita, M., Manceriu, L. M., Anastasescu, M., Nicolescu, M., Gartner, M., & Duta, A. (2014). Coloured TiO2 based glazing obtained by spray pyrolysis for solar thermal applications. *Ceramics International, 40*, 3903–3911.
20. Moldovan, M., Visa, I., & Burduhos, B. (2011). Energetic autonomy for a solar house. *Environmental Engineering and Management Journal, 10*, 1283–1290.

Lighting System Efficiency in the Industrial Plants

Mircea Draghici, Francisc Sisak and Anca Manolescu

Abstract The article presents the most important elements of a lighting installation of the existing industrial building, how to choose from the various optimization solutions and efficient power consumption for the facility using advanced equipment control and the proper use of them in order to reduce the time of using of the artificial lighting. Energy efficiency is one of the important issues concerning lighting system control. A very significant part of building consumed energy is the lighting systems consume. Providing lighting only in the areas and in the periods lighting is needed and providing the right level of lighting as needed are effective means of reducing the energy use of the lighting system. The main control action for this purpose are on/off switching and dimming using a central control system BMS. There are presented and simulated some efficiency solutions of the lighting system within an industrial production plant that currently uses fluorescent lighting T8. The main conclusion of this article is that replacing conventional lighting systems in the industrial sector with modern lighting systems using LED technology controlled by a centralized automated intelligent BMS type, leads to increased energy efficiency. The article shows that in certain moments of time when natural light enters the building from exterior spaces through the walls or ceiling glass by automatically adjusting light intensity of lighting or just by switching some of the lamps off via light sensors and an integrated BMS system can achieve a saving of electricity consumption of approx. 30 %. By replacing lamps using T8 fluorescent tubes with new LED based lighting electricity, consumption can be reduced to approx. 60 %, and if additionally use a lighting management system centralized BMS type, saving power consumption can reach up to approx. 70 %.

Keywords Lighting installation · Efficiency · Control intelligent · BMS

M. Draghici (✉) · F. Sisak · A. Manolescu
Faculty of Electrical Engineering and Computer Science, Transilvania University of Brasov, Brasov, Romania
e-mail: draghicimircea@gmail.com

I. Visa (ed.), *Sustainable Energy in the Built Environment - Steps Towards nZEB*, Springer Proceedings in Energy, DOI 10.1007/978-3-319-09707-7_5

1 Introduction

The main objective of the European Union in the energetic field is particularly achievement by 2020 of a 20 % reduction in greenhouse gas emissions, increasing to 20 % the share of renewable energy and increasing energy efficiency by 20 % [1].

The new energy strategy focuses on five priorities:

1. Achieving an energetic efficiency Europe;
2. Building a truly pan-European integrated energy market;
3. Empowering consumers and achieving the highest level of safety and security;
4. Extending Europe's leadership in energy technology and innovation;
5. Strengthening the external dimension of the EU energy market.

Energy efficiency is the most cost-effective way to reduce emissions, improve energy security and competitiveness, make energy consumption more affordable for consumers as well as create employment, including in export industries. Above all, it provides tangible benefits to citizens: average energy savings for a household can amount to €1 000 per year [1].

Fluorescent lamps are discharge lamps, mercury vapor, with or without addition of gases; light rays are not obtained because of this phenomenon but because of a substance (luminophore) placed on the inner surface of those.

Discharge in these environments is very rich in ultraviolet radiation.

Luminophore layer (covering the walls of the glass on the inside) is to convert the emitted energy spectrum ultraviolet radiation, fulfilling the following conditions:

- Good conversion efficiency,
- Transparency to visible radiation,
- Radiation resistance during time,
- Shockproof irradiation caused by frequently connections-disconnections

Luminophore layer composition determines the color of light source and also the color rendering index value.

The ignition is done by surge discharge (shock voltage), decreased slow ionization, and environmental resistance discharge or by combining the two systems.

To stabilize the discharge is necessary ballast [2].

Tubular fluorescent lamps are discharge lamps, mercury vapor at low pressure. Discharge fluorescent lamp type is "positive column" the majority of radiation in this type of lamps (95 %) occurring in the ultraviolet spectrum (253.7 and 185 nm bands) and only 5 % in the visible spectrum.

Electroluminescence as a phenomenon was discovered in 1907 by the British experimenter H. J. Round of Marconi Labs, using a crystal of silicon carbide and a cat's-whisker detector [3].

Russian Oleg Losev reported creation of the first LED in 1927. His research was distributed in Russian, German and British scientific journals, but no practical use was made of the discovery for several decades [3].

In 1961, James R. Biard and Gary Pittman found gallium arsenide (GaAs) emitted infrared light when electric current was applied [4].

The first visible-spectrum (red) LED was developed in 1962 by Nick Holonyak, Jr., while working at General Electric Company [5].

The first high-brightness blue LED was demonstrated by Shuji Nakamura of Nichia Corporation in 1994 and was based on InGaN [6].

2 Presentation of Existing Situation

Given the above issues, this paper focuses on reducing the power consumption, offering an alternative solution to optimize existing lighting system used in the production halls of a factory located in Brasov.

Production in this plant is organized around the clock (24 h/day), except on Sundays (just 2 shifts, 16 h) and public holidays resulting in 8,100 h/year of lighting operations.

The lighting performance connection is of 1.3 MW; consequently, the annual consumption is of approx. 8,340 MWh and the annual costs are (computed at an estimation of 0.33 lei/kWh) of approx. 2,75 mil lei, equivalent to some 610,000 €.

Every area of the production halls has few (3…6) electrical switchboards providing electrical energy for the lighting system in monophasic or three-phasic circuits mode, every three-phasic circuits supplying approx. 30…40 fluorescents lamps.

This analysis will focus on a reference area (Fig. 1), situated in one of the areas used as production space, which is considered later as the reference for the entire study.

The space is considered to be fit in areas with low height ($h < 6$ m), the hall is equipped with machines and technological designed production components and equipment for the automotive industry, having installed a lighting system evenly distributed lighting plan being placed height of 4.5 m above the finished floor and the lighting environment considered useful work level height ($h = 1$ m) of 300 lux (for example uses the picture of Fig. 2).

The lighting used in the analyzed room consist of lighting lamps with 1 × 58 W and 2 × 58 W type, degree of protection IP 20 (Fig. 3).

The current situation in the reference area is as follows:

- Number of lamps in room with 1 × 58 W 245 pieces.
- Number of lamps in room with 2 × 58 W 596 pieces.
- Number of lamps in the reference area with 1 × 58 W 90 pieces.
- Power installed in a luminaire 1 × 58 W with ballast included 60 W.
- Power installed in a luminaire 2 × 58 W with ballast included 120 W.
- The lighting power installed on the entire analyzed room 86.22 kW.
- The lighting power installed on the reference analyzed area 5.4 kW.

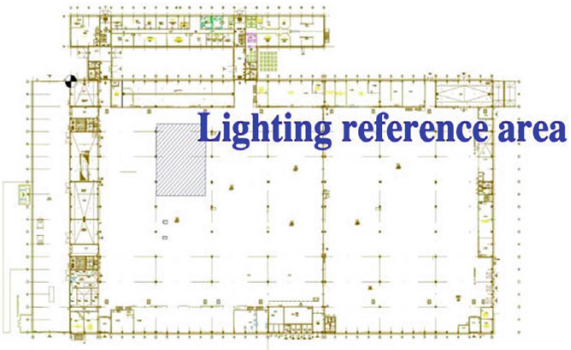

Fig. 1 Architectural plan of the building analyzed in Brasov/Romania, specifying the reference area chosen to be analyzed

Fig. 2 Picture that shows the layout of the lighting installation in the production hall analyzed

Using a measurement instrument I made measurements of the lighting in the reference area in the working plane (h = 1 m above ground level) resulting information in the below table.

The measurement instrument is a Lux meter Type: Tiede HD 2302.0, produced by DeltaOhm firm.

The HD2302.0 is a portable instrument with a large LCD display.

It measures illuminance, luminance, PAR and irradiance (across VIS-NIR, UVA, UVB and UVC spectral regions or measurement of irradiance effective according to the UV action curve).

The probes are fitted with the SICRAM automatic detection module: in addition to detection, the unit of measurement selection is also automatic. The factory calibration settings are already memorized inside the instruments.

Fig. 3 Fluorescent lamp used in the existing building

The *Max, Min* and *Avg* function calculate the maximum, minimum or average values.

Other functions include: the relative measurement REL, the HOLD function, and the automatic turning off that can also be disabled.

The instruments have IP67 protection degree.

I used for ILLUMINANCE measurement probe type: LP 471 PHOT with the followings characteristics, Table 1.

Measurement was done as follows:

- During daylight
- Grid 5 by 5 m
- Not considering additional lighting on specific workplaces
- Excluding all the areas separated by walls in the production hall (i.e. storage, offices, etc.)
- According the SR EN 12464 the measurement of the values starts after 100 h working of the lighting system.

(a) **Actual measured situation for the lighting in the existing industrial plant, chosen reference area** (Table 2, Fig. 4)

(b) **Actual simulated situation for the lighting in the existing industrial plant with Relux simulation program** (Table 4, Fig. 5)

Using simulation software Relux for the reference lighting area (the same grid of measurement points 5 m × 5 m) were obtained the following values (Fig. 5, Tables 3 and 4):

Table 1 Characteristics of the probe type: LP 471 PHOT

ILLUMINANCE measurement probe LP 471 PHOT				
Measurement range (lux)	0.01… 199.99	… 1999.9	… 19999	… $199.99*10^3$
Resolution (lux)	0.01	0.1	1	$0.01*10^3$
Spectral range	In agreement with standard photopic curve V(λ)			
Class	C			
Calibration uncertainty	<4 %			
f′1 [in agreement with pho-topic response V (λ)]	<8 %			
f2 (response according to the cosine law)	<3 %			
f3 (linearity)	<1 %			
f4 (instrument reading error)	<0.5 %			
f5 (fatigue)	<0.5 %			
α (temp. coefficient) f6 (T)	<0.05 % K			
Drift after 1 year	<1 %			
Functioning temperature	0…50 °C			
Reference standards	CIE n.69—UNI 11142			

Table 2 Measured values of the illuminance (lx) in the reference area

Measured values of the illuminance light intensity (lx)					
m	**5**	**10**	**15**	**20**	**25**
5	370	360	345	360	350
10	360	395	360	390	385
15	395	360	330	385	325
20	360	385	360	390	380
25	380	335	345	365	325
30	375	340	335	370	360
Average of the illuminance Em (lx) =					363

Grid of measurement points [m]

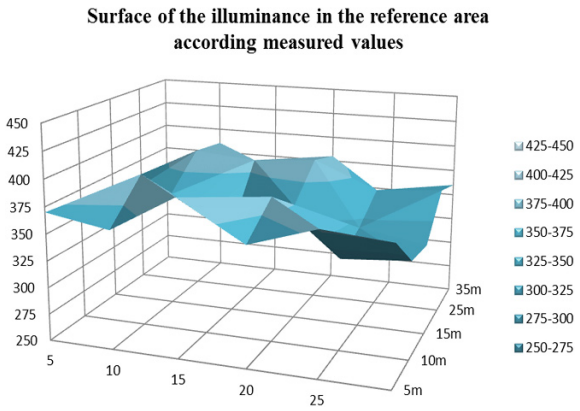

Fig. 4 Graphic of the measured values for the illuminance light intensity

Table 3 Relux simulated values of the illuminance light intensity

Relux simulated values of the illuminance light intensity (lx)					
m	**5**	**10**	**15**	**20**	**25**
5	341	337	337	332	328
10	450	436	433	433	436
15	462	446	443	444	489
20	464	449	446	441	406
25	462	451	449	448	444
30	455	450	446	447	447
Average of the illuminance Em (lx) =					428

Grid of measurement points [m]

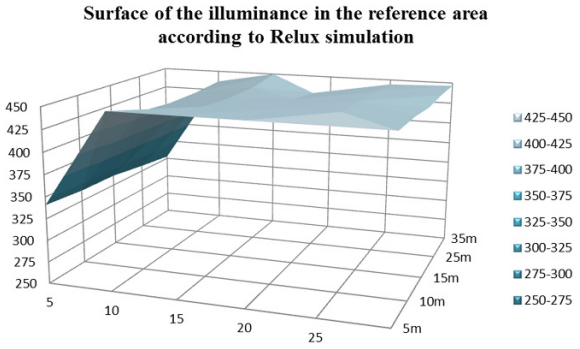

Fig. 5 Graphic of the simulated values for the illuminance light intensity

Table 4 Relux simulated values of the illuminance light intensity with LED lamps

Relux simulated values of the illuminance light intensity (lx)					
m	**5**	**10**	**15**	**20**	**25**
5	360	341	338	320	300
10	451	462	464	432	320
15	472	482	470	434	325
20	460	483	471	431	328
25	465	480	469	418	325
30	445	467	476	419	330
Average of the illuminance Em (lx) =					415

Grid of measurement points [m]

3 The Proposed Solution

(a) **Simulated situation for the lighting with changing of the fluorescent lamps with LED lamps**

Using simulation software Relux for the reference lighting area (the same grid of measurement points 5 m × 5 m), this time changing fluorescent lighting lamps with equivalent lighting as characteristics, LED lamps, built by the same manufacturer were obtained the following values (Table 4, Fig. 6):

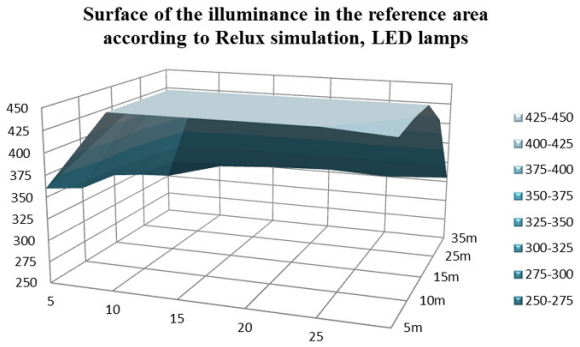

Fig. 6 Graphic of the simulated values of the illuminance light intensity, LED lamps

Table 5 Comparation led lamps with florescent lamps

Lamp type	Watts	Lumens	Operating lifetime (hrs)
CFL	58	5,000	8,500
LED lamps	32	4,800	50,000

The chosen LED lighting having similar characteristics of the emitted light intensity and have a power of 32 W/lamp.

In this situation in the reference chosen area the situation show as follows:

- Number of lamps in the reference area with (LED 32 W) 90 pieces.
- Power installed in a luminaire 32 W 32 W
- The lighting power installed on the reference analyzed area 2.88 kW

4 Results and Discussions

In the measurements and simulations above I wanted to show the following:

- Between measured values and calculated values derived from Relux simulation software, using the same type of lamp, there are some differences due to the influence of external light, shading or reflectance of equipment and machinery installed in the reference areas,
- The difference between the illuminance curve obtained from Relux simulation for fluorescent lamps and the illuminance curve obtained from Relux simulation for lamps with LED technology are relatively small, which leads to the conclusions sion that, in reality the measurement for the reference area with the Lux meter, using this time the LED lamps will be similar with the measurement for fluorescent lamps.

LED lightings represent a viable replacement of the T8 tubular fluorescent lamps, because there will be a reduction in energy consumption by 53 % from the

same stream of light the same area. Light cones as well as the amount of lumens are comparable to those of T8 fluorescent tubes. If the first generation LED lighting did not lend itself to production halls, further developed products can be applied successfully in them.

It can be seen that due to the influence of natural light during the day, light intensity measured in the reference is greater than the proposed 300 lux.

By implementing a lighting control system to measure light intensity in two measurement points on each circuit, closing one phase circuit if the measured light intensity is higher by 50 % than the 300 lux required, we can record savings an additional power to 10 % (Table 5).

5 Conclusions

The main conclusion of this article is that replacing conventional lighting systems in the industrial sector with modern lighting systems using LED technology controlled by a centralized automated intelligent BMS type, leads to increased energy efficiency.

Given the above analysis we can draw the following conclusions:

Fluorescent tubes contain mercury and phosphor, which present a number of health and environmental risks. The lights require ballast, which adds to the cost of the lamp and can cause a buzzing noise. Finally, they frequently flicker.

Installing a management system LMS to an existing lighting system which is uses fluorescent lighting do not show a high decrease of the cost to the fluorescent lamps is required to replace the electronic ballast with an dimmable electronic ballast, which represents also supplementary cost and even if this is done dimming light intensity can be achieved with less than 20 % because of the risk that lamp to is switched OFF during the dimming.

On the other hand, LED lamps live is longer than fluorescents, and they don't contain harmful ingredients like mercury. Perhaps most significantly, LEDs use much less power than fluorescent lamps and there are many other benefits, as well.

The article shows that in certain moments of time when natural light enters the building from exterior spaces through the walls or ceiling glass by automatically adjusting light intensity of lighting or just by switching some of the lamps off via light sensors and an integrated BMS system can achieve a saving of electricity consumption of approx. 30 %.

By replacing lamps using T8 fluorescent tubes with new LED based lighting electricity, consumption can be reduced to approx. 60 %, and if additionally use a lighting management system centralized LMS type, saving power consumption can reach up to approx. 70 %.

The LMS will decrease the electricity consumption at certain times of day when natural light affects the amount of artificial light, also can control switching ON/OFF lighting circuits in areas where at certain times light is not necessary due to lack of working staff.

Installing a LMS on a facility that uses LED lighting has the advantage that it can adjust the light intensity emitted by luminaries from 0—100 %.

Another important advantage that it shows the LED lighting to their lifespan is about 5,5 times longer than fluorescent lighting.

The main disadvantage is that the LEDs are currently more expensive, price per lumen, on an initial capital cost basis, than most conventional lighting technologies. As of 2010, the cost per thousand lumens (kilolumen) was about $18. The price is expected to reach $2/kilolumen by 2015 [7].

In conclusion, by replacing fluorescent lighting throughout the production hall with LED lighting and supplementary to install a LMS system will result in energy savings of up to 65 … 70 %. The total investment will have a cost of about 125,000 Euro and the economy will be about 45,000 Euro leading to a depreciation cost in about 3 years.

Similar results were obtained in a study conducted by a team of engineers from the University of Cluj. They analyzed lighting lamps mounted in suspended ceilings, fitted with fluorescent lighting comparing with lamps using the LED technology and controlled by a LMS system, similarly mounted [8].

References

1. Oettinger, G. H. (2013, November 10). Energy 2020_A strategy for competitive, sustainable and secure energy.
2. Manualul de instalatii electrice. (2002). Editura Artecno.
3. Round, H. J. (1907). A note on carborundum. *Electrical World, 19*, 309.
4. http://ro.wikipedia.org/wiki/LED.
5. Holonyak, N., Jr. (2004). Lemelson-MIT prize winner. Lemenson-MIT program. Retrieved August 13, 2007.
6. Nakamura, S., Mukai, T., & Senoh, M. (1994). Candela-class high-brightness InGaN/AlGaN double-heterostructure blue-light-emitting-diodes. *Applied Physics Letters, 64*(13), 1687.
7. LED Lighting Explained: Questions and Answers. www.energy.ltgovernors.com.
8. Mihai-Adrian Poop. (2013). Ingineria instalatiilor, editie studenteasca, nr. 2/2013 article Reabilitarea sistemelor de iluminat, studio de caz pe Aula facultatii de instalatii, Universitatea Tehnica din Cluj-Napoca.

Analysis of a CHP Plant Operation for Residential Consumers

Rodica Frunzulica, Andrei Damian, Radu Baciu and Cristian Barbu

Abstract All European Directives pleads for energy efficiency and, if it is possible, to implement Combined Heat and Power (CHP) high efficiency sources. The system composed by CHP and classical sources (as peak sources) needs to be studied, in order to respect the real scenario of the consumer functioning with optimum efficiency depending on fuel usage. According to this, a careful review and assessment of each potential application is needed. The small-scale CHP sources are suitable for industrial and commercial buildings, as well as for hotels, hospitals etc. Concerning residential consumers, it appears to be a considerable difference between winter and summer loads. The goal of the present article is to achieve reliable information for the assessment of performance capacity of CHP systems, as a key-point for the decision of using small-or micro-CHP. It might be useful for engineers in order to identify the most likely route for their particular duty. The investigation method will be based on the dynamic simulation of the performance of CHP system connected to a residential consumer, located in the city of Bucharest. The study will be performed using two specialized software, suitable for CHP sources and connections.

Keywords Small-scale and micro-CHP systems · Residential consumer · Heat and electric loads · Energy efficiency

1 Introduction

Cogeneration systems are defined as combined heat and power systems (abbrev. CHP) as energy providers for different type of consumers: domestic residences, industrial buildings, public and commercial buildings, hospitals etc. In most of East-European countries, large-scale CHP systems were imagined and implemented during the 1960s. Steam turbine was the most popular CHP technology at the time.

R. Frunzulica · A. Damian (✉) · R. Baciu · C. Barbu
Technical University of Civil Engineering Bucharest (T.U.C.E.B), Bucharest, Romania

I. Visa (ed.), *Sustainable Energy in the Built Environment - Steps Towards nZEB*,
Springer Proceedings in Energy, DOI 10.1007/978-3-319-09707-7_6

The plants were placed usually at the periphery of the urban communities in order to control and limit the carbon emissions resulting from the heat generation. Hundreds of combined energy units (thermal–kWh_t and electrical–kWh_{el}) were produced, transported and distributed through extended networks with some limits of monitoring possibilities. Many of these systems are still operating with poor or better efficiency. The efficiency values depend on several factors, such as: energy policies of the countries, rehabilitation measures, consumer's behaviour, and variety of new systems appeared. Some countries oriented their energy policies toward renewable energy, independent sources and high new technologies to produce heat and/or power. Some of the countries continue to maintain these large CHP systems but it is almost certain that some really measures are needed to be implemented in short time. All European Directives plead for energy efficiency and, if possible, for the set-up of Combined Heat and Power (CHP) high efficiency sources. Small-scale CHP and micro-CHP would fit very well in this scenario. These systems could produce energy rates ranging from a few kWh_{el} to 1 MWh_{el} [1, 2].

But are these systems always efficient and suited for the consumers? Apparently only realistic scenarios for electric and thermal loads variations will answer to this question. According to the recent studies in this field it results that a careful review and assessment must be taken into account for each specific application [3] Today, more CHP technologies are available (gas-turbines, engines, fuel cells etc.), so it is obvious that the engineers are confronted with the dilemma of the best choice for each application of a CHP system, in order to fulfil the services needed. Each technology has specific characteristics and performances which best suit only for specific duty requirements [4, 5].

In terms of residential consumers, duty requirements mean to cover their heating need, domestic hot water demands and electrical needs. Thinking at energy sources for new communities or at the replacement of existing large scale sources, we will focus in this paper on a group of residential consumers, represented by two blocks of flats located in Bucharest, the Romania capital.

2 Problem Formulation

For residential consumption there is a considerable difference between summer heat load and winter heat load. During summer, the heat demand is limited and the heat produced by the source is used usually, only for heating domestic tap water. The variation of heating load depends on climatic conditions [6, 7].

On the other hand, the electric loads depend on the appliances and other electric consumers in each apartment. As opposed to heat load, the electric load variation has little difference between summer and winter. However, some coefficients of consumers' simultaneous operation should be taken into consideration.

For an usual CHP engine operation, the heat is recovered as following: 30–35 % at 120 °C, from the exhaust gases with temperatures over 500 °C, 30–35 % at 80–95 °C from the cooling water circuit and 4–10 % from the lubrication oil at 45–65 °C.

The so called "recovering degree" *Xrec* express the ratio between the useful recovered heat and the maximum theoretical heat that could be recovered. An engine has the important advantage that the efficiency variation at different part loads is less affected compared with steam or gas turbines. The electrical efficiency of reciprocating engines, defined as the ratio between net electrical energy output and natural gas input, depends strongly on the electrical demand and system load. For energy rates below 15 kW_{el}, the electric efficiency does not exceed 26 % [7]. Thermal efficiency depends on the system and its level of heat integration (whether condensing heat is used). The total efficiency, (electrical and thermal) generally varies between 80 % and well above 90 %. These values are varying more or less depending on the engines manufacturers.

The design manner of a CHP source can be a function of the electrical demand or also of the heat demand. In both cases, peak sources (electrical and thermal) could be chosen in order to satisfy the maximum demands. On the other hand, coverage of about 60 % of the heat demand by the CHP system as a base source represents a good practice in order to obtain maximum energy efficiency. Another important recommendation is related to the number of the engine operational hours, in the range of more than 3,800–4,000 h/year.

We proposed in the present paper the utilization of a gas engine as a CHP base source which delivers heat and electric energy for two residential buildings (2 blocks with 58 apartments), located close to Bucharest, the Romania Capital. Each block has Ground Floor and four floors and the base design winter temperature, according to the Romanian standard SR 1907/1,2-2002, is −15 °C. The buildings envelopes have good thermal insulation, as illustrated in Table 1, when comparing the corrected thermal resistances of envelope elements, R_{cor} (m^2 K/W) with their minimum values, R_{min} (m^2 K/W) indicated by the Romanian norm C107/1-2010.

According to these values, and applying the calculation methodology corresponding to SR 1907/1,2-2002, a maximum heat demand Q_{heat_load} = 136 kW per block is calculated. The dynamic variation of the heat demand for each building during the heating season was also calculated. The selected engine is an internal combustion engine functioning on diesel fuel. Two plate heat-exchangers for heat recovery were connected to the engine: one on the water-cooling circuit and the other on the exhaust gas circuit. This engine will prepare hot water for heating and domestic hot water (DHW) purposes, and also electricity for the buildings. A calculation was made for the electric demand depending on the building operation (residential, weekday or weekend days). The preparation of domestic hot

Table 1 Thermal properties of the building envelope elements

Building element	R_{cor}	R_{min}	Condition $R_{cor} > R_{min\ fulfilled}$
	m^2 K/W	m^2 K/W	–
Upper slab	5,618	3	Yes
External walls	2,386	1.4	Yes
Lower slab	3.29	1.65	Yes
External windows and joinery	0.77	0.5	Yes

water is made by using a storage tank, equipped with two immersed heating coils: one coil connected to a primary water circuit issued from the jacket water flow cooling down the co-generation engine, and another electrical coil acting as auxiliary heater for the tank water, in order to reach a maximum temperature of 58 °C at the top of the tank. This electric coil will function with electricity produced by the engine. The secondary water circuit exiting from the tank supplies the DHW consumers at $t_{DHW\ supply}$ = 55 °C according to a residential daily water flow profile for the residential consumers. The total water flow passing through the first heating coil immersed in the tank is called $q_{DHW\ primary\ flow.}$ The heating circuit is supplied with water at 80 °C resulting from the same jacket water flow cooling down the CHP motor, as in the case of DHW preparation. The water temperature supplying the heating systems has the maximum temperature at 80 °C and decreases depending on the outdoor temperature ($t_{outdoor}$) following the supply fluid temperatures diagram, described by the relation (1):

$$t_1 = t_i + 0,5 \cdot \Delta t_n \cdot \frac{\Delta\theta}{\Delta\theta_n} + \delta_n \left(\frac{\Delta\theta}{\Delta\theta_n}\right)^{1+m} [^{\circ}C] \tag{1}$$

where Δt_n is the nominal logarithmic difference between supply/return heating temperatures at design outdoor temperature, t_i—indoor usual temperature for residential buildings (+20 °C); $\Delta\theta = t_i - t_{outdoor}$ and $\delta_n = (t_1 + t_2) - t_i$.

The electrical consumption depends on the electric appliances and their number of operation hours. At the same time, the calculation of the electric demand followed the variations registered for weekdays and weekend in every month of the year. A sketch of the dual system is presented in Fig. 1.

The hypothesis of the engine model needed to be selected are related to following parameters: 75/90 °C for the cooling water of the engine, the exhaust gas temperature at the evacuation from the heat exchanger in the atmosphere, 100 °C, the fluid nominal temperatures for heating process 80/60 °C in winter (heating season of about 226 days) and 60/35 °C in the rest of the year. The 60 °C temperature is related on the right temperature to prepare domestic hot water at 55 °C. The electric consumption of the coil which is functioning as a peak load for DHW will be added at the total electric demand of the consumer.

The cooling water leaves the motor with 90 °C and enters in the heat exchanger on the exhaust gas to cool them. The cooling water temperature rises with a value depending on the exhaust gases imposed at the output of the heat-exchanger (approx. 2 °C for each 100 °C variation of the output temperature from the heat-exchanger). In the same time, this temperature won't exceed the water vaporization temperature at the system's pressure. With these new parameters, the cooling water enters in the heat-exchanger to prepare the fluid for heating installations and for domestic hot water (process 3 in Fig. 2). The selected engine for the study case has 70 kW_{el} at nominal power and a total efficiency of 98.52 %. The dimensioning of the cogeneration system usually follows the thermal power. Because of the hourly variation of the electric demand, different part-loads for the engine functioning but

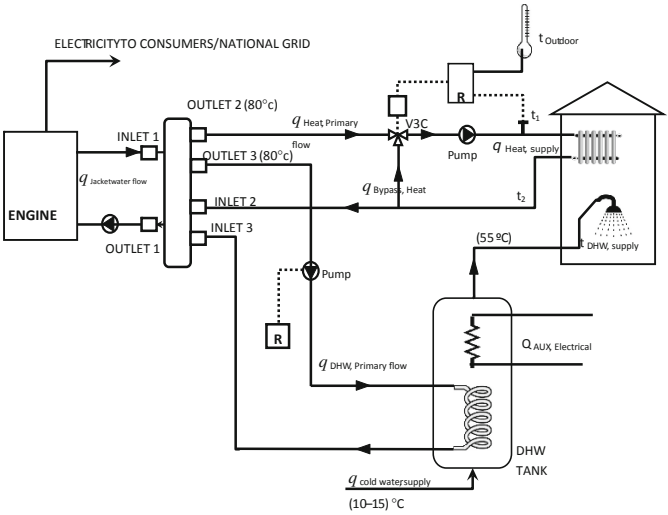

Fig. 1 The sketch of the CHP base system for heating and DHW production

not less than 50 % of the nominal power could be taken into consideration. The total efficiency of the engine is yet influenced by the part-load functioning, so a nominal charge of the engine is recommended.

The engine's performance for each part-load results from the utilization of THERMOFLEX software [8], which is a very useful and powerful tool for CHP

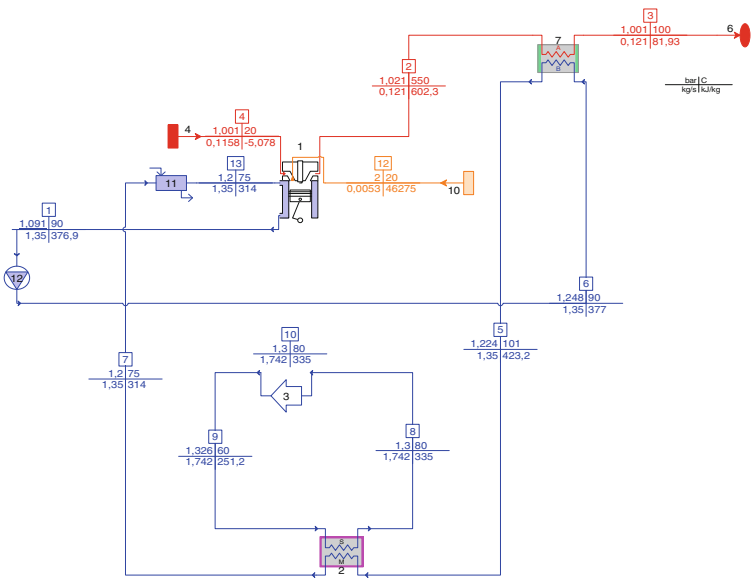

Fig. 2 The THERMOFLEX model for the CHP system, for the winter case

sources analysis. Twenty-four values of different parameters are provided by the software for every part-load. Important information such as fuel consumption, plant emissions, net power etc. can be analysed in order to evaluate the feasibility and benefits of the solution. These values, along with the building and CHP system characteristics, were then converted in the shape of TRNSYS model [9], in order to simulate the dynamic behaviour of the whole system under various climatic conditions. In the present paper the winter situation was studied, for the building located in Bucharest. The comparison between the electrical power supplied by the engine and the electrical needs of the consumers (including consumption for pumps and electric coil peak source for DHW) leads to the following possibilities: to inject the excess electricity production in the National Electric Grid (NEG) or to import electricity from NEG for very short periods of time. Taking into account the elements described before, the Fig. 3 outlines the TRNSYS representation of the system described in Fig. 1.

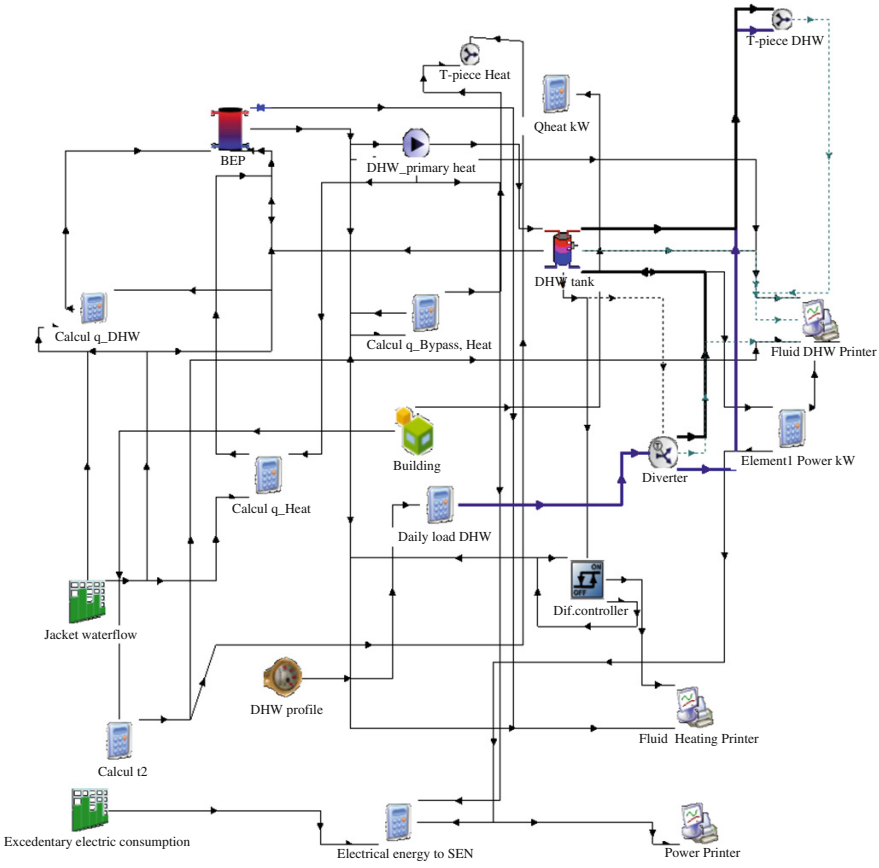

Fig. 3 The TRNSYS model of the system supplied by CHP source

3 Results and Discussions

The simulation of the system described in Fig. 3, follows the January demands for heating, DHW production and electricity purposes. The most interesting parameters were analysed and they were represented in Figs. 4, 5 and 6. The variation of the building heat load ($Q_{HeatLoad}$, kW) and the variation of the DHW load (Q_{DHW_load}, kW) depending on the water consumption are represented in Fig. 4. The supply/return temperatures for heating (t_1 and t_2 respectively, in °C) and the evolution of the DHW temperature ($t_{\_DHW}$, °C) are represented in Fig. 5. The balance between the electrical consumptions for the residential consumers, for the auxiliary heater immersed in the DHW tank and for the two circulating pumps (mounted on primary circuits) allows to finally assessing the amount of excess electricity available to be injected in the National Electricity Grid (NEG). In Fig. 6 there can be noticed the monthly variations of the electrical power consumed for the auxiliary coil immersed in the DHW tank (Power_consumed_DHW, kW), as well as the redundant electrical power returned to the NEG (Power_to_NEG, kW).

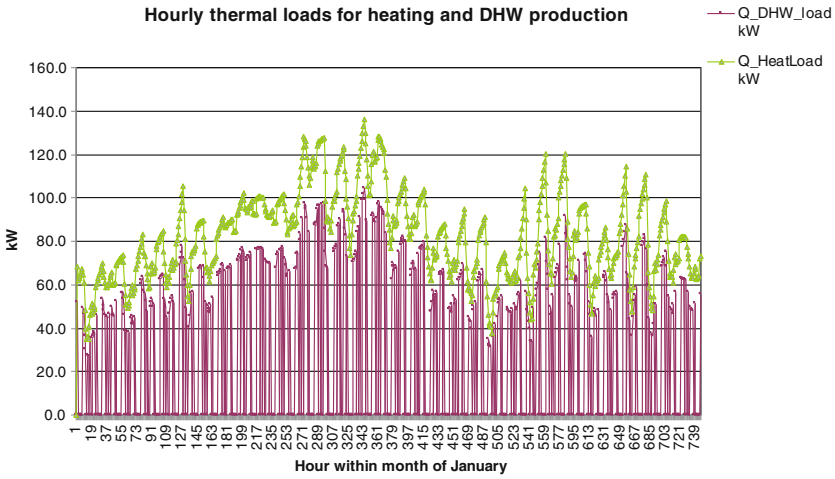

Fig. 4 The monthly variation of thermal loads for heating and DHW production

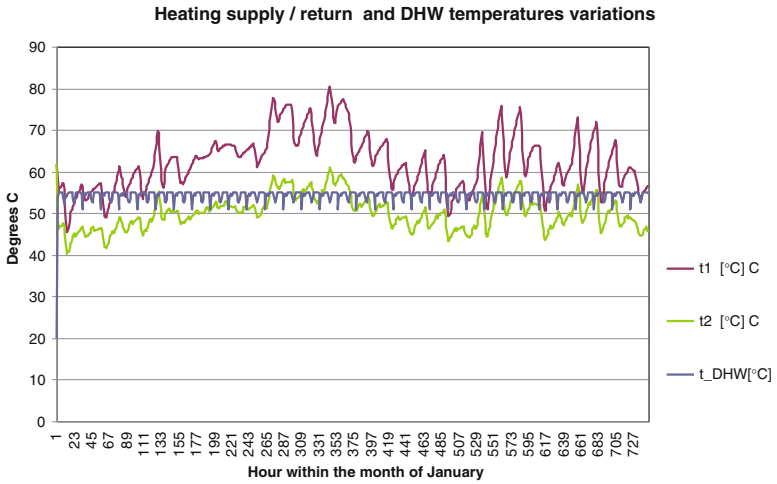

Fig. 5 The monthly variation of the heating supply/return and DHW temperatures

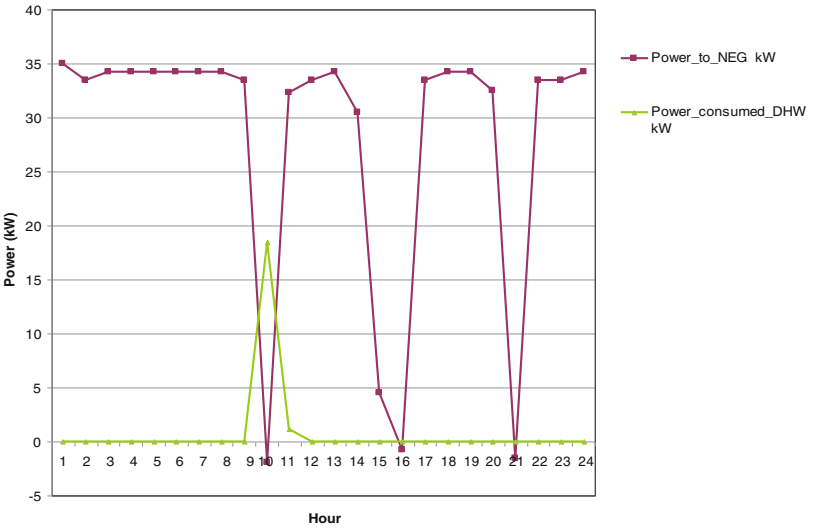

Fig. 6 The daily variation of the electrical powers consumed by the tank heater or provided/requested to/from the NEG

4 Conclusions

Using powerful software for simulation (TRNSYS) and for CHP sources (THERMOFLEX), a model for a system composed from a CHP source for residential consumers was developed. Both thermal loads (for heating and DHW preparation) can be assured by the CHP module by recovering the heat from the cooling water circuit and from the engine exhaust gas.

Most of the time, the electric demand is entirely covered by the CHP module, but there are 2 h when the electricity needs to be imported from the National Grid. An electric coil covers the peak loads for DHW, but the electricity is produced from the CHP module. The number of functioning hours during the heating season rises at 5,424 h, thus justifying the CHP solution.

The research opens new possibilities to identify the best choice for the type and size of CHP sources suited to residential consumers and not only. It was interesting for the authors to find the way to join the CHP source with the building system (which has electrical and thermal load variations depending on climatic factors and on the consumers' behaviour). The case study took into consideration the smallest engine from the available database in order to know and to follow the performances and efficiency for different demands. The residential consumers have their specific for the thermal loads and it was important to see the limits and constrains of the CHP solution. This study case is only the beginning for more complex analyses for small communities and to find the way to identify the most appropriate solution in heating extra-season. The joint of CHP source in winter and other renewable sources for summer will be studied.

Acknowledgments This work was prepared under the frames of a Master and a PhD work, both ongoing in 2014 at the Technical University of Civil Engineering Bucharest.

References

1. Beith, R. (2011). *Small and micro combined heat and power (CHP) systems: Advanced design, performance, materials and applications* (pp. 347–393). Cambridge: Woodhead Publishing Limited.
2. Pehnt, M., Cames, M., Fischer, C., Praetorius, B., Schneider, L., & Schumacher, K. et al. (Eds.) (2006). *Micro cogeneration—towards decentralized energy systems*. Berlin, Heidelberg: Springer.
3. Chamra, L. M., & Magom, P. J. (2008). *Micro-CHP power generation for residential and small commercial buildings* (pp. 1–75). New York: Nova Science Publishers, Inc. ISBN: 978-1-60876-334-4 (e-Book).
4. Catalog of CHP Technology. (2008, December). U.S. Environmental Protection Agency Combined Heat and Power Partnership.
5. Simader, G. R., Krawinkler, R., Trnka, G. (2006). Micro CHP systems: State of the art. *Final Report Deliverable 8 (D8) of Green Lodges Project* (EIE/04/252/S07.38608).

6. Obernberger, I. (2003). State of the art and future developments regarding small-scale biomass CHP systems with a special focus on ORC and stirling engines technologies. *International Nordic Bioenergy conference*.
7. Petchers, N. (2003). *Combined heating, cooling & power handbook: Technologies & applications: An integrated approach to energy resource optimization*. Lilburn: The Fairmont Press, Inc.
8. THERMOFLEX Software with Educational License for 2014.
9. TRNSYS Software with Educational License for 2014.

The Vibration Conversion Energy Harvesting on a Building

Mircea Ignat, Luca Florescu, Andrei Corbeanu and Raluca Turcu

Abstract The paper presents microstructure harvesting microgenerators based on the vibration conversion on electric energy with piezoelectric or electrical induction. We presented a study of vibration sources which can be found in the interior or exterior of a building. There are presented; the parameter and characteristics, the matrix microgenerator connection, the mounting of these harvesting microgenerators on the structure of buildings. The authors also present theoretical aspects; functional models, the specific relations of the conversion effects, and potential applications.

Keywords Energy · Building · Harvesting · Electrical microgenerators · Matrix

1 Introduction

Energy harvesting represents the conversion of energy from the environment and afterwards the generation of electricity, which can be used to power electronic and electric devices. Different technologies can be employed depending on the energy sources. For movement, mechanical harvesters can be used (which can work from electrostatic, piezoelectric and electromagnetic movement). Other energy sources include light, heat, EM transmission, biological energy sources and more. Some

M. Ignat (✉)
INCDIE ICPE CA, Bucurest, Romania
e-mail: mircea.ignat@icpe-ca.ro

L. Florescu
Excelency Centre for Young Olympics-ECYO (Collegium Sf.Sava), Bucharest, Romania

A. Corbeanu
ECYO (Collegium Iulia Hasdeu), Bucharest, Romania

R. Turcu
ECYO-Tudor Vianu National High School of Computer Science, Bucharest, Romania

I. Visa (ed.), *Sustainable Energy in the Built Environment - Steps Towards nZEB*,
Springer Proceedings in Energy, DOI 10.1007/978-3-319-09707-7_7

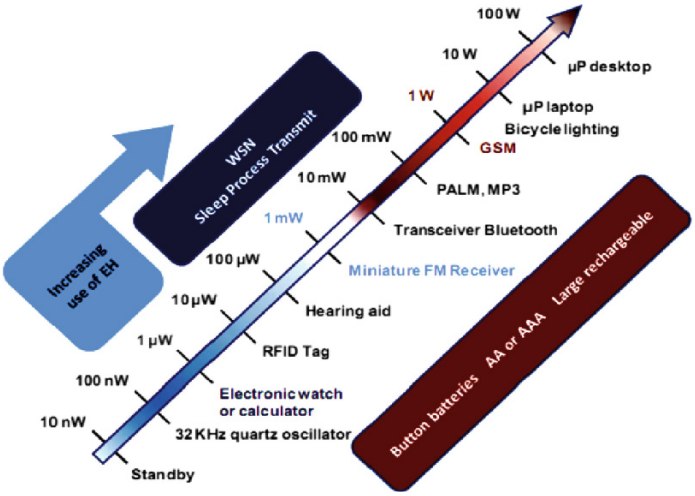

Fig. 1 A situation on the field of harvesting applications versus nano and micropower generated

versions are now even printed. Coupled with new forms of energy storage and lower power electronics, these energy harvesters can negate the need for small batteries in many applications enabling new markets, such as wireless sensors that last for decades or charging of consumer electronics devices.

An image of the harvesting energy applications is showed in Fig. 1 [1].

Table 1 [1] presents a comparison between energy sources from the environment versus harvesting power densities.

An evolution of the micropower supply in different periods is presented in Fig. 2.

An experimental study on the physiological harvesting sources (on the MEMS Laboratory of the National Institute of Electrical Engineering Research-Advanced Research of Bucharest makes the next results obvious (see Table 2):

Table 1 Energy sources from the environment and the densities of harvested power

Energy source	Harvested power
Vibration/motion	
Human	4 µW/cm^2
Industry	100 µW/cm^2
Temperature difference	
Human	25 µW/cm^2
Industry	1–10 mW/cm^2
Light	
Human	10 µW/cm^2
Industry	10 mW/cm^2
RF	
GSM	0.1 µW/cm^2
WIFI	0.001 mW/cm^2

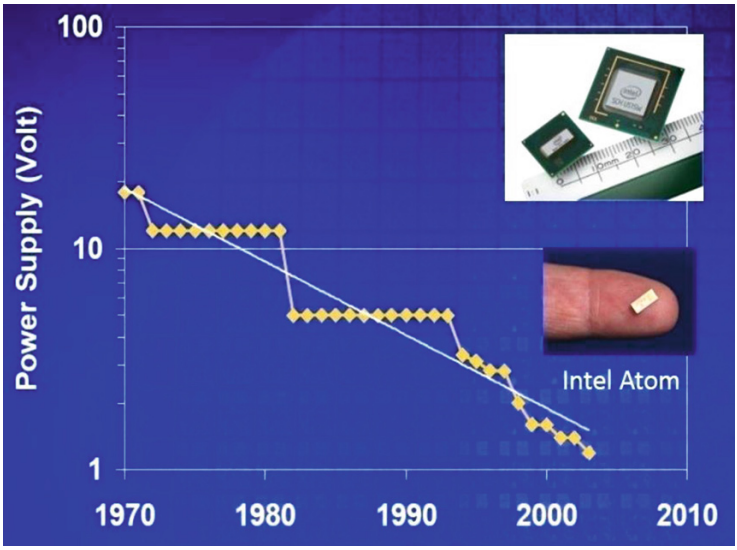

Fig. 2 The evolution of micropower supply from 1970 to 2010

Table 2 Physiological micromechanical harvesting

Query physiological	U_{ef} (mV)	I (μA)	P (mW)
Heartbeat	11	0.03–0.05	0.00033–0.00055
Breathing	105	0.05–0.1	0.00525–0.01
Cough	220	0.05–0.2	0.011–0.044
Spoken	36	0.05–0.15	0.0018–0.0054

The experimental results of the table was effected with the piezoelectric harvesting devices, spz.-planar microharvesting device (see Fig. 6), which was mounted in direct contact with the breast. This experiments was included on a medical rehabilitation project [2].

The data on the harvesting microsources offers a complete image on the harvesting application field.

A new research concept is the exploitation and the energy harvesting of buildings in the condition of decentralized energy production, resulting in the independence of the building's consumption [3]. In addition, the priority based control which is introduced to enable flexible control of building stress and processes, necessitates independent electric microsources.

For this case, a solution is represented by the harvesting of energy sources from ambiental building.

2 The Harvesting Microsources on the Buiding

The main microsources of energy of the buildings can be:

- The mechanical shock and vibration—on the interior and exterior of the building (the walls, the floors, the windows). With the piezoelectric or the electrostrictive conversion on the piezoelectric or the elastomer materials [4–6].
- The microeolian energy on the outer walls and on the roof, with rotating electromagnetic microgenerators.
- The microhydro energy of the small water flow to the nearness of the buildings or the rain. With the rotative electromagnetic microgenerators.
- The microphotovoltaic harvesting microsources to the windows, the outer walls and the roof.
- The electromagnetic radiation (RF waves)—with conversion of the antenna and the inductive—capacitive resonant circuits, on the outer walls.
- The electrochemical microsources, as a result of the pollution (rain or humidity).

In Figs. 3 and 4 there are presented the structure of a building and where and the placement of the main harvesting microsources.

We marked the great surface of the floor which can be used for vibration or shock energy harvesting: possible between 4–64 m^2 (for different room geometries). Also, we analysed the potential surface of the walls (inner or outer) and the windows.

If we consider an energy vibration harvesting density of $\sim 13,7\left[\frac{mW}{cm^2}\right]$ (in the case of the inertial piezoelectric microgenerators) [4, 7] it is possible to obtain a inner energy of the buiding in the field of: 548–0.8768 W!!

It is the ideal energy for supplying the lighting or the monitoring of the building (wireless system included).

In Fig. 5 we presented two piezoelectric harvesting microgenerators and in Fig. 6 different specific piezoelectric harvesting microgenerators for a building (inner or outer).

The harvesting devices presented in Fig. 6 are specific for conversion harvesting on the inner building and were realized by the Excellency Centre for Young Olympics-ECYO.

The authors effected an experimental study in the interior of a building for the vibration harvesting microenergy.

The parameters of the vibration to the inner of buildings were:

- Acceleration; 0.001–0.03 g (when are footsteps on the room),
- Speed; 0.02–0.04 mm/s,
- Amplitude; 0.04–0.09 μm.

The measurements were effected with Vibration Meter VM110 Monitran.

The harvesting device of Fig. 5b has the performances; voltage; 500 mV, and electric current; 1 mA.

Figure 7 represents a specific harvesting vibration signal on the floor, when somebody steps. The experiment was realized with the big inertial device of Fig. 5a.

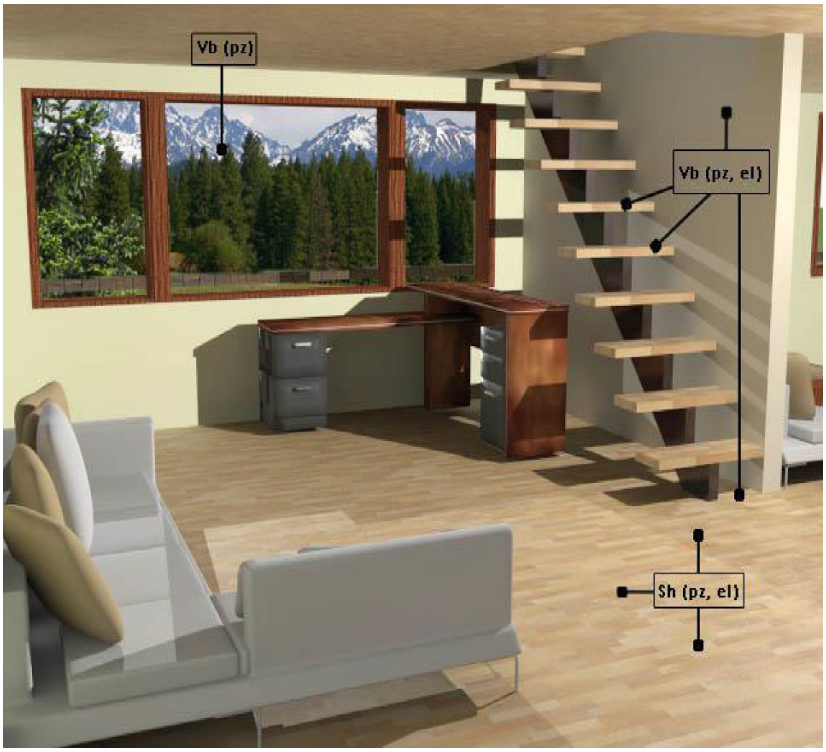

Fig. 3 The harvesting energy microsources in the interior of a building. *Vb* vibration microsource, *sh* mechanical shock, *pz* piezoelectric conversion (*I* piezoelectric effect), *el* electrostrictive conversion on the elastomeric materials

The big inertial harvesting device includes as inertial mass, a steel sphere (183 g), which is in tangential contact with a planar disc of a piezoelectric material PZT 5. The input vibration field is: $0.2\,\frac{mm}{s^2} - 20\,\frac{m}{s^2}$. The output characteristic points the approaching of a person(a men with 80 kg mass) which enters in a room and walks tot the harvesting device.

A characteristic of micromechanical energy versus mass for the inertial harvesting of Fig. 5b is presented in Fig. 8. We make experiments with different inertial mass, with the steel cylindrical geometry (with field: 7–45 g), and characteristic points the kinetic energy to input of the harvesting device. The output voltage of the device has the field: 0.2 mV−0.5 V.

The authors thought of other harvesting devices which can be used in a building; the electrical induction (or linear electromagnetic) harvesting microgenerator with the parameters; voltage; 0.05–1.46 V, micropower; 0.05–3 μW, stroke; 0.5 mm.

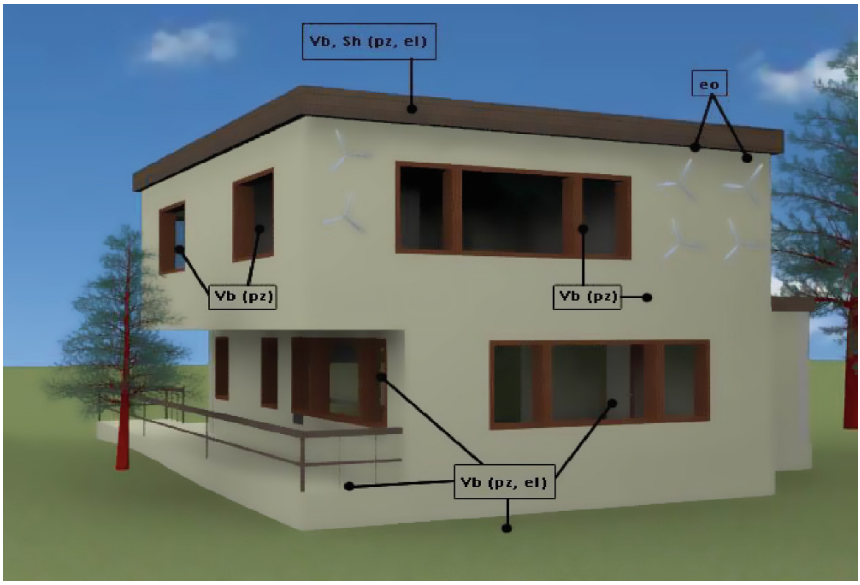

Fig. 4 The harvesting energy microsources on the outside of a buiding. *eo* microeolian energy

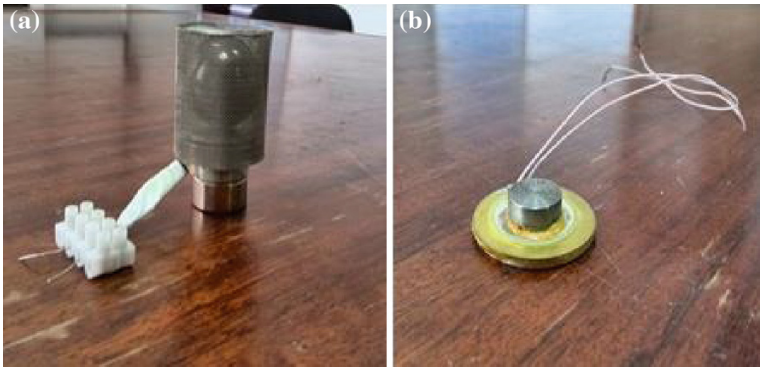

Fig. 5 The piezoelectric inertial harvesting microgenerators. **a** The big inertial system with 183 g mass *ball*, **b** the inertial system with 11.18 g disc geometry

3 A Hybrid Harvesting Generator

In the Excellency Centre for Young Olympics-ECYO, we designed and experimented on a independent hybrid harvesting source [8] (Fig. 9). This harvesting source is a demonstrator which combines all type of microenergies which could be

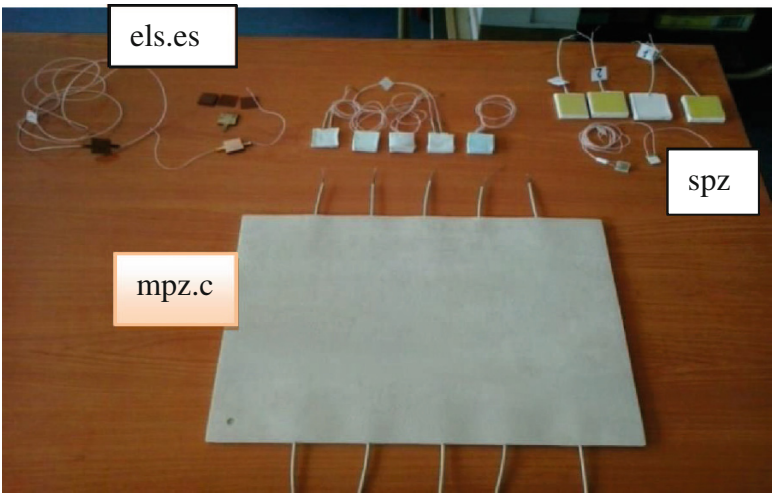

Fig. 6 The different harvesting specific convertors. *spz* single piezoelectric harvesting element, *els.es* the single elastomeric electrostrictive harvesting element, *mpz.c* the matrix piezoelectric carpet (for floor and staircase)

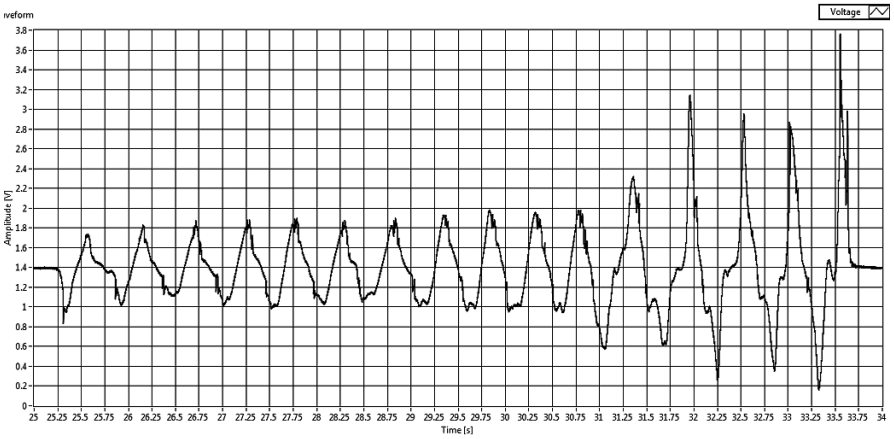

Fig. 7 A specific vibration harvesting signal to a big inertial device

harvested from a building (interior and exterior). In Table 3 is presented the harvesting microenergy specific to each surface of the cube.

The each surface of this hybrid generator represents an other energy form, see Fig. 10.

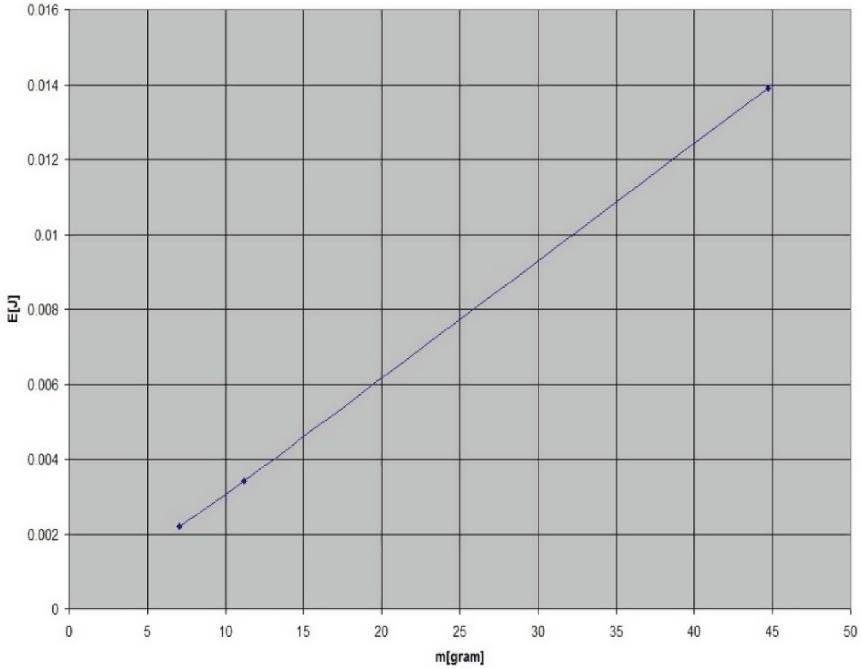

Fig. 8 The characteristic of the micromechanic energy versus mass of inertial element

Fig. 9 The energy harvesting cube

Table 3 Characteristic of the energy harvesting cube

The cube face/energy conversion	The convertor/microgenerator type/characteristics/gauge, dimensions	The microenergy produced experimental/theoretic maximum estimation
A. Microhidro electromagnetic generator	Electric DC rotative microgenerator	2 W/4 W
B. Microeolian electromagnetic generator	Electric DC rotative microgenerator	2 W/4 W
C. Piezoelectric harvesting conversion microgenerator	Piezoelectric disc	0.6 W/1 W
D. Electrochemical harvesting conversion	Pt-carbon-NaCl micro-source	0.5 W/1.5 W
E. Microgenerator harvesting of the residual electro-magnetic waves	Antenna-accord LC circuit-rectifier	2 mW/4 mW
F. Photovoltaic conversion harvesting energy	Photovoltaic cell	0.5 W/1.5 W

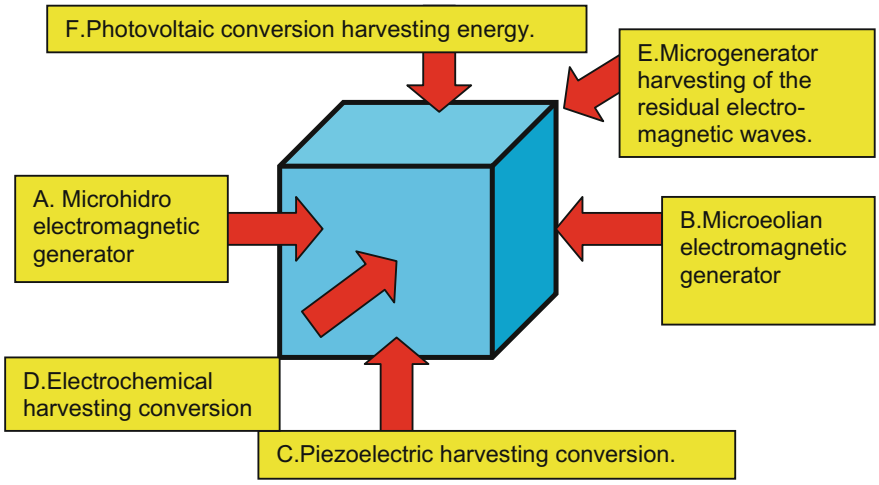

Fig. 10 The distribution of the energy to the cube surfaces

The electric micropower parameters are presented in Table 3, where **The microenergy produced**, represents the experimental results for each harvesting microgenerator (on each surface), and **Theoretic maximum estimation** represent the potential power to the ideal condition.

A. Microhidro electromagnetic generator and B. Microeolian electromagnetic generator are two DC permanent microgenerators with micromechanical multiplier with 1/10 ratio, C. Piezoelectric harvesting conversion microgenerator is based on

the PZT5 disc (typ spz), surface C is in contact with medium (floor by exemple), D. Electrochemical harvesting conversion is a neu electrochemical source, E. Microgenerator harvesting of the residual electro-magnetic waves, include an outlet antenna of minimum 5 m length, F. Photovoltaic conversion harvesting energy is a commercial photovoltaic cell with 81 cm^2.

4 Conclusions

The main purpose of this paper is to emphasize the possibilities of to harvest the existent microenergy in the inner of a building and the different modes of exploitation.

The buildings are responsible for 30–40 % of the primary energy demand. As such, energy efficiency is an important performance aspect. Thus, the usage of harvesting microgenerators represents a scientific and economic target.

The authors presented some experimental aspects of the use of the harvesting energy to the feed a building, certain needs; wireless, microsensor monitoring, the electric lighting and consider energy harvesting in building to be an important target and a great research challenge.

The new aspects that the paper presents are;

- The identification of the places with a distinct vibration or shock micromechanical energy, also and other energies;
- The different harvesting conversion microdevices;
- The harvesting piezoelectric microgenerator, the electromagnetic DC Microgenerator, the radio frequency microgenerator.

Acknowledgments This work was possible thanks to support programme PN-09-35-01-01/2009 of ANCS Romania.

References

1. Energy Harvesting and Storage for Electronic Devices 2014–2024, Forecasts, Technologies, Player.
2. Ignat, M., Hristea, G., Cazacu, M., & Nica, A.S. (2013). *Electrostrictive microsensors based on the elastomeric polymers for medical rehabilitation procedures*, EUROEAP2013, Dubendorf, Switzerland, 25–26 June, pp. 52–54.
3. van Goch T. A. J. (2014). *Connecting office buildings to the smart grid: harvesting flexibility*. Dissertation, Stan Ackermann Institute, Eindhoven.
4. Mitcheson, P. D., Reilly, E. K., Toh, T., Wright, P. K., & Yeatman, E. M. (2007). Performance limits of the three MEMS inertial energy generator transduction types. *Journal of Micromechanics Microengineering 17*, 211–216 (IOP Publishing).

5. Mitcheson, P. D., Green, T. C., Holmes, A. S., & Yeatman, E. M. (2004). Architectures for vibration-driven micropower generators. *Journal of Microelectromechanical Systems, 13*, 429–4240.
6. Church, A. H. (1957). *Mechanical Vibrations*. New York: Wiley.
7. Choi, W. J., Jeon, J. H., Jeong, J. H., Sood, R., & Kim, S. G. (2006). Energy harvesting MEMS device based on thin film piezoelectric cantilevers. *Journal of Electroceramics, 17*, 543–548.
8. Corbeanu, A., & Florescu, L. (2014). The harvesting energy cube. *Project to the INFOMATRIX 2014, International Project Olympiad*, *Bucharest*, 8–11 may.

Comparative Study on Achieving an Energy Efficient Lighting Using Classical and Modern Sources

Anca Manolescu, Francisc Sisak and Mircea Draghici

Abstract The article discusses how it is more efficient, from energy point of view, the achievement of a lighting system using lamps equipped with LED sources in comparison with fluorescent sources. The results obtained help specialists in the field to understand the importance of energy saving lighting in administrative buildings.

Keywords Lighting · Lighting source · LED · Efficiency

1 Introduction

Global climate changes, Kyoto Protocol objectives regarding CO_2 emissions and environmental legislation to promote energy efficiency, by reducing the volume of wasting resources and the use of hazardous substances, are factors to be taken into account when is established a lighting solution, both in the case of buildings located in service, as well in the case of newly constructed.

From the point of view of energy consumption, lighting allows significant savings that can be obtained if they opt for efficient lighting systems energy.

The energy efficiency of lighting systems follows three main directions: making light sources with more efficient light; implementation of auxiliary equipment with high efficiency and low noise transmitted in the mains power supply and with a suitable management of lighting systems.

Choosing a suitable light source is the most important role in providing energy performance of the system of lighting, this being the receiver with electrical consumption the largest of electricity within the lighting systems.

A. Manolescu (✉) · F. Sisak · M. Draghici
Faculty of Electrical Engineering and Computer Science, Transilvania University of Brasov, Brasov, Romania
e-mail: manolescuanca@yahoo.com

I. Visa (ed.), *Sustainable Energy in the Built Environment - Steps Towards nZEB*, Springer Proceedings in Energy, DOI 10.1007/978-3-319-09707-7_8

Table 1 Comparative luminotechnic features of lighting sources

Luminotechnic features	LFA	LED
Luminous flux—φ[lm]	1,300–8,850	150
Nominal power—P[W]	14–120	2–22
Luminous efficiency—e[lm/W]	61–109	20–75
Luminance—L[cd/m^2]	0.85–4.1	30×10^6
Colour temperature—T_c[K]	2,700–6,500	2,700–6,500
Color rendering—Ra[−]	50–93	65–90
The operating time [hours]	50,000–60,000	30,000–50,000

Light source type must be chosen in such a way as to ensure visual comfort required to carry out their duty or creating a suitable ambient light. Their choice shall be made taking into account the luminotechnic characteristics, among which, the most important ones are:

- Luminous flux;
- Nominal power;
- Luminous efficiency;
- Source luminance;
- Colour temperature;
- Color rendering;
- The operating time

By comparing from the point of view of luminotechnic features two types of lamps (fluorescent and LED), may be observed considerable differences (Table 1) [1, 2].

2 Study Case

For a better understanding of the differences described above, it may be possible to make luminotechnic studies using specialized computing programs.

The luminotechnic study was carried out on a space with destination office with an area of about 30 sqm, considering, in accordance with normative NP-061-2002, with a lighting level E = 500 lx and a height of the working plan 0.7 m [3, 4].

The results obtained are shown below.

2.1 Luminaire Fitted with Discharge Lamps Mercury Vapor at Low Pressure or Fluorescent Lamp Socket, Type ELBA, FIRI-04-418 P [5]

After calculations, has resulted in a need for 9 luminaires, uniformly placed (Figs. 1, 2, 3).

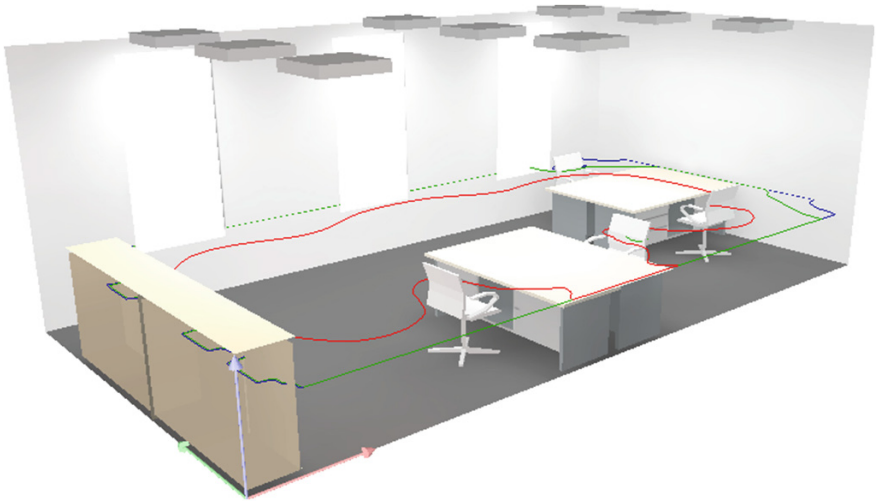

Fig. 1 Drawing isolux corresponding curves for luminaires equipped with fluorescent tube lamps —3D view

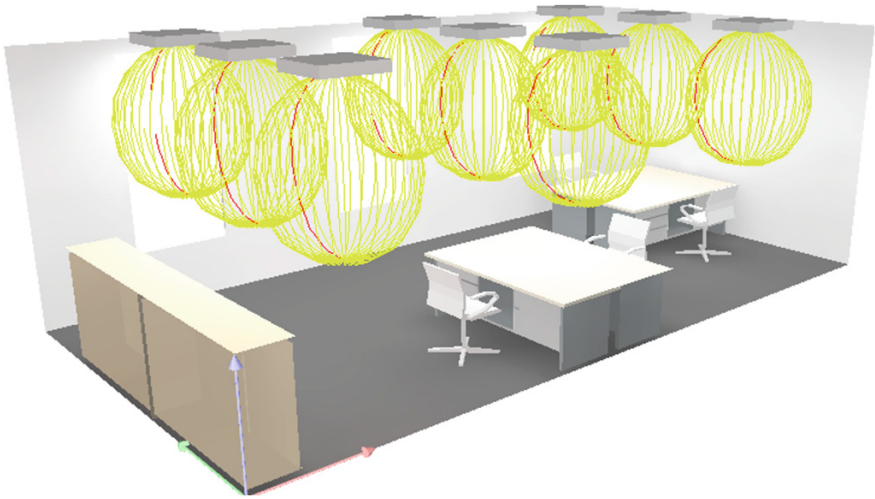

Fig. 2 Light dispersion for luminaires equipped with fluorescent tube lamps

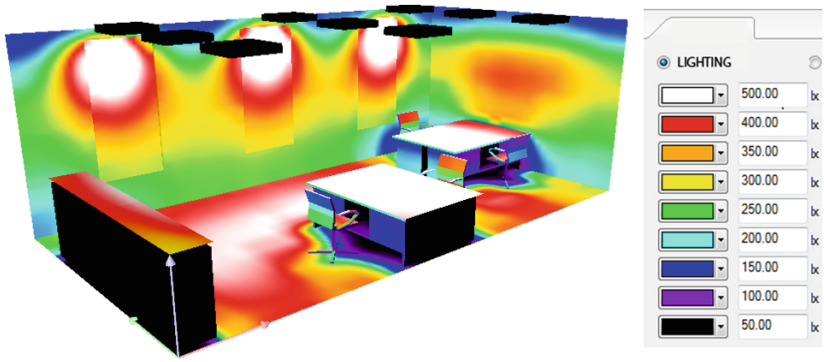

Fig. 3 Distribution of lighting for luminaires equipped with fluorescent tube lamps

2.2 LED source, ZUMTOBEL type, 42181854 LFE E56W LED 830 [6]

After calculations, has resulted in a need for 6 luminaires, uniformly placed (Figs. 4, 5, 6).

Compliance with the data entered in the calculation assumptions made has resulted in luminotechnic solutions different from the point of view of lighting values and coefficients of uniformity (Figs. 7, 8).

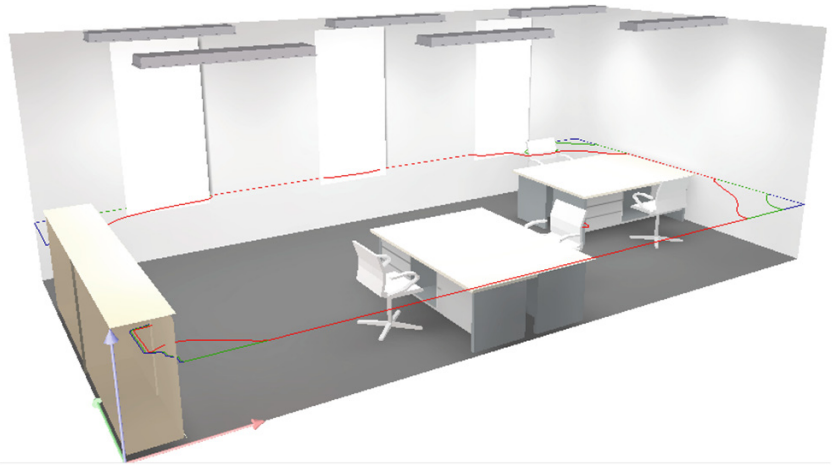

Fig. 4 Drawing isolux corresponding curves for luminaires equipped with fluorescent tube lamps —3D view

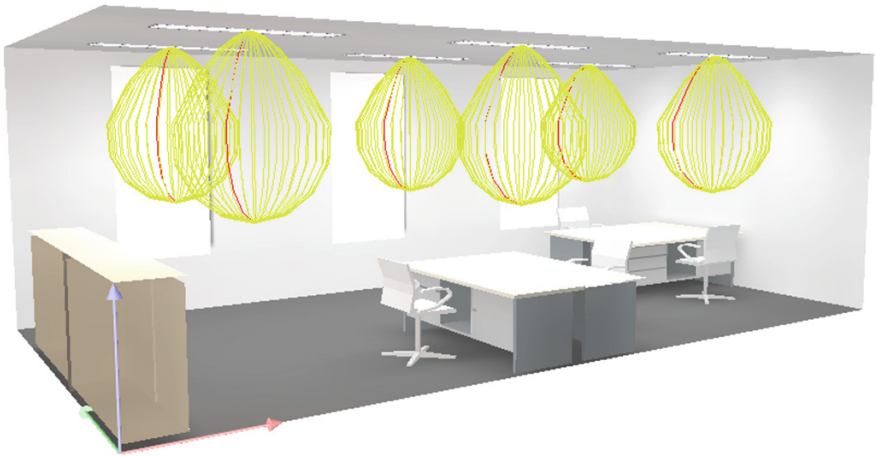

Fig. 5 Light dispersion for luminaires equipped with LED sources

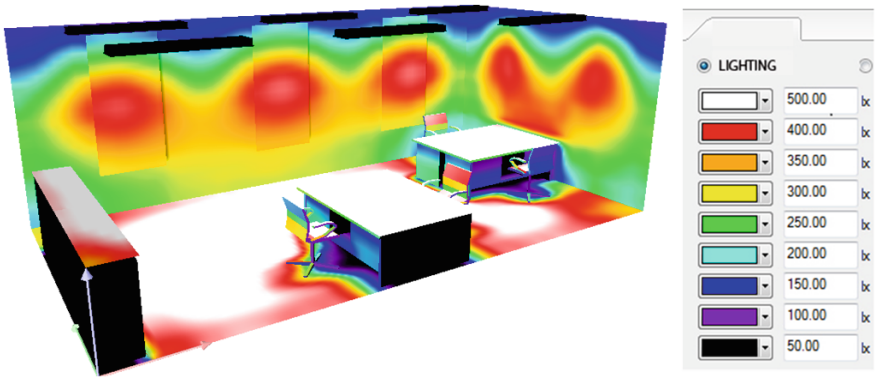

Fig. 6 Distribution of lighting for luminaires equipped with LED sources

3 Analysis of the Results Obtained and Remarks

By analysing compared the luminaries fitted with fluorescent tube lamps and those with LED, in accordance with schedule above, we could see the following photometric results (Table 2).

With all that they have been used luminaires fitted with 2 sources with LED light 56 W, total power output is 45 % less than that of the luminaire equipped with 4 fluorescent sources of 18 W.

Even if indirect lighting values are approximately equal, there is a significant difference between the average directly (75 %) and by default and between the total average.

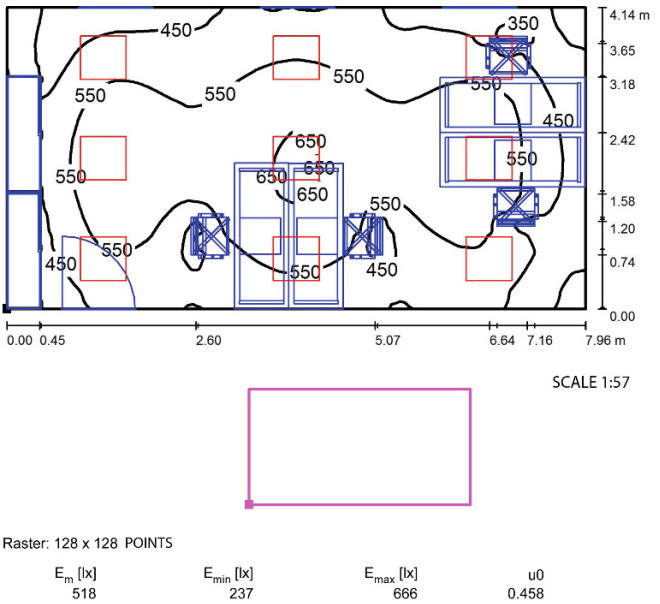

Fig. 7 The isolux corresponding distribution curves—luminaires equipped with fluorescent sources

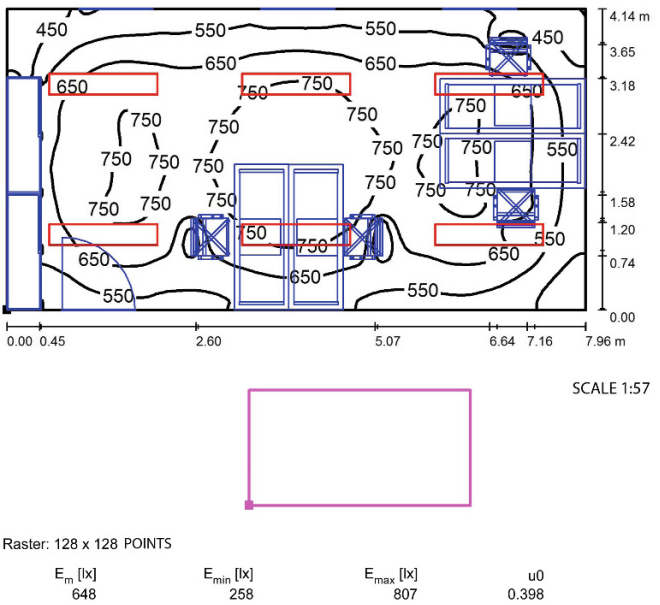

Fig. 8 The isolux corresponding distribution curves—luminaires equipped with LED sources

Table 2 Comparative results of photometric lighting sources

Photometric results	LFA	LED
Total luminous FLUX—φ—[lm]	28,887	31,534
Total power—P—[W]	756	336
Specific power—p_s—[W/m^2]	22.94	12.20
Direct lighting average E_{md}—[lx]	397	525
Indirect lighting average E_{mr}—[lx]	122	123
Total lighting average E_m—[lx]	518	648
E_{min}/E_{max} Effective working area	0.357	0.320
E_{min}/E_{med} Area for working plan	0.458	0.398

The coefficients of uniformity at the plan level useful are comparable (u = 0.458 as compared to the u = 0.398 in the case LED source).

Although they have low power, LED sources have a high luminous flux, in comparison with conventional sources.

In the case LEDs, the light is directed to a specific location without the use external reflector while in the case of sources incandescent is spread in all directions, depleting a great quantity of light.

Carrying out a system of LED lighting can achieve an economy of up to 80 % of the energy consumption, as compared to traditional lighting solutions.

In the case presented above, for a life of 50,000 h, the economy by achieving lighting using LEDs is approximately 2,500 €.

4 Conclusions

Even if they are more expensive, as investment, than most lights (a luminous flux of 1 lm is more expensive in the case of leds), especially because of technologies involved in the manufacturing process, this disadvantage is compensated for the advantages listed above, so that, overall, a lighting system with LED is cheaper (from the point of view of the investment, maintenance and exploitation) than one similar to fluorescent light [7].

Trend is waiving classical sources of light, energy and promotion inefficient light sources performance, category to which they belong LEDs. European legislation provides for replacing up to 2017 of the sources of light with plug and gas discharge.

References

1. Moroldo, H. (2013). Notes the progress—III-rd engineers day, specialized training facilities for civil engineering. Bucharest: Faculty of Engineering of Installations, U.T.C.
2. Mira, N., Bianchi, C., Moroldo, D. Georgescu, A., & Moroldo, H. (2011). ş. a.—The workshop electrical installations and automation. Bucharest: Publishing House Artecno Bucharest S.R.L.
3. NP-061-2002, Normative for the design and execution of artificial lighting systems in buildings.
4. Romanian National Committee of Lighting—CIE guide the interior lighting for workplaces (publication CIE DS 008.2 /E). (2001). Bucharest: Matrix Rom Publishing House.
5. SC ELBA SA—Luminaires catalog and lighting systems 2012–2013. Timisoara, 2013.
6. Zumtobel., Inc.—Technical Datasheet 42181854 LFE E 56 W LED830 M600L15 LDO KA SRE.
7. Ispas, G. (2008). Contributions to the study of the interior lighting systems specialized equipped with electroluminescent diodes (LED).

Characteristics of Electrical Energy Consumption in the Social Housing

Nikolay Mihailov, Todor Todorov, Aleksandar Evtimov, Daniel Todorov and Lyuben Iliev

Abstract In the period 2011–2013 a team from "Angel Kanchev" University of Ruse has worked within international project Balanced European Conservation Approach (BECA), financed under the Information and Communication Technologies Policy Support Program. The project's main goal was to provide energy services to social housing sector using modern measuring devices and licensed software. With them each consumer can track down online his own consumption of electrical energy. This article shows the results received from studying the load profiles of electric energy consumption in a residential block of apartments. The load profiles were analyzed using the software product Statgraphics. The dynamics of the studied random process is shown making a statistical analysis of the correlation functions and the spectral densities of the electrical consumption. As a result, the statistical assessments of the electrical consumption create the possibility for the consumers to efficiently manage their electrical loads.

Keywords BECA · Measuring devices · Electrical energy · Statistical analysis

1 Introduction

It is well known, that one of the main goals of the strategy EUROPE 2020 is connected with reducing consumption of electricity with 20 %, together with 20 % usage of renewable energy sources (RES) from the total energy mix, compared to the situation from the year 1990. This goal can be accomplished with studying the load profiles of different types of powerful users and studying the possibilities of using RES on the other hand. As a result from the reformation of Bulgarian industry, main user of electrical energy appears to be the residential sector.

N. Mihailov (✉) · T. Todorov · A. Evtimov · D. Todorov · L. Iliev
"Angel Kanchev" University of Ruse, 8 Studentska str., 7017 Ruse, Bulgaria
e-mail: mihailov@uni-ruse.bg

I. Visa (ed.), *Sustainable Energy in the Built Environment - Steps Towards nZEB*,
Springer Proceedings in Energy, DOI 10.1007/978-3-319-09707-7_9

2 Materials and Methods

The aim of this work is to study the consumption of electrical energy, inside a typical residential block of flats and to determine the parameters of load profiles for the different climate seasons.

A typical block of flats, with two sections of 24 apartments each, is chosen to be the object of investigation. On each floor there are one-room, two-room and three-room flats. There is no central heating system installation and there is no thermal insulation applied on the building. Accurate data for the energy consumption is being collected by the help of WiFi data acquisition (Fig. 1) [1–3].

The system allows measuring the used electrical energy and water for a certain period of time. The dynamics of the random processes of water and electricity consumption determines this particular period of time. The installed electricity meters and water meters inside each flat are connected to Industrial PLC device which acts like a Gateway. This device transmits the acquired data to a network router, through a cable using the IP protocol. The router is connected to the network of the network service provider (NSP), through a broadband PPPoE connection. A secondary tunnel type connection (from the type VPN) is configured to allow access through the university's network FireWall reaching the VPN&MSMQ Broker server. This server sends the data to a DATA BASE server. A WEB Server, is configured to visualize the collected data, which allows the end user to check the values of his consumption. The measuring devices are digital electricity meters for

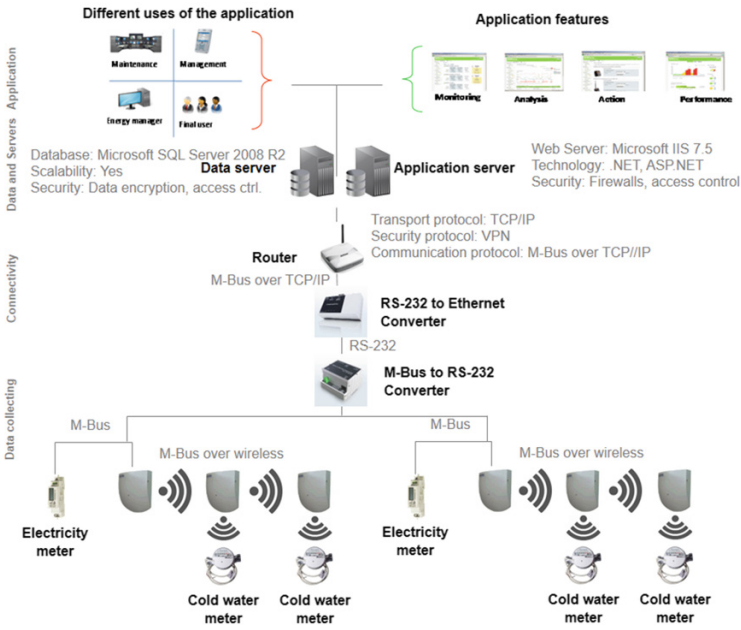

Fig. 1 Topology of data acquisition system, installed inside block 50, housing estate "Druzhba"

active energy with inbuilt M-BUS communication (DHZ 5/63M-BUS 2/230-1), installed inside the floor electrical panel for each flat. The water, consumed by the inhabitants, is measured by digital water meters (from the type ResidiaJet, Qn1.5, 3/4, 30 °C), with installed radio communication device (type Base R) and concentrators BaseNet. There is also one common electricity meter and water meter installed for each entrance of the block. The meters, power supply units and communication devices are placed inside electrical panel with IP65 degree of protection. Every user can monitor via internet his own consumption of water and electrical energy, thus providing a possibility for management.

The measurements are made in the period of years 2012–2013. For the needs of this work, only the electricity consumption is being analyzed.

A detailed knowledge of the electrical demand is required for building intelligent electricity network (smart grid), that distributes power accounting to the information for the behaviour of all of its components. Thus, improved efficiency, reliability, sustainability and economics of the electricity services are provided. Smart grid also helps increasing the power capacity using the available infrastructure. The reliability parameters are also improved—less time and number of power expectation interrupts, improved service life of assets of the system. Voltage control and two way flow of the energy also contributes for better efficiency. Smart grid also enables integration of modern technologies and integration compatibility.

The studies show, that electrical consumption is a random process. Its characteristics and parameters are determined by the software product STATGRAPHICS CENTURION XV. For example in Table 1 data is presented for December.

Some of characteristics of the consumption are calculated: mean value, standard deviation, coefficient of variation. Minimum and maximum value of the load are determined. The confidence intervals of the mean value and standard deviation are calculated at confidence probability 0.95.

The correlation of the energy consumption between different flats is determined (Table 2).

Table 1 Statistical analysis for electrical diurnal consumption in kWh for different flats (month December 2013)

Estimations	Flat 1	Flat 2	Flat 3	Flat 4
Sample	24	24	24	24
Mean value	0.18	0.21	0.13	0.21
Standard deviation	0.05	0.061	0.022	0.059
Coefficient of variation, %	27.05	28.46	16.79	28.05
Minimal value	0.105	0.1447	0.092	0.122
Maximal value	0.259	0.343	0.165	0.320
Confidential limits of mean value	0.161–0.202	0.19–0.241	0.120–0.140	0.185–0.234
Confidential limits of standard deviation	0.038–0.069	0.048–0.086	0.017–0.031	0.046–0.082

Table 2 The correlation of the energy consumption between different flats

	Flat 1	Flat 2	Flat 3	Flat 4
Flat 1		0.7676	0,5732	0,9100
		(24)	(24)	(24)
		0.0000	0.0034	0.0000
Flat 2	0.7676		0.7645	0.5734
	(24)		(24)	(24)
	0.0000		0.0000	0.0034
Flat 3	0.5732	0.7645		0.5931
	(24)	(24)		(24)
	0.0034	0.0000		0.0023
Flat 4	0.9100	0.5734	0.5931	
	(24)	(24)	(24)	
	0.0000	0.0034	0.0023	

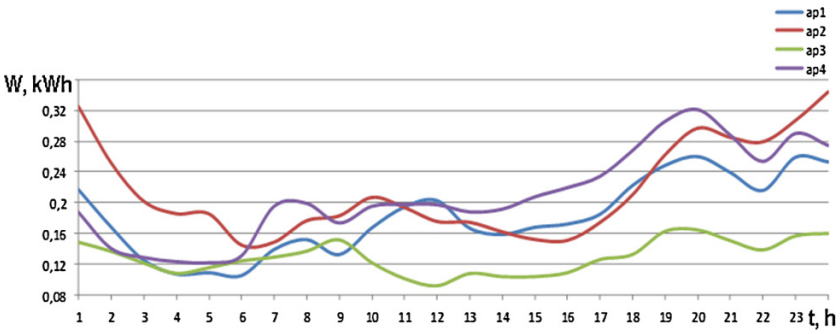

Fig. 2 Diurnal load profile of different flats

From the results inside the table, it is visible, that correlation between the daily hourly energy consumption for different flats is positive. Figure 2 shows the uneven distribution of the load.

Preliminary studies show, that energy profile of the demand and generated power from photovoltaic (PV) panels, intended to be integrated in the roofs, does not match. This means, that quantitative analysis is required for calculation of this difference, by calculating the seasonality factor [4–6]:

$$K_S = \frac{W_d \min}{W_d \max}, \tag{1}$$

Table 3 Minimal and maximal diurnal energy consumption and seasonality factor

Month	Minimal diurnal value for the energy consumed $W_{d\ min}$, kWh	Maximal diurnal value for the energy consumed $W_{d\ max}$, kWh	Seasonality factor K_S
January	3.61	5.96	0.61
February	3.81	5.35	0.71
March	3.02	5.43	0.56
April	2.38	4.43	0.54
May	2.21	2.84	0.78
June	1.75	2.74	0.64
July	1.31	2.53	0.52
August	1.89	2.74	0.69
September	1.93	2.74	0.70
October	2.27	3.98	0.57
November	1.75	4.17	0.42
December	3.37	5.58	0.60

where:

$W_{d\ min}$ is the minimal consumed diurnal active energy for the month, kWh;

$W_{d\ max}$ the maximal consumed diurnal active energy for the month, kWh.

The results show significant differences in the monthly consumption of electrical energy, in the block (Table 3, Fig. 3).

The explanation can be found in using electrical energy during autumn–winter season for heating, the schedule of usage of flats during the summer time, etc. On the other hand, the value and relatively constant demand, during the period May–

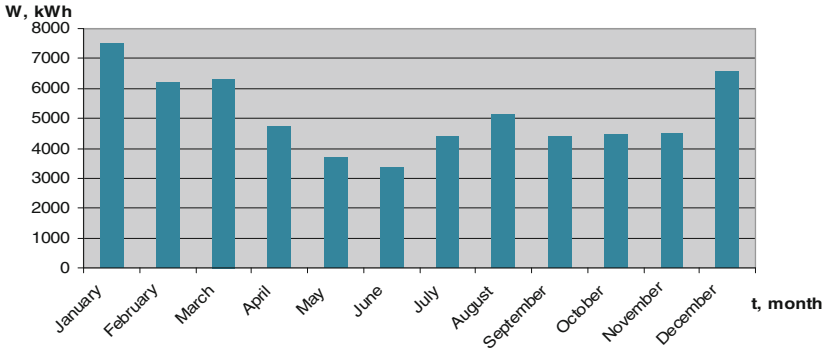

Fig. 3 Monthly load profile of a typical municipal block of flats

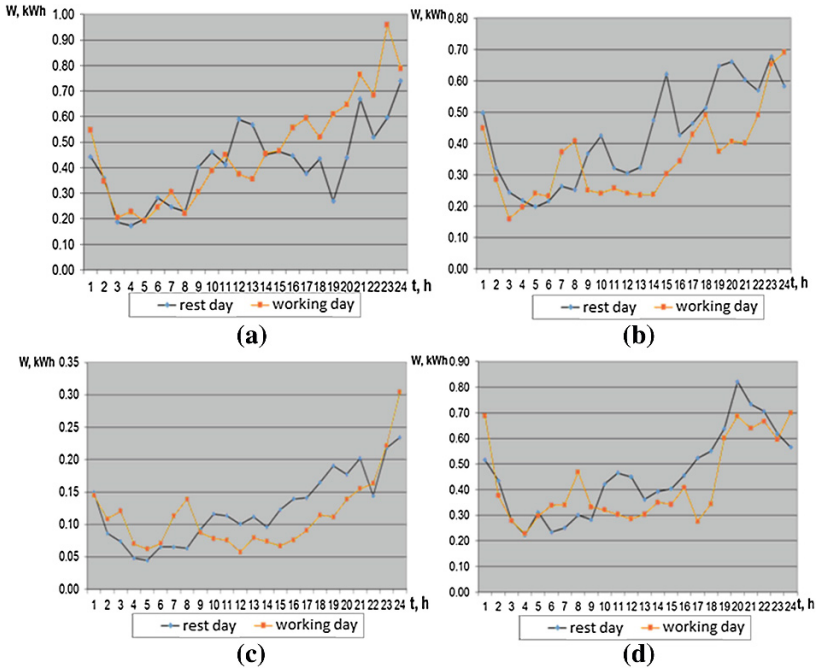

Fig. 4 Diurnal load profile of a typical summer day in May (**a**), June (**b**), July (**c**) and August(**d**)

September, are suitable for local PV generation. Good knowledge of the day-and-night energy profile is required at all cases (Fig. 4).

One of the most important analytical characteristics for evaluation of diurnal load profiles is the filling coefficient. It provides an opportunity to make decisions for equalization of the diurnal, monthly and seasonal load profiles. The obvious irregularity of the profile is estimated by the help of the filling coefficient:

$$K_f = \frac{W_d}{24 \cdot W_{d\max}}, \tag{2}$$

where:

W_d is the total diurnal value of the active energy used, kWh;

$W_{d\ max}$ maximal diurnal value, kWh

This coefficient varies for working and rest days respectively in the ranges (0.53–0,62) and (0.38–0.56). Through appropriate control of charge/discharge processes of the PV storage battery, better demand profile can be achieved.

3 Conclusions

The results can be used for making the following conclusions:

(a) An original measurement and information system, which provides new type of electrical service, where the users can monitor their diurnal consumption on-line, is developed. The user-friendly graphical and table visualization of the database allows the users to make comparative analysis and to reduce the energy consumption (for example, turning on/off power domestic loads, using only part of the installed power, etc.);
(b) Typical load profiles are created and investigated in the domestic sector. A database is collected for the minimal and maximal monthly electrical consumption, seasonal and filling coefficient for a typical load profile.
(c) The monthly electrical consumption for the studied residential block of flats varies between 3,383.9 kWh (June) and 7,522.1 kWh (January). It can be noted, that with the analysis of the demand profile factors of other buildings and facilities, a database can be acquired, that can be useful in solving various tasks, connected with design, building and exploitation of smart grid system in the residential sector.

Acknowledgments The present paper has been developed with the financial aid of the European social fund. The "Angel Kanchev" University of Ruse is solely responsible for the content of this document and it can in no circumstances be viewed as the official position of the European Union or the Ministry of Education and Science.

Project:No BG051PO001-3.3.06-0008 "Aiding the growth of researchers in the engineering field and the information technologies"

References

1. Ekanayake, J., Liyanage, K., Wu, J., Yokoyama, A., & Jenkins, N. (2012). *Smart grid: technology and applications*. London: Wiley.
2. Weranga, K., Kumarawadu, S., & Chandima, D. P. (2013). *Smart metering design and applications*. Berlin: Springer.
3. Project № 270981.Balanced European Conservation Approach-ICT services for resource saving in social housing (BECA), beca-ruse.eu
4. Feodorov, A. A., & Risthain, E. M. (1981). *Electrical power supply of factories*. Moscow: Energia.
5. Kudrin, B. I., & Prokopchin, V. V. (1988). *Electrical power supply of factories*. Minsk: University Press.
6. Platikanov, S. (2011). *Electrical supply*, TUG.

Towards nZEB—Sustainable Solutions to Meet Thermal Energy Demand in Office Buildings

Macedon Moldovan, Ion Visa and Daniela Ciobanu

Abstract The transition towards Nearly Zero Energy Buildings (nZEB) requires the implementation of clean, efficient and affordable energy mixes in buildings. While the first two pre-requisites are related to a technical breakthrough that is expected for increasing the efficiency and sustainability of the renewable-based energy mixes implemented in the built environment, the affordability is directly related to the costs of these mixes, particularly to the initial investment. The paper analyses the affordability of the renewable based energy mixes for thermal energy production and outlines that the initial investment is exponentially increasing with the specific energy demand of the building. The calculations are focused on office buildings, having specific features that impose a lower thermal energy demand as compared to residential or other buildings with special regime (hospitals, hotels, etc.). Even in these conditions, the analysis shows that installing a renewables-based energy mix that covers 50 % of the thermal energy demand represents an affordable action if the buildings have a specific thermal energy need less than 80 kWh/(m^2 year). A case study is discussed and support the general cost model, considering a thermal energy mix possible to be installed in the built environment and consisting of a solar-thermal system (with flat plate collectors) and a heat pump, along with a photovoltaic array able to deliver the energy required for powering the heat pump.

Keywords Energy efficiency · Low energy building · Nearly zero energy building · Renewable energy sources · Renewables energy mix

M. Moldovan (✉) · I. Visa · D. Ciobanu
Renewable Energy Systems and Recycling R&D Centre, RES-REC, Transilvania University of Brasov, Eroilor 29, Brasov 500036, Romania
e-mail: macedon.moldovan@unitbv.ro

I. Visa (ed.), *Sustainable Energy in the Built Environment - Steps Towards nZEB*, Springer Proceedings in Energy, DOI 10.1007/978-3-319-09707-7_10

1 Introduction

Nearly Zero Energy Building (nZEB) status will be mandatory for all new buildings starting with January 1st 2021 in European Member States [1]. Existent buildings undergoing major renovation shall also comply with these new regulations. This milestone is earlier set, on January 1st 2019, for public authorities' buildings. This is a necessary answer to the increase in the building stock and in the associated energy consumption expected due to the global population growth, estimated at 10 billion up to 2050 [2].

In a first step, to get the nZEB status, integrated design should consider cost-effective measures to reach high energy performance for buildings, considering the climatic conditions and the specific requirements of that buildings. The target is to lower the energy consumption used for heating, cooling, ventilation, hot water and lighting, while preserving the internal comfort. The second step focuses on the sustainable production of the needed energy, by on-site or nearby installed renewable energy systems.

The renewable energy systems (RES) implementation is related to the type of building, its location, the available space for RES installation, architectural design, but also initial and operating costs. There is a broad diversity of buildings types, out of which the residential sector has a major contribution (75 %) to the energy consumption, followed by the wholesale and retail (7 %), offices (5.75 %) and educational buildings (4.25 %) in EU [3].

This paper focuses on office buildings because large companies are likely to invest for reaching the nZEB status, as an open commitment towards sustainability. These buildings have some special features that influence the design criteria:

(a) shape, orientation and envelope;
(b) functional zones/rooms in which the office building is divided;
(c) use of space, the daily schedule, the occupancy;
(d) air pollution and odour control etc.

The consequences related to this specificity are further detailed.

(a) *Office buildings shape, orientation and envelope* influence the heating and cooling loads due to the exposure to sun and weather conditions, therefore passive design should be considered from the early design stages. There are many studies on the impact of the shape and orientation of the office buildings, from wide-spread, high-raised office buildings with vertical walls, optimized with simplified analysis methods [4, 5], parametric flexible system design [6, 7] or by multi objective genetic algorithm [8] up to studies on buildings with inclined walls having self-shading effect, cutting the cooling load in hot climatic zones [9, 10]. As compared to residential buildings, the office buildings envelope is often characterised by higher glazing-to-wall ratio reducing the insulation level and the thermal mass. The insulation quality determines the thermal resistance of the building envelope which is intensively investigated in literature and already regulated in national Building Codes, Standards and

Guides by mentioning the minimum permitted thermal resistance for the elements of the building envelope [11–13]. These thresholds are not differentiated by the type of buildings, but are low enough to be respected also by office buildings with high glazing-to-wall ratio. Recently, the effect on the heating and cooling demand of the office buildings was evaluated for different types of materials integrated in building walls for sensible heat storage, in solid and liquid state [14], for latent heat storage (organic and inorganic phase change materials [15, 16]) and for thermochemical heat storage based on adsorption and absorption phenomena [14]. Research on the thermal mass of exterior and interior construction elements show that, in certain conditions, the energy demand of the office building can be decreased [17, 18]. The glazing-to-wall ratio is important due to the compromise needed to be done between natural lighting, lighting savings and reducing heat losses [19]. Office buildings have large windows contributing to higher energy demand both for heating and cooling [20]. Besides better thermal resistance of both glazing and frames, smart windows with controlled optical properties [21, 22] and the integration of (semi)transparent photovoltaic modules [23, 24] are broadly investigated.

(b) *The functional zones in which the office buildings are divided* are located in peripheral and interior areas [25]. These zones may be or not extensively subdivided. In most cases, the peripheral zones are adjacent to large windows causing variable loads, due to the daily and seasonally changing of the weather conditions and of the apparent position of the sun on the sky. Compared to the interior zones, peripheral zones have higher heating demand in winter when the overall inside air temperature and relative humidity must be maintained, during the working schedule, between 21–23 °C, and 20–30 % respectively [26, 27], and have higher cooling demand in summer when the overall inside air temperature and relative humidity must be maintained, during the working schedule, between 23–26 °C, and 50–60 % respectively [26, 27]; in intermediate seasons, some peripheral zones may require heating while some other peripheral zones require cooling. Interior zones have an almost uniform cooling load during the year, depending mainly on interior sources as people, office equipment and lighting systems. While the heat load from people varies between 6 and 60 W/m^2 upon occupancy [26, 27], the usual electrical equipment and the lighting system add 10–50 W/m^2, and computers and office specific electronic equipment add another 50–110 W/m^2 [28].

(c) *The uses of an office building* is generally for office activities such as reading, writing and computer work, done during working days from 8 a.m. till 5 p.m.; some maintenance operations are done in a couple of hours before and/or after the main schedule, but usually during night these buildings can accept lower comfort parameters. These office buildings may contain also data centres, printing facilities, communications operations, and/or surveillance and security systems etc. which could operate up to 24/7. Occupancy varies upon the specific work done in a space, between 2 m^2/person for conference rooms and 19 m^2/person for private offices where a high concentration level is demanded;

for usual office activity, the average occupancy is approximately 7 m^2/person [28].

(d) *Air pollution and odour control* must be addressed besides indoor air temperature and relative humidity, defining the thermal comfort [29] that supports better performances of the occupants. Depending on the occupancy and on the type of equipment used in office buildings, rates of 4–10 air changes per hour must be insured, with maximum allowed air speed of 0.13–0.23 m/s [26, 27].

Overall, depending on the geographic location and on the above described characteristics, the total yearly energy demand of office buildings varies between 100–1,000 kWh/m^2 [30]. In order to reach the nZEB status, this yearly energy demand must be as low as economically feasible. In some European Member States there are already in-force requirements for the yearly energy demand between 60 and 150 kWh/m^2 [31] upon the geographic location and type of use.

After applying the measures required to reduce the yearly energy demand of the building, renewable energy systems (RES) must be designed to cover this. For existent buildings having already implemented RES, the energy provided by RES should be assessed and, if the energy demand is not covered "to a very significant extent by energy from renewable sources, including energy from renewable sources produced on-site or nearby" as stipulated in the recast of the energy performance of buildings directive [1], then the exiting RES capacity should be increased if possible; if not, new types of RES must be considered according to the renewable energy sources potential and available space for installation. In the case of office buildings, there are constraints both on potential and available space. Thus, due to their location in areas with high buildings density and restrictive construction permits, usually solar, geothermal and wind (only for higher buildings) sources of renewable energy can be taped. Among these RES, the best use of available space for installation is attained for air to air or vertical ground coupled heat pumps [32], followed by solar thermal collectors [33], photovoltaic modules [34, 35] installed on the buildings' rooftops or facades, and wind turbines [36]. Optimum results can be achieved if each RES is analysed not only as an entity, but also as part of an integrated and flexible energy mix able to meet the energy needs based on fluctuant renewable sources of energy [37, 38]. One important advantage of using RES on office buildings is given by the willingness of companies operating these office buildings to decrease operating costs, to improve employees' productivity and its "green" image.

The paper presents a method to evaluate the specific initial cost of a renewable energy mix (expressed in €/m^2 for the entire building), aiming at covering a given value of RES share in the total energy demand, and to offer an easy to use instrument to evaluate the feasibility of such renewable energy mixes for office buildings having different values of yearly specific energy demand.

2 Method

The method used in this paper rely on an algorithm previously developed in general terms to improve the renewable energy mix for a building toward the nZEB status [37], meshed on the particular case of office building types. The first two steps of the above mentioned algorithm (the assessment of the current energy status and the decrease of the energy demand) are skipped, considering a given range of values for the yearly specific energy demand for domestic hot water and space heating. The focus is on the third step: the selection of the optimal, feasible and affordable renewable energy mix.

The yearly energy demand for domestic hot water and space heating is calculated with:

$$E_{DHy} = e_{DHy} \cdot S \ [\text{kWh/year}] \tag{1}$$

where:

e_{DHy} is the given value of the yearly specific energy demand [kWh/(m^2 year)];
S is the entire floor surface of the building [m^2].

This yearly energy demand must be monthly divided as significant differences occur. To this end, the yearly energy demand for domestic hot water and space heating is separately calculated.

The yearly energy demand for heating domestic hot water is calculated with:

$$E_{Dy} = n_p \cdot q \cdot \rho \cdot c \cdot \Delta t \cdot N_{wdy}/3{,}600{,}000 \ [\text{kWh/year}] \tag{2}$$

where:

n_p is the number of persons occupying the office building [person];
q is the daily specific hot water demand [L/(person day)];
ρ is the density of water [kg/L];
c is the specific heat of the water [J/(kg K)];
Δt is the temperature difference between the hot and cold water [°C];
N_{wdy} is the number of working days in a year [days/year].

The yearly energy demand for space heating is calculated with:

$$E_{Hy} = E_{DHy} - E_{Dy} \ [\text{kWh/year}] \tag{3}$$

The monthly energy demand for domestic hot water heating is calculated with:

$$E_{Dm} = n_p \cdot q \cdot \rho \cdot c \cdot \Delta t \cdot N_{wdm}/3{,}600{,}000 \ [\text{kWh/month}] \tag{4}$$

where:
N_{wdm} is the number of working days in a month [days/month].

The monthly energy demand for space heating is calculated with:

$$E_{Hm} = \frac{E_{Hy} \cdot H_{DDm}}{H_{DDy}} \text{ [kWh/month]} \quad (5)$$

where:
H_{DDm} is the monthly heating degrees days [° days/month];
H_{DDy} is the yearly heating degrees days [° days/year].

Both, monthly and yearly heating degrees days are calculated based on the average monthly outdoor temperature. The monthly thermal energy demand for domestic hot water and space heating is calculated with:

$$E_{DHm} = E_{Dm} + E_{Hm} \text{ [kWh/month]} \quad (6)$$

Next, different mixes of RES are evaluated for an imposed share of yearly energy demand to be covered by RES (f_{RES}). For each RES component, the installed capacity and associated costs are calculated based on an algorithm presented in this paper for a solar thermal system (STS), a heat pump system (HPS) and a photovoltaic system (PVS) which provides the yearly electrical energy needed to drive the heat pump system.

Solar thermal systems (STS) are evaluated based on a methodology previously proposed [38], to cover different shares (f_{STS}) between 0 and 100 % of yearly energy demand for domestic hot water and space heating; the results are the installed power (P_{STS}) and the investment cost (C_{STS}). The STS specific cost (sc_{STS}) is calculated with:

$$sc_{STS} = \frac{C_{STS}}{S} \quad [€/m^2] \quad (7)$$

where:
C_{STS} is the investment cost for STS [€].

Heat pump systems (HPS) are evaluated based on the same methodology, to cover different shares (f_{HPS}) between 100 and 0 % of yearly energy demand for domestic hot water and space heating (complementary to STS); the results are the installed heating power (P_{hHP}), the investment cost (C_{HPS}) and the yearly electric energy demand to drive the HPS (E_{eHPy}). Due to the specific characteristic of implementation sites, for office buildings (usually located in places with less available ground surface) vertical ground heat exchangers are recommended,

usually increasing the initial investment cost in comparison with horizontal ones. The cost of the vertical ground heat exchanger is calculated with:

$$C_{VHX} = l \cdot L \ [€] \tag{8}$$

where:
l is the average market cost of vertical ground heat exchanger [€/m];
L is the depth of the vertical ground heat exchanger [m].

The L value is calculated with:

$$L = P_{hHP} \cdot \frac{COP - 1}{COP} \cdot \frac{1}{h} \ [\text{m}] \tag{9}$$

where:
P_{hHP} is the installed heating power of the heat pump [W];
COP is the coefficient of performance of the heat pump [−];
h is the amount of heat that can be transferred from the ground [W/m].

The HPS specific cost, considering both the heat pump and the vertical ground heat exchanger (sc_{HPS}), is calculated with:

$$sc_{HPS} = \frac{C_{HPS} + C_{VHX}}{S} \ [€/\text{m}^2] \tag{10}$$

where:
C_{HPS} is the investment cost for HPS [€];
C_{VHX} is the investment cost for the vertical ground heat exchanger [€].

Photovoltaic systems (PVS) should cover the yearly energy demand to drive the HPS and is designed based on the methodology proposed in [38], resulting the installed power (P_{PVS}) and the investment cost (C_{PVS}). The PVS specific cost (sc_{PVS}) is calculated with:

$$sc_{PVS} = \frac{C_{PVS}}{S} \ [€/\text{m}^2] \tag{11}$$

where:
C_{PVS} is the investment cost for PVS [€].

The specific cost of the entire RES mix is calculated for different combinations of shares covered by each component with:

$$sc_{RES} = sc_{STS} + sc_{HPS} + sc_{PVS} \ [€/\text{m}^2] \tag{12}$$

3 Case Study

The calculation method is applied considering the following hypotheses:

- One large office buildings (S = 1,350 m^2) occupied by 56 persons, 5 days/week with a schedule of 8 h/day (form 8:00 to 16:00);
- Iterative yearly specific thermal energy demand for space heating between 10 and 100 kWh/m^2/year and a constant daily specific hot water demand of 5 L/(person day);
- For the latitude corresponding to the implementation location (45.65°) and based on the solar radiation monitored over two years, it was concluded that the yearly collection efficiency of the solar radiation (obtained in simulation calculations) was 55 % for the fixed horizontal STS and 67.5 % for optimal fixed tilt STS at 37°;
- Continental temperate climatic profile, with winter and summer peak temperatures of −28 and 32 °C respectively, and values evaluated based on on-site measurements for: monthly available global horizontal solar radiation G_h, monthly average outdoor air temperature T_E, monthly heating and cooling degree-days H_{DDm} and C_{DDm}, as presented in Table 1.

In these conditions, the yearly energy demand for domestic hot water and space heating were calculated with Eqs. (1–3), and the results are presented in Table 2.

Based on the separately calculated values of the yearly energy demand for domestic hot water and space heating, monthly values are calculated using Eq. (4) and (5). The monthly energy demand for domestic hot water heating depends on the number of working days in the month, resulting 326, 349, and 360 kWh/month for the months with 28, 30 and 31 days respectively. The results obtained for the monthly energy demand for space heating are presented in Table 3.

Based on these results, the monthly thermal energy demand is calculated with Eq. (6), and the results are presented in Table 4.

Solar thermal systems (STS) are evaluated in following hypotheses:

- overall conversion efficiency of the STS 60%
- current average market prices for STS 750 €/kW

Based on these values, the installed power (P_{STS}), the investment cost (C_{STS}) and the specific cost (sc_{STS}) of the STS were calculated, Table 5.

Heat pump systems (HPS) are evaluated in following hypotheses:

- average coefficient of performance (COP) 4.50
- current average market prices for vertical ground heat exchanger (l) including the borehole, the U-tube and the grout: 50 €/m
- the heat that can be transferred from the ground (h) 50 W/m
- current average market prices for heat pumps based on the trend line equation presented in Fig. 1, where the significant dependence between the specific cost (sc_{HP}) of the heat pumps and its installed heating power is outlined.

Table 1 Monthly climatic parameters

Month	Jan	Feb	Mar	Apr	May	Jun	Jul	Aug	Sep	Oct	Nov	Dec
G_h, [kWh/m^2]	37.20	50.40	83.70	105.00	145.70	156.00	169.88	142.60	90.00	71.30	51.00	24.80
T_e, [°C]	−4.90	−2.50	2.60	8.50	13.30	16.10	17.50	17.00	13.40	7.90	2.80	−1.90
H_{DDm}, [° days]	772	630	539	345	47	0	0	0	53	375	516	679
C_{DDm}, [° days]	0	0	0	0	30	183	233	217	34	0	0	0

Table 2 Yearly energy demand for DHW (E_{Dy}) and space heating (E_{Hy}) [kWh/year]

e_{DHy}*	10	20	30	40	50	60	70	80	90	100
E_{DHy}	13,500	27,000	40,500	54,000	67,500	81,000	94,500	108,000	121,500	135,000
E_{Dy}	4,244	4,244	4,244	4,244	4,244	4,244	4,244	4,244	4,244	4,244
E_{Hy}	9,256	22,756	36,256	49,756	63,256	76,756	90,256	103,756	117,256	130,756

* e_{DHy}—yearly specific energy demand for domestic hot water and space heating [kWh/(m^2 year)]

Table 3 Monthly energy demand for space heating, E_{Hm} [kWh/month]

Month	e_{DHy}*									
	10	20	30	40	50	60	70	80	90	100
January	1,806	4,440	7,074	9,708	12,343	14,977	17,611	20,245	22,879	25,513
February	1,474	3,624	5,774	7,924	10,074	12,224	14,373	16,523	18,673	20,823
March	1,262	3,103	4,943	6,784	8,625	10,466	12,306	14,147	15,988	17,829
April	807	1,985	3,162	4,339	5,516	6,694	7,871	9,048	10,226	11,403
May	110	270	430	590	750	910	1,070	1,230	1,390	1,550
June	0	0	0	0	0	0	0	0	0	0
July	0	0	0	0	0	0	0	0	0	0
August	0	0	0	0	0	0	0	0	0	0
September	124	304	484	664	844	1,024	1,205	1,385	1,565	1,745
October	878	2,158	3,438	4,718	5,998	7,278	8,558	9,838	11,118	12,398
November	1,207	2,968	4,729	6,490	8,251	10,012	11,773	13,533	15,294	17,055
December	1,588	3,905	6,222	8,539	10,856	13,172	15,489	17,806	20,123	22,439

* e_{DHy}—yearly specific energy demand for domestic hot water and space heating [kWh/(m^2 year)]

Table 4 Monthly thermal energy demand, E_{DHm} [kWh/month]

Month	e_{DHy}*									
	10	20	30	40	50	60	70	80	90	100
January	2,166	4,801	7,435	10,069	12,703	15,337	17,971	20,605	23,240	25,874
February	1,800	3,949	6,099	8,249	10,399	12,549	14,699	16,849	18,999	21,149
March	1,622	3,463	5,304	7,145	8,985	10,826	12,667	14,508	16,348	18,189
April	1,156	2,333	3,511	4,688	5,865	7,043	8,220	9,397	10,575	11,752
May	470	630	790	950	1,110	1,270	1,430	1,591	1,751	1,911
June	349	349	349	349	349	349	349	349	349	349
July	360	360	360	360	360	360	360	360	360	360
August	360	360	360	360	360	360	360	360	360	360
September	472	653	833	1,013	1,193	1,373	1,553	1,734	1,914	2,094
October	1,238	2,518	3,798	5,078	6,358	7,638	8,918	10,198	11,478	12,758
November	1,556	3,317	5,078	6,839	8,600	10,360	12,121	13,882	15,643	17,404
December	1,949	4,266	6,582	8,899	11,216	13,533	15,850	18,166	20,483	22,800

* e_{DHy}—yearly specific energy demand for domestic hot water and space heating [kWh/(m^2 year)]

Table 5 Specific cost of the STS covering a share of f_{STS} in the energy mix [€/m^2]

f_{STS} (%)	e_{DHy}*									
	10	20	30	40	50	60	70	80	90	100
0	0.00	0.00	0.00	0.00	0.00	0.00	0.00	0.00	0.00	0.00
10	0.54	1.12	2.21	3.62	5.09	7.01	9.48	13.22	20.19	35.57
20	1.12	3.26	6.14	9.03	12.53	16.48	22.81	30.67	46.48	77.86
30	2.05	5.78	10.11	14.44	19.97	26.19	36.14	48.40	72.77	120.15
40	2.98	8.30	14.08	19.85	27.41	35.91	49.47	66.12	99.06	162.44
50	4.03	10.83	18.04	25.26	34.85	45.62	62.80	83.84	125.35	204.73
60	5.08	13.35	22.01	30.77	42.29	55.34	76.13	101.57	151.65	247.01
70	6.13	15.87	25.98	36.29	49.73	65.05	89.46	119.29	177.94	289.30
80	7.18	18.40	29.94	41.81	57.17	74.76	102.79	137.01	204.23	331.59
90	8.23	20.92	33.91	47.33	64.60	84.48	116.12	154.74	230.52	373.88
100	9.28	23.44	37.88	52.85	72.04	94.19	129.45	172.46	256.81	416.17

* e_{DHy}—yearly specific energy demand for domestic hot water and space heating [kWh/(m^2 year)]

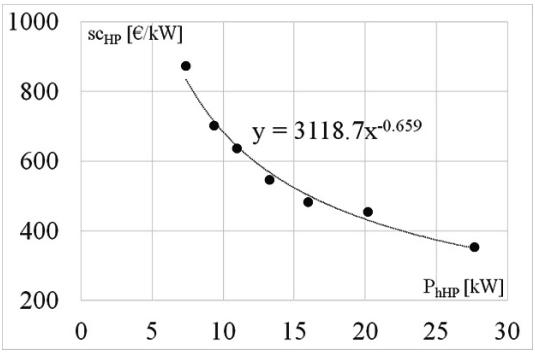

Fig. 1 The dependence between the specific cost of heat pumps and its installed heating power

Based on these values, the installed power (P_{hHP}) and the investment cost (C_{HPS}) of the HPS were calculated, along with the investment cost (C_{VHX}) of the vertical ground heat exchanger and, accordingly, the specific cost (sc_{HPS}) of the HPS; the results are presented in Table 6.

Photovoltaic systems (PVS) are evaluated in following hypotheses:

- overall conversion efficiency of the PVS 15 %
- current average market prices for PVS 1,500 €/kW

Based on these values, the installed power (P_{PVS}) and the investment cost (C_{PVS}) of the PVS were calculated and, accordingly, the specific cost (sc_{PVS}) of the PVS, the results being presented in Table 7.

The nZEB status requires to cover a significant share of the energy demand by using RES. Now-a-days it is usually considered that "significant" referred to a share (f_{RES}) above 50 %. Therefore, two cases were considered to discuss the optimal energy mix: f_{RES} = 70 % and f_{RES} = 50 %.

Table 6 Specific cost of the HPS covering a share of f_{HPS} in the energy mix [€/m^2]

f_{HPS} (%)	e_{DHy}*									
	10	20	30	40	50	60	70	80	90	100
0	0.00	0.00	0.00	0.00	0.00	0.00	0.00	0.00	0.00	0.00
10	1.31	1.72	2.04	2.39	2.79	3.15	3.47	3.82	4.22	5.00
20	1.72	2.39	3.06	3.70	4.28	4.82	5.33	5.99	6.69	8.08
30	2.04	2.99	3.92	4.75	5.51	6.23	6.94	7.86	8.86	10.82
40	2.39	3.55	4.69	5.69	6.63	7.53	8.44	9.60	10.90	13.41
50	2.70	4.07	5.39	6.58	7.69	8.75	9.87	11.27	12.86	15.92
60	2.98	4.55	6.05	7.41	8.70	9.94	11.25	12.89	14.76	18.36
70	3.25	5.01	6.69	8.23	9.68	11.09	12.60	14.47	16.62	20.76
80	3.50	5.45	7.30	9.01	10.64	12.21	13.92	16.02	18.45	23.13
90	3.74	5.87	7.90	9.78	11.58	13.32	15.22	17.55	20.26	25.47
100	3.97	6.28	8.49	10.54	12.50	14.40	16.50	19.06	22.05	27.78

* e_{DHy}—yearly specific energy demand for domestic hot water and space heating [kWh/(m^2 year)]

Table 7 Specific cost of the PVS covering a share of f_{HPS} in the energy mix [€/m^2]

f_{HPS} (%)	e_{DHy}*									
	10	20	30	40	50	60	70	80	90	100
0	0.00	0.00	0.00	0.00	0.00	0.00	0.00	0.00	0.00	0.00
10	0.24	0.48	0.72	0.96	1.20	1.45	1.69	1.93	2.17	2.41
20	0.48	0.96	1.45	1.93	2.41	2.89	3.37	3.85	4.34	4.82
30	0.72	1.45	2.17	2.89	3.61	4.34	5.06	5.78	6.50	7.23
40	0.96	1.93	2.89	3.85	4.82	5.78	6.74	7.71	8.67	9.63
50	1.20	2.41	3.61	4.82	6.02	7.23	8.43	9.63	10.84	12.04
60	1.45	2.89	4.34	5.78	7.23	8.67	10.12	11.56	13.01	14.45
70	1.69	3.37	5.06	6.74	8.43	10.12	11.80	13.49	15.18	16.86
80	1.93	3.85	5.78	7.71	9.63	11.56	13.49	15.42	17.34	19.27
90	2.17	4.34	6.50	8.67	10.84	13.01	15.18	17.34	19.51	21.68
100	2.41	4.82	7.23	9.63	12.04	14.45	16.86	19.27	21.68	24.09

* e_{DHy} - yearly specific energy demand for domestic hot water and space heating [kWh/(m^2 year)]

Eight different mixes can be obtained for f_{RES} = 70 %, using iterative shares for STS (f_{STS}) between 70 and 0 % with 10 % steps (and accordingly for HPS (f_{HPS}) between 0 and 70 %). The case considering f_{RES} = 50 % will follow the same approach. The specific costs obtained are presented in Table 8 and their graphical representation in Fig. 2.

Table 8 Specific cost of the RES mix

RES mix			Yearly specific energy demand, e_{DHY}, [kWh/(m^2 year)]									
			10	20	30	40	50	60	70	80	90	100
f_{RES} [%]	f_{STS} [%]	f_{HPS} [%]	STS + HPS + PVS specific cost [€/m^2]									
70	70	0	6.13	15.87	25.98	36.29	49.73	65.05	89.46	119.29	177.94	289.30
	60	10	6.63	15.56	24.77	34.13	46.28	59.93	81.29	107.31	158.04	254.43
	50	20	6.24	14.18	22.55	30.89	41.54	53.33	71.50	93.68	136.38	217.62
	40	30	5.74	12.74	20.17	27.49	36.53	46.47	61.47	79.76	114.43	180.49
	30	40	5.40	11.26	17.69	23.99	31.42	39.50	51.32	65.71	92.35	143.20
	20	50	5.03	9.74	15.15	20.42	26.24	32.46	41.11	51.58	70.18	105.82
	10	60	4.97	8.57	12.60	16.82	21.02	25.62	30.85	37.67	47.96	68.39
	0	70	4.94	8.38	11.75	14.97	18.11	21.20	24.40	27.96	31.80	37.62
50	50	0	4.03	10.83	18.04	25.26	34.85	45.62	62.80	83.84	125.35	204.73
	40	10	4.53	10.51	16.84	23.21	31.40	40.50	54.63	71.87	105.46	169.85
	30	20	4.25	9.13	14.62	20.07	26.66	33.90	44.84	58.24	83.80	133.05
	20	30	3.89	7.69	12.24	16.67	21.66	27.05	34.81	44.31	61.85	95.91
	10	40	3.89	6.60	9.79	13.17	16.54	20.32	24.66	30.53	39.76	58.62
	0	50	3.90	6.48	9.00	11.39	13.71	15.98	18.30	20.91	23.70	27.96

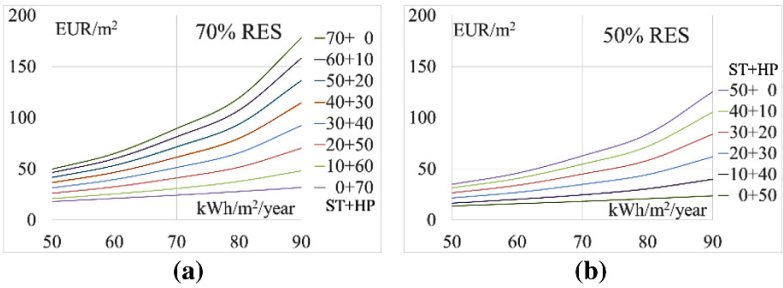

Fig. 2 **a** 70 % RES share; **b** 50 % RES share out of thermal energy demand

4 Results and Discussions

There is a direct correlation between the initial investment costs to implement renewables and the thermal energy demand of the building. The results show that specific RES cost increase exponentially starting from a threshold of 80 kWh/(m^2 year). Therefore, the first steps in developing Nearly Zero Energy Buildings, before implementing RES, should be made towards decreasing the specific energy demand of the building.

The lowest specific cost were obtained for systems based on HPS only, both when considering a RES share of 50 % and of 70 % respectively, due to the smaller specific energy demand for domestic hot water than space heating. This is characteristic to office buildings, having smaller DHW need, 5 L/(person day), as compared to residential buildings, 90 L/(person day).

For highly efficient buildings, with specific energy demand lower than 50 kWh/(m^2 year), the share of domestic hot water in the yearly energy demand increases, making almost no difference between different RES mixes.

A specific RES cost under 50 €/m^2 can be considered affordable for new buildings considering the average office building costs of 500–750 €/m^2. This threshold can be respected if the specific energy demand is lower than 90 kWh/(m^2 year).

Future developments will consider the increase of the building cost when improving its envelope thermal characteristics, the operating and maintenance cost of RES mix and finally the cost - benefit ratio.

5 Conclusions

It is common knowledge that the thermal resistance of the building envelope and consequently its specific energy demand have a major influence on the RES mix feasibility, but the extent of this influence is usually not outlined. Therefore, the

paper proposes a calculation model that correlates the yearly specific thermal energy demand of a building with the costs of the installed renewables.

The results outline the need to follow a stepwise development of Nearly Zero Energy Buildings, first by increasing the energy efficiency (and significantly cutting the thermal losses) and only afterwards to consider the implementation of renewables-based energy mixes.

Even so, covering 50 % of the thermal energy demand with RES represents a feasible and affordable path in the current development conditions, and well justifies the targeted values proposed for nZEBs.

Acknowledgement This paper is supported by the Sectoral Operational Programme Human Resources Development (SOP HRD), financed from the European Social Fund and by the Romanian Government under the project number POSDRU/159/1.5/S/134378.

References

1. The European Parliament. (2010). The directive 2010/31/EU of the European Parliament and of the Council of 19 on the energy performance of buildings. *Official Journal of the European Union, 53*, 2010.
2. Smalley, R. E. (2005). Future Global Energy: Prosperity The Terawatt Challenge. *MRS Bulletin, 30*, 412–417.
3. The Buildings Performance Institute Europe. (2011). *Europe's buildings under the microscope A country-by-country review of the energy performance of buildings*. ISBN: 9789491143014.
4. Ourghi, R., Al-Anzi, A., & Krarti, M. (2007). A simplified analysis method to predict the impact of shape on annual energy use for office buildings. *Energy Conversion and Management, 48*, 300–305.
5. Al-Anzi, A., Seo, D., & Krarti, M. (2009). Impact of building shape on thermal performance of office buildings in Kuwait. *Energy Conversion and Management, 50*, 822–828.
6. Granadeiro, V., José, P. D., João, R. C., & Leal, V. (2013). Building envelope shape design in early stages of the design process: Integrating architectural design systems and energy simulation. *Automation in Construction, 32,* pp. 196–209.
7. Granadeiro, V., João, R. C., Leal, V., & José, P. D. (2013). Envelope-related energy demand: A design indicator of energy performance for residential buildings in early design stages. *Energy and Buildings*, *61*, 215–223.
8. Wang, W., Rivard, H., & Zmeureanu, R. (2006). Floor shape optimization for green building design. *Advanced Engineering Informatics, 20*, 363–378.
9. Chan, A. L. S., & Chow, T. T. (2014). Thermal performance of air-conditioned office buildings constructed with inclined walls in different climates in China. *Applied Energy, 114*, 45–57.
10. Zerefos, S. C., Tessas, C. A., Kotsiopoulos, A. M., Founda, D., & Kokkini, A. (2012). The role of building form in energy consumption: The case of a prismatic building in Athens. *Energy and Buildings, 48*, 97–102.
11. ASHRAE Inc. (2013). ANSI/ASHRAE/IES Standard 90.1-2013: Energy standard for buildings except low-rise residential buildings, S-I and I-P Editions.
12. The Chartered Institution of Building Services Engineers London. (2004) *CIBSE guide F: Energy efficiency in buildings* (2nd edn.).
13. IPCT. (2010). *Norm C107/2010 on the thermo technical calculation of the buildings construction elements*.

14. Tatsidjodoung, P., Le Pierres, N., & Luo, L. (2013). A review of potential materials for thermal energy storage in building applications. *Renewable and Sustainable Energy Reviews, 18*, 327–349.
15. Memon, S. A. (2014). Phase change materials integrated in building walls: A state of the art review. *Renewable and Sustainable Energy Reviews, 31*, 870–906.
16. AL-Saadi, S. N., & Zhai, Z. J. (2013). Modeling phase change materials embedded in building enclosure: A review. *Renewable and Sustainable Energy Reviews*, *21*, 659–673.
17. Wang, L.-S., Ma, P., Hu, E., Giza-Sisson, D., Mueller, G., & Guo, N. (2014). A study of building envelope and thermal mass requirements for achieving thermal autonomy in an office building. *Energy and Buildings, 78*, 79–88.
18. Talyor, R. A. (2014). Mark Miner, a metric for characterizing the effectiveness of thermal mass in building materials. *Applied Energy, 128*, 156–163.
19. Thalfeldt, M., Pikas, E., Kurnitski, J., & Voll, H. (2013). Facade design principles for nearly zero energy buildings in a cold climate. *Energy and Buildings, 67*, 309–321.
20. Ochoa, C. E., Aries, M. B. C., van Loenen, E. J., & Hensen, J. L. M. (2012). Considerations on design optimization criteria for windows providing low energy consumption and high visual comfort. *Applied Energy, 95*, 238–245.
21. Dussault, J. M., Gosselin, L., & Galstian, T. (2012). Integration of smart windows into building design for reduction of yearly overall energy consumption and peak loads. *Solar Energy, 86*, 3405–3416.
22. Sbar N. L., Podbelski L., Yang, H. M., & Pease, B. (2012). Electrochromic dynamic windows for office buildings. *International Journal of Sustainable Built Environment*, *1*, 125–139.
23. Xu, S., Liao, W., Huang, J., & Kang, J. (2014). Optimal PV cell coverage ratio for semi-transparent photovoltaics on office building façades in central China. *Energy and Buildings, 77*, 130–138.
24. Didoné, E. L., & Wagner, A. (2013). Semi-transparent PV windows: A study for office buildings in Brazil. *Energy and Buildings, 67*, 136–142.
25. Korolija, I., Marjanovic-Halburd, L., Zhang, Y., & Hanby, V. I. (2013). UK office buildings archetypal model as methodological approach in development of regression models for predicting building energy consumption from heating and cooling. *Energy and Buildings, 60*, 152–162.
26. International Organisation for Standardisation. (2005). ISO 7730 Ergonomics of the thermal environment—Analytical determination and interpretation of thermal comfort using calculation of the PMV and PPD indices and local thermal comfort criteria.
27. American Society of Heating, Refrigerating and Air-Conditioning Engineers. (2004). ASHRAE Standard 55-2004 Thermal environmental conditions for human occupancy.
28. American Society of Heating, Refrigerating and Air-Conditioning Engineers. (2007). *ASHRAE handbook HVAC applications SI units*.
29. Taleghani, M., Tenpierik, M., Kurvers, S., & van den Dobbelsteen, A. (2013). A review into thermal comfort in buildings. *Renewable and Sustainable Energy Reviews, 26*, 201–215.
30. Santamouris, M., & Dascalaki, E. (2002). Passive retrofitting of office buildings to improve their energy performance and indoor environment: the OFFICE project. *Building and Environment, 37*, 575–578.
31. COWI. (2011). Mapping of strategies for low energy housing in the EU countries.
32. Sauchelli, Michele, Masera, Gabriele, D'Antona, Gabriele, & Manzolini, Giampaolo. (2014). ISIS Facchinetti: A nearly zero energy retrofit in Italy. *Energy Procedia, 48*, 1326–1335.
33. Visa, I., Comsit, M., & Duta, A. (2014). Urban acceptance of facade integrated novel solar thermal collectors. *Energy Procedia, 48*, 1429–1435.
34. Pikas, E., Thalfeldt, M., & Kurnitski, J. (2014). Cost optimal and nearly zero energy building solutions for office buildings. *Energy and Buildings, 74*, 30–42.
35. Aelenei, L., & Gonçalves, H. (2014). From solar building design to net zero energy buildings performance insights of an office building. *Energy Procedia, 48*, 1236–1243.

36. Walker, S. L. (2011). Building mounted wind turbines and their suitability for the urban scale—A review of methods of estimating urban wind resource. *Energy and Buildings, 43*, 1852–1862.
37. Visa, I., Moldovan, M. D., Comsit, M., & Duta, A. (2014). Improving the energy mix in a building toward the nearly zero energy status. *Energy and Buildings, 68*, 72–78.
38. Moldovan, M. D., Visa, I., Neagoe, M., & Burduhos, B. G. (2014). Solar heating & cooling energy mixes to transform low energy buildings in nearly zero energy buildings. *Energy Procedia, 48*, 924–937.

Heating Sources Switching System

Sorin-Aurel Moraru, Dominic Mircea Kristály and Milian Badea

Abstract This paper presents a system for automatic switching between thermal sources—a gas boiler, a heating pump and solar thermal collectors—in order to reduce the gas consumption in the ICDT Pro-DD Research Institute of Transilvania University of Brasov. An algorithm was devised and a software product developed that, by monitoring several temperatures collected from the sensors in the system, allows maximum use of the energy from the heating pump, achieving a high degree of economy of classic fuel (gas). The paper includes a synthesis of data collected from the gas boiler (temperatures and modulation), useful for designing the algorithm governing the switching between heating sources, temperatures from the solar thermal collectors (for the behavioural study of this type of heating source in the region of Brasov) and the electric energy consumption.

Keywords Switching system · Heating sources · Heating pump · Solar thermal collectors · Sustainability

1 Introduction

Energy—the quasi-permanent crisis—is always a present problem in terms of resources and sustainability. Civilization is dependent on finding new sources of energy and more efficient use of existing ones.

The gas heating boilers are the most commonly used in heating systems. To use renewable energy, the heat generator is supplemented by a heat pump and possibly solar thermal collectors for domestic heated water [1]. Because the maximum temperature on the tour circuit of the heat pump is 55 °C, in the systems where the temperature on the tour circuit of the system exceeds this maximum temperature, the heat pump will only function complementing the conventional heat generator [2, 3].

S.-A. Moraru (✉) · D.M. Kristály · M. Badea
Transilvania University of Brasov, Eroilor 29, 500036 Brasov, Romania
e-mail: smoraru@unitbv.ro

I. Visa (ed.), *Sustainable Energy in the Built Environment - Steps Towards nZEB*,
Springer Proceedings in Energy, DOI 10.1007/978-3-319-09707-7_11

Fig. 1 Positioning of laboratories at the Pro-DD Research Institute

A heating system relying on heat pumps to provide all the necessary power can be achieved in new buildings, in which case a heat distribution system with a maximum temperature in the tour circuit of 35 °C is chosen. This operating mode is called monovalent. The bivalent operating mode combines heat pumps with electric drive, with at least one heat generator that can use gas or other fuel.

If the heat pump is combined with a heat source that uses the same type of energy, the operating regime is called monoenergetic mode. An example of this is using an instant hot water heater on the primary tour circuit or an electric resistance in the hot water boiler [4, 5].

The heating system presented in this paper was developed for the ICDT Pro-DD Research Institute of Transilvania University of Brasov. Figure 1 shows the positioning of each laboratory in the complex. All laboratories buildings are connected through a glass hallway.

In the L1 laboratory of the Pro-DD Research Institute in Brasov is implemented such a bivalent system, consisting of:

- Gas boiler;
- Heat pump with depth wells;
- Two solar thermal collectors for domestic hot water.

In the gas boiler the temperature must be higher than the temperature of any other circuit. The implemented heating system contains three circuits. Two circuits with mixing valve and one direct circuit, as follows:

- circuit with mixing valve for underfloor heating;
- circuit with mixing valve for heating radiators;
- heating water boiler circuit for domestic hot water (DHW).

The temperature of each circuit is determined by the heating curves and the temperature for each circuit is set in the configuration menu of the heating system. Heating curves (Fig. 2) [4, 5] represents the connection between outside

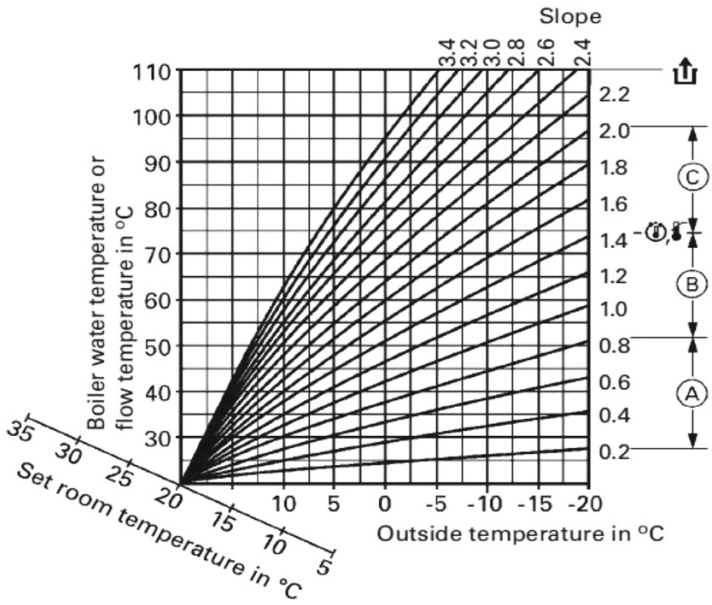

Fig. 2 Heating curves [4, 5]

temperature and heat supplied by the tour circuit. If the outdoor temperature is lower, the flow circuit temperature is higher.

The slope of the heating curve is chosen according to the heating system:

- The A area, with a slope between 0.2 and 0.8, is chosen for underfloor heating;
- The B area, with a slope between 1.0 and 2.0, is chosen for low temperature heating systems;
- The C area, with a slope over 2.0, is chosen for the heating systems with heating boilers in which the temperatures exceed 75 °C.

The adjustment of the heating curve according to the heating strategy, can be done in two ways:

- changing the slope of the heating curve by changing it in the configuration menu of the heating system;
- changing the ambient temperature, which is usually set at 20 °C, in this way changing the curve.

2 Profibus Network

In order for each laboratory to allow an easy expansion (adding new participants), the network was designed with scalability in mind, so that each laboratory is a segment. For this reason, seven repeaters were necessary, which made the connection of the segments to the network possible.

The elements connected to the Profibus network are:

- Monitoring devices for power, type Sentron PAC 3200, one for each laboratory. The devices are installed in the general electric panels;
- Compact PLCs for monitoring the solar thermal systems located in 9 laboratories;
- One PLC that performs the monitoring and control of the orientations systems on laboratory L7;
- One PLC that performs the monitoring and control the of mobile platforms;
- ET200S connected to the network by IM151 interface module for monitoring the wells for the heat pump [6];
- M-Bus master/slave Profibus converters for reading information from energy meters [7, 8].

Because of the length and the large number of repeaters and segments, the Profibus network was divided into two networks:

1. the first network for the first seven laboratories and wells; the PLC is located in the laboratory L1;
2. the second network for the last five laboratories and mobile platforms, the master PLC is located in the L9 laboratory.

The network configuration was made using Simatic Manager. The first step was to fill the rack with the modules that were included in the PLC configuration:

- The central unit CPU 315-2P;
- Communication processor CP 343-1 Lean for Ethernet connection to SCADA system;
- Analog input module for ambient temperature sensors;
- I/O module for control of the valves;

The Profibus network is configured as DP Master in the Operating Mode tab, with the following parameters:

- Master System No.1;
- Transmission Rate: 187.5 Kbps;
- Profile: DP;
- Number of repeaters: 3;
- Cable length: 500 m.

Next, the slave devices were introduced; they are participating in the communication. The repeaters, that are used to connect the segments to the network, were not introduced in the interface as devices, but only their number.

3 The Heating System

The heating system diagram is shown in Fig. 4. The gas boiler heats the thermal agent at a target temperature, which must be higher than the temperature of any circuit.

The heating circuit temperature is bigger with the target value set in the differential temperature variable set in the configuration menu of the boiler to the requested temperature at a given time. The temperature is set by the manufacturer at 8 °C. The boiler pump sends thermal agent to the feeder (distributor), from where it is taken up by each heating circuit through pumps and mixing valves.

All pumps and valves in the system are controlled by the boiler's controller, as follows:

- The first heating circuit with mixing valve is for the underfloor heating. The P1 pump is controlled by the boiler's controller and the pump sends thermal agent through the heating tubes. The temperature of the thermal agent results from the chosen heat curve and from the outdoor temperature. This is achieved through control of the three-way valve M1 that mixes the hot agent from tour circuit with the cold agent on the return circuit. The temperature is measured by the T1 sensor (Fig. 3);

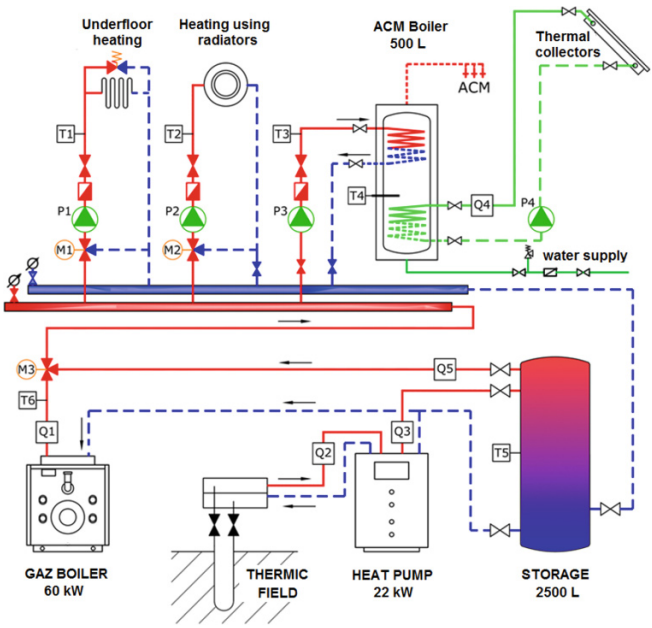

Fig. 3 Heating system diagram

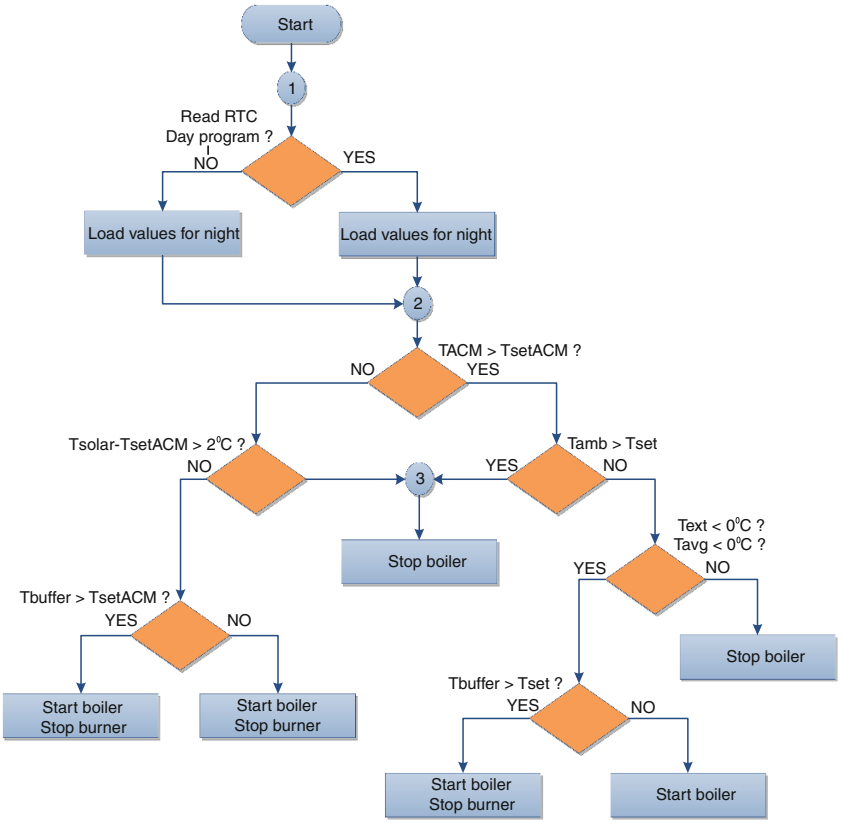

Fig. 4 Algorithm for switching between power sources

- The second heating circuit with mixing valve is for heating using radiators. The P2 pump, controlled by the boiler's controller sends the prepared thermal agent through the three-way valve M2. The temperature is measured by the sensor T2.

Hot water is prepared directly, without using the mixing valve. The pump P3 sends the thermal agent through the heating coil. The temperature is measured by the T3 sensor.

4 The Command and Control System

The command and control system is achieved through a PLC that is the master in the communication for the monitoring and data acquisition for the L1 laboratory. This system fulfils also the switch function.

The system has the following configuration:

- Central unit with two Profibus communication ports;
- Communication Processor CP 343-1;
- Analog input module for 8 RTD;
- Module Input /Digital Output 16DI/16DO
- Analogical I/O modules for 8 RTD;
- Digital I/O modules 16DI/16DO;
- The touch screen operator panel with MPI communication with the central unit for visualization of parameters and setting of the ambient temperature.

For implementing the switching function were necessary to:

- Establish the Modbus communication with the Hoval boiler for acquiring the temperature values, the state of elements of execution (circulation pumps, valves) and the state of the boiler (events and alarms);
- Establish Modbus the communications with Hoval boiler for exchanging information related to the setpoint and the boiler load;
- M-Bus communication with the energy meters for the acquisition of energy values, flow and temperature;
- Modbus communication with EEM-MA250 device for monitoring electric consumption of the heat pump;
- Connect the temperature sensors to the analog input module of the PLC, for monitoring ambient and floor temperature;
- Connect the PLC to the boiler's controller for the start /stop function;
- Connecting the PLC to the boiler's controller for the stop burner function (all installation functions remain active except the stop burner function).

After these changes and additions were made, it was possible to switch from heating using the boiler to heating using energy supplied by the heat pump and collected in the storage.

The PLC program has the following inputs:

- The tour circuit of the underfloor heating temperature (T1);
- The tour circuit radiator heating temperature (T2);
- The tour circuit of domestic hot water heating temperature (T3);
- The boiler's temperature (T4);
- The storage's temperature (T5);
- The tour circuit boiler temperature (T6);
- The ambient temperature;
- The floor temperature;
- Outside temperature;
- The average temperatures of the previous days.

For monitoring, viewing, acquisitioning and saving of the system parameters in a database, a SCADA/HMI application was created, application which runs on a computer in the L7 laboratory. Acquired data are taken from two Siemens PLCs, each of them master in the Profibus network. The connection between the fields

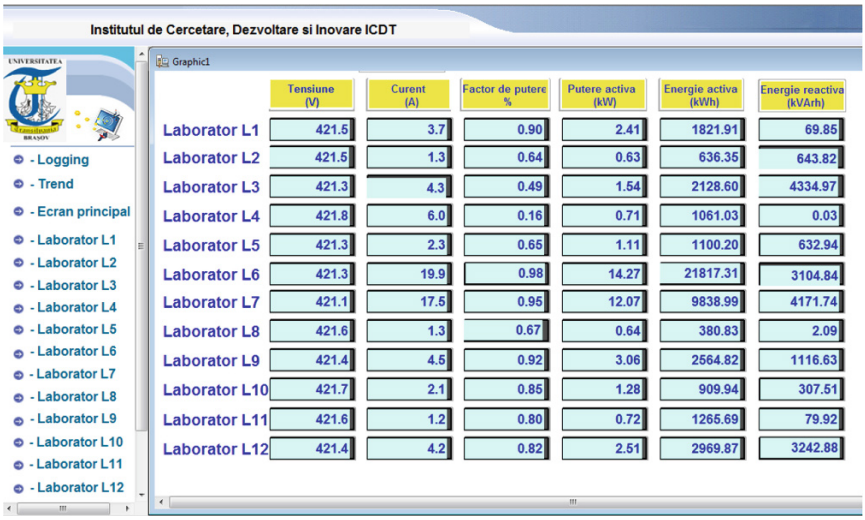

	Tensiune (V)	Curent (A)	Factor de putere %	Putere activa (kW)	Energie activa (kWh)	Energie reactiva (kVArh)
Laborator L1	421.5	3.7	0.90	2.41	1821.91	69.85
Laborator L2	421.5	1.3	0.64	0.63	636.35	643.82
Laborator L3	421.3	4.3	0.49	1.54	2128.60	4334.97
Laborator L4	421.8	6.0	0.16	0.71	1061.03	0.03
Laborator L5	421.3	2.3	0.65	1.11	1100.20	632.94
Laborator L6	421.3	19.9	0.98	14.27	21817.31	3104.84
Laborator L7	421.1	17.5	0.95	12.07	9838.99	4171.74
Laborator L8	421.6	1.3	0.67	0.64	380.83	2.09
Laborator L9	421.4	4.5	0.92	3.06	2564.82	1116.63
Laborator L10	421.7	2.1	0.85	1.28	909.94	307.51
Laborator L11	421.6	1.2	0.80	0.72	1265.69	79.92
Laborator L12	421.4	4.2	0.82	2.51	2969.87	3242.88

Fig. 5 Main screen

declared in the SCADA/HMI application and the data values in data blocks of the PLC memory is implemented through tags. The connection between the computer and the two PLCs is Ethernet.

The communication with the two PLCs is accomplished by declaring, in the Tag Management zone, two stations belonging to the same channel. Blocks are declared inside each station, each block accessing one block of the PLC memory. The driver supports a maximum of 240 bytes; if the data block is bigger, multiple readings are executed, until all data is consumed. For each block is set the block number, start address, where the reading begins, the length of the block, in bytes, and the period of the acquisition.

For the developed application, for most of the blocks an acquisition time of 500 ms was chosen. For easy access to data, a main screen was created, a screen for each laboratory, a Data Logging screen and a Trend Graph screen.

The Fig. 4 presents the algorithm for switching between the power sources. The priority is to use the energy produced by solar thermal collectors and heat pump; the gas boiler starts only if the two sources of energy fail to maintain the target ambient temperature. The values are set using the operator panel or the SCADA/HMI interface.

The main screen (Fig. 5) is the start screen of the application and it is displaying the values of the main parameters of the supply network (voltage, current, power factor, power, energy) for each laboratory. On the left side there are buttons that can open other screens.

For each laboratory one screen was created, to present the acquired values (Fig. 6). Each screen displays the network parameters and other specific values:

- temperatures and flow for the thermal solar collectors on 9 laboratories;

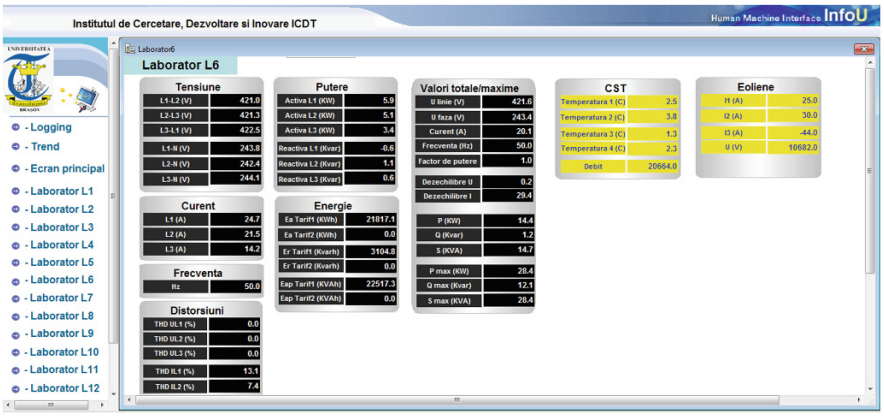

Fig. 6 Laboratory screen

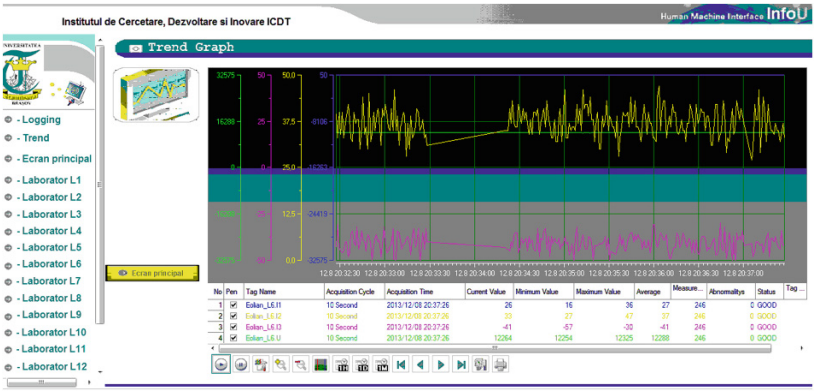

Fig. 7 Trend graph screen

- wells temperatures for laboratory L1;
- currents and voltages of the wind turbines located on laboratory L5 and L6; current and target angles for the orientation systems.

Trend Graph screen (Fig. 7) displays graphically the values of the parameters (you can view multiple values at once, with different scales). It is possible to change the viewing interval and to change the variables.

Data Logging screen (Fig. 8) displays the values of the parameters as a text. It is possible to view the real time values or the stored values. For the stored values a period of time must be selected, from 1 h to 1 month. The requested values can be exported into a CSV file for further processing and interpretation using other software applications.

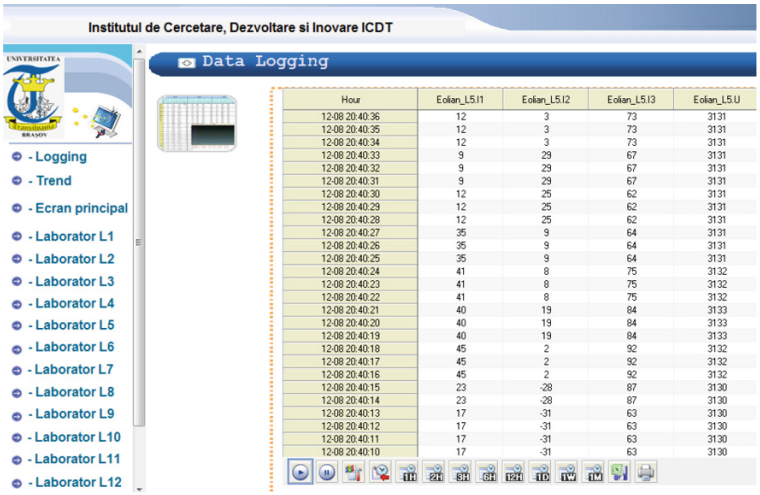

Hour	Eolian_L5.I1	Eolian_L5.I2	Eolian_L5.I3	Eolian_L5.U
12-08 20:40:36	12	3	73	3131
12-08 20:40:35	12	3	73	3131
12-08 20:40:34	12	3	73	3131
12-08 20:40:33	9	29	67	3131
12-08 20:40:32	9	29	67	3131
12-08 20:40:31	9	29	67	3131
12-08 20:40:30	12	25	62	3131
12-08 20:40:29	12	25	62	3131
12-08 20:40:28	12	25	62	3131
12-08 20:40:27	35	9	64	3131
12-08 20:40:26	35	9	64	3131
12-08 20:40:25	35	9	64	3131
12-08 20:40:24	41	8	75	3132
12-08 20:40:23	41	8	75	3132
12-08 20:40:22	41	8	75	3132
12-08 20:40:21	40	19	84	3133
12-08 20:40:20	40	19	84	3133
12-08 20:40:19	40	19	84	3133
12-08 20:40:18	45	2	92	3132
12-08 20:40:17	45	2	92	3132
12-08 20:40:16	45	2	92	3132
12-08 20:40:15	23	-28	87	3130
12-08 20:40:14	23	-28	87	3130
12-08 20:40:13	17	-31	63	3130
12-08 20:40:12	17	-31	63	3130
12-08 20:40:11	17	-31	63	3130
12-08 20:40:10	17	-31	63	3130

Fig. 8 Data logging screen

5 Data Acquisition Results

The data acquisition subsystem was used to collect the data that shaped the algorithm for the switching system and its parameters. Also, the developed system will empower further studies on the added value brought by renewable energy producing devices in the region of Brasov.

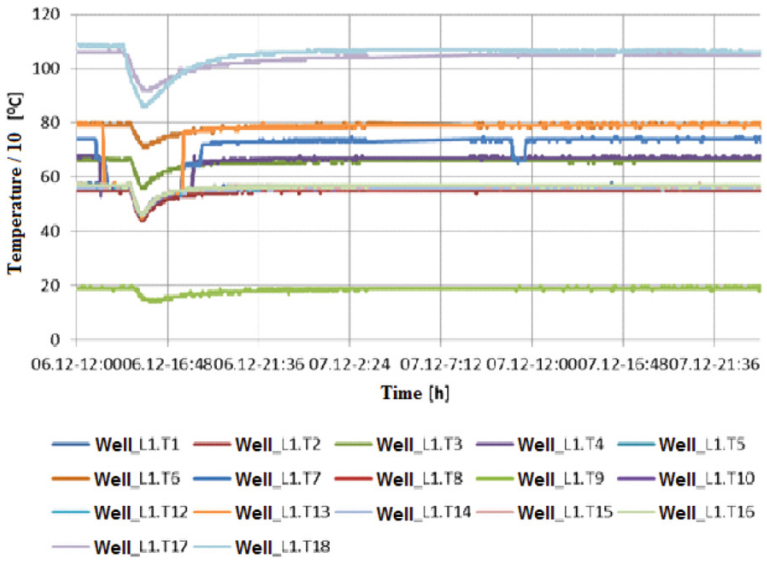

Fig. 9 Monitoring temperatures of wells

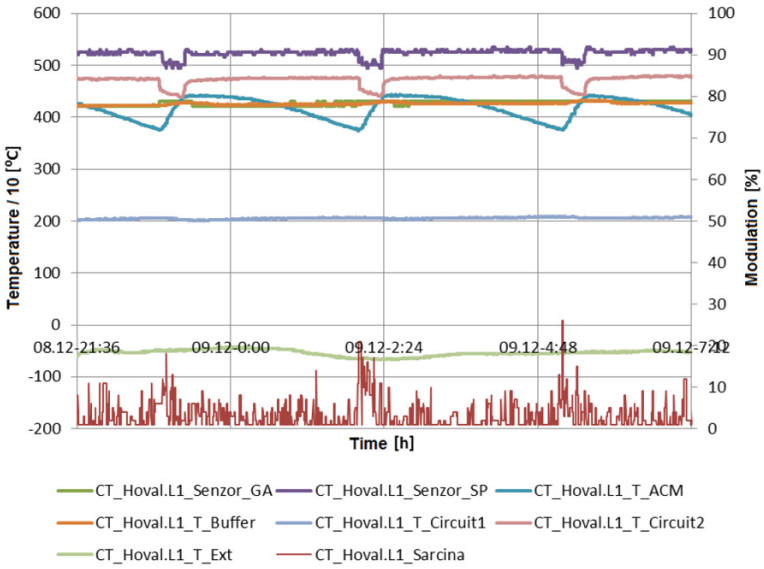

Fig. 10 Monitoring parameters on Hoval radiators

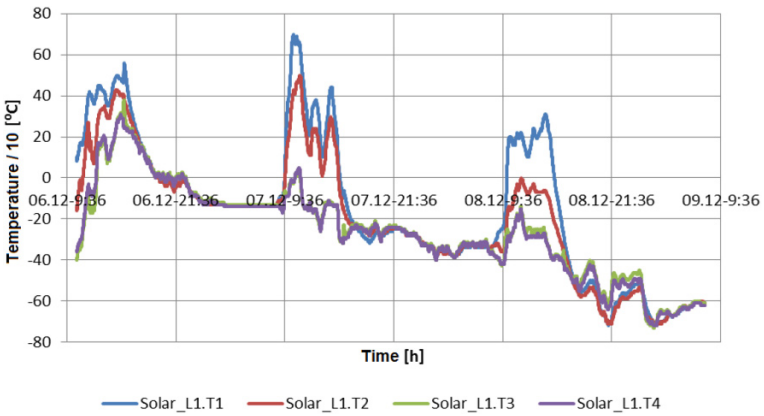

Fig. 11 Monitoring temperatures of the solar thermal collectors, laboratory L1

The Fig. 9 presents the evolution of temperatures for wells, acquired on December 7th 2013. When the heat pumps were installed and the wells were drilled, 18 PT100 temperature sensors were installed every five meters. The acquisition is useful for the study of the soil behaviour when the pump is working or in the passive cooling of the laboratory.

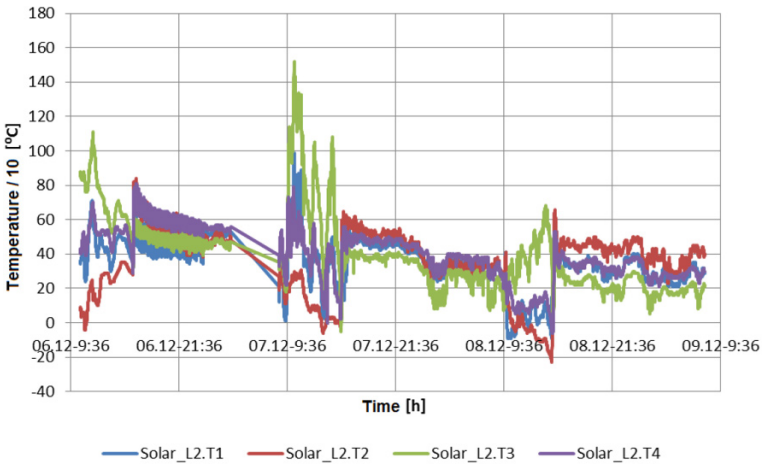

Fig. 12 Monitoring temperatures of the solar thermal collectors, laboratory L2

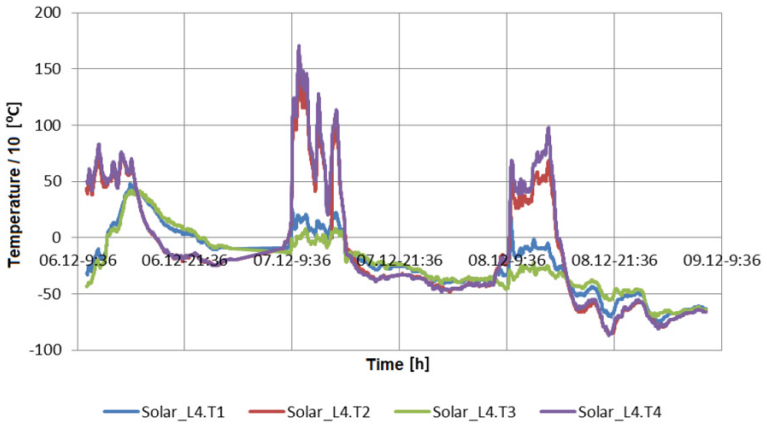

Fig. 13 Monitoring temperatures of the solar thermal collectors, laboratory 4

Figure 10 shows graphically the Hoval boiler parameters on radiators (underfloor heating was off) acquired on December 9th/2013. The temperatures and modulation are highlighted, useful data when deciding to switch between power supplies.

Figures 11, 12 and 13 show temperature of the solar thermal collectors acquired from laboratory L1, laboratory L2 and laboratory L4. The recording was made from December 6th to December 9th 2013. The acquired data will be used in further studies of the behaviour of the solar thermal collectors in Brasov.

Figures 14, 15 and 16 show the wind power acquired from aeolian collectors located on L5 laboratory. The recording was made from December 6th to December 9th 2013. The acquired data can be used to study behaviour of aeolian collectors in Brasov region.

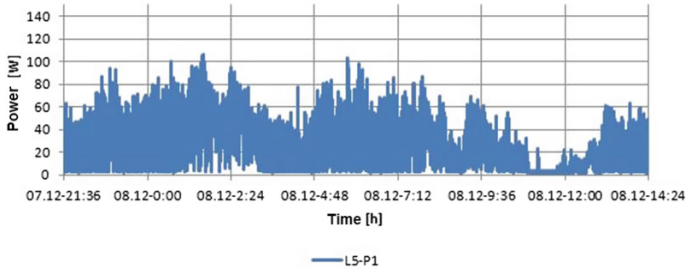

Fig. 14 Monitoring wind power 1—laboratory L5

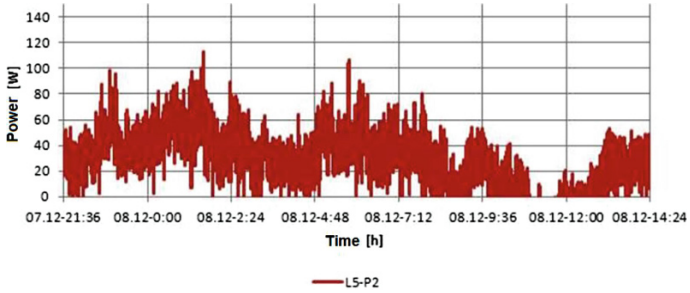

Fig. 15 Monitoring wind power 2—laboratory L5

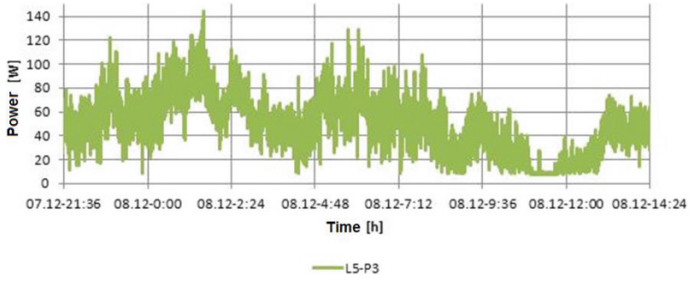

Fig. 16 Monitoring wind power 3 - laboratory L5

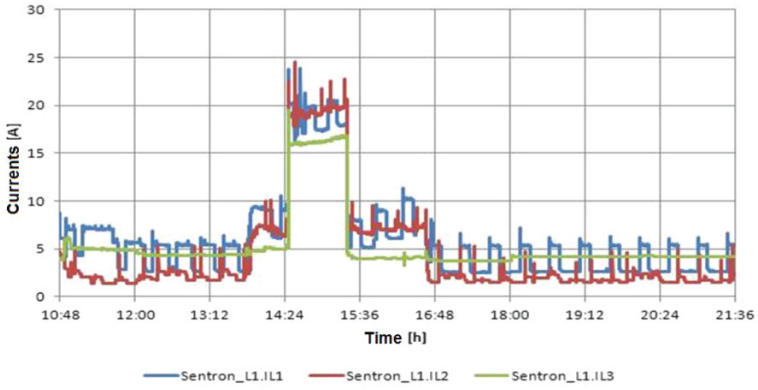

Fig. 17 Monitoring currents for laboratory L1 (06.12.2013)

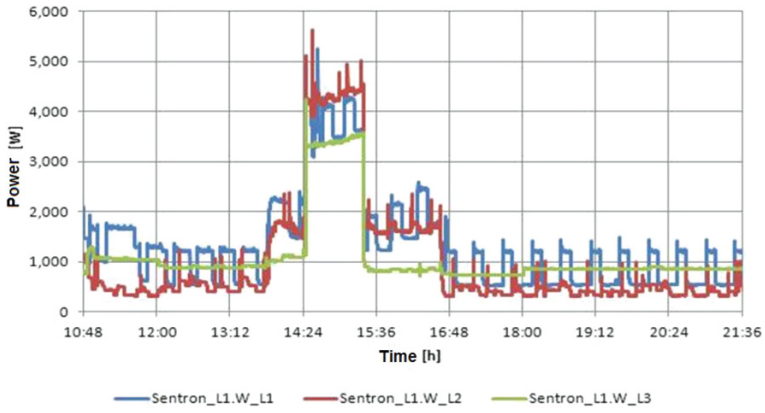

Fig. 18 Monitoring the active power per phase for laboratory L1 (06.12.2013)

The Figs. 17 and 18 show the active power per phase currents respectively for L1 laboratory. Electrical parameters that are acquired are used for monthly reports on consumption, but also to observe the qualitative parameters of the network, the load of each phase and types of consumers.

6 Conclusions

The switching system of heating sources designed, developed and implemented achieved its goal: to reduce the gas consumption. The devised algorithm and the developed software product allowed, through the monitoring of several temperatures collected from the sensors in the system, the maximum use of the energy from the heating pump, achieving a high degree of economy of classic fuel (gas).

Switching between sources was carried out taking into consideration the outside temperature, the storage tank temperature of the heating pump and the target temperatures for each enclosure.

The necessary data for switching between sources was read both directly from the sensors, as well as using communication channels and protocols (such as Profibus, Modbus or M-Bus), much of the data being provided by the gas boiler.

All the acquired data was grouped and stored inside the PLCs' memory, in data blocks that can be easily integrated into a variety of SCADA/HMI systems, allowing the visualization of the stored values, system messages, alarms, but also exporting the data onto PCs and generating reports.

The switching system was developed and implemented at the Institute for Research, Development and Innovation—High-Tech Products for Sustainable Development (ICDT—PRO-DD)—of the Transilvania University of Brasov.

References

1. Ochsner, K. (2011). *Pompe de caldura pentru tehnica incalzirii: ghid practic pentru instalatori si proiectanti*. Bucuresti: Matrix Rom.
2. Chisalita, D. (2007). *Heating pumps. Green energy for buildings*. Brasov: Editura Universitatii Transilvania din Brasov (in Romanian).
3. Chisalita, D. (2011). *Heating pumps*. Brasov: Editura Universitatii Transilvania din Brasov (in Romanian).
4. Viessmann. (2003). Design guidelines. On-line: http://www.viessmann.com/com/en.
5. Hovsl Ultragas, on-line: http://www.hoval.ro/produse/ultragas.
6. ***, Siemens Automation Technology, http://automation.siemens.com.
7. AdfWeb, M-Bus Analyzer/Scanner/Sniffer User Manual.
8. AdfWeb, M-bus Master/Profibus DP Slave User Manual.

Assessment of Wind Energy Resources in Communities. Case Study: Brasov, Romania

Radu Săulescu, Oliver Climescu and Codruţa Jaliu

Abstract The implementation of small wind turbines at community level is limited by the accurate data on wind resource, due to the influence of the built environment. The turbine position and mounting height are important in order to capture the maximum available wind energy, insuring the best power output. The paper is focusing on the wind characterization at community level (in the built environment and in the outskirts) using as case study the Brasov region, where data of five weather stations, distributed in the investigated area are comparatively analysed. The daily and monthly mean wind distribution and other wind speed parameters of the sites are measured and compared. The results of the wind potential parameters allow optimizing the specific implementation site for the small wind turbines in the built environment.

Keywords Wind energy · Potential · Built environment · Wind turbine

1 Introduction

The use of renewable energy sources (RES) increased significantly, mainly due to the need to reduce the fossil fuels consumption. Among the RES, wind became a feasible alternative to the conventional resources, due to its huge potential and low-cost investments for the conversion system. Large wind farms are installed worldwide, proving extended knowledge in this field. On the other hand, it is still a challenge to design small scale wind turbines to be implemented at community level because of the direct dependence of the wind resource characteristics on the implementation site. The built environment modifies the wind natural features and leads to turbulences and a variable potential, with a rather low predictability degree. Under these conditions,

R. Săulescu · O. Climescu · C. Jaliu (✉)
Renewable Energy Systems and Recycling Research Centre,
Transilvania University of Brasov, Brasov, Romania
e-mail: cjaliu@unitbv.ro

I. Visa (ed.), *Sustainable Energy in the Built Environment - Steps Towards nZEB*,
Springer Proceedings in Energy, DOI 10.1007/978-3-319-09707-7_12

the implementation location of small wind turbines for the built environment needs to be carefully chosen, as to maximize the output energy and to find the optimal places where the cut-in speed is reached during a large number of hours in the year. The turbine position and mounting height are important too, small changes in the location site producing a decrease in the generated power.

The amount of energy that can be generated by a wind turbine is directly linked to the wind potential of the implementation region. The daily, monthly and annual mean wind speeds, the speed frequency distribution, the dominant wind direction, the dependence wind speed—air temperature and humidity are the most important parameters that significantly influence the turbine output and efficiency [1–11]. In the communities' case, these parameters have to be very accurately assessed in order to get the optimal implementation site and the suitable configuration of the wind turbine.

Therefore, predicting wind speed in the built environment by using general wind models can lead to errors and a poor placement of the turbines, thus to lower power output. Many studies focused on the estimation of the wind energy potential in different parts of the world, most of them referring to the implementation of wind farms [12–18]. The complex behaviour of the wind resource in the built environment is studied based on simulations [3, 19–22], wind maps [23, 24], site monitoring [1, 2, 4, 5, 7–9, 25, 26] and/or the use of wind tunnels [21, 27]. The first method consists in analyzing the air flows around the virtual model of the built environment, based on specific software (e.g. CFD, ANSYS) [3, 19–22]. The software allows analyzing the air flows in all points around the model, but it also brings uncertainties [21]. The second method uses both wind maps and measurements to establish the wind potential, being reported as less accurate [23, 24]. The most accurate way is to measure the wind parameters at the implementation site, in different points, for at least one year period [1, 2, 4, 5, 7–9, 25, 26]. Another way is to build small scale models of the neighboring buildings and place them in the wind tunnel at different wind conditions [21, 27], respecting the scalability evaluated based on non-dimensional scaling criteria. Unlike software simulations, the last three methods provide wind information only in the measuring points.

Based on these methods, the wind potential had been assessed in urban environments, in different countries, and, subsequently, small scale turbines were implemented, either mounted on rooftops, or placed on buildings walls, corners [12, 18, 21, 28, 29]. The most common configurations recommended for the built environment are the lift-driven horizontal axis wind turbines and the drag-driven vertical axis wind turbines [28, 29].

In Romania, the first map containing the major wind characteristics was drawn in 1962 based on the meteorological measurements taken every hour over a ten-years period (1951–1960) [10], placing the country on the first position among the SE European countries in terms of wind potential. The recent Romanian wind atlases offer information mainly for the wind farms developers (thus in open fields), being based on estimated data [30]. The weather stations belonging to the Romanian Meteorological Administration are located infield, and, therefore, the wind data for urban locations can only be roughly estimated.

The paper discusses the influence of the built environment as compared to infield data for a given community location; a case study validates the assumptions based on the assessment and analysis of the wind energy potential for small wind turbines in the outskirts and in the urban Brasov area, based on the recorded data from five weather stations distributed in key-sites. The monthly mean wind distribution and other wind speed parameters are measured and compared. The results allow creating a database supporting the preliminary assessment of the wind potential in the Brasov area and allow concluding on the type and placement of small-scale wind turbines in the built environment, at communities' level.

2 Methodology

The design of small-scale RES systems based on wind turbines to be implemented in the built environment rely on the on-site data, thus there is a pre-requisite to accurately monitor the wind resource. Therefore, the assessment of wind potential in a community should be based on the data collected in the outskirts and in the core-community locations, for over one year period. For the investigated location (Brasov city and outskirts), the weather stations are implemented as presented in Fig. 1 (the arrows are indicating the position of the stations):

Brasov is a city in the centre of Romania, located in the curvature of the Carpathian Mountains. The relief in the area is mountainous in the South and East, and relatively flat in the North side.

The weather data are provided by five stations, located in the Northern part of Brasov; one station is located in Brasov city centre (Colina campus, 45.63°N/25.58°E) (Fig. 1b). The location is on a hill, with buildings of relatively uniform heights. The meteorological station is mounted on a building rooftop, at 2 m height (Fig. 1b) from the terrace (10 m from the ground), being of Delta-T type, with: an anemometer, a wind vane, a rain gauge, air temperature sensors, and a sunshine pyranometer. The wind speed sensor accuracy is ±0.1 m/s and for wind direction is less than ±2 %.

The other four stations are installed in the outskirts (the University Research Institute, 45.67°N /25.55°E) (Fig. 1a):

- three of the measuring instruments are located on the rooftop of the main buildings, in the Research Institute campus (Fig. 1a), in Southeast and Northwest positions (L11_NW, L11_SE and L7_NW). The buildings in the area are of uniform heights, being linked by a taller atrium and a lower spine (Fig. 2). The surroundings are crop fields. The meteorological stations are mounted at 4.8 m height from the terrace (16.8 m from the ground level). The instruments are produced by Adcon Telemetry and Delta-T Devices Ltd type, all of them meeting the WMO requirements;
- the fourth weather station (Fig. 1a) is mounted at a height of 10 m above ground level, 300 m far from the Research Institute, in the field.

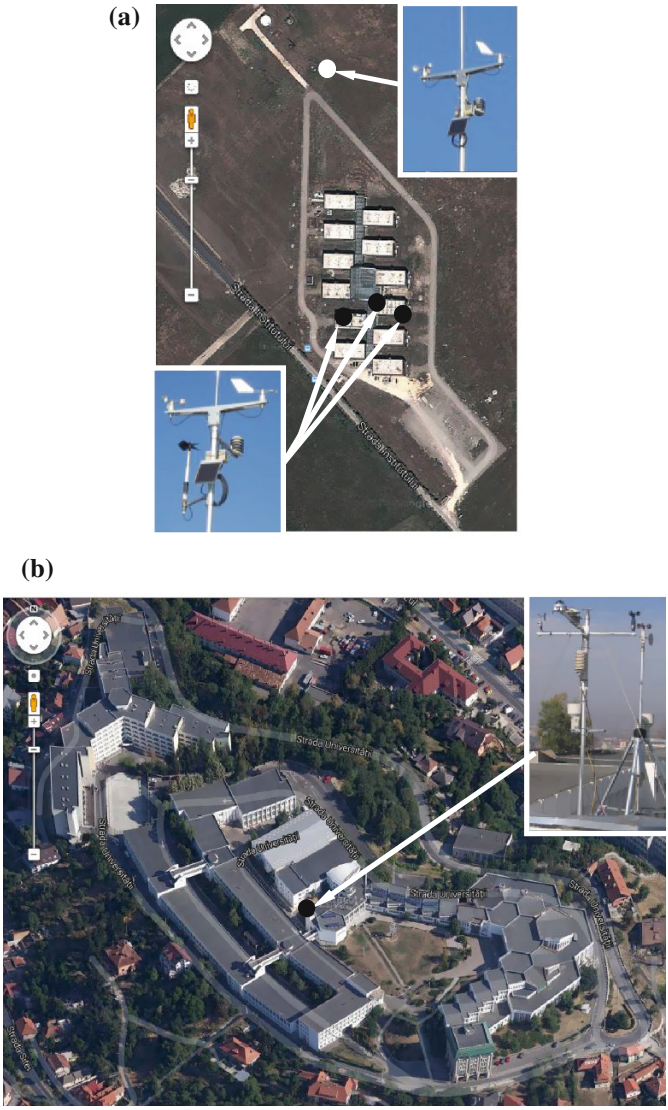

Fig. 1 The locations of the weather stations: Research Institute (**a**), Colina Campus (**b**)

Each of these four weather stations consists of: a cup anemometer and a wind vane, a combined air temperature—humidity sensor, and a solar cell providing the necessary energy. The wind speed sensor accuracy is ±0.1 m/s and starts at less than 0.4 m/s, while the accuracy for wind direction measurement is of ±2.5 %. Additionally, the three meteorological stations on the buildings terraces contain a Gill propeller type anemometer for measuring the vertical wind speeds.

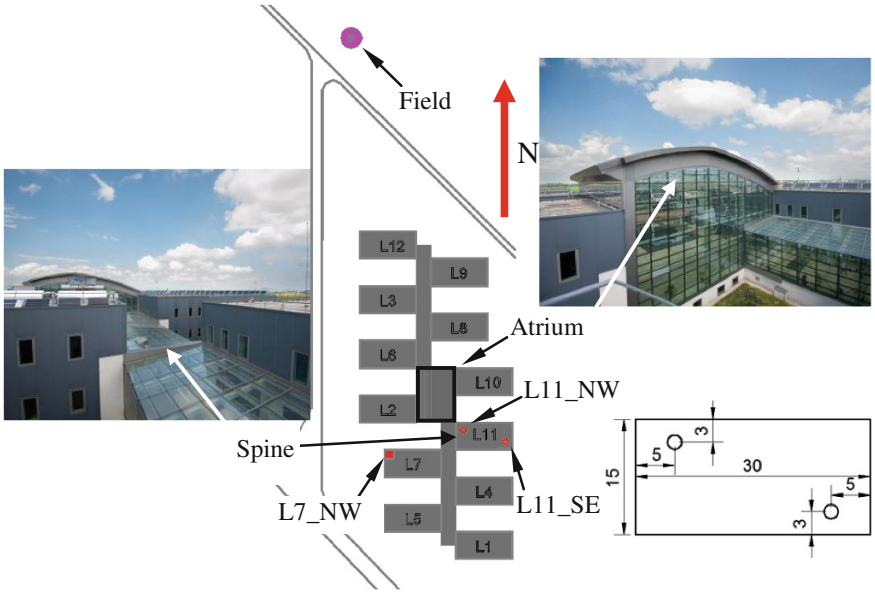

Fig. 2 The Research Institute buildings and the location of the four weather stations

The data are collected over 19 months (October 2012–April 2014) at the four stations located in the outskirts, and for over 5 years period (January 2009–April 2014) at the urban station. The measurements for wind speed, wind direction, air temperature, relative humidity and solar radiation are made every minute at the 4 stations from the Research Institute (for accurately defining the wind profile) and every 10 min at the urban station (as recommended by the National Meteorology and Hydrology institute).

The monthly mean wind distribution and other wind speed parameters of the sites across the years are determined. As the wind data are recorded at different elevations, it was necessary to adjust them to the standard height of 10 m to allow comparison [6, 18], using Eq. (1), [6]:

$$v_1 = v_2 \left(\frac{H_1}{H_2} \right)^{\alpha} \tag{1}$$

where v_1 is the computed mean wind speed at 10 m height, v_2 is the mean wind speed measured at the weather station, H_1 is the anemometer standard height (10 m), H_2 is the anemometer real height, α is the roughness factor with values from 0.1 to 0.4, depending on the surface roughness, the time of the day, the level of wind speed, the wind stability [6]. One way to get the value of the roughness factor α is by using Eq. (2) [31]:ą

$$\alpha = \frac{0.37 - 0.0881 \cdot \ln v_2}{1 - 0.0881 \cdot \ln(H_2/10)} \quad (2)$$

Literature [11] offers as appropriate a roughness factor value of 1/7, which suits the weather conditions of Brasov measurements, as well. The difference between the computed value and the measured one being less than 1 %, the value of 1/7 for the roughness factor is considered in the paper.

The scalar mean wind speed is computed on daily, monthly and annual basis as the arithmetic mean of the instantaneous values.

Beside the mean wind speed, the wind speed frequency distribution (the number of hours/month during which the given wind speeds occur) is also important in the wind potential assessment. It gives the information on the time in which the turbine is either out of action or generates the rated power. The frequency distribution (%) is obtained from the wind speed data as a function of time.

The wind direction is an important feature of the wind potential. The prevailing wind direction can be identified in the wind rose, and represents an important requirement in the implementation of a wind turbine. The five wind roses present the distribution of the wind direction over the monitoring period of time at the five measurement locations.

After the information that characterizes the wind potential in the five locations was collected, the values of the mean wind speeds, the frequency and the prevailing wind directions are further compared. Recommendations for small wind turbines implementation are formulated based on the results of wind potential assessment.

3 Results and Discussions

The most representative month in terms of wind speed is chosen to be discussed in the paper. The data recorded since 2009 at the urban weather station and in 2013–2014 at L7_NW (Tab. 1) prove that March is the month with the maximum wind potential in the year, the monthly speed exceeding the annual value. The year 2011 was less windy (wind class 1, according to Beaufort wind scale), the month with the best wind potential being July (Table 1).

Table 1 The mean wind speeds at two of the locations

Year	Monthly mean wind speed—March		Annual mean wind speed	
	Colina Campus	Research Institute	Colina Campus	Research Institute
2009	1.38	–	1.16	–
2010	1.62	–	1.18	–
2011	0.60	–	0.93	–
2012	1.81	–	1.25	–
2013	1.71	2.94	1.27	2.09
2014 (01–04)	1.64	2.62	1.16	1.96

Further, the most important wind potential parameters for March 2013, the month with the highest mean wind speed, at the five locations will be presented and analyzed comparatively.

Wind Speed

The first step in the analysis of the wind speed is to adjust the information recorded at the three stations mounted on the terrace of the Research Institute buildings at the standard height of 10 m by using relation (1). The calculated wind speed and the measured wind speed in March 2013 for the three stations on the Research Institute rooftop (Figs. 1a and 2) are presented in Fig. 3a–c. Thus, the wind characteristic parameters from the five stations can be further compared. The diagrams outline the influence of the neighboring buildings, group of buildings, and of the surrounding area on the air flows.

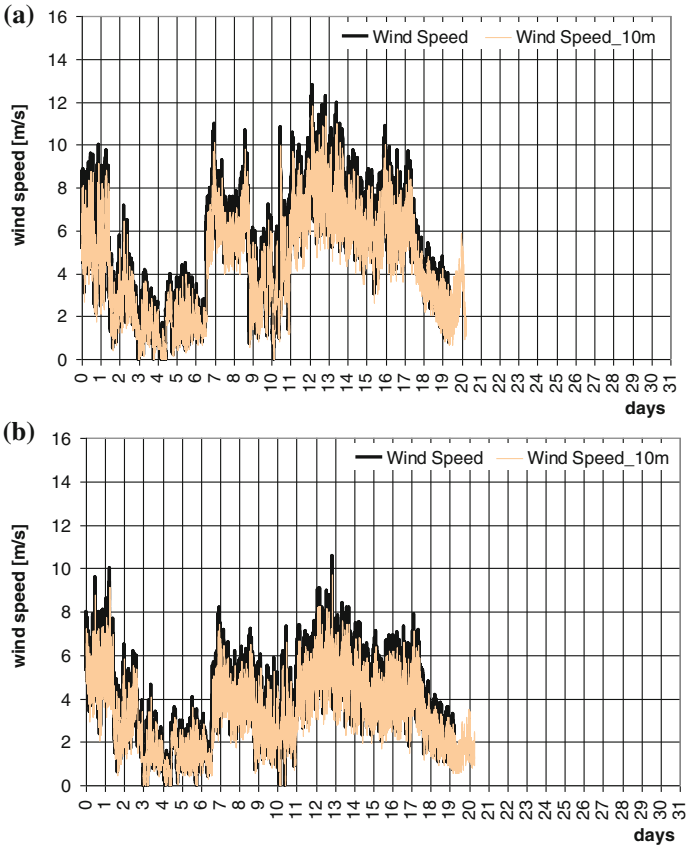

Fig. 3 Mean daily wind speeds for March 2013, in the five locations: L11_NW (**a**), L11_SE (**b**), L7_NW (**c**), Infield (**d**), Colina Campus (**e**)

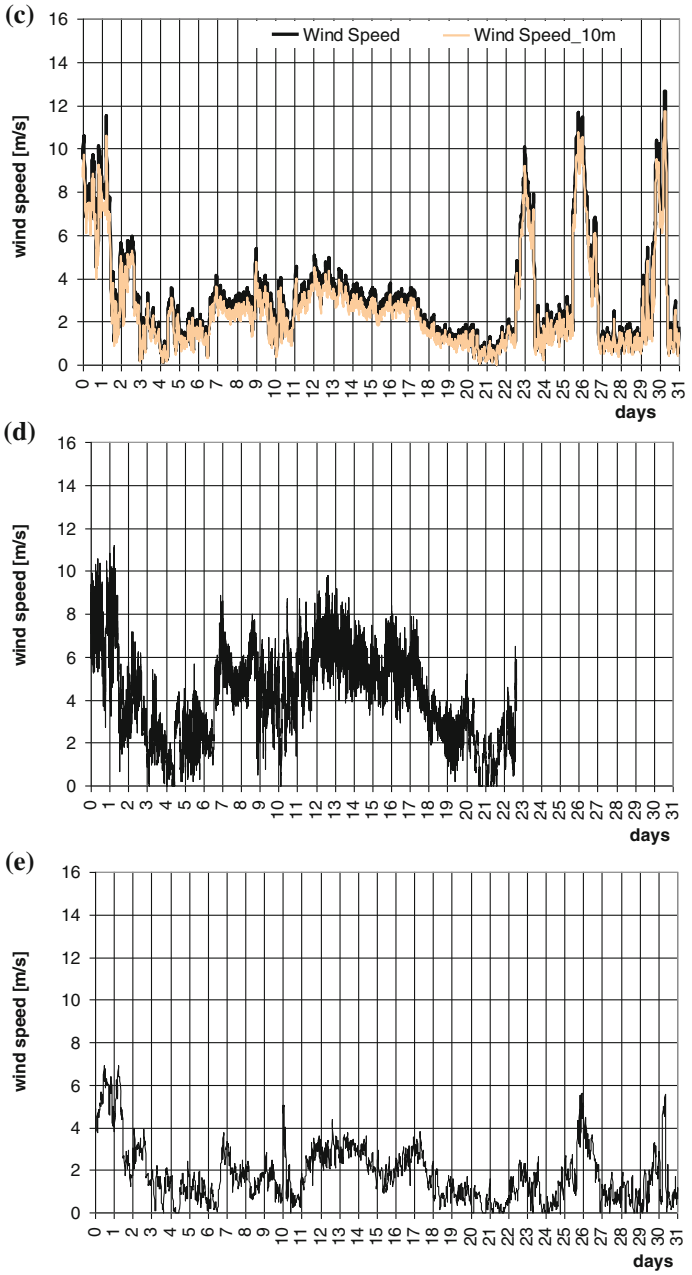

Fig. 3 (continued)

The area with the largest wind speed is located in the outskirts, in the infield site, North from the Research Institute, with a monthly average wind speed of 4.23 m/s and a peak value of 15.6 m/s. On the other hand, the light winds blow in the urban area, with average monthly speeds of 1.79 m/s, and peaks of 6.93 m/s in March. Among the rooftop locations, higher speeds are registered at L11_NW station due to the nearby atrium, which redirects the air flows coming from North, Northeast or East direction.

It is also clear from Fig. 3a–c that the wind speed increases with the hub height. The wind speeds at the L11_NW location registered at 16.8 m are higher than the peak speeds from all locations, at 10 m. These results justify the decisions regarding the implementation of small wind turbines on taller buildings, regardless of the wind profile and the relief.

Thus, it can be noticed that the urban area and the outskirts of Brasov are characterized by light winds of class 1; therefore, it becomes crucial to accurately select the optimal location for the small scale turbines implementation, in terms of wind speed and wind frequency. The comparison of the four rooftop wind speed data outlines the importance of monitoring the parameters at the implementation site, any obstacle significantly modifying the wind pattern.

The speeds at the urban site (Fig. 3e), which is located on a hill in the center of Brasov city (Fig. 1b) are strongly influenced by the hills and mountains that surround the place, as well as by the taller buildings in the area. The relief and the built environment break the air flows and, thus, reduce the wind speed.

The results for the outskirts are justified by the presence of a taller building (i.e. atrium) that increases the wind speeds over 6 m/s for the locations placed on the prevailing wind direction (L11_NW).

It may be therefore concluded that the buildings don't significantly influence the speeds over 12 m/s, but these values are not characteristic for the built environment. The buildings reduce the wind speeds below 6 m/s for the locations behind taller buildings, which redirect the air flows (i.e. L7_NW).

Wind Speed Distribution in Time

The frequency distribution of the wind speeds for each meteorological station, during March 2013, is presented in Fig. 4. The data allow characterizing the region as an area with preponderant light winds (<2 m/s). Over than 60 % of the time, the wind speeds at the urban location (Fig. 4e) are lower than 2 m/s, imposing the implementation of very light small scale wind turbines, with cut-in speeds less than 2 m/s.

In the outskirts, at the location near the tall atrium, the time-distribution of the wind speeds up to 10 m/s has small variations, between 8 and 21 %, allowing the implementation of wind turbines with higher cut-in speeds and rated speeds. The L7_NW location is also characterized by light winds, the wind being less than 2 m/s for about 40 % of the month time. The air flows coming from North or East meet the taller building (the atrium), which redirect them.

Thus, one may conclude that the sites near taller buildings against the wind are not suitable for turbines implementation; on the other hand, these are very good

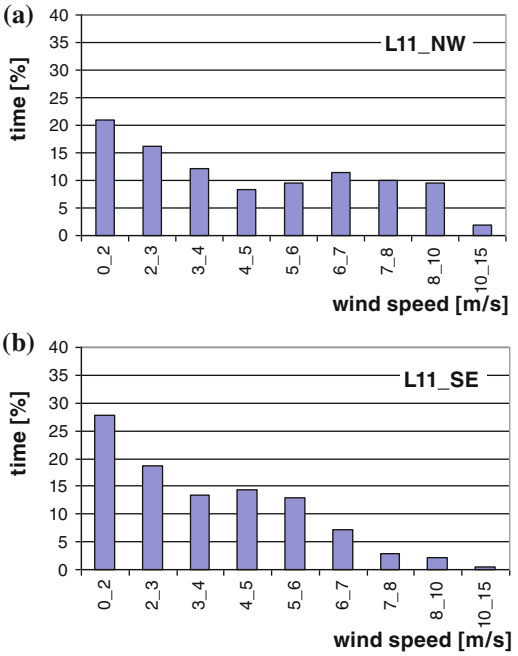

Fig. 4 The wind speeds distributions for March 2013, in the five locations: L11_NW (**a**), L11_SE (**b**), L7_NW (**c**), Infield (**d**), Colina Campus (**e**)

locations for giving use to the building terraces for gardening or recreation purposes.

It can be noticed that, for short periods of time, the wind had values over 7 m/s, values which could be recorded only in the outskirts. This behavior in the urban areas is justified by the neighboring buildings effect that fragments the air flows. As the wind speed frequency is low for speeds over 2 m/s, this type of urban locations could be equipped with vertical axis or light horizontal axis wind turbines, or could be used for recreation.

The infield location is characterized by a similar pattern as the L11_NW site, proving that the two areas are exposed to a dominant North or North-East wind flow and that the nearby buildings don't influence the air flows. Thus, the locations with no taller buildings in front of the air flows are characterized by higher wind speeds and allow implementing small scale wind turbines.

The wind direction frequency distributions and the prevailing wind directions for the five locations during March 2013 are presented in the wind roses from Fig. 5 [32]. The data show that most of the time, the prevailing wind in Brasov outskirts, was North for the station installed in the NW corner (L11_NW), being influenced by the neighboring atrium, (East positioned). For the other four locations, the wind flows from East and North-East due to the Nemir wind, which is blowing from the East Carpathians.

Fig. 4 (continued)

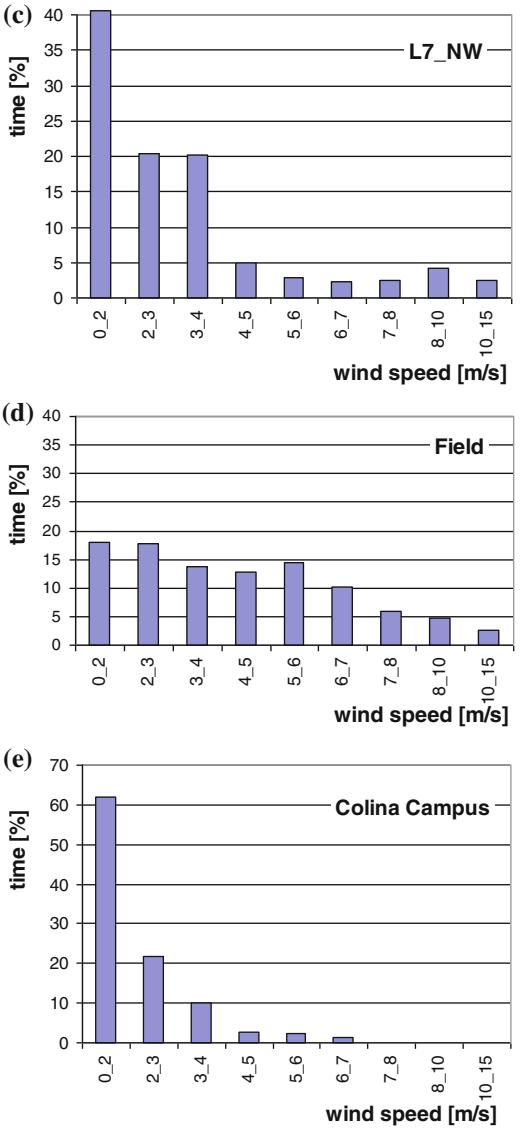

The urban location is characterized by a wind blowing from East, as well (Fig. 5e), with the highest percentage of the prevailing wind direction is 42.26 % from the North for L11_NW station, proving that the atrium redirects the air flows.

The highest percentage of windward direction for the other four locations varies from 25.54 % for the urban site from East and South-East, to 40.81 % for L7_NW

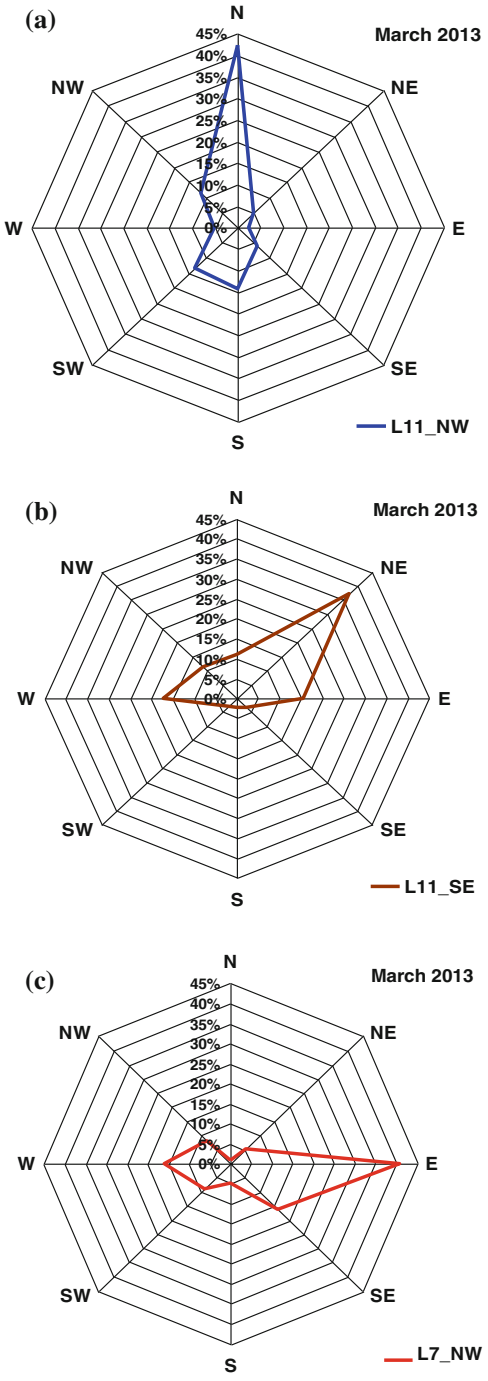

Fig. 5 The wind roses for the five locations, March 2013: L11_NW (**a**), L11_SE (**b**), L7_NW (**c**), Infield (**d**), Colina Campus (**e**)

Fig. 5 (continued)

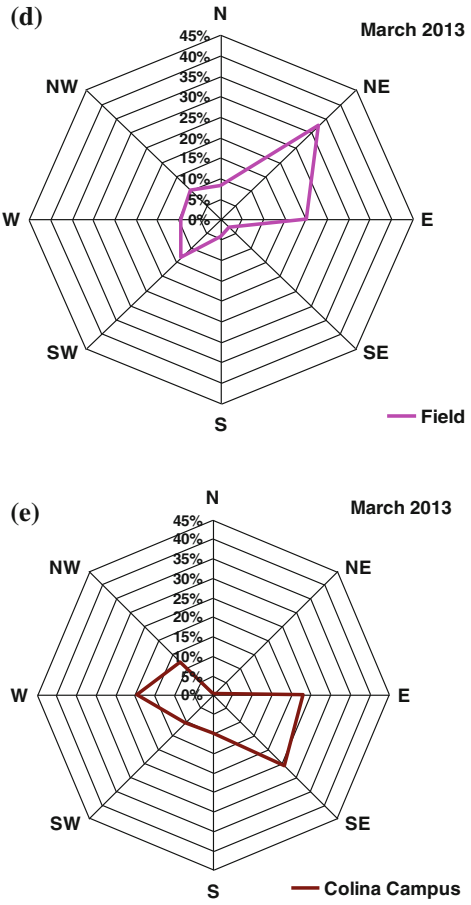

location from East and North-East. Thus, it can be concluded that the most frequent wind directions for the investigated area are North, North-East and East.

The variable wind potential imposes the implementation in the area of light, small scale wind turbines, easy to follow the wind flow and having a low cut-in speed. Therefore, six horizontal axis turbines were mounted on two terraces, two in the corners and one on a side at half distance (Fig. 6). The different wind characteristics of the six locations influence the turbines output power. Thus, the different behavior of the turbines in the same time proves the correctness of the wind potential data and demonstrates the importance of measuring the parameters at the implementation site, due to the influence of the neighboring built environment (i.e. the atrium).

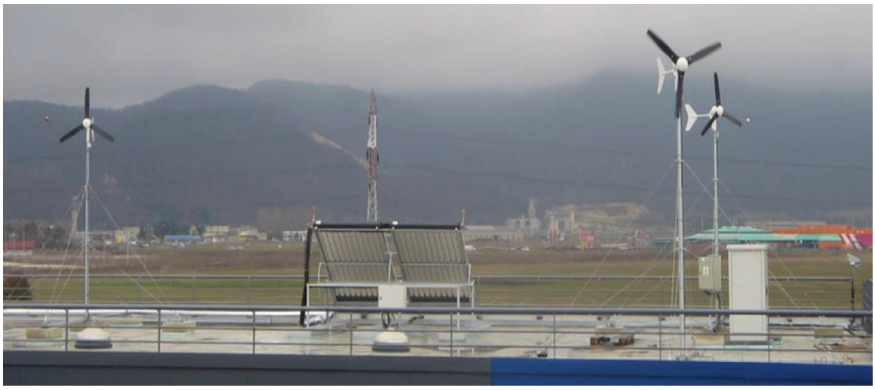

Fig. 6 Three wind turbines of 300 W each, installed on the terrace of one of the Research Institute buildings

4 Conclusions

The data outline the variability of the wind potential in the built environment, which can be registered even on very small differences of the possible implementation sites of small wind turbines (15–30 m). It is also evidenced that the infield features are reached close to the built environment (less than 50 m), thus allowing implementing small wind farms very close to the community built area.

These conclusions were formulated based on a case study—the Brasov community, characterized by a limited wind potential, which fits into the Class 1 wind classification. The differences between the data registered infield and at the urban station outline the influence of the built environment on the efficient and profitable running of a wind turbine.

The wind direction in Brasov is predominantly from North, North-East and East. Thus, the wind directions to be considered in the implementation of small-scale wind turbines in Brasov outskirts are East and North.

The wind resources in the Brasov area could be efficiently exploited by using either light, horizontal axis small wind turbines, specifically optimized for these conditions or vertical axis turbines that start/function independent of the wind direction. Another solution is represented by the concentrated wind turbines that use a nearby building as concentrator.

This analysis represents the basis for further research on designing and implementing optimized small wind turbine farms, according to the location characteristics and for selecting its proper implementation site.

Acknowledgments We hereby acknowledge the structural founds project PRO-DD (POS-CCE, O.2.2.1., ID 123, SMIS 2637, ctr. No 11/2009) for providing the infrastructure used in this work.

References

1. Ucar, A., & Balo, F. (2010). Assessment of wind power potential for turbine installation in coastal areas of Turkey. *Renewable and Sustainable Energy Reviews, 14*, 1901–1912.
2. Makkawi, A., Tham, Y., Asif, M., & Muneer, T. (2009). Analysis and inter-comparison of energy yield of wind turbines in Pakistan using detailed hourly and per minute recorded data sets. *Energy Conversion and Management, 50*, 2340–2350.
3. Sunderland, K. M., et al. (2013). Estimating the wind resource in an urban area: A case study of micro-wind generation potential in Dublin, Ireland. *Journal of Wind Engineering and Industrial Aerodynamics, 118*, 44–53.
4. Fagbenle, R. O., Katende, J., Ajayi, O. O., & Okeniyi, J. O. (2011). Assessment of wind energy potential of two sites in north-east, Nigeria. *Journal of Renewable Energy, 36*(4), 1277–1283.
5. Cabello, M., & Orza, J. A. G. (2010). Wind speed analysis in the province of Alicante, Spain. Potential for small-scale wind turbines. *Journal of Renewable and Sustainable Energy Reviews, 14*(9), 3185–3191.
6. Lashin, A., & Shata, A. (2012). An analysis of wind power potential in Port Said,Egypt. *Journal of Renewable and Sustainable Energy Reviews, 16*(9), 6660–6667.
7. Ouammia, A., Sacile, R., & Mimet, A. (2010). Wind energy potential in Liguria region. *Renewable and Sustainable Energy Reviews, 14*, 289–300.
8. Ullah, I., Chaudhry, Q. Z., & Chipperfield, A. J. (2010). An evaluation of wind energy potential at Kati Bandar, Pakistan. *Renewable and Sustainable Energy Reviews, 14*, 856–861.
9. Mirhosseini, M., Sharifi, F., & Sedaghat, A. (2011). Assessing the wind energy potential locations in province of Semnan in Iran. *Renewable and Sustainable Energy Reviews, 15*, 449–459.
10. Rusan, N. (2010). Wind energy potential in the east of Romania. *Romanian Journal of Geography*, *54*(1), 77–88.
11. Peterson, E. W., & Hennessey, J. P, Jr. (1978). On the use of power laws for estimates of wind power potential. *Journal of Applied Meteorology, 17*, 390–394.
12. Aslam Bhutta, M. M., Hayat, N., Farooq, A. U., Ali, Z. (2012). Vertical axis wind turbine—A review of various configurations and design techniques. *Journal of Renewable and Sustainable Energy Reviews*, *16*(4), pp. 1926–1939.
13. Millward-Hopkins, J. T., Tomlin, A. S., Ma, L., Ingham, D. B., & Pourkashanian, M. (2013). Assessing the potential of urban wind energy in a major UK city using an analytical model. *Renewable Energy, 60*, 701–710.
14. Calif, R., Emilion, R., & Soubdhan, T. (2011). Classification of wind speed distributions using a mixture of Dirichlet distributions. *Renewable Energy, 36*, 3091–3097.
15. Millward-Hopkins, J. T., Tomlin, A. S., Mab, L., Ingham, D. B., & Pourkashanian, M. (2013). Mapping the wind resource over UK cities. *Renewable Energy, 55*, 202–211.
16. Nor, K. M., Shaaban, M., Abdul Rahman, H. (2014). Feasibility assessment of wind energy resources in Malaysia based on NWP models. *Renewable Energy*, *62*, 147–154.
17. Ahmed, A. S. (2011). Analysis of electrical power form the wind farm sitting on the Nile River of Aswan, Egypt. *Renewable and Sustainable Energy Reviews, 15*, 1637–1645.
18. Ettoumi, F. Y., Adane, A. E. H., Benzaoui, M. L., & Bouzergui, N. (2008). Comparative simulation of wind park design and sitting in Algeria. *Journal of Renewable Energy, 33*(10), 2333–2338.
19. Lackner, M. A., deVelder, N., Sebastian, T. (2013). On 2D and 3D potential flow models of upwind wind turbine tower interference. *Computers & Fluids*, *71*, 375–379.
20. Drew, D. R., Barlow, J. F., & Cockerill, T. T. (2013). Estimating the potential yield of small wind turbines in urban areas: A case study for Greater London, UK. *Journal of Wind Engineering and Industrial Aerodynamics, 115*, 104–111.

21. Beller, C. (2011). Development of a simulation tool to predict Urban wind potential. In *Sustainability in energy and buildings, smart innovation, systems and technologies* (Vol. 7, pp. 111–120). Springer, Berlin.
22. Balduzzi, F., Bianchini, A., & Ferrari, L. (2012). Microeolic turbines in the built environment: Influence of the installation site on the potential energy yield. *Renewable Energy, 45*, 163–174.
23. McIntyre, J. H., Lubitz, W. D., Stiver, W. H. (2011). Local wind-energy potential for the city of Guelph, Ontario (Canada). *Renewable Energy*, *36*, 1437–1446.
24. Waewsak, J., Landry, M., & Gagnon, Y. (2013). High resolution wind atlas for Nakhon Si Thammarat and Songkhla provinces, Thailand. *Renewable Energy, 53*, 101–110.
25. Anagreh, Y., Bataineh, A., & Al-Odat, M. (2010). Assessment of renewable energy potential, at Aqaba in Jordan. *Renewable and Sustainable Energy Reviews, 14*, 1347–1351.
26. Dahmouni, A. W., Ben Salah, M., Askri, F., Kerkeni, C., & Ben Nasrallah, S. (2010). Wind energy in the Gulf of Tunis, Tunisia. *Renewable and Sustainable Energy Reviews, 14*, 1303–1311.
27. Fothergill, C. E., Roberts, P. T. (2002). Flow and dispersion around storage tanks: A comparison between numerical and wind tunnel studies. *Wind & Structures*, *5*(2–4), 89–100.
28. Dutton, A. G. et al. (2005). *The feasibility of building-mounted/integrated wind turbines (BUWTs)*: *Achieving their potential for carbon emission reductions*. Energy Research Unit. http://www.eru.rl.ac.uk/BUWT.html.
29. Webb, A. (2007). *The viability of domestic wind turbines for urban Melbourne*. Alternative Technology Association. http://www.ata.org.au/wpcontent/projects/ata_report_domestic_wind.pdf .
30. http://www.adrcentru.ro/Document_Files/ADStudiiRegionale/00000077/e6rq1_Analiza%20potential%20eolian%20Regiunea%20Centru1.pdf.
31. Coelingh, J. P., van Wijk, A. J. M., & Holtslag, A. A. M. (1996). Analysis of wind speed observations over the North Sea. *Journal of Wind Engineering and Industrial Aerodynamics, 61*(1), 51–69.
32. http://www.enviroware.com.

Part II
Renewable Based DHW, Heating and Cooling in the Built Environment

Biomass Potential for Sustainable Environment, Biorefinery Products and Energy

Maria Gavrilescu

Abstract The paper is a short survey on the potential of biomass to become the root source for the production of biobased products and bioenergy, in the circumstances where the 21st century released the challenge for increasing the use of renewable resources in the global economy so as to guarantee the production of new products and energy in an environmentally friendly manner. Some considerations and discussions are provided on global and European challenges like: population growth, rapid urbanization, food supply, water access, energy demand, climate change, resource scarcity, for shaping sustainable present and future. The focus of the paper is on exploring tools to develop and expand the bioeconomy, as a proficient pathway in exploiting biomass potential for sustainable environment, biorefinery products and energy. Also, the environmental impacts and safety of bioprocesses are analyzed, considering the relevant environmental aspects which could generate threats on environmental components. It was suggested that the life cycle analysis can offer the support for decisions making to reduce the environmental pressures of biorefinery processes. In the paper it has been pointed out that investments in research, development and innovation would supply the means to equally convert existing industries, by replacement of fossil resources with renewable ones.

Keywords Biobased products · Bioeconomy · Biofuel · Climate change · Environment · Feedstock · Impact · Sustainable growth

M. Gavrilescu (✉)
Faculty of Chemical Engineering and Environmental Protection, Department of Environmental Engineering and Management, "Gheorghe Asachi" Technical University of Iasi, 73 Prof. Dr. Docent D. Mangeron Street, 700050 Iasi, Romania

M. Gavrilescu
Academy of Romanian Scientists, 54 Splaiul Independentei, 050094 Bucharest, Romania

I. Visa (ed.), *Sustainable Energy in the Built Environment - Steps Towards nZEB*, Springer Proceedings in Energy, DOI 10.1007/978-3-319-09707-7_13

1 Global and European Challenges for Shaping Sustainable Present and Future

During the last decades, the world faced high competition for limited and finite natural resources, which will continue in the next decades, in parallel with opening new ways in using the renewable resources potential for ensuring sustainable environment, biorefinery products and energy. While the 20th century was an epoch of petro-chemistry, which provided the world with both energy and various products that have influenced nearly each part of modern life, a notable increase in energy demand estimated at over 50 % by 2025 is expected, emerging especially from the rapidly developing nations [69, 85].

However, the 21st century opened up new possibilities for increasing the use of renewable resources in the global economy in order to ensure the demands for new products and energy in an environmentally friendly manner. This is a sign that a transition occurs towards a most favorable use of renewable biological resources, by shifting to production and processing systems that can produce more food, fiber and other biobased products, as well as bioenergy, with fewer inputs, a reduction of environmental impact and reduced greenhouse gas emissions [9, 35, 60]. This trend is necessary to be further developed, when the global challenges are considered, such as: population growth, rapid urbanization, food supply, water access, energy demand, climate change, resource scarcity [6].

World population is anticipated to grow (Fig. 1), generating unmatched demand for food, water, energy, and employment. This increase is recorded since

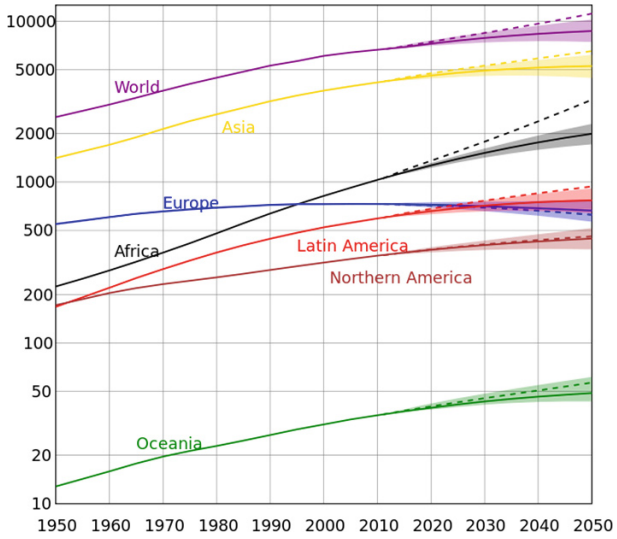

Fig. 1 The evolution of world population by continents between 1950 and 2050 (estimates) (according to the United Nations; the vertical axis is millions of people using logarithmic coordinates) (adapted upon [4, 48])

Table 1 Global proportion of the urban population increase [76]

Year	Urban population (million)	Proportion (%)
1900	220	13
1950	732	29
2005	3,200	49
2030	4,900	60

the end of the Great Famine and the Black Death in 1350, when it was near 370 million, to one billion humans in 1804, 2 billion in 1927, 6 billion in 1999, and 7.2 billion by 2013 [46, 47]. UN forecasts a range from 8.3 to 10.9 billion people by 2050, with 9.6 billion as the mid-projection [4, 48, 77].

Urbanization is a foremost change occurring worldwide. FIG Commission 3 [33] found that the urban global peak was achieved in 2007. Moreover, more than half of the Earth population, i.e. almost 3.3 billion people used to live in urban areas, while the estimates indicate that 60 % of the world's population will be urbanized by 2030 (Table 1) [76]. Figure 2 illustrates countries and territories with 2050 urban populations exceeding 100 millions inhabitants [79].

Food supply is a major challenge for the future, since to satisfy the needs of the ever-growing global population and to produce supplementary food should be done using less land, water and energy [54]. The concerns on food security concerns have evolved recently as a reaction to the problem of food price and increased food demand in the world. Various association such as the Food and Agriculture Organization of the United Nations (FAO) and the International Food Policy Research Institute (IFPRI) developed and published analyses on in global food demand out to 2050 [29, 30, 59].

It is predicted that the increasing in global population and daily food consumption will lead to an increase by 70 % of the world food production in the period to 2050 [13, 29–32] (Fig. 3).

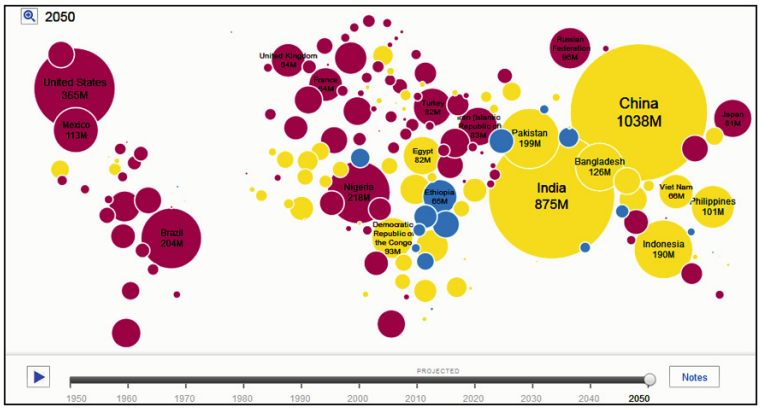

Fig. 2 The evolution of the urban population: 2050 [79]. Significance of colors: *Red* >75 %; *Yellow* 50–75 %; *Blue* 25–50 %; *Green* <25 %

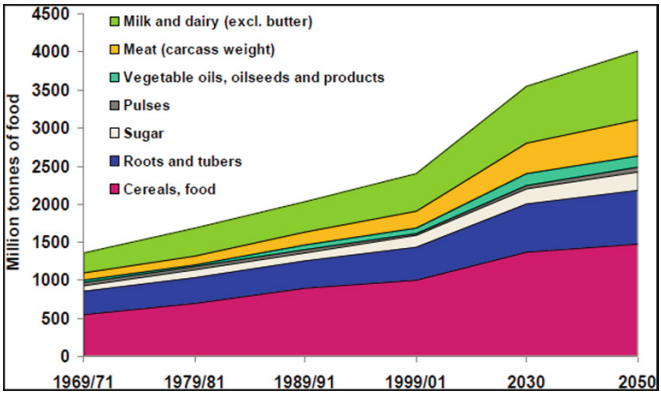

Fig. 3 The food worldwide demand by 2050 (adapted upon [32])

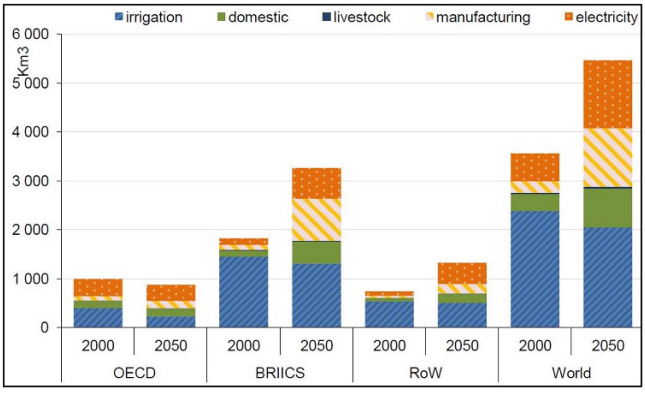

Fig. 4 Global water demand according to Baseline scenario (BRIICS—Brazil, Russia, India, Indonesia, China and South Africa; RoW—rest of the world [62])

Water access is a worldwide problem addressing the global crisis originating in scarce water provision, unable to ensure vital human requirements and growing demands for water resources so as to meet human, commercial and agricultural requests. Today, almost 3 billion of people are affected by water scarcity. Water demand is expected to increase by 55 % worldwide between 2000 and 2050 (Fig. 4) [55, 62]. This state is due to two factors: (i) the increasing in the number of people living in the neighborhoods of river basins supporting severe stress (almost 3.9 billion by 2050, meaning over 40 % of the world's population); (ii) groundwater reduction, which may become the furthermost hazard for agriculture and urban water supplies [55, 58].

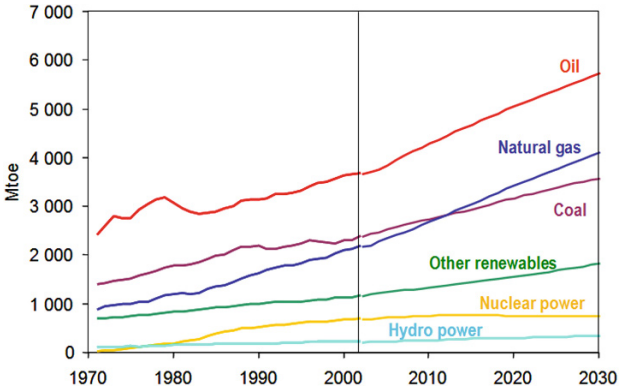

Fig. 5 World primary energy demand during 1970–2030 (taken from [11])

Energy demand will continue to increase, while fossil fuels shall account for almost 90 % of the growth in energy demand between now and 2030 (Fig. 5) [11]. The global energy system continues to be dependent on the fossil fuels.

Due to this situation, some challenges to sustainability are evident for the worldwide energy system [39, 44, 84]: reducing greenhouse gas (GHG) emissions resulted from fossil fuels use, also contributing to climate change at a global scale; energy security problem which results from the rising energy demand, but also from the limited fossil fuel provision; the geopolitical extent of the carbon economy; limited access to energy services in some parts of the world [81]. It is estimated that world energy-related CO_2 emissions will grow with 62 % in 2030, comparative to those in 2002 (Fig. 6) [11].

Climate change induced by human activities occurs in an unprecedented manner since 200 years, affecting life on Earth. The UN Framework Convention on Climate Change considers that climate change is ascribed directly or indirectly to human activities that modify the composition of the global atmosphere and, into a

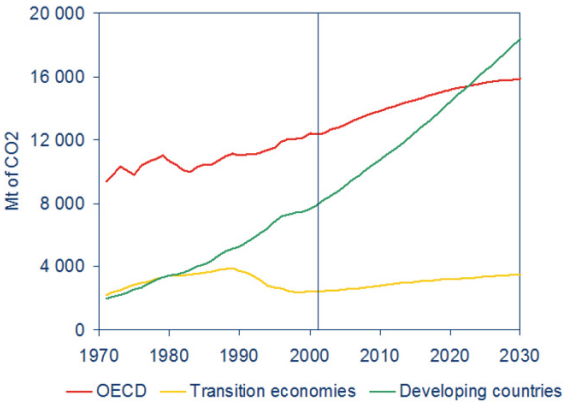

Fig. 6 World energy-related CO_2 emissions in different world economies (taken from [11])

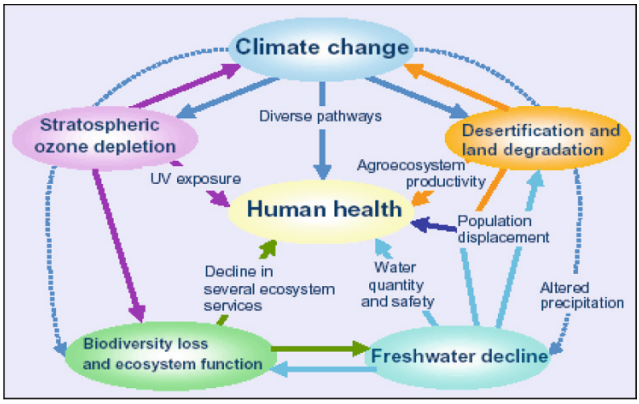

Fig. 7 Climate change impacts on human health and global environmental change (taken from [83])

lesser extent, to natural climate variability, observed over equivalent time phases [42, 83]. Global climate change makes threats on the well-being of society, damages economic growth and modify the natural environment (stratospheric ozone depletion, desertification and land degradation, biodiversity loss and ecosystem function, freshwater decline, all with effects on human health) (Fig. 7), so that it becomes more and more a key of the policy making and concerns of the 21st century.

Resource scarcity is strongly connected with the above-described world challenges and will affect increasingly more the world, since the global population will also continue to expand, boosting the worldwide claim for energy, water and food. In several parts of the planet, the impacts of climate change can produce increases in extreme weather, the levels of the sea and intensification in water scarcity. These effects will determine numerous difficulties in growing crops, animals, development of fish population etc. and will lead to significant increases in requirements for key resources expected to appear in the future, let's say until 2030 [28, 34]. They can be summarized as follows:

- the demand for food could increase with more than 50 % by 2030, while that for meat by 85 % [3];
- a 1 % per year increase in oil requirement of until 2030 (from 85 million barrels a day now to 105 mb/d in 2030) [63, 66];
- an increase by 32 % in global water use is expected between 2000 and 2025, while global water use has been rising almost two times as rapid as population for over a century [2, 78].

To meet **the growing worldwide population** with consequences on the depletion of natural resources (in particular, non-renewable), as well as on increasing environmental impacts and climate change, the current pathways of production, consumption, processing, storage, recycling and disposal of biological

resources [17]. Therefore, there is an obvious and emergent must for enhancing the capacity to foresee changes needed to be implanted in policy and strategy for future development to meet global challenges. In this context, the Europe 2020 Strategy advocates for **bioeconomy** as a key solution for smart, inclusive, sustainable, and green growth in Europe.

The aim of this work is to provide an illustration of the key trends forward and possible future strategies necessary to go beyond current and upcoming global and European challenges in order to shape sustainable present and future. The focus is on exploring tools to develop bioeconomy, able to exploit biomass potential for sustainable environment, biorefinery products and energy.

2 The New Age of Bioeconomy

The bioeconomy, a holistic strategy which involves the sustainable production and use of renewable resources from land, fisheries and aquaculture environments for food, feed, fiber bio-based products and bio-energy as well as the interrelated community supplies, constitutes a significant reply of Europe to the challenges that the humanity continues to rise in terms of resources, energy and environmental pressures. The European Commission characterizes the bioeconomy as: "the production of renewable biological resources and their conversion into food, feed, biobased products and bioenergy. It includes agriculture, forestry, fisheries, food and pulp and paper production, as well as parts of chemical, biotechnological and energy industries" [26]. Also, bioeconomy involves "the application of biotechnology to primary production, health and industry in order to contribute to economic output" [61]. All these issues entail [40]:

- biotechnical knowledge generated to develop new processes for manufacturing a large variety of sustainable products
- use of renewable biomass and proficient bioprocesses to reach sustainable production
- integrated application of knowledge-base sustainable bioeconomy framework across a range of application areas

The idea of a modern, viable, competitive and powerful knowledge-based bioeconomy was launched and established in 2000 at the Lisbon Summit. The EU 2020 Strategy, announced in 2010, includes the bioeconomy as an important component of the three key priorities of the Strategy: "**smart growth**: developing a knowledge and innovation based economy; **sustainable growth**: promoting a more resource efficient, greener and more competitive economy; **inclusive growth**: fostering a high employment economy delivering social and territorial cohesion" [27]. There is a continuous dynamic in the European bioeconomy, in terms of strategy and vision (Fig. 8), starting with the Lisbon Summit in 2000, and the re-launched Lisbon strategy, in 2005 [16, 17, 70].

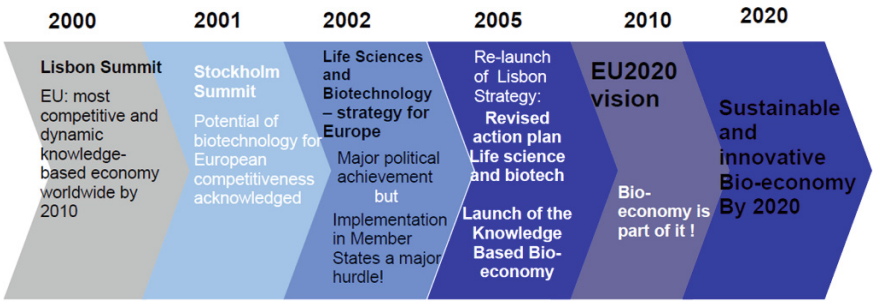

Fig. 8 Dynamics of European bioeconomy concept and vision (taken from [70])

The bioeconomy strategy is correlated with the concepts of *decoupling growth from resource use* and *achieving more at lower environmental costs,* also requiring ways for enhancing resource efficiency and reducing the amount of resources used to meet humanity needs. These also should contribute to the reduction of the environmental impacts on water, air, soil and biodiversity. Figure 9 shows how resource efficiency relates to the use of natural capital and ecosystem resilience [24, 29, 30]. Expected profits from the conversion in a bio-based economy embrace a lessening of greenhouse gas (GHG) emissions, reduction in the dependence on fossil resources, enhanced food security, advanced management of natural resources [20, 52, 57]. Therefore, there is a need to appraise the appearance of new

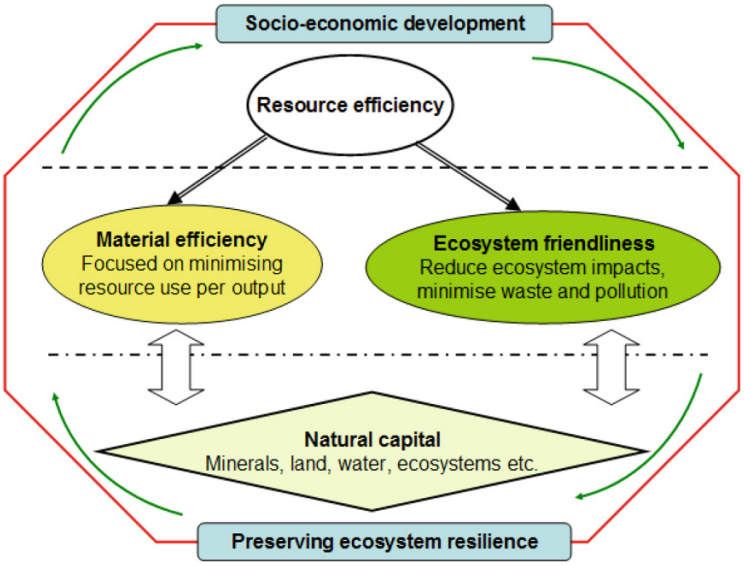

Fig. 9 The two key aspects of resource efficiency in the context of bioeconomy able to ensure the preservation of ecosystem endurance together with the socio-economic development (adapted from [24])

biobased industries and markets inside the wide structure of the bioeconomy, for bioenergy, bio-based products, biotechnologies and biorefineries. It is expected that innovation will supply the break to equally convert existing industries, by replacement of fossil resources with renewable ones (chemical industry, biofuel industry, physical share of foreign resources, development of biotechnology, advanced biorefinery for energy and materials) and to open new markets for new bio-based products [57, 72].

The bioeconomy is based on a variety of feedstocks and processes to convert these feedstocks into a large variety of products and energy, as illustrated in Fig. 10. As described in Fig. 10, the feedstocks are grouped in three generations, dependent on the easiness to access carbon. Processes are grouped in three categories: thermochemical, chemical and bioprocessing. It's also a hierarchy in products value, with the lowest value at the bottom [34, 36, 45]. The recognition of issues affecting the advance of the bioeconomy can operate as the root for elaborating ideas, objectives, strategies and measures to perform the shift in the direction of a bio-based economy. For example, the EU's Energy Roadmap 2050 [21] anticipates the crucial task of bioenergy by 2050 in ensuring a reduction of 80–95 % in gas emissions in EU, emphasizing the increasing bioenergy influence in facilitating major decrease in GHG emissions with impact on ecological resources. This also highlights the importance of biomass in the strategy for sustainability in the EU and the degree of its potential impacts [21–23, 37, 67].

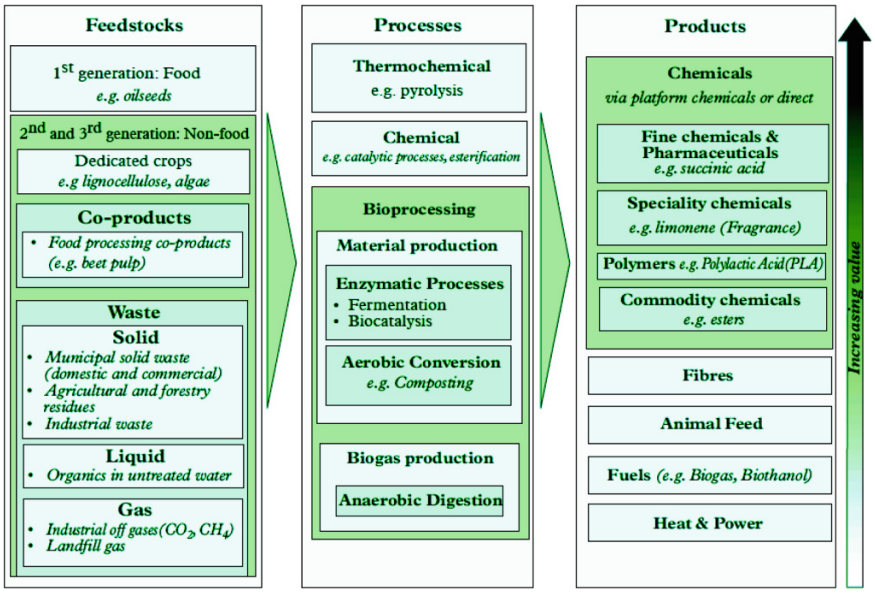

Fig. 10 Feedstock, process and product categories in the bioeconomy context (adapted from [45])

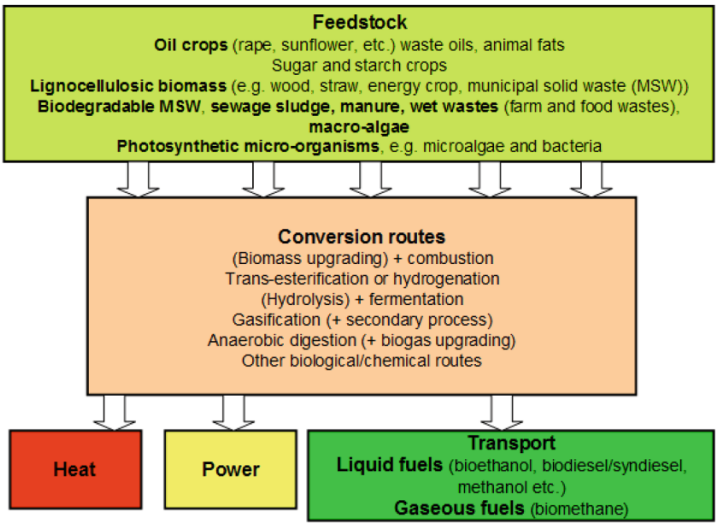

Fig. 11 Routes for converting biomass to energy (adapted from [24])

Specialists and decision makers can be helped to select resource-efficient renewable energy sources and the conversion routes, if costs and impacts of alternative technologies are determined, as well as of biomass categories resulting from agriculture, forests and wastes (lignocellulosic biomass, oil crops, biodegradable/organic waste, micro-, macro-algae etc.), so as to be able to implement economic alternatives by 2020, as those illustrated in Fig. 11.

To preserve its competitiveness, Europe guarantees adequate raw materials, energy and industrial products under conditions of decreasing fossil carbon resources. To handle the problems generated by an increasing global population, fast exhaustion of various resources, increasing environmental pressures and climate change, Europe should radically revolutionize its approach to production, consumption, processing, storage, recycling and disposal of biological resources [21–23]. The Communications from the Commission to the European Parliament [22, 23] mention that "Europe 2020 Strategy calls for a bioeconomy as a key element for smart and green growth in Europe. Advancements in bioeconomy research and innovation uptake will allow Europe to improve the management of its renewable biological resources and to open new and diversified markets in food and bio-based products".

Bioeconomy in Europe would ensure maintaining and generating economic development and jobs and improvement of economic and environmental sustainability. Therefore, the bioeconomy development should contribute to any decrease in the dependence on fossil resources by about 60 % by 2050. Moreover, the **biowaste** (estimated at up to 138 million tons per year in EU—up to 40 % being

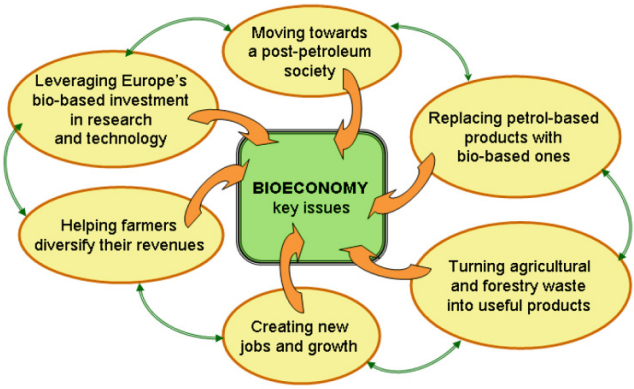

Fig. 12 Key issues in bioeconomy

currently land-filled) possesses high potential added value as a feedstock for additional productive processes, allowing that biological resources and ecosystems be used in a more sustainable, efficient and integrated manner.

The switch from a fossil **fuel-based economy** into a **bio-based economy** could be limited by the supply of ecologically sustainable biomass, which needs to be enough to meet at least 10–20 % of the final energy and feedstock consumption in 2030 [38, 67]. Therefore, from a sustainability perspective, there is an urgent need to guarantee ecologically sustainable biomass production. This way some key issues of European bioeconomy would be fulfilled (Fig. 12). Bio-based products (**bio-based:** derived from biomass; **bio-based product**: wholly or partly bio-based) are considered of high societal and economic interest due to several positive factors [23, 36, 37] illustrated in Fig. 13.

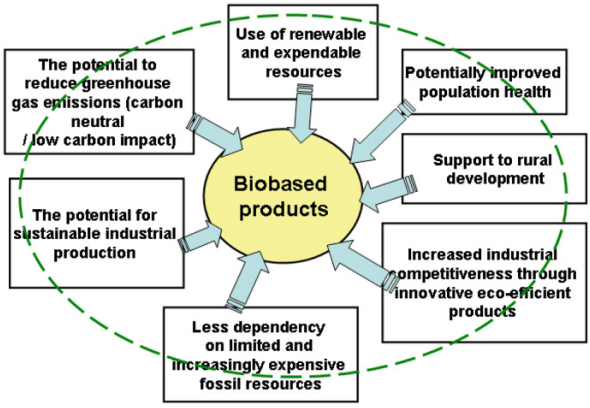

Fig. 13 Societal and economic interest of biobased products (adapted upon [23])

3 A Bioeconomy Strategy for Europe

The bioeconomy is assumed to add significantly new values to the objectives of the flagship initiatives associated to Europe 2020 strategy, specifically *Innovation Union* and *A Resource Efficient Europe,* since Europe keep on facing up to an unprecedented and unsustainable use of natural resources, even if numerous efforts in terms of research, development and innovation were invested in the last decades [16, 17, 67]. Moreover, considerable and potentially irrevocable alteration to its climate and a persistent loss in biodiversity continue to endanger the immovability of the living and socio-human systems.

The European Commission has established a coordinated approach to promote the use of biomass to support and facilitate the implementation of the European strategy for mitigating the climate change phenomenon and ensure the generation of renewable energy. In this context, some initiatives were launched such as the adoption of "Biomass Action Plan" and "EU Strategy for Biofuels" [12, 16]. In this context, EU should produce "more with less" and develop smart sustainable industry, agriculture—farming, fisheries and aquaculture so as to ensure balanced economic and social development, sustainable production, energy security, public health, preservation of natural resources, mitigating of climate changes, food security (Fig. 14). At present, biorefineries have progressed into integrated biorefineries (IBR) [1, 27, 38]. In fact the IBR idea considers a broad variety of technologies capable to split biomass resources (agricultural, woody,…) into their basic structures (carbohydrates, proteins, triglycerides…), which can be transformed to products with added value (biofuels and chemicals). Therefore, in order to continue to be competitive, the EU has to develop into a low carbon culture, based on sustainable process industry through resource and energy efficiency (SPIRE), bio-based products and bioenergy [75].

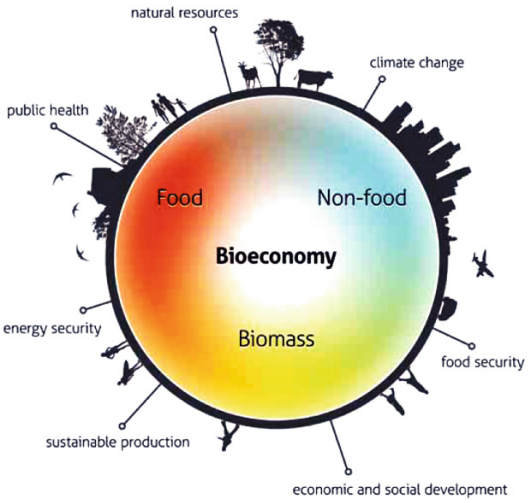

Fig. 14 The main goals of European bioeconomy (taken from [8, 26])

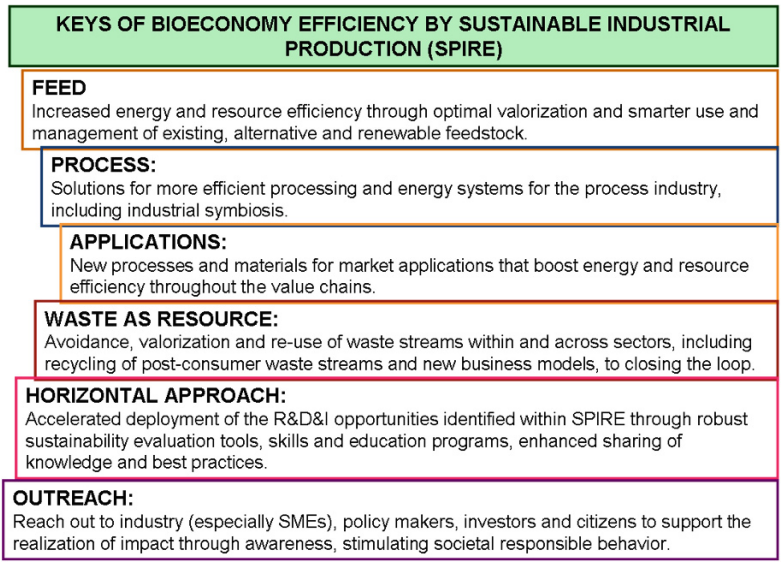

Fig. 15 Key components as the core of a resource and energy efficient process industry (adapted upon [76])

To achieve increased competitiveness in Europe, two main drivers of bioeconomy should be exploited: climate protection, particularly by reducing the greenhouse gases (GHG) emissions, and a sustainable reallocation of resources, from fossil-based to renewable feedstocks. Consequently, a relevant support for bioeconomy strategy consists in providing the pathway to decouple the resource consumption in industrial processes from human welfare achievement. Today, along Europe biomass is extensively acknowledged as the merely sustainable choice to fossil carbon sources and the main driver in developing production processes with a low, or even zero, carbon footprint.

SPIRE Roadmap [21, 76] identified six key components as the core of proficient and sustainable industrial system: feed, process, applications, waste as resource, horizontal approach, outreach (Fig. 15).

4 Biorefineries for Bioproducts and Bioenergy

As an essential part of the smart economy, the biological based feedstock could ensure the preservation and management of various resources in fundamental strategic lines to foster sustainability tasks in the 20th century [49]. The development of technologies for processing biogenic raw materials-biomass, with those for the production of intermediate and final products could be possible through an integrated production of food, feed, chemicals, materials, fuels, energy, goods [50].

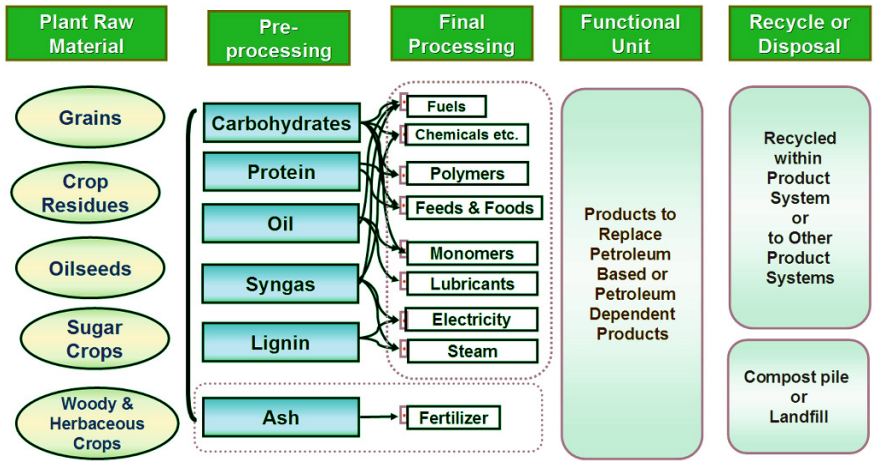

Fig. 16 Integrated production of biobased products from biogenic raw materials with specific technologies for biomass processing [38, 51]

The pressing demand for a green chemistry determined the international scientific community to launch the initiative for founding a scientific and technical platform based on the new industrial concept of biorefinery, having as fundament the innovative industrial biotechnological approaches [1, 38, 80]. Therefore, the accountable application of biotechnology to get economic, social and environmental profit is essentially interesting and can generate a impressive development of research from traditional fermentation technologies (cheese bread, beer making, animal and plant breeding), to modern techniques (gene technology, recombinant DNA technologies, biochemistry, immunology, molecular and cellular biology) to supply proficient synthesis of low toxicity products, renewable bioenergy and yielding new methods for environmental monitoring and protection [36, 37, 56]. These products can be generated by "*a biorefinery that integrates the biomass conversion processes*" [82]. Consequently, the biorefinery economy stands for an outlook in which the fossil fuels are replaced with biorenewables. The final products, termed as "bio-based products" include three categories: biofuels (biodiesel, bioethanol); bioenergy (heat, power); bio-based chemicals (Fig. 16).

A biorefinery should be supported by feedstock advancement processes, likewise to what happens in a conventional oil refinery, where raw materials are constantly upgraded and refined (Fig. 17). However, the biobased industrial products can go into a competition with petro-chemical based products when the biomass capital is processed optimally within biorefinery systems, by implementing new value chains. Consequently, since a biorefinery is designed to boost the value of the diverse biomass components as bioproducts and bioenergy, heat and electricity production should be produced from the residues and scraps of preceding technological treatments and conversion processes only [1, 38, 64]. The fundamental principles of the conventional oil refinery and the biorefinery are schematically represented in Fig. 17 [49].

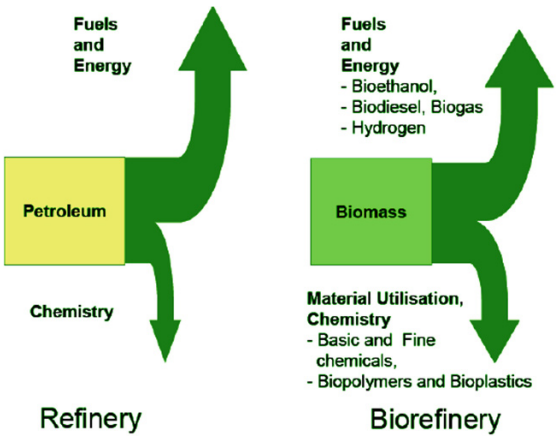

Fig. 17 Some characteristics of oil refinery and biorefinery [49]

Biorefinery concepts are being classified based on feedstock, type of technology, status of technology (first- and second-generation biorefinery), and intermediate (syngas platform, sugar platform etc.). Seven different biorefinery concepts are presented as follows [15, 19, 38]:

- Conventional Biorefineries (CBR)
- Green Biorefineries (GBR)
- Whole Crop Biorefineries (WCBR)
- Lignocellulosic Feedstock Biorefineries (LCFBR)
- Two Platform Concept Biorefineries (TPCBR)
- Thermo Chemical Biorefineries (TCBR)
- Marine Biorefineries (MBR)

Four classes of feedstocks for biorefinery are established [18, 38] (Fig. 18): *first generation*, including biomass from agricultural sources with food destination (rich in starch, oil); *second generation*, which use biomass as non-food sources and crops (residual non-food parts of crops, solid waste, wheat straw etc.); *third-generation*, including algae to produce vegetable oil; *fourth-generation*, which uses vegetable oil, biodiesel. A study of Raschka and Carus [68] takes into account the straightforwardly used main raw material (crop biomass) not including secondary raw materials (as waste for biorefinery). It was found that almost 147 million tonnes of fresh biomass are consumed for bioenergy and almost 175 million tonnes for biobased products (Fig. 19).

The selection among the four diverse alternatives to replace fossil based products with biomass based products depends largely on the costs [71] (Table 2). In the future, a more bio-based economy would stand for more substitution of fossil fuels and a clear increase in biomass requirement. Due to conversion losses during the production of bioenergy, the contribution necessary to substitute 1 exajoule of fossil fuel may be 1.5–2 exajoules of biomass [25].

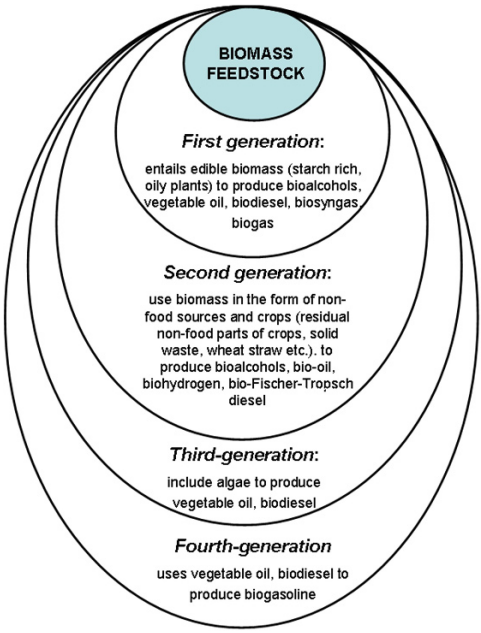

Fig. 18 Classes of various feedstock used in biorefinery (adapted upon [38])

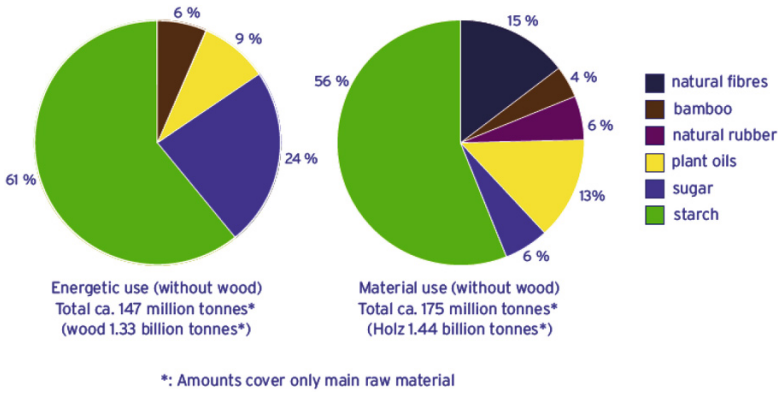

Fig. 19 Global use of renewable biomass for bioenergy and biobased products in 2008 (taken from [38])

A schematic overview of the added economic value of biomass uses can be ranked on the *value pyramid* (Fig. 20). The added value is the highest at the top of the pyramid, while and the volume of biomass needed for the applications is the lowest [25].

The efficient and effective use of biomass into biobased products and energy fits with the concept of 'cascading use', according to which the biomass is used for

Table 2 Costs associated to fossil based and biomass based products (adapted upon [71])

Product	Biobased integral costs (euro/GJ end-product)	Fossil based products (euro/GJ)
Average bulk chemicals	75	30 (oil)
Biofuels for transport	10	8 (oil)
Heat	4	3 (coal)

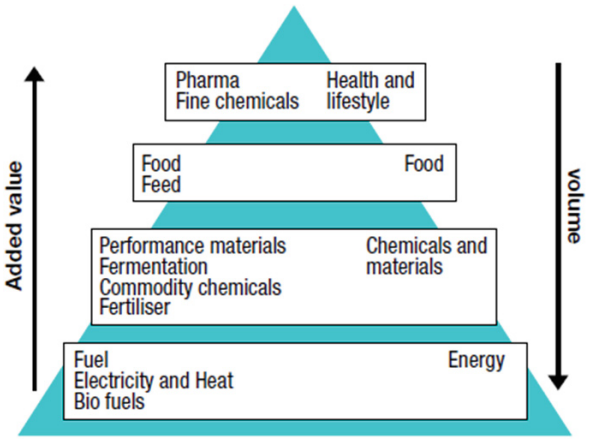

Fig. 20 The added value of biobased products and biomass requirement in biorefinery (taken from [25])

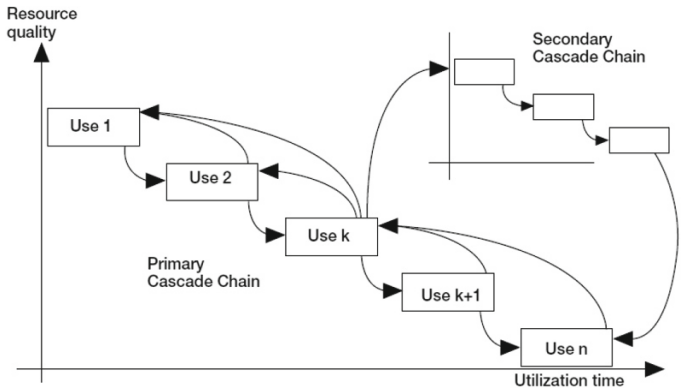

Fig. 21 The cascade of biomass use [73]

high-value materials, then "reused in bulk materials and finally used for production of biofuels and power" (Fig. 21). The diagram from Fig. 21 suggests the degree to which a resource quality can be recirculated, regenerated or reprocessed [25, 65, 73].

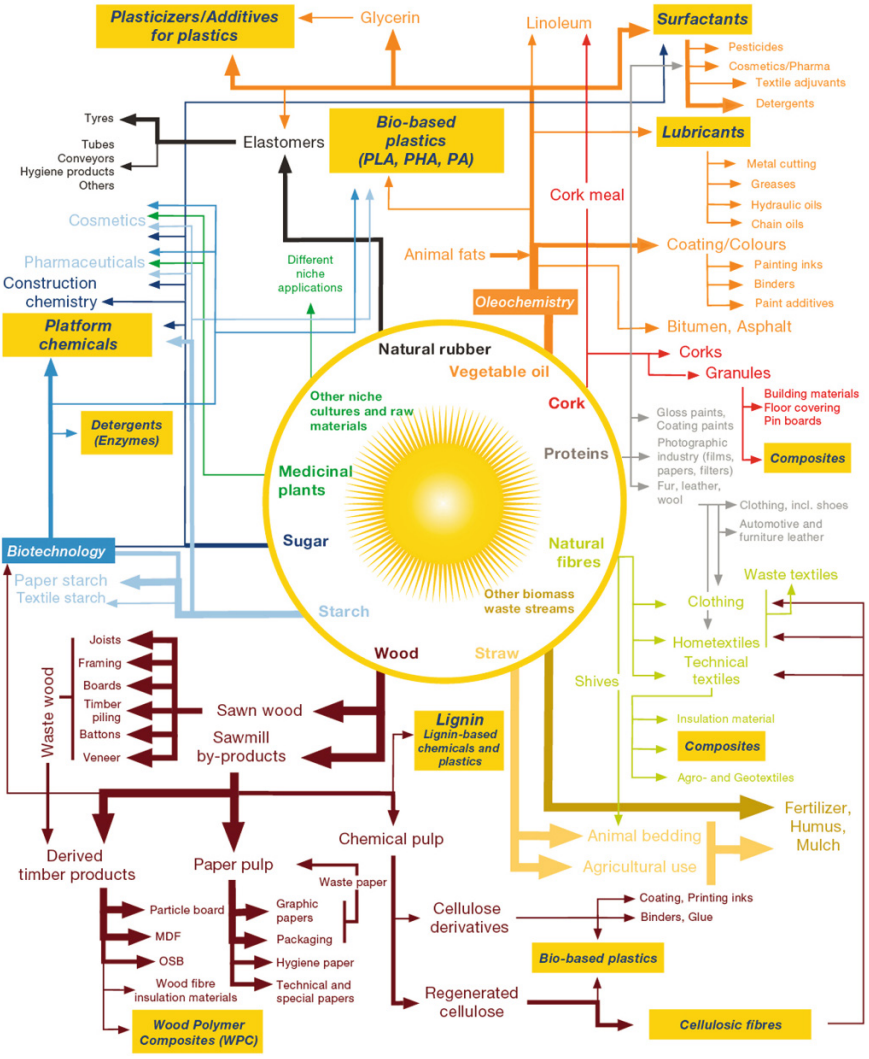

Fig. 22 The material flows of biomass use in Germany for the year 2008 (taken from [68])

The processing industry in Europe 2012 is notable considering the large number of applications comprised in the bio-based economy, which has to be sheltered by a wide-ranging market scrutiny (Fig. 22) [14, 68]. The figure illustrates the possibility by which several process options are accessible to attain the production of high added value molecules, contrasting with petroleum refineries where the raw material experiences definite lines of treatment. The same final product can be achieved during diverse pathways. Therefore, biomass use is characterized by a greater spectrum of applications. There is a wide range of bio-based products which

could eventually acquire a substantial market acceptance: fibre based materials (i.e. for construction sector or car industry); bio-plastics and other bio-polymers; surfactants; bio-solvents; bio-lubricants; ethanol and other chemicals and chemical building blocks; pharmaceutical products, vaccines; enzymes; cosmetics [38].

5 Environmental and Safety Concerns of Integrated Biorefineries

Various technological, economic, environmental, and social factors could influence the sustainability of integrated biorefineries and their products. These influences should be evaluated with awareness so as to ensure sustainable development of the biorefinery sector [1, 5, 6]. The expectances about the environmental and health risks posed by biorefineries are optimistic, in the sense that they are considered to be lower than those arising in the traditional chemical and petrochemical plants.

However, a lack of knowledge still exists regarding safety aspects of these new generations of production plants [9, 53]. Safety principles, a new proactive safety paradigm applied early in the design process could be the best way to ensure the security and sustainability of biorefinery plants, for the benefit of multiple stakeholders worried with the safety of the systems they exploit or mange [1, 74]. Moreover, the biorefinery plants should also be exploited in a sustainable way in the sense that all the energy supplies for biomass conversion processes have to be internally supplied by the production of heat and electricity from combustion of residues (within a properly sized set of processes/technologies) [37, 38, 43].

Forests and grasslands are converted to cultivate biofuel crops, and a loss of biological diversity can arise, but the biodiversity can recover if degraded lands are re-established for biomass production [7, 9, 74]. Additional environmental impacts related to the integrated biorefineries and their products can include soil erosion, water use, land availability, nutrients leaching, acidification, eutrophication, health issues (human toxicity, eco-toxicity), intergenerational issues, human and labour rights issues (Fig. 23) [10]. Based on the relevant environmental aspects which pose threats on environmental components, a specific assessment of environmental impacts, based on biomass life cycle analysis can be performed and various decisions can be made to reduce the environmental pressures.

Also, there are differences in the environmental impacts and risks associated to renewable (biobased) and conventional (fossil) feedstock types. It is expected that the impacts due to the provision of biobased feedstock to be generally reversible, while the largest part of impacts generated by the extraction and use of fossil feedstock is anticipated to be non-reversible and associated to long-term changes in environmental components. Figure 24 illustrates comparatively the main impacts supported by the environmental components due to biomass feedstock and fossil feedstock [10].

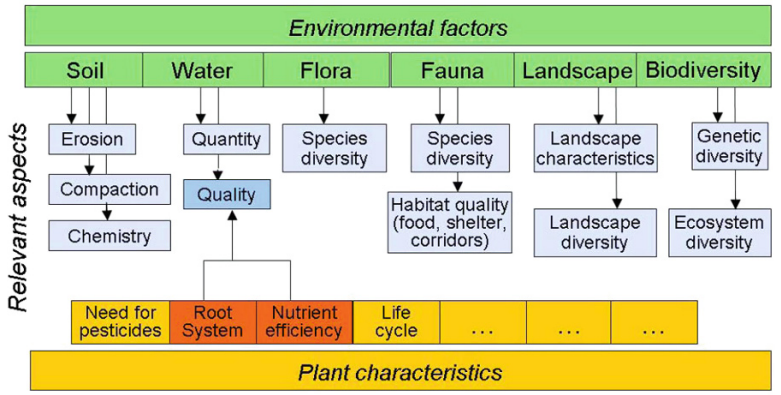

Fig. 23 Relevant aspects identified as factors with potential impacts on environmental components (taken from [10])

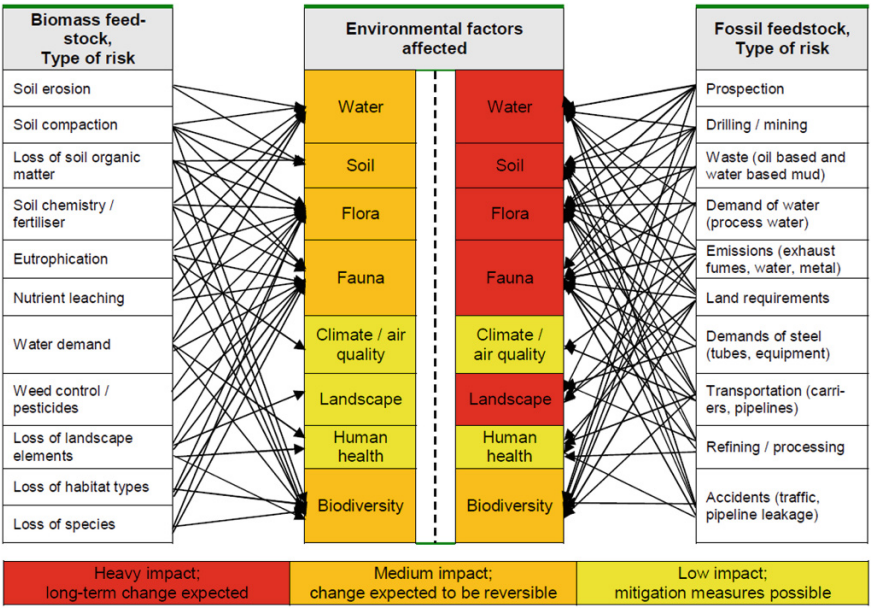

Fig. 24 Comparison of impacts on environmental factors due to provision of bio-based and conventional feedstock (taken from [10])

6 Concluding Remarks

New possibilities for increasing the use of renewable resources arise in the global economy in order to ensure the demands for new products and energy in an environmentally friendly manner, by shifting to production and processing systems

that can produce *more with less*. Biomass demonstrates to have a great potential to be exploited so as to ensure sustainable environment, biorefinery products and energy, in the today world which faced high competition for limited and finite natural resources, which will continue in the next decades. The new age of bio-economy would lead to sustainable production and use of renewable resources from land, fisheries and aquaculture environments for food, feed, fiber bio-based products and bio-energy, as well as the interrelated community supplies.

Investments in research, development and innovation will supply the break to equally convert existing industries, by replacement of fossil resources with renewable ones (chemical industry, biofuel industry, physical share of foreign resources, development. The greatest potential of the biorefinery is necessary to be exploited by means of progress in plant genetics, biotechnology, separation technologies, green chemistry and engineering. Moreover, biorefining of biomass into lots of products, such as energy, chemicals, and materials, should be designed and exploited in the direction of increasing the overall value of biomass and diminishing the environmental impacts generated by the extraction and use of fossil feedstock.

The biorefinery based bioeconomy would ensure the three main priorities of Europe 2020 strategy: smart, sustainable and inclusive growth, since it will be able to contribute to the development of an economy based on knowledge and innovation, to promote a proficient, green, and competitive economy, while fostering a high employment economy.

Acknowledgments This work was partially supported by the grant of the Romanian National Authority for Scientific Research, CNCS—UEFISCDI, project number PN-II-ID-PCE-2011-3-0559, Contract 265/2011.

References

1. Accardi, D. S., Bubbico, R., Di Palma, L., & Pietrangeli, B. (2013). Environmental and safety aspects of integrated biorefineries (IBR) in Italy, *Chemical Engineering Transactions*, *AIDIC 32*, 169–174.
2. Alavian, V., Qaddumi, H. M., Dickson, E., Diez, S. M., Danilenko, A. V., Hirji, R. F., et al. (2009). Water and climate change: Understanding the risks and making climate-smart investment decisions, World Bank, 2009. Available online at http://www-wds.worldbank.org/external/default/WDSContentServer/WDSP/IB/2010/02/01/000333038_20100201020244/Rendered/PDF/529110NWP0Box31ge0web0large01128110.pdf
3. Alexandratos, N., & Bruinsma, J. (2012) World Agriculture towards 2030/2050. The 2012 Revision, ESA Working Paper No. 12-03, FAO Agricultural Development Economics Division, Rome, 2012. Available online at http://www.fao.org/docrep/016/ap106e/ap106e.pdf
4. Andreev, K., Kantorová, V., & Bongaarts, J. (2013). Demographic components of future population growth. Technical Paper No. 2013/3, United Nations Department of Economic and Social Affairs, Population Division, New York, 2013. Available online at http://www.un.org/en/development/desa/population/publications/pdf/technical/TP2013-3.pdf
5. Azapagic, A., & Stichnothe, H. (2011). Assessing sustainability of biofuels. In A. Azapagic, S. Perdan (Eds.), *Sustainable development in practice: Case studies for engineers and scientists* (2nd ed., pp. 142–169). New Jersey: Wiley.

6. Azapagic, A. (2013). Sustainable chemical engineering: Challenges and opportunities for shaping our future, Plenary Lecture, WCCE9, Seoul, 2013. Available online at http://www.sustainable-systems.org.uk/files/Sustainable_chemical_engineering_-_Shaping_our_future_%28Azapagic%29.pdf
7. Azapagic, A. (2014). Sustainability considerations for integrated biorefineries. *Trends in Biotechnology*, *32*, 1–4 (Elsevier).
8. BECOTEPS, The European bioeconomy in 2030 (2012) Delivering sustainable growth by addressing the grand societal challenges. White Paper, Contract KBBE-2008-226526: BECOTEPS—Bio-Economy Technology Platforms, 2012. Available on line at http://www.epsoweb.org/file/560
9. Berndes, G., Bird, N., & Cowie, A. (2010). Bioenergy, land use change and climate change mitigation. IEA Bioenergy. Available online at http://task39.org/files/2013/05/Bioenergy-Land-Use-Change-and-Climate-Change-Mitigation.pdf
10. BIOCORE, Environmental sustainability assessment of the BIOCORE biorefinery concept (D7.5), BIOCORE Biocomodity Refinery, FP7-241566 Grant, 2013, Institute for Energy and environmental Research (IFEU), Heidelberg. Available online at http://www.biocore-europe.org/file/BIOCORE_D7_5_Environmental%20assessment_2014-05-15.pdf
11. Birol, F. (2004). World energy and environmental outlook to 2030. World Energy Outlook, International Energy Agency.
12. BP (2012). BP Energy Outlook 2030. London. Available online at http://www.bp.com/content/dam/bp/pdf/Energy-economics/Energy-Outlook/BP_Energy_Outlook_Booklet_2011.pdf
13. Bruinsma, J. (2009). *The resource outlook to 2050: By how much do land, water and crop yields need to increase by 2050? Expert Meeting on How to Feed the World in 2050*. Rome: FAO.
14. Carus, M. (2012). *Bio-based Economy in the EU-27: A first quantitative assessment of biomass use in the EU industry*. Hürth, Germany: Nova-Institut GmbH.
15. Cherubini, F., Jungmeier, G., Wellisch, M., Willke, T., Skiadas, I., van Ree, R., et al. (2009). Toward a common classification approach for biorefinery systems. *Biofuels, Bioproducts and Biorefining, 3*, 534–546.
16. COM. (2006). Communication from the Commission of the European Communities to the Council and the European Parliament. An EU Strategy for Biofuels, Communication of 8 February, 2006. Available online at http://ec.europa.eu/energy/res/biomass_action_plan/doc/2006_02_08_comm_eu_strategy_en.pdf
17. COM. (2012). Communication from the Commission to the European Parliament, the Council, the European Economic and Social Committee and the Committee of the Regions Innovating for Sustainable Growth: A Bioeconomy for Europe, European Commission, Brussels, 2012. Available online at: http://eur-lex.europa.eu/legal-content/EN/TXT/?uri=CELEX:52012DC0060
18. Demirbas, A. (2010). *Biorefineries: For biomass upgrading facilities*. Dordrecht, Heidelberg-London-New York: Springer.
19. Diep, N. Q., Sakanishi, K., Nakagoshi, N., Fujimoto, S., Minowa, T., & Tran, X. D. (2014). Biorefinery : concepts, current status, and development trends. *International Journal of Biomass and Renewables.* Available online at: http://ijbr.utp.edu.my/uploads/19_111_mqdnx13-02-14.pdf
20. EC. (2012). *Innovating for Sustainable Growth: A Bioeconomy for Europe*, COM (2012) final. European Commission, Brussels, Belgium.
21. EC. (2012). *Energy Roadmap 2050*. European Union, Luxembourg. Available online at http://ec.europa.eu/energy/publications/doc/2012_energy_roadmap_2050_en.pdf
22. EC. (2012). Communication from the Commission to the European Parliament, the Council, the European Economic and Social Committee and the committee of the Regions. Innovating for Sustainable Growth: A Bioeconomy for Europe, COM, Brussels.

23. EC. (2013). Bio-Based Industries Initiative: using renewable natural resources and innovative technologies for greener everyday products. Available online at http://ec.europa.eu/research/press/2013/pdf/jti/bbi_factsheet.pdf
24. EEA Report. (2013). EU Bioenergy potential from a resource efficiency perspective. Report No 6, European Environment Agency, Copenhagen.
25. Eickhout, B. (2012). A strategy for a bio-based economy. Green European Foundation for the Greens/EFA Group in the European Parliament, Brussels.
26. EuropaBio. (2013). *Boosting the EU Bioeconomy*. Brussels: The European Association for Bioindustries.
27. EUROPE 2020. (2010). Communication from the Commission Europe 2020: A strategy for smart, sustainable and inclusive growth. European Commission. Available online at http://ec.europa.eu/eu2020/pdf/COMPLET%20EN%20BARROSO%20%20%20007%20-%20Europe%202020%20-%20EN%20version.pdf
28. Evans, A. (2011). Resource scarcity, climate change and the risk of violent conflict. World Development Report 2011, Background Paper, Center on International Cooperation New York University. Available online at http://siteresources.worldbank.org/EXTWDR2011/Resources/6406082-1283882418764/WDR_Background_Paper_Evans.pdf
29. FAO. (2006). World agriculture towards 2030/2050: Interim report. Food and Agriculture Organization of the United Nations, Rome. Available on line at www.fao.org/fileadmin/templates/em2009/docs/FAO_2006_.pdf
30. FAO. (2009). How to feed the World in 2050. Food and Agriculture Organization of the United Nations, paper prepared for How to feed the World in 2050: High-level expert forum, 12–13 October, Rome. Available online at www.fao.org/fileadmin/templates/wsfs/docs/expert_paper/How_to_Feed_the_World_in_2050.pdf
31. FAO. (2010). The State of Food Insecurity in the World 2009. Food and Agriculture Organization of the United Nations FAO, Rome.
32. FAO. (2013). State of food insecurity in the World 2013. The multiple dimensions of food security. Food and Agriculture Organization of the United Nations, Rome
33. FIG Commission 3. (2010). Rapid urbanization and mega cities: The need for spatial information management, International Federation of Surveyors (FIG), Copenhagen. Available on line at: http://www.fig.net/pub/figpub/pub48/figpub48.pdf
34. Finley, M. (2012). The oil market to 2030—Implications for investment and policy. *Economics of Energy and Environmental Policy*, *1*, 25–36 (IAEE).
35. Fortună, M. E., Simion, I. M., Ghinea, C., Petraru, M., Cozma, P., Apostol, L. C., et al. (2013). Analysis and management of specific processes from environmental engineering and protection based on sustainability indicators. *Environmental Engineering and Management Journal*, *12*, 333–350.
36. Gavrilescu, M., & Chisti, Y. (2005). Biotechnology—a sustainable alternative for chemical industry. *Biotechnology Advances*, *23*, 471–479 (Elsevier).
37. Gavrilescu, M. (2010). Environmental biotechnology: achievements, opportunities and challenges. *Dynamic Biochemistry, Process Biotechnology and Molecular Biology*, *4*, 1–36 (Global Science Books).
38. Gavrilescu, M. (2014). Biorefinery systems: An overview. In V. K. Gupta, C. P. Kubicek, J. Saddler, F. Xu & M. G. Tuohy (Eds.), *Bioenergy Research: Advances and Applications* (pp. 227–246). Amsterdam: Elsevier.
39. GEA. (2012). *Global Energy Assessment—Toward a sustainable future*. Cambridge: Cambridge University Press.
40. Guy, K. (2012). Skills and the bioeconomy. Presentation for New Skills for a European Bioeconomy, Meeting, Division OECD, Brussels, November 20–21, 2012.
41. Hall, T. (2012). European bioeconomy: strategy and action plan. Directorate-General Research and Innovation European Commission. Available online at: www.rokfor.eu/openfile/575
42. Hardy, J. T. (2003). *Climate change: Causes, effects and solutions*. Chichester, England: Wiley.
43. Hatty-Kaul, R. (2010). Biorefineries, a path to sustainability. *Crop Science, 50*, S152–S156.

44. Hodbod, J., & Adger, W. N. (2014). Integrating social-ecological dynamics and resilience into energy systems research. *Energy Research and Social Science*, *1*, 226–231 (Elsevier).
45. House of Lords. (2014). Waste or resource? Stimulating a bioeconomy, Science and Technology Select Committee, 3rd Report of Session 2013–2014, Authority of the House of Lords, London, 2014.
46. http://www.census.gov/popclock/
47. http://www.millennium-project.org/millennium/Global_Challenges/chall-03.html
48. http://en.wikipedia.org/wiki/World_population
49. Kamm, B., Kamm, M., & Gruber, P. R. (2006). Biorefinery systems—an overview. In B. Kamm, R. Gruber, & M. Kamm (Eds.), *Biorefineries—Industrial processes and products. Status Quo and Future Directions* (Vol. 1, pp. 3–40). Weinheim, Germany: Wiley WCH Verlag GmbH and Co. KGaA.
50. Kamm, B. (2013). Introduction to biomass and biorefineries. In H. Xie & N. Gathergood (Eds.), *The role of green chemistry in biomass processing and conversion* (pp. 1–26). New Jersey: Wiley, Hoboken.
51. Kim, S., & Dale, B. E. (2004). Life cycle assessment of integrated biorefinery cropping systems: All biomass is local. Presentation within "Agriculture as a Producer and Consumer of energy" Michigan State University.
52. Langeveld, J. W., & Sanders, J. P. M. (2010). General introduction. In J. W. Langeveld, J. P. M. Sanders, M. Meeusen (Eds.), The biobased economy: Biofuels, materials and chemicals in the post-oil Era (pp. 3–17). London, UK: Earthscan.
53. Laser, M., Larson, E., Dale, B., Wang, M., Greene, N., & Lynd, L. R. (2008). Comparative analysis of efficiency, environmental impact, and process economics for mature biomass refining scenarios. *Biofuels, Bioproducts and Biorefining*, *3*, 247–270 (Wiley).
54. Leaver, J. D. (2011). Global food supply: a challenge for sustainable agriculture. *Nutrition Bulletin*, *36*, 416–421 (British Nutrition Foundation).
55. Leflaive, X. (2012). Water Outlook to 2050: The OECD calls for Early and Strategic Action, OECD Environment Directorate.
56. Liu, X. Y., Ding H. B., & Wang J. Y. (2010). Food waste to bioenginery. In S. K. Khanal, R. Y. Surampalli, T. C. Zhang, B. P. Lamsal, R. D. Tyagi, C. M. Kao (Eds.) *Bioenginery and biofuel from biowastes and biomass* (pp. 43–70). Reston, Virginia: ASCE.
57. McCormick, K., & Kautto, N. (2013). The bioeconomy in Europe: An overview. *Sustainability, 5*, 2589–2608. doi:10.3390/su5062589.
58. Mountford, H. (2011). Water: The environmental outlook to 2050, OECD global forum on environment: Making water reform Happe, 26 October 2011, Paris. Available online at: http://www.oecd.org/env/resources/49006778.pdf
59. Nelson, G., Rosegrant, M., Palazzo, A., Gray, I., Ingersoll, C., Robertson, R., et al. (2010). *Food security, farming and climate change to 2050: Scenarios, results, policy options*, Washington DC. Available online at: www.ifpri.org/sites/default/files/publications/rr172.pdf
60. Nikolaou, A., Remrova, M., & Jeliazkov, I. (2003). Biomass availability in Europe. In Bioenergy's role in the EU Energy Market, European Commission. Available online at: http://ec.europa.eu/energy/res/sectors/doc/bioenergy/cres_final_report_annex.pdf
61. OECD. (2009). The Bioeconomy to 2030, Designing a Policy Agenda, Organization for Economic Co-operation and Development, OECD, Paris.
62. OECD. (2012). Environmental Outlook to 2050. The Consequences of Inaction, OECD Publishing. doi:10.1787/9789264122246-en. Available online at: http://www.keepeek.com/Digital-Asset-Management/oecd/environment/oecd-environmental-outlook-to-2050_9789264122246-en#page1
63. OECD/IEA. (2009). World Energy Outlook 2009. International Energy Agency. Available online at: http://www.iea.org/textbase/npsum/weo2009sum.pdf
64. Ohara, H. (2003). Biorefinery. *Applied Microbiology and Biotechnology*, *62*, 474–477 (Springer).
65. Østergård, H., Markussen, M. V., & Jensen, E. S. (2010) Challenges for sustainable development in a biobased economy, In H. Langeveld., M. Meeusen., & J. Sanders. (Eds.),

The bio-based economy, biofuels, materials and chemicals in the post-oil era (pp. 33–48). New York: Earthscan.
66. Oxford Economics. (2005). The challenge of higher oil prices. Asian Development Outlook. Available online at https://www.oxfordeconomics.com/publication/open/222575
67. Perlack, R. D., Wright, L. L., Turhollow, A. F., Graham, R. L., & Stokes, B. J. (2005). Biomass as feedstock for a bioenergy and bioproducts industry: The technical feasibility of a billion-ton annual supply. U.S. Department of Energy and U.S. Department of Commerce. Available online on http://www1.eere.energy.gov/bioenergy/pdfs/final_billionton_vision_report2.pdf.
68. Raschka, A., Carus, M. (2012). Industrial material use of biomass. Basic data for Germany, Europe and the world, first part of the report on the R&D project In *Environmental Innovation Policy: more efficient resource use and climate protection through sustainable material use of biomass*. Hürth, Germany: Nova-Institute GmbH.
69. Ragauskas, A. J., Williams, C. K., Davison, B. H., Britovsek, G., Cairney, J., Eckert, C. A., et al. (2006). The path forward for biofuels and biomaterials. *Science, 311*, 484–489.
70. Rute, M. (2010). Bio-economy 2020 and priority setting for research 2011. *European Commission, Directorate General for Research, Directorate E: Biotechnologies, Agriculture and Food*.
71. Sanders, J., Scott, E., Mooibroek, H. (2005). Biorefinery, the bridge between agriculture and chemistry, In *Proceedings of the 14th European biomass conference and exhibition*: *Biomass for energy, industry and climate protection*. Paris, France, October 17–21, 2005.
72. SAT-BBE. (2013). Tools for evaluating and monitoring the EU bioeconomy: Indicators, report, EU FP 7 SAT-BBE project: Systems analysis tools framework for the EU bio-based economy strategy, 2013. Available online at http://www3.lei.wur.nl/SATBBE_Publications/SAT-BBE%20-%20WP2%20-%20Deliverable%202.2_FINAL_20140116.pdf
73. Sirkin, T., Ten Houten, M. (1994). The cascade chain: a theory and tool for achieving resource sustainability with applications for product design *Resource, Conservation and Recycling 10*, pp. 213–276, Elsevier.
74. Stephen, R. (2009). Climate change and environmental refugees part II: Can we decrease the number of environmental refugees? In *Elements: Environmental health intelligence.* Available online at http://www.elementshealthspace.com/2009/10/22/climate-change-and-environmental-refugees-part-ii-can-we-decrease-the-number-of-environmental-refugees/
75. Tello, P., Weerdmeester, R. (2013). SPIRE roadmap. Sustainable process industry through resource and energy efficiency, Brussels. Available online at http://www.spire2030.eu/uploads/Modules/Publications/spire-roadmap_december_2013_pbp.pdf
76. United Nations. (2013). World population prospects: The 2012 revision. Department of Economic and Social Affairs, Population, Division, volume I: Comprehensive Tables ST/ESA/SER.A/336, 2013.
77. UNPD. (2010). *World population prospects. The 2010 revision*. New York: United Nations Population Division.
78. UNESCO. (2010). Water in a changing world. The United Nations World Water Development, Report 3. Available Online at http://www.unesco.org/new/fileadmin/MULTIMEDIA/HQ/SC/pdf/WWDR3_Facts_and_Fig.s.pdf
79. UNICEF. (2012). An urban world, 2012. Available online at www.unicef.org/sowc2012/urbanmap/
80. van Ree, R., Annevelink, B. (2007). Status report biorefinery 2007. Wageningen: Agrotechnology and Food Sciences Group. Available online at http://www.biorefinery.nl/fileadmin/biorefinery/docs/publications/StatusDocumentBiorefinery2007final211107.pdf
81. Walker, G. (2014). The dynamics of energy demand: Change, rhythm and synchronicity, *Energy Research & Social Science*, *1*, pp. 49–55, Elsevier.
82. WEF. (2010). *The future of industrial biorefineries*. Cologny, Geneva, Switzerland: World Economic Forum. Available from URL http://www3.weforum.org/docs/WEF_FutureIndustrialBiorefineries_Report_2010.pdf

83. WHO. (2013). Global environmental change. Available online at http://www.who.int/globalchange/climate/en/
84. World Bank. (2010). World Development Report 2010: Development and climate change. Washington D.C.: World Bank. Available online at http://siteresources.worldbank.org/INTWDR2010/Resources/5287678-1226014527953/WDR10-Full-Text.pdf
85. Zadek, S., Forstater, M., & Naidoo, S. (2012). Shaping a sustainable future. In *Strengthening the role of development cooperation in delivering sustainable development*. New York: UN Development Cooperation Forum. July 2012. Available online at http://www.un.org/en/ecosoc/newfunct/pdf/dcf_australia_zadek_may_2012.pdf

The Usage of Earth's Natural Potential for Cooling and Heating in Industrial Building

Alin Ionuţ Brezeanu, George Dragomir, Mircea Horneţ, Cristian D. Năstac, Nicolae Iordan and Lucia Boieriu

Abstract This paper discusses the suitability of heat pump systems into industrial buildings and analyses the energy needed by a ground source heat pump system to heat, cool and to produce domestic hot water for a building in Bucharest. The energy used and thermal parameters were monitored for a year. Using these values we were able to determine the energy savings, the greenhouse gases emissions and the payback time compared to a hybrid system of fuel-oil heat and electric cooling.

Keywords Heat pump · Greenhouse gases emission · Efficiency

1 Introduction

Geothermal energy is usually associated with steam extracted from underground and used to produce electric energy. Today, a better and more convenient way to use geothermal energy is to connect ground source heat pumps (GSHPs) to commercial and residential buildings.

GSHP systems exchange heat with the ground, and maintain a high level of performance even in colder climates. This results in a more efficient energy usage, this being the reason why many countries support this type of equipment [7].

Traditionally, boilers based on fossil fuels (solid, liquid and gaseous) and electrical driven air conditioning systems have been used for heating and for cooling spaces. Heat pumps offer the same comfort level, being more sustainable and having less greenhouse gasses emissions (GHG).

The heat pump systems represent a proven technology, capable of significant energy use savings even in summer peak electrical demand in buildings is reduced.

A.I. Brezeanu (✉) · G. Dragomir · M. Horneţ · C.D. Năstac · N. Iordan · L. Boieriu
Department of Building Services, Transilvania University, Turnului Nr. 5,
Brasov, Romania
e-mail: alinlonut.brezeanu@gmail.com

I. Visa (ed.), *Sustainable Energy in the Built Environment - Steps Towards nZEB*,
Springer Proceedings in Energy, DOI 10.1007/978-3-319-09707-7_14

Recently, some studies involving GSHP were performed for a school building in Southern Korea [5], and for an office building in southern Germany [6]. The studies performed in Germany examined the thermal performance of a GCHP system installed in an office building in Nuremberg by continuously monitoring the system for 4 years [6].

Usually, in Romania, GSHP have been used in residential area and because of the advantages they bring, and the continuous rise of the energy price for space heating and cooling these systems started to be implemented in commercial and industrial buildings too.

The potential for significant energy savings of GSHP systems results from a lower electricity consumption necessary only for its operation, the main energy being extracted from the earth.

2 Building and HVAC Facilities

The 6,669 m^2 building houses offices, truck service, restaurant and training rooms. The mission of the new building is to provide new facilities for trucks servicing, along with dealer activities and technology integration.

The new building was especially designed to have low environmental impact by using LED lighting technology and also heat pump systems.

The building's envelope features exterior walls constructed of insulated panels, achieving additional energy savings. Their overall U-value of 0.48 W/m^2 K reduces heat losses. The roof is constructed of white EPDM membrane, insulation and concrete, having an overall U-value of 0.28 W/m^2 K. The exterior windows consist of low-e glazing with a U-value of 1.33 W/m^2 K.

Each of these features is factored into the performance of the building, and is part of a comprehensive system design that provides 56 % savings compared to the industrial buildings code's requirements for the envelope [9].

To meet the low environmental target impact and to comply with the comfort standards, a heat pump system was implemented, and the building was divided into two separate functional zones:

Zone 1—Service and Warehouse, where heating and cooling are provided by underfloor radiant surfaces.

Zone 2—Offices and Restaurant serviced by fan coils.

Thermal comfort is met in the building by supplying hot water to the above mentioned separate thermal zones:

A. The first one is served by an industrial radiant surface, made of peroxide cross linked polyethylene pipes 20 × 2.0 mm mounted on a 20 cm slab. The operating parameters of the system are: flow temperature 50 °C, return temperature 40 °C, the floor temperature 29.7 °C and the design temperature 18 °C. All these conclude to a 127 W/m^2 heat flow transferred to the thermal zone. The cooling

process: flow temperature 17 °C, return temperature 20 °C, floor temperature 21.5 °C. The designed internal temperature was 26 °C and the specific flux was 29 W/m^2. The flow temperature is limited to 17 °C by the heat pump's control system to prevent condensation on the slab.

B. The second thermal zone is served by a fancoil system working simultaneously with a ventilation system for fresh air supply. The operating parameters of the system in heating mode are: flow temperature 50 °C, return temperature 40 °C and the design temperature 20 °C. For the cooling time the operating parameters are flow temperature 12 °C, return temperature 16 °C and design temperature 25 °C.

The energy needed to operate the heating/cooling systems is provided by two ground- water heat pumps Vitocal 300 G Pro-240 kW each, operating in a master-slave system, each of them being equipped with two compressors [11]. The system has been designed for operation temperatures of 50–40 °C for heating periods, and 12–16 °C for cooling time. Technologically, the system allows a passive cooling operation, but active cooling is used only when peak loads occur.

During transition periods (warm to cold and vice versa) and according to each zone demand the system can operate simultaneously both on cooling and on heating. To achieve this, and to avoid cycling of the heat pump the system is equipped with two 10,000 l tanks.

Domestic hot water is produced through a 240 kW-plate heat exchanger being connected to the master heat pump, with priority over the heating and cooling procedures.

The primary flow for the heat pumps is achieved with 80 vertical earth loops, 100 m deep, placed at 6 m one from another, arranged into two fields.

For the first field, two drilling machines have been used simultaneously, considering the drilling of one bore lasts about one day and for the second field only one equipment was used, as can be seen in Fig. 1.

Fig. 1 The drilling process for the vertical earth loops

3 Heat Pump System Efficiency and Energy Savings

The cost efficiency depends on various parameters such as:

- Coefficient of performance (COP) of the heat pump;
- Number of working hours during a year;
- Cost of the investment;
- The cost of the electricity;
- Additional expenses.

Efficiency of a heat pump increases as the annual operating hours are higher and as the coefficient of performance of the heat pump increases. Unfortunately, no general predictions are possible. For this reason, each case must be analyzed separately by comparing costs involved in various heating systems.

The Seasonal Performance Factor, SPF defined as the average coefficient of performance of a heat pump over the full heating season, is useful to compare different heat pumps with conventional heating systems such as boilers, in terms of primary energy savings and CO_2 emission reductions.

SPF values are usually lower than the instantaneous COP as results from field measurements. To determine the efficiency of the system we used the data provided by the equipment's internal software as shown in Table 1. During the last year, the two heat pumps have provided 1,333 MWh energy for space heating, 63 MWh energy for DHW and 108 MWh energy for active space cooling. The rest of the cooling load 612 MWh were achieved by means of passive cooling. All the data were provided by the energy meters installed on the system.

To obtain the above amount of energy the heat pump system consumed 256.35 MWh for space heating, 14.32 MWh for DHW and 31.58 MWh for active cooling.

To obtain a real and concrete efficiency of the heat pump system we compared it with a traditional gas-fired boiler for heating and with a conventional chiller for cooling. The seasonal efficiency of typical fuel gas boilers throughout the heating period is evaluated between 75 and 80 % [3]. Using these data and considering the average price for natural gas of 0.03 Euro/kWh [13] and 0.13 Euro/kWh [12] for

Table 1 Working hours, COP and SPF for the two Vitocal 300 G Pro Heat Pumps

		Working hours-heating	Working hours-DHW	Working hours-cooling	COP DHW	SPF heating
Heat pump-master	Compressor 1	3474	245	303	4, 4	5, 2
	Compressor 2	2513		240		
Heat pump-slave	Compressor 1	2514		241		
	Compressor 2	2612		201		

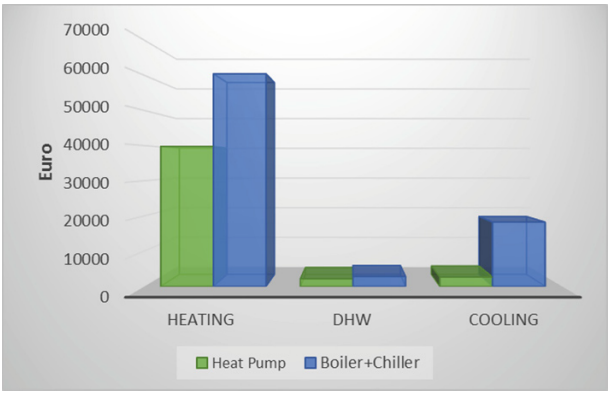

Fig. 2 Comparison of the cost of heating, cooling, and DHW between heat pump system and the classic one

electricity we were able to calculate the savings in thermal energy costs during the year as shown in Fig. 2.

Comparing the heat pump system with the gas-fired boiler and considering the working hours of the heat pump, the COP values and the price for gas and electricity, the energy costs for heating the two thermal zones was 50 % lower, and for the DHW were 26 % lower. During the summer time passive cooling was mostly used, and a significant reduction was achieved, about 85 %. All these were determined using:

$$E = \frac{P_g \cdot COP}{P_e \cdot \eta_{cz}} \tag{1}$$

where

E	cost operation ratio between heat pump and boiler;
P_e	price of the electricity (Euro/kWh);
COP	coefficient of performance for heating, DHW and cooling;
η_{cz}	conventional boiler efficiency (for a gas fired boiler is 0,75 ÷ 0,8);
P_g	price for natural gas (Eur/kWh).

Using the above data, gas price, electricity price and the energy consumption over last year we were able to determine the savings amount: 40,000 Euro.

To evaluate whether the lower energy costs of the ground-source heat pump system are worthwhile, we estimated the costs of each system over a period of ten years, assuming that electricity cost is increasing 5 % per year, and gas cost 10 % every year.

The difference of the initial investment cost between the heat pump system and a conventional one for this building was about 300,000 Euro. Considering the higher heat pump investment and the energy price savings provided by it every year, the

initial costs can be recovered in approx. 7.5 years. The rate of price increase for natural gas is twice the electricity, leading to a recovery of initial investment in a much shorter period of time, approx. 6 years.

4 Greenhouse Gas Emissions

The reduction of the greenhouse gas emissions (GHG) is essential for limiting the global warming. This leads to the replacement of the existing solutions for heating/cooling based on fossil fuels with heat pumps, especially those that use ground as a source of energy [2]. The overall potential for GHG reductions is determined by life cycle emissions of each energy source, and the efficiency of energy conversion used to meet heating/cooling [1].

$$GHG = C_e \cdot \left(\frac{I_f}{\eta_{sources}} - \frac{I_e}{3,6 \cdot COP} \right) \times 10^{-3} \, (t_{co_2}/\text{year}) \tag{2}$$

where

I_f the intensity of the greenhouse gases production, specific for every fossil fuel (natural gas 50 kg CO_2/GJ) [4];

COP coefficient of performance of the heat pump for heating, DHW and cooling;

$\eta_{sources}$ conventional boiler efficiency (for a gas fired boiler is 0.75 ÷ 0.8);

C_e energy used for heating, DHW and cooling (MWh/year);

I_e emission intensity, specific for the efficiency of the electricity production (tones of CO_2/GWh).

An important role in reducing GHG is the share of renewables in the electricity production-mix for the heat pump system. In Romania they have a pronounced variation throughout the day, months and year (Fig. 3).

All energy systems emit greenhouse gases (GHG) and contribute to anthropogenic climate change. It is now widely recognized that GHG emissions resulting from the use of a particular energy technology need to be quantified over all stages of the technology and its fuel life-cycle [8]. Emission intensity, specific for the efficiency of the electricity production for Romania is 326 gCO_2/kWh, which was calculated using for the average data of the share type electricity producers, presented in Fig. 4 and the data in Table 2 (Fig. 4a).

Based on the data obtained by monitoring the heat pump system through last year, it can be expected to reduce greenhouse gas emissions, in comparison to conventional gas boiler and chiller with the values shown in Fig. 4b.

Due to high values of heat pump's COP and the large share of the total electricity produced in Romania from renewable sources (hydro, photovoltaic and wind), greenhouse gas reduction in our case has a significant value.

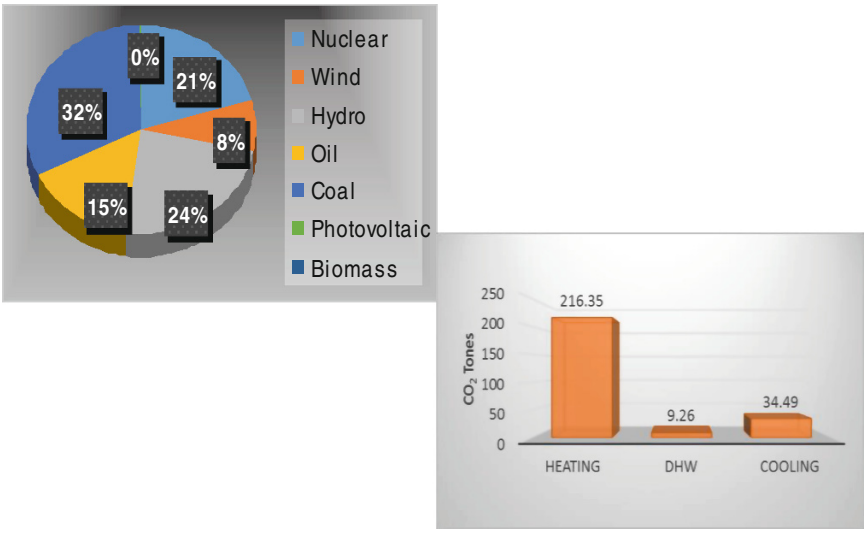

Fig. 3 Electric energy production in Romania for different production types during the last year [10]

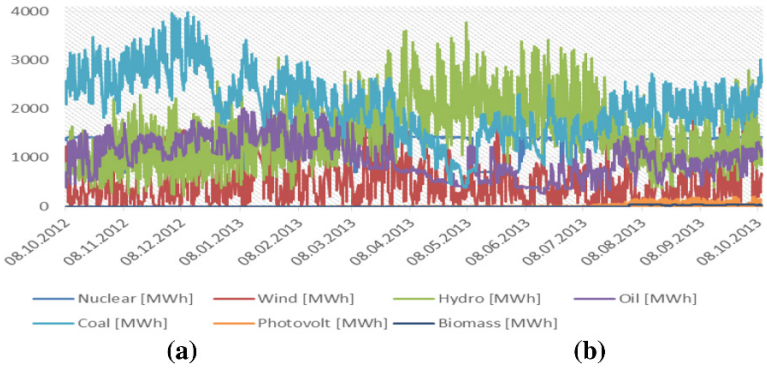

Fig. 4 **a** Total electricity production by share type (Oct. 2012–Oct. 2013) [10]. **b** GHG reduction due to the heat pump usage

Relative to natural gas and heating oil, the threshold of electric CO_2 intensity at which heat pumps become environmentally feasible varies with the efficiency levels of both conventional and GSHP systems.

Table 2 GHG emissions by energy type [8]

Fuel type	gCO_2/kWh
Coal	800–1,000
Oil	400
Wind	8–32
Photovoltaic	43–73
Biomass	35–99
Nucear	2.8–28
Hydro	0.35–30

5 Conclusions

Heat pumps are an economical, and sustainable source for thermal energy, partial dependent to fossil fuel price fluctuations, being also a measure of greenhouse gases emissions reduction.

Energy savings and CO_2 emission reductions that will result from the expansion to industrial area of the heat pump systems are expected to be substantial. Improved green electricity generation systems will lead to lower emissions and improved heat pumps (higher SPF) will increase the share of energy taken from environment renewable energy.

Heat pump systems have the potential to lower both average and peak energy costs for homeowners and industrial customers.

Acknowledgments This paper is supported by the Sectoral Operational Programme Human Resources Development (SOP HRD), ID134378 financed from the European Social Fund and by the Romanian Government.

References

1. Blumsack, S., Brownson, J., Witme, L. (2009). Efficiency, economic and environmental assessment of ground-source heat pumps in central Pennsylvania. In *42nd Hawaii International Conference System Sciences, HICSS '09*.
2. Boian, I. (2007). Sustainable development. Building facilities based on renewable energies (in Romanian language). Transilvania University.
3. Boian, I., Dragomir, G. (2012). The efficiency of the heat pump systems and CO_2 emissions (in Romanian language). In *Building facilities and environmental comfort conference*, April 2012, pp. 160–168.
4. Boian, I.,Chiriac, F. (2013). Heat pump systems, matrix rom (in Romanian language). Bucharest, Romania.
5. Hwang, Y., Lee, J., Jeoung, Y., Koo, K., Lee, D., Jin, S., et al. (2009). Cooling performance of a vertical ground-coupled heat pump system installed in a school building. *Renewable Energy, 34*(3), 578–582.

6. Luo, J., Rohn, J., Bayer, M., Wilkmann, L., & Xiang, W. (2014). Heating and cooling performance analysis of a ground source heat pump system in Southern Germany. *Geotermics, 53*, 57–66.
7. Thompson, C., Kelbis, W. (2013). Aquathermal systems. *ASHRAE Journal*.
8. Weisser, D. (2007). A guide to life-cycle greenhouse gas (GHG) emissions from electric supply technologies. *Energy, 32*(9), 1543–1559.
9. ***C107-2/1997 Standard for the calculation of the global coefficient of thermal insulation in buildings other than residential destination.
10. http://transelectrica.ro. Accessed 10 Apr 2014.
11. http://viessman.ro. Accessed 19 Apr 2014.
12. https://www.enel.ro/ro/clienti/energiaafacereata/clientii_nostri/download/Tarife_energie_agenti_economici_EEM_zona_Muntenia_iulie_2013.pdf. Accessed 19 Apr 2014.
13. https://www.gdfsuez.ro/energie-pentru-acasa/vreau-gaze-naturale/pretul-gazelor-naturale/. Accessed 12 Apr 2014.

Outdoor and Indoor Testing to Increase the Efficiency and Durability of Flat Plate Solar Thermal Collectors

Daniela Ciobanu, Ion Visa, Anca Duta and Monica Enescu

Abstract This paper presents the test performed on the solar thermal flat plate collector and the effect of saline aerosol on the solar thermal conversion; an assembly of testing rigs developed in the R&D Centre Renewable Energy Systems and Recycling, in Transilvania University of Brasov, Romania is presented; the rigs allow outdoor testing of solar thermal flat plate collector in accelerated aging conditions: under stagnation and in saline aerosols. The corrosion/erosion effect of saline aerosols is investigated according to an original testing method. The results allow to formulate the preliminary prerequisites for developing novel standardized testing procedures.

Keywords Flat plate solar thermal collector · Outdoor testing · Durability · Accelerated aging test

1 Introduction

Large scale implementation of solar-thermal systems as part of the development of Nearly Zero Energy buildings requires efficient and durable flat plate collectors (STFPC). Standard testing is already formulated at international level for the main output properties, being linked to the conversion efficiency and durability, and represents a support in the developing novel, performance and cost-effective solutions. The International Association European Solar Thermal Industry Federation [1] reports on currently running testing procedures for the solar collectors: internal pressure, high-temperature resistance, exposure, external thermal shock,

D. Ciobanu · I. Visa · A. Duta (✉) · M. Enescu
Renewable Energy Systems and Recycling Research Centre, Transilvania University of Brasov, Brasov, Romania
e-mail: a.duta@unotbv.ro

D. Ciobanu
e-mail: daniela.ciobanu@unitbv.ro

I. Visa (ed.), *Sustainable Energy in the Built Environment - Steps Towards nZEB*, Springer Proceedings in Energy, DOI 10.1007/978-3-319-09707-7_15

internal thermal shock, rain penetration, freeze resistance, mechanical load, impact resistance (optional), final inspection and thermal performance tests [1–3]. To perform all these tests, literature mentions the need for at least three collectors: one collector for assessing the thermal performance, the second for testing the durability, and the third is used for mechanical load and rain penetration tests.

There are two methods to evaluate the thermal performance of a solar collector: steady state and quasi dynamic test methods [4]. Each of these methods has advantages and disadvantages. In case of steady state method the advantage is its simplicity but the main disadvantage is related to a very large period of testing time in which the tests can be run due to the reduced number of days when all conditions are fulfilled (solar radiation, wind speed, etc.). In the case of the quasi dynamic testing method, the advantage is related to the reduced solar radiation intensity acceptable according to the standards, thus, for outdoor testing rigs, a triple number of days is available over one year, when the tests can be done.

Most of the performance standards are specifically designed for in-door or outdoor testing rigs and address the functional properties of un-used FPSTCs. On the other hand, the durability assessment requires accelerating aging tests, mimicking extreme operation conditions and registering the consequences on different parts of the collector and on the entire device. The focus is on two main causes that are responsible for the efficiency loss: (1) overheating during stagnation, responsible for the system's wearing, but mainly for the development of micro-cracks on the absorber plate and (2) corrosion/erosion of the absorber plate under saline aerosols that are likely when installing FPSTC on the seashore areas. Both causes lead to fast degradation and losses in the spectral selectivity, thus to a significant decrease in the conversion efficiency.

So far, the rain penetration standard addresses only the collectors' tidiness, and the corrosion/erosion measurements are standardized only for the absorber plate, ranking these according to their loss in the spectral selectivity, after the climatic chamber test. But, the tidiness (the polymeric sealing) can significantly be affected by the combination of heat and saline aerosols (common for many sea shore locations where solar thermal systems are installed), allowing the penetration of the latest and the reaction on the absorber plate during the working period, thus under solar irradiation (including UV and heat). This combination, having a significant variability in the content/ratio of the aggressive factors during the diurnal and seasonal cycles, needs to be initially tested in outdoor conditions and, after outlining the most important parameters, it can be transferred in in-door standardized procedures.

Thus specific aging tests are required, to investigate the FPSTC durability under these conditions and to validate the viability of the proposed solutions aiming at mitigating the effects of overheating, saline corrosion and their combination.

The paper presents an assembly of testing rigs developed in the R&D Centre Renewable Energy Systems and Recycling, in the Transilvania University of Brasov, Romania, supporting the quality assessment of FPSTC, under standardized and non-standardized procedures. Further on, the paper discusses the effect of saline aerosols on the solar-thermal conversion and, based on the outdoor testing results, preliminary prerequisites for developing novel standardized testing procedures are outlined.

2 FPSTC Testing Infrastructure

In order to evaluate the thermal performance of FPSTC, standard test EN 12975 describes in EN 12975-1:2006 the general requirements for solar thermal collectors and the first part and in second part are describing the testing methods [2]. To perform these tasks, certification stands can be either in-door or outdoor [5, 6].

As for the durability tests in saline environment for FPSTC, currently there is no standard in the word. In R&D Centre Renewable Energy Systems and Recycling (RES-REC), from Transilvania University of Brasov, Romania, has installed out-door and in-door testing rigs for assessing the solar thermal performance of FPSTC and an out-door test rig for corrosion/erosion tests. The outdoor testing rigs are implemented on the rooftop of the laboratory building of the RES-REC Center, in the R&D Institute of the Transilvania University of Brasov. The location is at 45°66′ latitude, 25°55′ longitude, at 600 m above the sea level in a mountain region with an average amount of solar energy of 1,200 kWh/m^2/year, with large variations between the winter months (lower than 45 kWh/m^2/month during winter) and the summer months (over 150 kWh/m^2/month during summer).

For various tests related to FPSTC and their components, the relevant input data are measured on the testing rig (as required by the testing procedure). Additionally, the ambient parameters (solar radiation, wind speed and direction, temperature and humidity) are measured by the weather station Delta T installed near the outdoor testing rigs.

The out-door test rig presented in Fig. 1 was designed considering the specific objectives of the standard outdoor testing procedures. The testing rig also supports the research on overheating mitigation by using complex algorithms [7], thus it can be tracked by a bi-axial mechanical tracking system.

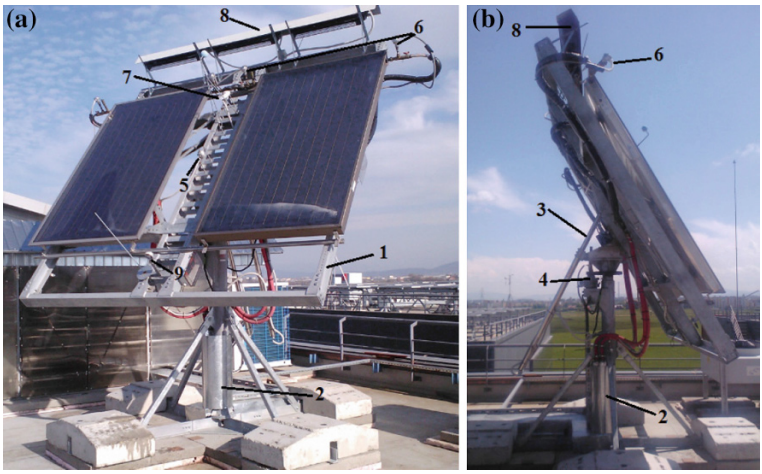

Fig. 1 Outdoor test rig for thermal performance. **a** Front view. **b** Left view

It consists of:

1. Solar-thermal platform frame (3 × 3 m^2) where two solar collectors with identical or different dimensions can be mounted;
2. Platform pillar; where the solar collector is mounted.
3 and 4. Bi-axial tracking system allowing the diurnal motion with an angular stroke of ±110° (gear based mechanism), while the elevation is insured by a linear actuator, (angular stroke of 10°–90°);
5. Pyranometer (class A) for global solar radiation measurement, installed in the solar collector plane;
6. PT100 sensors for inlet and outlet fluid temperatures;
7. Pyranometer with shadow ball (class A) for diffuse solar radiation measurement;
8. Ventilation units (maxim air speed 4 m/s);
9. Anemometer for wind speed measurement.

The regular tracking, for evaluating the collector's performance, follows the concept of theoretical maximum gain of available solar radiation. It is reached through a program that calculates the position of the sun in the sky depending on the day number and local time. Following data are subject of acquisition: global solar radiation; diffuse solar radiation, fluid inlet and outlet temperatures, mass flow, wind speed, elevation and diurnal angles.

Indoor FPSTC testing always brings complementary information on the FPSTC and allows ranking the collectors according to their functional performance. The indoor test rig, Fig. 2, consists of the following components:

1. Sun simulator; the intensity of solar radiation is of max. 1,000 W/m^2; the irradiation source is a mix of Vis- and UV bulbs, well mimicking the part of interest of the solar spectrum when analysing the conversion processes. The simulator allows therefore also PV testing;
2. Solar collector frame (1 × 2 m^2);
3. Pyranometer (class A), for global solar radiation measurement;
4. PT 100 sensors for inlet and outlet fluid temperature measurements;
5. Ventilation unit for wind simulation (wind speed 2 m/s);
6. Anemometer for wind measurement; temperature sensor (environment);
7. Sensor for mass flow measurement;
8. One axis tracking system, with linear actuator that allows an angular stroke of 0°–90°.

Following the need identified for extending durability tests on solar-thermal collectors by considering saline aerosols, a novel out-door test rig for corrosion/erosion tests was designed and developed, Fig. 3:

1. STFPC frame, tilted at 45°;
2. Nozzles for spraying the saline aerosol; 25 nozzles are equidistantly installed on a pipe, allowing a homogeneous coverage of the collector's surface;
3. Plastic trough to collect the saline water at the bottom of the collector;

Fig. 2 Indoor test rig

Fig. 3 Out-door test rig for corrosion/erosion test

4. Storage tank (30 L) for the saline solution;
5. Recirculation pump (T.I.P. GPK46/42) with controllable flow;
6. Flow-meter (FIP FSIV032T, accuracy ±1.875 %).

The temperature and the humidity inside the collector are registered using a TPI597 device (Wales, ±0.5 % accuracy).

3 Results and Discussions

Complementary information is received from outdoor and indoor testing:

- Outdoor testing allows the acquisition of specific data that are close to the real output of the FPSTC, in the testing location; by extension it may be suppose a similar behaviour in geographic areas with a climatic profile close to the testing one. Outdoor testing also gives valuable information on the efficiency variation with the solar radiation profile (allowing the development of tracking algorithms for increasing the amount of solar input on the FPSTC surface) and gives an idea about the correlation solar radiation—duration—overheating, allowing the design of the algorithms aiming at mitigating the overheating effects.
- Indoor testing, under controlled radiation and wind speed allows differentiating among FPSTC and gives an accurate view on the tracking effect, since on the solar simulator there is only direct radiation.

If in the case of the outdoor rig information related to the method of testing, the place where the equipment is installed, the method to present the recorded data are clear, for indoor tests, the analysis of the existing standards allows the conclusion that the information on the testing procedure could be improved. The main improvement that could be done is to include an exactly specification of the devices used to measure solar radiation simulated. The measurement devices of the solar radiation are usually mentioned as pyranometer class A. Still comparative investigations, below described, suggest the need for a better description of the pyranometer.

3.1 Indoor Test

Indoor test of solar collectors involved to use a sun simulator. According to standard EN 12975:2-2006, light used to simulate the solar radiation must be in the range of 700 W/m^2, but can vary between 300 and 1,000 W/m^2. The spectral distribution of the simulated solar radiation shall be approximately to that of solar spectrum at optical air mass 1, 5 [2].

On the sun simulator described in Fig. 2, measurements of the input radiation were done using a pyranometer class A (Delta Ohm, LP PYRAN 03AC) and a lux-meter (MAVOLUX, 5032C/B). The results, expressing the global radiation should be equivalent. The correlations between the values recorded by the two devices are shown in Fig. 4.

As the results show, there is a good correlation at high irradiation but the values of the simulated solar radiation, between 200 and 400 W/m^2, there are certain differences between the recorded values from the pyranometer and the lux-meter.

Further on, a comparison between the measured values recorded by the pyranometer and the lux-meter when only the VIS lamps are switch on, is shown in

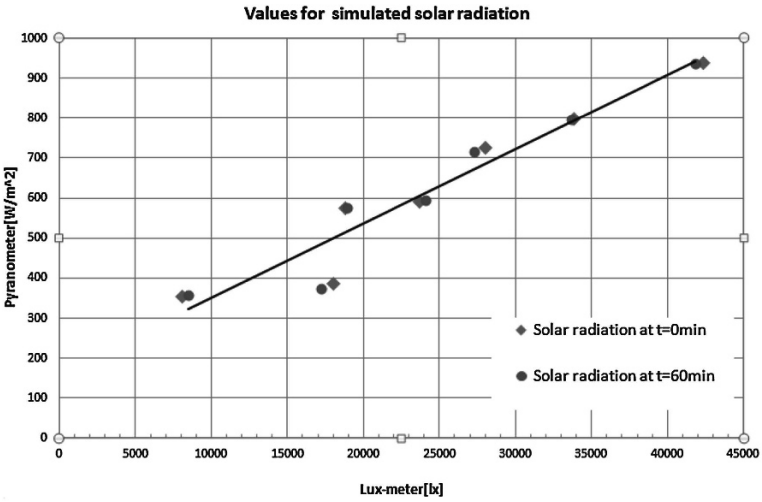

Fig. 4 Equivalent values of the simulated solar radiation (UV+VIS) as recorded by the pyranometer class A and by the lux-meter

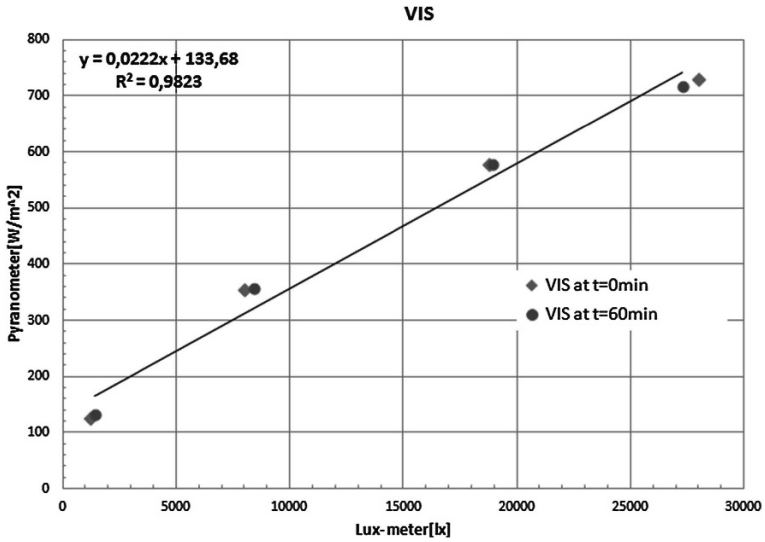

Fig. 5 Simulated solar radiation with VIS lamps

Fig. 5. The overlapping is good, leading to the conclusion that the differences registered in Fig. 4 are mainly connected to the measurement values in the UV spectral range. By applying linear regression on the measured values, the regression coefficient R is 0.9823, showing that, although an equivalency exists between the two types of measurements, these are not fully inter-changeable in Vis.

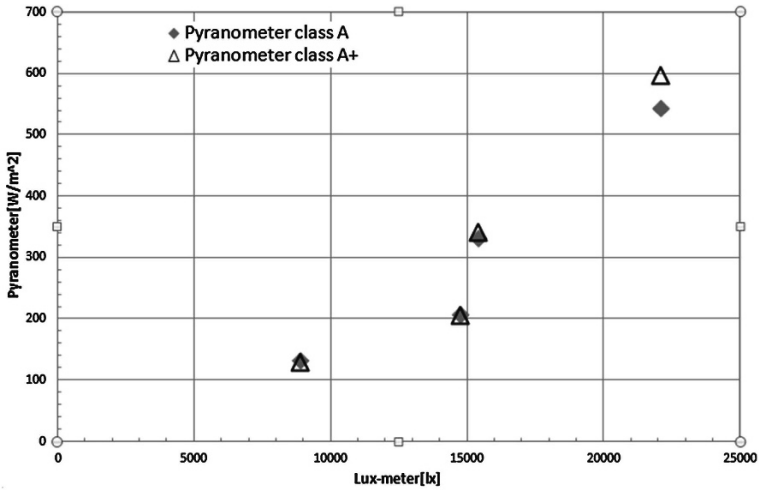

Fig. 6 Comparison between measure solar radiation with pyranometer class A or A+

In order to further investigate the pyranometer measurements similar measurements were performed using a pyranometer class A + (LSI LASTEM, BSR 153). By comparing the measured values using the two pyranometers (class A and class A+), Fig. 6, differences are outlined between the recorded values, considering as reference the data recorded by the lux-meter. The largest difference 54 W/m^2 occurs at high intensities of the solar radiation.

These results outline the need for specifying the type and accuracy of the device used for measuring the simulated solar radiation, for a correct estimation of the conversion efficiency.

Obviously, these conclusions can be extended also to outdoor measurements.

3.2 Outdoor Test for Saline Aerosol

Many applications of the residential solar thermal systems are in seashore areas where the climatic profile is mild and the number of sunny days is high. Because of this, there is an increased interest on the durability tests in saline environment applied to the solar thermal collectors (and to their components), [8, 9]. Several tests are developed for the casing and for the absorber plate, similar to the regular corrosion test of metals in the fog chamber (e.g. ASTMB117 and ISO 9227), but for the entire solar thermal collector there is no durability standard in saline environment (yet).

In an attempt to formulate a new quality criteria (durability in saline environment), a testing rig and a testing procedure were developed. Testing was conducted on the flat plate solar collector having air in the pipes and no circulation. This setup

was chosen considering the different specific heats of air (1.005 kJ/kg K) and water (4.180 kJ/kg K) and the very large density differences (1,000 kg/m^3 for water and 1.12…1.29 kg/m^3 for air); using air allows thus sensing small variations in the temperature inside the pipes, under the outdoor irradiation conditions.

The tests covered 60 days, in three periods: in July–August 2013 (20 days) and in March–May 2014 (20 days from March 24 and 20 days from May 7); the first period is usually characterized by sunny days with high outdoor temperatures during the day; the second time interval is typical for a transient season (early to late spring) with significant and sudden variations in the solar radiation and with average outdoor temperatures (thus the risk of overheating is very low). Thus, the main functional situations were covered, corresponding to the periods when the collector is expected to well perform. From September to February, the FPSTC was left at rest outdoor.

Preliminary data on the July–August time interval were already reported [10], and allowed to identify two possible functions that could characterize the decay of the FPSTC, involving the FPSTC output temperature and the outdoor temperature: their difference and their ratio. Further on, to extend the database and to validate the conclusions already presented, the tests run during 2014 followed the same procedure; the recorded values were: the inlet and outlet air temperature inside the solar collector registered at 9, 12 and 15 o'clock, and the outdoor conditions at these moments (outdoor temperature, wind speed, humidity, and solar radiation). The comparative charts of the outlet temperatures obtained in the three periods is presented in Fig. 7.

The main challenge is to identify the most relevant experimental conditions and the optimal correlations between selected input and output data.

The solar radiation is not a fully useable data for a temperate climate as high intensity can be registered at very low outdoor temperatures (e.g. during sunny, frosty winter days), thus for the solar-thermal conversion, this is not the best parameter to be directly linked to the conversion efficiency and its decay. As the most important input data in efficiency calculations is the outdoor temperature, this was also hereby used.

In terms of output, the temperature at the FPSTC outlet (the outlet temperature) was considered as the suitable indicator of the solar-thermal conversion (as generally used in solar-thermal calculations).

A first correlation was attempted between the outlet FPSTC temperature and the ambient temperature. As expected, a similar trend was registered, for all three periods (in 2013, 2014) thus the correlation was not conclusive in either of the investigated moments: at 9:00, at 12:00 and at 15:00. Additionally, the data collected at 9:00 proved to be highly irrelevant as result of the low radiation profile. Therefore, in further correlations these data were no longer used.

Following the conclusions presented in [10], two functions were further investigated: the difference between the outlet and the ambient temperature ($T_{out} - T_{amb}$) and the ratio between these two: T_{out}/T_{amb}.

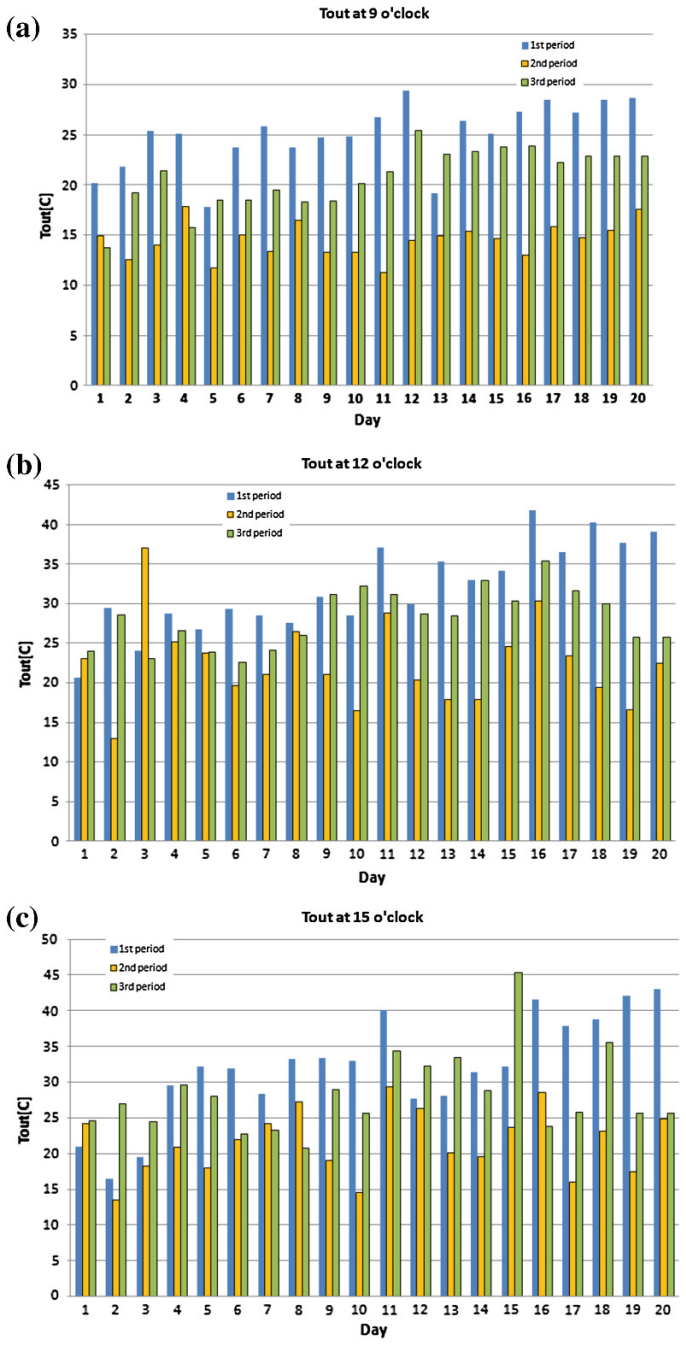

Fig. 7 Difference of outlet temperature for **a** 9 o'clock; **b** 12 o'clock and **c** 15 o'clock

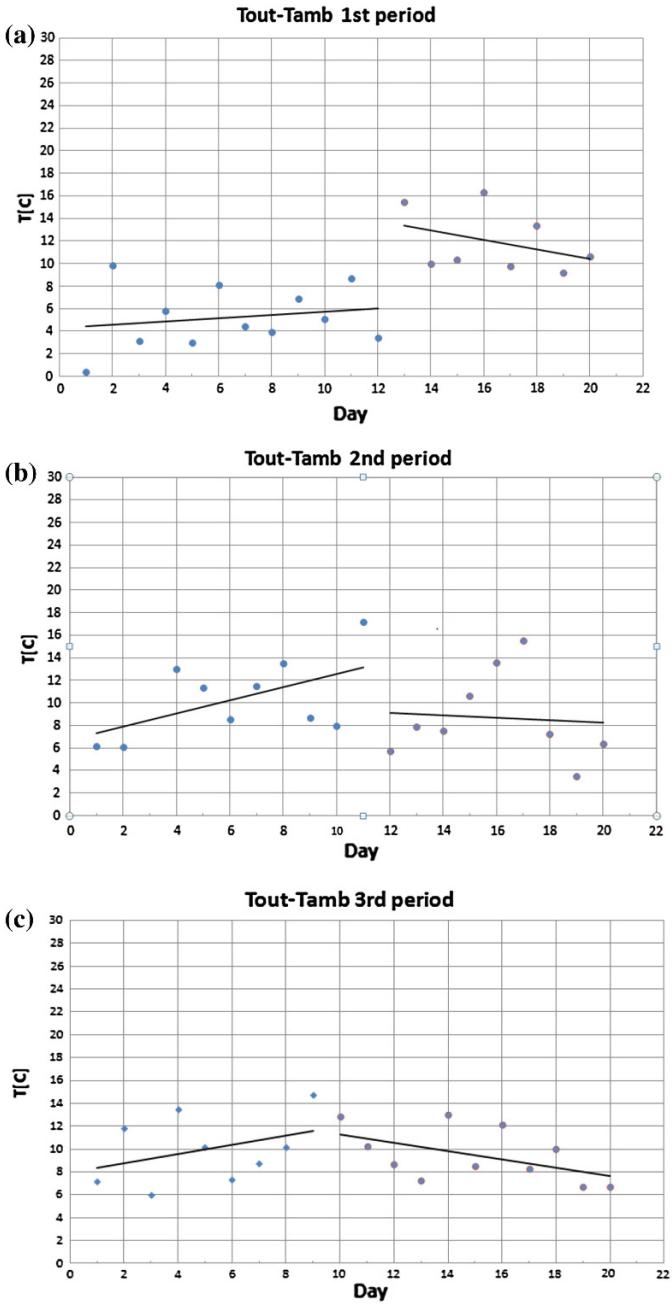

Fig. 8 Difference between the outlet and outdoor temperature at 12:00 during: **a** 1st period, **b** 2nd period and **c** 3rd period

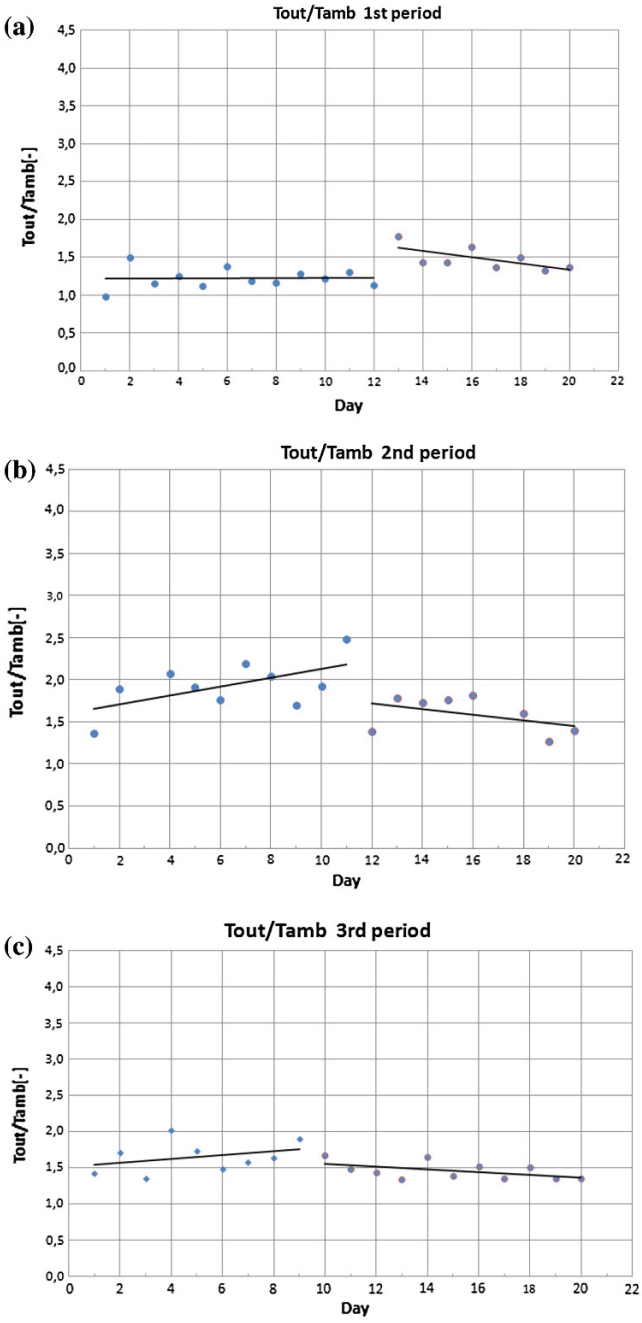

Fig. 9 Ratio between the outlet and outdoor temperature at 12:00 during: **a** 1st period, **b** 2nd period and **c** 3rd period

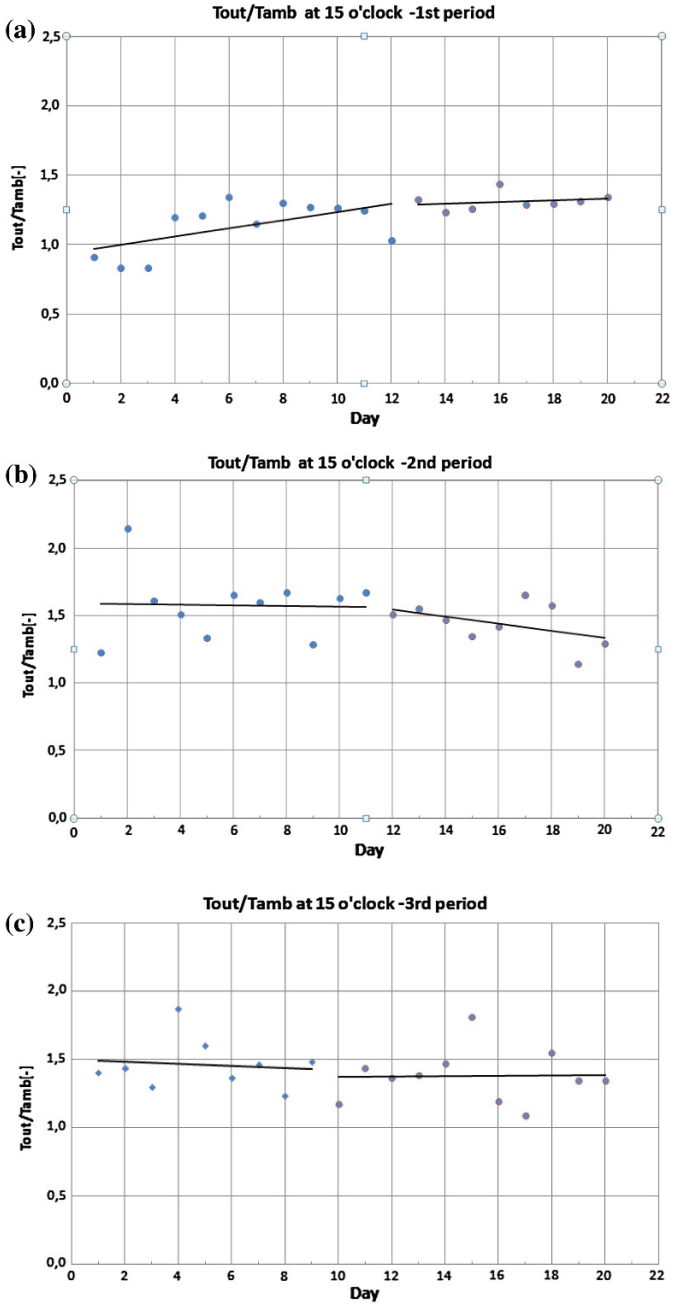

Fig. 10 Ratio between the outlet and outdoor temperature at 15:00 during: **a** 1st period, **b** 2nd period and **c** 3rd period

To give evidence on the best outdoor conditions able to outline the changes in the conversion efficiency (due to aging), these functions were calculated both for the data collected at 12:00 and for those registered at 15:00.

The graph variations over the three periods of 20 days represented based on the data collected at 12 o'clock are given in Fig. 8 and ($T_{out} - T_{amb}$) in Fig. 9 (T_{out}/T_{amb}). The same correlation functions ($T_{out} - T_{amb}$ and T_{out}/T_{amb}) were analysed also for the data collected at 15:00 but the slope changes are less evident thus the degree of uncertainty is higher. The ratio T_{out}/T_{amb} for the three investigated periods is presented in Fig. 10.

This recommends 12:00 (noon) as best testing period, outlining that the decay effect is more sensitive at higher ambient temperatures, thus it has the strongest influence when the output is at its best. This result outlines again the need for such tests as part of the re-design of the FPSTC components, particularly of the sealing which is mostly sensitive to the combination of heat and saline aerosols.

By analyzing the diagrams following observation can be obtained:

1. The outlet temperature has a decreasing trend for similar conditions of solar radiation and ambient temperature, as Fig. 7;
2. The saline aerosol test led to changes in the solar thermal flat plate collector behavior (abrupt change in the function variation); during the first testing period, changes in solar collector behavior appeared of the 12th day, in the second period changes occurred after 11 days, and during the third period changes were starting in the 9th days.
3. By comparing the set of measurements it can be concluded that the most sensitive to the changes in the solar collector behavior is the parameter given by the difference between outdoor temperature and the outlet temperature.
4. As Fig. 8 shows, this difference is decreasing from one testing period to another, showing the irreversible destruction of the absorber plate.

4 Conclusions

In assessing the efficiency (thus quality) of solar thermal flat plate collectors thermal performance and durability tests are required. Complementary indoor and outdoor tests can give a quite accurate evaluation of the new (un-used) FPSTC by following standardized procedures run on specific rigs. To get a common ground all over the world for the testing results, the paper shows that for indoor testing rigs additional info should be included in the testing methodology, especially related to the device that measures the input simulated solar radiation.

For the durability tests, saline aerosol/rain penetration tests were run outlining the influence of three sets of 20 days testing on the FPSTC performance. The results show that the tests are more relevant if run at higher outdoor temperatures (at noon). The most sensitive function in evaluating the decay due to accelerate aging was found to be the difference between the outdoor and outlet temperature.

Acknowledgments We hereby acknowledge the structural founds project PRO-DD (POS-CCE, O.2.2.1., ID 123, SMIS 2637, ctr. No 11/2009) for providing the infrastructure used in this work and the project PNII Cooperation Project, EST in URBA no. 28/2012 financially supported by the Romanian National Research Council.

References

1. http://www.estif.org/solarkeymarknew/index.php.
2. Standard EN 12975.
3. ESTIF and intelligent energy Europe, QAiSt a guide to the standards EN 12975, Renewable Energy House. www.estif.org. Accessed 9 May 2014.
4. Osorio, T., & Carvalho, M. J. (2014). Testing of solar thermal collectors under transient conditions. *Solar Energy, 104*, 71–81.
5. Nielsen, J. E., et al. (2012). Towards global certification of solar collectors. *Energy Procedia, 30*, 1339–1343.
6. Serrats, E. M., et al. (2012). IEA-SHC task 43: Research and standardization on solar collector testing and towards a global certification scheme. *Energy Procedia, 30*, 162–167.
7. Neagoe, M., Visa, I., Burduhos, B. G., & Moldovan, M. D. (2014). Thermal load based adaptive tracking for flat plate solar collectors. *Energy Procedia, 48*, 1401–1411.
8. Kaltenbach, T., et al. (2014). Testing of components for solar thermal collectors in respect of saline atmospheres. *Energy Procedia, 48*, 731–738.
9. Kaltenbach, T., et al. (2014). Aging tests of components for solar thermal collectors. *Energy Procedia, 30*, 805–814.
10. Ciobanu, D., Visa, I., & Duta, A. (2014). Solar thermal collectors outdoor testing in saline environment. *Energy Procedia, 48*, 707–714.

Study of Adaptability of Solar Thermal Systems on Merchant Ships

Alexandru Cotorcea and Ion Visa

Abstract In recent years, sustainability in a climate and an environmental perspective has become an issue of highest priority. This is an agenda that cannot and should not be ignored and transportation, including shipping should be part of the general effort towards green and affordable solutions. Nowadays, energy consumption in shipping depends on fossil fuels. As oil price is constantly increasing, solutions must be found in order to ensure sustainability. Developing and implementing energy efficient and environmentally friendly technologies for energy production and propulsion of the ship will conduct to a valid non-fossil future. In this context, the paper analysis an alternative solution for meeting the thermal energy demand of the vessels. This solution consists in implementing solar thermal collectors on board merchant ships. Also, an algorithm of implementation is proposed considering the specificity of the activities.

Keywords Shipping industry · Renewable energy sources · Solar thermal systems

1 Introduction

About 80 % of the world trade by volume is carried by sea [1]. In 2007, international shipping was responsible for approximately 870 million tones of CO_2 emissions, or 2.7 % of the global anthropogenic CO_2 emissions [2]. Domestic shipping and fishing activity bring these totals up to 1,050 million tones of CO_2, or 3.3 % of the global anthropogenic CO_2 emissions. Despite the undoubted CO_2 efficiency of shipping in terms of CO_2 amount emitted per tone-km, it is recognized within the maritime sector that reductions in these totals must be made. Shipping is

A. Cotorcea (✉) · I. Visa
Transilvania University of Brasov, Brasov, Romania
e-mail: alexandru.cotorcea@unitbv.ro

I. Visa (ed.), *Sustainable Energy in the Built Environment - Steps Towards nZEB*,
Springer Proceedings in Energy, DOI 10.1007/978-3-319-09707-7_16

responsible for a greater share of NOx (37 %) and SOx (28 %) emissions [3] and recent legislation is aimed at reducing these emissions through the introduction of emission control areas and requirements on newly built marine diesel engines [4]. The base scenarios regarding CO_2 emissions from shipping from 2007 to 2050, modeled by the International Maritime Organization (IMO), indicate an annual increase of CO_2 emissions in the range 1.9–2.7 % with the extreme scenarios predicting changes of 5.2 % and −0.8 %, respectively. If global emissions of CO_2 are to be stabilized at a level consistent with a 2 °C rise in global average temperature by 2050 it is clear that the shipping sector must find ways to stabilize or reduce its emissions; otherwise the projected values will account for 12–18 % of all total permissible CO_2 emissions.

On the other hand, the European Union (EU), in the strategy described in [5], marks a turning point in the protection policy against atmospheric pollution from vessels. About 42 % of the EU's domestic shipping and 90 % of its trade with non-European countries is transported by sea. The energy consumption and CO_2 emissions per ton and mile traveled by ship represents about 25 % of the fuel consumption by road. Therefore, the EU has established as a fundamental strategic objective the pollution and greenhouse gas emissions reduction by transferring the transport of goods to motorways on the sea. Despite these measures, it is estimated that, by 2020, vessel emissions of sulphur oxides (SO_x), nitrogen oxides (NO_x) and particulate matter (PM2.5) in EU waters will increase by 40, 50 and 55 %, respectively, compared with the 2000 levels.

Studies made by the International Council on Clean Transportation [6] and IMO [2] concur on the range of technological and operational strategies available to the current global fleet [7]. In 2010, IMO introduced "Technical measures", "Operational measures" and "Economic instruments" as instruments for reducing CO_2 emissions. IMO also introduced the Energy Efficiency Design Index (EEDI), as the index for evaluating the technical measures [8]. Main categories of EEDI reduction technologies and opportunities include the following:

- Policy issues on shipping logistic;
- Modified hull form (reduction in propulsion resistance);
- Modified propeller (enhanced propulsion efficiency);
- Energy-saving appendages on hull;
- Increase in deadweight capacity by increasing the hull size;
- Use of energy from exhaust heat recovery;
- Use of renewable energy (wind, solar, etc.).

Further, there are presented alternative sources of energy used in shipping industry, novel solutions recently identified and our perspective on the technical solution focusing on the solar-thermal systems. These efforts are made for reducing emissions from ships and, as ultimate goal, obtaining a zero emission vessel.

2 Methodology for Solar Thermal Collectors Integration as Alternative Source of Energy in Shipping

Several alternatives are proposed to reduce or to replace fossil fuels onboard a ship: sails, kites, received electricity in ports, use of biodiesel, wind turbines, photovoltaic modules and hydrogen fuel cells. They can be used on their own or as hybrid systems for power generation onboard a ship. These are green energy systems that use renewable or clean energies.

Sails and kites reduce fuel by 20–27 %, respectively 15 % for certain routes, depending on the average speed of the vessel. In wind turbines (horizontal/vertical axis), wind energy acts on the blades making a generator spin. This in turn converts rotational mechanical energy into electrical energy [9]. Their most significant application on vessels is as part of a hybrid energy system, working in combination with hydrogen fuel cells. Thus, the electricity produced by wind turbines is used to generate hydrogen through the electrolysis of water and this is used to feed the fuel cells.

Feasibility of installing photovoltaic modules onto vessels is considering the payback time from the adopted investment with respect to fuel oil savings. Thus, the two important parameters incorporated for a good parametric analysis are the solar radiation density and the fuel cost. For one square meter of the considered solar modules the peak output power is taken equal to 130 W [10]. For a reasonable fuel price annual increase at about 10–15 % the estimated payback period varies from 16 to 27 years. The methodology shows that by increasing the fuel oil price (according to a realist scenario), the payback time will decrease down to a minimum of 10 years [11].

As the synthetic literature review shows, the solar thermal solution is not even mentioned as an option when consider alternative sources of energy in shipping. Reviewed literature reveal some concern related to usage of additional thermal energy onboard vessels, especially those which are involved in short maritime transportation. Identified solutions mostly rely on storing the thermal energy onshore produced and transferred to the ship before going on sea.

Thermal energy obtained through conversion of solar energy can be used onboard ships in domestic hot water and steam generation processes. In order to adapt and implement solar thermal systems onboard merchant vessels, an algorithm is proposed:

(a) *Evaluation of the thermal energy demand onboard the ship*; this step makes an assessment of all systems and consumers that require thermal energy in order to work.
(b) *Design and sizing the area of the solar thermal collectors*, considering the available surface for installation according to the ship characteristics; limitations in adapting the solar thermal systems on vessels include effect of ship's swing movement, influence of salty environment to collectors efficiency, horizontal area available for the collectors—without hindering the work carried onboard or assuming safety risks of the operations with cargo.

(c) *Evaluation of the thermal energy gained through the solar thermal system*, considering the yearly solar radiation on the main transit routes of the vessel; the available solar radiation on the transit routes of a specific vessel represents the input for an accurate evaluation of the produced thermal energy through the solar thermal system. Solar collectors are expected to better perform on the sea due to the amount of solar radiation, as compared with land [12].
(d) *Design of the solar-thermal system*; this requires the optimal integration of the solar thermal platform/system with the other systems and installations already existing on board and their usual positioning (solar collectors on deck and ship's installations, usually, in engine room).
(e) *Cost-benefit analysis of the implemented system*, as a comparison of operating costs before and after implementation; analysis will consider firstly the already known operating costs of the vessel. Secondly, there are calculated the costs associated with the initial investment (installation and implementation) related to the solar collectors on the available surface. This results are further correlated with the thermal energy obtained gained due to use of the solar-thermal system (thus cost savings); additional factors in assessing the feasibility are the selection of the optimal, and the fuel savings.
(f) *Detailed design and installation of the optimized solar thermal system*; as a consequence of step (e), the optimization of the system will consider reducing cost of installation (accordingly to thermal demand of the ship and collectors efficiency) and optimal positioning of the collectors for increased output.

A case study is further presented, starting with the evaluation of the thermal energy demand for domestic hot water and heating of heavy fuel oil (step a) for an 8,700 tdw general cargo ship, *the Albatros*. The vessel is owned by Mircea cel Batran Naval Academy of Constanta, Romania. Following the algorithm described, the surface of the solar collectors that must be installed in order to cover the thermal energy need is calculated.

3 Case Study: Evaluation of Thermal Demand for a 8,700 tdw General Cargo

The *Albatros* vessel is intended for general cargo, bulk cargo (exclude minerals), equipment, containers and timber (in warehouses or on the deck). Main dimensions and general characteristics of the ship are presented in Table 1.

The ship has a capacity of 564 tons of heavy fuel oil (HFO), 260 tons of diesel oil (DO) and 208 tons of water. Average daily cruising consumptions consist of 12 tons of HFO, 2.5 tons of DO and 8 tons of water.

Thermal energy is used on board for domestic hot water and steam generation. Therefore, an CAVNO 1000 naval boiler is design to provide the necessary thermal energy. The naval boiler operates normally with HFO, but can also operate with DO in emergency situations. Main characteristics include a steam flow of 1,000 kg/h, a

Table 1 Dimensions and general characteristics of *Albatros*

Maximum length	$L_{max} = 130.86$ m
Maximum width	$B_{max} = 17.70$ m
Maximum draft	$T_{max} = 8.10$ m
Maximum speed	$V_{max} = 15$ kn
Cruising speed	$V = 10$ kn
Displacement (full load)	$\Delta = 12{,}350$ tons

working pressure of 7 bar, temperature of feed water of 40 °C and a consumption of 95 L/h.

In Fig. 1 the main components of the steam circuit are represented. It consists of fresh water and HFO service tanks, naval boiler and steam mainline. Dashed lines are used to represent the components of the proposed solar thermal system and outlines its integration into the standard system.

The thermal energy demand consists of:

- Domestic hot water produced to meet the daily requirements of the crew (44 sailors of which: 20 safe crew, 12 auxiliary personnel and 12 cadets).
- Steam used for heating HFO tanks (storage, settling, service), "defrost" of heavy fuel (steam piping doubling of heavy fuel pipes, diesel mixing tube—heavy fuel), heating the castle, wash tanks system and fire fighting system.

The steam used to heat tanks has a pressure of 5 bar and is collected from the steam mainline leaving from naval boiler. Heating heavy fuel is up to 95 °C and is done by two coil serpentines in each tank, independent one of another. The first coil makes a spiral around the fuel transfer system strainer, then is carried out to the half-length tank. The second coil has direct input and runs the rest of the tank. This solution was adopted as usually it is not necessary to heat the entire mass of fuel once.

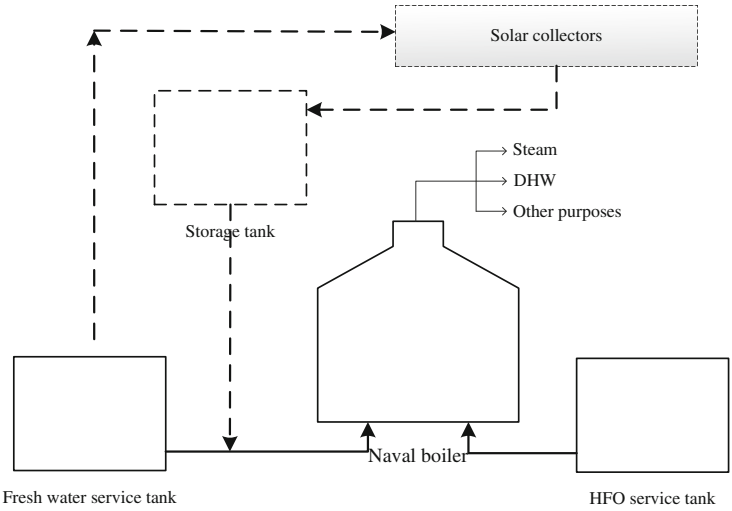

Fig. 1 Block diagram of naval boiler circuit

While on sea, fuel consumption is 500 kg/h. To heat this quantity in an hour the necessary mass flow is:

$$m_{HFO} = \frac{m_h}{\tau \times 3600} = \frac{500}{1 \times 3600} = 0.14\,(\mathrm{kg/s}) \tag{1}$$

Thus the thermal power required for heating heavy fuel will be:

$$Q_{HFO} = m_{HFO} \times c_{HFO} \times (T_{out} - T_{in}) = 0.14 \times 2.1 \times 80 = 23.5\,(\mathrm{kW}) \tag{2}$$

where:

C_{HFO} = 2.1 kJ/Kg × deg	specific heat of heavy fuel oil
T_{out} = 95 °C	temperature of heavy fuel oil before use
T_{in} = 15 °C	temperature of heavy fuel oil in storage tanks

On the other hand, domestic hot water consumption is derived from 75 liters per crew member per day. According to the number of crew members (44) it results 3,300 l per day or 137.5 per hour. In order to heat up this quantity of fresh water will be necessary a mass flow:

$$m_{DHW} = \frac{m_h}{\tau \times 3600} = \frac{137.5}{1 \times 3600} = 0.038\,(\mathrm{kg/s}) \tag{3}$$

The thermal power required for heating fresh water will be:

$$Q_{DHW} = m_{DHW} \times c_W \times (T_{out} - T_{in}) = 0.038 \times 4.19 \times 50 = 8\,(\mathrm{kW}) \tag{4}$$

where:

$c_{HFO} = 4.19\,\mathrm{kJ/kg} \times \mathrm{deg}$	specific heat of water
T_{out} = 60 °C	temperature of water before use
T_{in} = 10 °C	temperature of water in storage tanks

From Eqs. (2) and (4) results an hourly demand of thermal power of 31.5 kW. Further, to ensure this amount of energy from solar power, the solar radiation intensity, collector's efficiency and available installation surface must be known.

In this calculation, the solar radiation intensity is considered 150 W/m^2 (horizontal) as an average of the values identified in literature [13]. However, for a better evaluation of thermal energy gained to a specific maritime route (step b from algorithm) solar radiation intensity must be determined in situ. Also, the energy output of solar-thermal systems using flat plate collectors can be improved by tracking [14], but this subject is not covered in the present study. For collector's efficiency there were considered two values (50 and 75 %) allowing to compare among the commercial flat solar thermal collectors. The *Albatros* vessel has a total horizontal surface exposed to sun of about 2,000 m^2. Still, much of this surface can not be used for installation of solar collectors because of other usage.

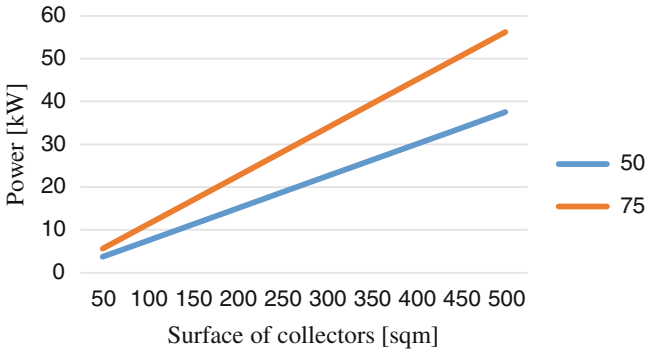

Fig. 2 Power gain depending on surface of collectors

In Fig. 2 there can be seen the variation of power gain through solar collectors for surfaces between 1 and 500 m^2.

In order to comply with hourly demand of thermal power of the ship (31.5 kW), surface required varies from 400 m^2 for an efficiency of 50 % to approximately 300 m^2 for an efficiency of 75 %. These correspond to 15–20 % of total available surface. By increasing the area covered by collectors (up to 2,000 m^2), amount of energy thus obtained reach up to 225 kW. In current situation this amount of energy can not be used, but retrofitting the propulsion system of the ship (into steam turbine) can be a viable solution. As a result, given the free surfaces available for installation of such systems, is recommended the use of solar thermal collectors with high efficiency and the possibility of tracking. However, adding a tracking system requires additional investments, but the cost raise is covered by the increase in the amount of solar radiation received by the collectors.

Substituting energy obtained by fuel consumption with energy derived from solar thermal system will conduct to an economy of 400 kg of HFO per day. This amount represents 3.3 % of the total consumption of the ship and fits the reduction potential provided in [15]. Considering a price of 600 $/ton, use of solar technologies will save up to 240 $/day or 72,000 $ annually (for an average of 300 operation days). Also, reduction of carbon dioxide emissions (360 tons per year) is another key aspect.

4 Conclusions

In search of a “green” ship, it was presented an algorithm for adapting and implementing solar thermal systems onboard merchant vessels. Results obtained so far will be used in further studies that will evaluate feasibility of solar thermal systems for oil tankers or dry bulk carriers.

Further work will focus on efficiency and feasibility of this kind of collectors in different sea conditions, with emphasis on reduction of greenhouse gases and perspective of continuously rising price for fuel because of dwindling oil reserves.

However, ship-owners are skeptical regarding implementing renewable sources of energy onboard ships, due primarily to high costs associated with these technologies. Efforts must be made, generally by policies and incentives for encouraging development of "greener" ships outlining economic and environmental benefits.

Acknowledgments This paper is supported by the Sectoral Operational Programme Human Resources Development (SOP HRD), financed from the European Social Fund and by the Romanian Government under the project number POSDRU/159/1.5/S/134378.

References

1. UNCTAD. (2008). Review of maritime transport. In: *Proceedings of the United Nations Conference on Trade and Development*, Accra (Ghana).
2. IMO. (2009). MEPC59—Second IMO green house emission study. International Maritime Organisation.
3. AEA Energy and Environment. (2008). Greenhouse gas emissions from shipping: Trends, projection and abatement potential. Didcot, Final Report ED43808, Issue 4.
4. MARPOL. (2005). MARPOL 73/78 revised ANNEX VI, MEPC59. IMO.
5. Communication from the Commission COM (2002) 595 final, The Clean Air for Europe (CAFE) Programme: Towards a Thematic Strategy for Air Quality.
6. International Council on Clean Transportation. (2011). *Reducing greenhouse gas emissions from ships: cost effectiveness of available options*. Washington: ICCT.
7. Nuttall, P., Newell, A., Prasad, B., Veitayaki, J., & Holland, E. (2014). A review of sustainable sea-transport for Oceania: Providing context for renewable energy shipping for the Pacific. *Marine Policy, 43*, 283–287.
8. International Maritime Organization, Marine Environment Protection Committee (2009) Interim guidelines on the voluntary verification of the energy efficiency design index for new ships, MEPC.1/Circ.682.
9. Spera, D. A. (ed) (1998). Wind turbine technology. Number 0-7918-1205-7. ASME.
10. Kagaraki, K. (2001). Photovoltaic technology (pp. 52–129). Symmetria Publications, Greece. ISBN: 978-960-266-183-3, .
11. Glykas, A., Papaioannou, G., & Perissakis, S. (2010). Application and cost-benefit analysis of solar hybrid power installation on merchant marine vessels. *Ocean Engineering, 37*, 592–602.
12. Jiménez-Munoz, J. C., Sobrino, J. A., & Mattar, C. (2012). Recent trends in solar exergy and net radiation at global scale. *Ecological Modelling, 228*, 59–65.
13. Frouin, R., Gauttier, C., Katsaros, K. B., & Lind, R. J. (1988). A comparison of satellite and empirical formula techniques for estimating insolation over the oceans. *Journal of Applied Meteorology, 27*, 1016–1023.
14. Neagoe, M., Visa, I., Burduhos, B. G., & Moldovan, M. D. (2014). Thermal load adaptive tracking for plate solar collectors. *Energy Procedia, 48*, 1401–1411.
15. International Maritime Organization, Marine Environment Committee (2010) Reduction of GHG emissions from ships, July, 2010.

Recycling Biomass Waste to Compost

Lucia Dumitrescu, Ileana Manciulea, Claudia Zaha and Anca Sauciuc

Abstract Composting is nowadays an important and efficient process in sustainable organic waste management. Recycling process of biodegradable organic waste (animal and agriculture residues, sewage sludge, household refuse) by composting, also represents an ecological solution to synthesize new materials used as biofertilizers or adsorbents in wastewater treatment. The paper presents results obtained in composting vegetables waste, sewage sludge, beech sawdust and beech ash, monitoring the parameters of the composting process and investigation of the nutritional quality of the compost by germination test.

Keywords Compost · Recycling biomass · Sawdust · Sewage sludge · Wood ash

1 Introduction

Implementing in practice the principles of sustainable development, both on soil eco-fertilization and wastewater treatment, imposed to identify new, green technologies, based on low cost eco-materials obtained by recycling different types of waste [8, 45, 59]. Nowadays there is an increased interest in using biological processes to solve environmental problems such as solid waste disposal, hazardous waste remediation and treatment of contaminated water [19, 50].

Composting is a biological aerobic decomposition process which received considerable attention for the remediation of organic solid waste and also an important part of the European Union waste management strategy for reducing waste volume going to landfill, being considered one of the most suitable ways for

L. Dumitrescu (✉) · I. Manciulea · C. Zaha
Renewable Energy Systems and Recycling Center,
Transilvania University of Brasov, Brasov, Romania
e-mail: lucia.d@unitbv.ro

A. Sauciuc
Research and Development, ROCAT Synfuels, Brasov, Romania

I. Visa (ed.), *Sustainable Energy in the Built Environment - Steps Towards nZEB*,
Springer Proceedings in Energy, DOI 10.1007/978-3-319-09707-7_17

disposing unpleasant wastes and increasing the amount of organic matter that can be used to restore and preserve the environment [18, 20, 25, 32].

Composting is generally defined as the biological oxidative decomposition of organic constituents in wastes of almost any nature under controlled conditions. As a biological process of decomposing organic materials, composting requires special conditions such as: temperature, moisture, aeration, pH and C/N ratio, related to optimum biological activity in the various stages of the process. The main products of aerobic composting are carbon dioxide, water, mineral ions and stabilized organic matter, also called humus [6, 12, 39].

The biofertilizer compost is an ecological soil conditioner, increasing soil structure and fertility, porosity, soil organic matter and also may contribute to destroy plant pathogens [10, 22, 35]. The recycling of organic matter by composting process represents a sustainable solution for obtaining ecological materials used both, as biofertilizers and adsorbents of heavy metals from polluted waters [5, 13]. High prices of raw materials and adsorbent substrates, for example activated carbon, used as heavy metals adsorbent from wastewater determined and encouraged the research on synthesis/identifying of new low-cost adsorbent materials from cheap waste such as agricultural or industrial waste available in large quantities, sewage sludge, sawdust, compost [2].

Sewage sludge is a residue generated from the treatment of wastewater. Taking into account that annual production of the sewage sludge in the EU exceeds 10 million tones there is a great concern regarding the disposal of sewage sludge, and environmental protection legislation and perspectives for valorization. Due to the complex chemical structure: (a) organic compounds: proteins, fats, soap, urea, cellulose, (b) inorganic compounds: silica, nitrogen, phosphoric acid, iron, calcium oxide, alumina, magnesium oxide, potash, sewage sludge seems to be a promising feedstock both, for the production of adsorbents and bio fertilizer compost [33, 34, 44, 47].

Sawdust is a biodegradable waste generated in large quantities from the wood industry, with great impact on environment, contributing on land degradation and water pollution. The chemical structure consists of principal wood constituents poly carbohydrates cellulose, hemicelluloses and aromatic polymer lignin, secondary constituents of wood, especially tannins. All these compounds posses hydroxyl and carboxyl groups able to bind heavy metal ions from wastewater through different mechanisms [1, 27, 42]. As organic biodegradable material, sawdust can also be recycled by composting with vegetable waste, sewage sludge, ashes to biofertilizer compost [16].

Wood ash and coal fly ash has a higher carbon content, lower nutrient content and exhibits some of the physiochemical properties of activated carbon. The wood ash is a carbon source in the composting recipe and helps to decreasing bulk density and providing potassium, calcium and magnesium to the final product [47, 54]. High-carbon wood ash was examined for its ability to control green material compost odours because it has been shown to be effective in reducing odour emissions from related waste streams such as biosolids and municipal wastewater effluent [40]. The presence of wood ash as raw material in compost has little effect

on compost quality from an agronomic perspective. Composting biomass waste with coal fly ash to obtain manufactured soil for landscaping use increases the available water holding capacity of the manufactured soil product [7, 21, 53].

The intense industrialization generated major environmental pollution problems and global concern regarding waste production and its management. Especially concern is dedicated to the water pollution with heavy metals (arsenic, cadmium, chromium lead, mercury, copper) which are non-biodegradable, accumulates along the food chain and can causes different problems for human health [36, 37]. Conventional methods for removing the heavy metals from aqueous environment such as chemical precipitation, ion-exchange, coagulation, flotation, evaporation, oxidation, adsorption, membrane separation, solvent extraction, reverse osmosis are applied on a large scale in practice [24, 26]. Adsorption is the most recommended physical-chemical treatment process applied for heavy metals removal from wastewater samples because it is a simple, economical, effective and environmental friendly method. Various organic and inorganic low-cost adsorbents have been investigated and used for the removal of toxic metals from wastewaters [28, 41, 51–54]. Naturally poly carbohydrates, modified or unmodified, such as chitosan and lignocellulosic materials containing in their structure hydroxyl and carboxyl functional groups were investigated and proposed as bio adsorbents [38, 49].

2 Synthesis and Characterization of Ecological Biofertilizer Compost

New, inexpensive and effective biofertilizer compost samples were synthesized and characterized at the Research Centre Renewable Energy Systems and Recycling (RES and Recycling) from the Transilvania University of Braşov. The new ecological bio materials were the result of the composting a complex mixtures of vegetable waste, sewage sludge, beech sawdust and beech ash.

2.1 Composting Waste

Materials and Methods

A series of 8 typs of composts were synthesized (at laboratory scale) and characterized (*in triplicate*) based on different ratios of biodegradable waste: vegetables (carrots, cabbage, potatoes, bananas and apples), sewage sludge (from Brasov Wastewater Treatment Plant), beech sawdust and beech wood ash (from wood industry), in order to obtain the best biofertilizer compost. The composition of the compost samples is presented in Table 1.

Table 1 The composition of the compost samples

Compost Sample	Vegetables (%)	Sewage sludge (%)	Sawdust (%)	Wood ash (%)
BN1	90	10	–	–
BN2	80	20	–	–
BC1	80	–	–	20
BR1	90	–	10	–
BR2	80	–	20	–
BNR1	80	10	10	–
BNR2	70	20	10	–
BNR3	70	10	20	–

The parameters of raw materials were previously determined and reported [55].

The samples of vegetable waste, sewage sludge, sawdust and wood ash and 60 % water were mixed with a blender to obtain a homogeneous size of grains of organic matter, allowing rapid biodegradation and stored in open 5 l PET containers, shaken every day for efficient aeration. In order to obtain good quality composts, the composting process was monitored, during the 9 weeks of composting, by investigating weekly (in compost extract 10 % in distilled water) some physical- chemical parameters: pH, electrical conductivity (EC), content on carbohydrates and amino acids and C/N ratio. The compost maturity and stability was also investigated by germination tests (already described) [57] performed with dry samples of compost added to the soil and seeds of radish (Raphanus sativus) and cabbage (Brassica oleracea).

The pH values were measured in the filtrate solution using the pH-meter 340 I/SET and Electrical Conductivity was performed with 315 I/SET Conductometer. The FT-IR analysis of the surface structure and biodegradation products during composting was performed with a Spectrometer BX II (Perkin Elmer 2005). The content on monocarbohydrate glucose was determined by Willstätter-Schull method, based on oxidation of aldehyde group with iodine in alkaline medium and the content on amino acids was determined by Sörensen method [15].

C:N ratio was determined with analyzer TruSpec CHN, Leco Elementar (2008).

3 Results and Discussions

3.1 Monitoring the Composting Process

pH Evolution During Composting

pH is a very important parameter for the microorganism metabolism, the quantity of nutrients formed by biodegradation processes of organic matter being a good indicator of the development of composting [48]. Analyzing the variation of pH

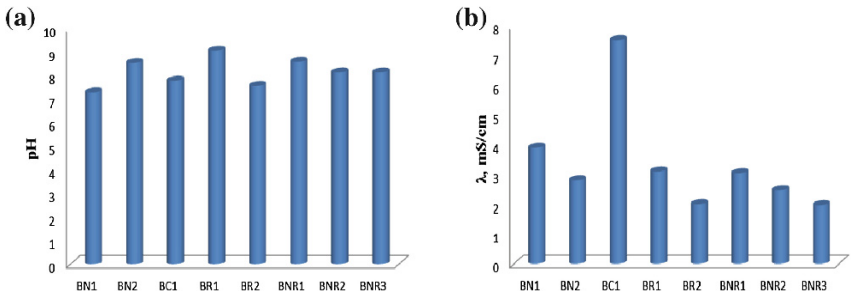

Fig. 1 **a** pH values of the composts. **b** EC values of the composts

during composting it can be observed the correlations between the stages of biodegradation, respectively the formation of specific biodegradation products. At the beginning of the composting process, the presence of biomass, sewage sludge and sawdust rich in poly carbohydrates, proteins, lipids, determine low pH values in the first 3 weeks indicating an energic aerobic biodegradation, releasing acid metabolic products of Krebs cycle (carbon dioxide, piruvic acid, acetic acid, citric acid etc.) and decarboxilation products of proteins and lipids [3, 15]. Further increasing of pH (weeks 4–9) may be caused by decomposition of organic matter containing nitrogen (proteins, amino acids) and mineralization of organic nitrogen through microbial activities leading to formation of ammonia [56]. The pH values at the end of composting period (9 weeks) are between 7.28 and 9.00, decreasing after the maturation period at 6.68–6.96, a pH value considerate optimum for using as bio fertilizers (see Fig. 1a) [60].

Electrical Conductivity Evolution During Composting

Electrical conductivity (EC) can be associated with the release, during composting, of easily biodegradable organic compounds and salts of mineral acids into the solution [4, 19, 31].

Monitoring the composting process it was observed that the presence of sawdust with polymeric structures such as cellulose and lignin in the raw material, as well as sewage sludge containing lipids and proteins, hard to biodegrade, determine a slower biodegradation of organic matter in the first 3 weeks of composting and low values of conductivity. When composting process advances in time and more ionic, metabolic compounds are released into the solution (ammonium, calcium, magnesium carbonates, phosphates, lactates, citrates, acetates, etc.) the values of the electrical conductivity increased [57]. The final values of the EC for the composts are presented in the Fig. 1b.

Evolution of the Content of Amino Acids During Composting

The content on N of the organic matter biodegraded by composting represents an important parameter of the composting process. Amino acids are fundamental structural units of proteins, nucleic acids, enzymes etc., being involved in construction and functionalization of microorganisms and plants cellules. Meantime,

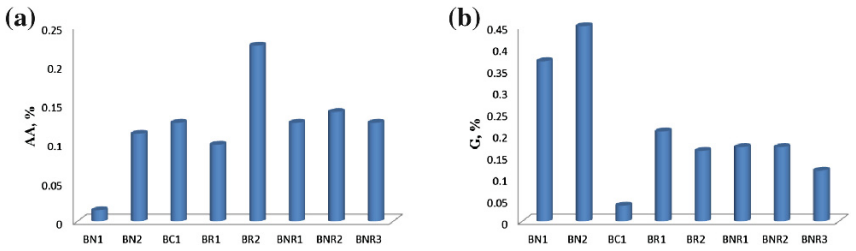

Fig. 2 **a** Content of amino acids from the composts. **b** Content of carbohydrates from the composts

they are acting as reagents and buffers in the metabolism and also can bind heavy metal ions [14]. The hydrolysis of proteins, biocatalyzed by complex enzymes, results in amino acids, which are further biodegraded by specific reactions of deamination and decarboxylation to micro molecular organic compounds amides, amides, carboxylic acids etc., determining the decreasing of amino acids content during composting [17, 58]. Evolution of amino acids concentration during composting depends on the type and biodegradability of the proteins from compost. An increasing of the content in amino acids are registered at the end of composting (see Fig. 2a) for the compost samples with sawdust and sewage which improves the decomposition process by adding nutrients, proteins and enzymes [60].

Evolution of the Content of Carbohydrates During Composting

Carbohydrates represent over 50 % of the dry matter of vegetables, as simple mono carbohydrates (glucose, fructose, ribose, deoxyribose etc.) or poly carbohydrates (starch, cellulose) [9, 29]. Biodegradation of poly carbohydrates is an oxidative process which generates energy by exothermic reactions. In the presence of biocatalyst enzymes, the poly carbohydrates are split into mono carbohydrates (glucose being the main component) which are decomposed into simpler compounds with lower molecular mass [55].

The compost samples rich in easily decomposable vegetable biomass, biodegrade more rapidly in time. The compost samples with sawdust and sewage sludge, having poly carbohydrates and less biodegradable polymer lignin, decomposed slowly, but continuously, having at the end of composting greater content of mono carbohydrates (as can be seen in Fig. 2b), benefic for the compost quality.

This behaviour can be correlated with the presence of extra biocatalysts enzymes able to biodegrade the lignocellulosic structure of the sawdust and sewage sludge.

The lowest content on carbohydrates was registered for the compost with wood ash, due to the mineral structure [60].

Evolution of C/N Ratio During Composting

C/N ratio is an important parameter for evaluating both, the composting process and compost maturity and stability [10, 12]. During the composting process, C/N ratio decreased for all samples of composts because the total N content increased faster than organic C content, due the rapidly biodegradation of proteins and amino acids

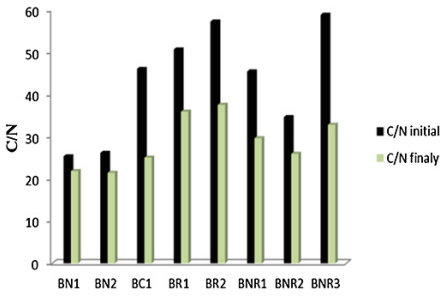

Fig. 3 Evolution of C/N ratio of the compost samples

from biomass into simpler organic compounds amides, amines, etc. The poly carbohydrates (cellulose, hemicelluloses, starch, etc.) components of organic matter are hydrolyzed by enzymes to mono carbohydrates, which further are partially transformed into inorganic, volatile compound, carbon dioxide. The presence o sawdust and sewage sludge in compost samples promotes a slower biodegradation of poly carbohydrates due to inhibiting influence of sawdust over micro organisms' activity [11, 55].

The C/N ratios of the composts at the end of the composting process (illustrated in Fig. 3) are within the favorable range to be used as fertilizers in agriculture [30, 31, 57].

FT-IR Analysis

FT-IR analysis supports the results of the others tests performed during composting (content in mono carbohydrates and amino acids, etc.) certifying both, the presence in all composts samples of complex, macro molecular compounds: poly carbohydrates, proteins, lignin, lipids etc., and their biodegradation process forming simpler products: mono carbohydrates, aldehydes, ketones, alcohols, amines, phenols, carboxylic acids and their derivatives (amides, esters, nitriles, etc.) [55, 56, 58].

The interpretation of FT-IR spectra of the samples of compost (presented in Table 2) enables the investigation of the evolution of the stages of biodegradation and composition of organic matter during the composting process [23, 43, 46].

The absorbance bands at 3,200–3,400 cm^{-1} attributable to the long chain aliphatic structures (poly carbohydrates, lipids, proteins) decreased during composting process, as result of organic waste biodegradation and formation of micro molecular compounds: carboxylic acids, aldehydes, ketones, amines, amides, phenols having absorption bands at 1,070–1,300 cm^{-1}.

At the end of composting, as result of aerobic oxidative biodegradation of organic matter by composting, a reduction of numbers of bands characteristic to the aliphatic polymeric compounds (poly carbohydrates, proteins, lipids) and an increasing of absorption bands (700–1,000 cm^{-1}) characteristic to the aliphatic and oxidized aromatic organic compounds such as carboxylic acids (–COO– ions in organic acids and their salts), carbonyl compounds (aldehydes, ketones, quinones), aromatic compounds formed by lignin biodegradation (phenols, amides, aromatic aldehydes, monosubstituted arenes were observed [12, 56, 60]).

Table 2 Attribution of absorbance bands (cm^{-1}) for FT-IR spectra of composts [23, 43, 46, 60]

Absorbance band (cm^{-1})	Attribution
3,200–3,400	• C–H group in unsaturated aliphatic alkenes and alkynes
	• N–H bonds in amines, amides
	• O–H aliphatic and aromatic groups from poly carbohydrates (starch, cellulose, hemicelluloses) and lignin
	After 30 days of composting the absorption bands become sharp, indicating the occurrence of several compounds from biodegradation of biomass forming amides, amines, alcohols and phenols
2,800–3,200	• O–H group in carboxylic acids (biodegradation products of poly carbohydrates)
	• C–H group in long chains aliphatic structures (lipids, fatty acids, waxes, other aliphatic structures)
	• C=O groups from poly carbohydrates
2260–2150	• C≡C and C≡N groups in aliphatic or aromatic structures formed by biodegradation of biomass components
1,550–1,650	• Confirming the presence of C=C in alkenes and aromatic rings
	• NH group in aliphatic or aromatic amines
	• NO_2 group in nitro compounds
	• Functional groups $–COO^-$ and C=O in amides, C=O in ketones, aromatic carboxylic acids, quinones
	• Band at 1,600 cm^{-1} rises with increase of carboxylic acids, aldehydes, amides originating from degradation of proteins, poly carbohydrates, lignin
	Samples with larger quantities of poly carbohydrates present sharper absorption bands. Samples with high concentrations of sewage sludge show strong biodegradation due to the presence of microorganisms in sludge
1,415–1,465	• CH, $–CH_3$ and CH_2 groups
	• C=C group from lignin component of sawdust and vegetable biomass
1,070–1,300	• C–O group in alcohols, ethers, carboxylic acids, esters, anhydrides
	• Certifies the amide formation (by degradation of amino acids and carboxylic acids), ethers and phosphorus compounds (due to the biodegradation of nucleic acids and enzymes)
700–970	• C–H group in aromatic compounds from lignin biodegradation (phenols, amides, aromatic aldehydes, arenes, etc.)

Germination Test

The germination test represents the most important parameter for determining the nutritional quality, toxicity and maturation degree of the compost [35]. It is established that a germination index (GI) between 80–85 % or a percentage of seeds germinated (PSG) greater than 60 % indicates a matur compost, without fitotoxines [10, 30, 39]. The indices of germination (performed during 7 days) combined relative seed germination (a) and relative root growth (b) for (Raphanus sativus and

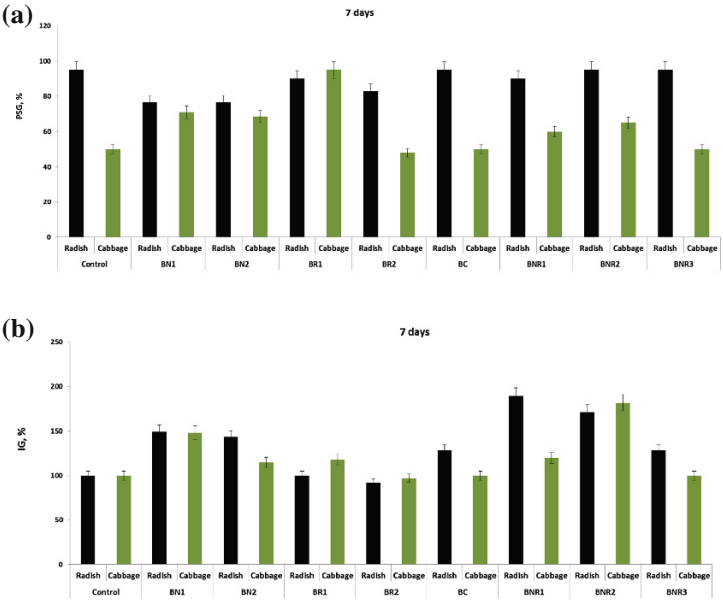

Fig. 4 Germination test for the compost samples. **a** Relative seed germination of the composts. **b** Relative root growth of the composts

Brassica oleracea, comparable with the control sample (GI considerated 100 %). As shown in Fig. 4a, b all the compost samples had good results for both radish and cabbage seeds. The best results were obtained using as biofertilizers the compost samples with biomass, sewage sludge and sawdust due to its enriched content in nutrients and biocatalysts enzymes [16, 55, 60].

From all the compost samples synthesized and characterized were selected 3 organic substrates with the best results regarding maturation and stability, established by literature [10, 12, 30, 31, 33, 39] as optimum for a biofertilizer:

- pH = 6–9;
- Electrical conductivity: 2.0 ÷ 3.5 mS/cm;
- C/N ratio: 20 ÷ 35;
- Germination test: PSG > 60 %; and GI > 85 %.

The compost samples selected as biofertilizers are:

- BN2 (80 % vegetable waste and 20 % sewage sludge)
- BNR1 (80 % vegetable waste,10 % sewage sludge, 10 % sawdust)
- BNR2 (70 % vegetable waste, 20 % sewage sludge, 10 % sawdust).

4 Conclusions

Implementing in practice the principles of sustainable development, both on soil eco-fertilization and wastewater treatment, imposed to identify new, green technologies, based on low cost eco-materials obtained from different types of waste.

The research revealed that the recycling of biodegradable waste by composting represents a sustainable solution of organic waste valorization.

This paper seeks to review the published research in the field of recycling biodegradable waste by composting, the characteristics and the potential applications of these ecological materials.

The results obtained in the RES-REC group put into evidence the synthesis of new, ecological materials by aerobic biodegradation of sewage sludge, sawdust, wood ash and vegetable biomass, used as ecological biofertilizers.

It can be appreciate that a ratio of (10–20 %):(90–80 %) between sewage sludge and sawdust: vegetable waste is adequate for obtaining a good biofertilizer compost, in which the sewage sludge and sawdust were valorized and recycled together with vegetable waste.

Future research will be dedicated to investigate compost as ecological adsorbent material for toxic metals from polluted waters.

Acknowledgments This paper is supported by the Sectoral Operational Programme Human Resources Development (SOP HRD), financed from the European Social Fund and by the Romanian Government under the project number POSDRU/159/1.5/S/134378.

References

1. Ahmad, A., Rafatullah, M., Sulaiman, O., Ibrahim, M. H., Chii, Y. Y., & Siddique, B. M. (2009). *Removal of Cu(II) and Pb(II) ions from aqueous solutions by adsorption on sawdust of Meranti wood*, Desalination 247 (pp. 636–646). Amsterdam: Elsevier.
2. Ali, M. (2012). New generation adsorbents for water treatment. *Chemical Reviews, 112*, 5073–5091.
3. Alvarenga, P., Palma, P., Gonçalves, A. P., Fernandes, R. M., Cunha-Queda, A. C., Duarte, E., et al. (2007). Evaluation of chemical and ecotoxicological characteristics of biodegradable organic residues for application to agricultural land. *Environment International, 33*, 505–513.
4. Amir, S., Benlboukht, F., Cancian, N., Winterton, W., & Hafidi, M. (2008) Physico-chemical analysis of tannery solid waste and structural characterization of its isolated humic acids after composting. *Journal of Hazardous Materials 160*, 448–455.
5. Bailey, S. E., Olin, T. J., Bricka, R. M., & Adrian, D. D. (1999). A review of potentially low-cost sorbents for heavy metals. *Water Research, 33*, 2469–2479.
6. Barberis, R., & Nappi, P. (1996). Evaluation of compost stability. In M. de Bertoldi, P. Srequi, B. Lremmes, & T. Papi (Eds.), *The science of composting, Part 1* (pp. 175–184). London: Chapman and Hall.
7. Belyaeva, O. N., & Haynes, R. J. (2009). Chemical, microbial and physical properties of manufactured soils produced by co-composting municipal green waste with coal fly ash. *Bioresource Technology 100*, 5203–5209.

8. Bhatnagar, A., & Sillanpaa, M. (2010). Utilization of agro-industrial and municipal waste materials as potential adsorbents for water treatment. *A review, Chemical Engineering Journal, 157*, 277–296.
9. Bijaya K., Barrington S., Martinez, J., & King S. (2008). Characterization of food waste and bulking agents for composting. *Waste Management, 28*, 795–804.
10. Boulter-Bitzer, J. I., Trevors, J. T., & Bolanda, G. J. (2006). A polyphasic approach for assessing maturity and stability in compost intended for suppression of plant pathogens. *Applied Soil Ecology, 34*, 65–81.
11. Bustamante, M. A., Paredes, C., Marhuenda-Egea, F. C., Perez-Espinosa, A., Bernal, M. P., & Moral, R. (2008). Co-composting of distillery wastes with animal manures: carbon and nitrogen transformations in the evaluation of compost stability. *Chemosphere, 72*, 551–557.
12. Castaldi, P., Alberti, G., Merella, R., & Melis, P. (2005). Study of the organic matter evolution during municipal solid waste composting aimed at identifying suitable parameters for the evaluation of compost maturity. *Waste Management, 25*, 209–213.
13. Cochrane, E. L., Lua, S., Gibb, S.W., & Villaescusa, I. (2006). A comparison of low-cost biosorbents and commercial sorbents for the removal of copper from aqueous media. *Journal of Hazardous Materials, 137*, 198–206.
14. Dumitrescu, L. (2004). Elements of vegetable biochemistry (pp. 50–90). Transilvania University Ed., ISSN 158-0506; ISBN 973-635-292-7.
15. Dumitrescu, L., Manciulea, I., Isac, L. (2007). *Recycling waste by composting*. Bulletin of the Transilvania University of Brasov 4 (pp. 679–684) Brasov: Transilvania University Press.
16. Dumitrescu, L., Manciulea, I., Sauciuc, A., Zaha, C. (2009). *Obtaining fertilizer compost by composting vegetable waste, sewage sludge and sawdust*, Bulletin of the Transilvania University of Braşov 2 (pp. 117–122) Brasov, Romania: Transilvania University Press.
17. Eklind, Y., & Kirchmann, H. (2000). Composting and storage of organic household waste with different litter amendments. II: nitrogen turnover and losses. *Bioresource Technology, 74*, 125–133.
18. EU Commission. (2010). *Biodegradable waste*. http://ec.europa.eu/environment/waste/compost/index.htm.
19. Fernández, J. M., Hernández, D., Plaza, C., & Polo, A. (2007). Organic matter in degraded agricultural soils amended with composted and thermally-dried sewage sludges. *Science of the Total Environment, 378*, 75–80.
20. Fytili, D., & Zabaniotou A. (2007). Utilization of sewage sludge in EU application of old and new methods—A review. *Renewable and Sustainable Energy Reviews, 12*, 116–140.
21. Gaind, S., & Gaur, A. C. (2003). Quality assessment of compost prepared from fly ash and crop residue. *Bioresource Technology, 87*, 125–127.
22. Godfree A. (2003). Health constraints on the agricultural recycling of wastewater sludge. In N. J. Horan (Ed.) *Handbook of water and wastewater microbiology* (pp. 281–296). New York: Academic Press.
23. Inbar, Y., Chen, Y., & Hadar, Y. (1991). Carbon-13 CPMAS NMR and FTIR spectroscopic analysis of organic matter transformations during composting of solid wastes from wineries. *Soil Science, 152*, 272–282.
24. Kim H., Baek, K., Kim, B. K., Shin, H. J., & Yang, J. W. (2008). *Removal characteristics of metal cations and their mixtures using micellar-enhanced ultrafiltration*. *Korean Journal of Chemical*, *25*, 253–258.
25. Laturnus, F., von Arnold, K., & Gron, C. (2007). Organic contaminants from sewage sludge applied to agricultural soils – false alarm regarding possible problems for food safety. *Environmental Science and Pollution Research*, *14*, 53–60.
26. Lin, L. C., Li, J. K., Juang, R. S. (2008). Removal of Cu(II) and Ni(II) from aqueous solutions using batch and fixed-bed ion exchange processes. *Desalination*, *225*, 249–259.
27. Lucaci, D., & Vişa, M. (2011). Adsorption of methyl orange from wastewater using sawdust and sawdust-fly ash substrates. *Revista de Chimie*, *62*, 741–745.
28. Lucaci, D., Vişa, M., & Duță, A. (2011). Cooper removal on wood-Fly ash substrates—Thermodinamic study. *Revue Roumaine de Chemie*, *56* 1067–1074.

29. Mondini, C., Sánchez-Monedero, M. A., Sinicco, T., & Leita, L. (2006). Evaluation of extracted organic carbon and microbial biomass as stability parameters in ligno-cellulosic waste composts. *Journal of Environmental Quality, 35*, 2313–2320.
30. Moral, R., Paredes, C., Bustamante, M. A., Marhuenda-Egea, F., Bernal, M. P. (2009). Utilization of manure composts by high-value crops: safety and environmental challenges. *Bioresource Technology*, *100*, 5454–5460.
31. Mote, C. R., & Griffis, C. L., Variations in the composting process for different organic carbon sources. *Agricultural Wastes*, *2*, 215–223.
32. OECD. (2002). Household energy & water consumption and waste generation: Trends (pp. 62–67). Environmental Impacts and Policy Responses, ENV/EPOC/WPNEP(2001)25, Paris: Organisation for Economic Co-operation and Development.
33. Oleszczuk, P. (2008). The toxicity of composts from sewage sludges evaluated by the direct contact tests phytotoxkit and ostracodtoxkit. *Waste Management, 28*, 1645–1653.
34. Pagnanelli, S., Mainelli, L., Bornoroni, D., & Dionisi, L. (2009). Mechanisms of heavy metal removal by activated sludge. *Chemosphere*, *75*, 1028–1034.
35. Papadopoulos, A. E., Stylianou, M. A., Michalopoulos, C. P., Moustakas, K. G., Hapeshis, K. M., Vogiatzidaki, E. E. I., et al. (2009). Performance of a new household composter during in-home testing. *Waste Management, 29*, 204–213.
36. Pino, G. H., de Mesquita, L. M. S., & Torem, M. L. (2006). Biosorption of heavy metals by powder of green coconut shell. *Separation Science and Technology*, *41*, 3141–3153.
37. Rafatullah, M., Sulaimana, O., Hashima, R., & Ahmad, A. (2009). Adsorption of copper (II), chromium (III), nickel (II) and lead (II) ions from aqueous solutions by meranti sawdust. *Journal of Hazardous Materials, 170*, 969–977.
38. Rezaeia, R., Mirghaffaria, N., & Rezaeib, B. (2012). Kinetic isotherms study of copper adsorption from solutions by a low-cost adsorbent. *International Journal of Chemical and Environmental Engineering*, *3*, 225–229.
39. Rynk, R. et al. (1992). *On farm composting handbook* (pp. 255–7654). Northeast Regional Agricultural Engineering Service. Available from NRAES, Cooperative Extension, 152 Riley-Robb Hall, Ithaca, NY 14853-5701, (607).
40. Rosenfeld, P., & Henry, C. (2001). Activated carbon and wood ash sorption of wastewater, compost and biosolids, odorants. *Water Environment Research*, *73*, 388–393.
41. Sciban, M., Klasnja, M., & Skrbic, B. (2008). Adsorption of copper ions from water by modified agricultural by-products. *Desalination*, *229*, 170–180.
42. Shukla, A., Zhang, Y. H., Dubey, P., Margrave, J. L., & Shukla, S. S. (2002). The role of sawdust in the removal of unwanted materials from water. *Journal of Hazardous Materials*, *95*, 137–152.
43. Silverstein, R. M., Webster, F. X., & Kiemle, D. J. (2005). *Spectrometric identification of organic compounds*. New Jersey: Wiley.
44. Simantiraki, F., Kollias, C. G., Maratos, D., Hahladakis, J., Gidarakos, E. (2013). Qualitative determination and application of sewage sludge and municipal solid waste compost for BTEX removal from groundwater. *Journal of Environmental Chemical Engineering*, *1*, 9–17.
45. Sisca, O. L., Novie, F., Soetaredjo, F. E., Sunarsob, J., & Ismadji, S., Studies on potential applications of biomass for the separation of heavy metals from water and wastewater. *Biochemical Engineering Journal*, *44*, 19–41.
46. Smidt, E., & Meissl, K., The applicability of Fourier transform-infrared (FT-IR) spectroscopy in waste management. *Waste Management*, *27*, 268–276.
47. Smith, K. M., Fowler, G. D., Pullket, S., & Graham, N. J. D. (2009) Sewage sludge-based adsorbents: A review of their production, properties and use in water treatment applications. *Water Research*, *43*, 2569–2594.
48. Sundberg, C., J., & önsson, H. (2008). Higher pH and faster decomposition in biowaste composting by increased aeration. *Waste Management*, *28*, 518–526.
49. Ulmanu, M., Maranon, E., Fernandez, Y., Castrillon, L., Anger, I., & Dumitriu, D. (2003). Removal of copper and cadmium ions from diluted aqueous solutions by low cost and waste material sorbents. *Water, Air, and Soil Pollution*, *142*, 357–373.

50. vanHerwijnen, R., Hutchings, T. R., Al-Tabbaa, A., Moffat, A. J., Johns, M. L., Ouki, S. K. (2007). Remediation of metal contaminated soil with mineral-amended composts. *Environmental Pollution*, *150*, 347–354.
51. Vișa, M., & Duță, A. (2013). Methyl-orange and cadmium simultaneous removal using fly ash and photo-Fenton systems. *Journal of Hazardous Materials*, *244–245*, 773–779.
52. Vișa, M., Isac I., & Duță, A. (2012). Fly ash adsorbents for multi-cation wastewater treatment. *Applied Surface Science*, *258*, 6345–6352.
53. Vargas, C., Brandão, P. F. B., Ágreda, J., & Castillo, E. (2012). Cr(VI) removal by compost. *Bio Resources*, *7*(3), 2711–2727.
54. Wei, Y. L., Lee, Y. C., Yang, Y. W., & Lee, J. F. (2004). Molecular study of concentrated copper pollutant with a compost. *Chemosphere*, *57*, 1201–1205.
55. Zaha, C., Manciulea, I., & Sauciuc, A. (2011). Reducing the volume of waste by composting vegetable waste, sewage sludge and sawdust. *Environmental Engineering and Management Journal*, *10*, 1415–1423.
56. Zaha, C., Sauciuc, A., Dumitrescu, L., & Manciulea, I. (2011). Aspects regarding recycling sludge by composting. *Environmental Engineering and Management Journal*, *10*, 1589–1594.
57. Zaha, C., Dumitrescu, L., & Manciulea I. (2013). Correlations between composting conditions and characteristics of compost as biofertilizer. *Bulletin of the Transilvania University of Brasov*, *6*, 51–58.
58. Zaha, C., Sauciuc, A., Manciulea, I., & Dumitrescu, L. (2011). Sustainable development by recycling waste as biofertilizer compost. In *Proceedings of 1st International Conference on Quality and Innovation in Engineering and Management* (pp. 535–538), Cluj-Napoca, Romania.
59. Zaharia, M., Robu T., & Irimia, N. (2010). Ecological agriculture: dynamics of the biological activities in soils cultivated with maize under the influence of organic fertilization. *Environmental Engineering and Management Journal*, *9*, 1437–1441.
60. Zaha, C. (2013). Ecological biomaterials used as bio fertilizers and as heavy metals removers from wastewater. PhD Thesis, Transilvania University of Brasov.

A Novel Spray Pyrolysis Deposition Procedure on Planar and Non-planar Surfaces

Monica Enescu

Abstract The paper refers to a process of materials deposition through spray pyrolysis in open environment, using an automatic robotic system (industrial robot with six axes—degrees of freedom). The advantage of this automatic system is the minimization of the spraying cycle time and material losses, which leads to low-cost production. The procedure allows the obtaining of thin films on large planar and non-planar surfaces, with superior characteristics to those obtained by manual spray pyrolysis, or through the deposition systems in closed environment. The quality of the obtained film is strongly influenced by the uniformity of spray thickness. The proposed method allows the automatic generation of the sprayer trajectory by using off-line programming and simulation in virtual environment (RobotStudio). There are the following steps for the automatic generation of the trajectory: selecting the substrate (deposition surface) from a computer database, setting the spray pyrolysis deposition parameters, and generating the trajectory. This in-step process is based on the execution of the CAD model of the substrate on which the spraying will be carried out. The uniformity of the deposited films depends on the input data referring to the specific parameters of spray pyrolysis deposition. The following parameters have been considered as design variables in the spray pyrolysis deposition procedure: the inclination angle of the sprayer, the step between two successive spraying sequences, the spraying height, the pressure of the carrier gas, the number of consecutive spraying sequences on the substrate, the speed of the sprayer, and the time (named pause) between two spraying sequences.

Keywords Spray pyrolysis deposition · Open environment · Automatic system · Optimization

M. Enescu (✉)
Transilvania University of Braşov, 29 Eroilor Bvd, 500036 Braşov, Romania
e-mail: monicaenescu@unitbv.ro

I. Visa (ed.), *Sustainable Energy in the Built Environment - Steps Towards nZEB*,
Springer Proceedings in Energy, DOI 10.1007/978-3-319-09707-7_18

1 Introduction

Lately, the technologies for obtaining thin films have been studied and analyzed in order to use them to obtain anti-reflection layers, passivation layers, or absorbent material for solar-thermal collectors. The literature presents different techniques and procedures for obtaining thin films, such as Chemical Vapor Deposition (CVD), Electro Spray Deposition (ESD), doctor blade, pulsed laser deposition, spin deposition [1–5]. The spray pyrolysis can be also performed by using the classical methods including manual spraying or by using a spray pyrolysis equipment. A disadvantage of these techniques is that they do not allow a large variety for changing the spraying parameters, but usually only for the substrate temperature, which can vary between 250 and 4,000 °C. Typically, the spraying height can be adjusted up to 300 mm [6].

The spray pyrolysis procedure described in [7] has the advantage of using more spray guns, allowing the deposition on larger surfaces. There are the following parameters that can be varied in this procedure: the spraying height (100–300 mm), the substrate temperature (2,800–5,000 °C), the flow of the precursor solution (1–100 ml/min), and the spraying duration (30–40 min). The main disadvantage of this method is that it does not allow the adjustment of the spraying angle and of the spraying speed. The procedure allows only the use of an alcohol-based precursor solution, and not water-based.

Another deposition technique used in the domain is Physical Vapor Deposition (PVD) [8]. The main disadvantage of this procedure is the small dimension of the flat (plane) substrate due to the need to ensure the vacuum, and due to the systems that are required for plasma production. Moreover, the PVD technique is a high cost technology.

For the chemical vapor deposition technique, there is the disadvantage of the high power consumption which is necessary for obtaining higher temperatures. Another disadvantage of the CVD technique is that the materials with low melting point cannot be deposited due to the high temperatures of the sprayed substrate [9]. The technique also has the disadvantage of limiting the surface of the substrate due to the relatively small dimensions of the furnace. The precursor required by this procedure is an expensive solution, and the substrate must be chemically and thermally stable at the deposition temperature.

The conclusion that can be drawn is that the existing methods involve various drawbacks, such as the difficulty to adjust the spraying angle and the sprayer speed —thus, the result being a more limited diversity of the obtained morphology. The deposition is not uniformly executed for the surfaces that are not perfectly flat/plane (leading to variations in efficiency, and a low energetic capacity of these surfaces), and the system flexibility in relation to the variety of the surfaces that have to be coated is low, these being standardized procedures.

The deposition procedure presented in this paper eliminates the above mentioned drawbacks in that the deposition is executed in an open environment. For the deposition, an industrial robot, equipped with a spray gun, containing the precursor

solution to be sprayed on a substrate heated at a constant temperature, is used. In order to use a precursor solution, for instance TiCl4, the deposition surface with certain geometry is heated, the carrier gas pressure can be set to different values, the spraying height and angle are adjustable, and the sprayer speed is variable. At the same time, the program designed for the industrial robot allows the adjustment of the step between two spraying sequences, the dimension of the deposition surface, the number of successive spraying sequences on the substrate, and the time between two spraying sequences.

2 The Spray Pyrolysis Process

For obtaining thin films with applications in the conversion systems of the solar energy into electricity and/or thermal energy [10–14], the spray pyrolysis deposition (SPD) in open environment requires the use of a robotic system, in this case, an ABB industrial robot with six axes/degrees of freedom—see Fig. 1, the representation of the SPD process being shown in Fig. 2.

The deposition is performed by using a liquid precursor solution (1), by forming certain aerosols that are dispersed in the carrier gas (2), they are deposited on the

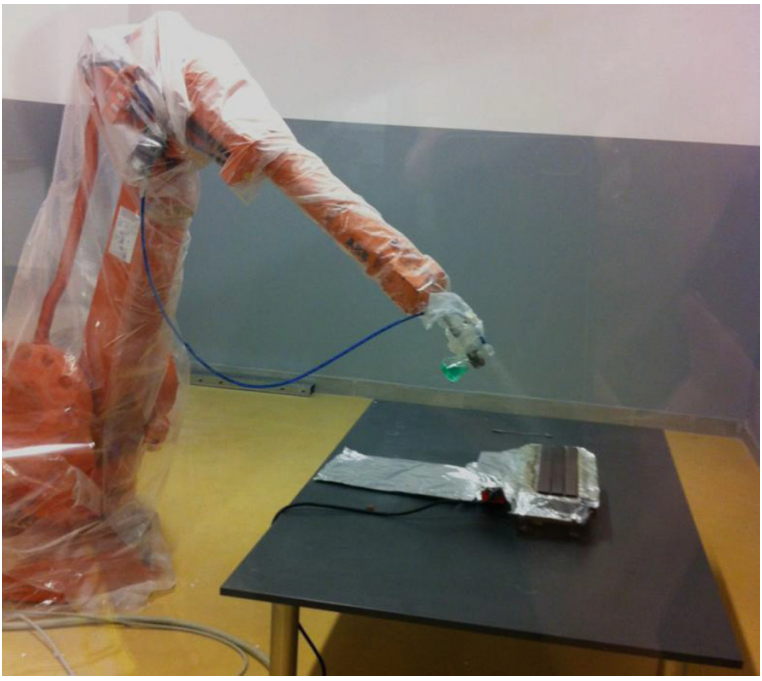

Fig. 1 The industrial robot with six degrees of freedom used in the SPD process

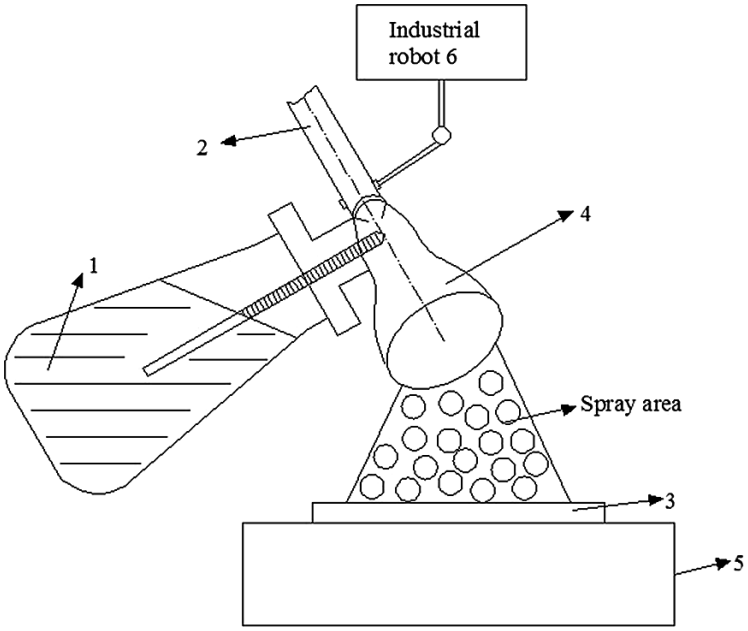

Fig. 2 The schematic representation of the spray pyrolysis procedure

heated substrates (3). The sprayer (4) is connected to a carrier gas source (such as a compressor, a recipient with gas under pressure, or another similar system), which creates a pressure in the precursor solution with values between 1–1.5 bar.

The precursor solution is sprayed on the surface heated by a hot plate (5) at a temperature of 100–500 °C. On the heated substrate the precursor reacts and forms the film and secondary by-products.

The spray gun is installed through an attachment system on the end-effector of the industrial robot (6), which follows to execute the trajectory necessary for deposition on the substrate.

In accordance with Fig. 3, the working stages for the spray pyrolysis procedure are: preparing the precursor solution (**a**); loading the sprayer with precursor solution, which can be water-based or alcohol-based (**b**); cleaning the sample substrate (**c**); placing the substrates with different geometries on the heating plate (**d**); heating the substrate by using an isothermal plate (**e**); checking the temperature, the pressure of the carrier gas, and the sprayer position (**f**); controlling the characteristic parameters of the deposition procedure, which is applied throughout the process (**g**); executing a control and self-adjustment loop of the parameters (**h**); loading the input data into the microprocessor of the system (**i**); spraying the precursor solution from the sprayer on the substrate (**j**).

After the deposition on the substrate, which is performed in accordance with the input data of the system, the sample is cooled down (**k**), and the control of the parameters is executed (**l**).

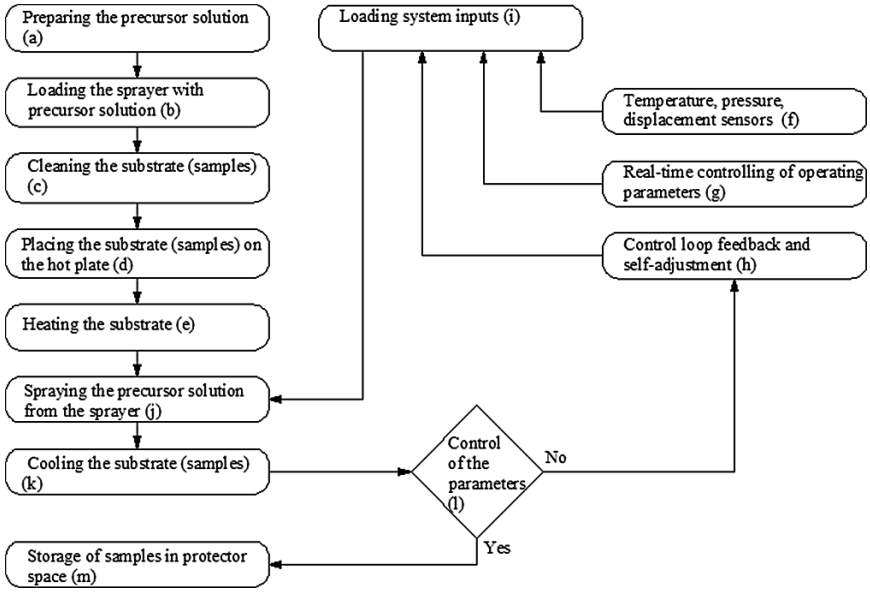

Fig. 3 The working stages diagram of the SPD process in open environment

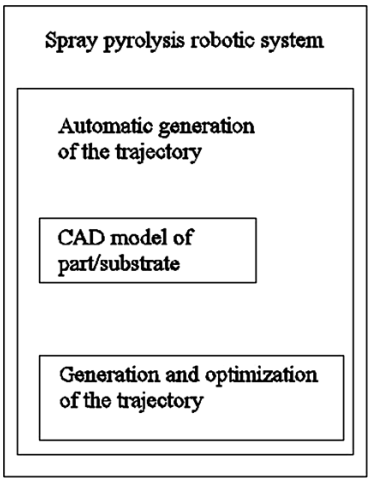

Fig. 4 The stages for the automatic generation of the trajectory

If the control parameters are corresponding, then the sample will be deposited in a protective space (**m**), otherwise (non-corresponding parameters) a return to the control and self-adjustment loop will be performed.

Figure 4 shows the stages for the automatic generation of the trajectory, when the deposition is performed with a robotic system, in open environment. For beginning, it is necessary to execute the CAD model of the surface that will be coated, but also of the virtual working environment, which is identical to the real

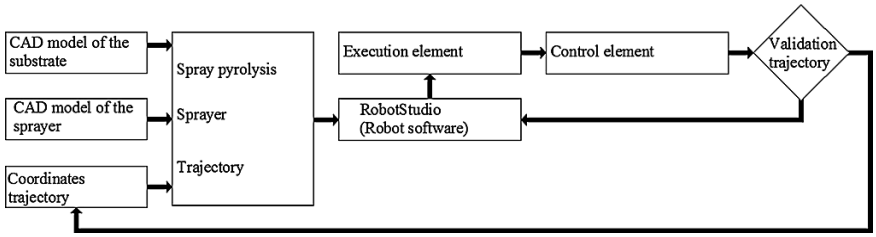

Fig. 5 Block diagram for obtaining the spray gun trajectory

one, namely: the CAD model of the industrial robot with six degrees of freedom, the worktable, a plate for heating the substrate, the system for attaching the sprayer on the robot, and the glass sprayer.

The CAD model of the substrate, having a triangulated geometry, is saved in a VRML format, after which it is introduced in the created virtual environment. Then, from the program menu, the specific settings of the spraying are executed, as follows: the spraying height, the spraying angle, the spraying step, the pressure of the carrier gas, the number of spraying sequences, and the time between two spraying sequences. After these steps, the generation of the trajectory is performed, obtaining the global coordinates X, Y and Z of the points that are necessary for generating the trajectory in relation with the considered deposition surface. The block diagram for obtaining the 3D coordinates of the points that define the necessary trajectory of the sprayer is shown in Fig. 5.

In these terms, the CAD model of the surface that follows to be coated—it can be both plane and non-planar—is generated, then the robot "learns" the specimen and generates the trajectory by returning the coordinates of the points which define it. The program allows the setting of the following parameters: the spraying height, the spraying angle, the step between two paths, the pressure of the carrier gas, the number of spraying sequences, and the time between two spraying sequences. The optimal design of these parameters is approached in the next section of the paper.

3 The Optimization Strategy

In order to comply with the condition for obtaining a uniform thin film, with different thicknesses and morphologies, on relatively large surfaces, both for flat (polished) and shaped (textured) substrates, it is necessary to obtain the optimal values of the specific parameters used in the spray pyrolysis [15]. The uniformity of the deposited films depends on the input data referring to the specific parameters of spray pyrolysis deposition.

The methodology for establishing the film thickness has been elaborated based on the experimentally obtained data, by using existing methods and instruments (e.g. the UV-VIS spectrophotometer), the measurement of the film thickness being

performed in two different points on the sample. There are the following stages used in this methodology:

- evaluating the characteristic deposition parameters of the spray pyrolysis deposition, which have influence on the thin film thickness; seven deposition parameters (i.e. design variables) have been used in this study, as follows: the substrate temperature (X_1), the pressure of the carrier gas (X_2), the spraying height (X_3), the spraying angle (X_4), the time between two successive spraying sequences on the substrate (X_5), the number of spraying sequences of the sprayer on the substrate (X_6), and the step between two spraying sequences (X_7);
- establishing the mathematical model for predicting the values of the deposition parameters that give the smallest difference in thickness in the two measuring points on the sample, namely the response:

$$Y3 = |Y2 - Y1|, \tag{1}$$

  where Y_1 and Y_2 are the film thicknesses in the two measuring points, determined by using specific devices and measurement methods (e.g. UV-VIS, Ball-Cratering);
- optimizing the spraying model, i.e. obtaining the optimal values of the deposition parameters, by minimizing the response Y_3, improving in this way the uniformity of the thin film.

The seven deposition parameters, named design variables, are defined by variation domains (fields), as follows: $X_j[\min(X_j), \max(X_j)]$, where j = 1:7, in accordance with Table 1.

Several statistical investigation strategies (Perimeter, Sweep, Screening, Response Surface) and DOE (Design of Experiments) design types (Fractional Factorial, Full Factorial, Plackett-Burman, D-Optimal, Latin Hypercube) have been tested for generating the optimal combinations of deposition parameters—samples properties shown in Table 1. The best results, in terms of goodness of fit, have been obtained for the DOE Screening (2 Level) investigation strategy with the Plackett-Burman design type. This technique involves at least eight samples (tests)—S_i, i = 1:8, for which the film thicknesses in two points of the sample have been measured.

Table 1 The optimal combinations of deposition parameters

Sample	X_1	X_2	X_3	X_4	X_5	X_6	X_7
S_1	$\max(X_1)$	$\min(X_2)$	$\min(X_3)$	$\max(X_4)$	$\min(X_5)$	$\max(X_6)$	$\max(X_7)$
S_2	$\max(X_1)$	$\max(X_2)$	$\min(X_3)$	$\min(X_4)$	$\max(X_5)$	$\min(X_6)$	$\max(X_7)$
S_3	$\max(X_1)$	$\max(X_2)$	$\max(X_3)$	$\min(X_4)$	$\min(X_5)$	$\max(X_6)$	$\min(X_7)$
S_4	$\min(X_1)$	$\max(X_2)$	$\max(X_3)$	$\max(X_4)$	$\min(X_5)$	$\min(X_6)$	$\max(X_7)$
S_5	$\max(X_1)$	$\min(X_2)$	$\max(X_3)$	$\max(X_4)$	$\max(X_5)$	$\min(X_6)$	$\min(X_7)$
S_6	$\min(X_1)$	$\max(X_2)$	$\min(X_3)$	$\max(X_4)$	$\max(X_5)$	$\max(X_6)$	$\min(X_7)$
S_7	$\min(X_1)$	$\min(X_2)$	$\max(X_3)$	$\min(X_4)$	$\max(X_5)$	$\max(X_6)$	$\max(X_7)$
S_8	$\min(X_1)$	$\min(X_2)$	$\min(X_3)$	$\min(X_4)$	$\min(X_5)$	$\min(X_6)$	$\min(X_7)$

Fig. 6 The interface designed to introduce the SPD parameters

By comparing the difference in thickness between the two points for each of the eight samples, the sample with the smallest difference of the film thickness has been identified, thus the optimal values for spraying has been obtained, in compliance with the precursor solution. These values were introduced through the user interface, shown in Fig. 6, to control the motion of the robot end-effector (which holds the spray gun). This optimization algorithm is part of the proposed SPD procedure.

The stages of this procedure are described in Fig. 7, as follows: the user is questioned about the shape of the surface (flat or non-planar); for the flat surfaces, the length and the width that define the surface are introduced; for the non-planar surfaces, the previous executed CAD model is introduced; selecting the precursor solution, for example $TiCl_4$, which is an alcohol-based precursor solution; determining the optimal values of the seven specific deposition parameters (parameters) of the spray pyrolysis deposition (X_j, j = 1:7); cleaning the sample and placing it on the plate; the introduction in the deposition procedure of a self-control and adjustment loop of the parameters; after obtaining the optimal temperature of the substrate, the spraying is performed; after executing all the "n" successive spraying sequences on the substrate, the sample is cooled and deposited in a specially designed place.

In a case study, the following variation fields of the seven deposition parameters have been used: $X_1 \in [300, 450]$, $X_2 \in [1, 1.5]$, $X_3 \in [200, 300]$, $X_4 \in [45, 75]$, $X_5 \in [5, 75]$, $X_6 \in [5, 15]$, $X_7 \in [20, 30]$. An ethanolic solution of TiCl4 with 0.05 molar concentration was used as precursor solution. The deposition was performed on glass substrates, the flat plane surface was selected into the program, and was defined by the length & width of the substrate. Then, the type of precursor solution was selected, in this case: an alcohol-based solution. The ranges of values (meaning variation fields) of the seven deposition parameters were defined, and then all eight depositions corresponding to the chosen strategy (see Table 1) were performed.

The optimization process aims to obtain the smallest difference in thickness at two points of interest on the sample. The optimization is performed by minimizing the appropriate regression function for the response Y_3. In these terms, a relationship between the seven deposition parameters and the response has been obtained, by a multiple regression to a specified order: linear, quadratic or cubic, the best results (in terms of goodness of fit) being obtained for the linear order.

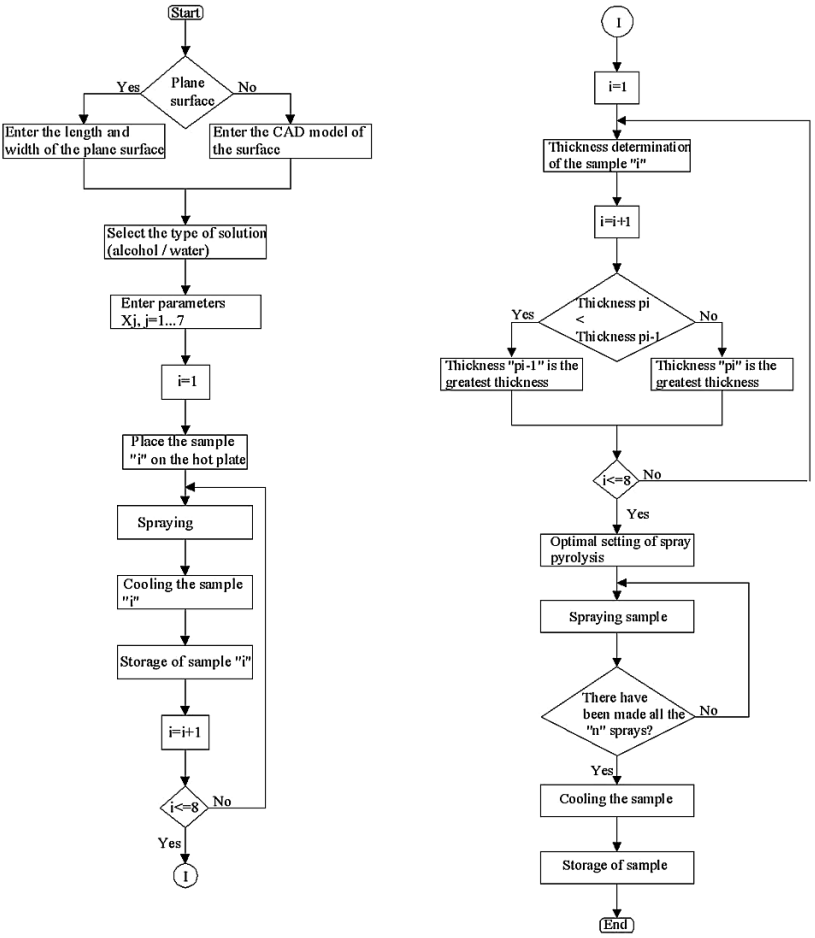

Fig. 7 The block scheme of the deposition procedure in open environment

The corresponding equation of the regression model has the following form:

$$Y_3 = c_0 + c_1 \times X_1 + c_2 \times X_2 + c_3 \times X_4 + c_5 \times X_4 + c_5 \times X_5 + c_6 \times X_6 + c_7 \times X_7, \quad (2)$$

where c_0 is the constant term, and c_i (i = 1:7) are the regression coefficients (each deposition parameter X_i has a regression coefficient c_i associated with it).

The goodness of fit is defined by the following statistical measures [16]: R-squared (R2), R-squared-adjusted (R2adj), regression significance (P), range-to-variance (R/V), and F-ratio (F). R-squared indicates the variance in the predicted results versus the real data, a score of "1" indicating a perfect fit. R-squared-adjusted

Fig. 8 The fit table for the regression function Y_3

	DOF	SS	MS	F	P
Model	7	1.3e+03	186	1e+20	0
Error	0	2.34e-27	0		
Total	7	1.3e+03			
R2	1				
R2adj	1				
R/V	1e+20				

Fig. 9 The terms table for the regression function Y_3

	Coef	+/-	Std. Error	Beta	T	P	Term
1	8.3521	0	0	0	1e+20	0	1 (constant)
2	0.0069017	0	0	0.040616	1e+20	0	f_7
3	19.801	0	0	0.38842	1e+20	0	f_6
4	0.021098	0	0	0.082773	1e+20	0	f_2
5	-0.26469	0	0	-0.31154	1e+20	0	f_1
6	-0.12306	0	0	-0.33797	1e+20	0	f_5
7	1.8225	0	0	0.71502	1e+20	0	f_4
8	-0.87593	0	0	-0.34365	1e+20	0	f_3

is similar to R2, but it is adjusted to account for the number of terms. Regression significance indicates the probability that the fitted model has no useful terms. Range-to-variance ratio indicates how well the model predicts values at the data points. F-ratio is used in the regression to test the significance of the regression, high values suggesting that the regression model is useful. The fit table (shown in Fig. 8) contains also the number of independent variables used into the estimation of a parameter (DOF—Degrees Of Freedom), the sum of squares (SS), and the mean square (MS), for the three parts—regression (model), residual (error), and total.

The terms for the regression function (response) Y_3 are presented in Fig. 9, the following values being displayed / evaluated: coefficient, confidence interval, standard error, beta (standardized coefficient), T statistic, term definition (Term). The confidence interval measures uncertainty in an estimate. The confidence limits about the estimate contain the true value, with a specified level of confidence. The standard error of a coefficient is an estimate of the standard deviation that would be obtains by repeatedly estimating the coefficient with new data. Standardized coefficients are the results of fitting the model to transformed data, where the response and term values have been centered and scaled to give a mean of zero and a unit variance.

Figure 10 shows the residuals for the response Y_3. Residual is the difference between the predicted (estimate) and observed (actual) values of the response. Studentized residuals are residual values that are scaled to make them independent of the magnitude of the actual residuals. For an appropriate model, the studentized residuals should be between −3 and 3. Cook's statistics measure the influence of each trial/experiment on the fit; for an appropriate model, the values should be between 0 and 1 [17].

Fig. 10 The residuals table for the regression function Y_3

	Actual	Estimate	Raw Residual	Studentized	Cook's
1	16.07	16.07	0	0	0
2	7.072	7.072	7.1054e-15	0	0
3	44.78	44.78	-3.5527e-14	0	0
4	8.82	8.82	-7.1054e-15	0	0
5	0.1	0.1	1.7764e-14	0	0
6	25.08	25.08	-1.4211e-14	0	0
7	16.471	16.471	2.1316e-14	0	0
8	13.51	13.51	0	0	0

The results shown in Figs. 8, 9 and 10 indicate that the regression model for the selected strategy (DOE Screening—2 Level, Plackett-Burman design, and linear regression order) matches the test data very well, the "green" bullets indicating the results soundness (i.e. the entity is likely appropriate). All these results demonstrate the viability of the proposed regression model.

Once the deposition has been completed, the thin film thicknesses $Y_{1,2}$ in the two interest points have been measured, corresponding to the eight samples. The optimization has been performed with the purpose to minimize the response Y_3 (see Eq. 1). The algorithm used to perform the optimization is OPTDES-GRG, which requires that deposition parameters have range limits, since it works in scaled space [18]. In this way, the optimal values of the deposition parameters and the corresponding response have been obtained, as follows: X_1 = 450 °C, X_2 = 1 bar, X_3 = 300 mm, X_4 = 75°, X_5 = 75 s, X_6 = 7 spraying sequences, X_7 = 20 mm, Y_3 = 2 nm (Y_1 = 148 nm, Y_2 = 151 nm). Using these optimized deposition parameters, a thin film of TiO_2 was deposited by SPD. The surface morphology of the obtained film (Fig. 11.), as control property, is porous with agglomerated nanostructured crystalline aggregates of TiO_2.

4 Conclusions

In this paper, a novel procedure for the spray pyrolysis deposition of thin films in open environment was proposed. The procedure was implemented for obtaining thin films of TiO_2, using planar glass samples (as substrate) that are placed on a plate having the dimensions 400 × 200 mm^2. The deposition performed in these conditions represents only a variant for applying the procedure, the application domain being much larger (including non-planar surfaces).

The utilization of an industrial robot in the SPD process allows to attenuate the material loses by covering just the heated layer. At the same time, the errors caused by the human operator on manual deposition have been eliminated, increasing the quality of the thin films. The specific parameters of the spray pyrolysis deposition are obtained in an optimal design process, which is performed by using DOE and

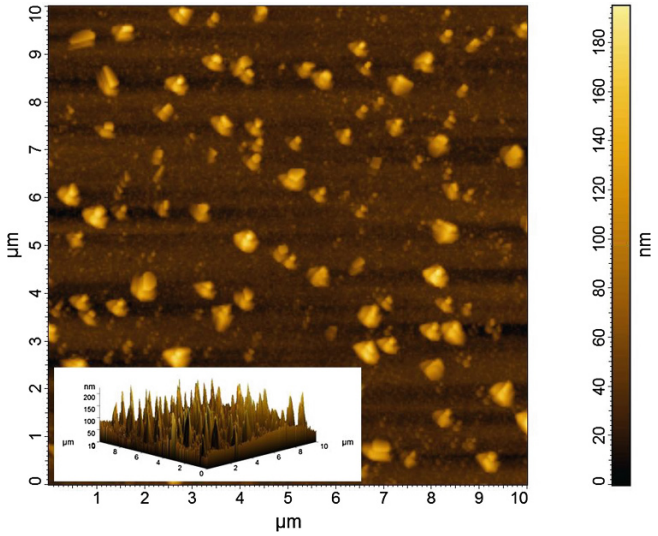

Fig. 11 The 2D and 3D (inset) AFM images of TiO_2 film obtained with optimized deposition parameters

regression models, considering as design objective the minimization of the difference in thickness between two interest points on the sample (in other words, to improve the film uniformity).

Integrating the optimization algorithm into the deposition procedure allows obtaining better surfaces (from structural and morphological point of view), and it also reduces the duration of the whole process. Future development is needed to test the proposed procedure for more complex geometry surfaces. At the same time, we intend to improve the SPD process by a more accurate investigation, with a larger number of experiments, and more responses for verifying the thin film quality.

References

1. Liu, Z. L., & Xiang, L. (2014). Effects of working pressure and substrate temperature on the structure and mechanical properties of nanocrystalline SiC thin films deposited by bias-enhanced hot filament chemical vapor deposition. *Thin Solid Films, 562*, 24–31.
2. Kim, Y., et al. (2012). Controlled electro-spray deposition of highly conductive PEDOT: PSS films. *Solar Energy Materials and Solar Cells, 98*, 39–45.
3. Dinh, N. N., et al. (2011). Highly-efficient electrochromic performance of nanostructured TiO_2 films made by doctor blade technique. *Solar Energy Materials and Solar Cells, 95*, 618–623.
4. Luttrell, T., et al. Photocatalytic activity of anatase and rutile TiO_2 epitaxial thin film grown by pulsed laser deposition, *Thin Solid Films*, In Press, Accepted Manuscript.
5. Dahman, H., et al. (2014). Structural, morphological and optical properties of Cu2SnS3 thin film synthesized by spin coating technique. *Vacuum, 101*, 208–211.

6. US 7838403 B1/2010. Spray pyrolysis for large-scale production of chalcopyrite absorber layer in photovoltaic devices.
7. US 0064699 A1/2012. Methods and systems for spray pyrolysis with addition of volatile non-polar materials.
8. US 0011582 A1/2009. Method for depositing a vapour deposition material.
9. US 0232723 A1/2011. Layer system for solar absorber.
10. Spasevska, H., et al. (2012). Optimised In_2S_3 thin films deposited by spray pyrolysis. *International Journal of Photoenergy, 2012*, 7.
11. Kang, H. W., et al. (2008). Preparation of by spray pyrolysis and evaluation of apparent photocatalytic activity for hydrogen production from water. *International Journal of Photoenergy, 2008*, 8.
12. Ito, S., & Ryo, T. (2012). Segregation of Cu-In-S elements in the spray-pyrolysis-deposited layer of CIS solar cells. *Advances in Materials Science and Engineering, 2012*, 6.
13. Patil, G. E., et al. (2012). Spray pyrolysis deposition of nanostructured tin oxide thin films. *ISRN Nanotechnology, 2012*, 5.
14. Xie, R., et al. (2013). Structural and photoelectrochemical properties of Cu-doped CdS thin films prepared by ultrasonic spray pyrolysis. *International Journal of Photoenergy, 2013*, 7.
15. Enescu, M., & Alexandru, C. (2012). Optimal algorithm for spray pyrolysis deposition of TiO_2 films by using an industrial robot. *Journal of Renewable and Sustainable Energy, 4*(5), 053126-1–053126-11.
16. Manteiga, W. G., & González, A. P. (2006). Goodness-of-fit tests for linear regression models with missing response data. *Canadian Journal of Statistics, 34*(1), 149–170.
17. Orwin, R. G., & Cordray, D. S. (1985). Effects of deficient reporting on meta-analysis: A conceptual framework and reanalysis. *Psychologica, 97*(1), 134–147.
18. Sohoni, V. N., & Haug, E. J. (1982). A state space technique for optimal design of mechanisms. *ASME Journal of Mechanical Design, 104*(4), 792–798.

Valorification of Renewable Ground Energy in a Building Heating

Mircea Horneţ, Cristian D. Năstac, George Dragomir, Bolocan I. Sorin, Nicolae F. Iordan and Lucia M. Boeriu

Abstract The major impediments in adopting in Romania the solution of a building heated with heat pump are the high value of the investment in such a facility and the high cost of electricity compared to that obtained by using methane gas. This makes the payback period of an investment in such a system to be long. To reduce the value of the investment it is important to perform an accurate sizing of the system and to adopt a heating solution that is suitable for use with a heat pump as a heat source for heating. Therefore in this article is presented a solution for heating a building with heat pump. For the solution to be cost effective, it has been adopted in accordance with rigorous sizing of thermal loads for heating and adoption of appropriate solutions for heating. To argue the correctness of adopting such a solution, a comparison calculation was performed for the estimated thermal load and energy consumption for heating the building in two versions namely designing the installations with steady-state methods used in Romania, respectively, using a program of numerical simulation namely TRNSYS.

Keywords GSHP · Ground renewable energy · Radiation heating systems

1 Introduction

Lately in Romania it is discussed ever more the fact that the heat pump solution for buildings heating is appropriate and the fact that the coefficient of performance COP of such a system is between 4 and 5. In fact these things must be considered with much more realism to the following reasons:

1. On the one hand, the average potential that can be "squeezed" from the ground in the most favorable pipe and borehole assembly is in the range 30–50 W/m depending on the thermal conductivity of soil, and not 50 W/m under all conditions [4].

M. Horneţ (✉) · C.D. Năstac · G. Dragomir · B.I. Sorin · N.F. Iordan · L.M. Boeriu
University Transilvania of Brasov, Brasov, Romania
e-mail: mircea.hornet@unitbv.ro

I. Visa (ed.), *Sustainable Energy in the Built Environment - Steps Towards nZEB*,
Springer Proceedings in Energy, DOI 10.1007/978-3-319-09707-7_19

2. On the other hand, the literature and the applications studied by the team of authors reveals a coefficient of performance on entire duration of the heating period (winter) of about COP = 3, or slightly more to the south, where the air temperatures are higher [3]. Considering the maximum yield of production of electricity from conventional fuels, resulting maximum energy economy is found to be only 20 % (not 300 %). Of course, things are better for producing electricity from sources other than fossil fuels.
3. In our country, the price of 1 kWh of electricity is almost three times higher (2.89 times) than 1 kWh of heat produced by a boiler that uses natural gas (price of electric energy p = 0.081 €/kWh—the price for non industrial consumers, for a reservation-monome contract at between 0 and 1 kV, provided by the ENEL official web site [8], price of energy obtained from gas p = 0.028 €/kWh). So, although in the use of a heat pump is obtained about three times more energy than is consumed (average approximately value throughout the heating season), monthly operating costs are approximately equal because of the price three times lower thermal energy produced by burning natural gas [2]. Obviously, this situation creates further difficulties in terms of a return on investment in such a system.

These are the main reasons that the team of authors has correlated to develop a viable, technical and economic way to take advantage of the renewable energy of the ground via a GSHP (ground source heat pump) in buildings heating.

2 Problem Formulation

When we consider adopting a GSHP for heating a building, it is essential to correlate, from a technical standpoint, some elements, namely:

a. the actual temperature (and also the one that leads to a coefficient of performance of heat pump appropriate to ensure the effectiveness of its use), of the heating agent (hot water) the GSHP can provide is approx. 40 °C, or even less for some periods of operation [1]. Of course, some equipment providers indicate higher maximum temperatures of the heating agent, of about 60 °C, but these values are:

   - On the one hand, we might say, only theoretical. They can only get such high temperatures under the most favorable operation conditions that are met hard enough in a practical application of heating a building;
   - On the other hand, when the heat pump is required to supply heat to a temperature of 60 °C, its coefficient of performance decreases greatly at levels that render the GSHP heating system uneconomic in usage.

b. However, in order to heat a building with heating agent hot water at 40 °C the heat flow through the envelope should be as low as possible, a condition which requires that the building envelope should be well insulated.
c. In addition to that, the heating system should be as effective at such low temperatures. For example, a conventional heating system with static radiators would be ineffective and therefore not suitable in this case.

3 Problem Solution

Given the above, we believe that, the necessary condition for heat pump to be a viable solution for heating a building is that the solution will be adopted concurrently with other two measures, strictly necessary, namely:

- a well-insulated envelope,
- a heating system that operates efficiently with heating agent warm water at a temperature of 40 °C i.e. under floor heating system.

3.1 Comparative Study on Heat Load Calculation and Energy Consumption for Buildings Heating

In the economic conditions specific to Romania, for an owner to decide to invest in an GSHP system he should consider, in addition to the investment in the heat pump to invest in an very well insulated envelope. That's why, the sizing of the heating loads (and consequently the energy consumption for heating the building) to be made as judiciously as possible (in a way to exclude an unnecessary oversizing both of the heating system and the degree of thermal insulation of the envelope).

According to Romanian norms, heat load calculation and energy consumption for heating is carried out according to the "Methodology for calculating the energy performance of buildings" MC001-2006. Below are reproduced some details of the scope and method of application.

- Designing the building elements in terms of heat transfer, shall be made to achieve the following goals:
  - Minimum thermal resistance necessary to ensure the appropriate indoor climate, to limit the heat losses and to save energy in operation of buildings;
  - Resistance to water vapour permeability, in order to limit or to prevent condensation of water vapor inside the building elements;
  - Thermal stability required both in winter and in summer, to limit fluctuations in indoor air temperature and on the inner surface of building elements [7].

- The methodology is written in the following general assumptions:
  - Heat transfer is in steady state;
  - All thermo physical characteristics of materials are independent of temperature;
  - The main calculations are based on automatic numerical calculations of temperature fields;

The fact that accordingly to the mentioned methodology the calculation of heat loads and energy consumption for heating is carried out in steady state heat transfer, obviously leads to oversizing. Therefore, in this paper we propose to perform a comparative study of such calculation in two ways: steady state thermal regime, and transient thermal.

Experiments to validate this comparative study were conducted on a building with basement, 7 stories and terrace roof, the headquarters of the Faculty of Civil Engineering. The building's main facade is East oriented and is moderately sheltered. The structure of the building is in reinforced concrete beams and pillars. The envelope is made in light concrete blocks, with a thickness of 30 cm. Horizontal elements are monolithic reinforced concrete slabs, with thickness of 15 cm. Figure 1 presents an overview of the building.

Fig. 1 Overview of the studied building

Calculation of Heating Loads and Energy Consumption for Heating in Steady State

In order to determine the energy consumption for heating we have performed on the experimental building the energy certification in accordance with the "Methodology for calculating the energy performance of buildings" MC 001/2006.

According to the above mentioned methodology, the annual specific energy consumption for heating is Q = 205 kWh/m^2/year. In this value, the specific loses trough the exterior walls is Q = 104 kWh/m^2/year.

In the whole building—3,096 m^2, the annual energy consumption due to the losses through exterior walls is Q = 104 × 3,096 = 321,984 kWh/year.

Calculation of Thermal Load and Energy Consumption for Heating under Transient Thermal

In the simulation with TRNSYS we have obtained the total annual energy consumption of our building—the subject of this investigation being: Q = 602,220 kWh/year [8]. In the simulation we have considered the influence that thermal bridges have on the heat transfer between building and environment. This value obviously includes all categories of energy losses in our building, namely:

- Energy consumption due to heat loss through the building envelope;
- Energy consumption for heating the cold outdoor air that infiltrates the building trough leaks;
- Energy consumption for artificial lighting;
- Energy consumption for DHW heating. In this case, the value is zero (the building has no DHW heating);
- Energy consumption for ventilation and cooling of the building. In this case, its value is also zero (the building has no ventilation system and air conditioning) (Fig. 2).

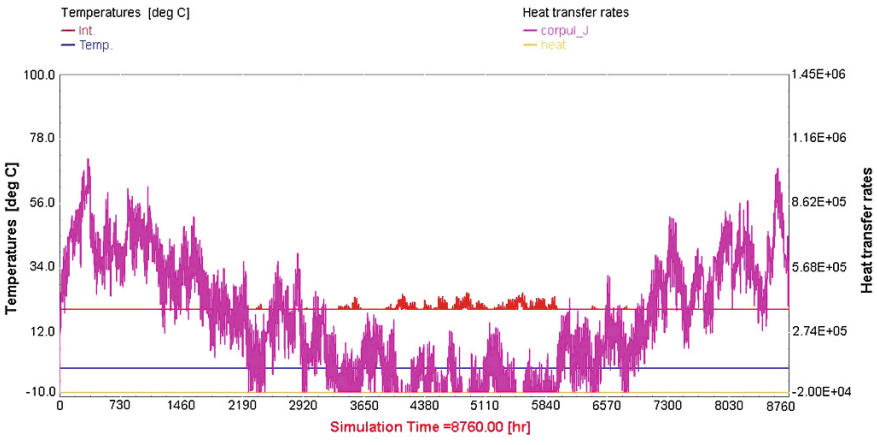

Fig. 2 Energy demand of the studied building over a year

Results of Heat Transfer in Steady State and Transient Thermal Experimental Validation Study

Experimental research objective is to determine which of the two approaches to the calculation leads to results closer to the actual thermal stresses on the studied building, and consequently to the proper sizing of both facilities and envelope (which removes the possibility of unnecessary oversizing).

For this, it was necessary to monitor on the duration of the heating period (October 26, 2013–April 15, 2014), physical parameters necessary for evaluation of energy performance in real operating conditions.

To validate which of the two methods of calculation gives results closer to the actual one we have performed in the same period (October 26, 2013–April 15, 2014) a measurement of the heat flux through the exterior wall and trough an exterior window. Measurements were carried out on their surface temperatures also. Heat flux measurement was performed using data logger digital multimeters TESTO 435-2 (2 pieces, one for opaque wall and one for the window). This measures the thermal transmittance (and calculates the heat flux) of a building element by measuring the following temperatures: the temperature on the inner surface of the construction element considered, the indoor air temperature and the outdoor temperature. To measure the temperature of the inner surface (T_{pi}) of the element of construction, the apparatus is equipped with three probes that are fixed on its surface at a distance of 30 cm between them. This probe has integrated connection socket TESTO 435-2 and a sensor for measuring indoor air temperature (T_i). Outdoor air temperature (T_e) is measured with a special wireless probe located outside (Figs. 3 and 4).

Monitoring was done through a complex system consisting of the measurement sensors for physical parameters, data acquisition and processing system.

The measurement sensors for physical parameters is composed of [5]:

- Sensors for measuring outside air temperature, type ATF01_PT1000 according to DIN EN 60751, class B, measurement range (−50, +90) °C;
- Sensors for measuring the temperature of the outer and inner surfaces of construction elements of the building envelope OFTF_PT1000_PVC1 type 5 according to DIN EN 60751, class B, measurement range (−30, +105) °C;

Fig. 3 Digital multimeter and data logger TESTO 435-2

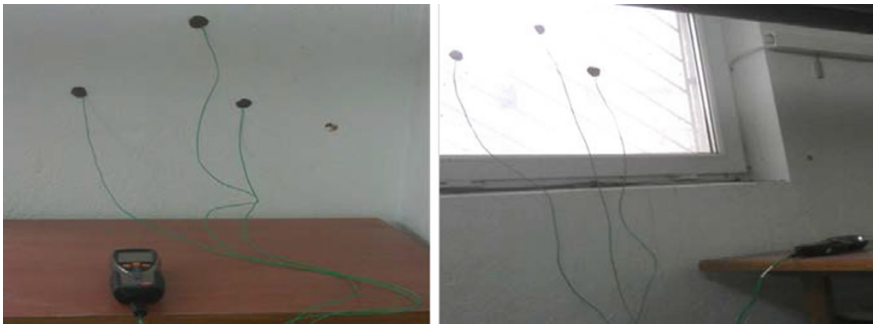

Fig. 4 TESTO sensors mounted on the inner surface of the exterior wall and window

Fig. 5 Electrical board of the data acquisition and processing system

- Sensors that measures the relative humidity of the outside air type AFF-I, DIN EN 60751, class B, measurement range (0, 100) %;
- A system for measuring the heat flux through the opaque outside wall and the window, respectively, the digital multimeter and data logger TESTO 435-2, together with the wall temperature probe and a wireless probe for measuring the outdoor temperature;
- Gas meter, to measure the energy consumed for heating the building and determine the thermal power of the heat source.

All the equipment for the data acquisition and processing system are mounted on a board specially tailored to this, as shown in Fig. 5.

Fig. 6 Temperature sensors that have been mounted on the inner and outer surfaces of the wall and window

Experimental measurements were performed in the "Radiating surfaces laboratory", the building elements tested (opaque wall and window), representing the outer wall of the laboratory.

To obtain the maximum accuracy of measurement results, both the system sensors that measures heat flow through opaque outer wall and the temperature on inner and outer surfaces were installed in areas uninfluenced by thermal bridges, or where their effect is minimal. To identify these areas we have used infrared thermography camera.

Figure 6 presents the temperature sensors mounted both inside and outside wall surface, i.e. one of the glass windows.

The Results of the Measurements

In this paper we present only the strictly necessary measurements for comparing the results of the study of heat transfer in steady state and transitory thermal regime. These results are shown in Figs. 7, 8, 9 and 10.

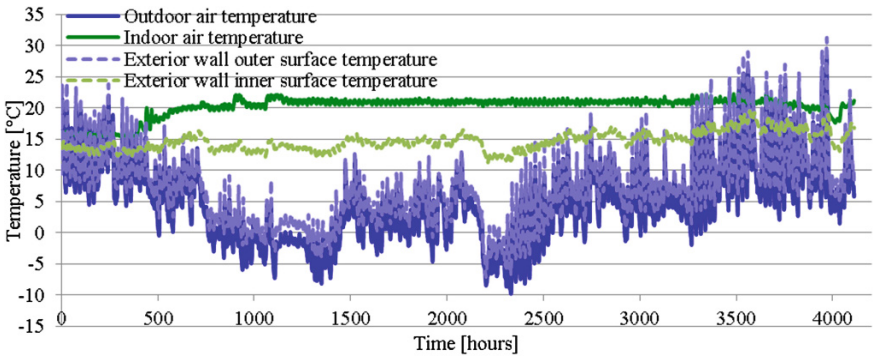

Fig. 7 Measured temperatures on the inner and outer surfaces of the exterior wall and the indoor and outdoor air temperature

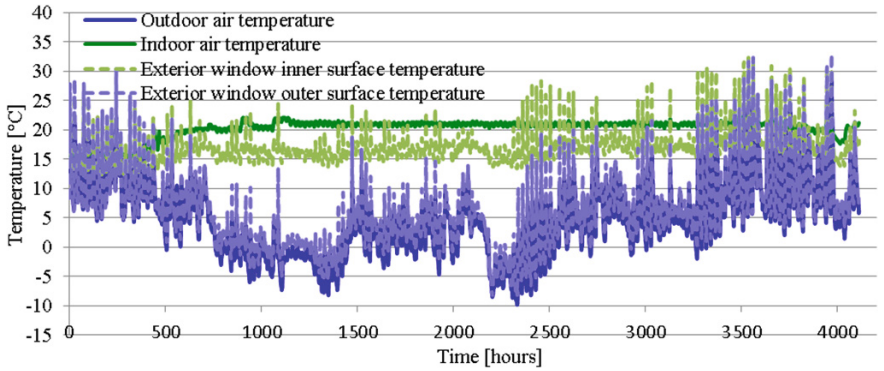

Fig. 8 Measured temperatures on the inner and outer surfaces of the exterior window and the indoor and outdoor air temperature

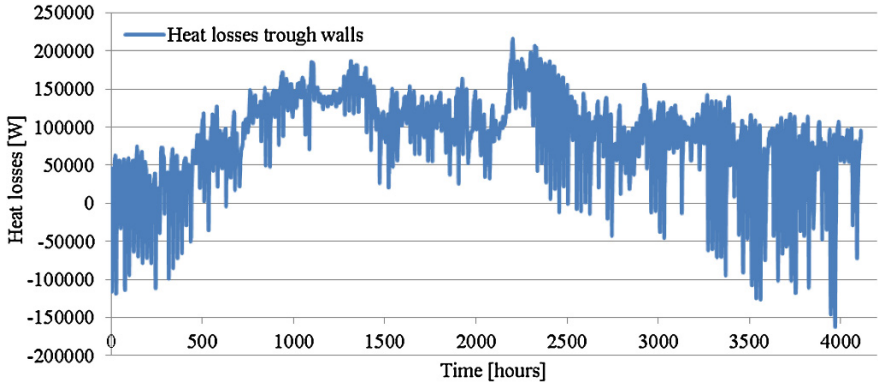

Fig. 9 Measured heat losses through the exterior walls

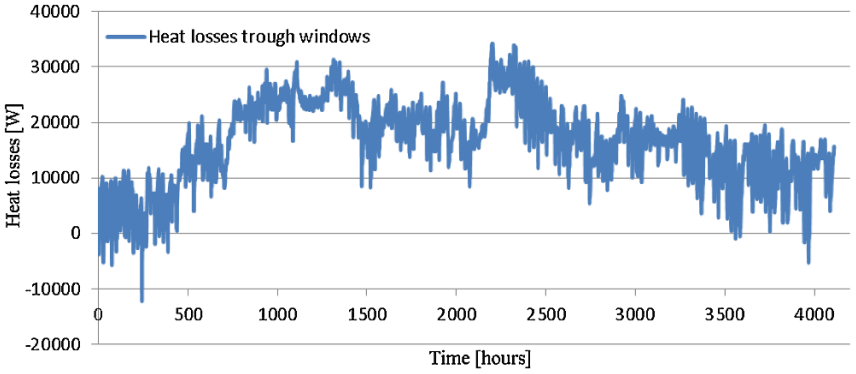

Fig. 10 Measured energy consumption through the exterior windows

Results of the Study of Heat Transfer in Steady State and Transitory Thermal Regime Comparison

Measurements that have been carried out to validate the results of calculus done by MC001/2006 and those of TRNSYS simulation provides the heat losses (and consequently energy consumption) through the vertical elements of the building envelope (only opaque walls and window surfaces, were not measured heat losses to the ground and trough the terrace, those have been considered equal with those obtained by MC001/2006).

When calculating the heating load and energy consumption for heating was determined under steady state, the calculus was done for the entire building. Compared to the results obtained in the measurements, the calculus under steady state comprises more elements: energy losses to the ground, those trough the terrace and the energy consumption required for heating the air infiltrated into the building through leaks.

When calculating the thermal load and energy consumption for heating in transient thermal we have determined the total energy consumption of the building (because TRNSYS determine total energy and not a component). Compared to the results obtained with the calculation in steady state, it also contains the energy consumption for lighting.

Therefore, in order to make a fair comparative analysis of the results obtained in the three cases described, we had to choose one value, namely the energy consumption trough opaque exterior walls. Thats why, the energy consumption written in columns 2–6 of Table 1 have been considered equal for all four situations. In Table 1 below we reproduce the values considered in the comparative analysis.

The comparative analysis was done considering the measured values for about 6 months (between October 26, 2013–April 15, 2014) given the fact that in Braşov climate, **outside this period**, there is no real need for heating.

As mentioned above, the energy values that we have compared are analyzed in column 7 of Table 1. Comparing the values listed in Table 1 above we can draw the following observations:

1. First we have compared the energy consumption due to heat transfer through opaque exterior walls obtained from measurements "in situ" i.e. Q = 271,039 kWh/year, with the percent in the total readout of the gas meter (519,464 kWh/year), namely the one thet corresponds to the energy consumption due to heat transfer through opaque exterior walls, respectivly Q = 264,430 kWh/year. We can see that the value obtained from the measurements is correct (which is 2.5 % higher than that indicated by the gas meter), which validates the correctness of the measurements.
2. Energy consumption due to heat transfer through opaque exterior walls obtained from calculations according to Romanian methodology MC 001/2006—"Methodology for calculating the energy performance of buildings" (computing in steady state thermal regime) i.e. Q = 321,984 kWh/year, is greater than that measured, that is Q = 271,039 kWh/year with 18.8 %.

Table 1 Comparative values of the energy consumption of the building, obtained in the research and experimenting

Conducted studies	Total energy consumption	Components of the energy consumption					
0	1	2	3	4	5	6	7
		Air in trough leakages [kWh/year]	Lighting [kWh/year]	Energy losses to ground [kWh/year]	Energy losses through terrace [kWh/year]	Energy losses through windows [kWh/year]	Energy losses through walls [kWh/year]
MC 001/2006 [kWh/year]	634,680	12,5913	57,658	5,918	52,424	70,783	321,984
TRNSYS [kWh/year]	602,220	12,5913	57,658	5,918	52,424	70,783	289,524
Measured values [kWh/year]	–	–	–	–	–	70,783	271,039
Gas meter readout	519,464	125,913	–	5,918	52,424	70,783	264,430

3. Energy consumption due to heat transfer through opaque exterior walls obtained by numerical simulation software TRNSYS (computing in transitory thermal regime), Q = 289,524 kWh/year, is higher than that obtained by the measurements, i.e. Q = 271,039 kWh/year with 6.8 %.

As can be seen, the results closest to the given measurements are those obtained by numerical simulation software TRNSYS (computing transitory thermal regime). Good correlation of the results of this calculation with the measured values proves that the use of numerical simulation software TRNSYS is an adequate solution both to calculate the energy consumption of a building and dimensioning of the elements that make up the building envelope. Moreover, the TRNSYS software is useful in designing and sizing facilities in buildings.

4 Conclusions

As we have said at the beginning of this paper, the major impediments in the adoption in Romania of such a solution with GSHP for heating and DHW in buildings are the high value of the investment in such a facility and practical impossibility of recovering the investment. The situation is the following:

- If the GSHP solution for heating is implemented in an average building (as happens in many cases), the average coefficient of performance (COP) of the heat pump during the cold season can only be: COP = 3.
- As said before, in our country the price of electricity is about three (2.89) times higher than the price for the energy produced by a boiler that uses natural gas. Although a heat pump produces about three times more energy than consumes, monthly operating costs of the two heating solutions (gas operated boiler, and heat pump) are approximately equal. Obviously, this situation makes it impossible for the investment in a solution with heat pump to pay back.

In order to recover the investment in the solution of heating with GSHP of a building, should the average coefficient of performance (COP) of the heat pump during the heating season to be between 4 and 5. This consists in a temperature of the heating agent as low as possible. To heat a building with heating agent at 33–34 °C, two conditions must be met simultaneously, namely:

- A highly insulated envelope;
- A heating system to operate efficiently at low temperatures i.e. 33–34 °C, namely a radiation heating system mounted in the floor.

Making an envelope very well insulated implies additional investment costs. As shown in the presented paper, the usual methods for sizing of both heating facilities and building are based on the assumption that the thermal regime is steady state. The consequence of this is an unnecessary oversizing, which will only increase the cost of investment.

In this paper, the authors have argued that the use of a numerical simulation software, such as TRNSYS in designing the buildings and building facilities can remove the oversizing, both of the installations and of envelopes components. This leads to reduced investment costs and increase investor confidence to adopt a system for heating a building with GSHP.

References

1. Afify, R. (2013). Sustainable design of water source VRH. *ASHRAE Journal*, *55*(10).
2. Boian, I. (2007). *Dezvoltarea durabilă (Sustainable development)*. Braşov: Transilvania University Press.
3. Chiriac, F., & Boian, I. (2013). *Pompe de căldură (Heat pumps)*. Bucharest: Editura Matrix Rom.
4. Collins, P. A., Orio, D. C., & Smiriglio, S. (2002). *Geothermal heat pump manual*. New York: Department of Design and Constructions.
5. Drăghici, M. (2012). *Măsurarea mărimilor fizice în construcţii-achiziţia datelor măsurate*., Bulletin of the Transilvania University of Braşov Brasov: Transilvania University Press.
6. https://www.enel.ro/crosweb/calculator/factura_casnic?p_loccons.id=
7. MC001/2006. (2006). *Calculation methodology for buildings performance*, Romania.
8. Năstac, C. D. (2014) *Reasearch on reducing energy consumption by envelope retrofit and usage of earth's natural energy*. PhD thesis, Iaşi, Romania.

Efficiency of the Flat Plate Solar Thermal Collector

Florin Iordache and Vlad Iordache

Abstract The paper aims at establishing the theoretical efficiencies of flat plate solar thermal collector with improved properties regarding the absorption and the transparency of the collector plate and that of the transparent element. The paper presents the thermal balance equations corresponding to the plate of the solar collector and to its transparent element. The mathematical model developed was implemented in an automated computational tool and it was used in order to determine the energy performance. The graphical variation of the efficiencies as a function of the outdoor parameters offers a synthetic image of the energy performance for this type of solar collectors.

Nomenclature

t_m	Average temperature of the thermal agent in the flat plate solar thermal collector (^oC)
t_e	Outdoor temperature (^oC)
t_E	The sol-air temperature (^oC)
I	Global intensity of solar radiation (W/m^2)
α_{ap}	Absorption coefficient of the absorption plate, in visible spectrum (-)
α_{ag}	Absorption coefficient of the glazing, in visible spectrum (-)
α_{rg}	Reflexing coefficient of the glazing, in visible spectrum (-)
τ	Glass transparency (-)
α_i	Convection coefficient inside the pipe for the thermal agent [$W/(m^2\ K)$]
α_e	Convection coefficient outside the solar panel [$W/(m^2\ K)$]
k_i	Descending heat transfer coefficient of the solar panel [$W/(m^2\ K)$]
k_s	Upward heat transfer coefficient of the solar panel [$W/(m^2\ K)$]
q_s	Surface specific heat flux for the upward of the solar panel (W/m^2)
q_i	Surface specific heat flux for the downward of the solar panel, (W/m^2)
l	Half the distance between two consecutive pipes of the solar panel (m)
d_i	The inside diameter of the solar panel pipes (m)

F. Iordache (✉) · V. Iordache
CAMBI Research Center, Technical University
of Civil Engineering of Bucharest, Bucharest, Romania
e-mail: fliord@yahoo.com

I. Visa (ed.), *Sustainable Energy in the Built Environment - Steps Towards nZEB*,
Springer Proceedings in Energy, DOI 10.1007/978-3-319-09707-7_20

d_e Outside diameter of the solar panel pipes (m)
R_c Contact thermal resistance between the pipes and the absorbent panel, (m K/W)
λ_p Thermal conductivity of the absorbent panel [W/(mK)]
δ_p Width of the absorbent panel (m)
δ_{iz} Width of the insulation layer (m)
λ_{iz} Thermal conductivity of the insulation layer [W/(mK)]
ε_p Emissivity of the absorber panel (-)
ε_g Emissivity of the glazing (-)
t_g Glazing temperature (^oC)
t_p Absorber panel temperature (^oC)
S The flat plate solar thermal collector surface (m^2)
α_{cv} Convective heat transfer coefficient between panel and glass [W/(m^2K)]
α_r Radiant heat transfer coefficient between panel and glass [W/(m^2K)]
α_{pg} Radiant and convective coefficient between panel and glass [W/(m^2K)]
φ_I Heat flux incident on the solar panel (W)
φ_U Heat flux absorbed by the thermal agent (W)
Φ_o Optic flux loss (W)
F′ Geometric-structural factor for the solar panel (-)
β Outdoor parameter, ratio between the average logarithmic difference of the temperatures and the solar intensity radiation (m^2 K/W)
γ Temperature difference ratio (-)
η The efficiency of the flat plate solar thermal collector (%)
k_c Heat loss global coefficient of the flat plate solar thermal collector (W/m^2 K)
k_{c1} The first heat loss global coefficient of the flat plate solar thermal collector (W/m^2 K)
k_{c2} The second heat loss global coefficient of the flat plate solar thermal collector (W^2/m^4 K^2)

1 Introduction

The flat, absorption, solar collectors represent the main component of the unconventional energy plants used for domestic water heating. Therefore, it is important to be given special attention in order to achieve high efficiency. The temperatures of the absorber plate and the transparent element and different heat flows are estimated based on the steady thermal balances equations for several constructive solutions of these devices. Further, the efficiency of the solar panel is estimates as the ratio between the heat flow and the incident heat flow.

In this paper we analyzed the variation of the solar collector efficiency while operating in different scenarios, characterized by different temperatures of the water circulated through the collectors and different climatic conditions (ambient air temperature and solar radiation intensity).

2 Heat Transfer Processes Associated with the Absorption of the Solar Collectors

The structure of the analyzed solar collector is described in Fig. 1: glass, air, plate, thermal agent, plate and thermal insulation.

Thermal balance equations corresponding to the steady state for main elements of the solar collector are presented below:

- Steady state heat balance of the transparent element:

$$\alpha_{pg} \cdot (t_p - t_g) + \alpha_e \cdot (t_e - t_g) + \alpha_{ag} \cdot I = 0 \tag{1}$$

- Steady state heat balance of the absorber plate:

$$\alpha_{pg} \cdot (t_g - t_p) + k_i \cdot (t_e - t_p) + \alpha_i \cdot (t_m - t_p) + \alpha_{ap} \cdot \tau \cdot I = 0 \tag{2}$$

The global heat transfer coefficient (convection + radiation) between the plate and the glass is calculated as follows:

$$\alpha_{pg} = \alpha_{cv}/2 + \alpha_r \tag{3}$$

The solar collector performance depends on the average temperature of the thermal agent inside the collector. The global coefficient of heat transfer at the lower part of the solar collector is calculated as follows:

$$k_i = \left(\frac{\delta_{iz}}{\lambda_{iz}} + \frac{1}{\alpha_e}\right)^{-1} \tag{4}$$

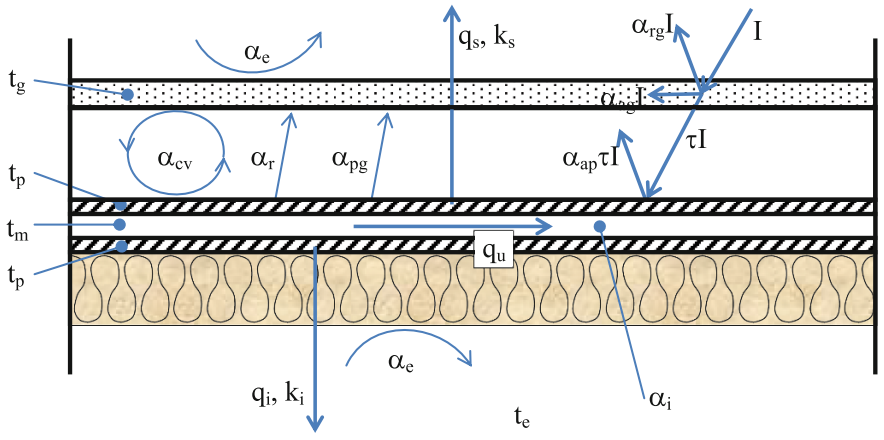

Fig. 1 Scheme of the heat transfer phenomena inside a thermal agent solar panel

The glazing transparency coefficient is calculated:

$$\tau = 1 - \alpha_{ag} - \alpha_{rg} \tag{5}$$

Temperatures t_p and t_g represents the unknowns of the system formed of Eqs. (1) and (2). After a short shape-shift of the two equations we obtain the following algebraic system:

$$\begin{aligned} -\alpha_{pg} \cdot t_p + \left(\alpha_{pg} + \alpha_e\right) \cdot t_g &= \alpha_e \cdot t_e + \alpha_{ag} \cdot I \\ \left(\alpha_{pg} + k_i + \alpha_i\right) \cdot t_p - \alpha_{pg} \cdot t_g &= k_i \cdot t_e + \alpha_i \cdot t_m + \alpha_{ap} \cdot \tau \cdot I \end{aligned} \tag{6}$$

Or its vectorial form:

$$\begin{pmatrix} -\alpha_{pg} & \left(\alpha_{pg} + \alpha_e\right) \\ \left(\alpha_{pg} + k_i + \alpha_i\right) & -\alpha_{pg} \end{pmatrix} \cdot \begin{pmatrix} t_p \\ t_g \end{pmatrix} = \begin{pmatrix} \alpha_e \cdot t_e + \alpha_{ag} \cdot I \\ k_i \cdot t_e + \alpha_i \cdot t_m + \alpha_{ap} \cdot \tau \cdot I \end{pmatrix} \tag{7}$$

Thus the solution of the system is:

$$\begin{pmatrix} t_p \\ t_g \end{pmatrix} = \begin{pmatrix} -\alpha_{pg} & \left(\alpha_{pg} + \alpha_e\right) \\ \left(\alpha_{pg} + k_i + \alpha_i\right) & -\alpha_{pg} \end{pmatrix}^{-1} \cdot \begin{pmatrix} \alpha_e \cdot t_e + \alpha_{ag} \cdot I \\ k_i \cdot t_e + \alpha_i \cdot t_m + \alpha_{ap} \cdot \tau \cdot I \end{pmatrix} \tag{8}$$

The heat flux incident on the solar panel is calculated as the difference between the incident energy flux and the optic flux loss,

$$\Phi_I = I * S - \Phi_o. \tag{9}$$

The heat flux absorbed by the thermal agent is calculated with

$$\Phi_U = \Phi_I - q_i * S - q_s * S. \tag{10}$$

The efficiency η of the solar panel is calculated as the ratio between the absorbed and the incident heat flux,

$$\eta = \Phi_U / \Phi_I. \tag{11}$$

The outdoor parameter β is calculated:

$$\beta = (t_m - t_e)/I. \tag{12}$$

This algorithm leads to the correlation between the efficiency η of the flat plate solar thermal collector and the outdoor parameter β.

3 Processing Results Based on Simulation

The solution of the system proposed in the previous chapter has been implemented in a computational program for the solar panel operation. This computational program allows user to set the configuration of the solar panel from a structural and operational viewpoint and also to choose the test conditions, consisting in the thermal agent temperatures involved in the heat transfer phenomena.

The following scenarios had been tested: (1) intensity of the solar radiation I = 200, 500, 800 (W/m^2) and (2) logarithmic average temperature of the thermal agent t_m = 30, 50, 70 (^{o}C). Concerning the solar panel, two structural solutions had been tested: a higher quality and a lower quality of the heat transfer phenomena. The higher quality solar panel with one glazing (CB1) is characterized by the values: $l = 0.04$, $d_i = 0.015$, $d_e = 0.017$, $R_c = 0.0$, $\lambda_p = 360$, $\delta_p = 0.0005$, $\alpha_{rg} = 0.05$, $\alpha_{ag} = 0.03$, $\alpha_{ap} = 0.9$, $\varepsilon_p = 0.9$, $\varepsilon_g = 0.1$, and the lower quality of the solar panel with one glazing (CS1) is characterized by the values: $l = 0.06$, $d_i = 0.015$, $d_e = 0.017$, $R_c = 0.1$, $\lambda_p = 160$, $\delta_p = 0.001$, $\alpha_{rg} = 0.1$, $\alpha_{ag} = 0.05$, $\alpha_{ap} = 0.8$, $\varepsilon_p = 0.9$, $\varepsilon_g = 0.9$.

Following the nine simulated scenarios (three values of I × three values of t_m), the variation of several parameters were analyzed:

- The surface density of heat flux that is not used from the received solar energy due to structure of the solar panel;
- The surface density of the lost light energy flux;
- The surface density of the heat flux dissipated to the outside environment;
- The useful surface density of the heat flux transmitted to the thermal agent; and
- The ratio between the average logarithmic difference of the thermal agent temperatures and the solar radiation intensity.

For each simulation, several steps were followed:

- determining the temperatures t_p and t_g of the absorption plate and of the glass;
- determining the heat flux incident on the solar panel, Φ_I, and the heat flux absorbed by the thermal agent Φ_U;
- the calculation of the solar panel efficiency, η, and
- the evaluation of the outdoor parameter $\tilde{\beta}$

The nine simulation scenarios (for three I values and three t_m values) were used to form a graphical representation of the solar panel behavior. Using these nine points of coordinates (β, η) a multiple polynomial regression curve was learned. Finally, we calculated the correlation between the (1) solar panel efficiency η (%) and the (2) ratio between the average logarithmic difference of the thermal agent temperatures and the solar radiation intensity β (m^2 K/W). This correlation (Fig. 2) represents the thermal characteristic of the solar panel and represents a synthesis of the energy performance of the solar panel for different exploitation scenarios.

We note that the solar panel efficiency is inverse correlated with the coefficient β. For higher β values the efficiency can become negative—it corresponds to the case where the solar panel losses heat towards the outdoor environment.

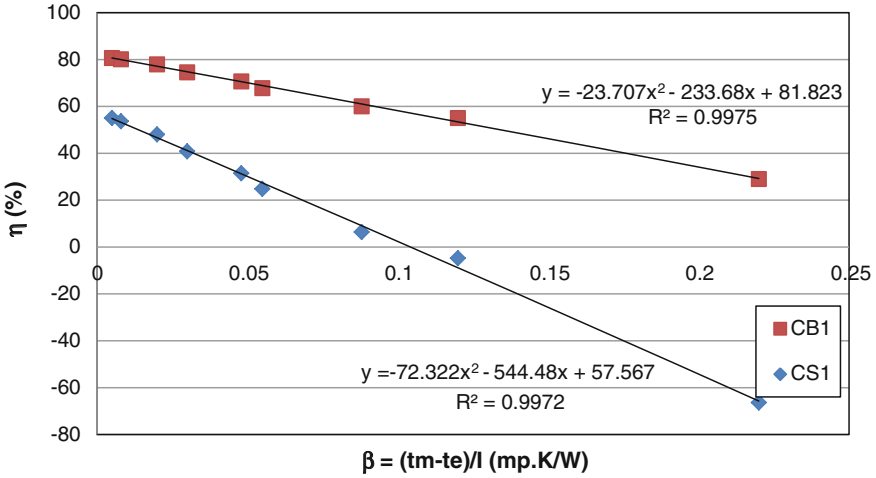

Fig. 2 Thermal characteristics of two, one glazing, different solar panels η = η(β)

The solar panel efficiency can be usually estimated as a polynomial function of coefficient β [1]. Further, we use this formula (Eq. 13) and the regression equations in Fig. 2 in order to identify the average values of the parameters F', k_{C1} and k_{C2},

$$\eta = F' \cdot \left(\alpha_{ap}\tau\right) - F' \cdot k_{C1} \cdot \beta - F' \cdot k_{C2} \cdot \beta^2 \tag{13}$$

During this analysis, the absorption coefficient of the solar panel and the transparency coefficient were constant, while the global heat transfer coefficient of the solar panel, k_C, was variable as a function of the energy parameters characterizing the solar panel [2, 3]. Finally, we obtained for the lower quality solar panel (CS1), the average values for these parameters: $F' = 0.85$, $k_{C1} = 6.43$, $k_{C2} = 0.85$; and for the higher quality solar panel (CB1), the average values: $F' = 0.99$, $k_{C1} = 2.36$, $k_{C2} = 0.24$.

The solar panel efficiency can also be calculated as a linear function of temperature difference ratio, γ, with no free term.

$$\begin{aligned} &\eta = F' \cdot (\alpha\tau) \cdot \frac{t_E - t_m}{t_E - t_e} = F' \cdot (\alpha\tau) \cdot \gamma \\ &\textit{where}: \\ &\gamma = \frac{t_E - t_m}{t_E - t_e}; \quad \text{and} \quad t_E = \frac{\alpha_{ap}\tau \cdot I}{k_C} + t_e \end{aligned} \tag{14}$$

The variation of the solar panel efficiency as a function of the temperature difference ratio is graphically presented in Fig. 3.

Parameter F′ was again calculated according to the new regression curves established for the two types of solar panel CS1 and CB1. Thus, for the solar panel

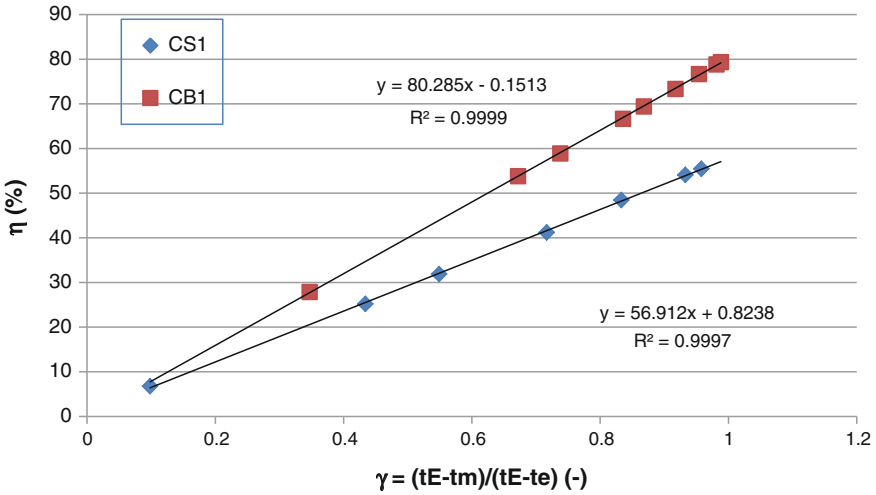

Fig. 3 Thermal characteristics of two, one glazing, different solar panels $\eta = \eta(\gamma)$

with a lower quality, $F' = 0.84$ for the solar panel with a higher quality $F' = 0.97$. One can easily note that these new values are close to those obtained previously.

For this second type of thermal characteristic of the solar panel, the ratio of the temperature differences, γ, which is also the input data of this thermal characteristic, depends on the equivalent temperature t_E (Eq. 14), which is different according to the structure of the solar panel. For the first type of thermal characteristic, the input data, β, is totally independent of the structure of the solar panel.

4 Conclusions

The aim of this paper was to identify the thermal characteristic of the solar panel by means of computer simulation during their usual operation. The computation software is based on the absorption phenomenon radiant energy and all heat transfer phenomena inside the solar panel. In this software the global heat transfer coefficient, k_C and the factor F' depend on the several energy parameters that influence the solar panel.

The values presented in chapter three are average values determined from the regression curve of the solar panel characteristic (Fig. 2). In this paper we propose a new and simpler form of the solar panel characteristic that is based on the temperature difference ratio, which depends on the constructive structure of the solar panel.

The thermal characteristic of the solar panel is a global parameter that reflects the energy performance of the solar panel. During the operation of the solar panel in different types of installations, the value of the efficiency depends on the outdoor parameter, β, parameter that need to be taken into consideration during design stage of such installations.

References

1. Duffie, J. A., & Beckman, W. A. (1980). *Solar engineering of thermal processes*. New York: Wiley.
2. Iordache, F. (2010). *Energy aspects of the thermal device and systems in buildings*. Bucharest: Conspress (in Romanian).
3. Iordache, F. (2014). *Flat plate solar thermal collectors*. Energy aspects—revista romana de inginerie civila—2014 (in Romanian).

Spectrally Solar Selective Coatings for Colored Flat Plate Solar Thermal Collectors

Luminita Isac, Alexandru Enesca, Ciprian Mihoreanu, Dana Perniu and Anca Duta

Abstract The paper is a review on the state-of-the-art on colored materials (absorbers and glazings) for solar thermal flat plate collectors obtained world-wide. The best results obtained by the group active in the R&D Centre Renewable Energy Systems and Recycling are also reported and they are related to the steps followed in developing and optimizing the absorber plate (substrate, the alumina matrix, the colored coatings and the anti-reflexion layer) and the glazing (as anti-reflexive coating and/or as colored component). These results represent a promising input for novel, market-acceptable flat plate solar-thermal collectors, with increased architectural acceptance, for facades integration in Nearly Zero Energy Buildings.

Keywords Colored solar thermal collectors · Absorbers · Glazings · Spray pyrolysis deposition · Solar spectral selectivity

1 Introduction

Solar energy is the most abundant renewable energy source. The simplest and direct way of harnessing solar energy is the solar thermal conversion using solar thermal collectors. Solar thermal systems with flat plate collectors are environmental friendly, non-polluting and market competitive systems, used to convert incident solar radiation (direct and diffuse) in thermal energy and therefore to fulfil the ever increasing demand of the future green energy supply [1].

Flat plate collectors are mainly designed for solar hot water and industrial process heat applications and have as main components: a metal casing (bottom and side-walls insulated), the tubes for the heat agent circulation (water, ethylene glycol solution, air), the absorber plate and the glazing. The active component in a flat

L. Isac (✉) · A. Enesca · C. Mihoreanu · D. Perniu · A. Duta
Renewable Energy Systems and Recycling R&D Centre (RES-REC), Transilvania University of Brasov, Eroilor 29, 500036 Brasov, Romania
e-mail: isac.luminita@unitbv.ro

I. Visa (ed.), *Sustainable Energy in the Built Environment - Steps Towards nZEB*, Springer Proceedings in Energy, DOI 10.1007/978-3-319-09707-7_21

plate solar thermal collector is the absorber plate, a spectrally selective coating used to convert the UV-VIS part of the solar radiation into heat and to allow the convection of the IR part of the spectrum, towards the tubes [2]. As pre-requisite, the solar radiation has to reach the absorber plate in a high percentage. Thus, carefully engineered optical properties are required for:

- *the absorber plate*: high absorptance ($\alpha_s > 0.9$) over the solar spectrum ($\lambda = 0.28–2.5$ μm) and low thermal emittance ($\varepsilon_T < 0.1$) in the IR region ($\lambda > 2.5$ μm), at the operating temperature; usually, commercial absorbers have solar spectral selectivity ($S = \alpha_s/\varepsilon_T$) higher than standard values ($S > 9$) and even much higher, e.g. 54.5 for Mo-Si_3N_4 black multilayered coating [3] and 21.3 for a colored (red) titanium nitride coating [4]; to reduce scattering and reflection, an anti-reflective coating is recommended to be added.
- *the glazing*: high transmission all over the solar spectrum, low reflectance (for avoiding reflection and light scattering), combined with low absorptance (as heating the glazing actually represents a thermal energy loss).

Most of solar-thermal collectors are installed on roof tops, facade integration being still seldom, mainly because of black or dark bluish color of the selective absorber and the visibility of corrugated metal sheets, welding traces and tubing that have low architectural acceptance. Thus, facades solar collectors must be compatible with the architectural design and colored solar collectors are aesthetically preferable.

There are two main approaches for developing colored flat plate solar thermal collectors: by coloring the absorber plate or by coloring the glazing. Colored absorber coatings can be obtained by direct deposition of the colored pigment (Fe_2O_3, Cr_2O_3, CoO_x) on metal (Al, Ti, Si) substrate (*Thickness Insensitive Solar Selective coatings, TISS*) or as a combination of multilayers with variable refractive index, deposited on the metal or ceramic/cermet substrates (*Thickness Sensitive Solar Selective coatings, TSSS*).

Colored TISS coatings, integrally obtained using spray pyrolysis technique (SPD), by embedding oxides (Fe_2O_3, V_2O_5) and sulphide (CuS) pigments in an alumina matrix were recently developed in our research group [5]. Bright red spectral selective coatings with spectral selectivity of 12.4 were obtained using Fe_2O_3 pigment with embedded Au NPs, deposited on Al/Al_2O_3 matrix.

The good reciprocal infiltration pigment-matrix, thus the controlled morphology of each layer and of the assembly represents the key issue in obtaining high spectral selectivity. Therefore, it is very important to well prepare the substrate/matrix interface and one alternative is the anodization of the Al substrate in nitric acid solution (HNO_3:H_2O = 1:1). Due to the economic and environmental issues, the industrial-scale implementation of this method is cost effective, therefore an alternative is to use sulfuric acid solution to Al anodization.

Our recent experimental results showed that SPD deposited red coatings with Al/Al_2O_3/Fe_2O_3-Au NPs structure have S = 6.75–9.60, promising values for selective absorber coatings in colored solar thermal flat plate collectors.

To increase the durability and the amount of useful solar energy, anti-reflective coatings (AR) need to be deposited on the spectral selective coating. As AR have no role in conversion, they need to be transparent in UV and VIS (thus very large band gap semiconductors or insulators) and must have low IR absorptance, thus they should be deposited as very thin films. Additionally, AR should have the proper refractive index, low thermal emittance, good flexibility and long-term stability [6].

2 Solar Absorber Coatings

Most of the highly spectrally selective absorber layers reported so far consists of a matrix, inorganic or polymeric coating deposited on metallic substrate (Al, Cu, Si, stainless steel), in which nano- or micro-sized ceramics and metals (Au, Ag, Pt or Cu) are embedded, for increasing the spectral selectivity by lowering the thermal emittance value. Nanosized metals and semiconductor particles show specific physical properties which are related to both classical and quantum size effects. The changes in optical properties can be qualitatively explained by resonant oscillations of surface charges in electromagnetic field. Differences in optical properties are attributed to particles size, shape, concentration, distribution and the dielectric environment of the host matrix [1, 7, 8].

High performing selective absorbers already exists on the market, still they represent the most costly high technology component of a solar thermal collector. In this context, the development of highly efficient, flexible, durable, up-scalable and, most of all, low-cost absorber materials for solar-thermal applications, using simple deposition techniques, continues to be important research targets. Recently, an exhaustive review of selective coatings materials prepared by PVD techniques has been reported [9]. Among PVD methods (e.g. evaporation, ion plating, pulsed laser deposition, sputtering), magnetron sputtering seems to be the most suitable for industrial deposition of large-area solar selective coatings [1, 3, 10–12]; although efficient and allowing a perfect control, these techniques are intensive energy consumers, making the overall energy balance of the product quite unsustainable. A broad range of these materials are mainly deposited using wet chemical techniques: electrodeposition, anodization, sol–gel, solution growth, spray pyrolysis etc. [2, 9, 11, 13–19]. Spray pyrolysis deposition (SPD) has the advantage of low complexity, good reproducibility, up-scalable applications and, last but not least, low cost.

The absorber materials obtained by one or more of the above-mentioned techniques, with high solar spectral selectivity values (S = 7.92–54.5), are mainly black or with blue shades (because of the thin TiO_2 anti-reflective layer), and only several papers reported the developing of colored absorber coatings with still low but promising S values (2.67–21.3). Most of black solar absorber coatings are formed by cermets composed of metals such as Mo, Ni, Cu, Fe, Cr, Au or Pt embedded in ceramic matrixes of (a) metal oxides: Al_2O_3 [1, 11, 14, 20–23], NiO [18, 24],

Table 1 Solar spectral selectivity of black absorber coatings

Absorber coating	S	Ref.
Ni-Al_2O_3	28.33	[11]
Ni-Al_2O_3/AR	18.6	[11]
Ni-Al_2O_3	4.5–8.5	[20]
Ni-Al_2O_3/SiO_2/TiO_2	19.4	[22]
Ag-Al_2O_3	23.25	[1]
Al/Ni-Al_2O_3/Al_2O_3	13.43	[21]
Ni-NiO	19.4	[24]
Ni-NiO_x	13	[18]
$NiCrO_x$	43.6	[25]
Cu-CuO	>12	[26, 29]
ZnO-C	11.83	[30]
NiO-C	21	[30]
Cu-Co-Mn-Si-O	7.92	[31]
CuO_x-NiO_x	19–30	[19, 27]
NbAlN/NbAlON/Si_3N_4	13.65	[28]
Si_3N_4/Mo-Si_3N_4	54.5	[3]
CrMoN(H)/CrMoN(L)/CrON	6.1–6.9	[12]
HfMoN(H)/HfMoN(L)/HfON	6–7	[32]

$CrNiO_x$ [14, 25], Cu_xO [19, 26–29] and SiO_2 [1], (b) oxynitrides: NbAlON [28], CrON [12], or (c) nitrides: NbAlN [28], Si_3N [3], CrMoN [12].

The solar performances, according with spectral selectivity (S) values of a wide range of black absorber coatings, are presented in Table 1.

Alumina-based cermets have been widely used as solar absorber surfaces because they have excellent optical properties and thermal stability. Ni-Al_2O_3 solar selective absorbing coatings, with or without anti-reflective layer (AR), Table 1, were obtained on Al substrate by a facile chemical-solution methods [11, 22] and by electroplating [20].

In the last years, the use of nanocermets (i.e. Ag or Au metal nanoparticles embedded in a dielectric matrix) has attracted considerable attention due to their wide range of applications: solar energy conversion, photo-chromic, photo-electrochemical materials and gas sensors. Nanocermets are considered promising candidates for solar energy conversion because they exhibit a strong absorption of solar radiation (usually in the VIS region of solar spectrum), as result of the quantum confinement effect, called surface plasmon resonance phenomenon (SPR) —collective oscillations of the conduction electrons of noble metal nanoparticles (NPs) embedded in a dielectric matrix. Barshilia and coworkers [1] reported the obtaining of Ag-Al_2O_3 nanocermet solar selective coating, deposited on copper, silicon and glass substrates, using magnetron sputtering technique. The optimized coating exhibited a solar spectral selectivity higher than 23 (Table 1), depending on size distribution and concentration of Ag NPs embedded in alumina matrix.

Cermets coatings with composition Ni-NiO, on Al substrate, having spectral selectivity from 13 [18] to 19.4 [24], and Ni-NiCrOx with S = 43.6 [25] are recognized as versatile materials, suitable for solar selective absorbers. The infiltration of metallic Ni particles in the dielectric NiO or $NiCrO_x$ matrix represents a prerequisite for efficient solar selective absorption NiO-based cermets, confirmed by high S value obtained for Ni-$NiCrO_x$ cermet (Ni-NiO particles embedded in Cr_2O_3-NiO matrix).

Mixed CuO_x-NiO_x based cermets were developed by our research group, using SPD as a single deposition technique of spectral selective coatings on Cu substrate [27]. By controlling the film morphology using maleic anhydride copolymers as additives into the precursors' solution, solar absorber with good selectivity (19) were obtained. The high selectivity values (S > 30) of the optimized CuO_x-NiO_x composite coatings, obtained on Cu substrate using nickel and copper acetate, dissolved in mixed solvents with various water: ethanol ratios, were explained based on two parallel mechanisms: intrinsic absorption and multiple reflections generated when absorbers with controlled roughness are deposited [19].

Related to nitrides and oxynitrides based cermets (Table 1), only few examples are reported in literature [3, 12, 28, 32] and recently, a selective coating based on Mo–Si_3N_4 was reported [3]. Accurate combination of the individual component layers based on optical simulations and precise control of layers thickness and composition leads to the highest solar spectral selectivity (S = 54.5), known so far to the best of our knowledge. This is why, in the latest report, the European association of solar-thermal systems, ESTIF nominated these types of coatings as a breakthrough.

Nowadays, intensive researches are devoted to increase the efficiency and durability, but also to architectural integration of solar energy conversion systems into buildings. This is part of the effort towards reaching the Nearly Zero Energy Building status, as set by the EU directives that will enter in force by 2020.

Because of architectural and social (lack of) acceptance, most solar-thermal collectors are installed on roof tops, facade integration being still seldom. For developing on-site solar-thermal energy convertors, able to totally meet the need for domestic hot water, and partially the need for heating and cooling, the use of the facades-mounted solar-thermal arrays becomes an alternative that needs to be supported. Therefore, colored solar collectors were outlined as being aesthetically preferable if installed on the visible parts of these buildings [33, 34].

3 Colored Absorber Coatings

In 1955, Tabor patented an absorber coating produced by electrogalvanization. Since then, so-called "black chrome" has become one of the standard products on the market [8]. To avoid the monotony of black absorber flat plate collectors, and also to provide an aesthetic integration in the built environment, colored absorbers were developed and investigated, representing an attractive perspective for the

modern architecture, even if a lower solar thermal efficiency would have to be expected [35–37]. As the working environment is close to the dew point of water, the colored absorbers should be stable and water-insoluble, thus inorganic pigments are used in spectrally selective absorber plate [7]: ceramic multi-materials as stacked layers or 3D composites, cermets. As already mentioned, two types of spectrally selective coatings are reported in the literature, differentiated by the effect of the layer (paints) thickness on the absorber performance:

(a) *Thickness sensitive spectrally selective (TSSS) coatings*, mostly based on black inorganic oxides, that are currently dominate the market; the paints are incorporated as so-called "tandem structures"; the paint forms the top layer of these two-layered structures (having short wavelength absorbing properties and infrared transparency), while an infrared reflective metal surface accounts for the bottom, ensuring low thermal radiation losses [15];
(b) *Thickness insensitive spectrally selective (TISS) coatings* combine the advantages of paints (durability, chemical resistance achieved by a high thickness of the applied layer, variety of colors and simple application) with spectral selectivity, which does not depend on the thermal emittance of the substrate [38].

A synthesis of several colored absorber coatings is presented in Table 2.

For paint coatings prepared as thickness-dependent spectrally selective surfaces, both the solar absorptance and the thermal emittance increase with the coating thickness [15, 16, 37]. Still, there is a maximum thickness that allows a certain flexibility of the colored layer(s) that is necessary as the dilatation coefficient of the metal substrate is much higher than those of the ceramic coating. Once this limit is exceeded, the thermal dilatation (during day) leads to micro-cracks when the collector cools down (during night).

Nowadays TiAlN is considered the state of the art spectrally selective absorber material. The optical properties of the reported TiAlN TSSS coatings [4] are shown in Table 2, along with other several colored TISS.

More recently, spectral selective coatings for absorbers in solar thermal flat plate collectors with high architectural acceptance were obtained by our group as composite structures of colored pigments embedded in alumina matrix. Three types of TISS structures were analyzed with Fe_2O_3, V_2O_5 and CuS as red, green-yellow and dark green pigments [5].

The results showed that the most important aspect in getting competitive spectral selectivity (over 12 for red TISS absorber) is represented by the good and uniform reciprocal infiltration of the composites layers; this was obtained for composites containing Fe_2O_3 pigment, with extended crystallinity and high roughness. By adding gold nanoparticles (10 nm Au NPs, prepared as described in [40]), depending on the precursor type, the growth is uniform, embedding the Au NPs in the layer (for Fe_2O_3-based absorber, Fig. 1), or preferentially runs on the Au NP, when a separate layer above the matrix (as for V_2O_5) is obtained; thus, controlling the Au NPs surface charge and adequately matching the precursor represents a path for optimizing the composite structure, towards enhanced spectral selectivity.

Table 2 Optical properties and spectral selectivity of colored absorber coatings

Absorber type	Absorber coating	Color	α_s	ε_T	S	Ref.
TSSS	Silicone paints	Green, blue	>0.85	<0.25	>3	[37]
	Ti-AlN	Purple, green, red	0.84–0.94	0.05–0.27	3.5–16	[39]
	TiAlN	Red	0.86	0.04	21.5	[4]
	TiAlN	Yellow	0.81	0.06	13.5	[4]
	TiAlN	Blue	0.86	0.08	10.7	[4]
	TiAlN/TiAlON	Green	0.92	0.08	11.5	[4]
	TiAlN/TiAlON/ AR	Dark red	0.95	0.09	10.5	[4]
TISS	TiMEMO paint + Al flakes	Red, green, blue	>0.9	<0.3	>3	[38]
	Fe_2O_{3+} Al flakes pigment	Red	0.27	0.14	1.92	[16]
	Al flakes pigment	Green, blue	0.58	0.35	1.67	[16]
			0.25	0.03	8.33	
	$Al/Al_2O_3/Fe_2O_3$-Au NPs ($/TiO_2$)	Red	0.62	0.05	12.4	[5]
			0.65	0.07	9.28	
	$Al/Al_2O_3/V_2O_5$-Au NPs ($/TiO_2$)	Yellow	0.52	0.17	3.06	[5]
			0.53	0.14	3.79	
	Al/Al_2O_3/CuS-Au NPs ($/TiO_2$)	Green	0.75	0.23	3.26	[5]
			0.69	0.20	3.45	

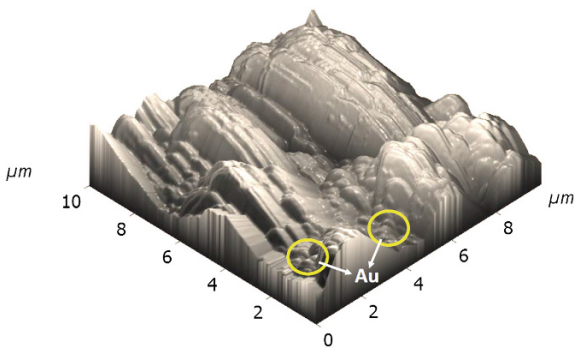

Fig. 1 AFM image of the Al/Al_2O_3/Fe_2O_3-Au absorber coating

Durability tests (Table 3) on the best performing coating ($Al/Al_2O_3/Fe_2O_3$–Au, with or without TiO_2 AR layer) showed that the optical properties and spectral selectivity for the coating with AR layer are not influenced by the aggressive working environment, due to the homogeneity and chemical stability of the TiO_2 layer. The absence of anti-reflection protective layer causes morphological changes (Figs. 2 and 3), with effect on the solar absorptance and thermal emitatance values and decreasing of spectral solar selectivity, from 12.4 to 8.71 (climatic chamber tests), and

Table 3 Results of durability tests on the absorber coating $Al/Al_2O_3/Fe_2O_3$-Au

Sample	Initial optical properties			Optical properties after 144 h in the climatic chamber[a]			Optical properties after electrochemical corrosion in NaCl 3.5 %		
	α_s	ε_T	S	α_s	ε_T	S	α_s	ε_T	S
Without TiO_2	0.62	0.05	12.40	0.61	0.07	8.71	0.68	0.09	7.56
With TiO_2	0.65	0.07	9.28	0.65	0.07	9.28	0.65	0.07	9.28

[a] NaCl 3.5 %, at 35 °C (± 0.5 °C)

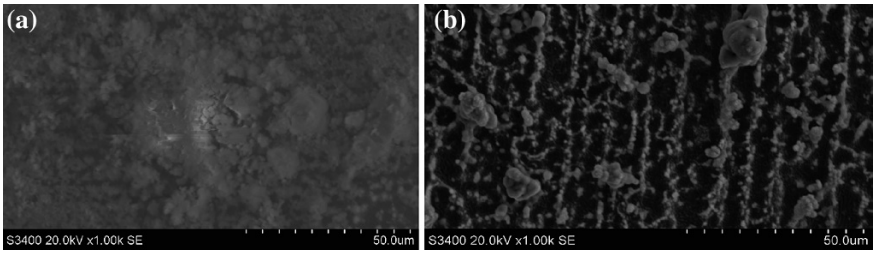

Fig. 2 SEM image of the samples **a** $Al/Al_2O_3/Fe_2O_3$-Au and **b** $Al/Al_2O_3/Fe_2O_3$-Au/TiO_2 tested in the climatic chamber

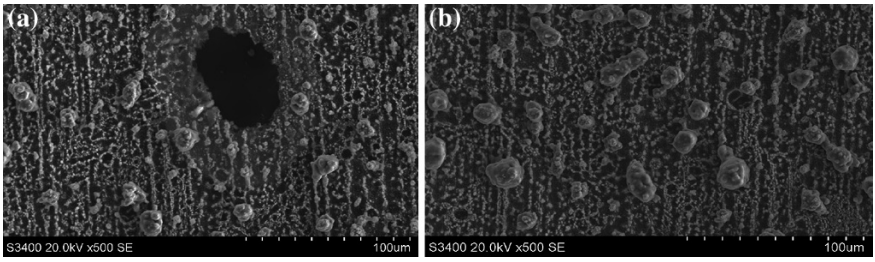

Fig. 3 SEM image of the samples **a** $Al/Al_2O_3/Fe_2O_3$-Au and **b** $Al/Al_2O_3/Fe_2O_3$-Au/TiO_2 electrochemically tested in NaCl 3.5 %

respectively to 7.56, after electrochemical corrosion tests. After the tests in climatic chamber, the morphology of absorber coating without AR layer is denser (Fig. 2a) with relative low porosity, reducing the solar absorption capacity. Electrochemical corrosion tests in saline working conditions show a decrease of the spectral selectivity value for the coating without AR layer (TiO_2), due to the morphological changes occurred at the contact of absorber coating with aggressive solution (Fig. 3a) when a local electrochemical cell can be formed with the Au NPs.

For large scale implementation, the use of alumina-matrix obtained by Al anodization in HNO_3 solution is quite expensive and environmental problems are encountered. In this context, our group used as alternative solution of H_2SO_4 to Al

anodization, and red coatings with $Al/Al_2O_3/Fe_2O_3$-Au NPs structure were deposited on alumina substrate.

In developing these coatings, several steps needed to be optimized, using the spectral selectivity as output property:

1. *The substrate pre-treatment*: a thin Al_2O_3 layer with controlled thickness and porosity is obtained by anodization, in sulfuric acid solution (c = 200 g/L) for 35 min at 0.1, 0.2, 0.5, 0.8 and 1 A on the commercial Al substrate (99.5 % Beofon, thickness 0.7 mm) previously degreased and conditioned in alkaline solution (65 g/L NaOH, at 60 °C) and in nitiric acid solution (HNO_3:H_2O = 1:1, at 40 °C, for 10 min); samples of 3 cm × 4 cm were used as substrates in the spray pyrolysis deposition of active layers; the best spectral selectivity values were obtained for layers prepared at a current of 1 A, therefore these substrates were further studied and nominated as "A1";
2. *The Al_2O_3 layer* was deposited by SPD from aqueous solution of 0.25 mol/L $AlCl_3$ and acetyl acetone as additive on the preheated substrate at 400 °C, by 30 spraying sequences, using air as carrier gas, at 1.5 bar; the samples are further nominated as "A1/AO";
3. The red pigment (thin film of Fe_2O_3) was deposited by SPD from precursor solution of 0.2 mol/L $FeCl_3$ in water—ethanol mixtures (1:1 vol), at deposition temperature T = 400 °C, using 20 spraying sequences, and 1.5 bar pressure of air; 10 nm Au nanoparticles (Au-NPs, prepared as described in [40]) were dispersed in the pigment precursor solution to obtain concentration of 35 µmol/L; the samples without SPD Al_2O_3 layer are nominated as "A1/Fe_2O_3-Au" and the samples containing SPD Al_2O_3 layer are labeled as "A1/AO/Fe_2O_3-Au".

For samples optical properties (α_s, ε_T) evaluation, the Fourier Transform Infrared Spectroscopy (FTIR, Bruker Vertex 70) and UV-VIS-NIR spectrophotometry (Perkin Elmer Lambda 950) were used. The optical properties were correlated with the crystalline structure (XRD, Bruker D8 Discover) and with the surface composition (EDS) and morphology (SEM 3500N, Hitachi).

The pigment absorber coating and components layers have polycrystalline structures (Fig. 4), containing crystalline phases of Al_2O_3, aluminum oxy-hidrogenated compounds and Fe_2O_3. The composition of the crystalline phases and the overall crystallinity degree (estimated using the device software EVA 1.4) are presented in Table 4.

The absorber stacked layers, developed by infiltrating the A1/OA matrix, causes an increase in the crystallinity degree of the pigments and a significant increase in polymorphism is registered for the A1/AO/Fe_2O_3-Au coating: six different crystalline phases, including three Fe_2O_3 polymorphs. The presence/absence of the SPD Al_2O_3 as matrix influences the composition and the pigment structure in the absorber coating: the predominant Fe_2O_3 crystalline phase (46.91 %) with cubic lattice is infiltrated in alumina matrix, while, in coating obtained by directly deposition of the pigment on the substrate, Fe_2O_3 with orthorhombic lattice (40.62 %) is obtained. The difference in the pigment composition and structure may influence the optical properties of the investigated red absorber coatings. Moreover,

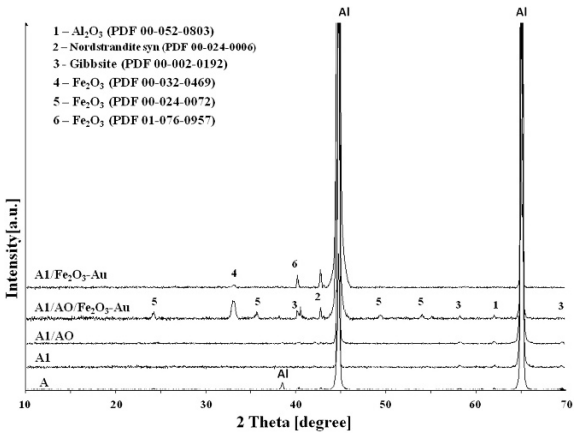

Fig. 4 XRD patterns of substrate, alumina matrix and red absorber coatings

Table 4 The composition of the crystalline phases in the absorber layers

Sample	Crystallinity (%)	Crystalline structure and composition
A1	74.6	Al_2O_3, orthorhombic (22.54 %)
		Gibbsite, $Al_2O_3 \cdot 3H_2O$, monoclinic (61 %)
		Nordstrandite syn, $Al(OH)_3$, triclinic (16.46 %)
A1/AO	92.6	**Al_2O_3, orthorhombic (54.5 %)**
		Gibbsite, $Al_2O_3 \cdot 3H_2O$, monoclinic (23.94 %)
		Nordstrandite syn, $Al(OH)_3$, triclinic (21.56 %)
A1/AO/Fe_2O_3-Au	94.5	Al_2O_3, orthorhombic (2.84 %)
		Gibbsite, $Al_2O_3 \cdot 3H_2O$, monoclinic (4.59 %)
		Nordstrandite syn, $Al(OH)_3$, triclinic (10.43 %)
		Hematite, Fe_2O_3, rhombohedric (29.42 %)
		Fe_2O_3, cubic (46.91 %)
		Fe_2O_3 (5.87 %)
A1/Fe_2O_3-Au	97.7	**Nordstrandite syn, $Al(OH)_3$, triclinic (48.38 %)**
		Fe_2O_3, cubic (11 %)
		Fe_2O_3, orthorhombic (40.62 %)

it was already reported [5] that tailoring the surface charge of the matrix (OA is slightly negatively charged) and of the Au NPs may represent an instrument in tuning polycrystallinity.

The elemental composition analyzed by EDS, represented in Fig. 5, gives information on the surface composition and consequently on the growth and adherence of each layer on the previous one, allowing the accurate design of the final absorber coating.

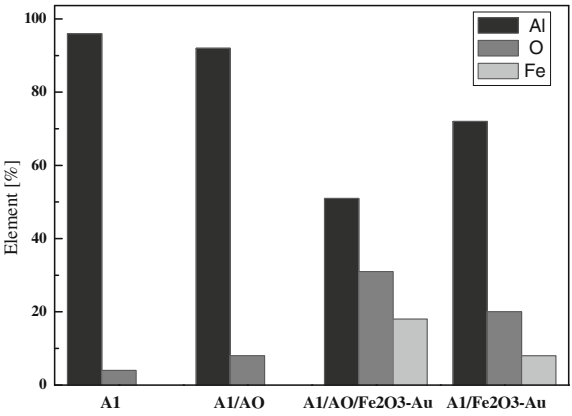

Fig. 5 Elemental composition of the absorber layers

As expected, the SPD Al_2O_3 and Fe_2O_3 layers deposition on the anodized aluminum substrate closely respects the substrate composition and shows an increase in the oxygen content. For the A1/Fe_2O_3-Au sample, the difference registered in the XRD composition is sustained by EDS results that indicate a decrease of about 50 % in the estimated Fe weight content, in comparison with about 37 % estimated from the XRD patterns. This indicates that more Al–O based compounds could be present on the surface and, due to the large variations registered in the Al content, the pigment coating has different thicknesses.

Besides differences in composition and structure, the differences in surface morphology represent an important factor in controlling and tailoring the optical properties of the absorber material. The morphologies of the investigated samples are shown in Fig. 6.

Previous results reported by our group [5] showed a very good infiltration of the Fe_2O_3 pigment, particularly when Au NPs are included in the coating structure, when Fe_2O_3 layers infiltrate the small Au NP among the columnar oxide structures. In this study, the morphology of sample A1/AO/Fe_2O_3-Au show that Fe_2O_3 pigment is mostly good infiltrated in the alumina matrix (A1/AO) but large agglomerates are formed also on the alumina matrix and/or grow on the Au NPs. This may be due to the Al substrate (A1), obtained by Al anodization in sulfuric acid, with small differences in composition and structure.

The morphology of the sample without SPD alumina matrix shows that pigment and Au NPs are on the substrate, as aggregates, and noinfiltration is observed. It is obvious that this morphology will not allow multiple reflections and multiple scattering in the absorber material, and the optical parameters are not convenient for a selective solar absorber coating.

The optical properties (α_s, ε_T) and spectral selectivity (S) values are presented in Table 5 and can be explained, based on the above results. As expected, the best result (S = 9.60) is obtained for absorber coating with structure A1/AO/Fe_2O_3-Au, as consequence of the optimized composition, structure and morphology. This result is slightly lower than the previous one [5], but is promising for obtaining large-scaled, lower cost red absorber coatings, for solar-thermal flat plate collectors.

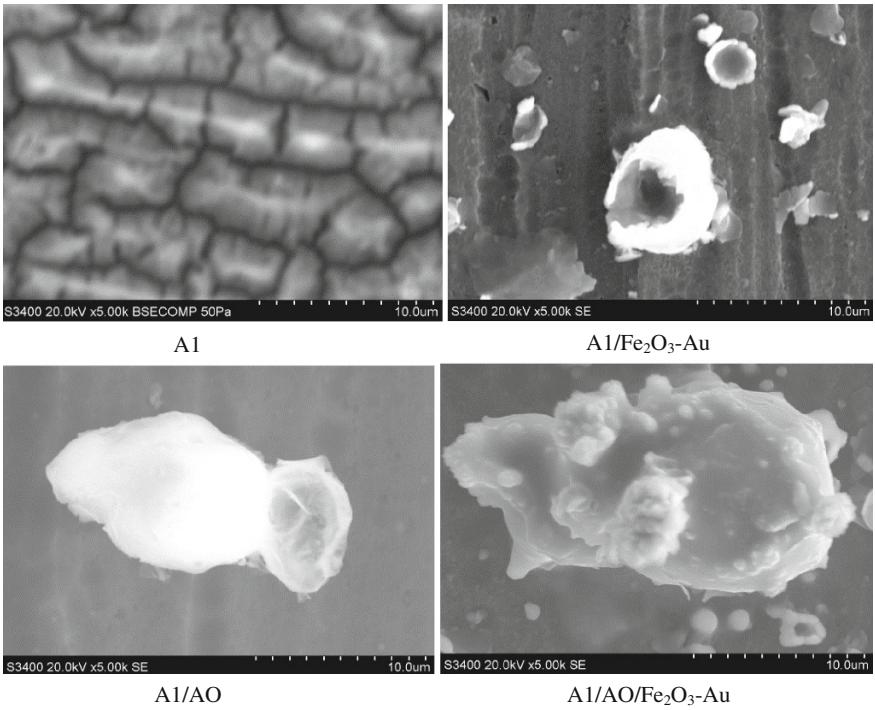

Fig. 6 SEM micrographs of the substrate, matrix and absorber layers

Table 5 Optical properties and spectral selectivity of the absorber layers

Sample	α_s	ε_T	S
A1	0.21	0.85	0.24
A1/AO	0.01	0.15	0.07
A1/AO/Fe_2O_3-Au	**0.48**	**0.05**	**9.60**
A1/Fe_2O_3-Au	0.37	0.13	2.84

4 Glazings

A perfect architectural integration of common glazed or unglazed solar thermal collectors in a building is difficult to obtain. Perfect integration means that the collector is part of the building's envelope or an architectural design element and can therefore not be recognized immediately as solar collector [41].

The pre-requisite for optimal coating glazing in solar thermal application is represented by the conjunction of three factors: high transmittance in UV-VIS-IR, low reflectance in VIS-IR and high chemical stability in the working environment (humidity, dust, hail-stone, salts, high and low temperatures).

Thermal transmittance, visual transmittance and solar factor are only several parameters that should be carefully examined during the design phase. The adoption of double and triple glasses, or modern double-skin façades, could optimize the transmission/reflection ratio [42]. Consequently it is possible to modify the surface properties of glass by using metal oxides coatings, aiming to improve the visual transmittance (antireflective coatings), thermal transmittance (low-E coatings), solar factor (solar control filters) and glass maintenance (self-cleaning coatings).

Different deposition techniques have been employed for coating glasses with different thin films materials. One of the most preferred for large-scale applications is E-beam evaporation [43]. Better uniformity for smaller area coatings is provided by magnetron sputtering techniques [44]. The metal oxides optical coatings can be deposited on glass substrates by CVD (chemical vapor deposition) [45] and PVD (physical vapor deposition) [46]. The heterogeneity between the deposit and the glass substrate is the main cause of the lack of durability of these coatings. Other techniques that have been intensively used in preparation of optical coatings were ion assisted and laser ablation deposition techniques [47, 48]. Both E-beam evaporation and magnetron sputtering require high cost equipment for low vacuum and the size is also limited at the chambers dimension. The high temperatures reached during this process and the high value of pressure is the main limits of these methods from an environmental point of view. The use of metal oxides containing silver or other elements can have environmental implications concerning the entire life-cycle of the treated glass.

The relevance of the sol-gel method basically consists of (1) improvement of processing and properties of conventional materials and (2) development of novel materials. This technique supports the self-assembly of nanostructured surfaces when combined with a low cost dip-coating thin layer deposition.

The sol-gel method for fabricating materials starts with a solution consisting of the organic or inorganic metal precursors (e.g. TEOS ($Si(OC_2H_5)_4$) for silica synthesis), water as hydrolysis agent, ethanol (C_2H_5OH) as solvent and hydrochloric acid as catalysts. Metal compounds undergo hydrolysis and polycondensation at 60 °C, giving rise to the sol, in which fine particles are dispersed. Further reactions connect the particles, solidifying the sol into a wet gel, which still contains water and ethanol. Usually, various shapes are formed during the sol to gel transformation. Vaporization of water and solvents produces a dry gel, one of the final products. Optionally, heating the gels to several hundred degrees or higher temperatures produces dense SiO_2.

Our recent studies targeted the SiO_2 thin films that were obtained by dip-coating using the diluted gel. The gel dilution was varied from 1.0 g/100 mL up to 4.0 g/100 mL, and the use of additives (Dodecyltrimethylammonium bromide DTAB, C_{15} $H_{34}BrN$) was investigated as coherence agents. As dilution solvent, a mixture of water:ethanol (1:1 vol) was used. The SiO_2 films were deposited, using 6 or 10 deposition sequences, on microscopic glass, previously cleaned by successive immersion in ultra-sound bath containing ethanol. The samples abbreviations and the deposition parameters are presented in Table 6. The samples codes were attributed according to samples preparation conditions, e.g.:

Table 6 Parameters for samples deposition

Samples	Quantity of sol-gel (g/100 mL solvent)	Quantity of DTAB (g/100 mL solvent)	Number of deposition sequences
A0_6	1.0	–	6
A0_10	1.0	–	10
A1_6	1.0	0.02	6
A1_10	1.0	0.02	10
B0_6	2.0	–	6
B0_10	2.0	–	10
B1_6	2.0	0.02	6
B1_10	2.0	0.02	10
C0_6	4.0	–	6
C0_10	4.0	–	10
C1_6	4.0	0.02	6
C1_10	4.0	0.02	10

- sample A0_6: SiO_2 film deposited with 6 deposition sequences using 1 g diluted gel;
- sample A1_6: SiO_2 film deposited with 6 deposition sequences using mixture of 1 g diluted gel and 0.02 g DTAB.

Selective results considered to be most relevant for this study will be presented. High transmittance and low reflectance are a compulsory for coatings used in solar-thermal glazing. The Figs. 7 and 8 show that the transmittance and reflectance values vary with the depositions conditions and the additives addition. Consequently, in the case of 6 immersions without additive the sample containing 4 g of sol-gel has the best combination of optical properties (high transmittance/low reflection) and if the additive is used, the sample containing 2 g of gel has the best combination. Contrary, in the case of 10 immersions with DTAB the sample containing 4 g gel has better optical properties. However, comparing with all samples (with or without DTAB) the most favorable ratio between the transmittance and the reflectance values correspond to sample B1_6.

The antireflection properties can be explained by the double interface. In this case the presence of a thin film will generate two reflected waves which should be out of phase (they partially or totally cancel). If the coating is a quarter wavelength thicknesses and has a refractive index (1.503) lower than the glass index (1.518) in air, then both reflections are out of phase. Single layer anti-reflective coatings can lead to an increase of light transmittance consisting in about 5–7 % points, with a consequent increase in terms of thermal efficiencies.

This is a significant increase considering that the overall efficiency of a collector is about 65–85 %.

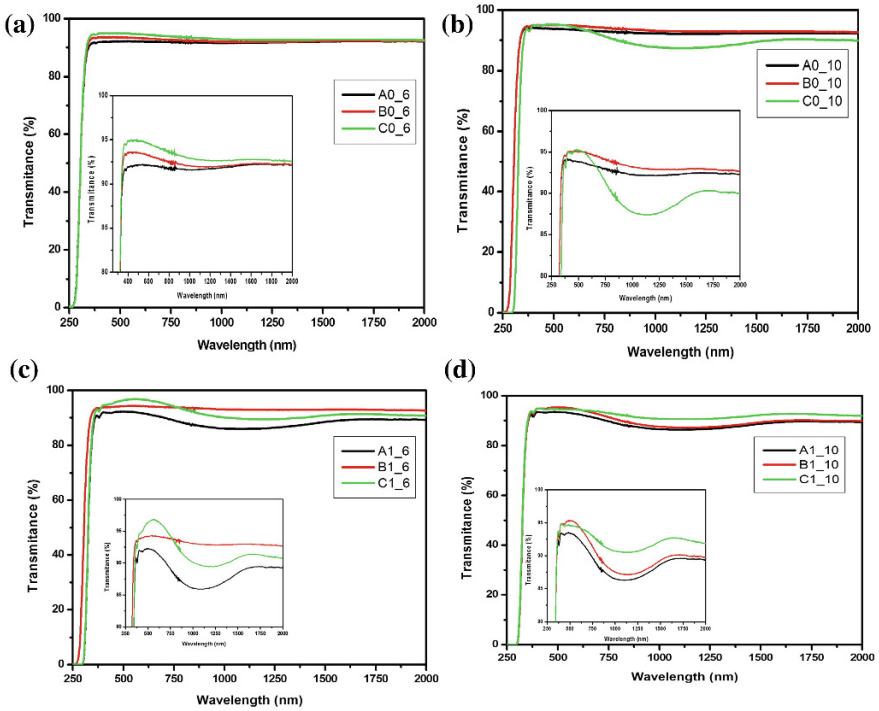

Fig. 7 Transmittance spectra for SiO_2 samples obtained by dip-coating: **a** 6 and **b** 10 immersions without DTAB; **c** 6 and **d** 10 immersions with DTAB

Considering the influence of additives on the optical properties it is important to investigate the morphology changes in the presence and in absence of DTAB. Atomic force microscopy (Fig. 9) has been used in the evaluation of coatings morphology for the samples which shows good optical properties. The roughness and the thickness values of the tested coatings are presented in Table 7.

The AFM shows that all samples have a dense morphology with grains between 20–50 nm. The highest roughness values correspond to the sample B0_10 obtained by 10 immersions without additive, while the use of DTAB increases the surface uniformity and homogeneity as result of the templating effect (re-organizing the active center on the surface). This allows the formation of uniform morphologies, without any cracks or defects which are considered the weak points of the antireflection coatings.

A second research direction of our group, following the concept of colored glazing, was focused on titanium dioxide thin films with colored reflections obtained by robotic spray pyrolysis deposition using titanium (IV) isopropoxide as precursor and air as a carrier gas [49]. Thin films with low roughness (<4.5 nm), high transparency (>70 %) in the UV–Vis–NIR region and hydrophilic properties were obtained. The optical properties, particularly transmittance are not influenced

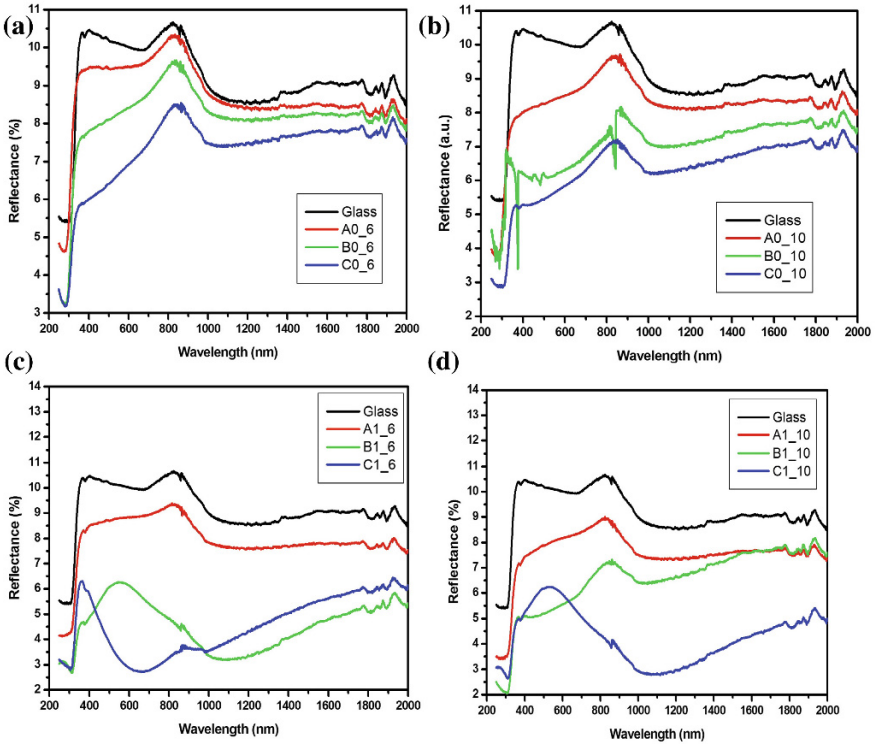

Fig. 8 Reflectance spectra for SiO_2 samples obtained by dip-coating: **a** 6 and **b** 10 immersions without DTAB; **c** 6 and **d** 10 immersions with DTAB

by humidity exposure. The films color depends on the number of deposition sequences (10, 20, 30 and 40) due to changes induced in thickness and surface topology. Colored TiO_2 films with different thickness shows a decrease of the visible transmittance compared to the glass substrate (as expected), but still convenient, above 80 %. All the samples have very low diffuse reflectance (<2 %), matching the requirements for quality glazing. The surface roughness is also expected to be reduced.

The number of the interference fringes is increasing with the number of deposition sequences, influencing the films' color. Consequently the thin films growth respects with Frank van der Merwe mechanism involved in the formation of the TiO_2 layers deposited with 20 and 30 spraying sequences. Thus, TSSS layers with shades varying from light blue to light violet were obtained. Green or brownish apparent colors could be further obtained by combining the TiO_2 layers with cobalt oxides, while colors ranging from orange to red were obtained by combining TiO_2 with iron oxide(s), without significant transmittance loss.

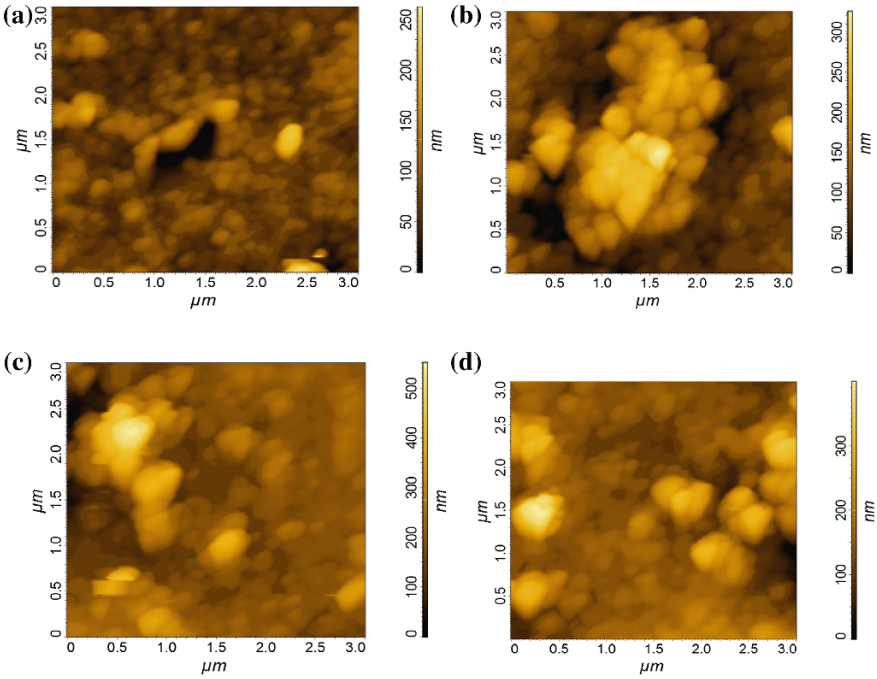

Fig. 9 AFM 2D morphology for: **a** C0_6, **b** B1_6, **c** B0_10 and **d** C1_10

Table 7 Roughness and thickness values

Sample name	Roughness (nm)	Thickness (nm)
B0_10	40.7	182.1
C0_6	28.0	510.8
B1_6	38.5	178.6
C1_10	39.5	547.2

5 Conclusions

The research on solar-thermal flat plate collectors is nowadays focusing on the increase of the efficiency, durability, affordability and acceptance for integration in the built environment. Thus, flat plate solar-thermal collectors, differently colored than the traditional black or dark blue, need to be developed and represent a topic much investigated. A review of the best solutions reported for colored solar thermal flat plate collectors obtained world-wide is presented, along with the results obtained by the group active in the R&D Centre Renewable Energy Systems and Recycling. There are reviewed the steps followed in optimizing the substrate, the red spectral selective coatings, the anti-reflection coating for developing the

absorber plate; further on the versatility of the glazing coatings is outlined, as anti-reflexive coating and as colored component.

These results were obtained by spray pyrolysis deposition and represent a promising input for novel, market-acceptable flat plate solar-thermal collectors, with increased architectural acceptance, for facades integration in Nearly Zero Energy Buildings.

Acknowledgments We hereby acknowledge the structural founds project PRO-DD (POS-CCE, O.2.2.1., ID 123, SMIS 2637, No 11/2009) for providing the infrastructure used in this work and the project EST IN URBA, PN-II-PT-PCCA-2011-3.2-051, in the frame of the Program: Cooperation in Priority Fields—PNII, developed with the support of ANCS, CNDI-UEFISCDI, Romania.

References

1. Barshilia, H. C., Kumar, P., Rajam, K. S., & Biswas, A. (2011). Structure and optical properties of Ag–Al_2O_3 nanocermet solar selective coatings prepared using unbalanced magnetron sputtering. *Solar Energy Materials and Solar Cells*, *95*, 1707–1715.
2. Kalogirou, S. A. (2004). Solar thermal collectors and applications. *Progress in Energy and Combustion Science*, *30*, 231–295.
3. Céspedes, E., Wirz, M., Sánchez-García, J. A., Alvarez-Fraga, L., Escobar-Galindo, R., & Prieto, C. (2014). Novel Mo–Si_3N_4 based selective coating for high temperature concentrating solar power applications. *Solar Energy Materials and Solar Cells*, *122*, 217–225.
4. Zhu, D., & Zhao, S. (2010). Chromaticity and optical properties of colored and black solar–thermal absorbing coatings. *Solar Energy Materials and Solar Cells*, *94*, 1630–1635.
5. Duta, A., Isac, L., Milea, A., Ienei, E., & Perniu, D. (2014). Coloured solar-thermal absorbers —a comparative analysis of cermet structures. *Energy Procedia*, *48*, 543–553.
6. Boström, T. K., Wäckelgård, E., & Westin, G. (2005). Durability tests of solution-chemically derived spectrally selective absorbers. *Solar Energy Materials and Solar Cells*, *89*, 197–207.
7. Wijewardane, S., & Goswami, D. Y. (2012). A review on surface control of thermal radiation by paints and coating for new energy applications. *Renewable and Sustainable Energy Reviews*, *16*, 1863–1873.
8. Oelhafen, P., & Schüler, A. (2005). Nanostructured materials for solar energy conversion. *Solar Energy*, *79*, 110–121.
9. Selvakumar, N., & Barshilia, H.C. (2012). Review of physical vapor deposited (PVD) spectrally selective coatings for mid- and high-temperature solar thermal applications. *Solar Energy Materials and Solar Cells*, *98*, 1–23.
10. Wu, L., Gao, J., Liu, Z., Liang, L., Xia, F., & Cao, H. (2013). Thermal aging characteristics of $CrNi_xO_y$ solar selective absorber coating for flat plate solar thermal collector applications. *Solar Energy Materials and Solar Cells*, *114*, 186–191.
11. Li, Z., Zhao, J., & Ren, L. (2012). Aqueous solution-chemical derived Ni–Al_2O_3 solar selective absorbing coatings. *Solar Energy Materials and Solar Cells*, *105*, 90–95.
12. Selvakumar, N., Santhoshkumar, S., Basu, S., Biswas, A., & Barshilia, H. C. (2013). Spectrally selective CrMoN/CrON tandem absorber for mid-temperature solar thermal applications. *Solar Energy Materials and Solar Cells*, *109*, 97–103.
13. Granqvist, C. G. (2003). Solar energy materials. *Advanced Materials*, *15*, 1789–1803.
14. Ding, D., Cai, W., Long, M., Wu, H., & Wu, Y. (2010). Optical, structural and thermal characteristics of Cu–$CuAl_2O_4$ hybrids deposited in anodic aluminum oxide as selective solar absorber. *Solar Energy Materials and Solar Cells*, *94*(10), 1578–1581.

15. Orel, B., Spreizer, H., Slemenik Perše, L., Fir, M., Sûrca Vuk, A., & Merlini, D. (2007). Silicone-based thickness insensitive spectrally selective (TISS) paints as selective paint coatings for coloured solar absorbers (part I). *Solar Energy Materials and Solar Cells*, *91*, 93–107.
16. Orel, B., Spreizer, H., Sûrca Vuk, A., Fir, M., Merlini, D., & Vodlan, M. (2007). Selective paint coatings for coloured solar absorbers: Polyurethane thickness insensitive spectrally selective (TISS) paints (part II). *Solar Energy Materials and Solar Cells*, *91*, 108–119.
17. Kunič, R., Kozelj, M., Orel, B., Sûrca Vuk, A., Vilčnik, A., & Slemenik Perše, L. (2009). Adhesion and thermal stability of thickness insensitive spectrally selective (TISS) polyurethane-based paint coatings on copper substrates. *Solar Energy Materials and Solar Cells*, *93*, 630–640.
18. Purghel, E., Voinea, M., Isac, L., & Duta, A. (2008). Optical properties of Ni/NiO_x as infiltration agent in cermet solar Ir absorber. *Revista de Chimie, 59*, 469–471.
19. Dudita, M., Isac, L., & Duta, A. (2012). Influence of solvents on properties of solar selective coatings obtained by spray pyrolysis. *Bulletin of Materials Science*, *35*, 997–1002.
20. Wazwaz, A., & Al-Salaymeh, A. (2013). Photothermal testing before and after degradation of nickel-pigmented aluminium oxide selective absorber prepared by alternate and reverse periodic plating technique. *Energy Conversion and Management*, *65*, 770–776.
21. Xue, Y., Wang, C., Wang, W., Liu, Y., Wu, Y., & Ning, Y. (2013). Spectral properties and thermal stability of solar selective absorbing $AlNi–Al_2O_3$ cermet coating. *Solar Energy*, *96*, 113–118.
22. Cheng, J., Wang, C., Wang, W., Du, X., Liu, Y., & Xue, Y. (2013). Improvement of thermal stability in the solar selective absorbing $Mo\text{-}Al_2O_3$ coating. *Solar Energy Materials and Solar Cells*, *109*, 204–208.
23. Boström, T. K., Westin, G., & Wäckelgård, E. (2007). Optimization of a solution-chemically derived solar absorbing spectrally selective surface. *Solar Energy Materials and Solar Cells*, *91*, 38–43.
24. Zhao, S., & Wäckelgård, E. (2006). Optimization of solar absorbing three-layer coatings. *Solar Energy Materials and Solar Cells*, *90*, 243–261.
25. Gaouyat, L., He, Z., Colomer, J. F., Lambin, Ph., Mirabella, F., & Schryvers, D. (2014). Revealing the innermost nanostructure of sputtered $NiCrO_x$ solar absorber cermets. *Solar Energy Materials and Solar Cells*, *122*, 303–308.
26. Kumar, S. K., Suresh, S., Murugesan, S., & Raj, S. P. (2013). CuO thin films made by nanofibers for solar selective absorber applications. *Solar Energy*, *94*, 299–304.
27. Voinea, M., Ienei, E., Bogatu, C., & Duta, A. (2009). Solar selective coatings based on nickel oxide obtained via spray pyrolysis. *Journal of Nanoscience and Nanotechnology*, *9*, 4279–4284.
28. Barshilia, H. C., Selvakumar, N., Rajam, K. S., & Biswas, A. (2008). Spectrally selective $NbAlN/NbAlON/Si_3N_4$ tandem absorber for high temperature solar applications. *Solar Energy Materials and Solar Cells*, *92*, 495–504.
29. Kumar, S. K., Murugesan, S., & Suresh, S. (2014). Preparation and characterization of CuO nanostructures on copper substrate as selective solar absorbers. *Materials Chemistry and Physics*, *143*, 1209–1214.
30. Katumba, G., Olumekor, L., Forbes, A., Makiwa, G., Mwakikunga, B., & Lu, J. (2008). Optical, thermal and structural characteristics of carbon nanoparticles embedded in ZnO and NiO as selective solar absorbers. *Solar Energy Materials and Solar Cells*, *92*, 1285–1292.
31. Joly, M., Antonetti, Y., Python, M., Gonzalez, M., Gascou, M., Scartezzini, J-L. (2013). Novel black selective coating for tubular solar absorbers based on a sol–gel method. *Solar Energy*, *94*, 233–239.
32. Selvakumar, N., Manikandanath, N. T., Biswas, A., & Barshilia, H. C. (2012). Design and fabrication of highly thermally stable $HfMoN/HfON/Al_2O_3$ tandem absorber for solar thermal power generation applications. *Solar Energy Materials and Solar Cells*, *102*, 86–92.
33. Tripanagnostopoulos, Y., Souliotis, M., & Nousia, Th. (2000). Solar collectors with colored absorbers. *Solar Energy*, *68*, 343–356.

34. Sun, X-Y., Sun, X-D., Li, X-G., Wang, Z-Q., He, J., & Wang, B-S. (2014) Performance and building integration of all-ceramic solar collectors. *Energy and Buildings*, *75*, 176–180.
35. Kalogirou, S., Tripanagnostopoulos, Y., & Souliotis, M. (2005). Performance of solar systems employing collectors with colored absorber. *Energy and Buildings*, *37*, 824–835.
36. Baneshi, M., Maruyama, S., & Komiya, A. (2011). Comparison between aesthetic and thermal performances of copper oxide and titanium dioxide nano-particulate coatings. *Journal of Quantitative Spectroscopy and Radiative Transfer*, *112*, 1197–1204.
37. Crnjak Orel, Z., Klanjšek Gunde, M., & Hutchins, M. G. (2005) Spectrally selective solar absorbers in different non-black colours. *Solar Energy Materials and Solar Cells*, *85*, 41–50.
38. Japelj, B., Sûrca Vuk, A.,Vilčnik, A., Orel, B., Slemenik Perše, L., & Jerman, I. (2008). Preparation of a TiMEMO nanocomposite by the sol–gel method and its application in coloured thickness insensitive spectrally selective (TISS) coatings. *Solar Energy Materials and Solar Cells*, *92*, 1149–1161.
39. Wu, Y., Zheng, W., Lin, L., Qu, Y., & Lai, F. (2013). Colored solar selective absorbing coatings with metal Ti and dielectric AlN multilayer structure. *Solar Energy Materials and Solar Cells*, *115*, 145–150.
40. Mihaly, M., Fleancu, M. C., Olteanu, N. L., Bojin, D., Meghea, A., & Enachescu, M. (2012). Synthesis of gold nanoparticles by microemulsion assisted photoreduction method. *Comptes Rendus Chimie*, *15*, 1012–1021.
41. Mertina, S., Hody-Le Caër, V., Joly, M., Mack, I., Oelhafen, P., & Scartezzini, J. L. (2014). Reactively sputtered coatings on architectural glazing for coloured active solar thermal facades. *Energy and Buildings*, *68*, 764–770.
42. Cannavale, A., Fiorito, F., Manca, M., Tortorici, G., Cingolani, R., & Gigli, G. (2010). Multifunctional bioinspired sol–gel coatings for architectural glasses. *Building and Environment*, *45*, 1233–1243.
43. Borge-Diez, D., Colmenar-Santos, A., Pérez-Molina, C., & Castro-Gil, M. (2013). Passive climatization using a cool roof and natural ventilation for internally displaced persons in hot climates: Case study for Haiti. *Building and Environment*, *59*, 116–126.
44. Arnaud, A. (1997). Industrial production of coated glass: Future trend for expanding needs. *Journal of Non-crystalline Solids*, *218*, 12–18.
45. Dong, Z. B., Lu, Y. F., Gao, K., Shi, L. Q., Sun, J., & Xu, N. (2008). Thermal stability of carbon nitride thin films prepared by electron cyclotron resonance plasma assisted pulsed laser deposition. *Thin Solid Films*, *516*, 8594–8598.
46. Zuo, J., Keil, P., & Grundmeier, G. (2012). Synthesis and characterization of photochromic Ag-embedded TiO_2 nanocomposite thin films by non-reactive RF-magnetron sputter deposition. *Applied Surface Science*, *258*, 7231–7237.
47. Jäger, T., Bissig, B., Döbeli, M., Tiwari, A. N., & Romanyu, Y. E. (2014). Thin films of SnO_2: F by reactive magnetron sputtering with rapid thermal post-annealing. *Thin Solid Films*, *553*, 21–25.
48. Amoruso, S., Nedyalkov, N. N., Wang, X., Ausanio, G., Bruzzese, R., & Atanasov, P. A. (2014). Ultrashort-pulse laser ablation of gold thin film targets: Theory and experiment. *Thin Solid Films*, *550*, 190–198.
49. Dudita, M., Manceriu, L. M., Anastasescu, M., Nicolescu, M., Gartner, M., & Duta, A. (2014). Coloured TiO_2 based glazing obtained by spray pyrolysis for solar thermal applications. *Ceramics International*, *40*, 3903–3911.

Working Fluids for Organic Rankine Cycles Comparative Studies

Mahdi Hatf Kadhum Aboaltabooq, Horatiu Pop, Viorel Bădescu, Valentin Apostol, Cristian Petcu and Mălina Prisecaru

Abstract The paper presents a comparison between working fluids selection using energy and exergy analysis to recover waste heat from Diesel engine (DE). This study involves the use of a 40 kW Diesel engine with basic configuration for Organic Rankine Cycle (ORC). The independent parameters are the turbine inlet temperature, working fluid type and exhaust gases mass flow rates and temperature. A comparison of results for nine working fluids is showed in this paper. To know what is the best choice of working fluid for ORC is not an easy process; there are many different criteria to deal with. These criteria mainly has to do with working fluids thermodynamic and heat transfer properties from a side and safety and environmental aspects from other side. The process needs building thermodynamic models and running numerical calculations

M.H.K. Aboaltabooq (✉) · H. Pop · V. Bădescu · V. Apostol · M. Prisecaru
University Politehnica of Bucharest, Splaiul Independenţei 313,
Bucharest 060042, Romania
e-mail: hatfmahdi@yahoo.com

H. Pop
e-mail: pophoratiu2001@yahoo.com

V. Bădescu
e-mail: badescu@theta.termo.pub.ro

V. Apostol
e-mail: apostol.crvprofesional@gmail.com

M. Prisecaru
e-mail: malina_prisecaru@yahoo.com

M.H.K. Aboaltabooq
Technical College Najaf, Foundation of Technical Education,
Najaf, Iraq

C. Petcu
Rokura Company, Bucharest, Romania
e-mail: crispet@gmail.com

I. Visa (ed.), *Sustainable Energy in the Built Environment - Steps Towards nZEB*,
Springer Proceedings in Energy, DOI 10.1007/978-3-319-09707-7_22

in Engineering Equation Solver program (EES).The performance of the ORC system including the first and second law efficiencies is showed under different operating loads (50, 75 and 100 %). Some of the results demonstrate that ORC using Ethanol shows the maximum efficiency and maximum turbine work whereas those using R245fa shows the worst efficiency and turbine work among selection of organic fluids but the first favorite choice is R123 and the second favorite is divided between R245fa and R141b. Therefore, chosen of the working fluid do not depend on just the maximum turbine work and thermal efficiency but depends on the other important factors such as safety, Ozone Depletion Potential (ODP) and Global Warming Potential (GWP).

Keywords Waste heat recovery · Organic rankine cycle · Working fluid

1 Introduction

There are many reasons to deal with waste heat as example the increasing in fuel consumption for all the world in recent years, the increasing of fuel price and the high percentage losses of waste heat as seen in factories, steam and gas power stations, and internal combustion engines. It is interesting to recover this waste energy and converted back into useful energy. Waste heat recovery system is the best way to recover energy and save fuel. Organic Rankine cycle systems is one of many ways to recover waste heat but is the best. Many studies analyzing the ORC performances have been conducted recently [1–7]. In this paper the mathematical model of ORC combined with DE in steady state condition under different loads is developed to make comparison between nine working fluids. The turbine work, the thermal efficiency and exergy efficiency of organic Rankine cycle as well as the total irreversibility for the system are taken in consideration.

2 System Description

2.1 Diesel Engine Description

In this study, a 40 kW diesel generator is considered as a heat source. The specifications of diesel engine are: 3.3 L (0.83 L/cylinder), compression ignition, four-cylinder engine and engine speed about 1,500 rpm. The studies are performed with different engine loads (50, 75 and 100 %). The first important parameter in the engine is the temperature of exhaust gases which is measured after supercharger with values between 170 and 480 °C depending on the load and the second parameter is water jacket temperature outlet which is between 71 and 74 °C while water jacket temperature inlet 33–54 °C for different loads (50–100 %). The two major primary sources of waste heat from internal combustion engine (ICE) are the exhaust gases (medium-grade) and engine coolant (low-grade) [8].

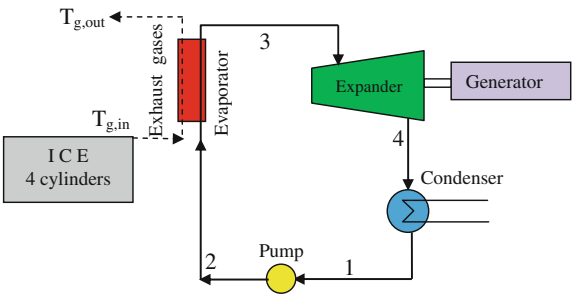

Fig. 1 Basic ORC system combined with the ICE

2.2 Organic Rankine Cycle Description

As shown in Fig. 1, the ORC heat recovery power plant used in this paper is composed of an expander, a condenser, an evaporator, a working fluid pump and other auxiliary equipment. The waste heat from internal combustion engine is pumped into evaporator (process 2–3) where refrigerant is evaporated, then delivered to expander inlet (process 3–4).The refrigerant drives the expander to generate electricity along with pressure and temperature decreasing. The low pressure and temperature refrigerant is cooled to refrigerant liquid when passing through the condenser (process 4–1) and collected into a receiver. The working fluid pump lefts the liquid refrigerant back into evaporator (process 1–2) to absorb the heat again then the above process repeats.

3 Mathematical Modeling

To develop the mathematical model for this system some simplifications are assumed and formulated as follows:

(1) Steady-state and steady-flow condition.
(2) No pressure drop in heat exchangers and connecting pipes.
(3) The external heat loss from pipes and equipment are negligible.
(4) The expander and pump efficiency are 90 % [9–11].
(5) Ambient temperature (t_o) is 22 °C.
(6) Flue gas mass flow rate is 192.6, 177.8, 171 kg/h for 100, 75 and 50 % load respectively, from experimental work [8].
(7) Exhaust gas temperature after evaporator is 140 °C for different loads [12].

3.1 Process 1–2 (Across Pump)

The working fluid leaves the condenser as saturated liquid and then it is pumped from point (1) to point (2s) theoretically isentropic process while in a real process to point (2r) as shown in Fig. 2. The pump power can be expressed as [13]:

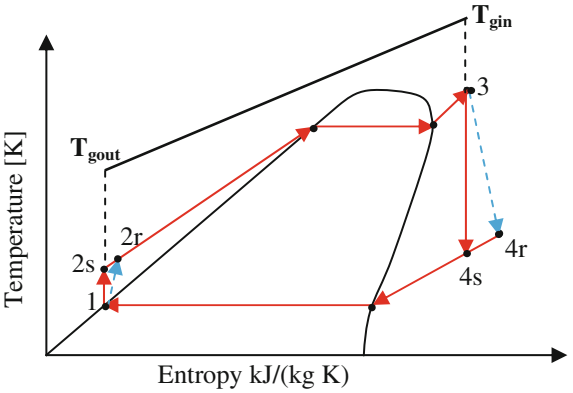

Fig. 2 T-S diagram of the ORC system

$$\dot{W}_{P,actual} = \frac{\dot{W}_{P,ideal}}{\eta_P} = \frac{\dot{m}_{ref}(h_1 - h_{2s})}{\eta_P} = \dot{m}_{ref}(h_1 - h_{2r}) \quad (1)$$

where $W_{p,\ ideal}$ is the ideal power of the pump, $\dot{m}_{ref}$ the working fluid mass flow rate, η_p is the isentropic efficiency of the pump, h_1 enthalpy of the working fluid at the inlet and h_{2s} and h_{2r} the ideal and real enthalpies of the working fluid at the outlet of the pump, respectively, for the ideal case. Enthalpy at point (1) is determined depending on ambient temperature and pressure by EES program. The irreversibility rate for pump can be expressed as [13]:

$$\dot{I}_p = \dot{m}_{ref} T_o[(s_{2r} - s_1)] \quad (2)$$

where s_1 and s_{2r} are the specific entropies of the working fluid at the inlet and exit of the pump for the actual conditions, respectively, T_o is the ambient temperature in kelvin scale.

3.2 Process 2–3 (Across Evaporator)

The amount of heat, which is used in working fluid evaporation in the evaporator is taken from of the heat in the exhaust gases, of course not all the heat which the exhaust gases carry is transfer to the evaporator, therefore part of this heat can be transfer to the evaporator for evaporate the working fluid. This value of heat is equal to the heat addition to the evaporator. From the above clarification previously can be use the following equation to calculate the heat source:

$$\dot{Q}_g = \dot{m}_g\ c_{p,g}(T_{g,in} - T_{g,out}) = \dot{m}_{ref}(h_{out}\ -\ h_{in}) = \dot{m}_{ref}(h_3\ -\ h_{2r}) \quad (3)$$

where $\dot{m}_g$ is the exhaust gas mass flow rate (kg/s) and $c_{p,g}$ is specific heat of exhaust gas (kJ/kg K), $T_{g,in}$, $T_{g,out}$ are the exhaust gas temperature at inlet to the evaporator and outlet from evaporator, h_3 is the enthalpy of the fluid at inlet to the expander.

Typically, the exhaust temperature is between 170 and 480 °C depending on the load, and the exhaust pressure is slightly higher than atmospheric pressure. Therefore, the exhaust gas can be treated as a mixture of ideal gases [14]. Thus, the specific heat of the exhaust gas can be calculated as:

$$c_{p,g} = \sum_{i=1}^{4} g_i \; c_{Pi} \tag{4}$$

where g_i is the percentage volume of flue gas component and c_{pi} is the specific heat of flue gas component (kJ/kg K).

The main components in the exhaust gas of a diesel engine are CO_2, H_2O, N_2, and O_2. Moreover, the mass fractions of these components vary with the engine operating condition [15]. So, the percentage volume of components for flue gases theoretically as follow: g_{co_2} 15.1 %, g_{H2_O} 5.5 %, g_{N_2} 71.6 % and g_{O_2} 7.8 % [16].

When calculate the specific heat at constant pressure of exhaust gases for evaporator as a whole can be use the medium temperature (T_m) as shown in the following equation:

$$T_m = \frac{T_{g,in} + T_{g,out}}{2} \tag{5}$$

The enthalpies of refrigerant on the inlet to evaporator (point 2r) and outlet from evaporator (point 3) depend on the properties of working fluid and can be calculated by using the EES program. With some changes at Eq. (3), the refrigerant mass flow rate can be calculated as:

$$\dot{m}_{ref} = \frac{\dot{Q}_g}{h_3 - h_{2r}} \tag{6}$$

To determine the exergy destruction rate in the evaporator as shown in Eq. (7):

$$\dot{I}_e = \dot{m}_{ref} T_o \left[(s_3 - s_{2r}) - \frac{h_3 - h_{2r}}{T_H} \right] \tag{7}$$

where s_3 and s_{2r} are the actual specific entropies of the working fluid at the inlet and exit of the evaporator, respectively. In order to transfer heat to the working fluid a temperature differential ΔT_H exists such that, $T_H = T_3 + \Delta T_H$.

3.3 Process 3–4 (A Cross Turbine)

This is an expansion process and the absorbed energy at the evaporator is converted to useful mechanical work by an expander or a turbine. The turbine power is given by Eq. (8) [4, 17]:

$$\dot{W}_t = \dot{W}_{t,ideal}\eta_t = \dot{m}_{ref}\ (h_3 - h_{4s})\eta_t = \dot{m}_{ref}\ (h_3 - h_{4r}) \tag{8}$$

where $W_{t,ideal}$ is the ideal power of the turbine, η_t the turbine isentropic efficiency, h_{4s} and h_{4r} the isentropic and real enthalpies of the fluid at the turbine outlet. To calculate the exergy destruction rate in the turbine can be expressed as Eq. (9) [4]:

$$\dot{I}_t = \dot{m}_{ref} T_o (s_{4r} - s_3) \tag{9}$$

where s_3 and s_{4r} are the specific entropies of the working fluid at the inlet and exit of the turbine for the actual conditions, respectively.

3.4 Process 4–1 (Across Condenser)

In this process the heat is rejected in condenser in order to condensate the working fluid and re-circulates it in the cycle. The heat rejection process is considered to be isobaric process. The heat transfer equation for this condition is given by Eq. (10):

$$\dot{Q}_{Rej} = \dot{m}_{ref}(h_1 - h_{4r}) \tag{10}$$

where h_1 and h_{4r} are the actual enthalpies of the working fluid at the outlet and inlet of the condenser, respectively. Assuming that the temperature difference between the fluid and the condenser is ΔT and $T_L = T_1 - \Delta T$. Then, the exergy destruction rate in this process is [4, 17]:

$$\dot{I}_c = \dot{m}_{ref} T_o \left[(s_1 - s_{4r}) - \frac{h_1 - h_{4r}}{T_L} \right] \tag{11}$$

where s_1 and s_{4r} are the actual specific entropies of the working fluid at the inlet and outlet of the condenser, respectively. Combining Eqs. (2), (7), (9) and (11) the total exergy destruction rate of the cycle can be obtained by Eq. (12 or 13) [4, 17]:

$$\dot{I}_{Total} = \dot{I}_p + \dot{I}_e + \dot{I}_t + \dot{I}_c \tag{12}$$

$$\dot{I}_{Total} = \dot{m}_{ref}\ T_o \left[-\frac{h_3 - h_{2r}}{T_H} - \frac{h_1 - h_{4r}}{T_L} \right] \tag{13}$$

The exergy efficiency (the second law efficiency) is defined by the ratio of the turbine output power to the summation of the turbine output power and the total exergy of destruction rate of the cycle, and it is shown by Eq. (14) [4, 17]:

$$\eta_{ex} = \frac{\dot{W}_t}{\dot{W}_t + \dot{I}_{Total}} \tag{14}$$

Availability ratio (Φ) is the ratio of the available energy to the total energy obtained from the thermal source, and is expressed as [17]:

$$\Phi = \frac{\dot{Q}_g - \dot{I}_{Total}}{\dot{Q}_g} \tag{15}$$

Finally the thermal efficiency, defined as the ratio between the net power of the cycle to the heat addition, can be expressed as:

$$\eta_{th} = \frac{\dot{W}_n}{\dot{Q}_g} = \frac{\dot{W}_t - \dot{W}_p}{\dot{Q}_g} \tag{16}$$

Thermal efficiency increases as turbine work increases and pump of work decreases according to the Eq. (16).

3.5 Selection of Working Fluids in Organic Rankine Cycle

Many of scientific publications deals with selection of working fluids [18–24]. Choosing the best working fluid used in ORC depends on many factors therefore is not an easy task.

The following criteria should be taken in consideration in order to figure out the best candidates as shown in Fig. 3.

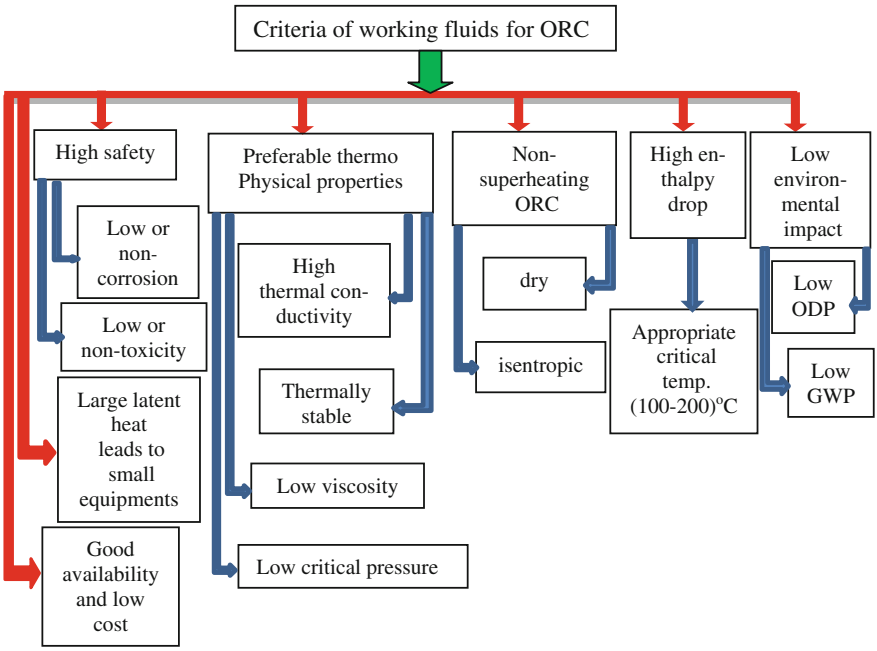

Fig. 3 Selection criteria of organic working fluid using in ORC

Table 1 Characteristic parameters to choice of working fluid

N	Fluid (%)	GWP	ODP	W_{max} kW	η_{th} (%)	η_{ex} (%)	I	Safety	Points
1	R245fa								
	100	**1030[4]**	**0[5]**	**3.743[2]**	**17.26[2]**	**57.53**	**2.763**	**Non-F[5]**	**18**
	75			**2.77**	**17.26**	**57.53**	**2.045**		
	50			**1.9**	**17.26**	**57.53**	**1.402**		
2	R113								
	100	6,000[2]	0.8[1]	3.864[3]	18.9[3]	61.33	2.436	Non-F[5]	14
	75			2.859	18.9	61.33	1.803		
	50			1.961	18.9	61.33	1.236		
3	R123								
	100	*77[5]*	*0.02[4]*	*3.964[4]*	*19.25[4]*	*62.64*	*2.364*	*Non-F[5]*	22
	75			*2.934*	*19.25*	*62.64*	*1.749*		
	50			*2.012*	*19.25*	*62.64*	*1.2*		
4	R601								
	100	11[5]	0[5]	3.766[2]	18.39[3]	59.75	2.537	F[1]	16
	75			2.787	18.39	59.75	1.877		
	50			1.911	18.39	59.75	1.287		
5	Butane								
	100	20**[5]**	0**[5]**	3.843**[3]**	18.06**[3]**	59.61	2.604	F**[1]**	17
	75			2.844	18.06	59.61	1.927		
	50			1.95	18.06	59.61	1.321		
6	Ethanol								
	100	n. a	n. a	4.393[5]	21.86[5]	70.44	1.844	F[1]	11
	75			3.251	21.86	70.44	1.364		
	50			2.23	21.86	70.44	0.9357		
7	R141b								
	100	**725[4]**	**0.12[1]**	**4.074[4]**	**19.77[4]**	**64.31**	**2.261**	**Non-F[5]**	**18**
	75			**3.015**	**19.77**	**64.31**	**1.673**		
	50			**2.067**	**19.77**	**64.31**	**1.147**		
8	n-hexane								
	100	n. a	n. a	3.705[1]	18.53[3]	59.86	2.51	F[1]	4
	75			2.769	18.53	59.86	1.857		
	50			1.899	18.53	59.86	1.274		
9	Toluene								
	100	n. a	n. a	4.23[5]	20.44[5]	66.55	2.126	F[1]	11
	75			3.13	20.44	66.55	1.573		
	50			2.147	20.44	66.55	1.079		

First favorite: *bold value*; Second favorite: *italic value*; Non-F: non-flammable; F: Flammable; η_{ex} : exergy efficiency; η_{th}: thermal efficiency; I: irreversibility; W_{max}: maximum net work; n. a: not applicable (no rank due to no reference yet) (1)–(5): represent the increasing of rank from poor (min.) to rich (max.)

4 Results and Discussion

The proposed mathematical modeling in this paper is solved using EES program [25] which includes thermodynamic properties for a large number of natural and manufactured fluids to show the comparison between fluids under different operating loads in steady state condition. Table 1 is constructed under the following conditions: evaporation temperature (t_{ev}) is 145 °C, ambient temperature (t_o) is 22 °C, flue gas temperature at evaporator exhaust $T_{g,in}$ is 477, 403, 327 °C at 100, 70 load and 50 % load respectively, flue gas temperature at evaporator inlet ($T_{g,out}$) is 140 °C, pump efficiency (η_p) is 0.9, expander efficiency (η_{ex}) is 0.9, gas mass flow rate ($\dot{m}_g$) is 0.05352, 0.0494 and 0.0475 kg/s at 100, 70 and 50 % load respectively. Superheating degree (DS) is 10 °C.

In current study adopted methodology is used for selection working fluid. The method depend on the allocation rank for each important parameter and the parameters used are maximum turbine work, thermal efficiency, ODP, GWP and safety. Every parameter ranked between minimum value (1) to maximum value (5). Finally the points of the parameters are summed to give the rank of the working fluid selection.

From above methodology can be concluded that the best choice for working fluid in our case is R123 and the second rank is R245fa and R141b depending on the total points.

5 Conclusions

In this study, a mathematical model of ORC combined with ICE is presented and developed to compare nine working fluids depending on many of characteristic parameters such as maximum turbine work, thermal efficiency from side and environmental effects from another side such as safety, ODP and GWP by using measured data such as flue gas mass flow rate and flue gas temperature at evaporator inlet and outlet. The performance of the ORC is evaluated under different engine operation loads. Based on our analysis, the followings can be concluded:

(a) The results presented in this paper show the maximum turbine power and thermal efficiency for Ethanol and minimum turbine power for n-hexane but the first favorite choice is R123 and the second favorite is R245fa and R141b. Therefore the chose of working fluid do not depend on just the maximum turbine work and thermal efficiency but depends on the other important factors such as safety, ODP and GWP.
(b) Using the methodology to choice working fluid for ORC system is reasonable.
(c) The maximum turbine work is given by increasing the engine operating load.

In the future work could be use many of configurations for ORC to see the effect of configuration on the selection of working fluid.

Acknowledgments One of the authors (M. H. K. Aboaltabooq) acknowledges support from the Iraqi government through grant and the Romanian government through Research grant "Hybrid micro-cogeneration group of high efficiency equipped with an electronically assisted ORC", 1st Phase Report, 2nd National Plan, Grant Code: PN-II-PT-PCCA-2011-3.2-0059, Grant No.: 75/2012.

References

1. Kang, S. H. (2012). Design and experimental study of ORC (organic Rankine cycle) and radial turbine using R245fa working fluid. *Energy, 41*, 514–524.
2. He, C., Liu, C., Gao, H., Xie, H., Li, Y., Wu, S., et al. (2012). The optimal evaporation temperature and working fluids for subcritical organic Rankine cycle. *Energy, 38*, 136–143.
3. Sun, J., & Li, W. (2011). Operation optimization of an organic Rankine cycle (ORC) heat recovery power plant. *Applied Thermal Engineering, 31*, 2032–2041.
4. Wang, E. H., Zhang, H. G., Fan, B. Y., Ouyang, M. G., Zhao, Y., & Mu, Q. H. (2011). Study of working fluid selection of organic Rankine cycle (ORC) for engine waste heat recovery. *Energy, 36*, 3406–3418.
5. Rentizelas, A., Karellas, S., Kakaras, E., & Tatsiopoulos, I. (2009). Comparative technoeconomic analysis of ORC and gasification for bioenergy applications. *Energy Conversion and Management, 50*, 674–681.
6. Gewald, D., Karellas, S., Schuster, A., & Spliethoff, H. (2012). Integrated system approach for increase of engine combined cycle efficiency. *Energy Conversion and Management, 60*, 36–44.
7. Vélez, F., Chejne, F., Antolin, G., & Quijano, A. (2012). Theoretical analysis of a transcritical power cycle for power generation from waste energy at low temperature heat source. *Energy Conversion and Management, 60*, 188–195.
8. Research Grant. (2012). *Hybrid micro-cogeneration group of high efficiency equipped with an electronically assisted ORC*, 1st Phase Report, 2nd National Plan, Grant Code: PN-II-PT-PCCA-2011-3.2-0059, Grant No.: 75/2012.
9. Meinel, D., Wieland, C., & Spliethoff, H. (2014). Effect and comparison of different working fluids on a two-stage organic Rankine cycle (ORC) concept. *Applied Thermal Engineering, 63*, 246–253.
10. Bao, J., & Zhao, L. (2013). A review of working fluid and expander selections for organic Rankine cycle. *Renewable and Sustainable Energy Reviews, 24*, 325–342.
11. Fu, B. R. & Liu, C. H. (2014). *Performance of a 250 kW organic rankine cycle system for off-design heat source conditions*, *1st International E-Conference on Energies* (pp. 14–31).
12. Panoiu, N. (Ed.). (1982). *Cazane de abur.* Bucuresti: Didactica si pedagogica.
13. Mago, P. J., Chamra, L. M., & Somayaji, C. (2007). Performance analysis of different working fluids for use in organic Rankine cycles. *Proceedings of the Institution of Mechanical Engineers, Part A: Journal of Power and Energy*, *221*(3), 255–263.
14. Cengel, Y. A, Boles, M. A. (2008). *Thermodynamics an engineering approach* (pp. 681–709, 6th ed.). London: McGraw-Hill.
15. Zhang, H. G., Wang, E. H., & Fan, B. Y. (2013). Heat transfer analysis of a finned-tube evaporator for engine exhaust heat recovery. *Energy Conversion and Management, 65*, 438–447.
16. Yu, G., Shu, G., Tian, H., Wei, H., & Liu, L. (2013). Simulation and thermodynamic analysis of a bottoming Organic Rankine Cycle (ORC) of diesel engine (DE). *Energy, 51*, 281–290.
17. Roy, J. P., et al. (2011). Performance analysis of an organic rankine cycle with superheating under different heat source temperature conditions. *Applied Energy, 88*(9), 2995–3004.
18. Badr, O., et al. (1990). Rankine-cycle systems for harnessing power from low-grade energy sources. *Applied Energy, 36*(4), 263–292.

19. Liu, B., Chien, K., & Wang, C. (2004). Effect of working fluids on organic rankine cycle for waste heat recovery. *Energy, 29*, 1207–1217.
20. Mago, P., et al. (2008). An examination of regenerative organic Rankine cycles using dry fluids. *Applied Thermal Engineering, 28*, 998–1007.
21. Facão, J., & Palmero, A. (2009). Oliveira A. Analysis of a solar assisted micro cogeneration ORC system. *International Journal of Low Carbon Technologies, 3*(4), 254–264.
22. Tchanche, B., et al. (2009). Fluid selection for a low-temperature solar organic Rankine cycle. *Applied Thermal Engineering, 29*, 2468–2476.
23. Dai, Y., et al. (2009). Parametric optimization and comparative study of organic Rankine cycle (ORC) for low grade waste heat recovery. *Energy Conversion and Management, 50*, 576–582.
24. Guoquan, Q. (2012). Selection of working fluids for micro-CHP systems with ORC. *Renewable Energy, 48*, 565–570.
25. http://www.fchart.com/ees/

Tunning the Colour of Solar Absorbers by Changing Chromophore Nature and Nanoparticle Size

Maria Mihaly, Elena Adina Rogozea, Nicoleta Liliana Olteanu, Adina Roxana Petcu, Cosmina Andreea Lazar and Aurelia Meghea

Abstract In this paper some metallic (Au) and oxide (NiO and Cr_2O_3) nanoparticle dispersions are proposed as optical enhancers for solar collectors. The metallic nanoparticles are synthesised by photoreduction technique whereas the oxide nanoparticles are obtained by precipitation method, their shape and size being confined in a template of water-in-oil microemulsion. By using the mentioned template, monodispersed nanoparticles could be prepared, which have been further characterized by dynamic light scattering, transmission electron microscopy, diffuse reflectance spectroscopy and chromatic analysis. Correlation of these results is useful to obtain criteria for the design of Au or metallic oxides nanoparticles based solar absorbers.

Keywords Metallic and oxide nanoparticles · Solar absorbers · Size tunning · Colour analysis

1 Introduction

Nanoparticles have become the subject of intensive research because of their scientific and technological importance [1]. As a result of their unique optical, electronic, catalytic and magnetic properties, compared with the corresponding bulk materials, the number of potential applications of these colloidal particles is growing rapidly [2]. Nanoparticles are employed in many fields such as energy science, biotechnology, industry, catalysts, optics, life sciences, pharmacy, medicine, mechanics and magnetism [3–5].

Due to their special properties, synthesis of nanoparticles with specific compositions, sizes, shapes and controlled dispersion is very important for their

M. Mihaly · E.A. Rogozea · N.L. Olteanu · A.R. Petcu · C.A. Lazar · A. Meghea (✉)
Research Centre for Environmental Protection and Eco-friendly Technologies, University Politehnica of Bucharest, Polizu 1, 011061 Bucharest, Romania
e-mail: a.meghea@gmail.com

I. Visa (ed.), *Sustainable Energy in the Built Environment - Steps Towards nZEB*, Springer Proceedings in Energy, DOI 10.1007/978-3-319-09707-7_23

applications in energy. In general a selective solar absorber is based on the deposition of metal particles into a porous substrate, such as anodic aluminium. The porous alumina provides an ideal dielectric matrix for the nano-sized metal particles, which provides a major absorption in the solar region. The nickel pigmented aluminium oxide solar absorber was first documented by Andersson et al. [6]. It has a good optical performance (solar absorbance, $\alpha = 0.95$ and thermal emittance, $\varepsilon = 0.12–0.20$) but its service life time can be shortened by too high temperature, humidity or atmospheric pollution such as sulphur dioxide. Enhancement of solar radiation absorption using a nanoparticle suspension was also demonstrated [7]. A nanoparticle suspension, in which Ni nanoparticles having average diameter of 4.9 nm were dispersed with volume fraction of 0.001, was shown to have much higher absorption coefficient than the base fluid over visible and near-infrared wavelengths which are characteristic of solar radiation. At the same time, absorption coefficient of the suspension in the infrared region, which dominates thermal radiation emitted from the suspension, remains the same as one of the base fluid. Recently, Hirsch and colab [8] introduced nanoparticles in the structure of selective solar absorbers as nano-metal-ceramic (cermet) or metal-semiconductor composites types. NiO [9], Cr [10] or Co [11] pigmented porous alumina is a well-known selective absorber for its high absorbance and low emittance at temperatures below 100 °C. In the speciality literature were also reported different deposition materials from cermet class like: Pt-Al_2O_3 [12], Ni-Al_2O_3 [13], Mo-Al_2O_3 [14], W-AlN [15], Au-MgO [16], Cr-Cr_2O_3 [17, 18], Au-Al_2O_3, Ag-Al_2O_3 [19, 20], etc. Nano-cermet materials can be used in the conversion of solar energy because they absorb very well the solar radiation (usually in visible) due to their quantum confinement effect also known as surface plasmon resonance phenomenon (SPR) met in the collective oscillation of conduction electrons from noble nanoparticles (Ag and Au) incorporated in a dielectric matrix [21]. The matrices that were used for Ag are: SiO_2, ZnO, Bi_2O_3, DLC, Si_3N_4, BN, WO_{3-x}, Al_2O_3 [22–25]. The optical properties of nano-cermets are dependent of the size, concentration and distribution of the particles and the dielectric properties of the host matrix [21].

Solar collectors improved with metal nanoparticles, existent in present on the market, are restrictive as colours, only shades of black and grey. In this context, using Au or metallic oxides nanoparticles based solar absorbers might overcome this drawback leading to absorbent materials with diversified colours.

Therefore, in this paper some metallic (Au-MS) and oxide (NiO and Cr_2O_3) nanoparticles dispersions are proposed as optical enhancers for solar collectors as new solutions for improving the solar absorbers. The metallic nanoparticles are synthesised by photoreduction [26] whereas the oxide nanoparticles are obtained by precipitation method [27], their shape and size being confined in a template of water-in-oil microemulsion. By using the mentioned template, dispersed nanoparticles could be prepared. Tunning the nanoparticles size, the colour of solar collectors could be designed.

2 Results and Discussions

2.1 Materials

Hydrogen tetrachloroaurate ($HAuCl_4$), chromium nitrate (III) nonahydrate, n-heptane, cycloxexane, polyoxyethylene 4-lauryl ether (Brij 30), sodium 3-mercaptopropanesulfonate (MS) cysteamine hydrochloride (Cis), acetone were purchased from SIGMA–ALDRICH. Nickel(II)-nitrate-hexahydrate, ammonia solution 25 % (NH_4OH) were purchased from MERCK. All chemicals were of analytical grade and used without further purification. Ultra-pure water (Millipore Corporation) was used.

2.2 Synthesis

2.2.1 Metallic Nanoparticles

Au and Au functionalised with MS and Cis nanoparticles (Au, Au-MS, Au-Cis NP) were synthesized in a water-in-oil (water droplets dispersed in oil phase) microemulsion (μE) (Fig. 1). Their synthesis involves the preparation of the initial solutions, $HAuCl_4$ (1 g/L), MS/$HAuCl_4$ 0.05 M or Cis/$HAuCl_4$ 0.01 M at 25 °C

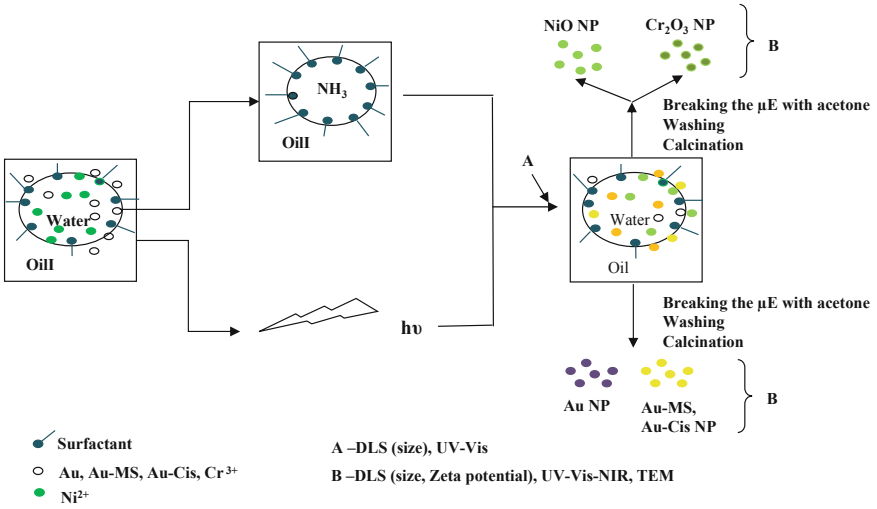

Fig. 1 Synthesis procedure of metallic and oxide nanoparticles

that were consequently stirred for 30 min. These solutions were then added in n-heptane (82.5 % (w/w)) and Brij30 (15 % (w/w)) to form a μE. UV irradiation was carried out in a photoreactor containing a medium-pressure UV lamp at 254 nm. After 3 h irradiation, the microemulsion turns from colourless to yellow or dark red indicating the formation of Au-MS, Au-Cis and Au NPs, respectively with specific sizes. The colour is defined by the nanoparticle size and shape. The resulted NPs were five times alternatively washed with acetone and ethanol in order to remove the oil, surfactant and excess of thiol compounds.

2.2.2 Oxide Nanoparticles

Oxide nanoparticles (NiO NP and Cr_2O_3 NP) were prepared by mixing two water-in-oil microemulsions. First μE contained Brij 30/organic phase/Ni^{2+} water solution and Brij 30/organic phase/Cr^{3+} water solution for NiO and Cr_2O_3 NP, respectively. The organic phase was represented by heptane or cyclohexane. The second μE was formed from Brij 30, an organic phase and an aqueous solution of NH_4OH. The two mixed μE, were stirred for 45 min at 25 °C and then the nanoparticles were recover after breaking the microemulsion with acetone. The nanoparticles were washed five times with acetone, dried at 25 °C and then calcined in static conditions at 550 °C for 5 h.

2.3 Instrumental Techniques

Size and zeta potential measurements were realised using Malvern Nanosizer equipment. Size was performed on both media, the microemulsion and the solid nanoparticles dispersed in water (0.01 g/L) whereas zeta potential was done only on the later. UV-Vis measurements and color analysis were performed using a Jasco V570 spectrophotometer. When the spectra of NiO and Cr_2O_3 NP, with different sizes, were recorded, the same quantity of solid materials was used. Morpho-structural characterization of Au-MS was carried out using transmission electron microscopy (TEM) Philips EM 410 and of NiO NPs with PHILIPS CM 120 ST HRTEM microscope equipped with a surface area electron diffraction system (HR-TEM-SAED operating at 200 kV). The pore structure of the materials was determined using nitrogen adsorption/desorption method, carried out on a Quantachrome instrument NOVA 2200e. Samples were degassed at 250 °C under a pressure of 0.334 MPa for 3 h in nitrogen atmosphere. The specific surface area was calculated by applying standard BET equation. The instrument error is ±5 %.

3 Results and Discussion

3.1 Nanoparticle Characterization

3.1.1 Metallic Nanoparticles

Size estimation of $HAuCl_4$-MS, dispersed in microemulsion, before irradiation, and of Au-MS NP, after irradiation, was obtained by DLS measurements. Inspecting Fig. 2 one can observe that the size of $HAuCl_4$-MS nanodroplets is around 6 nm. Au-MS NP's have a smaller size (5 nm) as, after the irradiation process Au^{3+} is reduced to Au^{o}. The size distribution exhibits a narrow peak due to the high degree of homogeneity, affirmation sustained by the small value of polidispersity index (0.125).

In order to confirm the size and morphology of Au-MS and Au-Cis NP's, TEM microscopy was realised on the nanoparticles in powder form. TEM images of functionalised Au NP are shown in Fig. 3 where one can see that the size of the nanoparticles is very small, 5 nm for Au-MS and 7 nm for Au-Cis, respectively. The nanoparticles have spherical shape and a high degree of homogeneity, in accordance with DLS measurements.

3.1.2 Oxide Nanoparticles

In Figs. 4 and 5 are shown the DLS spectra of $Ni(OH)_2$ and $Cr(OH)_3$ nanodroplets dispersed in water-in-oil microemulsion, respectively. Small sizes are obtained for these nanoparticles too, around 6.5 nm for $Ni(OH)_2$ and 8.5 nm for $Cr(OH)_3$. The high degree of homogeneity of these two systems was demonstrated by the narrow

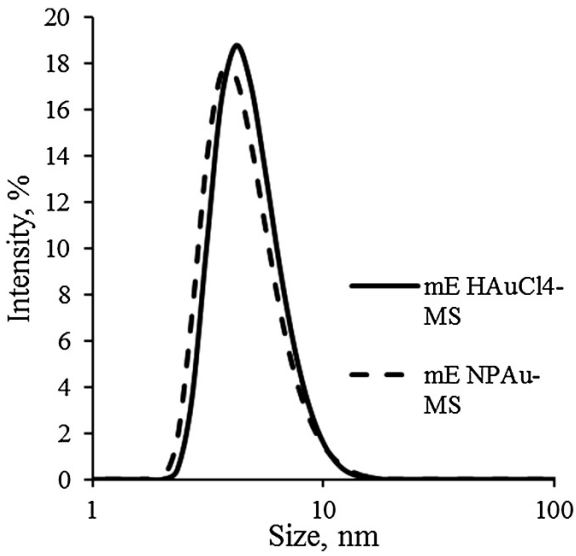

Fig. 2 Size distribution of Au-MS NP's

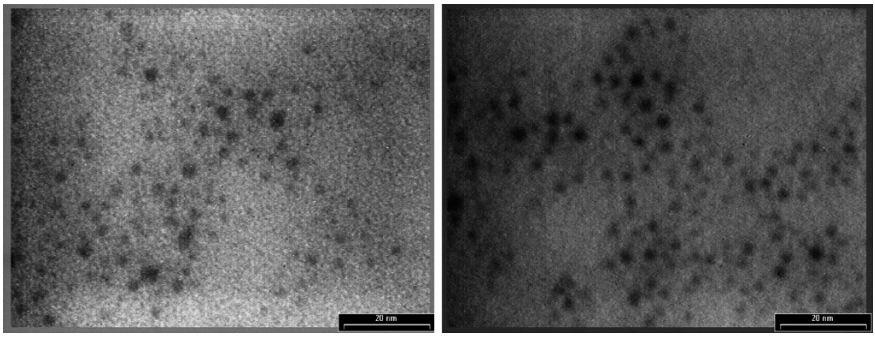

Fig. 3 TEM micrographs of Au-MS (*left*) and Au-Cis NP's (*right*)

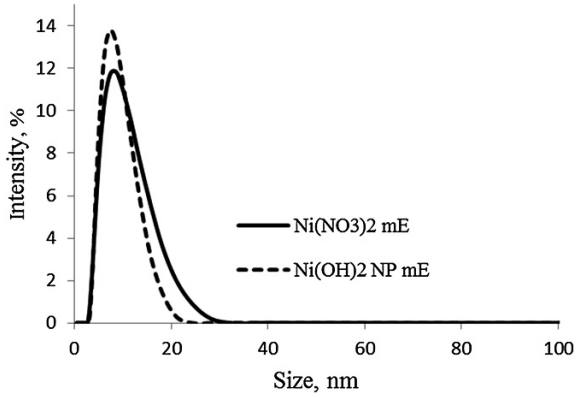

Fig. 4 Size distribution of NiO NP's

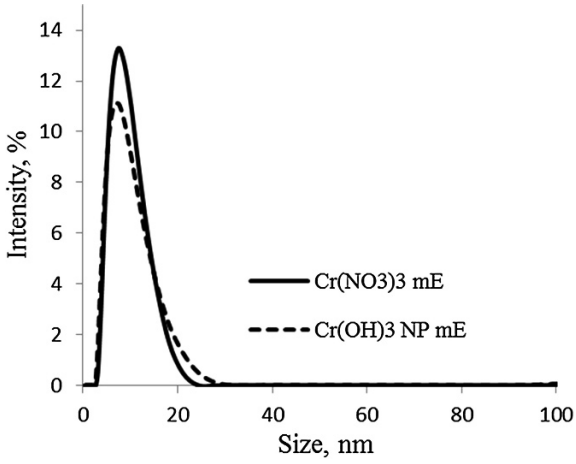

Fig. 5 Size distribution of Cr_2O_3 NP's

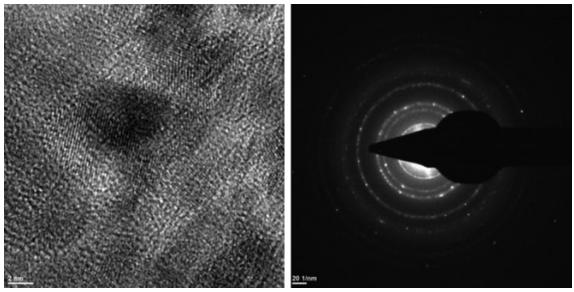

Fig. 6 HR-TEM micrograph of NiO NP and the corresponding electron diffraction image (SAED)

distribution of the nanoparticles sizes and the polidispersity index, 0.187 and 0.285 for $Ni(OH)_2$ and $Cr(OH)_3$, respectively.

The TEM image of NiO nanoparticles is shown in Fig. 6. The size of the nanoparticles is 6 nm. The presence of NiO crystallites is evidenced by diffraction image which shows 5 well-defined diffraction rings which can be indexed as (111), (200), (220), (311) and (222) crystal planes corresponding to the cubic phase structure.

3.2 Tunning the Nanoparticle Size in Different Microemulsion Templates

3.2.1 Spectral and Chromatic Analyses

The microemulsion method has the advantage that nanoparticles with very well organized sizes and structures can be obtained. In Tables 1 and 2 are listed the DLS diameters of NiO and Cr_2O_3, respectively, in different microemulsion templates.

Table 1 Microemulsion templates for NiO nanoparticles with different sizes

Size (nm)	Organic phase (%)	Aqueous phase (%)	Brij 30 (%)
6.5	80.0 (cyclohexane)	5.0	15.0
22.0	87.5 (heptane)	2.5	1.0
70.0	94.0 (cyclohexane)	1.0	5.0

Table 2 Microemulsion templates for Cr_2O_3 nanoparticles with different sizes

Size (nm)	Organic phase (%)	Aqueous phase (%)	Brij 30 (%)
8.5	85.0 (cyclohexane)	5.0	10.0
40.0	87.5 (heptane)	2.5	10.0
80.0	94.0 (cyclohexane)	1.0	2.5

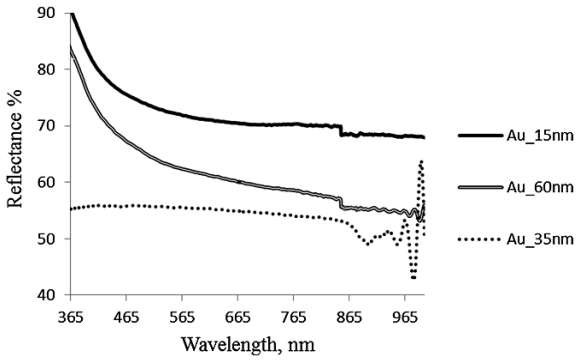

Fig. 7 Electronic spectra of Au nanoparticles with different sizes

Inspecting these tables, one can see that by increasing the organic phase concentration the size of the nanoparticle is raising accordingly.

The electronic spectra of Au, Cr_2O_3 and NiO NPs, which were recorded in diffuse reflectance mode, were shown in Figs. 7, 8, 9 and 10. For Au NPs (Fig. 7) a continuous absorbance monotonous increasing towards NIR domain is evidenced, corresponding to specific plasmon resonance of metallic nanoparticles, which confers a gray-bluish nuance. This spectral behaviour is different from that of functionalized Au NP (Fig. 8) where the yellow colors is characteristic for charge transfer tranzitions of Au^{3+} with thiol ligands (MS and Cis). The more intensive band obtained for Cis as ligand suggests a better accommodation of d-orbitals within tetrahedron conformation round Au^{3+} as the central ion.

Electronic spectra for Cr_2O_3 NPs (Fig. 9) of various sizes show more or less distinct bands located round 360, 455, 620 nm, with dominant intensity towards UV side, thus conferring a yellow-greenish color to these complex structured systems. NiO spectrum, shown in Fig. 10, has two peaks, one at 385 nm and the other at 700 nm. The two peaks in the visible region can be the result of the different forms

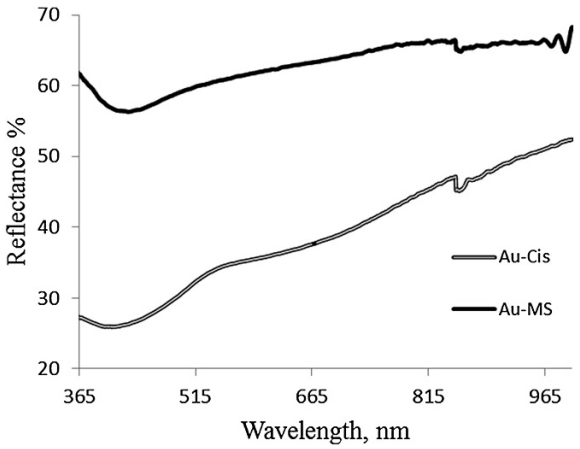

Fig. 8 UV-Vis spectrum of Au-MS NP's realised in diffuse reflection

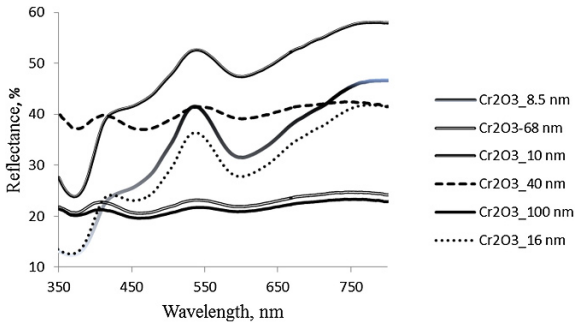

Fig. 9 Electronic spectra of Cr_2O_3 nanoparticles with different sizes

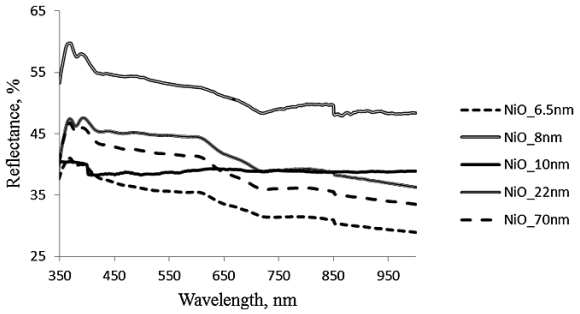

Fig. 10 Electronic spectra of NiO nanoparticles with different sizes

of NiO NP produced during nucleation. The last more intensive band is specific for green color of this compound, which combined with significance absorbance at 650 nm (blue) and 400 nm (orange) results in various tents of turquoise-bluish.

Based on electronic spectra registered in diffuse reflectance, all chromatic parameters in CIE L*a*b* system have been monitored for nanoparticles of various sizes (Table 3).

Apparently, no regular dependences between particle size and these trichromatic parameters can be established. However, a detail analysis highlights interesting aspects on how color analysis can be applied for understanding structural evolution in such nanodisperse systems and finding adequate criteria for selection them as candidates for solar thermal chromophores.

Indeed, one may notice that the three NP types presented here show completely different chromatic characteristics as follows:

- For Cr_2O_3 NP at all sizes negative values for a* and positive values for b* are obtained, this being specific for tents between green and yellow;
- For NiO NP negative values for both a* and b* are obtained, specific for colors between green and blue;
- For Au-MS/Cis NPs values for $a^* = \pm 0.2$, $b^* > 0$ correspond to pure yellow;
- For Au NPs values for $a^* \geq 0$, $b < 0$ correspond to pure blue.

Table 3 Trichromatic parameters for synthetized NP of various sizes

Sample	Size (nm)	L*	a*	b*	dEab*	C*	H
Cr_2O_3	100	63.06	−9.56	11.87	37.34	11.20	128.86
	68	53.20	−0.93	2.24	42.43	2.43	112.54
	40	69.60	−1.85	2.90	26.60	3.44	122.47
	16	75.89	−5.34	8.34	23.73	9.91	122.63
	13	65.23	−10.54	10.60	35.28	14.95	134.82
	10	54.52	−1.44	2.44	41.18	2.83	120.65
	8.5	85.62	−6.68	11.20	19.51	13.04	120.80
NiO	70	70.55	−0.61	−1.55	24.77	1.66	248.52
	22	72.59	−0.75	−0.79	22.84	1.09	226.52
	10	72.31	−0.70	−1.77	23.02	1.90	248.42
	8	77.93	−0.50	−1.47	17.47	1.55	251.07
	6.5	66.19	−0.10	−1.86	29.05	1.86	267.02
Au-MS	5	82.31	0.12	3.36	14.73	3.36	88.03
Au-Cis	7	65.07	−0.39	9.22	32.80	9.23	92.41
Au	15	88.11	0.32	−3.35	7.13	3.36	275.53
Au	35	80.91	1.07	−4.42	14.25	4.54	283.59
Au	60	83.39	0.41	−4.78	11.84	4.89	274.96

In this table, L* is defined as the position on the light-dark axis (white-black color), a*—the position on the green-red axis, b*—the blue-yellow axis, chroma, dEab*—the total color difference, C*, (the distance between the chromatic point to L* axis) and the hue angle, H [28]

This chromatic differentiation based on structural reasons is more clearly underlined in Fig. 11, where the hue angle, H, which reflects simultaneously the weight of a* and b* parameters, is represented as function of size. Except for small size region, one may notice that H angle is determined in a decisive manner, by the chromophore nature, thus allowing obtaining a desired and controlled color for new solar collectors.

3.2.2 Textural Properties

In order to demonstrate in what extent the pore size influences the textural properties of Cr_2O_3 nanoparticles, adsorption-desorption nitrogen isotherms were also performed and the corresponding curves are presented in Fig. 12. All isotherms were type IV according to the IUPAC classification and the hysteresis loop type H3. Typically, if the material under investigation presents a N_2 isotherm of type IV accompanied by a type H3 hysteresis loop, then, the solid is purely mesoporous containing non-intersecting mesopores of cylindrical geometry and similar size. However, the hysteresis loop presented in Fig. 12 corresponds to type H3 which is

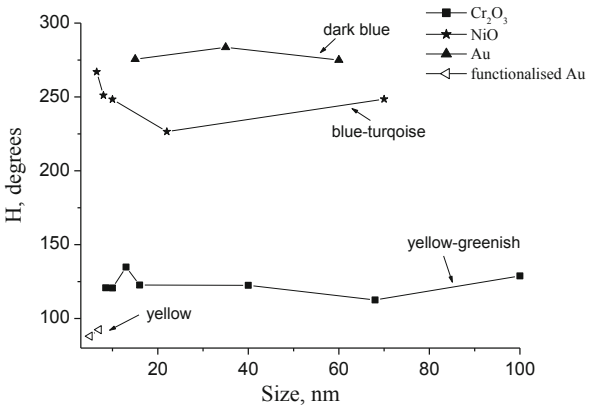

Fig. 11 Correlation between hue angle and nanoparticles size

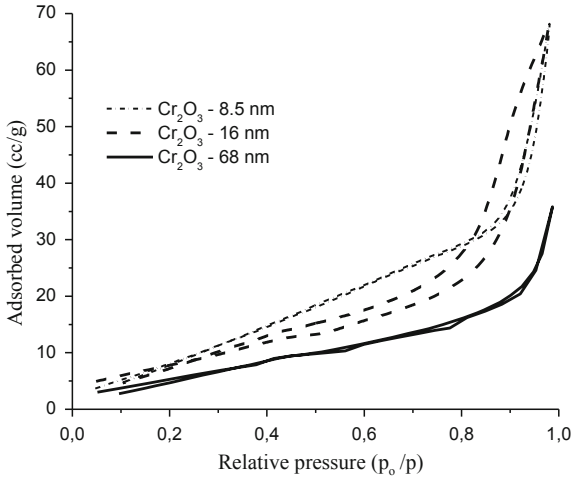

Fig. 12 Nitrogen adsorption-desorption isotherms of Cr_2O_3 with different sizes

the case of more random distribution of pores and interconnected pore systems. Type H3 hysteresis loops also suggest that the mesopores have a slit-shaped structure. The specific surface area, pore volume and average pore size calculated with Barrer Joiner Hallenda (BJH) equation according to the size distribution curve for the desorption branch of the Cr_2O_3 nanoparticles are given in Table 4. The

Table 4 Textural properties of Cr_2O_3 with different sizes derived from nitrogen adsorption isotherms

Size DLS (nm)	Specific surface area (m^2/g)	Pore volume (cm^3/g)	Pore diameter (nm)
8.00	36.86	0.11	9.06
16.00	20.53	0.10	15.87
68.00	17.01	0.05	65.87

Table 5 Sizes and zeta potential values for metallic and oxide nanoparticles

NP	Size in microemulsion (nm)	Size (nm)	Zeta potential (mV)
Au-MS	9.6	253	−34.8
Cr_2O_3	8.5	157	−39.5
NiO	6.5	137	−30.7

results from Table 4 show that both surface area and pore volume are decreasing with nanoparticle size. One may also notice that the pore diameters are in excellent accordance with DLS measurements.

3.3 Nanoparticles Dispersability in Water

As the nanoparticles are deposited by spraying on the flat collector surface, it is very difficult to use them in microemulsion phase. That is why it is essential to know the dispersability of these solid nanoparticles in aqueous phase. In this direction the dispersability of the nanoparticles in water was studied. In Table 5 are listed the sizes and zeta potential values for metallic and oxide nanoparticles. The zeta potential value of Au-MS NP is around -34.8 mV which indicates a good stability of the nanoparticles and their negative charge due to SO_3^- ions remained free after the covalent coordinative binding of gold to sulphur. NiO and Cr_2O_3 nanoparticles are also very stable and negatively charged at the surface.

In the microemulsion media, the size of the nanoparticles is very small, around 10 nm. After being processed by multiple ultrasonication and washing steps, the sizes of the solid nanoparticles dispersed in water are much higher, in general above 100 nm. This phenomenon is explained by the small size of the nanoparticles which gives an excess of energy due to the high number of atoms that are exposed on the nanoparticle surface and their tendency to reach the minimum free energy level (thermodynamic equilibrium) by phase transformations, structural changes of the surface or by aggregation phenomena [29]. The values of the zeta potential showed that these aggregates are stable as a result of their high sizes.

4 Conclusions

Disperse metallic (Au) and oxide (NiO and Cr_2O_3) nanoparticles were synthesized in a microemulsion template, the former by photoreduction technique and the later by precipitation method. Nanoparticles with size ranging between 5 and 100 nm have been obtained and characterized for their morpho-structural properties by DLS and TEM measurements.

Textural properties of Cr_2O_3 NPs have been determined by nitrogen adsorption/desorption isotherms, and correlations has been established between specific surface area, pore volume and NP diameter, in accordance with DLS measurements.

NP dispersability in water has been studied and good stability has been demonstrated by high zeta potential values.

Based on electronic spectra of NP powders registered in diffuse reflectance mode, a systematic color analysis has been made, allowing nominating the hue angle as relevant criterion for selecting specific NPs of various cromophore natures as optimal candidates for solar thermal collectors.

Acknowledgments This work was done in the frame of the Program: Cooperation in Priority Fields—PNII, developed with the support of ANCS, CNDI-UEFISCDI, Romania, in the project EST IN URBA, PN-II-PT-PCCA-2011-3.2-051, contract no. 28/2-11.

References

1. Wu, B., Kuang, Y., Zhang X., & Chen J. (2011). Noble metals nanoparticles/carbon nanotubes nanohybrids: Synthesis and applications. *Nano Today 6*, pp. 75–90, Elsevier.
2. Zhou, J., Ralston, J., Sedev, R., Beattie, D. (2009). Functionalized gold nanoparticles: Synthesis, structure and colloid stability. *Journal of Colloid and Interface Science 331*, pp. 251–262, Elsevier.
3. Narayanan, K. B., & Sakthive, N. (2010). Biological synthesis of metal nanoparticles by microbes. *Advances in Colloid and Interface Science, 156*, pp. 1–13, Elsevier.
4. Javadi, F. S., Saidur, R., & Kamalisarvestani, M. (2013). Investigating performance improvement of solar collectors by using nanofluids. *Renewable and Sustainable Energy Reviews, 28*, pp. 232–245, Elsevier.
5. Filho, E. P. B., Hernandez Mendoza, O. S., Beicker, C. L., Menezes, A., & Wen, D. (2014). Experimental investigation of a silver nanoparticle-based direct absorption solar thermal system. *Energy Conversion and Management*, *84*, pp. 261–267, Elsevier.
6. Andersson, A., Hunderi, O., & Granqvist, C. G. (1980). Nickel pigmented anodic aluminum oxide for selective absorption of solar energy. *Journal of Applied Physics, 51*, 754–764.
7. Kameya, Y., & Hanamura, K. (2011). Enhancement of solar radiation absorption using nanoparticle suspension. *Solar Energy, 85*, 299–307.
8. Hirsch, L. R., Stafford, R. J., Bankson, J. A., Sershen, S. R., Rivera, B., Price, R. E., et al. (2003). Nano shell mediated near-infrared thermal therapy of tumors under magnetic resonance guidance. *Proceedings of the National Academy of Sciences of the United States of America, 100*, 13549–13554.
9. Chou, C. S., Lin, Y. J., Yang, R. Y., & Liu, K. H. (2011). Preparation of TiO_2/NiO composite particles and their applications in dye-sensitized solar cells. *Advanced Powder Technology*, *22*, pp. 31–42, Elsevier.
10. Sebastian, P. J., Quintana, J., & Avila, F. (1997). Retention of the high optical absorptance in thermally aged black chrome on variably sensitized Cu. *Solar Energy Materials and Solar Cells*, *45*, pp. 65–74, Elsevier.
11. Nahar, N. M., Mo, G. H., & Ignatiev, A. (1989). Development of an Al_2O_3-Co selective absorber for solar collectors. *Thin Solid Films*, *172*, pp. 19–25, Elsevier.
12. Nuru, Z. Y., Arendse, C. J., Nemutudi, R., Nemraoui, O., & Maaza, M. (2012). Pt–Al2O3 nanocoatings for high temperature concentrated solar thermal power applications. *Physica B*, *407*, pp. 1634–1637, Elsevier.

13. Stephen Sathiaraj, T., Thangaraj, R., AlSharbaty, H., & Agnihotri O. P. (1991). Optical properties of selectively absorbing R.F. sputtered Ni-Al2O3 composite films. *Thin Solid Films, 195*, pp. 33–42, Elsevier.
14. Zhang, Q.-C., Yin, Y., & Mills, D. R. (1996). High efficiency Mo-Al_2O_3 cermet selective surfaces for high-temperature application. *Solar Energy Materials and Solar Cells*, *40*, pp. 43–53, Elsevier.
15. Zhanga, Qi.-C., & Shenb, Y. G. (2004). High performance W-AlN cermet solar coatings designed by modelling calculations and deposited by DC magnetron sputtering. *Solar Energy Materials and Solar Cells*, *81*, pp. 25–37, Elsevier.
16. Maziere-Bezes, D., & Valignat, J. (1982). Optical properties of gold-magnesia selective cermets. *Solar Energy Materials 7*, pp. 203–211, Elsevier.
17. Smith, G. B., Mcphedran, R. C., & Derrick, G. H. (1985). Surface structure and the optical properties of black chrome. *Applied Physics A*, *36*, pp. 193–204, Springer.
18. Khamlich, S., Nemraoui, O., Mongwaketsi, N., McCrindle, R., Cingo, N., & Maaza M. (2012). Black Cr/a-Cr2O3 nanoparticles based solar absorbers. *Physica B, 407*, pp. 1509–1512, Elsevier.
19. Radeka, M., Gorzkowska-Sobas, A., Zakrzewska, K., & Sobas, P. (2004). Nanocermet TiO2: Au thin film electrodes for wet electrochemical solar cells. *Opto-Electronics Review*, *12* (1), pp. 53–56, Springer, 2004.
20. Zakrzewska K., Radecka M., Kruk A., & Osuch W. (2003). Noble metal/titanium dioxide nanocermets for photoelectrochemical applications. *Solid State Ionics*, *157*, pp. 349–356, Elsevier.
21. Mandal, S. K., Roy, R. K., & Pal, A. K. (2002). Surface plasmon resonance in nanocrystalline silver particles embedded in SiO_2 matrix. *Journal of Physics D Applied Physics, 35*, 2198–2205.
22. Toudert, J., Camelio, S., Babonneau, D., Denanot, M. F., Girardeau, T., Espinos, J. P., et al. (2005). Morphology and surface-plasmon resonance of silver nanoparticles sandwiched between Si3N4 and BN layers. *Journal of Applied Physics, 98*(114316), 1–10.
23. Deng, H., Yang, D., Chen, B., & Lin, C.-W. (2008). Simulation of surface plasmon resonance of Au–WO3 − x and Ag–WO_{3-x} nanocomposite films. *Sensors and Actuators B*, *134*, pp. 502–509, Elsevier.
24. Camelio, S., Toudert, J., Babonneau, D., & Girardeau, T. (2005). Tailoring of the optical properties of Ag:Si3N4 nanocermets by changes of the cluster morphology. *Applied Physics B*, *80*, pp. 89–96, Springer.
25. Barshilia, H. C., Prashant Kumar, Rajam, K.S., & Biswas, A. (2011). Structure and optical properties of Ag–Al_2O_3 nanocermet solar selective coatings prepared using unbalanced magnetron sputtering. *Solar Energy Materials and Solar Cells*, *95*, pp. 1707–1715, Elsevier.
26. Mihaly, M., Fleancu, M. C., Olteanu, N. L., Bojin, D., Aurelia Meghea, A., & Enachesc,u M. (2012). Synthesis of gold nanoparticles by microemulsion assisted photoreduction method. *Comptes Rendus Chimie*, *15*, pp. 1012–1021, Elsevier.
27. Mihaly, M., Comanescu, A. F., Rogozea, A. E., Vasile, E., & Meghea, A. (2011). NiO–silica based nanostructured materials obtained by microemulsion assisted sol–gel procedure. *Materials Research Bulletin*, *46*, pp. 1746–1753, Elsevier.
28. Feraru, D. L., & Meghea, A. (2014). Comparative forensic analysis of ballpoint pen inks. *Revista de Chimie, 65*, 421–425.
29. Rusanov, A. I. (2005). Surface thermodynamics revisited. *Surface Science Reports*, *58*, pp. 111–239, Elsevier.

Evaluation of Various Hybrid Solar Collector Configurations for Water and Air Heating

Qahtan Adnan Abed, Viorel Badescu and Iuliana Soriga

Abstract In this paper a mathematical model has been developed to study the thermal efficiency of a water-air hybrid solar collector (HSC). The model, implemented in MATLAB, was used to evaluate the collector in the real operation conditions of Timisoara, Romania. The effect of solar irradiation, ambient temperature and air inlet temperature on the useful energy collected by air and water has been investigated. Absorber plate temperature variation, water and air outlet temperatures, collector efficiency and air flow rate effects are presented. Moreover, the efficiency of the collector for three different configurations of the air channel is computed and compared: triangular fins, rectangular fins and without fins. The simulation results show that the configuration with triangular fins has better performance compared with the others.

Keywords Hybrid solar collector · Water heater · Air heater · Modeling · Effectiveness

1 Introduction

The use of solar heating systems had increased based on the reasonable initial costs and relatively simple structure, especially the solar water heating and air heating are widely used in most of the countries. There are many studies about the hot water and air heated by solar radiations. Among these, one analysis focused on the performance of solar thermosiphon water heaters with heat exchangers in storage tanks [1]. Another study [2] made a review on element geometries used as artificial roughness in solar air heaters in order to improve the heat transfer capability of solar air heater

Q. Adnan Abed (✉) · V. Badescu · I. Soriga
University Politehnica of Bucharest, Bucharest, Romania
e-mail: qahtan77@yahoo.com

Q. Adnan Abed
Foundation of Technical Education, Najaf Technical College, Najaf, Iraq

I. Visa (ed.), *Sustainable Energy in the Built Environment - Steps Towards nZEB*,
Springer Proceedings in Energy, DOI 10.1007/978-3-319-09707-7_24

ducts. In the agricultural domain, a simple solar air heater from cheap plastic wrapping film with air bubbles, for use in drying operations on a farm, has been proposed [3]. These studies had been performed on a single-purpose collector, where the operating fluid is only air or liquid. For the collectors whose working fluid is water, thermal transfer rate is acceptable because water is a good conductor of heat. However, for solar air collectors, heat transfer is low, therefore, the use of fins or corrugated surfaces is required, for the improvement of the heat transfer [4]. In order to increase the efficiency, some researchers studied the thermal performance of solar collectors working with two different types of fluids simultaneously. In this regard, studies were made on the performance of an air and water collector combined in a single solar collector, also called a Dual Purpose Solar Collector (DPSC) [5]. Energy and exergy study of air-water combined solar collector was also investigated [6] observing the water inlet temperature and air flow rate effects. A dynamic numerical model has been developed and validated by experimental data [7], for a new proposed building- integrated dual-function solar collector that is able to provide passive space heating in cold winter, and water heating in warm seasons.

In this work the thermal performance of the Hybrid Solar Collector (HSC) for water and air heating was studied. The mathematical model used for the HSC assessment in the real operating conditions of Timisoara, Romania, was implemented in MATLAB.

2 Description of the HSC

The studied collector is a flat-plate collector, in which both working fluids receive heat from the absorbing plate, as shown in Fig. 1. The length of collector is 1.94 m and width 0.94 m [8]. The transparent cover is made from glass. The gap between the glass cover and the absorber plate is 3 cm. The water is flowing through pipes located in the top of the absorber plate, and the air flows through a channel in the

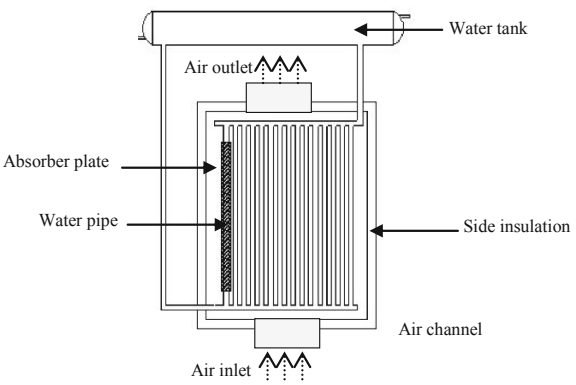

Fig. 1 Schematic layout of a typical solar water and air heater system

Table 1 Detail specification and input parameter of the hybrid solar collector

HSC detail specification		
Transparent cover and absorber plate	Material	Glass and aluminium
	Emissivity	0.88 and 0.17
	Thickness	4 and 2 mm
Insulation	Thermal conductivity	0.04 W/(m.K)
	Rear and the side thickness	5 and 2 cm
Water pipes	Number	10
	Diameter	7 mm
Air channel (heat transfer area)	Without fins	4.24 m^2
	Rectangular fins	7.6 m^2
	Triangular fins	8.16 m^2
HSC input parameter		
Solar global irradiance		11.5–883.8 W/m^2
Inlet air temperature		294.25–308.05 K
Water inlet temperature		313.15 K
Mass flow rate of water and air		0.02 and 0.1 kg/s
Wind speed		1.5 m/s

bottom side of the absorber plate with height 6 cm. The rear and the side insulation are provided by a polystyrene sheet. The detail configuration and input parameter of HSC for water and air are tabulated in Table 1.

3 Theoretical Analysis: Assumptions and Collector Model

The suitable sizing of the components of the solar system is a complex problem which includes both predictable (collector and other performance characteristics) and unpredictable (weather data) components, so the following assumptions were made to simplify the analysis of the HSC:

(a) The absorber plate, water tube surface and air channel surface, have the same temperature.
(b) The conduction and radiation heat transfer in water tubes and air channel was neglected.
(c) The heat losses by convection and radiation from the rear and side surfaces was neglected.
(d) Flow inside water pipes and air channels was assumed to be laminar.

The first step in the HSC thermal model is the computation of the heat loss from the collector. Top, rear and side heat loss was calculated according to Ref. [8]. The heat transfer coefficient between water and the tubes is calculated from the Nusselt number:

$$h_w = \frac{k_w}{d} Nu_w \tag{1}$$

where: k_w—thermal conductivity (W/(m.K)), d—diameter of the tube (m) and Nu_w—Nusselt number.

For the circular tube the average Nusselt number for the thermal entrance region can be determined from [9]:

$$Nu_w = 3.66 + \frac{0.0667(\frac{d}{L_1})\mathrm{Re}_w.\,\mathrm{Pr}}{1 + 0.04\left[(\frac{d}{L_1})\mathrm{Re}_w.\,\mathrm{Pr}\right]^{\frac{2}{3}}} \tag{2}$$

where: Re_w—Reynold number, L_1—length of absorber plate (m) and Pr—Prandtl number.

Also, the convection heat transfer coefficient in the air channel of the collector for the three different configurations (without fins, rectangular fins and triangular fins), can be estimated by Eqs. (3)–(5), respectively [10–12].

$$Nu_D = 0.0158\mathrm{Re}_D^{0.8} \tag{3}$$

$$Nu_D = 0.023\mathrm{Re}_D^{0.8}.\,\mathrm{Pr}^{0.4} \tag{4}$$

$$Nu_D = Nu_o + \beta\frac{b}{L_1}n, \left\{\begin{array}{lll} Nu_o = 2.821 & \beta = 0.126\mathrm{Re}_D & \mathrm{Re}_D < 2800 \\ Nu_o = 1.9 * 10^{-6}\mathrm{Re}_D^{1.79} & \beta = 225 & 2800 < \mathrm{Re}_D < 10^4 \\ Nu_o = 0.0302\mathrm{Re}_D^{0.74} & \beta = 0.242\mathrm{Re}_D^{0.74} & 10^4 < \mathrm{Re}_D < 10^5 \end{array}\right\} \tag{5}$$

where: β—tilt angle (degrees), b—half height of the triangular fins (m) and n—number of collectors connected.

The heat exchange effectiveness is defined as heat delivery to maximum heat delivery that can transfer to fluids. Heat exchange effectiveness for water can be obtained from the following equation [13]:

$$\varepsilon_w = 1 - \exp\left[-\frac{h_w A_w}{\dot{m}_w C_{p,w}}\right] \tag{6}$$

The performance of a hybrid solar collector for water and air can be described by the useful heat gain from the collector, which is defined as the difference between the absorbed solar energy and the thermal loss of a collector. Finally the amount of useful heat gain (q_u), is calculated from summation of the absorbed heat for water and air by using the two following equations respectively [8]:

$$q_{u,w} = \left(\frac{\varepsilon_w \dot{m}_w C_{p,w}}{U_{L,w}A_p + \varepsilon_w \dot{m}_w C_{p,w}}\right)\left[A_p S - U_{L,w}A_p\left(T_{w,in} - T_{amb}\right)\right] \quad (7)$$

$$q_{u,a} = \left(\frac{\varepsilon_a \dot{m}_a C_{p,a}}{U_{L,a}A_p + \varepsilon_w \dot{m}_a C_{p,a}}\right)\left[A_p S - U_{L,a}A_p\left(T_{a,in} - T_{amb}\right)\right] \quad (8)$$

where: ε_w—heat exchange effectiveness of water and air, $\dot{m}_w$—water mass flow rate (kg/s), $C_{p,w}$—specific heat (J/kg. K), A_p—collector area (m^2), S–absorbed solar radiation (W/m^2), $T_{w,in}$—water inlet temperature (K), $T_{a,in}$—air inlet temperature (K) and T_{amb}—ambient air temperature (K).

The thermal efficiency of the HSC is defined as the ratio of useful absorbed energy by the fluid to the solar energy received by the collector.

$$\eta = \frac{q_u}{A_p I_T} \quad (9)$$

The individual component models are coded into "MATLAB" software and the simulation program is used to predict system parameters such as hot water and air temperature, fluid absorbed useful energy, heat exchange effectiveness and the performance of HSC for various solar global irradiance values various air inlet temperatures and constant water inlet. The computation algorithm is represented in the flow chart shown in Fig. 2.

4 Results and Discussions

Useful heat gain, efficiency and working fluids outlet temperatures, were obtained from the numerical simulation, using as input data values characteristic to Timisoara, Romania (45° 44′N / 21° 13′E). Fig. 3 shows the variation of solar global irradiance and ambient air temperature on a sunny day (01/July/2010). The ambient air temperature was high throughout the day, with maximum value 308.05 K and a minimum value 294.25 K, and the maximum solar global irradiance was 883.8 W/m^2 at the midday.

The variation of water outlet and air outlet temperatures of HSC for three types of air channels: without fins, with rectangular fins and triangular fins are shown in Fig. 4. Here, it can be observed that the collector without fins in the air channel (first case), obtained highest water outlet temperature and lowest air outlet temperature, while in the other two cases temperatures were identical.

Figure 5 shows the useful heat gain of water and air during the day that are obtained from HSC model. The average value of the useful heat gain for water is 534 W, ranging between 24 and 924 W, and the average value of the useful heat gain for air is 124 W, ranging between 37.8 and 173.4 W.

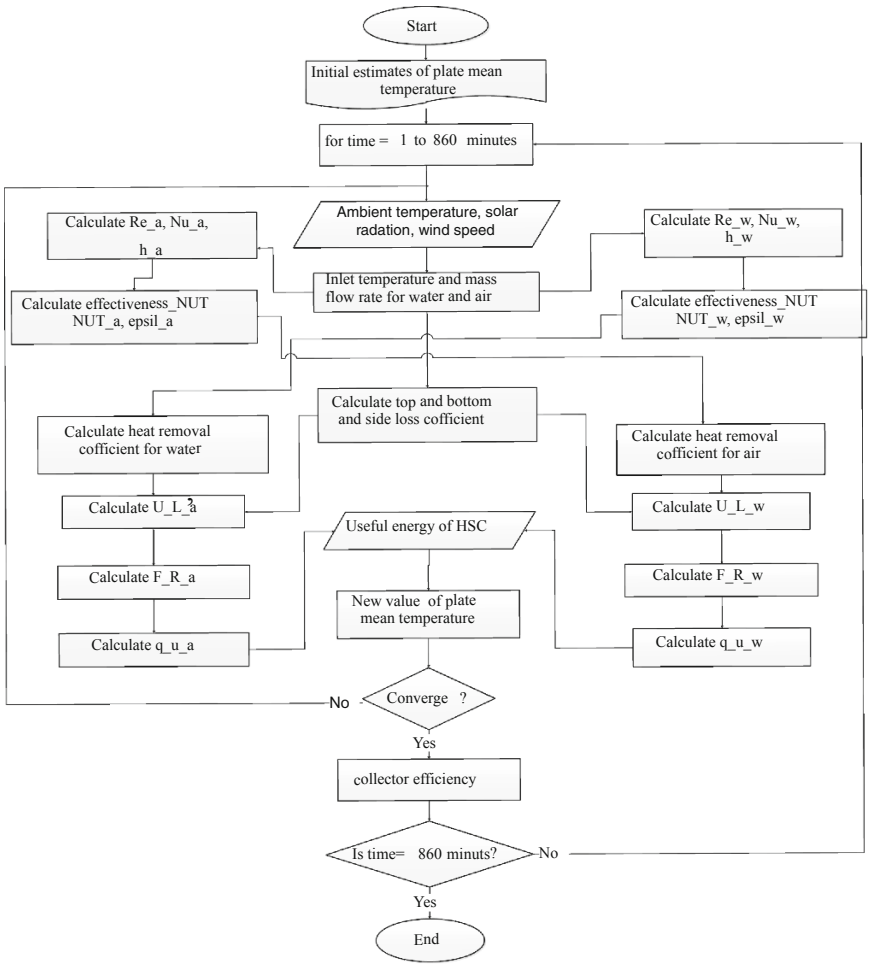

Fig. 2 Simple flow chart of simulation process

The useful heat gain of air increases when adding the fins for constant water and air mass flow rate equal to 0.02 and 0.1 kg/s, respectively. Figure 6 shows the maximum heat gain for air in the collector that uses triangular fins. The average value of the useful heat gain for the three types of air channel: without fins, rectangular fins and triangular fins was 72.3 W varying from 3.4 to 113.7 W, 110.4 W varying from 4.6 to 173.5 W and 111.8 W varying from 4.6 to 176.2 W, respectively.

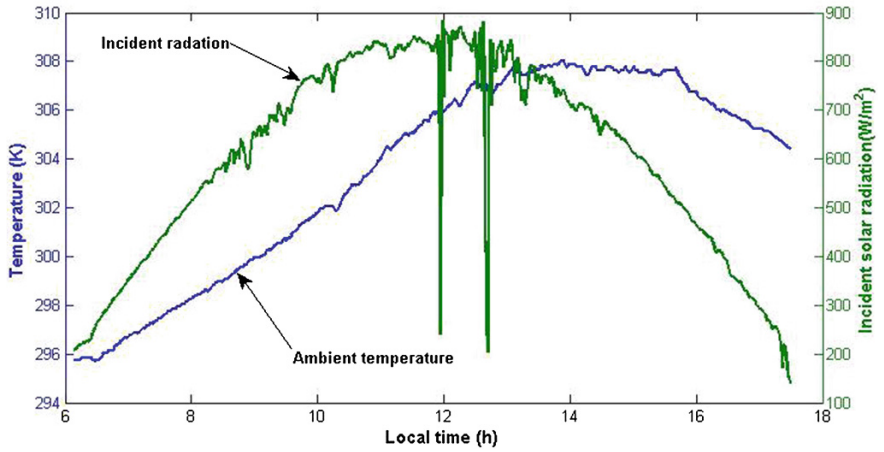

Fig. 3 Variation of ambient air temperature and solar radiation intensity on 01/July/2010

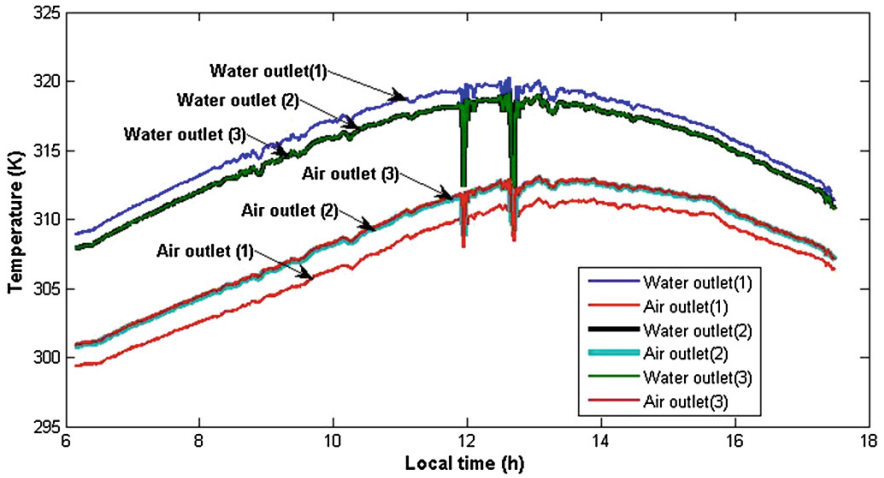

Fig. 4 Variation of water outlet and air outlet temperature for three types of air channels: (*1*) without fins, (*2*) with rectangular fins and (*3*) with triangular fins

The thermal efficiency of HSC is shown in Fig. 7, also for the three different types of air channels. It can be observed that it is higher for the configurations with fins. The maximum HSC efficiency was 67.9 % and it was obtained at noon for the air channel with triangular fins and constant air mass flow rate of 0.1 kg/s. This efficiency increased from morning until noon and then decreased. The maximum efficiency of the air channel without fins was 61 % and with rectangular fins, 65.8 % (Fig. 7).

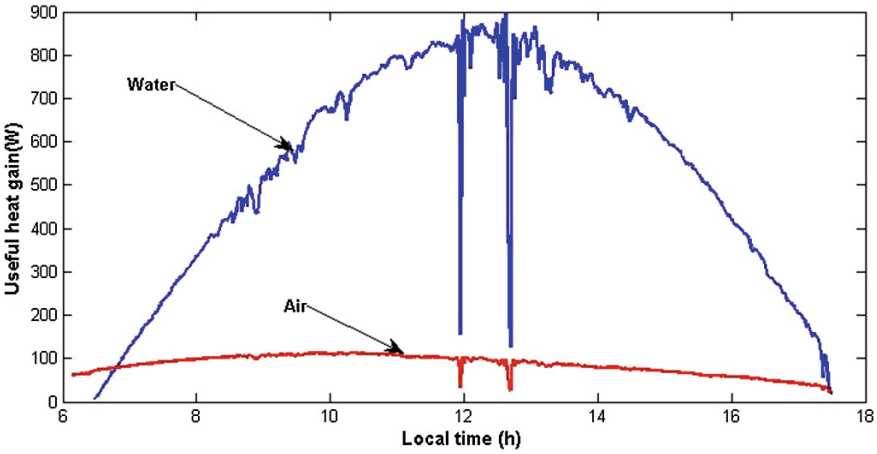

Fig. 5 Useful heat gain from HSC for air cannel without fins

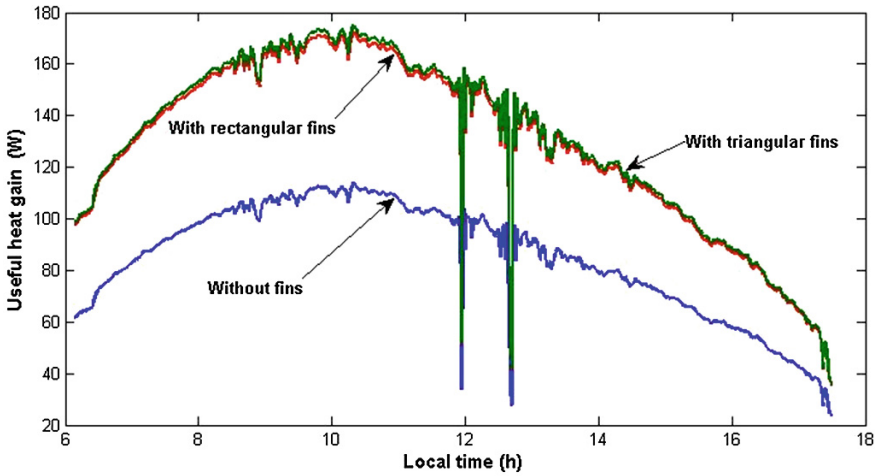

Fig. 6 Comparison of air useful heat gain for three types of air channel

5 Conclusion

A mathematical model for the simulation of HSC for water and air heating was developed. The performance of the solar collector was simulated with variable solar radiation, variable air inlet temperature, and constant water inlet temperature. The air channel type has an effect on the thermal efficiency. Because the heat transfer area of the air channel with triangular fins is higher compared to the other types, the

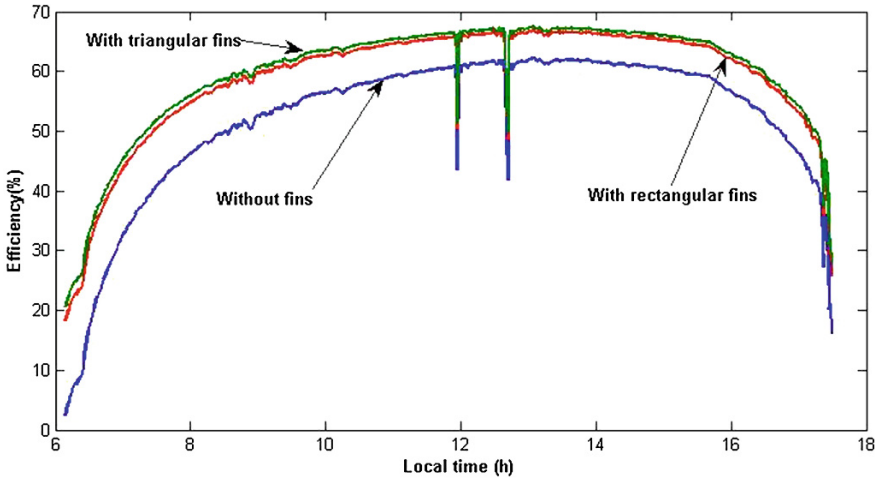

Fig. 7 Thermal efficiency for HSC during the day for different types of air channels

highest obtained thermal efficiency for the HSC, was for the configuration with triangular fins. The average efficiency of the HSC without fins, rectangular fins and triangular fins was 50.2, 56.6 and 57.4 % respectively.

Acknowledgments The authors thank Dr Marius Paulescu (West University of Timisoara) for providing meteorological data.

Author (Qhtan A. Abed) thank the Ministry of Higher Education in Iraq.

References

1. Mertol, A., Place, W., Webster, T., & Greif, R. (1981). Detailed loop model (DLM) analysis of liquid solar thermosiphons with heat exchangers. *Solar Energy, 27*, 367–386. (Elsevier).
2. Varun, Saini, R. P., & Singal, S. K. (2007). A review on roughness geometry used in solar air heaters. *Solar Energy, 81*, 1340–1350. (Elsevier).
3. Ahmad, N. T. (2001). Agricultural solar air collector made from low-cost plastic packing film. *Renew, Energy, 23*, 663–671. (Elsevier).
4. Youcef-Ali, S., & Desmons, J. Y. (2006). Numerical and experimental study of a solar equipped with offset rectangular plate fin absorber plate. *Renew Energy, 31*, 2063–2075. (Elsevier).
5. Assari, M. R., BasiratTabrizi, H., Kavoosi, H., Moravej, M. (2006). Design and performance of dual-purpose solar collector. In *Proceedings of 3rd International Energy, Exergy and Environment Symposium*, IEEES-3. Portugal: University of Evora.
6. Jafari, I., Ershadi, A., Najafpour, E., & Hedayat, N. (2011). Energy and exergy analysis of dual purpose solar collector, World Academy of Science. *Engineering and Technology, 57*, 242–244.
7. Ji, J., Luo, C., Chow, T. T., Sun, W., & He, W. (2011). Thermal characteristics of a building-integrated dual-function solar collector in water heating mode with natural circulation. *Energy, 36*, 566–574. (Elsevier).

8. Assari, M. R., Basirat Tabrizi, H., & Jafari, I. (2011). Experimental and theoretical investigation of dual purpose solar collector. *Solar Energy, 85*, 601–608. (Elsevier).
9. Edwards, D. K., Denny, V. E., & Mills, A. F. (1979). *Transfer processes* (2nd ed.). Washington: Hemisphere.
10. Sukhatme, S. P. (1996). *Solar energy* (2nd ed.). India: McGraw-Hill.
11. Kays, W. M., Crawford, M. E., & Weigand, B. (2005). *Convective heat and mass transfer* (4th ed.). Singapore: McGraw-Hill.
12. Hollands, K. G. T., & Shewen, E. C. (1991). Optimization of flow passage geometry for air handling plate type solar collectors. *Journal of Solar Energy, 103*, 323–330. (Elsevier).
13. Incropera, F. P., & Dewitt, D. P. (1996). *Introduction to heat transfer* (3rd ed.). USA: Wiley.

Characterization of Biomass Used for Fischer-Tropsch Diesel Synthesis

Anca Sauciuc, Lucia Dumitrescu, Ileana Manciulea, Reinhard Rauch and Hermann Hofbauer

Abstract The characteristics of biomass used at Combined Heat and Power (CHP) plant Güssing (Austria) were determined over three samples taken from the wood chips, including proximate analysis: moisture, ash, cellulose and lignin content, and ultimate analysis: total organic carbon, concentration of H, S, N, and O, high and low heating value and FT-IR. Based on the characteristics of biomass, investigation of the syngas composition has been performed. The results showed that most of the proximate and ultimate analysis, as well as FT-IR analysis of wood chips were comparable with the standards and with other results found in literature. Extrinsic moisture higher than the standard value was obtained due to high humidity in the atmosphere during harvesting, causing difficulties of the feeding inside the fluidized bed gasifier and affecting the quality of the syngas. Low concentrations of S and N determined low emissions of NH_3 and H_2S, providing a synthesis gas suitable for Fischer-Tropsch synthesis.

Keywords Biomass · Fischer-Tropsch · Gasification · Syngas

1 Introduction

The continuous demand for fossil fuels energy correlated with the decreasing of the reserves and the increase of the prices and environmental pollution, due to greenhouse gases emissions, have determined the focus on clean and renewable energy

A. Sauciuc (✉)
ROCAT Synfuels, Research and Development, Brasov, Romania
e-mail: Anca.sauciuc@rocatsynfuels.com

L. Dumitrescu · I. Manciulea
Department of Product Design, Mechatronics and Environment, Transilvania University of Brasov, Brasov, Romania

R. Rauch
Bioenergy 2020+, Research and Development, Güssing, Austria

H. Hofbauer
Department of Chemical Engineering, Vienna University of Technology, Vienna, Austria

I. Visa (ed.), *Sustainable Energy in the Built Environment - Steps Towards nZEB*, Springer Proceedings in Energy, DOI 10.1007/978-3-319-09707-7_25

technologies for biofuel production [1–4]. Biomass plays an important role in the sustainable policies, being a renewable resource that has the economic potential to be used as substitute for fossil fuels [5]. The benefits for using biomass for biofuels production consist in:

- Abundant resource all over the world, more than 65 billion tone of dry plant biomass being produced annually by world's forests [6];
- Biomass is considered neutral regarding the CO_2 emissions, as biomass is formed through photosynthesis and the CO_2 generated during energy conversion is consumed during the growth of the new biomass, based on Calvin cycle [1, 2, 6];
- The possibility to produce heat, electricity, biofuels and chemicals [7, 8].

Bioethanol and biodiesel (as first generation of biofuels) and Fischer-Tropsch synthetic diesel (as second generation of biofuels) obtained from biomass conversion can replace conventional gasoline and diesel. First generation of biofuels – biodiesel, relies on well-established technologies, however, the feedstock availability, the competition between biodiesel production and food industries, the toxicity of the process (using methanol, NaOH and H_2SO_4 as catalysts, fertilizers for plant growth) and the necessity of pretreatment stage for feedstock and purification stage for biodiesel, determine the focus on the second generation of biofuels derived from biomass, so called biomass-to-liquid technology BtL [9–12].

The principle of Fischer-Tropsch diesel production from biomass by BtL technology consists in five main processes: pretreatment of biomass, like drying or grinding, gasification of biomass with synthesis gas production (H_2 and CO), cleaning stage of syngas, in order to remove the poisoning component (H_2S, HCl, NH_3, COS, tars, particles), Fischer-Tropsch synthesis and finally upgrading the products by hydroprocessing and distillation in order to obtain a high quality diesel compatible with the automotive engines. The key concept of Fischer-Tropsch synthesis is to chemically convert the synthesis gas to longer chain hydrocarbons over the surface of catalysts based on Co or Fe. The Fischer-Tropsch reaction is highly exothermic, producing alkanes, alkenes, as primary components, respectively alcohols, carboxylic acids, aldehydes or ketones, as secondary components, undesirable [13, 14].

BtL technology is still under development and the worldwide research focus currently on the high-efficiency conversion of biomass to energy, heat and especially to Fischer-Tropsch liquid fuels. The choice of gasifier, operating conditions—temperature, oxidation agent, residence time, as well as composition of synthesis gas produced and the solid and flue gaseous emissions are directly influenced by the biomass physical and chemical characteristics [6]. The chemical properties of the greatest importance which affect the thermochemical conversion processes and fuels quality produced are the proximate analysis (moisture, ash content, volatile and fixed carbon content), ultimate analysis (cellulose, lignin, hemicellulose and extractive content, as well as elemental composition C, H, N, S and O), heat value, bulk density and alkali metal content. The characteristics of biomass vary based on the source and need to be known in detail before the thermochemical processes are developed [15]. The properties has to be taken into consideration also for the overall investment and operating costs of the biomass-to-liquid technology in order

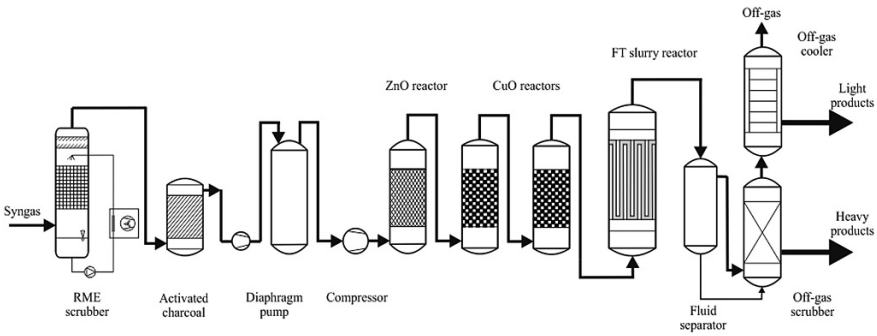

Fig. 1 Fischer-Tropsch pilot plant Güssing

to bring it at commercial scale. BtL technology is successfully demonstrated in Güssing, at the combined heat and power (CHP) plant, a gasification system with an installed power of 8 MW and a dual fluidized bed reactor for biomass gasification. The first FT plant from Austria (Fig. 1), in Güssing is in operation since 2005, producing 1 t/year FT products (0.03 t/year of diesel) at standard operation conditions: temperature 230 °C, pressure 20 bar, gas flow 5 Nm^3/h, Co catalyst.

The main objectives of the work were to establish the chemical characteristics of the biomass wood chips used at CHP plant Güssing. The research aims to determine by analytical methods the proximate analysis (moisture, ash content and total solids content), bulk density, cellulose, lignin and extractive content, FT-IR analysis over biomass, ultimate analysis (C, H, O, N and S) and heat value. Based on the characteristics of biomass, the syngas produced after gasification was analyzed in order to establish the concentration of the main components (CO, H_2, CO_2, CH_4) BTXN (benzene-toluene-xylene-naphthalene) and sulfur content.

2 Materials and Methods

2.1 Methods

At CHP Güssing plant, the tree trunks are stored on the ground, near the plant in order to dry through solar radiation. The harvested biomass is then size reduced, before it is gasified. From the wood chips, three samples were collected from different parts of the storage. For each of these samples, the analyses were performed three times, in order to get reproducibility and reliable results.

The moisture content was established by oven drying method, according to ASTM D 4442-07. Two types of moisture were determined in the wood chips from CHP Güssing plant: the extrinsic moisture, influenced by weather conditions during harvesting and the intrinsic moisture, the one contained in biomass without the

influence of water. Extrinsic moisture was measured immediately after sampling, while intrinsic moisture was determined after air-drying in laboratory for several days of the samples. Total solids content was determined by difference of intrinsic moisture from the total 100 %. Ash content was determined by applying the loss of ignition method. After measuring the moisture, the dried sample was placed in a crucible and heated to 550 °C for 4 h. Density of air-dried sample was determined as for irregular shaped objects with cylinder method. Quantitative cellulose determination was carried out with nitro-alcoholic dozing method. Determination of lignin content was similar to the cellulose one, but instead of nitro-alcoholic solution, H_2SO_4 72 % was used (Klason-Komarov method). Extractive content of biomass samples in water has been determined by boiling the samples with distilled water for 3 h to remove organic and inorganic substances, like part of the ash, saccharides, tannins, hemicelluloses, or pectin and gums.

The mass fraction of C, H, N, H were determined with an elemental analyzer (EuroVector EA 3000) equipped with TCD detector them. Oxygen is determined by difference from 100 %. High and low heating values were determined with established empirical equations from International Energy Agency. These formulas were used also by other researchers [15, 16] who made comparison between heat value measured and calculated and showed that a good estimation of the heating value is possible by using the equations:

$$HHV = 0.349\,\%C + 1.178\,\%H + 0.1005\,\%S - 0.015\,\%N - 0.103\,\%O - 0.21\,\%Ash$$

$$LHV = HHV\left(1 - \frac{\%Moisture}{100}\right) - 2.447 \cdot \frac{\%Moisture}{100} - \frac{\%H}{200} \cdot 18.02 \cdot 2.447 \cdot \left(1 - \frac{\%H}{100}\right)$$

IR spectra of the dried biomass samples were obtained with an ATR-FTIR spectrophotometer from Perkin Elmer, at spectral resolution of 4 cm^{-1}, 16 scans.

The composition of the syngas produced by biomass gasification was determined by online measurements with the gas chromatograph (GC) Clarus 500 Perkin Elmer, equipped with three different column (2 apolar—Porapak and 1 molar sieve) and two detectors—thermal conductivity detector (TCD) for permanent gases (CO, CO_2, N_2, O_2) and flame ionization detector (FID) for C_1–C_3 hydrocarbons. For the naphthalene and BTX content from syngas, another gas chromatograph from Perkin Elmer equipped with a 60 m MXT1 capillary column and FID detector, while the sulfur content was measured with a Clarus 500 Perkin Elmer with chemiluminescence detector and a 30 m MXT1 capillary column.

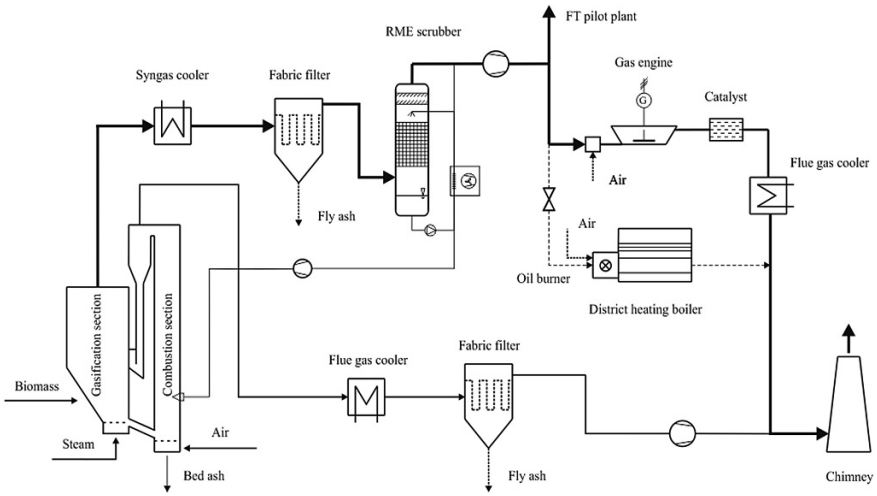

Fig. 2 Flow sheet of CHP plant

2.2 Technical Equipment for Biomass Gasification

The flow sheet of the CHP plant used for biomass thermochemical conversion is presented in Fig. 2. The wood chips are fed into the stationary fluidized bed reactor, named the gasification zone, where steam is used as oxidant to convert the biomass in CO, H_2, CO_2, CH_4 and H_2O. Non-gasified carbon is transported together with the bed material, via a chute, in the circulating fluidized bed reactor, the combustion section, where char is fully combusted in the presence of air. The heated bed material is separated by the flue gas with a cyclone and feed back in the gasification section, providing energy necessary for gasification The syngas produced is cooled down from 850–900 to 150–180 °C with a water heat exchanger and cleaned by tars, particles, ammonia and aromatics with a fabric filter and a rapeseed methyl ester (RME) scrubber. The scrubber is also used to cool the syngas to about 40 °C, necessary for the gas engine. The clean gas is transported simultaneous to the Fischer-Tropsch pilot plant and a gas engine to produce electricity and heat. The flue gas produced in the combustion section is cooled, cleaned by ash and released in the atmosphere by a chimney. CHP plant had more than 7,000 h of operation in 2011, with a thermal efficiency of 56 % and an electrical efficiency 25 %. About 2 t/h of biomass are used, in order to produce 2,500 Nm^3/h for an electrical output of 2 MW and a thermal output of 4.5 MW.

3 Results and Discussions

3.1 Proximate and Ultimate Analysis

The results of the wood chips analysis from Güssing Centre, Austria are presented in Table 1, including the measured values for three samples collected, the mean value, standard deviation and different references found in literature for the same type of biomass. As it can be observed, the water content of the biomass samples was in the range of 39.3 and 42.8 %, for the extrinsic moisture, and in the range of 6.3 and 7.6 for the intrinsic moisture, with standard deviations of 1.5, respectively 0.5, an acceptable precision of the method obtained also by [16–18]. The high extrinsic moisture is due to the weather conditions (rainy period) when the samples have been collected. Normally, the extrinsic moisture of woody biomass should be approximately 30 % [6]. Water content of biomass has direct influence on the gasification because excessive levels decrease the heating value, the combustion temperature by consuming heat in water evaporation. Thus, the efficiency of the conversion and the quality of the syngas are affected. The heating value (MJ/kg) can be reduced with more than 65 % if the moisture content of biomass is increasing from 0 to 40 %. Also, high moisture content lowers the capacity, causing maintenance difficulties. Because moisture promotes the microbial decomposition activity, the physical and chemical quality of the fuel can be deteriorated.

Table 1 Characteristics of biomass used at CHP Güssing

Property	M.U.	Wood chips Güssing						
		I	II	III	Mean	σ	[16]	[6]
Extrinsic moisture	wt.%	42.85	39.31	39.77	40.64	1.57	–	–
Intrinsic moisture	wt.%	7.63	6.38	6.73	6.91	0.52	7.7	9.2
Total solids	wt.%	92.37	93.62	93.27	93.09	0.52	92.3	90.8
Ash content	wt.%	1.76	1.95	1.71	1.81	0.1	0.51	0.6
Bulk density	kg/m^3	517.8	472.3	500.8	496.9	0.02	591	–
Cellulose content	wt.%	34.89	27.47	35.66	32.65	3.68	–	–
Lignin content	wt.%	37.89	26.47	38.08	34.13	5.42	–	–
Extractive content	wt.%	8.66	7.53	7.48	7.89	0.55	–	–
pH (aqueous extract)		6.85	6.37	6.66	6.63	0.2	–	–
C	wt.%	46.94	47.45	46.9	47.1	0.25	50.3	45.9
H	wt.%	5.78	5.87	5.99	5.88	0.09	5.7	5.13
N	wt.%	0.4	0.64	0.37	0.47	0.12	0.22	0.12
S	wt.%	0.57	0	0.01	0.19	0.27	–	0.24
O	wt.%	46.31	46.05	46.72	46.36	0.28	0	48.5
HHV	MJ/kg	18.42	18.66	18.56	18.55	0.1	20.3	18.2
LHV	MJ/kg	14.43	14.88	14.67	14.66	0.18	–	–

σ—standard deviation

Thermochemical conversion processes require lower moisture content of biomass, comparative with biochemical conversion processes. However, some moisture is required also in the thermochemical conversion processes, especially gasification, for H_2 production [14, 19]. It was established that 70 % moisture is the maximum permissible value and biomass which exceeds the value has to be treated first by drying or to be mixed with drier materials in order to meet the permissible value [20].

The lower the moisture content, the higher the total solids content of the biomass, thus more carbon and hydrogen to be oxidized during combustion, increasing the heating value. In case of biomass samples from CHP plant Güssing, after water excess evaporation, the total solid content had a mean value of 93.1 %.

The ash content of the biomass is essential for the choice of the appropriate type of gasifier and gas cleaning technology [6]. Biomass with high ash content has to be avoided, due to increasing danger of slag and deposit formation of the gasifier components, as well as increasing dust emissions and waste stream that will need to be removed and disposed [16]. In case of wood chips from Güssing, the analysis showed a low ash content, 1.81 % the average, which normally corresponds for mixed wood samples, containing bark, coniferous and deciduous species. The usual ash content for softwood is between 0.5 and 0.8 %, for hardwood is between 1 and 1.3 %, coniferous and deciduous wood without bark have an ash content of 0.3 %, while the ash content of the coniferous and deciduous bark range between 4 and 5 %. Even so, the ash content of wood is less than in coal (bituminous coal—9 %, lignite coal—6 %) or agriculture residues [14].

Bulk density of wood chips samples varied between 470 and 520 kg/m^3, with an average value of almost 497 kg/m^3, similar with other values found in literature [22, 27, 29]. This characteristic of biomass has significance influence over the transportation costs, storage capacity and handling equipment, as well as combustion behavior. Higher density reaches longer burnout time. The bulk density determines also the radius from which the biomass has to be acquired and as higher the bulk density, lower are the transportation costs [14].

The samples of wood chips collected from Bioenergy 2020+, Güssing, had an average cellulose content of 32.65 %, lignin content of 34 % and extractive content 7.89 %. The nitro-alcoholic dozing method (for cellulose) and the Klason-Komarov method (for lignin) had the highest standard deviation, showing the complexity and the difficulty of a quantitative and complete isolation of these polymers. Lower cellulose and lignin content than the ones expected, were obtained in the biomass sample, especially in case of sample II. It is possible that the high extrinsic moisture content favored the polysaccharides decomposition, due to biochemical fermentation.

The extractive content in the biomass samples was in the range of 7.48 and 8.66 % (7.8 % mean value) and the aqueous extracts had a slightly acidic pH (6.63). It is important to analyze the aqueous extracts because the high content of water from biomass, the extractive content can leach into the soil, where the biomass is stored, with potential pollution, especially in case the biomass represents industrial residues, like wood treated with dye.

In case of ultimate analysis (C, H, N, S content), significant variation of concentration appears for N, the range of 0.37–0.64 %, respectively S, in the range of

0–0.57 %. It has been demonstrated that coniferous wood have lower N concentration (0.1 %) than bark wood (0.5 %). The same observation can be done also for S, coniferous and deciduous wood having 0.02 % S, while bark has 0.1 % S [6]. This could be an explanation for the variations appeared in the biomass samples Güssing, which are mixture of different wood species and bark wood. During gasification, N is converted to N_2, NH_3, HCN, while S is converted to H_2S, organic sulfides, like carbonyl sulfides, methylmercaptane or thiophene, poisoning the syngas produced. Thus, the concentration of N and S should be as low as possible.

Wood chips samples analyzed had similar HHV, average value of 18.55 MJ/kg (standard deviation 0.1), respectively LHV of 14.66 MJ/kg (standard deviation 0.18). The results were in agreement with other research, where the HHV of wood based biomass is from 18 to 20 MJ/kg [6, 16].

3.2 FT-IR Spectroscopy

The spectra of wood chips samples are presented in Fig. 3, showing three important regions in all samples: 3,000–3,800; 1,400–1,600 and 750–1,180 cm^{-1}.

The small peaks at 3,740 cm^{-1}, seen in samples II and III could be related to the absorbed water in the wood [21, 22], while the broad bands at 3,330–3,340 cm^{-1} are attributed to the hydroxyl groups of the phenol and aliphatic OH stretching [23]. The peaks from 2,920 cm^{-1} are characteristic for C–H stretching in methyl and methylene groups from cellulose, lignin and hemicelluloses. The band at 1,600–1,620 cm^{-1} is attributed to the unconjugated and conjugated C=O stretching from lignin and xylan [24]. A small peak is observed at 1,510–1,520 cm^{-1}, representative for the aromatic skeleton vibration, while at 1,460 cm^{-1} the peaks are assigned to C–H deformation or aromatic ring stretch from lignin, xylan and cellulose [25]. Important peaks appear also in the region of 1,230 cm^{-1}, indicative of the syringyl ring and O–C–O stretching in lignin and xylan [22], at 1,020–1,180 cm^{-1} characteristic to C–O–C stretching in

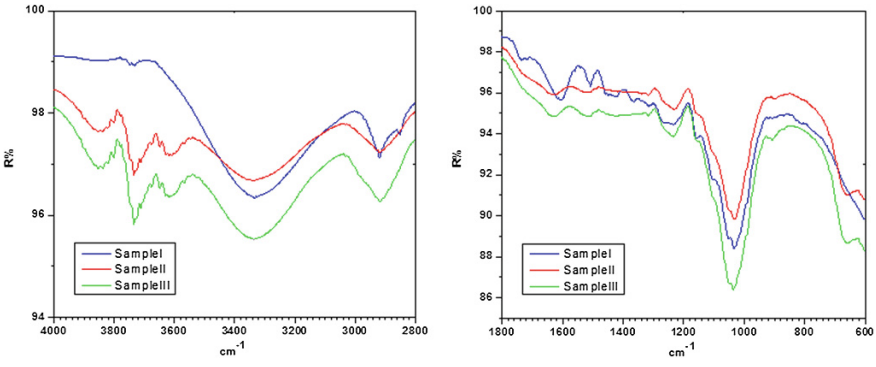

Fig. 3 IR spectra of wood chips samples

pyranose rings and C–O deforming in secondary alcohols and aliphatic ethers [26]. Other peaks could be detected at 905 cm^{-1} which corresponds to C–H deformation in cellulose and at 670 cm^{-1}, ascribed to O–H groups of non-free and involved in hydrogen bonds.

3.3 Syngas Analysis

The syngas obtained after wood chips gasification at CHP plant consists in high concentration of H_2–39 %, CO—21 %, CO_2–23 %, CH_4—10 % and N_2—1.85 %. The type of gasifier, the oxidant agent, the ratio oxidant/biomass, temperature, retention time, influence directly the composition of syngas produced from biomass. Dual fluidized bed gasifier (as presented in Fig. 2) gives syngas with high quality, due to high content of H_2 and low content of tars, without the necessity to preheat the biomass and with the possibility to gasify biomass with high moisture content [27].

Secondary compounds determined in the syngas produced at the CHP plant with the wood chips biomass are C_2 and C_3 alkanes and alkenes, more than 0.18 % for ethane and 0.02 % for propane, respectively 3 % for ethene and 0.3 % for propene. Comparative with GtL technology, in BtL technology the syngas derived from biomass has a lower H_2/CO ratio and contains contaminants—H_2S, COS, NH_3, HCl, tars and dust [28]. H_2/CO ratio has a significant impact over the FT synthesis, lower H_2/CO determining in increase of the C_{5+} selectivity. In Table 2 are presented the concentration of syngas impurities produced at CHP plant and their specific cleaning stages.

The analysis made on the syngas obtained from the biomass analyzed, after cleaning stages at CHP plant Güssing and FT plant are presented in Table 3. It was clearly seen the good efficiency of the cleaning stages of CHP plant, due to lower content of BTX and sulfur components. However, subsequent cleaning stages of syngas are necessary in order to decrease the concentrations of BTX to less than 0.5 g/Nm^3 and sulphur to 1 ppm. Due to the RME scrubber, activated charcoal, ZnO and CuO reactors from the FT plant, the BTX and sulfur content decreased to 0,1 g/Nm^3 and 0.02 ppm, making the syngas suitable for FT synthesis.

Table 2 Undesirable components in synthesis gas from CHP plant [29]

Component	Raw gas
Tars (mg/Nm^3)	1,500–4,500
Particles (mg/Nm^3)	5,000–50,000
NH_3 (ppm)	1,000–2,000
H_2S (ppm)	~150
Organic sulfur (ppm)	~20

Table 3 Composition of syngas after cleaning stages at CHP plant

Component	M.U.	CHP plant	FT plant
Main components			
H_2	Vol%	39	36.35
CO	Vol%	21.04	21.58
CO_2	Vol%	23.94	24.35
N_2	Vol%	1.85	2.73
O_2	Vol%	0.23	0.08
CH_4	Vol%	10.34	10.86
C_2H_6	Vol%	0.18	3.86
C_2H_4	Vol%	3.16	0.14
Undesirable components			
Benzene	g/Nm^3	6.88	0.03
Toluene	g/Nm^3	1.30	0.01
Xylene	g/Nm^3	0.49	0.02
Naphthalene	g/Nm^3	0.95	0.06
H_2S	ppm	64.81	0.02
Organic S	ppm	27.27	0

4 Conclusions

The analysis made over biomass wood chips from Güssing Centre, Austria, used for Fischer-Tropsch diesel synthesis, showed that:

(a) The results of the proximate and ultimate analyses were similar with the ones obtained by other research, with intrinsic moisture of almost 7 %, ash content 1.8 % and bulk density of 500 kg/m^3; higher extrinsic moisture (40 %) than the standard value (30 %) was obtained due to the bad weather conditions (winter time) during harvesting the biomass samples;
(b) Ultimate analyses of the biomass samples have been done by determining the content of cellulose, lignin and extractive and the concentration of C, H, N, S and O; Lower content of cellulose (34 %) and higher content of lignin (35 %) than the expected values were obtained probably due to the higher water content which favored the decomposition of the polysaccharides;
(c) FT-IR spectra of biomass gave more details about the structure of the biomass wood chips, being in good correlation with the ultimate analysis regarding the cellulose and lignin content, the main components of wood chips samples;
(d) Low concentration of S and N were found and the variations of the mass fraction for each biomass sample could be due to the mixture of different species of wood and bark; the low concentration of S and N determined low

emissions of NH_3 and H_2S during gasification of biomass and the cleaning stages of the CHP plant and FT plant, delivered to the FT slurry reactor a synthesis gas suitable for Fischer-Tropsch synthesis and middle distillate fraction selectivity.

Acknowledgments This work has been supported by the CHP plant Güssing by offering the wood chips biomass samples, Bioenergy 2020+ Centre of Güssing and by the Sectoral Operational Programme Human Resources Development (SOP HRD), financed from the European Social Fund and by the Romanian Government under the contract number ID59321.

References

1. Stöcker, M. (2008). Biofuels and biomass-to-liquid fuels in the biorefinery catalytic conversion of lignocellulosic biomass using porous materials. *Angewandte Chemie International Edition, 47*, 9200–9211.
2. Rapagnà, S., Gallucci, K., Di Marcello, M., Matt, M., Nacken, M., Heidenreich, S., et al. (2010). Gas cleaning, gas conditioning and tar abatement by means of a catalytic filter candle in a biomass fluidized-bed gasifier. *Bioresource Technology, 101*, 7123–7130.
3. Tock, L., Gassner, M., & Maréchal, F. (2010). Thermochemical production of liquid fuels from biomass: Thermo-economic modelling, process design and process integration analysis. *Biomass and Bioenergy, 34*, 1838–1854.
4. Bremaud, M., Fongarland, P., Anfray, J., Jallais, S., Schweich, D., & Khodakov, A. Y. (2005). Influence of syngas composition on the transient behaviour of a Fischer-Tropsch continuous slurry reactor. *Catalysis Today, 106*, 137–142.
5. Pfeifer, C., Puchner, B., & Hofbauer, H. (2009). Comparison of dual fluidized bed steam gasification of biomass with and without selective transport of CO_2. *Chemical Engineering Science, 64*, 5073–5083.
6. García, R., Pizarro, C., Lavin, A. G., & Bueno, J. L. (2012). Characterization of Spanish biomass wastes for energy use. *Bioresource Technology, 103*, 249–258.
7. Fischer, G., Prieler, S., van Velthuizen, H., Lensink, S. M., Londo, M., & de Wit, M. (2010). Biofuel production potentials in Europe: Sustainable use of cultivated land and pastures: Part I: Land productivity. *Biomass and Bioenergy, 34*, 159–172.
8. Tijmensen, M. J. A., Faaij, A. P. C., Hamelinck, C. N., & van Hardeveld, M. R. M. (2002). Exploration of the possibilities for production of Fischer-Tropsch liquids and power via biomass gasification. *Biomass and Bioenergy, 23*, 129–152.
9. Chum, H. L., & Overend, R. P. (2001). Biomass and renewable fuels. *Fuel Processing Technology, 71*, 187–195.
10. Damartiz, T., & Zabaniotou, A. (2011). Thermochemical conversion of biomass to second generation biofuels through integrated process design—A review. *Renewable and Sustainable Energy Reviews, 15*, 366–378.
11. Sauciuc, A., Dumitrescu, L., Manciulea, I., & Zaha, C. (2011). Studies on recycling of waste cooking oils for biodiesel production. *Environmental Engineering and Management Journal, 10*, 205–211.
12. Zwart, R. W. R., Boerrigter, H., & van der Drift, A. (2006). The impact of biomass pretreatment on the feasibility of overseas biomass conversion to Fischer-Tropsch products. *Energy and Fuels, 20*, 2192–2197.
13. Naik, S. N., Goud, V. V., Rout, P. K., & Dalai, A. K. (2010). Production of first and second generation biofuels: A comprehensive review. *Renewable and Sustainable Energy Reviews, 14*, 578–597.

14. Bao, B., El-Halwagi, M. M., & Elbashir, N. O. (2010). Simulation, integration, and economic analysis of gas-to-liquid processes. *Fuel Process Technology, 91*, 703–713.
15. Cheng, J. (2010). *Biomass to renewable energy processes*. Boca Raton, USA: CRC Press Taylor & Francis Group Publishing.
16. Obernberger, I., & Thek, G. (2004). Physical characterization and chemical composition of densified biomass fuels with regard to their combustion behaviour. *Biomass and Bioenergy, 27*, 653–669.
17. Samuelsson, R., Burvall, J., & Jirjis, R. (2006). Comparison of different methods for the determination of moisture content in biomass. *Biomass and Bioenergy, 30*, 929–934.
18. Neves, D., Thunman, H., Matos, A., Tarelho, L., & Gómez-Barea, A. (2011). Characterization and prediction of biomass pyrolysis products. *Progress in Energy and Combustion Science, 37*, 611–630.
19. Wankhade, P.P., Jajoo, B.N., Wankhade, R.P. (2009). Performance evaluation of parameters of biomass gasifier-diesel engine setup using woody biomass (Subabool). In *IEEE International Conference Emerging Trends in Engineering and Technology*, *Nagpur*, *India* (pp. 25–29).
20. Faaij, A., Van Ree, R., Waldheim, L., Olsson, E., Oudhuis, A., Van Wijk, A., et al. (1997). Gasification of biomass wastes and residues for electricity production. *Biomass and Bioenergy, 12*, 387–407.
21. Strezov, V., Moghtaderi, B., & Lucas, J. A. (2004). Computational calorimetric investigation of the reactions during thermal conversion of wood biomass. *Biomass and Bioenergy, 27*, 459–465.
22. Mohebby, B. (2005). Attenuated total reflection infrared spectroscopy of white-rot decayed beech wood. *International Biodeterioration and Biodegradation, 55*, 247–251.
23. She, D., Xu, F., Geng, Z. C., Sun, R. C., Jones, G. L., & Baird, M. S. (2010). Physicochemical characterization of extracted lignin from sweet sorghum stem. *Industrial Crops and Products, 32*, 21–28.
24. Popescu, C. M., Popescu, M. C., & Vasile, C. (2010). Characterization of fungal degraded lime wood by FT-IR and 2D IR correlation spectroscopy. *Microchemical Journal, 95*, 377–387.
25. Zmora-Nahum, S., Hadar, Y., & Chen, Y. (2007). Physico-chemical properties of commercial composts varying in their source materials and country of origin. *Soil Biology and Biochemistry, 39*, 1263–1276.
26. Huang, A., Zhou, Q., Liu, J., Fei, B., & Sun, S. (2008). Distinction of three wood species by Fourier transform infrared spectroscopy and two-dimensional correlation IR spectroscopy. *Journal of Molecular Structure, 883*, 160–166.
27. Göransson, K., Söderlind, U., & Zhang, W. (2011). Review of syngas production via biomass DFBGs. *Renewable and Sustainable Energy Reviews, 15*, 482–492.
28. Tristantini, D., Lögdberg, S., Gevert, B., Borg, Ø., & Holmen, A. (2007). The effect of synthesis gas composition on the Fischer-Tropsch synthesis over Co/γ-Al2O3 and Co-Re/γ-Al2O3 catalysts. *Fuel Processing Technology, 88*, 643–649.
29. Sauciuc, A., Potetz, A., Weber, G., Rauch, R., Hofbauer, H., Dumitrescu, L. (2011). Synthetic diesel from biomass by Fischer-Tropsch synthesis. In *Proceedings of International Conference on Renewable Energies and Power Quality, Gran Canary, Spain* (pp. 1–6).

Part III
Renewable Based Electricity Production in the Built Environment

New Priorities in Solar Photovoltaic Applications

Istvan Farkas

Abstract This paper deals with the new priorities and application possibilities of the photovoltaic technology. No doubt that the photovoltaic (PV) technologies will show their significance for longer period. The most important standpoints characterising the PV industry are to be discussed. The new features of the PV technology and the applications are also studied in a great extent. It includes new type of modules along with their colouring, extra size and the fixation system. Examples are shown for such application possibilities.

Keywords Thin film · Colouring · Transparency · New fixation system · Applications

1 Introduction

Within the use of solar energy the solar thermal field identified at a lower innovation potential however their application shows large varieties. Especially the production of electricity from solar thermal is a preferred solution.

In spite of the recent economic situation all over the world a significant yearly increase of photovoltaic module production and their installation were performed in last couple of year period. However it can be observed sensitivity of the market change on the photovoltaic industry, the PV technologies still show increasingly high priority.

At the same time, there are some very important features which are characterising and influencing the PV manufacturing and applications industry. The most important standpoints could be summarized as follows:

I. Farkas (✉)
Department of Physics and Process Control, Szent István University,
Gödöllő Pater K. u. 1, 2100, Hungary
e-mail: farkas.istvan@gek.szie.hu

I. Visa (ed.), *Sustainable Energy in the Built Environment - Steps Towards nZEB*,
Springer Proceedings in Energy, DOI 10.1007/978-3-319-09707-7_26

- 20–30 % of the part of renewables in the energy mix,
- at around 30–40 % yearly decrease of the PV cell and module prises,
- the cell efficiency in market products does not increase in a great extent as expected,
- strong competition between the crystalline and the thin film technologies,
- multi-Gigawatts applications are getting into the practice,
- widening the feed-in tariff system in several countries in worldwide,
- presence of the Chinese PV products in worldwide and especially in the European Union market.

Due to the growing market demand of the solar photovoltaic applications several new specific issues came to the light. These factors include new type of modules along with their colouring and extra size, wide range application of thin film technologies, colouring of the modules, transparency of the modules, extra size of modules and new type of fixation systems.

At the Department of Physics and Process Control at Szent István University (SIU) Gödöllő, Hungary as a part of research activities there were performed several solar installations. Among them the largest solar photovoltaic application is a 10 kWp capacity grid-connected system including two different module technologies as polycrystalline and amorphous silicon ones. During the new photovoltaic installation plans at the campus the above mentioned factors are also taking seriously consideration.

2 Recent PV Installation at the Campus Area

In the framework of the PV Enlargement Project of the European Union, a 10 kWp photovoltaic system was constructed (Fig. 1) in the central campus of the SIU. This set-up was the largest grid-connected PV installation in Hungary that time, and beside of the energy production it serves demonstrational, educational and research purposes, too. For the PV modules two different options were proposed as polycrystalline and amorphous silicon technologies. The reason for the use of different technologies is the comparison of the different technologies at the same location under the same operating conditions [1].

The system is installed on the flat roof of a student hostel building of the campus. The azimuth angle is 5° to East and the tilt angle is 30°, which is a good yearly average value for the site. The system consists of three different subsystems, having an own inverter, the same type for each. The PV system is structured into 3 subsystems. One subsystem has 32 pieces of ASE-100 type modules, and the remaining two identical subsystems are planned for using 77 pieces of DS40 type of modules each. The total power of the system is 9.5 kWp.

The main variables measured by the data logging system can be seen in the operational scheme in Fig. 2 as:

Fig. 1 The existing grid-connected PV installation

- Irradiation (in the panel plane by a silicon reference sensor, and the total radiation by a pyranometer),
- Temperature (environmental and module temperature for each type, measured by Pt100 sensors),
- PV array (DC) voltage, current and power,
- AC voltage, current and power supplied to the electrical grid.

Beside an installed PC based data logger, an authorized two way electrical meter was also installed as a control unit for the energy data. The metering unit can store the measured data of a 3 month period and the data can be read out through a telephone modem.

3 New Plans for PV Application Possibilities

Beside the 10 kWp capacity of grid-connected PV plan several new installation plans of about 50 kWp capacity each were considered at the campus of the SIU [2]. Among them four important building were identified showing a kind of priority among the sites of applications:

Laboratory building,
Dormitory building,
Knowledge Transfer Centre building,
Aula building.

The roof area and structure of the selected building were analysed taking into consideration of the size, orientation and tilt. After that preliminary design installation plans were performed along with the energetic estimations. During the calculations the internet-based PVGIS [3] simulation software was applied.

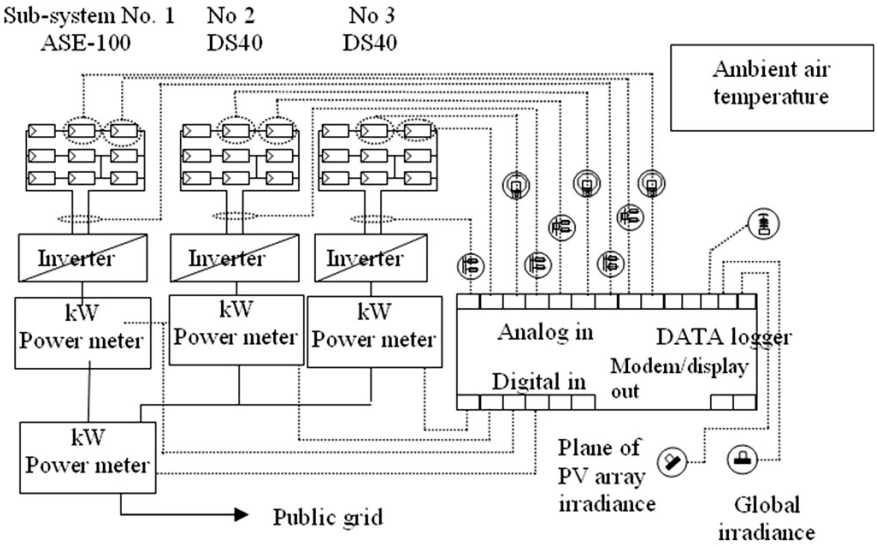

Fig. 2 Operational scheme and data acquisition system of the PV installation

Fig. 3 Picture of the laboratory building

Laboratory Building

The roof structure of the Laboratory building has got a very special shape as it can be seen in Fig. 3.

Table 1 Possible area for PV installation in laboratory building

Notation	Number of roofs (db)	Roof size	Total area (m^2)
North wing	5	19 m × 2 m	190
South wing	6	13 m × 2 m	156
Total			346

The freely available are for the location of the photovoltaic modules is given in Table 1.

The main data of the grid-connected installation are as follows:

Number of modules: 168 pcs (90 for North and 78 for South building)
Capacity of one crystalline module: 265 Wp
Total capacity: 44.52 kWp

Based on the PVGIS [3] simulation the specific energy production of the system is around 1,110 kWh/kWp.

Dormitory Building

The picture of the Dormitory building consisting of two parts (D1 and D2) can be seen in Fig. 4.

Fig. 4 Picture of the dormitory building

Table 2 Possible area for PV installation in dormitory building

Notation	Direction of the roof to south degree	Tilt angle degree	Specific energy production kWh/kWp	Area m^2
D1 east	−105	8	951	150
D1 west	75	8	987	150
D2 north	165	10	882	180
D2 west	75	10	988	220

The freely available are for the location of the photovoltaic modules avoiding the shaded parts is given in Table 2.

The main data of the grid-connected installation are as follows:

Number of modules: 138 pcs (69 for D1 East, 69 D1 West and 62 for D2 building)
Capacity of one crystalline module: 240 Wp
Total capacity: 48 kWp

Knowledge Transfer Centre Building

The front side picture of the Knowledge Transfer Centre building can be seen in Fig. 5.

This building has recently been reconstructed and having a quite large flat roof area of about 3,000 m^2 which is available are for the location of the photovoltaic modules. Furthermore, it is beneficial that the modules can be positioned ideally at 33–35° of tilt angle along with South facing orientation.

Fig. 5 Picture of the knowledge transfer centre building

Fig. 6 Tectum flat roof system

In return the roof is covered with a special plastic cover which causes some difficulty in the fixation of the support for the modules. For such a purposes, for example, it can be used the solution of Tectum flat roof system [4], which has a feature of quick installation, lightweight ($\sim$12 kg/m^2) and high yields (Fig. 6).

The main data of the grid-connected installation are as follows:

Number of modules: 200 pcs
Capacity of one crystalline module: 256 Wp
Total capacity: 53 kWp

Based on the PVGIS [3] simulation the specific energy production of the system is around 1,200 kWh/kWp.

Aula Building

The picture of the Aula building can be seen in Fig. 7.

For the location of the PV modules the following solutions can be considered:

(a) Changing glass surfaces with transparent thin film modules,
(b) Installing green colour PV modules in front of the green building plastic elements,
(c) Installing modules with low tilt on the flat roof area just above the office rooms.

The freely available area for the location of the photovoltaic modules is given in Table 3.

The main data of the grid-connected installation are as follows:

For the vertical arrangement (in front of the green plastic elements):

Number of modules: 78 pcs

Fig. 7 Picture of the dormitory building

Table 3 Possible area for PV installation in aula building

Notation	Direction of the roof to south degree	Tilt angle degree	Specific energy production kWh/kWp	Area m^2
West (entrance)	80	90	586,951	105
South	−10	90	757	30
West (entrance flat)	−10	10	1,050	100
South (entrance flat)	−10	10	1,050	180

Capacity of one crystalline module: 250 Wp
Total capacity: 19.5 kWp

For the low tilted flat arrangement:

Number of modules: 110 pcs
Capacity of one crystalline module: 265 Wp
Total capacity: 29.15 kWp

4 Transparent PV Applications

With the support of the British Council a Climate Office has been established at the campus dealing with all the aspects of the climate change, environmental issues related to the energy consumption.

Fig. 8 Glass PV plan

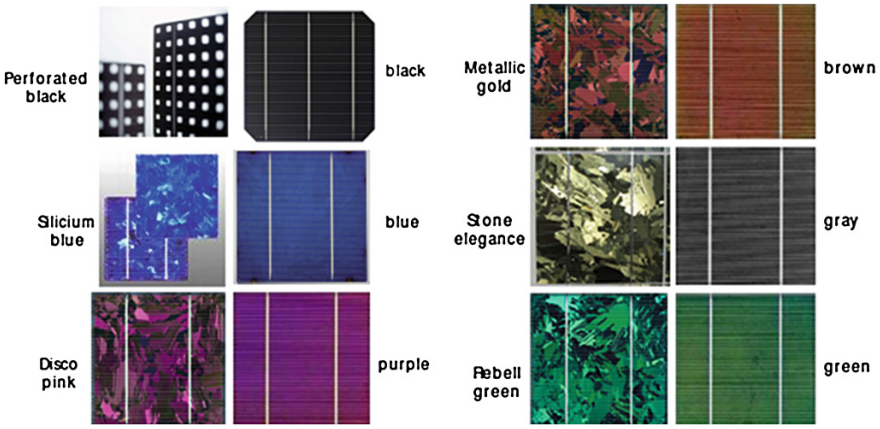

Fig. 9 Suntech glass PV colours

The Climate Office has made several plans for the use of renewable energy resources at the campus including also the solar energy. Among them one important idea was to use semi-shade PV modules located at the corridor of the Climate Office rooms. The preliminary plan of that unit is shown in Fig. 8.

The attractiveness of the applications is increased with the use of the different colours of modules. The possible colours of the planned semi-shade cells [5] can be seen in Fig. 9.

The main features of the Suntech modules are the standard framed unit with a tempered front glass and the durable clear polymer substrate. The module has got 50 % transparency, so it can be used to increase natural light behind the module along with providing energy production and surely some shading.

5 Environmental Influences

The applicability of solar energy is favourable in Hungary especially in the sense of radiation characteristics. The yearly sunny hours varies between 1,990 and 2,200. The average value of solar irradiation is 1,300 kWh/m^2. As a matter of fact, there is a significant difference between the summer and winter radiation conditions. In winter period there are some obstacles which have to be taken seriously into account.

Concerning to the photovoltaic applications the roof integrated and the ground positioned autonomous and grid-connected solutions are the most typical solutions.

The solar photovoltaic potential can be calculated on the basis of the available area all through the country which is estimated as: 4051.48 km^2 including the fields located along with the highways and railways. Considering the tilt angle of the available areas and the efficiency of the solar modules the entire solar photovoltaic potential was estimated as: 1,749 PJ/year.

Beside the energy saving opportunities the environmental impact of the use of photovoltaic technology can also be significant effect. For the estimation of the total reduction of the CO_2 emission the relative value of 0.82 kg/kWh is to be applied.

6 Conclusions

The priority of the use of PV installations at the campus is obvious as electric power generation is basically required.

Preliminary technical design of four typical 50 kWp capacity grid-connected PV system design has been completed along with the energetic and financial calculations.

Additionally some the environmental and social impacts of the plan were also taken into consideration.

Acknowledgment This work was carried out within the project OTKA K 84150.

References

1. Farkas, I. (2011). Solar energy applications. In R. Kovács (Ed.), *Hungarian renewable energy handbook 2011, Poppy Seed 2002 Bt* (pp. 32–34).
2. Farkas, I., Seres, I., Kocsany, I., & Zs, Termann. (2014). Installation possibilities of photovoltaic energy utilization systems, Magyar Energetika. *Hungarian, XXI*(2), 30–33.
3. Photovoltaic Geographical Information System (PVGIS)—Interactive maps (2014).

4. Soltecture, Tectum flat roof system. http://www.soltecture.com/uploads/media/Datasheet_TECTUM_EN_REV2.3_02.pdf, 15.15.2014.
5. Suntech, Semi-shade modules. www.suntech-power.com, 15.05.2014 http://re.jrc.ec.europa.eu/pvgis/apps4/pvest.php, 15.05.2014.

Improved Performance of Quasi-solid State Dye-Sensitized Solar Cells After Photoanode Surface Treatment with Novel Materials

D. Sygkridou, A. Rapsomanikis, A. Apostolopoulou, A. Ifantis and E. Stathatos

Abstract At the present work, we investigate the effect of TiO_2 nanocrystalline films surface treatment with two titanium based organic materials using chemical bath deposition technique. The two novel materials are titanium(IV) (triethanolaminato) isopropoxide and titanium(IV) bis(ammonium lactate)dihydroxide which are structural different from $TiCl_4$ which is a common material for TiO_2 post-treatment. The treated and untreated films are examined as negative photoelectrodes in quasi-solid state dye sensitized solar cells. The cells were characterized in terms of their electrical characteristics while direct comparisons based on the structural properties of the films were also made. Both treated films as photoelectrodes in dye sensitized solar cells exhibited better performance compared to the untreated films with recorded 26–30 % increase to the overall efficiency depending on the material used for the treatment. Dark current measurements were also performed in order to evaluate the effect of both materials as reducers of charge recombination rates.

Keywords Dye sensitized solar cells · Nanocrystalline materials · Photoelectrode treatment

1 Introduction

Over the past decades dye sensitized solar cells (DSSCs) have attracted intense interest mainly owing to the simplicity of their fabrication procedures, practically under ambient conditions with mild chemical processes and the fact that it is

D. Sygkridou · A. Rapsomanikis · A. Apostolopoulou · A. Ifantis · E. Stathatos (✉)
Department of Electrical Engineering, Technological-Educational Institute of Western Greece, 26334 Patras, Greece
e-mail: estathatos@teipat.gr

D. Sygkridou · A. Apostolopoulou
Department of Physics, University of Patras, 26500 Patras, Greece

I. Visa (ed.), *Sustainable Energy in the Built Environment - Steps Towards nZEB*, Springer Proceedings in Energy, DOI 10.1007/978-3-319-09707-7_27

possible to manufacture transparent cells that can be used in a variety of applications [1–3]. Although the overall efficiency has reached the record efficiency of 12 % (for laboratory small size) there is still space for further improvements at different fabrication steps of cells realization [4]. In order for DSSCs to become a commercially attractive alternative to conventional photovoltaic solar cells, improvements concerning their cost, overall efficiency and long-term stability are required. In particular, the control of the quality, morphology and design of the mesoporous titanium dioxide as basic photoanode material is of high interest among suggested improvements [5–7].

To enhance the DSSCs performance, the recombination rate, which is considered to be responsible for the dark current and represents the major source of current loss, needs to be reduced [8]. Therefore many researcher's attention has been focused to finding ways to achieve a better contact between the conductive glass (SnO_2:F) and the semiconductor used to manufacture the DSSC and suppress the charge recombination. Throughout the literature there is evidence that an additional layer covering the TiO_2 surface can block the recombination of conduction band electrons with the oxidized dye molecules or the redox system at the TiO_2/electrolyte interface, increasing the photocurrent [9–11]. A widely known procedure to improve the efficiency of the cells is the treatment of the conductive FTO substrate and TiO_2 mesoporous film with an aqueous solution of $TiCl_4$. However, except the use of $TiCl_4$ as a basic material for surface treatment of TiO_2 electrodes many studies have focused on the interface controlling of TiO_2/electrolyte to reduce the loss of the generated electrons especially by introducing Al_2O_3, Nb_2O_5 and $SrTiO_3$ for surface modification of mesoporous electrode [12–14]. The pre-treatment enhances the bonding strength between FTO substrate and porous TiO_2 film while blocks the charge recombination between electrons at FTO and electrolyte. However, the treatment of TiO_2 mesoporous film also improves the connection between nanoparticles and finally increases the current at the cells.

In this work, we demonstrate that the cell's overall efficiency can be enhanced by TiO_2 particles' surface treatment. The TiO_2 nanocomposite films are dipped in a sol containing the surface modifier molecules and stayed for short time succeeding the particles coverage according to chemical bath deposition technique. We studied the effect of two different solutions of (Titanium(IV) (triethanolaminato) isopropoxide (TTAI) and Titanium(IV) bis(ammonium lactate)dihydroxide (TALD) to the short circuit current density, open circuit voltage, fill factor and overall efficiency of quasi-solid state dye sensitized solar cells and finally the results were compared with differences monitored at the structural properties of the films. The TiO_2 films treated with the two aforementioned titanium precursors using chemical bath deposition method showed an increase to their electrical performance under full sunlight exposure. Treated cells with the new precursors are compared with reference cells without TiO_2 particle surface treatment to determine which electrical parameters are most affected. The effect of the annealing temperature of the treated films is also examined.

2 Experimental Section

2.1 Materials

Commercially available lithium iodide, iodine, 1-methyl-3-propylimidazolium iodide, guanidine thiocyanate, chloroplatinic acid hexahydrate (H_2PtCl_6), poly (propylene glycol) bis(2-aminopropyl)ether, 3-isocyanatopropyltriethoxysilane and all solvents were purchased from Sigma-Aldrich and used as received. Titanium (IV) (triethanolaminato) isopropoxide, 80 wt.% solution in 2-propanol and Titanium(IV) bis(ammonium lactate)dihydroxide, 50 wt.% solution in water were also purchased from Sigma-Aldrich and were further diluted using their solvent until their concentration was 1 M. 3-*Cis*-diisothiocyanato-bis(2,2′-bipyridyl-4,4′-dicarboxylato) ruthenium(II) bis(tetrabutylammonium), N719 was purchased from Solaronix S.A, Switzerland. SnO_2:F transparent conductive electrodes (FTO, TEC15) 15 Ohm/square were purchased from Hartford Glass Co., USA. Commercial ultrapure titanium isopropoxide (TTIP, 97 %, Aldrich), Triton X-100 (polyethylene glycol p-tert-octylphenyl ether) surfactant (99.8 %, Fisher Scientific), glacial acetic acid (AcOH, Aldrich) were used to make precursor TiO_2 sols and form a blocking layer among FTO and TiO_2 paste. Titania powder P25 was provided by Degussa, (Germany, 30 % Rutile and 70 % Anatase).

2.2 Preparation of TiO_2 Photoanodes Sensitized with Dye

TiO_2 thin films were first deposited on FTO glasses as blocking layers by following a previously reported procedure [15, 16]. Briefly, for 5.4 ml solution, 0.72 g of Triton X-100 were mixed with 4 ml of ethanol, followed by addition of 0.4 ml of glacial acetic acid and 0.32 ml of titanium isopropoxide under vigorous stirring. After a few minutes stirring, FTO glasses were dipped in the above sol and withdrawn with 2 cm/s. The films were heated up to 500 °C for 30 min using 20 °C/min heating ramp rate. The procedure was applied for the deposition of only one TiO_2 layer while the film thickness was approximately 150 nm. Then a layer of TiO_2 paste was deposited by doctor blading followed by heating to 500 °C. The fabrication of TiO_2 paste is as follows: 3 g of Degussa P25 was mixed with 0.5 ml of acetic acid in a mortar for about 3 min. After that, 2.5 ml of Millipore water and 17.5 ml of ethanol were alternately added to break all TiO_2 aggregates and form a homogenous solution. The solution was transferred to a crucible with 50 ml of ethanol and was mixed with 10 g of terpineol and an amount of ethyl cellulose. The solution was ultrasonicated for about 2 min and then the crucible was placed in a rotary evaporator at 40–45 °C to remove the excessive solvent and form the TiO_2 paste.

After cooling down at around 100 °C, some of the glasses were dipped for 30 min either to the 1 M Titanium(IV) (triethanolaminato) isopropoxide solution

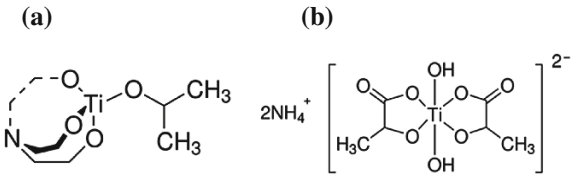

Scheme 1 **a** Titanium (IV) (triethanolaminato) (TTAI) and **b** Titanium(IV) bis(ammonium lactate)dihydroxide (TALD)

(hereafter denoted as TTAI) or to the 1 M Titanium(IV) bis(ammonium lactate) dihydroxide (hereafter denoted as TALD) with two different annealing temperatures (hereafter denoted as i.e. TTAI-300, TTAI-500 and meaning that the films were dipped in 1 M Titanium(IV) (triethanolaminato) isopropoxide solution and sintered at 300 and 500 °C respectively). The chemical structures of TTAI and TALD appear in Scheme 1. The cells fabricated with these glasses were compared with cells with photoanodes that weren't dipped in any of the above solutions (hereafter denoted as reference). BET measurements were performed to determine the pore size distribution, the pore volume and the films' porosity and they were conducted with Micromeritics Tristar 3,000 while film morphology and film thickness were characterized by Scanning Electron Microscopy (FE-SEM, FEI Quanta) and Veeco profilometer respectively. Finally, all the TiO_2 films were immersed in an ethanol/acetonitrile (1/1 v/v) solution of N719 (the dye concentration was 5×10^{-4} M) in order to sensitize the TiO_2 electrode in the visible region.

2.3 *Fabrication and Characterization of Quasi-Solid Dye-Sensitized Cell*

In the construction of the solar cells a quasi-solid state electrolyte was used. This was chosen as a promising approach to DSSC technology as it combines the high ionic conductivity of liquids while it reduces the risk of leaks and minimizes sealing problems in the cells. For the gel electrolyte applied to the DSSCs, we used a hybrid organic-inorganic material which was prepared according to a procedure described in previous publications [17, 18]. Briefly, poly(propylene glycol) bis(2-amino-propylether) of molecular weight 230 and 3-isocyanatopropyltriethoxysilane (ICS; molar ratio ICS/diamine = 2/1) react in a vessel (acylation reaction), producing urea connecting groups between the polymer units and the inorganic part. The gel electrolyte was synthesized by the following procedure: 0.7 g of the functionalized alkoxide precursor (hereafter ICS-PPG230) were dissolved in 1.6 g of sulfolane and 0.8 g of methoxypropionitrile under vigorous stirring. Then, 0.6 ml AcOH were

added followed by 0.3 M 1-methyl-3-propylimidazolium iodide, 0.1 M LiI and 0.05 M I_2 in a final molar ratio AcOH:LiI:MPImI:I_2 = 2.5:0.1:0.3:0.05. After 6 h stirring, one drop of the obtained sol was placed on the top of the titania electrode with adsorbed dye molecules and a slightly platinized FTO counter electrode was pushed by hand on the top. The platinized FTO glass was made by casting a few drops of a H_2PtCl_4 solution (5 mg/1 ml of ethanol) followed by heating at 450 °C for 10 min. The two electrodes tightly stuck together by Si–O–Si bonds developed by the presence of the hybrid material.

2.4 Characterization of the DSSCs

For the *J-V* curves, the samples were illuminated with Xe light using a Solar Light Co. solar simulator (model 16S-300) equipped with AM 0 and AM 1.5 direct Air Mass filters to simulate solar radiation at the surface of the earth. The light intensity was kept constant at 1,000 W/m^2 measured with a CMP 3 Kipp and Zonen pyranometer. Finally, the *I-V* curves were recorded by connecting the cells to a Keithley Source Meter (model 2601A) which was controlled by Keithley computer software (LabTracer). The cell active area was constant to 0.3 cm^2 using appropriate mask while back reflectors were not used in the measurements. For each case, we made two devices which were tested under the same conditions in order to avoid any misleading estimation of their efficiency. Cell performance parameters, including short-circuit current density (J_{SC}), open circuit voltage (V_{OC}), maximum power (P_{max}), fill factor (*FF*) and overall cell conversion efficiency, were measured and calculated from each *J-V* characteristic curve. Two devices were prepared for each case of TiO_2 surface modifier (Titanium(IV) (triethanolaminato) isopropoxide sintered at 300 and 500 °C) and (Titanium(IV) bis(ammonium lactate)dihydroxide sintered at 300 and 500 °C).

3 Results and Discussions

TiO_2 films are fabricated in two steps before their treatment with the two different structured titanium precursors. A thin layer of TiO_2 on FTO glass substrates was applied via sol-gel method while a second thicker layer was coated on top of the above layer made of nanocomposite TiO_2 paste using P25 commercial powder by doctor blade technique. The final thickness of the film was approximately 4 μm according to profilometer measurement. After the preparation of the two different layers of TiO_2, the films were dipped in 1 M titanium(IV) (triethanolaminato) isopropoxide solution in isopropanol or to a 1 M Titanium(IV) bis (ammonium lactate)dihydroxide in water followed by heating either to 300 or 500 °C. The final thickness of the TTAI or TALD treated films were approximately 3.7 and 3.8 μm respectively. The SEM images of treated and untreated films are presented in Fig. 1.

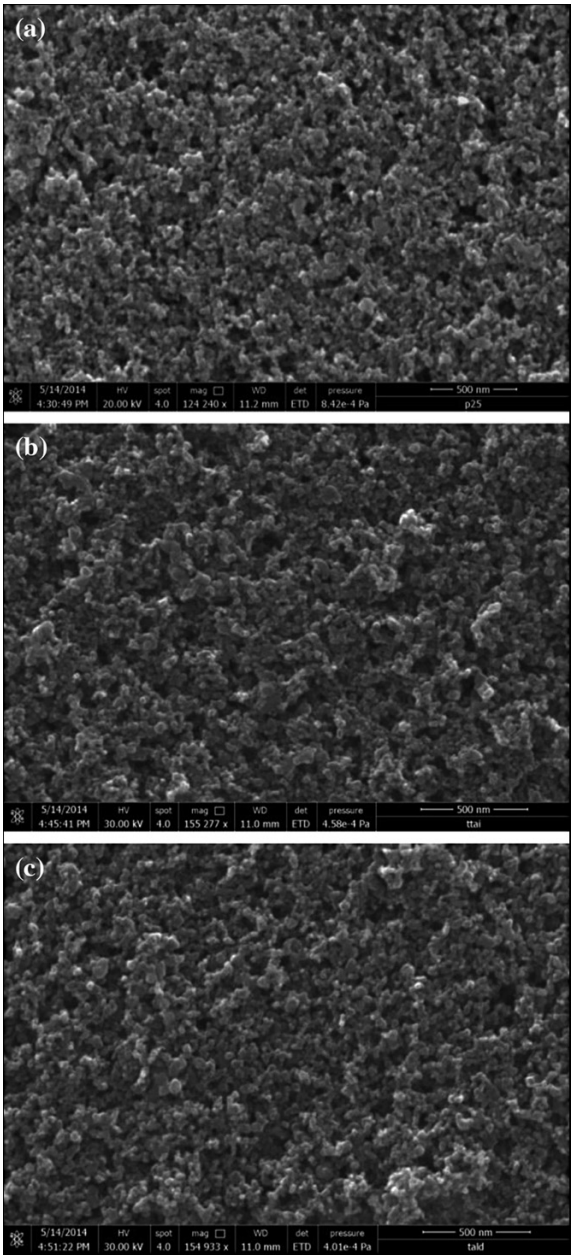

Fig. 1 SEM images of: **a** pure P25-TiO_2, **b** TTAI modified P25-TiO_2 and **c** TALD modified P25-TiO_2 films sintered at 500 °C

As it can be seen the untreated film is consisted of nanoparticles with an average size of 25 nm as it was expected because of the use TiO_2-P25 as starting material. However, no serious deviations are displayed in the presence of TTAI or TALD after films' treatment. The homogeneity of the films and the particle average size

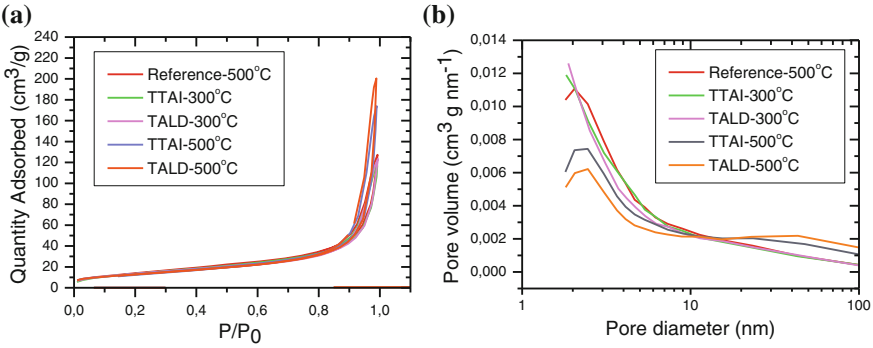

Fig. 2 Sorption-desorption isotherms **a** and pore size distribution **b** for treated and untreated TiO_2 films

look similar among the three images of Fig. 1. This means a very thin coverage of TiO_2 particles in films which does not affect to the increase of the total thickness of the film and particle size. Finally, TTAI and TALD treated TiO_2-P25 films look more porous than untreated films, therefore porosimetry measurements were performed to estimate structural properties of all films.

The texture of untreated P25 powder based nanocrystalline films and TTAI, TALD treated were analyzed by N_2 adsorption and desorption. The results are shown in Fig. 2a, b. In addition, their BET surface area and pore structure are also summarized in Table 1. From Fig. 2a, the hysteresis loop appear in relatively high pressure region ($0.8 < P/Po < 1.0$), which suggests that Degussa P25 particles could lead to the formation of larger pores. For treated and untreated TiO_2 matrix leads to the formation of enhanced mesopore structure. Moreover, treated samples seem to exhibit relatively wider pore size distribution (22–26 nm) compared to the untreated and treated at lower temperature samples (14–15 nm). This behavior to the pore size distribution affects the porosity and total pore volume of the samples which are at the same order. Such large pores are expected to have a beneficial effect on the electrolyte solution wetting and filling in the TiO_2 films. However, the specific surface area of particles is lower in the case of treated samples heated at 500 °C. From Table 1, it can be seen that the BET surface area of the untreated TiO_2 films is 53.01 m^2/g which is getting lower $\sim$51 m^2/g for treated TiO_2 films at 300 °C. Finally the surface area is getting even lower 47–48 m^2/g for treated samples at 500 °C. However, the difference between untreated and treated samples at 500 °C is only 11 %. Finally, as the specific surface area decreased after surface treatment the roughness factor of the treated films was also decreased (500 °C) after compared with the value of the untreated samples.

Figure 3 shows the absorbance of N-719 dye after detachment from all TiO_2 films exposed to 1 M NaOH for the same time (10 min). It is obvious that the quantity of the dye detached from all treated samples is higher than the untreated sample. The exact intensity of the dye's absorbance at both wavelengths in the

Table 1 Structural characteristics of treated and untreated TiO_2 films

Sample	Pore size (nm)	Porosity, P (%)	Total pore volume, Vp (cm^3/g)	Specific surface area, S (m^2/g)	Roughness factor (μm^{-1})[a]
Reference	14.86	0.43	0.197	53.01	2.43
TTAI-300	13.99	0.41	0.181	51.67	2.09
TALD-300	14.96	0.42	0.191	51.01	2.76
TTAI-500	22.14	0.50	0.269	48.57	1.76
TALD-500	26.32	0.54	0.310	47.11	2.37

[a] roughness factor was obtained by multiplying the specific surface area and TiO_2 weight

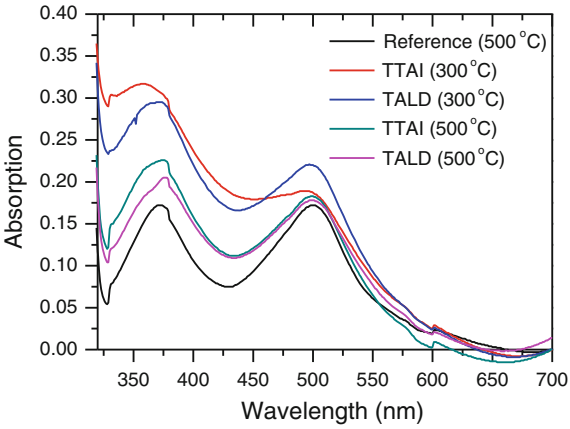

Fig. 3 UV-Vis absorption of dye N-719 detached from untreated and TTAI, TALD treated TiO_2 nanocrystalline films after exposition in 1 M NaOH

visible is presented in Table 2. TTAI, TALD surface treatment of TiO_2 films increased the amount of adsorbed dye. This may be caused due to passivation of TiO_2 surface and increased pore size distribution, pore volume and porosity of the films. The effect of higher adsorbed amounts of dye on TiO_2 films' surface was examined in the performance of DSSCs constructed in quasi-solid state electrolyte configuration.

The current-voltage (*J-V*) characteristic curves of quasi solid-state dye sensitized solar cells for all TiO_2 films are presented in Fig. 4. As it can be seen the quasi-solid state DSSCs constructed with untreated and treated TiO_2 films showed different energy to power conversion efficiencies under AM 1.5 simulated Xe-light of 100 mW/cm^2. In the case of TALD treated TiO_2 film the overall efficiency was slightly higher than the case of TTAI surface treated TiO_2 film. In particular, the open circuit voltage for TALD treated sample was 0.71 V and the short circuit current was 8.35 mA/cm^2. The overall efficiency for this cell was measured 4.04 %. For the cell containing TALD treated photoelectrode, with exactly the same electrolyte

Table 2 Absorbance of N-719 dye after detachment from TiO_2 films

Sample (°C)	Wavelength (nm)	Absorbance
Reference (500)	372.5	0.173
	500.5	0.171
TTAI-300 (300)	356.5	0.316
	490.5	0.191
TALD-300 (300)	371.5	0.294
	497.0	0.219
TTAI-500 (500)	374.5	0.183
	499.0	0.226
TALD-500 (500)	377.0	0.205
	499.0	0.178

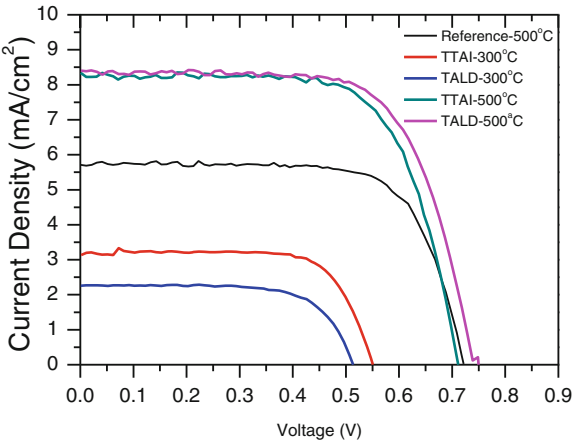

Fig. 4 Photocurrent-voltage curves of DSSCs based on treated and untreated TiO_2 nanocrystalline films

composition, the open circuit voltage was measured 0.74 volts and the short circuit current was 8.42 mA/cm^2. The overall efficiency for this cell was slightly increased to 4.25 %.

In both cases, the active area of the cells was 0.3 cm^2. We attribute the difference in overall efficiencies of the cells to the different textural and morphological characteristics of the two films as they were described in this section. Specifically, the difference may be explained by the higher number of active sites for the adsorption of dye molecules, the larger average pore size for effective mass transfer of electrolyte and light harvesting.

It is worth of noting that the efficiency of the untreated TiO_2 sample is much lower (2.97 %) mainly caused from lower recorded current density.

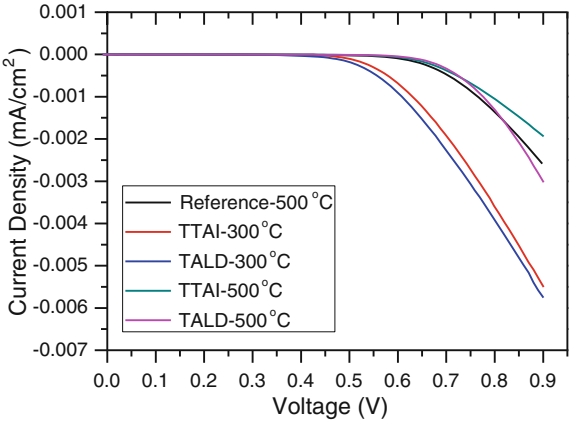

Fig. 5 Dark current-voltage characteristic curves of dye-sensitized solar cells before and after TTAI, TALD treatment

Table 3 Solar cells parameters for DSSCs with TTAI, TALD treated or untreated TiO_2 photoelectrodes

Sample (°C)	J_{SC} (mA/cm^2)	V_{oc} (V)	FF	n (%)
Reference (500)	5.71	0.72	0.721	2.97
TTAI-300 (300)	3.11	0.55	0.753	1.29
TALD-300 (300)	2.26	0.51	0.693	0.80
TTAI-500 (500)	8.35	0.71	0.683	4.04
TALD-500 (500)	8.42	0.74	0.684	4.25

Consequently, a 26.5 and 30.1 % increase to the overall efficiency was recorded for the TTAI and TALD treated photoanodes respectively. Finally, the treated samples heated at lower temperature (300 °C) exhibited poor performance mainly due to the carbon content which is still present as the temperature exposed the films was not enough elevated to remove carbon. The TiO_2 treated samples were also examined as efficient photoelectrodes in DSSCs measuring the dark current suppression. Figure 5 shows that the electron leakage, in the cells made with TTAI, TALD surface treated TiO_2 films at 300 °C is noticeably higher compared to the cells with untreated and TTAI, TALD treated TiO_2 films at 500 °C which leads to a reduced overall performance under light exposure (Table 3).

Among untreated and treated with TTAI, TALD photoelectrodes but all heated up to 500 °C it is monitored a very slight performance in case of the presence of TTAI.

4 Conclusions

Two titanium based materials were used for TiO_2 mesoporous films surface treatment. The treated and untreated films were examined as photoanodes in dye sensitized solar cells and their performance was evaluated in terms of photocurrent,

photovoltage and overall efficiency. Differences to their performance were attributed to the different structural properties and different recombination rate of the carriers in the films. In particular, the treated films with Titanium(IV) (triethanolaminato) isopropoxide and Titanium(IV) bis(ammonium lactate)dihydroxide were exhibited more porous structure and roughness while the amount of the absorbed dye was higher compared to the untreated samples. Finally, 26–30 % increase to the overall performance of the cells with TTAI and TALD treated photoanodes was measured.

Acknowledgments This research has been co-financed by the European Union (European Social Fund - ESF) and Greek national funds through the Operational Program "Education and Lifelong Learning" of the National Strategic Reference Framework (NSRF)—Research Funding Program: ARCHIMEDES III, Investing in knowledge society through the European Social Fund.

References

1. Yum, J.-H., Chen, P., Grätzel, M., & Nazeeruddin, M. K. (2008). Recent developments in solid-state dye-sensitized solar cells. *ChemSusChem, 1*(8–9), 699–707. Wiley.
2. Nazeeruddin, Md. K., Baranoff, E., & Graetzel, M. (2011). Dye-sensitized solar cells: A brief overview. *Solar Energy, 85*, 1172–1178. Elsevier.
3. Durrant, J., Haque, S. A., & Palomares, E. (2006). Photochemical energy conversion: From molecular dyads to solar cells. *Chemical Communications, 31*, 3279–3289. RSC.
4. Yella, A., Lee, H. W., Tsao, H. N., Yi, C., Chandiran, A. K., Nazeeruddin, M. K., et al. (2011). Porphyrin-sensitized solar cells with cobalt (II/III)–based redox electrolyte exceed 12 percent efficiency. *Science, 334*, 629–634. AAAS.
5. Huang, C.-Y., Hsu, Y.-C., Chen, J.-G., Suryanarayanan, V., Lee, K.-M., & Ho, K.-C. (2006). The effects of hydrothermal temperature and thickness of TiO2 film on the performance of a dye-sensitized solar cell. *Solar Energy Materials and Solar Cells, 90*, 2391–2397. Elsevier.
6. Hagfeldt, A., Boschloo, G., Sun, L., Kloo, L., & Pettersson, H. (2010). Dye-sensitized solar cells. *Chemical Reviews, 110*, 6595–6663. ACS.
7. Jose, R., Thavasi, V., & Ramakrishna, S. (2009). Metal oxides for dye-sensitized solar cells. *Journal of the American Ceramic Society, 92*, 289–301. ACS.
8. Ito, S., Murakami, T. N., comte, P., Liska, P., Graetzel, C., Nazeeruddin, M. K., et al. (2008). Fabrication of thin film dye sensitized solar cells with solar to electric power conversion efficiency over 10 %. *Thin solid films, 516*, 4613–4619. Elsevier.
9. Park, J.-H., Kim, J.-Y., Kim, J.-H., Choi, C.-J., Kim, H., Sung, Y.-E., et al. (2011). Enhanced efficiency of dye-sensitized solar cells through $TiCl_4$-treated nanoporous layer covered TiO_2 nanotube arrays. *Journal of Power sources, 196*, 8904–8908. Elsevier.
10. Vesce, L., Riccitelli, R., Soscia, G., Brown, T. M., Di Carlo, A., & Reale, A. (2010). Optimization of nanostructured titania photoanodes for dye sensitized solar cells: Study and experimentation of $TiCl_4$ treatment. *Journal of Non-crystalline solids, 356*, 1958–1961. Elsevier.
11. Roy, P., Kim, D., Paramasivam, I., & Schmuki, P. (2009). Improved efficiency of TiO_2 nanotubes in dye sensitized solar cells by decoration with TiO_2 nanoparticles. *Electrochemistry communications, 11*, 1001–1004. Elsevier.
12. Sun, X., Chang, X., Tuo, W., Wang, D., & Li, K. (2014). Performance comparison of dye-sensitized solar cells by using different metal oxide- coated TiO_2 as the photoanode. *Advances, 4*, 031304. AIP.

13. Xia, J., Masaki, N., Jiang, K., & Yanagida, S. (2007). Fabrication and characterization of thin Nb_2O_5 blocking layers for ionic liquid-based dye-sensitized solar cells. *Journal of Photochemistry and Photobiology A: Chemistry, 188*, 120–127. Elsevier.
14. Diamant, Y., Chen, S. G., Melamed, O., & Zaban, A. (2003). Core—shell nanoporous electrode for dye sensitized solar cells: The effect of the SrTiO3 shell on the electronic properties of the TiO2 core. *The Journal of Physical Chemistry B, 107*(9), 1977–1981. ACS.
15. Stathatos, E., Lianos, P., & Tsakiroglou, C. (2004). Highly efficient nanocrystalline titania films made from organic/inorganic nanocomposite gels. *Microporous and Mesoporous Materials, 75*, 255–260. Elsevier.
16. Makris, T., Dracopoulos, V., Stergiopoulos, T., & Lianos, P. (2011). A quasi solid-state dye-sensitized solar cell made of polypyrrole counter electrodes. *Electrochimica Acta, 56*, 2004–2008. Elsevier.
17. Stathatos, E. (2005). Organic-inorganic nanocomposite materials prepared by the sol-gel route as new ionic conductors in quasi solid state electrolytes. *Ionics, 11*, 140–145. Springer.
18. Stathatos, E., Lianos, P., Stangar, U. L., Orel, B., & Judeinstein, P. (2000). Structural study of hybrid organic/inorganic polymer gels using time-resolved fluorescence probing. *Langmuir, 16*, 8672–8676. ACS.

Azimuth-Altitude Dual-Axis Tracking Systems for Photovoltaic Panels

Milian Badea, Sorin-Aurel Moraru and Dominic-Mircea Kristály

Abstract This paper tackles the current theme of the renewable electric energy in general and increasing efficiency of its production, in particular. Two designs and implementations of azimuthal biaxial orientation systems are presented, one using a mobile platform driven by two linear actuators controlled by a PLC and one built on the principle of increasing the perceived radiation by focusing it using two flat mirrors, also using a PLC. The first system uses two actuators to move a mobile platform in order to optimally position the photovoltaic panel in relation to the sun's position in the sky. The optimal position is predefined for each day, hour of the day and the geographic position inside the PLC that controls the two actuators. The second system uses a rotating actuator and a linear actuator to position the photovoltaic panel, the altitude and azimuthal angles being computed by the PLC used to control the movement, allowing smaller steps in the adjustment. The results of the implementation of the two systems are illustrated through comparisons with fixed, respectively standard photovoltaic panels, proving the increased efficiency of electric energy production.

Keywords Renewable electric energy · Photovoltaic panel · Azimuthal orientation · Optimization

1 Introduction

The azimuth system consists of the horizontal plane of the observer and a vertical line at this point, being also called the local system. The two angles that describe the current point position of the sun (Figs. 1 and 2) [3]) are:

M. Badea · S.-A. Moraru (✉) · D.-M. Kristály
Transilvania University of Brasov, Eroilor 29, 500036 Brasov, Romania
e-mail: smoraru@unitbv.ro

I. Visa (ed.), *Sustainable Energy in the Built Environment - Steps Towards nZEB*,
Springer Proceedings in Energy, DOI 10.1007/978-3-319-09707-7_28

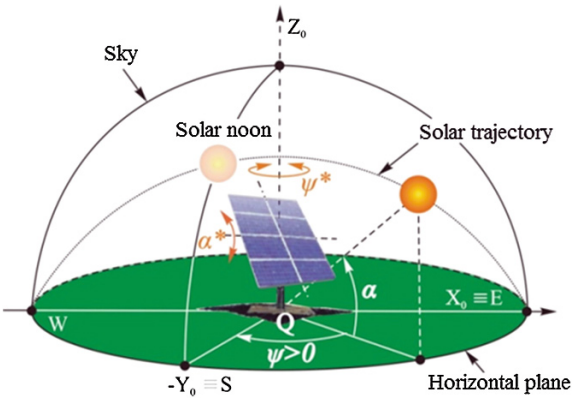

Fig. 1 The angles of the azimuthal system

Fig. 2 The experimental model

1. Altitude angle (α) is the angle between the solar ray and the horizontal plane where the observer is positioned, the angle is calculated with the Eq. (1).

$$\alpha = \arcsin(\sin\delta \sin\phi + \cos\delta \cos\phi \cos\omega) \tag{1}$$

where:
δ angle of declination
φ latitude
ω hour angle

2. Azimuth angle (ψ) it is the angle between the projection of the solar rays on the horizontal plane and a north to south oriented line in the same plane. The equation is (2) [1].

$$\Psi = (\text{sgn}\omega)\arccos\left(\frac{\sin\alpha\sin\phi - \sin\delta}{\cos\alpha\cos\phi}\right) \quad (2)$$

The following are used for azimuthal systems (especially medium and large ones):

- mechanical gear or hydraulic transmission for the azimuth axis;
- linear actuators for altitude axis.

The following were used for the small biaxial azimuthal orientation system:

- PLC GM7 PLC-DT02U (N);
- linear actuators with DC motors having permanent magnets and planetary gear, one for driving each axis;
- incremental rotating transducers with 2,500 pulses/rotation in order to establish the current position of the photovoltaic panel;
- proximity transducers for the limitation of displacement.

2 Dual Axis Azimuthal Orientation System with Two Linear Actuators

The orientation system follows the position of the sun by moving on two axis using steps that are saved in the PLC memory. A step represents the hour, the minute and the angle for each of the two axis. The days were divided into intervals, which can use the same sets of values. The following limits were established:

- maximum number of intervals: 40;
- maximum number of azimuth angles in an interval: 25;
- the maximum number of altitude angles in an interval: 10.

Figure 3 shows the positioning algorithm scheme. The PLC has four fast counter channels that can be configured as four counters on one phase or two counters on two phases. When using both pulse trains from the incremental transducers, the counter is bidirectional. The value of each counter is the real angle converted to impulses, for each axis. An action is performed only if the absolute value of the differences between the programmed angles and current angles are greater than 5.

Because incremental transducers are sensible to voltage falls and returns, the real rate must be adjusted:

- by saving it in a non-volatile memory and uploading it quickly into the counter upon power return;
- by an initialization sequence of the two axis, using fixed positions established at commissioning.

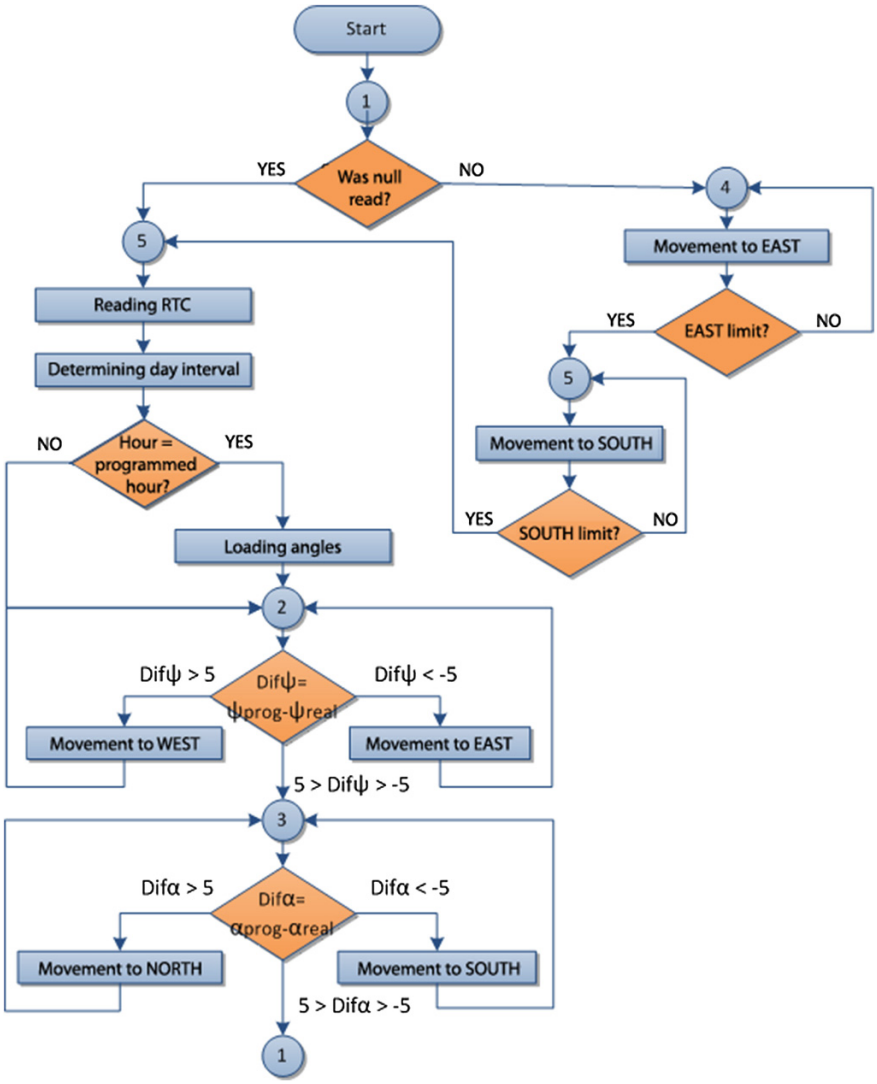

Fig. 3 The positioning algorithm scheme

This orientation system was developed using the second method. The first method has the following disadvantages:

- when the voltage falls happens while moving, it is possible for the real rate to be incorrectly stored;
- while voltage is absent the system may change its position due to mechanical reasons so the the real rate may be distorted, and errors can accumulate;
- when power failure is frequent, the errors become very large.

The fixed marks for null acquisition on each axis were chosen accordingly: the eastern stop detector for the azimuthal axis and the south stop detector for the altitudinal axis. This is the standby position for the orientation system overnight.

Upon system startup two bits are tested; they store whether or not a null position must be acquired. If these bits have the logic value 0 the following initialization sequence begins:

- the command is given to move the system on the azimuth axis to the east until the positive front of input I0.4 (east end of the course).
- a fast counter is reset and the byte "azimuthal axis initialized" becomes logical 1;
- the command is given to move the system on the altitude axis to the south until the positive front of input I0.6 (south end of the course).

If initialization was achieved, the normal tracking program begins:

1. Determining the range for the current day:

The system date and hour (RTC) is read and the _RTC_TIME vector (year, month, hour, minute, second and day of the month) is extracted. With this data it is calculated which day of the year the current day is. By successive comparisons, it is determined which is the range that the current day belongs to. The number of the current day interval represents the index for the subsequent searches (hours, minutes and angles).

2. Hour, minute, angle search:

The positioning steps are stored at fixed addresses in memory. The determination of the start address of the memory area for day time interval previously determined is as follows:

$$\text{Adr\_hour} = \text{Base\_hour} + \text{Index\_day} * 25$$

The system hour is compared with the 25 values stored in memory starting with the address Adr_hour and up. Upon coincidence, the number of comparisons becomes the new index for minute loading. Minute is uploaded from:

$$\text{Adr\_minute} = \text{Base\_minute} + \text{Index\_day} * 25 + \text{Index\_hour}$$

The value loaded to the minute Adr_minute is compared with the minute of the system given it from RTC. Upon coincidence the angle and start positioning sequence are uploaded.

The search algorithm for a certain hour in a certain interval covering the situation where two placements happen in the same hour, at different minutes, is shown in Fig. 4.

3. Positioning sequence:

The angle is loaded from address Adr_angle when the hour and minute loaded from memory are equal to the hour and minute of the system.

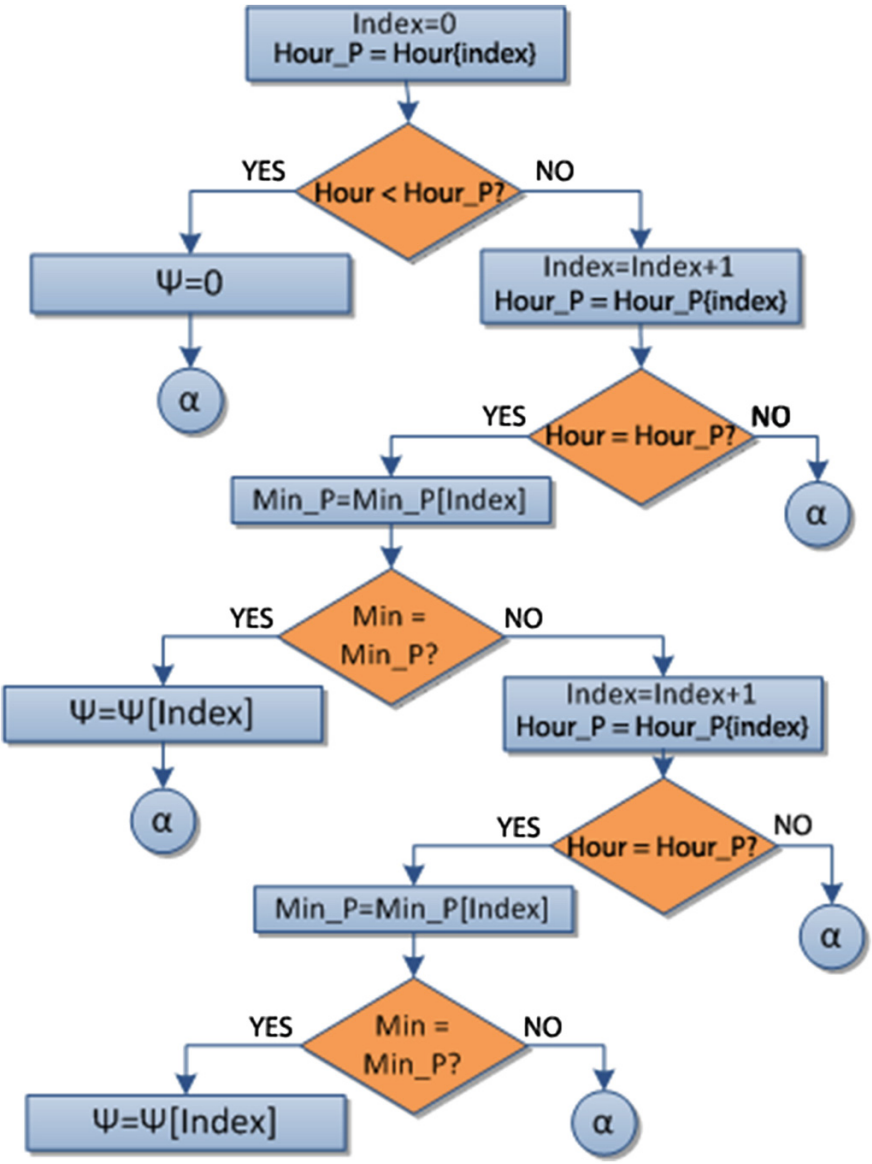

Fig. 4 Loading azimuthal angle algorithm flow chart

$$\text{Adr\_angle} = \text{Base\_angle} + \text{Index\_day} * 25 + \text{Index\_hour}$$

The program is designed so it continuously monitors the difference between the prescribed angle (loaded in memory) and the actual angle (current value of the fast counter). If this difference is greater, in absolute value, than the maximum

positioning error, the axis starts automatically reducing the difference. Positioning sequence for loading a new angle is as follows:

- the difference between actual and prescribed position for each axis is calculated;
- if both axis must execute a movement, the azimuthal axis is the one to start first. Depending on the sign of the difference, the axis starts in the right direction towards reducing the difference.

A smaller difference than the maximum positioning error means the positioning sequence is complete and the next set of memory values is retrieved.

4. The error system:

For the protection of actuators and overall mechanical system, the following error system was designed:

- In the case of a command to move the tracking system on the azimuthal axis or on altitude axis, the fast counter doesn't change its value after 2,000 ms, the system stops by switching to manual mode. Possible causes:
  - the actuator is faulty;
  - the incremental transducer is faulty;
  - the control voltage does not reach the actuator's motor (defective PLC output).
- If during the positioning sequence for azimuthal axis the digital input I0.5 (west endpoint reached) becomes logical 1, the system switches to manual mode (on normal operation the western endpoint cannot be reached). Possible causes:
  - the incremental transducer is faulty;
  - the elastic coupling on the incremental transducer's axle is weakened or damaged.
- If during positioning sequence for altitudinal axis the digital input I0.7 (north proximity detector limit) becomes logical 1, the system switches to manual mode (in normal operation, the north proximity detector is not triggered). Possible causes:
  - the incremental transducer is faulty;
  - the elastic coupling on the incremental transducer's axle is weakened or damaged.

Switching to manual mode, due to errors, determines the resetting of the bits indicating a performed initialization. Initialization is performed when switching back to automatic operation mode.

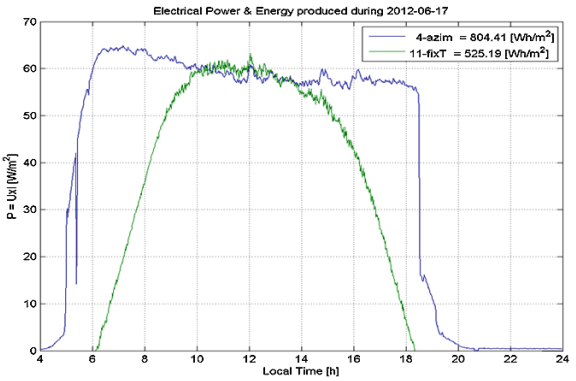

Fig. 5 Results of measurements (17.06.2012)

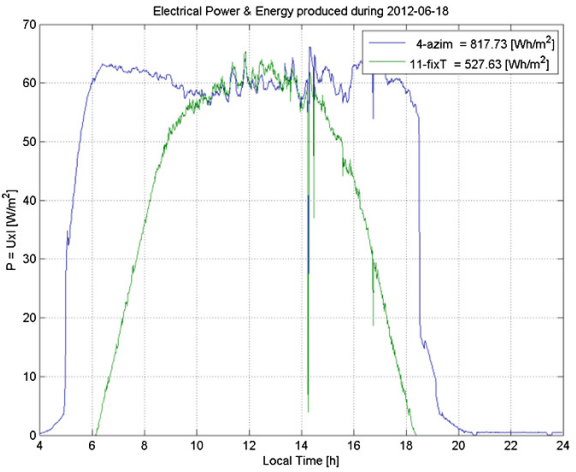

Fig. 6 The results of measurements (18.06.2012)

2.1 Results

In Figs. 5 and 6 are presented the results of measurements for a photovoltaic panel mounted on a biaxial orientation system (blue graph) and for a fixed panel with the same electrical characteristics (green in the chart). The graph shows an increase of approximately 30 % of the energy produced by the photovoltaic panel installed on the orientation system comparative to the energy produced by a fixed photovoltaic panel with identical features.

3 Dual Axis Azimuthal Orientation System and Flat Mirrors Radiation Focus System

Because the solar panels still have a fairly high price, increasing their effectiveness is still being pursued. The implementation of this orientation system (Fig. 7) uses two methods:

- increasing the radiation perceived through biaxial orientation using 4/8 min steps for the azimuth angle (ψ) and 8 min steps for the altitude angle (α);
- increasing the radiation perceived through focusing radiation with flat mirrors.

The following were used in building the orientation system with the radiation concentration system:

- PLC GM7-DT02U(N);
- A rotary actuator, model H-Fang-62-R-24E010, for the azimuthal axis and a linear actuator ELERO ATON 2 for the altitudinal axis;
- incremental transducer to read the current position on each axis, which are included in the actuators;
- proximity transducers for each end.

For this orientation system, calculations are performed to determine angles in impulses.

Because memorizing each step for the two axis requires 6 bytes it is possible that, in the case of orientation systems having short spans between steps, the PLC memory is insufficient.

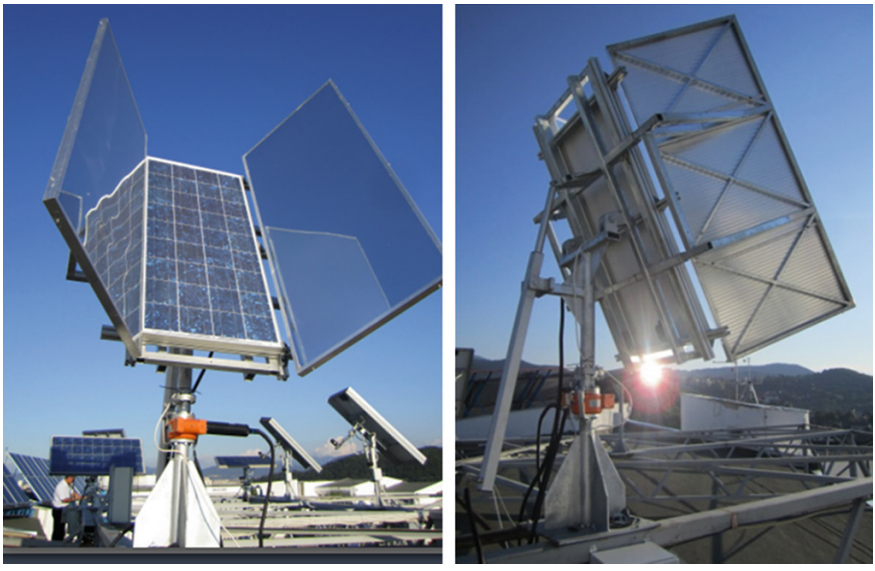

Fig. 7 Orientation system by focusing radiation with plane mirrors

For the biaxial azimuth orientation system having steps every 8 min, the PLC can store data for up to 40 days, which is a disadvantage.

Eliminating this drawback was done by implementing calculation of the positioning angles in the PLC program. The PLC GM7-DT02U(N) was replaced with XBC-DR32H for the necessary calculations with LREAL and REAL values for the trigonometric functions.

To compute the altitude angle and azimuth, the following must be calculated: declination (δ) and hourly angle (ω) with the Eqs. (3) and (4) [1, 2].

$$\delta = 23.45 \cdot \sin\left(\frac{360 \cdot (n - 80)}{365}\right) \tag{3}$$

where:
n day's number of the year

$$\omega = 15 \cdot (12 - t) \tag{4}$$

where:
t solar time expressed in hours

The altitude angle and azimuth are computed with Eqs. (1) and (2) [1, 2].

Figure 8 shows the flow chart with the positioning algorithm used in the azimuthal orientation system with flat mirrors. The declination, solar time, hourly angle, altitude angle and azimuth are computed continuously.

The computed values for the angles are used as prescribed values only if, from the last position, an interval of time has passed equal with the time that was set as the value of the step.

Upon system start-up the bit indicating working operating mode is tested. If this bit is 0 logic, the system is in manual operating mode and each axis of the orientation system moves individually through a command from the operator panel. In order to move each axis in the manual operating mode, an XP10 operator panel was used, with the following schedule:

- The operator panel can communicate with the PLCs of all guidance systems mounted on the roof of the University Hill Campus E building, in a 1:N communication.
- For each orientation system, a screen that displays the actual quota in impulses and in degrees, along with the working operating mode was created.
- The screen's number is a PLC network address. The address for each PLC must be unique. Four function keys were programmed to order the movements: East–West for azimuthal axis, North–South for altitude axis. Depending on selected screen, pressing a key for displacement sets the corresponding bit a specific orientation system.
- Two keys were programmed to change the operating mode. In Manual mode, the commands are received from the operator panel and in automatic mode the

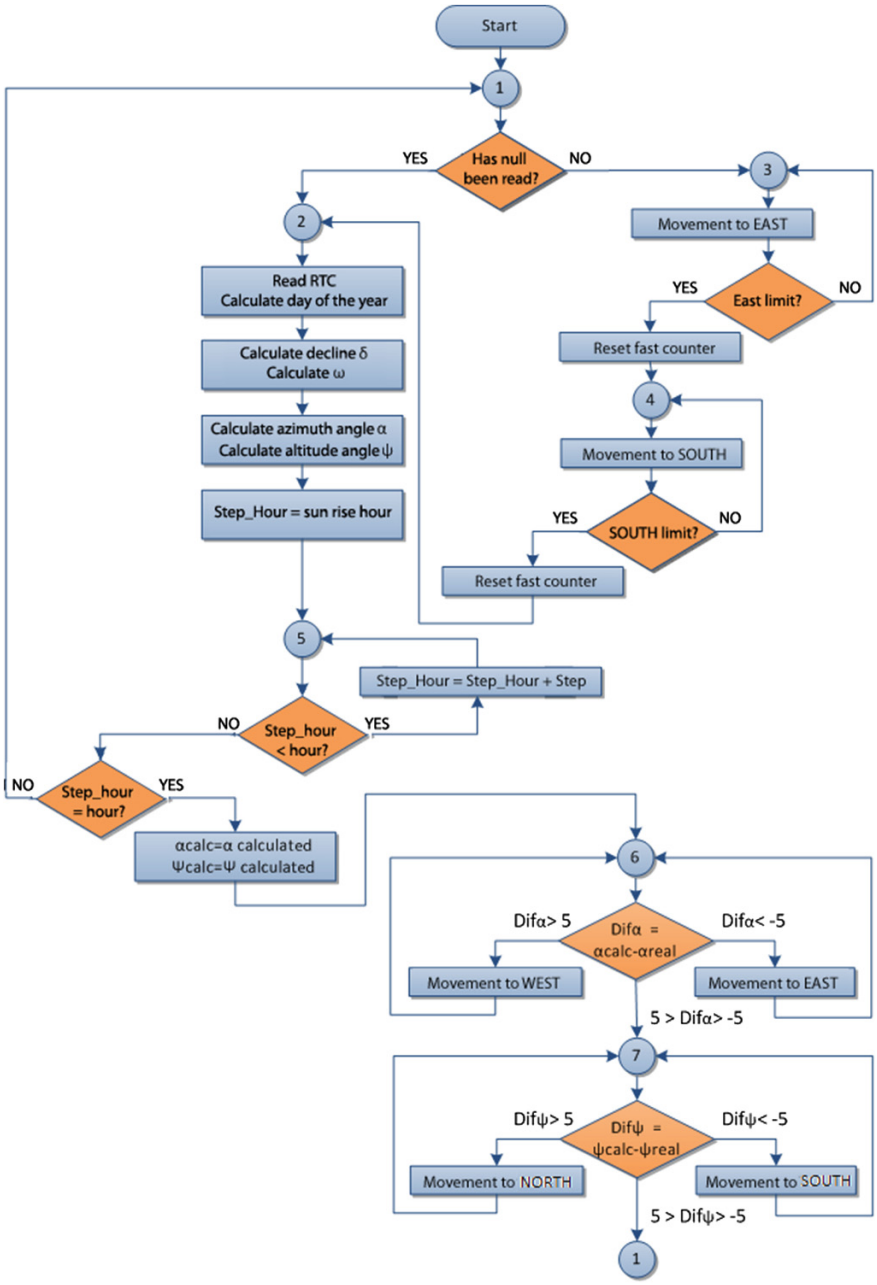

Fig. 8 Flow chart for the positioning algorithm used in the azimuthal orientation system with flat mirrors

program follows computed angles. The operator panel is permanently connected to the PLCs (it is especially useful to test the limits of the end point, the directions of movement etc.).

If the system is in automatic mode, two bits memorizing acquisition or not of the null position are tested. If these bits have the logic value 0, the initialization sequence starts:

- The command is given to move the system on the azimuth axis to the east until the positive front of input I0.4 (east end of the course).
- The fast counter is reset and the byte "azimuthal axis initialized" becomes logical 1;
- The command is given to move the system on the latitude axis to the south until the positive front of input I0.6 (south end of the course).

If initialization was achieved the normal tracking program begins:

1. Determining the range for the current day:

The system date and hour (RTC) is read and the _RTC_TIME vector (year, month, hour, minute, second and day of the month) is extracted. Because in this vector the values are grouped two in a 16 bits word and coded BCD, the function MOV8 moves each byte in 16 bits words, on low position, and then are converted to binary. The day's position in a year is calculated, for it is necessary further to compute the value of the declination.

2. The calculation of the altitudinal and azimuthal angles:

For the calculation of the two angles, necessary for the orientation process, Eqs. (1)–(4) have been implemented in the PLC.

Most calculations are in LREAL format, used for the syntax of the trigonometric functions. Finally, the values of the two angles are multiplied with the number of pulses/degree; the difference between this value and the value of the rapid counter represents the next quota that will be set for each axis.

3. The sequence of positioning:

Taking into account the fact that the positioning is performed in steps, the angles calculated and converted into pulses are not automatically set as the new values for positioning.

The time difference between two consecutive steps is written in a non-volatile memory, on the PLC and is optimized taking into account the fact that, on one hand, radiation captured via photovoltaic panel is desired, and secondly, that running too many steps increases wear and the energy gain can be insignificant. The calculation of time for positioning (hereinafter hour_step) begins with uploading from memory the hour when the sun rises for the current day of the year and this value becomes hour_step. Hour_step is compared to the real hour obtained from the RTC. The following situations are considered:

- if hour_step is less than the real hour, add the value of step time to hour_step until this value is greater than or equal to the actual hour. No movement on the two axis is executed;
- if hour_step is equal to the actual hour, the positioning of the two axis is set to values calculated according to the sequence described below;
- if hour_step is greater than the actual hour the system is in standby.

Angle positioning sequence is as follows:

- the difference between the current position and the calculated position for altitudinal axis is computed;
- depending on the sign of that difference, the axis starts movement in the correct direction in order to reduce the difference. If the difference is less than the maximum positioning error, the sequence is complete and azimuth axis positioning sequence begins, following the same algorithm.

4. The error system:

For the protection of actuators and overall mechanical system the following error system was implemented:

- In the case of a command to move the tracking system on the azimuthal axis or on altitude axis, the fast counter doesn't change its value after 2,000 ms, the system stops by switching to manual mode. Possible causes:
  - the actuator is faulty;
  - the incremental transducer is faulty;
  - the control voltage does not reach the actuator's motor (defective PLC output).
- If during positioning sequence for azimuthal axis the digital input I0.5 (west endpoint reached) becomes logical 1, the system switches to manual mode (in normal operation the western endpoint cannot be reached). Possible causes:
  - the incremental transducer is faulty;
  - the elastic coupling on the incremental transducer's axle is weakened or damaged.
- If during positioning sequence for altitudinal axis the digital input I0.7 (north proximity detector limit) becomes logical 1, the system switches to manual mode (in normal operation, the north proximity detector is not triggered). Possible causes:
  - the incremental transducer is faulty;
  - the elastic coupling on the incremental transducer's axle is weakened or damaged.

Switching to manual mode, due to errors, determines the resetting of the bits indicating a performed initialization. Initialization is performed when switching back to automatic operation mode.

3.1 Results

Figures 9 and 10 show the diagrams of the orientation angles, the real values and calculated values of the diurnal and seasonal. This diagram shows that the positioning accuracy is very good and steady over the day, the maximum deviation between the actual and the calculated values is maximum 5 pulses. Given the number of pulses generated by the incremental encoder, the error is less than 5 tenths of a degree.

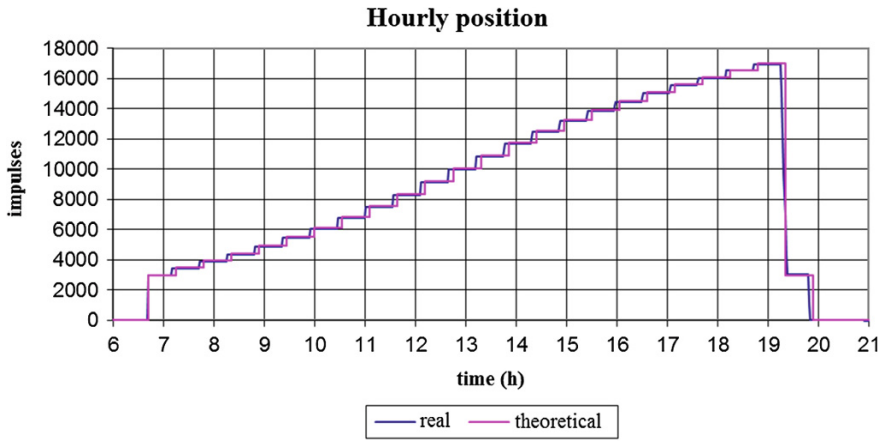

Fig. 9 The superposition between theoretic time position and real time position

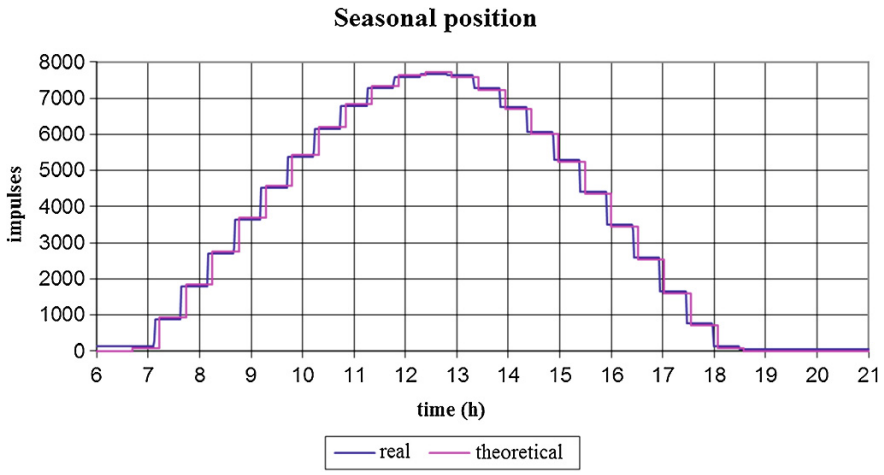

Fig. 10 The superposition between theoretic seasonal position and real seasonal position

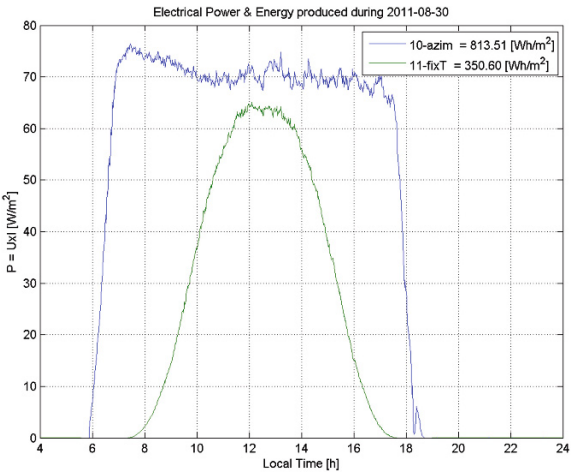

Fig. 11 The results of measurements (30.08.2011)

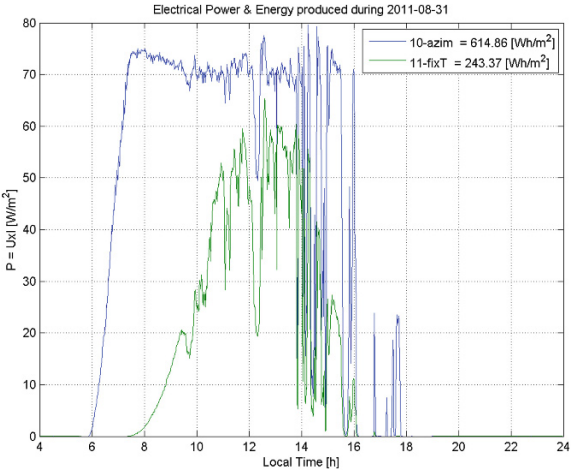

Fig. 12 The results of measurements (31.08.2011)

In Figs. 11 and 12 are the results of measurements of a photovoltaic panel mounted on a biaxial orientation system with flat mirrors (blue graph) and for a fixed panel with the same electrical characteristics (green in the chart).

The measurements were done out in a sunny day on 30.08.2011 and in an afternoon, when the sky was partially cloudy on 31.08.2011 (graphic area in which there are sudden changes of power).

4 Conclusions

The azimuthal orientation systems take into consideration the values stored in the PLC or compute the angle values directly. The PLC can work independently or networked with an operator panel in 1:N connection or through MODBUS communication.

The presented systems achieve a significant increase of efficiency of the panels in producing electrical energy which proves the importance of such systems.

Both positioning systems have two operation modes: automatic (the position is taken from the predefined values) and manual (which allows to position manually the panel). The systems also implement mechanisms for dealing safely with mechanical or electrical faults.

Both systems were developed, tested and implemented at the Institute for Research, Development and Innovation—High-Tech Products for Sustainable Development (ICDT—PRO-DD) of the Transilvania University of Brasov.

References

1. Diaconescu, D. V., Vişa, I., Burduhos, B. G., & Popa, M. V. (2006). Analysis of the Sun-Earth angles used in the design of the solar collectors' trackers. *Bulletin of the Transilvania University of Brasov, Romania, 13*(48), 99–104. ISSN 1223-9631, (without ACK).
2. Diaconescu, D., Vişa, I., & Burduhos, B. (2007). On the received direct solar radiance of the PV panel orientated by pseudoequatorial tracker. In *COMEC—The 2nd International Conference On Computational Mechanics And Virtual Engineering*, (pp. 43–48), Brasov, Romania. ISBN 978-973-598-117-4, ISSN 1844-9336, 11–13 October 2007.
3. Dinicu (Popa), V. M. (2009). *Increasing the energy efficiency of photovoltaic panels using azimuthal tracking mechanisms*. PhD thesis, Braşov, (in Romanian).
4. Messenger, R., & Ventre, J. (2003). *Photovoltaic systems engineering* (2nd ed.). Boca Raton: CRC, ISBN 978-0849317934.

Environmental Effects of the Large Scale Photovoltaic Investments in Covasna County

Sándor Bartha, Noémi Antal and Réka Incze

Abstract Renewable energy sources in electrical energy production means one way to reduce the greenhouse gas emission. The present paper describes one model for evaluation of the energy production of the large scale photovoltaic solar energy conversion systems and it also establishes the environmental impacts assessment. The article starts with one presentation of the solar energy potential for the application sites; it shows the incident global solar irradiation for the chosen locations. In this part is presented different techniques and device used in this evaluation process. The paper indicates the cumulated energy demand in case of energy production using different photovoltaic modules in solar park construction. Additionally, a case study is presented for one of the new solar photovoltaic parks recently built in Covasna County. The new installed PV plant capacity in this region today is 40–50 kW_p, based on the ANRE-Romanian Energy Regularity Authority data, but it can be increased up to 40 MW_p in the following years. New PV plants can influence the environment, including the land aspects and the land usage but they have an important role in reducing the CO_2 emission. All of these aspects are presented in this article. The paper also indicates the recycling procedures of the photovoltaic modules and shows the legal aspects for this process. In the second part of the study, the actual electricity production is presented; it includes PV conversion systems in Romania and it compares this trend with the local investment market. In a separate chapter, a case study is presented regarding the administrative labyrinth and legal aspects for implementing one photovoltaic park. Finally, the study indicates the environmental impact of the target value from the perspective of the energy mix established by certain EU directives. The paper also will be focused to indicate the impact of these solar parks to the biodiversity present in land, based on initially evaluation of the land biodiversity in case of these large scale solar parks.

S. Bartha (✉)
ICPE-Institute for Electrical Research, Bucharest, Romania
e-mail: sbartha@freemail.hu

N. Antal · R. Incze
Faculty of Environmental Science and Engineering, Extension Sf. Gheorghe,
Universitatea Babeş Bolyai, Cluj-Napoca, Romania

I. Visa (ed.), *Sustainable Energy in the Built Environment - Steps Towards nZEB*,
Springer Proceedings in Energy, DOI 10.1007/978-3-319-09707-7_29

Keywords Solar energy · Photovoltaics · Greenhouse gas emission · Environmental impact · Administrative issues

1 Introduction

Based on different predictive study the 21st century is called the Solar Age, the society can be able to achieve a 100 % renewable energy supply in the following 40 years. In this case, the European society do not need oil from the Middle East, nor gases from Siberia and nor uranium from Australia. For this period the EC prognoses the following structures for the energy mix: 40 %, solar power, 30 % Biomass, 15 % Wind power, 10 % Hydro power and 5 % Oil. Today this structure is relative stabile, substantial changes in this energy production values cannot be observed, the energy production from cool presented an increasing trend in the studied period (1990–2011) from 27 to 17 values the contribution of gas increased 18–24 % and the oil contribution remained broadly unchanged [1].

Recently the EU 27 economy remains heavily dependent on fossil fuels, which arrived 76 % of primary energy consumption. From statistical data about the EU energy mix in 2012 the PV contribution has been covered 2.6 % of the electricity demand and 5.2 % of the peak electricity demand in Europe [2]. The European PV market presents a growing trend, on end of 2012 year the cumulative installed PV capacity arrived 70 GW, this represents about 70 % of the world's cumulative PV capacity. The global PV market evolution is represented on Fig. 1.

In the presented graph we use the following notation for the geographical regions, APAC-Asia Pacific regions, MEA-North America and Middle East, Americas represents the South and Central America regions and ROW is the rest o word region.

1.1 EU Targets and Potential in 2020

Take into account the EPIA's report about the future of the PV market we can identified three possible PV development scenario to 2020. That is the following:

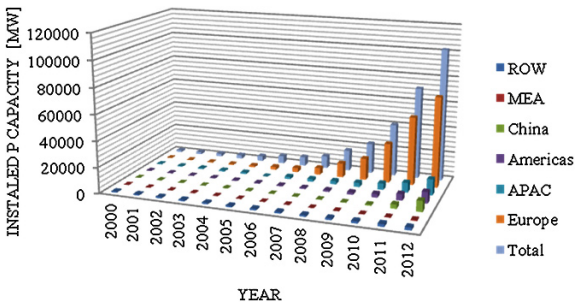

Fig. 1 Evolution of global PV cumulative installed capacity 2000–2012 (Based on EPVA data)

The baseline scenario envisages that 4 % of the electricity demand in Europe will be provided by PV. That represents about 130 GW cumulative capacities by 2020.

The second scenario name is the accelerate scenario in this case the PV electricity demand will be arrived 8 %, that is equivalent with 260 GW cumulative capacity. Finally the three is called the "Paradigm Shift" scenario in this case the PV Power Station will be supplied up to 12 % in EU electricity demand by 2020. That will represent approximate 390 GW cumulative PV capacities.

1.2 The Romania PV Market Study and the Cumulative PV Capacity in Covasna County

On end of July 2013 in Romania were installed and in use 474 MW_p power photovoltaic, solar parks. From statistical study based on Romanian National Grid Company —Transelectrica the top ten of the solar parks locations are presented in Table 1 [3].

That new PV installation has been built under financial support of the Romanian and European programs for green energy markets. The National Energy Action Plan for Romania indicated a target of 24 % RES in the energy mix; this target can be achieved by installing important new RES capacities. The PV sector shows growing trend; thus it achieves the energy production values presented in EU Action Plans. As consequence, Romanian authorities offer a favorable support framework for the investors. Legal framework concerning energy (published in 2011) indicates 6 green certificates for each MWh energy produced by this photovoltaic grid connected sources; today this value is reduced. Today Covasna County is present with 2 MW_p functioning grid connected capacity in this PV market; this value may increase up to 30–40 MW_p in this year after approved this investments. The location of some PV parks proposed to build in Covasna County is marked on Fig. 2.

Table 1 The top ten of the solar parks in Romania

Location/district	Installed power, MW_p	Investment value, mil euro
Comuna Slobozia, Giurgiu	45	100
Izvoarele, Giurgiu,	20	31
Targu Carbunesti, Gorj	10	15.5
Targu Carbunesti, Gorj	10	15.5
Grojdidobu, Olt	9.9	15.4
Uliesti, Giurgiu	9.5	14.7
Izvoru, Arges	8.8	13.6
Vanju Mare, Mehedinti	8.7	13.40
Frasint Calarasi	8.3	12.8
Uliesti, Giurgiu	8	12.4

Fig. 2 Map of the new solar park locations in Covasna County

2 Problem Formulation

The paper formulates the principals techniques and evaluation methods to energy balance and the parameters which is necessary to evaluating the environmental assessments impact of the PV grid connected system.

2.1 Energy Balance and Energy Yield of the Grid Connected Systems

For performance study of the grid connected PV system one of the principles parameters is the energy production that can be represented in daily or monthly values.

The monthly and annual energy yield of the PV system can quit and simple determine using standardized diagrams and tables. One of those parameters is the normalized yield. This parameter could be evaluated based on energy yield during a reference period (day, month, year) which is divided by the solar generator nominal output at STC power output, that indicates the installation yield and can be expressed in final and array yield, the mathematical expression for this parameters are taken from reference [4].

Final yield, Y_F, that is equal to time which the PV plan has to operate with nominal solar generator power to generate the useful output energy [h/d]

$$Y_F = \frac{E_{use}}{P_{G0}}. \tag{1}$$

Array yield, Y_A, is equal to the time which the PV plant has to operate with nominal power, [h/d]

$$Y_A = \frac{E_{Ae}}{P_{G0}}. \tag{2}$$

Reference yield, Y_R, is equal to the time which the Sun has to shine with 1 kWh/m^2, to irradiate the energy onto the solar generator

$$Y_R = \frac{H_G}{G_{STC}}. \tag{3}$$

where:

E_{use} PV installation power output during the reference period,
E_A solar generator output during the reference period,
P_{G0} nominal solar generator power under STC condition
H_G the irradiated energy in kWh/m^2, during the reference period
G_{STC} the irradiance under standard condition

Performance ratio, PR, is equal to the ratio of the useful energy to the energy which would be generated by lossless, ideal PV plant with solar cells at STC

$$PR = \frac{Y_F}{Y_R}. \tag{4}$$

The ideal values of the PR are between 0.8–0.84, if the performance ratio registers a significant decreasing value that means that the inverters are not operating in their optimal power.

2.2 The Challenge and Land Use in PV Projects

The renewable energy sector offered excellent investment possibility. Many projects were started in solar energy sector, but just a low number of projects were finalized. The explanation of the phenomena is the complicated process which led from a defined land trough a completed file to an accomplished project.

Firstly, you need about 2 hectares land for 1 MW photovoltaic park. As a consequence, for an average size of 5 MW Park you need approximately 10 hectares. The unclear ownership conditions mean the biggest difficulty; very few areas have complete land register documents. The commonage usually has the appropriate status and size but in these cases the group of commoners and the strict rules (e. q. the land cannot be sold) make complicated the progress. If you find an appropriate land from size and status perspective, you have to pay attention to the accessibility (roads) and the distance from the electrical network too. Usually, the

deal with the commoners ends up with a tenement contract for a long period (20–25 years). The sale and purchase contract is more common if the land has a private owner.

Secondly, you need a gross file which requires some sense of locality in the administrative labyrinth. You have to collect a whole set of permits, licenses and certificates from different institutions, such as Environment Protection Agency, Fire Service, Local Authorities etc. Particular documents have certain validity periods, which mean some extra-deadlines to you. Additionally, you have to order a set of studies, such as topographical, technical and geological. Of course, all these documents have their own money and time requirements. Additional tasks occur when certain institutions oblige you to modify some parts of the projects, so you have to repeat several processes. The biggest trial is that the rules and requirements are unstable.

Thirdly, the changing legal framework makes unstable the whole process. For example, the Emergency Ordinance no. 57/2013 introduced modifications in the supporting system of renewable energy. Among others, it affirms that those projects which are on agricultural land do not benefit of certain subsidies. Obviously, the majority of projects were planned on agricultural areas. Additionally, the process of taking out a land from agricultural usage was unclear. As a consequence, many projects fail at this criterion. Many investors are discouraged by the unstable legal framework and some of them stand off.

2.3 Recycling of the PV Modules

There are three major reasons why it is important to develop procedures to recycle used PV modules:

- The need to capture toxic substances contained in many thin-film solar cells (discussed in Sect. 3.2),
- The chance to reduce the cumulated energy demand of PV modules significantly,
- The use of recycled material might reduce the overall production costs of PV systems.

From the energy balance of the solar cell technologies, the most energy-intensive part of the production process of crystalline silicon PV modules is the generation of the silicone slices. Therefore, the recycling of used silicon from worn-out modules could reduce the CED of solar cells drastically

The recycling strategies developed to date include

- Separation of silicon wafers from the module compound acid digestion,
- Separation of glass, solar cells and metal fractions from modules by burning the polymer laminate,

- "Down-cycling" of frameless modules by melting the modules into FeSi, which can be used for steel production.

The following requirements for an optimal recycling system have been identified.

- High coverage of collection systems for used PV modules,
- Large volumes of recyclable material,
- Sorting the used modules by manufacturer,
- Separation of PV modules into their main fractions,
- Recycling of glass components,
- Recycling of silicon wafers for cell production.

The silicon based modules consist of 80 % glass therefore the flat glass recycling industries can treat this product in their current recycling lines, due to similar morphology, structure and composition of the PV modules and flat glass products [5].

2.4 Environmental Impacts of the Large Scale PV System

The environmental assessments impact can be structured in land use, social impacts and environmental benefits. That is the principal elements which are necessary to take into account in case of the building of the large scale solar parks. In special cases is necessary to realizing different study for evaluate the ecological effects of this PV application to flora and fauna, to the biological diversity to the visual effect to the landscape the effect to the soil erosion and land degradation [5].

This impact may appear in different case to natural recourses, like effect on agricultural land forest resources, water supplies, etc. The impact of land use on natural ecosystem is depended on specific factors such as the topography, the area and the type of the land covered by the system, the distance from areas of natural beauty.

Also an application of a system in once-cultivable land is possible to reserve soil productive areas. Thus the sitting in arid areas is recommended. Analysis has shown, however, that because these materials used in PV modules technologies appear in such minute quantities, in thin film PVs, anyone approaching close enough to encounter significant exposure to any of toxins would face significantly more dander from the fire itself. For example only 400 g Cd are present in a 1 MW CIS system. Whereas 5 g/m^2 of cadmium is present in Cd Te system or about 25 times the amount in CIS system. Other dangers associated with the installed system include, of course the possibility of electric shock hazard [6].

3 Results

3.1 Energy Balance and Reduction of the CO_2 Emission Used the PV Conversion System

In this paper the energy balance of the photovoltaic conversion system is presented for on 1,000 kW_p power grid connected system that is a reasonably practical size limit for studying the PV conversion grid connected system. This balance is presented to on PV grid connected system generally for Romanian market and representatives for the studied region. Also we established the principals' performance indicators for the one ideal PV grid connected system with 1,000 kW_p power. For this evaluation we has been used on commercial PV sizing tools, this tools allow to dimensioned the photovoltaic system taking into account the site location, energy requirements, and system cost and evaluate the principal parameters of the application. This software tools are relatively simple and help the user automatically to solve the energy balance of the system considering different combination of the system elements, like PV modules and inverters. The system simulation results are presented in Table 2. This simulation results presented the solar energy potential of the location, the monthly value of the energy production and the performance indicators of the PV conversion unit. These technical parameters have been evaluated with helpful of the relations presented in Sect. 2.1.

The values of the monthly energy production of the conversion system are presented on Fig. 3. That has been evaluated for the classical Si based modules.

Table 2 Simulation result of the 1 MW_p grid connected system

Month	Glob, Inc, [kWh/m^2]	E array [kWh/month]	E–Grid, [kWh/month]	Efficiency [%]	PR
Jan.	59.70	54,358.00	51,430.00	17.21	0.86
Feb	97.10	89,391.00	85,326.00	17.46	0.80
March	138.20	121,670.00	116,195.00	14.33	0.84
April	144.00	125,088.00	119,398.00	12.27	0.83
May	182.00	153,807.00	146,992.00	11.20	0.81
Jun.	166.30	141,094.00	134,774.00	10.85	0.81
Jul.	158.70	134,101.00	127,956.00	10.97	0.81
Aug.	168.70	142,362.00	136,079.00	11.80	0.81
Sept.	114.90	98,973.00	94,281.00	12.86	0.82
Oct.	76.60	67,457.00	63,913.00	14.66	0.84
Nov.	62.60	56,551.00	53,577.00	17.04	0.86
Dec.	45.00	40,668.00	38,278.00	17.59	0.85
Year	1413.80	1,225,520.00	1,168,199.00	12.77	0.83

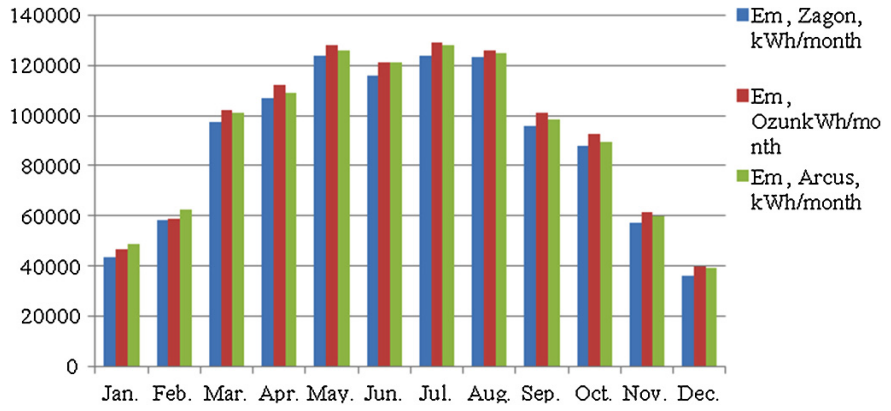

Fig. 3 The monthly energy production of the 1,000 kW_p power PV system, (in kWh/month) builds in different solar parks in Covasna County

The Fig. 3 compares the energy production values of the different solar parks, which will be developed in Covasna County.

Using the conversion method indicated by the National Energy Authority (ANRE), [7, 8] we has been evaluate the equivalent CO_2 quantity for this energy conversion system. In generally in phase of design of the PV system, reduction of the greenhouse-gas emission is evaluated base on reference level indicated by the National Authority that is 566 g CO_2/kWh in electrical energy production. The designer need to take into account this specific factor and need to evaluate the energy production of the solar park in every year based on energy balance. For electricity production in Romanian energy market this factor is 0.701 kg CO_2/kWh at the final consumer. That value can be measured or estimated using different predictive models. The monthly values for the conversion system built with classical Si based modules that can be seen in Fig. 4. From this data can be seen, that the CO_2 emission is reduced yearly with 1,386 tones in case of 1,000 kW_p power conversion grid connected system. Take into account the 20–30 years for the life period that conversion system can be reduced the CO_2 emission representatively. In evaluation of the global CO_2 emission reduction we can be take into account to the emission associated with transport of the modules and another row materials. The transport emission was still only 1 % of the components manufacturing related emissions. This value is for PV cell manufacturing between 50–100 g CO_2/kWh and in case of the glass substrate manufacturing have an important contribution [9], [10].

The reducing of the CO_2 quantity is of for the studied solar parks are presented on Fig. 4.

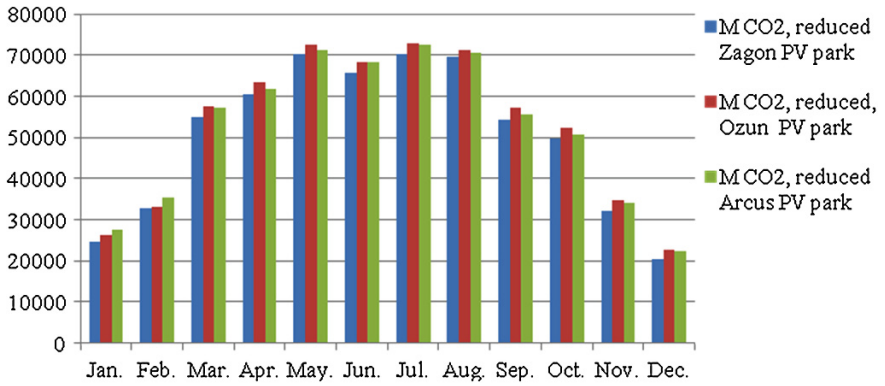

Fig. 4 The monthly CO_2 emission reduction, (in kg/month) in case of the 1,000 kW_p power PV system builds in different solar parks in Covasna District

3.2 Recycling Results of PV Modules

We have to take into account the physical structure of the PV conversion systems, including mechanical parameters of the PV modules, such as dimension, mass, number of modules integrated in the conversion system. Because the indicated solar parks in this paper are in design and approval tasks, we has been collected technical information from functioning solar parks.

We received this data from an important photovoltaic installer, from Renovatio Solar LTD. This integrator has been realized different large scale PV grid connected application in South Romania. The technical parameters of the studied system are presented in Table 3.

Generally, from the PV modules can be recycled the glass, the aluminum frame and different organic materials. Today the first generation of PV modules should be recycled; it has in their structure also different heavy metals like Pb, Cd, Zn. One of PV modules from the old generation (its weight is about 22 kg) contain also 12.67 g Pb. If the modules are not deposited properly, they may produce the following

Table 3 Technical parameter of a Solar Park, build by Renovatio Solar LTD

Location	Size of PV Park/perated by Renovatio	Capacity, MW_p	Nr. of integrated PV modules	Modules capacity, W_p	Area [mp]/ module
Singureni, _Giurgiu	1	1	4,176	240	1.65
Scornicesti, Olt	1	1	4,176	240	1.65
Crevedia, Dambovita	2	2	8,400	240	1.65
Corabia, Olt	7	7	28,602	245	1.65

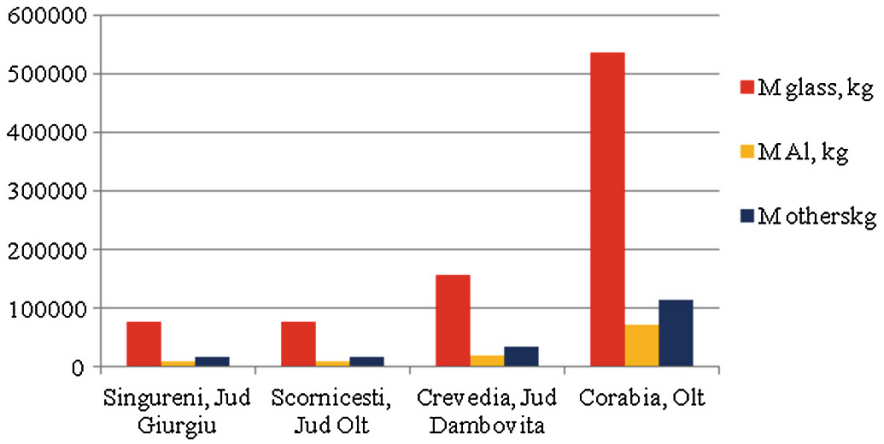

Fig. 5 The estimated weight of recycled materials in case of solar parks

negative impacts on the environment and human health: leaching of lead, cadmium, loss of conventional resources (primarily glass and aluminum) and loss of rare metals (Ag, In, Ga etc.). In this paper, we also estimate the quantity of the principal raw material which can be recycled at the end of the life of a solar park; the diagram could be seen in Fig. 5.

3.3 Environmental Impacts

Environmental benefits:

The energy production with PV system has significant emission reduction, this process not generate noise, or chemical pollutants during their normal operation, biased the PV panels help the increase of the soil humidity and improve the flora formation in dry/areas, that in all represent the environment benefits of this type of application.

Social impact, same benefits are related to lighting for domestic and community activities and creating new jobs improves the quality of life and reduced the migration.

Land use, the impact of land use on natural ecosystem is dependent on specific factors such as topography of the land covered by the system, the distance from areas of natural beauty or sensitive ecosystems and the biodiversity. Solar PV arrays could have implications for habitat loss, fragmentation and modification and displacement of species, however this solar parks may also be capable of delivering environmental gains such creating habitats trough undisturbed grassland for many years wildflower etc.

4 Conclusion

The energy production with photovoltaic conversion of the solar energy is a clean technology and it has a positive impact to reduction the CO_2 emission. Theoretically, in case of 1,000 kW_p power conversion grid connected system the CO_2 emission is reduced with 1,386 tones yearly. This value can be used to evaluate the total CO_2 reduction quantity, if the Romanian energetic industry achieves the target values establish in RES strategy this emission model can be represents a reference value for PV park emissions evaluation.

The presented application is in design and approved phase and from our information this investment projects in Covasna County will be connected to national grid in 2015 and will be contribute substantial to reducing the CO_2 emission in this region. Take into account the 20–30 years for the life period that conversion system can be reduced the CO_2 emission representatively.

These solar parks we consider will be integrated environmentally friendly in the region landscape. In generally the land use for this type of solar park is 2 hectares. In generally the connection box and the transformer are installed near the local grid.

From the year 2013 in EU legislation the PV modules are included in WEEE (waste electrical and electronic equipment, 2012/19/EU directives). That reduces the negative environmental impact produced by the inappropriate disposal. Base on this Directives the PV modules are included in WEEE category in class 4 "Household equipment and Photovoltaic panels". The Romanian low for the present time not mentioned these changes in the "Low HG 1037/2010" for waste electrical and electronic equipment, which transposes the Directive 2002/96/EC of the European Parliament in Romanian legislation [11, 12]. Is necessary the amendment of the actual Romanian legislation, for protecting the environment [13].

The lead and cadmium leaching can be reduced by limiting the quantity of improper disposal in case of photovoltaic panels; so the negative environmental impact can be also reduced. PV modules contain different toxic components; thus, it is necessary to establish the way of a good management for each phase of their life cycle.

Recycling these products on the end of their life cycle we can protect the land and the water sources from pollination with toxic elements. Studies have projected this recycling cost of approximately 0.01–0.04$/W for both materials using relatively standard separation techniques.

Acknowledgments This work was done with helpful of technical dates indicated by Renovatio Solar LTD.

References

1. Masson, G., Latour, M., Rekinger, I., Theologits, T., Papoutsi, M. (2013). Global market outlook for photovoltaic 2013–2017 (pp. 13–23), EPIA.
2. Hoogeven, Y., Asquith, M., Jarosinka, D. (2013). *Environmental Indicator Report* (pp. 75–88), European Environment Agency.

3. Roger, A. (2010). Messenger, Ventre, Jerry, *Photovoltaic system engineering* (pp. 351–367) Boca Raton: CRC Press.
4. Haberlin, H. (2012). *Photovoltaic system design and practice* (pp. 60–69). New York: Wiley.
5. Boxwell, M. (2012). Solar Electricity Handbook, pp. 89–99.
6. Grenstream Publishing, 2011.
7. Glipin, A. (2006). *Environmental imact assestment* (pp. 4–16) Cambridge: Cambridge University Press.
8. https://www.transelectrica.ro/web/tel/home
9. http://www.anre.ro/
10. Pacca, S., Sivaraman, D., & Keoleian, G. A. (2007). Parameters affecting the life cycle performance of PV technologies and systems. *Energy Policy, 35*(6), 316–326.
11. Pehnt, M. (2006). Dynamic life cycle assessment (LCA) of renewable energy technologies. *Renewable Energy, 31*(1), 55–71.
12. Directive 2012/19/Eu. (2012). On waste electrical and electronic equipment (WEEE).
13. Government Decision, Low Nr. 1037/2010. (2010). On waste electrical and electronic equipment.
14. Directive 2002/96 /EC of the European Parliament and of the Council, 2002.

CFD Analysis and Theoretical Modelling of Multiblade Small Savonius Wind Turbines

Mihai Lates and Radu Velicu

Abstract Vertical wind turbines are used in areas with non-stable wind directions or with turbulent air flows due to the reason that for a vertical wind turbine the wind direction is not an input design data—the functioning of the vertical wind turbine is not influenced by the wind direction. Built environments are characterized by turbulent air flows and small open spaces; due to that, according to the wind turbines applications, small Savonius wind turbines are used in these areas. The paper presents the finite element modeling (FEM) by using the CFD based Ansys 14.0 software of a multiblade small Savonius wind turbine and the theoretical modelling of it; the purpose of the modeling consists in finding out the wind turbines behavior depending on its blades number.

Keywords Savonius wind turbine · FEM · CFD · Power coefficient

1 Introduction

Vertical wind turbines are used in areas with non-stable wind directions or with turbulent air flows due to the reason that for a vertical wind turbine the wind direction is not an input design data—the functioning of the vertical wind turbine is not influenced by the wind direction [12].

Due to the action of the wind, on the wind turbines are acting *drag* $\boldsymbol{F_D}$ and *lift* $\boldsymbol{F_L}$ *forces*; Fig. 1 presents a general sketch of the drag and lift forces. The vertical wind turbines are designed according to the type of the acting force: the functioning of Savonius type wind turbines is based on the action of the drag forces and the functioning of the Darrieus wind turbines is based on the action of the lift forces. Hybrid vertical wind turbines are using both of the forces as acting forces [6].

M. Lates (✉) · R. Velicu
Product Design Mechatronics and Environment Department, Transilvania University of Brasov, Brasov, Romania
e-mail: latesmt@unitbv.ro

I. Visa (ed.), *Sustainable Energy in the Built Environment - Steps Towards nZEB*, Springer Proceedings in Energy, DOI 10.1007/978-3-319-09707-7_30

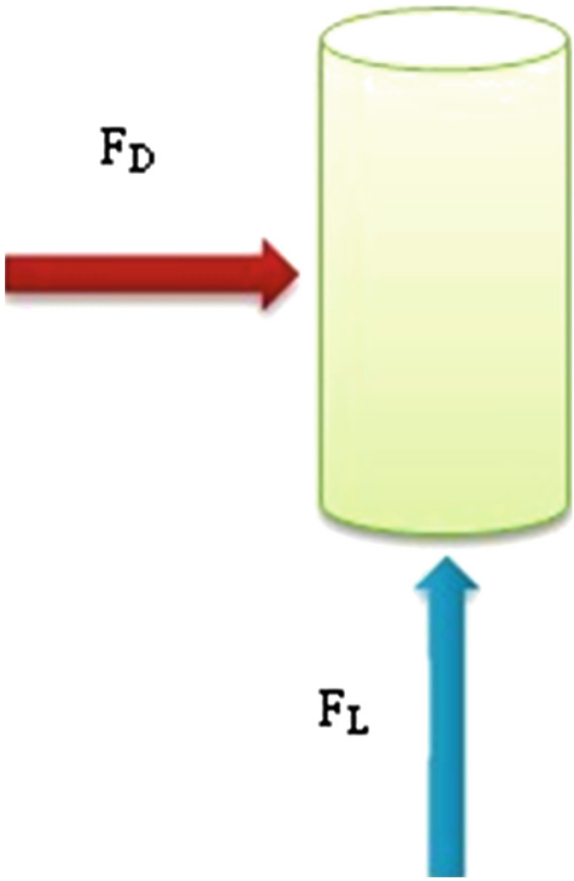

Fig. 1 The drag F_D and lift F_L forces which are acting on a general shaped system

Built environments are characterized by turbulent air flows mainly in the horizontal directions [16] and due to that there are preferred solutions with small vertical wind turbines which are functioning due to the action of the drag forces instead of the lift forces [3, 6]. These are the arguments which are on the base of using Savonius type wind turbines instead of Darrieus wind turbines [3, 6] in built environments.

The main parameter which characterizes a wind turbine is the *power coefficient* C_P which defines its aerodynamic efficiency and generally, the researches on the wind turbines development are focused on finding solutions with higher aerodynamic efficiencies combined with simple constructions. According to that, the literature offers new wind turbine solutions which are quantified by the power coefficient or/and the variation of the rotor's torque with the wind speed or/and the variation of the generated power with the wind speed or/and the values of the drag force.

The performance prediction of the Savonius wind turbine is depending on the computational methodology, on the wind turbines geometric parameters and on the number of blades [1, 13, 15].

The paper [20] has studied the parameters which are influencing the design of a 5 kW two bladed Savonius wind turbine. As geometric parameter, the *aspect ratio* $\boldsymbol{\alpha}$ [6, 7, 11, 20] (the ratio between the wind turbines height and the rotor's diameter) should be two, for a better stability and high efficiency. The results are represented by the pressure distribution and the value of the drag force by achieving a Computational Fluid Dynamics (CFD) analysis by using SolidWorks Flow Simulation. The general design steps are presented in [2] and are referring on the conceptual design, virtual prototyping testing and implementation of Savonius wind turbines.

The paper [8] concludes by measurements that a two blades Savonius rotor is more efficient than a three [8, 15] or four blades rotor. These measurements and the measurements from [4, 10, 11, 14, 17] validate the CFD analysis results and certify the CFD tools as a proper analysis tool of the Savonius wind turbines; the paper [11] offers CFD and measurements results regarding the turbulences created by a Savonius wind turbine.

The study of the references concludes that the measurements in wind tunnels and the CFD simulations are the only tools available to study the Savonius rotors behaviour.

2 Problem Formulation

The paper presents a theoretical study of a set of small Savonius wind turbines with different number of blades and same overall dimensions. The wind turbines are implemented in a built environment and, by using CFD simulations in Ansys software, the pressures, the velocities and the turbulences are obtained. By using the results data from the CFD simulations, the power coefficient, the acting torque, the drag forces and the generated power variation with the wind velocity are determined.

The theoretical simulations are achieved for an end plated Savonius wind turbine with the aspect ratio $\boldsymbol{\alpha} = 2$ and a diameter of $\boldsymbol{D} = 3.5$ m; the parameter which is varying is the number of the blades, from 2 to 8.

In the first step, in order to achieve the CFD simulation, the geometrical model of the Savonius wind turbines with 2–8 blades is made by using Catia software (see Fig. 2).

For all the Savonius wind turbines is defined a box type enclosure which represents the volume where the air will flow. The geometrical models are meshed in Ansys 14 software with a medium smoothness of the tetrahedral type elements and a fine transition of the finite elements in the border areas; the span angle centre is imposed to be fine, also. These settings are chosen in order to achieve the convergence of the results.

The meshed geometry is presented in the Fig. 3, where, in the middle of the enclosure the Savonius wind turbine is placed.

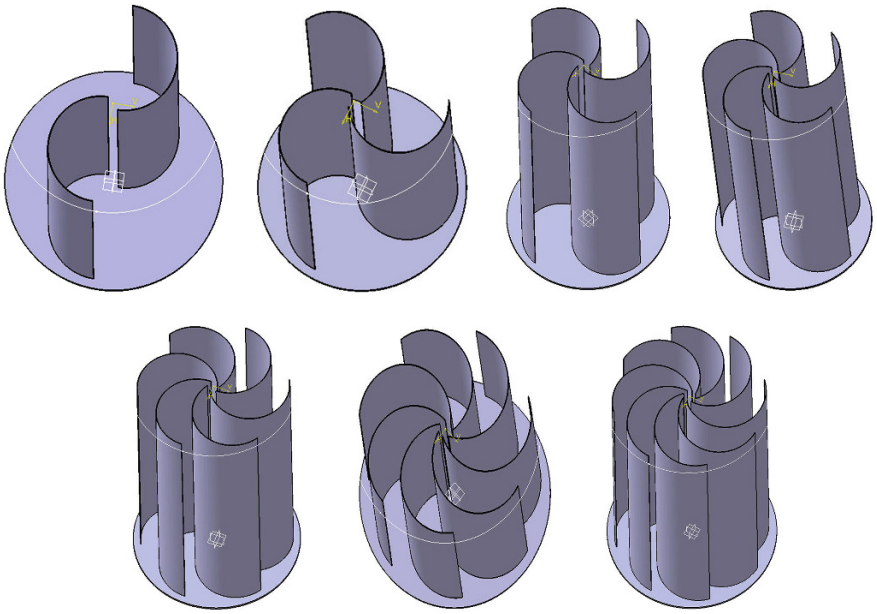

Fig. 2 The 2–8 bladed Savonius wind turbines models

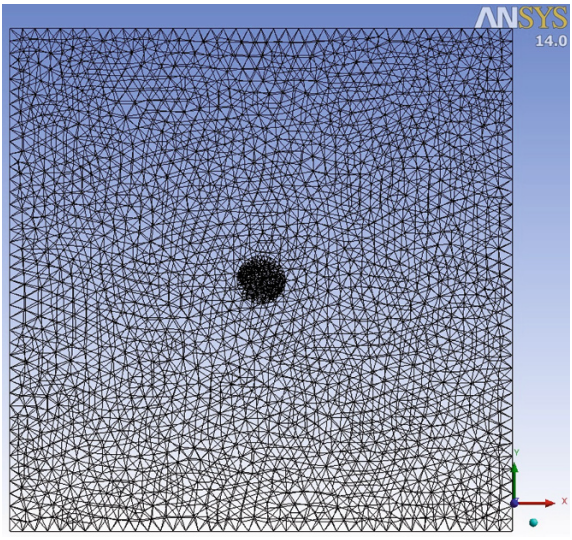

Fig. 3 The meshed model

For the CFD analysis the border conditions are modelled for the inlet and the outlet of the enclosure. On the inlet is imposed the wind velocity with a range of values between 5 and 25 m/s; on the outlet there are imposed pressure conditions

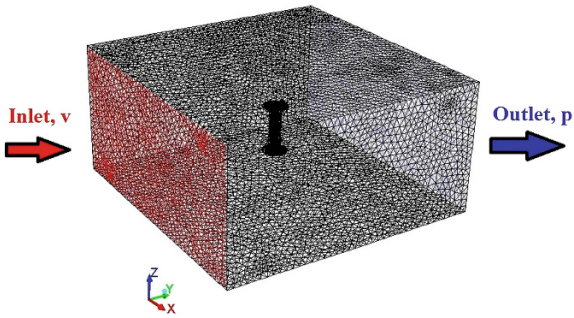

Fig. 4 The CFD model

—the pressure should be equal with the atmospheric pressure by considering the value of 101,325 Pa. The CFD model is presented in the Fig. 4.

The computational model which is used for the CFD analysis is the *K-epsilon turbulence model* which is based on two transport equations: one equation for the *turbulent kinetic energy* (***k***) and one equation for the *rate of dissipation of the turbulent kinetic energy* (***τ***). This model is the most validated turbulence theory with many applications, from industrial to environmental flows in the case of planar shear layers and recirculating flows; generally, in the case of the wind turbines, the planar shear layers are considered as solving assumptions [4–7, 9, 11, 14, 15, 17, 19]. In [7, 11, 15] were performed both tests and CFD analyses based on the main turbulence theories for Savonius wind turbines and the results are validating the *K-epsilon turbulence model* as base theory which can be used for CFD analyses in the case of Savonius wind turbines.

The iterations number which should be set up for the solving process is established according to convergence considerations; during model computations, a number of 80 iterations have been imposed in order to achieve the convergence—Fig. 5.

The results are referring on the pressures gradient (pressure difference between two sides of one face of the wind turbine), turbulence intensity, velocity magnitude, drag forces and torques which are acting on the turbine's rotor. The pressure gradients, the turbulence intensity and the velocity magnitude distribution for all the 2–8 blades Savonius wind turbines, in the case of a 20 m/s wind velocity, are presented in Figs. 6, 7 and 8, respectively.

According to the results, the pressure gradient has a distribution on a larger area of the 2 and 3 blades Savonius rotor than in the other cases, meaning that these two rotors are preferred in order to reduce the stresses on the blades. The pressure gradient, in these two cases, has a uniform distribution on the blades, instead of the other variants, which is generating stabile functioning of the turbines.

The turbulence intensity has a uniform distribution on the blades in the case of 2, 3 and 4 blades rotors; in the other cases, the turbulences intensities have a non-uniform distribution on all the blades which induces non-uniformities during the

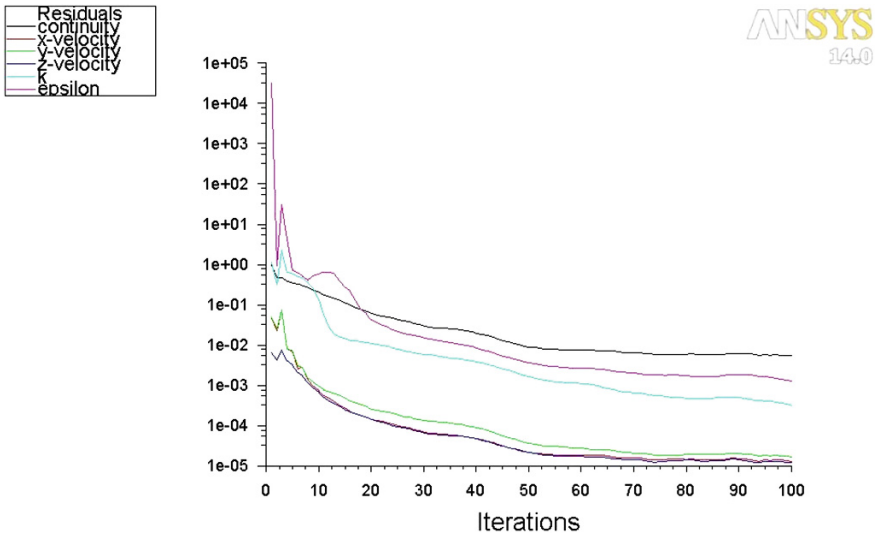

Fig. 5 The solutions convergence

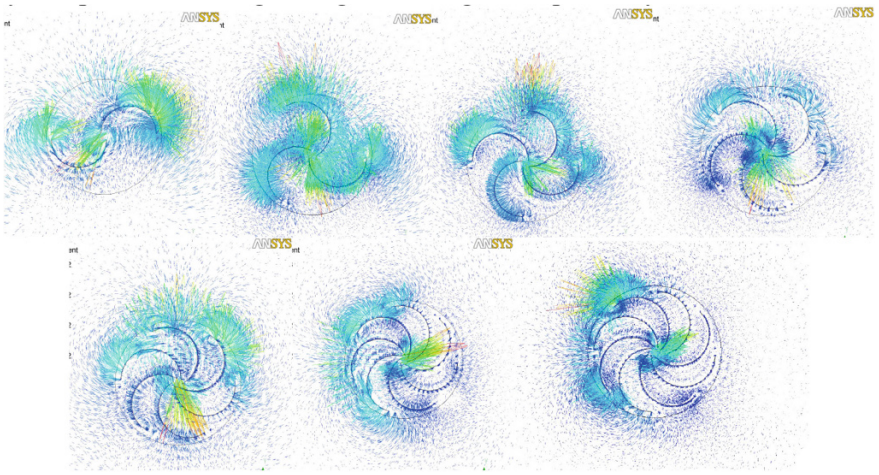

Fig. 6 The distribution of the pressure gradient

turbines functioning and reduce the efficiency of the wind turbine; same conclusion may be assumed in the case of the velocity magnitude.

The variation of the *drag force* $\boldsymbol{F_D}$ and of the *rotor's torque* $\boldsymbol{M_w}$ is presented in Figs. 9 and 10, respectively. According to the results, the 2 blades rotor has the highest values for the drag force and for the torque meaning that this type of rotor

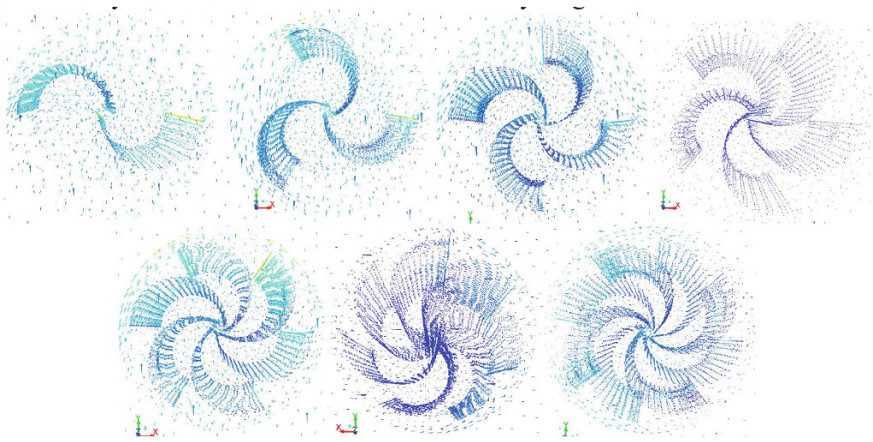

Fig. 7 The distribution of the turbulence intensity

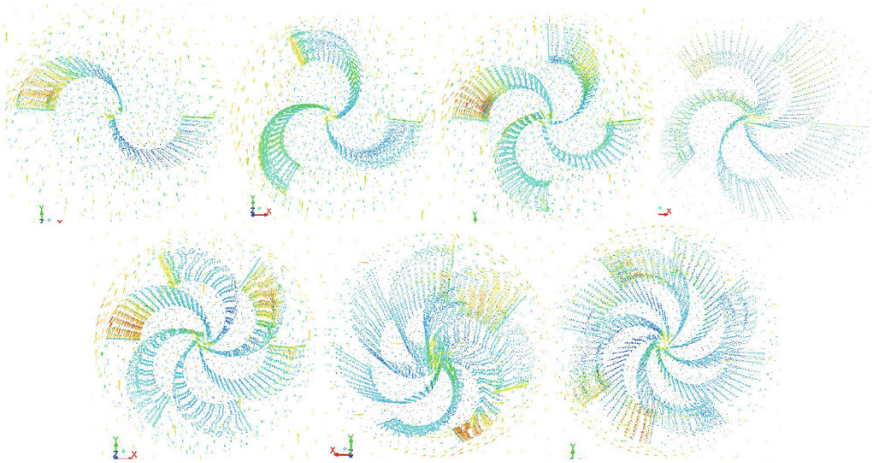

Fig. 8 The distribution of the velocity magnitude

has a highest efficiency than the others; all the other rotors have close values, one to the other, for the drag forces and for the torques.

The *torque at the rotor* is the parameter which is indicating in which conditions the turbine is starting to move; the condition that should be accomplished in order to put the rotor in motion is

$$M_w \geq M_r, \tag{1}$$

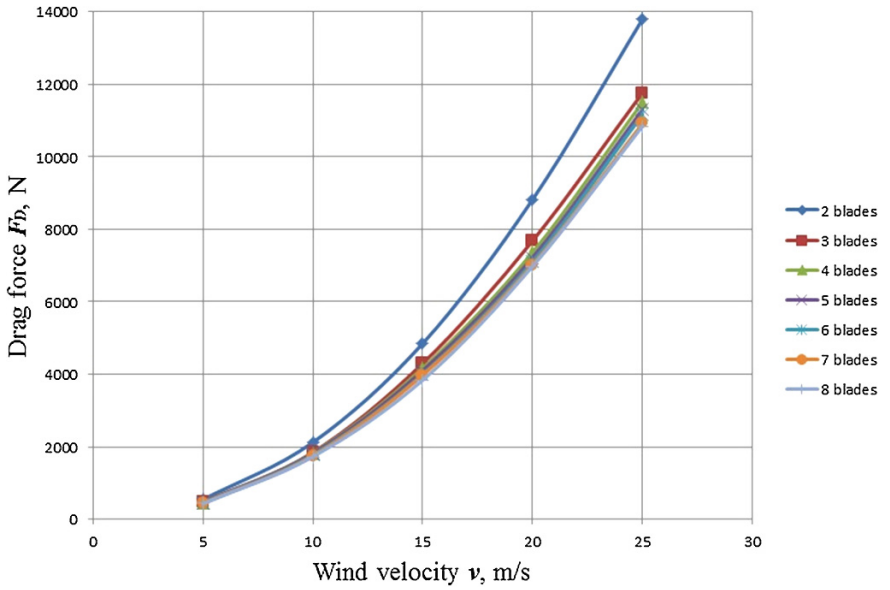

Fig. 9 The variation of the drag force

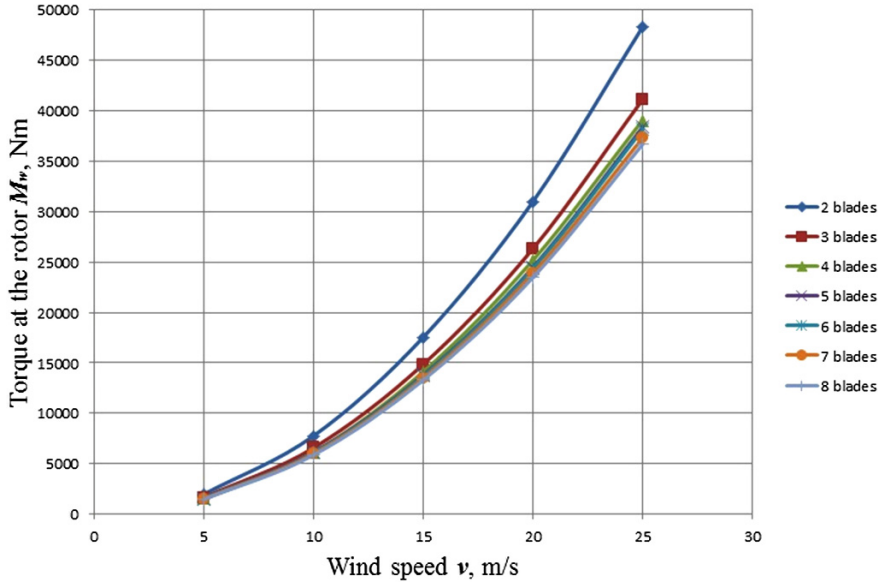

Fig. 10 The variation of the torque at the rotor

where $\boldsymbol{M_r}$ represents the *resistant torque* which includes the *inertial torque* $\boldsymbol{M_i}$ of the Savonius rotor and the *friction torque* $\boldsymbol{M_f}$; so

$$M_r = M_i + M_f. \tag{2}$$

The *generated power* by a wind turbine is determined with [4, 6, 8, 11]

$$P = 0,5 \cdot C_P \cdot \rho \cdot A \cdot v^3, \tag{3}$$

where: $\boldsymbol{C_P}$ is the *power coefficient*; $\boldsymbol{\rho}$ = 1.22 kg/m^3 represents the *density* of the air; $\boldsymbol{A}$ is the *area* of the rotor $\boldsymbol{A = H \cdot D}$ with the height $\boldsymbol{H}$ = 7 m and the diameter $\boldsymbol{D}$ = 3.5 m; $\boldsymbol{v}$ is the wind speed.

The only unknown parameter from the relation (3) is the power coefficient $\boldsymbol{C_P}$; its value can be determined according to the CFD theories and according to the results from the CFD simulations by using Ansys. From [6] the expression of $\boldsymbol{C_P}$ is

$$C_P = \frac{\left(1 + \frac{v_{p0}}{v}\right) \cdot \left(1 - \frac{v_{p0}^2}{v^2}\right)}{2}, \tag{4}$$

where $\boldsymbol{v}$ is the imposed *wind velocity in the inlet* of the analysis domain and $\boldsymbol{v_{p0}}$ is the *wind velocity* at the section where the pressure is equal with the atmospheric pressure of 101,325 Pa; so, in the CFD analysis case with Ansys, the $\boldsymbol{v_{p0}}$ wind speed is measured in the area where the pressure is equal with the atmospheric pressure.

In the case of relation (2) of the resistant torque $\boldsymbol{M_r}$, the inertial torque $\boldsymbol{M_i}$ is determined automatically by the Catia software for each of the rotors and for the *friction torque* $\boldsymbol{M_f}$ is made the assumption that 20 % from the total *resistant torque* $\boldsymbol{M_r}$ is represented by the friction [18]. According to these, the total *resistant torque* $\boldsymbol{M_r}$ can be calculated.

The *mechanical power* $\boldsymbol{P_M}$ is the power which is generated by the wind, so

$$P_M = P. \tag{5}$$

The mechanical power is depending on the *torque at the rotor* $\boldsymbol{M_w}$ and on the *pulsation* $\boldsymbol{\omega}$ as

$$P_M = M_w \cdot \omega, \tag{6}$$

where the *pulsation* $\boldsymbol{\omega}$ is

$$\omega = \frac{v}{R}, \tag{7}$$

where $\boldsymbol{v}$ is the *wind speed at the end of the blade* (known from the CFD simulation in Ansys) with the radius $\boldsymbol{R}$.

At the limit, in order to determine the start-up wind speed of the wind turbines, in the relation (6) is considered that $M_w = M_r$.

3 Results and Discussions

By using the relation (4) and the results from the CFD analyses in Ansys software, the power coefficient C_P calculated and its variation is presented in the Fig. 11.

Highest values for the power coefficient are obtained for the 2 blades Savonius rotor; the power coefficient for the 3 blades rotor is almost half as values from the values of the 2 blades rotor. Bigger number than 3 for the blades produce a dramatic reduction of the power coefficient.

The results for the power coefficient are validated by the references [6, 8, 15].

With the relation (3), by knowing the values of the power coefficient C_P, the generated power is determined; its variation is presented in Fig. 12.

As in case of the power coefficient, also for the generated power, higher values are obtained in the case of the 2 blades Savonius wind turbines; the 4–8 blades wind turbines are generating, almost, the powers small as values. The 3 blades wind turbine is generating a power between the two rotors categories, as values.

The relations (3), (4), (6), (7) are used to determine the start-up wind speed of the wind turbines and its variation is presented in Fig. 13.

The 2 blades Savonius wind turbine has the smallest start-up wind speed which means that is the most suitable to be used.

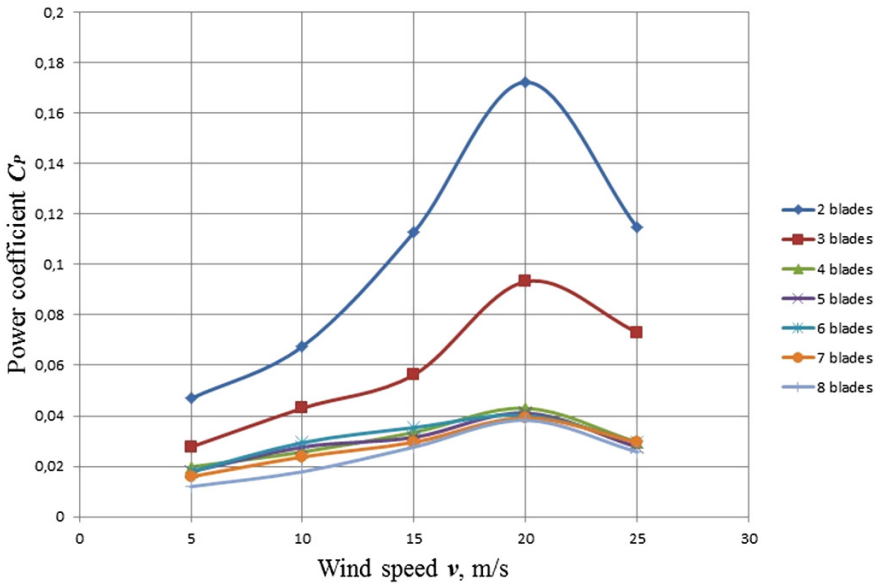

Fig. 11 The variation of the power coefficient

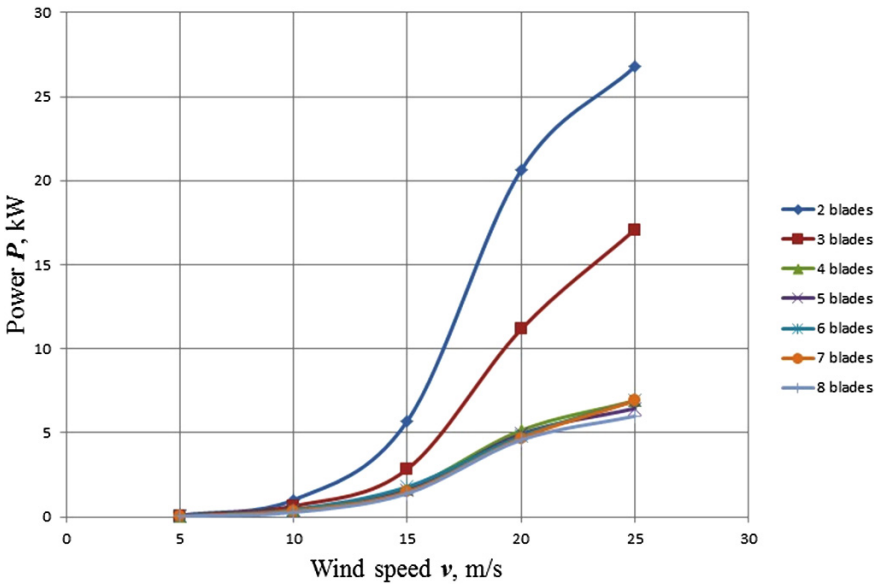

Fig. 12 The variation of the generated power

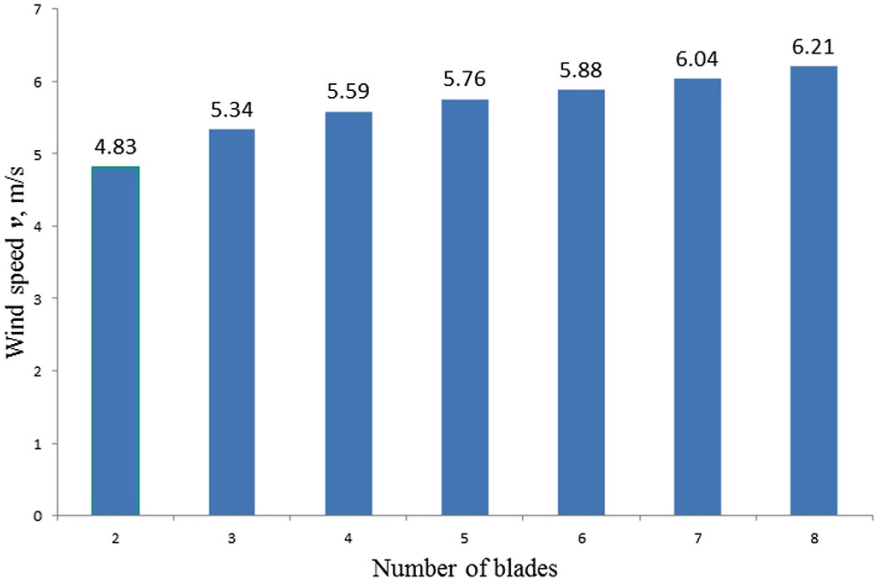

Fig. 13 The start-up wind speed

4 Conclusions

The CFD analysis combined with analytical modelling represent a modern and useful technique which can be used to analyse and predict the wind turbines behaviour.

For the Savonius multiblade wind turbines the results obtained from the CFD analyses and from the theoretical modelling can be concluded with:

(a) the novel part of the paper is referring on the finite element analysis, on the determination method of the power coefficient, of the generated power and on the start-up wind speeds;
(b) the pressure gradient has a distribution on a larger area of the 2 and 3 blades Savonius rotor than in the other cases, meaning that these two rotors are preferred in order to reduce the stresses on the blades and to assure a stabile functioning of the turbines;
(c) the turbulence intensity has a uniform distribution on the blades in the case of 2, 3 and 4 blades rotors which is an advantage according to the their functioning efficiency;
(d) the 2 blades rotor has the highest values for the drag force and for the torque meaning that this type of rotor has a highest efficiency than the others;
(e) the power coefficient, as the most important parameter which indicates a wind turbine's efficiency, has higher values for the 2 blades Savonius rotor; the power coefficient for the 3 blades rotor is almost half as values from the values of the 2 blades rotor. Bigger number than 3 for the blades produce a dramatic reduction of the power coefficient. The values of the power coefficient are influencing in the same way the values of the generated power;
(f) the start-up wind speed has the smallest values for the 2 blades wind turbine, so, according to that, this turbine is more suitable to be used in the case of the small wind speeds;
(g) as general conclusion, from the all analysed points of view, the 2 blades Savonius wind turbine is recommended to be used insteads of Savonius wind turbines with higher number of blades.

References

1. Akwa, J. W., Vielmo, H. A., & Petry, A. P. (2012). A review on the performance of Savonius wind turbines. *Renewable and Sustainable Energy Reviews, 16*, 3054–3064.
2. Albani, A., & Ibrahim, M. Z. (2013). Preliminary development of prototype of Savonius wind turbine for application in low wind speed in Kuala Terengganu, Malaysia. *International Journal of Scientific and Technology Research, 2*(3), 102–108.
3. Can, K., Haixia, L., & Xin, Y. (2014). Review of fluid dynamics aspects of Savonius-rotor-based vertical-axis wind rotors. *Renewable and Sustainable Energy Reviews, 33*, 499–508.
4. D'Alessandro, V., Montelpare, S., Ricci, R., & Secchiaroli, A. (2010). Unsteady aerodynamics of a Savonius wind rotor: a new computational approach for the simulation of energy performance. *Energy, 35*, 3349–3363.

5. Gupta, A., Biswas, A., & Sharma, K. K. (2008). Comparative study of a three-bucket Savonius rotor with a combined three-bucket Savonius—three bladed Darrieus rotor. *Renewable Energy, 33*, 1974–1981.
6. Ionescu, M. D., Haraguta, C., Ignat, M., Silivestru, V., Petcu, R., & Fetea, G. (2012). *Turbine eoliene cu ax vertical*. Contributii Romanesti: Graph Byte Press.
7. Jaohindy, P., McTavish, S., Garde, F., & Bastide, A. (2013). An analysis of the transient forces acting on Savonius rotors with different aspect ratios. *Renewable Energy, 55*, 286–295.
8. Kadam, A. A., & Patil, S. S. (2013). A review study on Savonius wind rotors for accessing the power performance. *Journal of Mechanical and Civil Engineering*, *5*, 18–24.
9. Kakcprzak, K., Liskiewitz, G., & Sobczak, K. (2013). Numerical investigation of conventional and modified Savonius wind turbines. *Renewable Energy, 60*, 578–585.
10. Kamoji, M. A., Kedare, S. B., & Prabhu, S. B. (2009). Experimental investigations on single stage modified Savonius rotor. *Applied Energy, 86*, 1064–1073.
11. Nasef, M. H., El-Askary, W. A., AbdEl-hamid, A. A., & Gad, H. E. (2013). Evaluation of Savonius rotor performance: static and dynamic studies. *Journal of Wind Engineering and Industrial Aerodynamics, 123*, 1–11.
12. Pope, K., Dincer, I., & Naterer, G. F. (2010). Energy and exergy efficiency comparison of horizontal and vertical axis wind turbines. *Renewable Energy, 35*, 2102–2113.
13. Shigetomi, A., Murai, Y., Tasaka, Y., & Takeda, Y. (2011). Interactive flow field around two Savonius turbines. *Renewable Energy, 36*, 536–545.
14. Sukanta, R., & Saha, U. K. (2013). Computational study to assess the influence of overlap ratio on static torque characteristics of a vertical axis wind turbine. *Procedia Engineeering, 51*, 694–702.
15. Sukanta, R., & Saha, U. K. (2013). Review on the numerical investigations into the design and development of Savonius wind rotors. *Renewable and Sustainable Energy Reviews, 24*, 73–83.
16. Toja-Silva, F., Colmenar-Santos, A., & Castro-Gil, M. (2013). Urban wind energy exploitation systems: bahaviour under multidirectional flow conditions—opportunities and challenges. *Renewable and Sustainable Energy Reviews, 24*, 364–378.
17. Tong, Z., & Dietmar, R. (2013). Numerical study of detailed flow field and performance of Savonius wind turbines. *Renewable Energy, 51*, 373–381.
18. Velicu, R., Lates, M. T., Saulescu, R., & Todi-Eftimie, A. (2013). Theoretical and experimental study of friction in bearing mountings. In *Presentation at VII Iberian Conference on Tribology, Porto*.
19. Yan-Fei, W., & Mao-Sheng, Z. (2013). 3-dimensional cfd simulation and analysis on performance of a micro-wind turbine resembling lotus in shape. *Energy and Buildings, 65*, 66–74.
20. Widodo, W. S., Chin, A. C., Sihombing, H., & Yuhazri, M. Y. (2012). Design and analysis of a 5 kw Savonius rotor blade. *Global Engineers and Technologists, 2*(8), 1–8.

Decreasing the Susceptivity of the Electric Equipment to Voltage Dips—A Way to Increase the Energy Sustainability

Elena Helerea, Corneliu Ursachi and Ionel Lepadat

Abstract This paper analyzes the intrinsic sensitivity of different types of electrical equipment, which is caused by the specific constructive operating principle. In the case of electric motors, their ability to function close to the normal operation regime, even in the case when certain events caused by various electromagnetic disturbances occur, is determined by the electrical and mechanical characteristics of the electric drive. The paper describes the test bench developed within the Electromagnetic Compatibility Laboratory of the Research-Development-Innovation Institute of Transilvania University of Brasov, with a view to establishing the effect of the three-phase voltage dips on the induction motors. The bench allows the generation of three-phase symmetrical dips of abrupt and gradual types with a magnitude ranging between 0 and 90 %. Experimental determinations and measurements of the shape of phase voltages, current, and active power are used to establish the effect of dips supply regimes, and to evaluate the induction motor efficiency.

Keywords Disturbances · Voltage dips · Induction motor · Susceptivity · Test bench · Measurement procedure

1 Introduction

The need for long-term sustainability of energy requires finding viable solutions applied on the entire chain of production, transport, distribution and use of energy [1]. One aspect of the energy sustainability is the safety and security afferent to the consumer supply. From this point of view, it has been found that along with increasing power consumption, extending the working frequency range, introducing widespread electric and electronic control, more and more events are reported due

E. Helerea (✉) · C. Ursachi · I. Lepadat
Transilvania University of Brasov, Braşov, Romania
e-mail: helerea@unitbv.ro

I. Visa (ed.), *Sustainable Energy in the Built Environment - Steps Towards nZEB*,
Springer Proceedings in Energy, DOI 10.1007/978-3-319-09707-7_31

to the electromagnetic disturbances which affect the quality and efficiency of the power delivered to consumer.

The implementation of distributed energy generation units, the formation of micro-grids power system interfaced with the mains through AC rotating machines or through power electronic converters increase the risk of the electromagnetic disturbances in the consumer networks [2–4].

Reducing electromagnetic disturbance requires a systemic approach to develop a unified view of the power supplier, the equipment manufacturer and the consumer. Although the power supplier should ensure the good working of their supply system installations at the highest level, however, economically, the effort to eliminate any risk of electromagnetic disturbances in the network is not justified. The important role is incumbent on the manufacturer and consumer.

Voltage dips are generally recognized as the most common type of power quality disturbance. The impact of voltage dips on consumer equipment is complex and includes two aspects of electromagnetic compatibility:

- Emissivity of electromagnetic disturbances—how equipment operation influences the voltage of power networks;
- Susceptivity to electromagnetic disturbances—how power network through voltage dips influences equipment performances.

From the point of view of sensitivity to voltage dips, these disturbances can disrupt or damage industrial equipment, processes, and commercial equipment. Therefore, many testing procedures have been developed, whereof many are now the bases for international standards, such as IEC 61000-4-11 and 61000-4-34, and industry standards, such as SEMI F47 in the semiconductor industry.

This paper analyzes the voltage dip characteristics, the procedure for determining the sensitivity of various types of electrical equipment to the voltage dips, and as case study, the sensitivity of the induction motor to the balanced three-phase voltage dips is determined and analyzed.

2 Voltage Dips and Equipment Sensitivity Testing

2.1 Voltage Dips Characteristics

The voltage dip, according to IEEE 1159–1995 standard, is a momentary decrease (10–90 %) in the RMS voltage magnitude for a time interval from 0.5 cycles to 1 min. The main causes of voltage dips are short-circuit type faults in the power networks or disconnection/connection of large loads in electric network of consumers.

Depending on the type of short-circuits, voltage dips can be single-phase, two-phase or three-phase. In three-phase power systems, dips can be balanced or unbalanced. A three-phase short-circuit may generate balanced voltage dips, in which the

phase voltages are equal. The short-circuit between a phase and earth or between two phases cause unbalanced voltage dips, in which the RMS values of the phase voltages are not equal, and/or their phase angles are different from 120° [5, 6].

The characteristics of the voltage dips are magnitude, duration and phase angle shift.

Depending on the type of fault which initiated the voltage dips, different dips models have been developed [5–7].

The basis for the determination of three-voltage dip magnitude is fault analysis. The fault analysis program can predict the voltage dip magnitude for any type of fault, anywhere in the network, if the accurate information of all impedances including the positive-, negative-, and zero-sequence resistances and reactances of the power components, and the fault impedance is available.

Thus, for a radial distribution system, shown as a voltage divider model, the voltage dip magnitude can be obtained:

$$\underline{U}_d = \frac{\underline{Z}_F}{\underline{Z}_F + \underline{Z}_S} \cdot \underline{U}_{pf} \tag{1}$$

where $\underline{Z}_F$ is the impedance of the feeder between the fault point and the PCC, $\underline{Z}_S$ is source impedance $\underline{U}_{pf}$ is the pre-fault voltage at the PCC.

If the pre-fault phase angle of $\underline{U}_{pf}$ is 0^o, the phase angle shift will be given by the difference between the pre-fault and the during-fault voltage phase angle:

$$\Delta\varphi_d = arctg\frac{X_F}{R_F} - arctg\frac{X_S - X_F}{R_S - X_F} \tag{2}$$

where $\underline{Z}_F = R_F + jX_F$ şi $\underline{Z}_S = R_S + jX_S$.

In the event of a fault, the voltage dip will last until a protective device interrupts the flow of the fault current. Thus, determining/calculating the duration of the voltage dip needs complete information on the type, location, and settings of the protective relays [7].

For unsymmetrical faults, the symmetrical component method is applied to obtain the characteristics of unbalanced voltage dips [5–7].

The shape of the voltage dip is rectangular if the impedance of the system remains constant over time (Fig. 1a). In the case when a time variation of impedances is produced, the shape of the voltage dip is not rectangular, being often of a trapezoidal shape (Fig. 1b).

In the case of non-rectangular voltage dip, the voltage recovery time t_r is higher than the pre-voltage dip time t_{dc}. This can lead to an incorrect assessment of the voltage dip effect on sensitive loads [8–10].

Voltage dips characteristics change by their propagation in power networks, depending on many factors: the network topology, line and cable impedance, transformers connections, protection and earth systems, load dynamics and connection types.

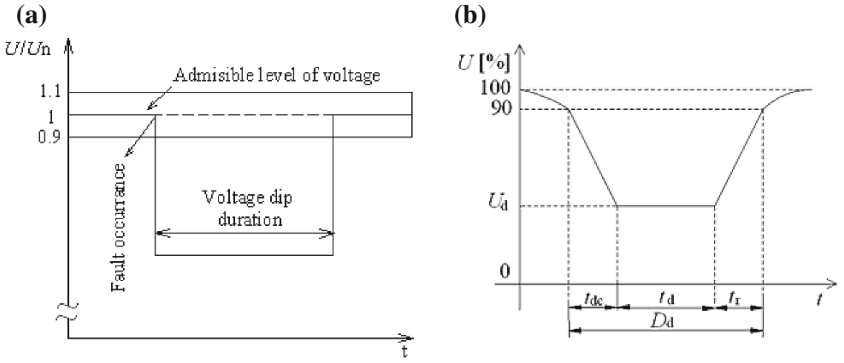

Fig. 1 Voltage dip with: **a** rectangular shape, **b** trapezoidal shape

In this paper, as a case study, the effect of the balanced three-phase voltage dip over induction motor is analyzed.

2.2 Testing Methods to Voltage Dips

The susceptivity of the equipment to voltage dips is expressed by the tolerance curves [7]. Generally, two tolerance curves of the equipment–namely the Information Technology Industry Council (ITIC) curve and the SEMI F47 curve—are used (Fig. 2a). Each point on the curve indicates how long the equipment is able to ride through certain voltage dips. The first curve, ITIC curve, was formerly called the Computer and Business Equipment Manufacturer Association (CBEMA) curve. It represents the voltage variation tolerance requirements of information technology equipment as defined by the Information Technology Industry Council, formerly known as CBEMA curve. The second curve specifies the voltage dip immunity of the semiconductor manufacturing equipment [9].

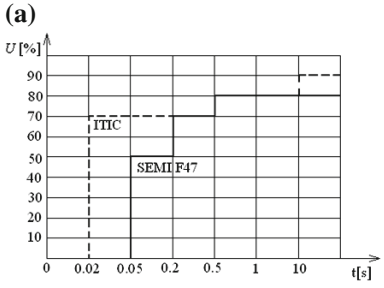

(b)

Ud %	Dip duration [cycles]					
	1	7	40	50	100	500
80				x	x	x
60			x	x	x	
40		x	x	x		
20	x	x	x	x		
10	x	x	x	x		
0	x	x	x	x		

Fig. 2 Example of tolerance curves (**a**) and testing program (**b**) containing the voltage dips magnitude and dip duration

As voltage dips are characterized by magnitude as well as duration, the important issue is how to obtain an accurate assessment—which is the way for quantifying the number of voltage dip events needed for testing plan.

The testing plan includes magnitude and duration ranges of voltage dips (Fig. 2b), which should be correlated with the real number of voltage dip events having voltage magnitude and duration within a certain range (dip density table), and with the total number of voltage dip events that have voltage magnitude lower than a given value and duration lasting longer than a specific time interval (cumulative dip table).

Thus, in this testing process, the duration must be carefully chosen to fit the equipments tolerance curves. The tests for establishing the voltage dip tolerance curves usually consider the case of rectangular dips [10].

In [11] the current methods of testing equipment to voltage dips are analyzed; likewise, new voltage dip indices based on scaling and wavelet coefficient energy analysis are proposed.

In this paper the effect of three-phase balanced individual voltage dip on induction motor is determined by theoretical and experimental investigations.

2.3 Voltage Dips Impact on the Electric Equipment

The voltage dips, as deviation of supplying voltage from the rated one, can cause important damages to end-user equipment. The voltage dip impact on the power network and on the sensitive consumers depends on the specific characteristics of the dip: magnitude, duration, phase angle jump, dip shape, etc.

Thus, the sensitivity of the electric equipment and the level of different voltage dips can be analyzed, respectively determined, through mathematical modeling of equipment, supplied in different regimes of voltage variation.

The model for AC magnetic contactor has been analyzed in [12], where for voltage sag assessment, the voltage sag ride through capability curves were constructed. The results reveal that the non-trip sag should be concerned because they may cause the decrease in operation lifetime of contactor.

The behavior of digitally controlled boost PFC converter in case of voltage sags is analyzed in [13]. Fault tolerant control algorithm is designed, implemented and is discussed.

The effects of voltage sags on domestic and office equipment are studied in [14] and the sensitivity of this kind of equipment for different magnitudes, durations and angle of incidence of voltage sag are experimentally obtained.

A preliminary study aimed at developing an ITI style curve to suit 230 V, 50 Hz electricity networks is developed in [15]. The results for domestic appliances show that equipment connected to the 230 V and 50 Hz electricity network has voltage sag immunity considerably better than that defined by the ITI curve. New investigations should be developed to clarify this aspect.

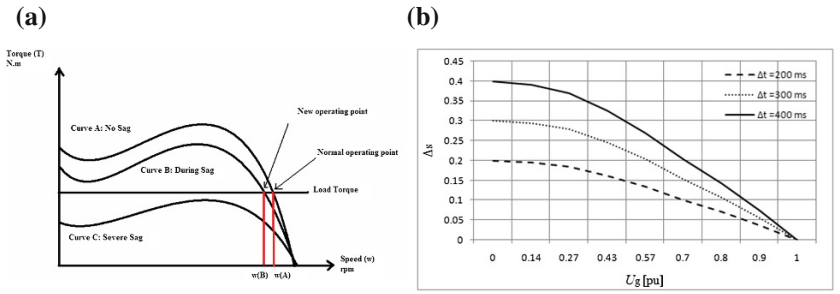

Fig. 3 Motor torque dependence on motor slip for different voltage dips (**a**) and motor slip variation for different magnitude and time values of the voltage dips (**b**)

The impact of the voltage dip on the performances of induction motor with applications in electric drives has been analyzed by researchers, mainly considering three-phase rectangular and non-rectangular voltage dips, using analytical methods and simulations [16–21].

The decrease in the performances of the induction motor is driven by the direct relationship between motor torque and the square of the supply voltage. When the induction motor supply voltage drops, the torque will drop sharply and with it the rotation speed (Fig. 3a). Depending on the depth and the voltage dip time, motor speed and motor slip can return to its normal value after supply voltage amplitude is restored.

Figure 3a shows three mechanical characteristics of the torque-speed induction motor, namely without voltage dips supplying (A curve), with voltage dips supplying (B curve) and severe voltage dip (C curve). The supply with voltage dips determines the reduction of the motor torque in direct proportion to the square of the supply voltage of the motor: the induction motor has a speed variation, but the operation is still stable (B curve). For a severe voltage dip, the torque produced by the induction machine is lower than the load torque; the induction machine slows its operating regime until it stops (C curve).

Considering the equivalent scheme of the induction motor, Golovanov and Lăzăroiu [18] established a dependency relationship between the slip variation Δs and voltage dip magnitude U_d and dip time t_d:

$$\Delta s = \frac{1 - U_d^2}{2H} \cdot t_d \tag{3}$$

where H is the inertia constant of the motor, which characterizes the ratio of the kinetic energy of moving masses at synchronous speed and rated power.

Figure 3b shows the slip variation along with the voltage dip amplitude for an induction motor at different H and t_d. One can observe a speed reduction at low amplitudes and longer voltage dip times.

Motor speed and torque reduction change motor dynamics, affecting the supply network and security systems. Thus, it is possible to trigger the under voltage

protection at voltage dip having dip time higher than the protection threshold. In this paper the experimental tests are described, and the wave forms obtained for voltages, currents and power are analyzed.

3 Experimental Tests

The experimental tests have been conducted on various types of electrical equipment. In this paper, we submit the results obtained in the case of the induction motor supplied with three-phase individual balanced voltage dips.

3.1 Description of Set-Up

The set-up from the Electromagnetic Compatibility Laboratory of the Research—Development—Innovation Institute of Transilvania University of Brasov allows the equipment testing to the various regimes of voltage dips. The configuration of testing bench is shown in Fig. 4.

The set-up has the following components:

- Dip generator—it is a three-phase controlled source of Netwave 30 type, with power of maximum 30 kVA which generates the voltage dips of various types;
- Power analyzer—it is a three-phase digital power analyzer of DPA 503 N type, which allows the measurement of RMS phase voltages, RMS currents, phase angles, and power;
- PC—it is a control and calculus system, with *dpa.control* software for controlling the parameters of the multifunctional three-phase source, and processing the data: voltage variations, harmonics and flicker.
- Mechanical DAQ allow measuring the mechanic characteristics of the induction motor.

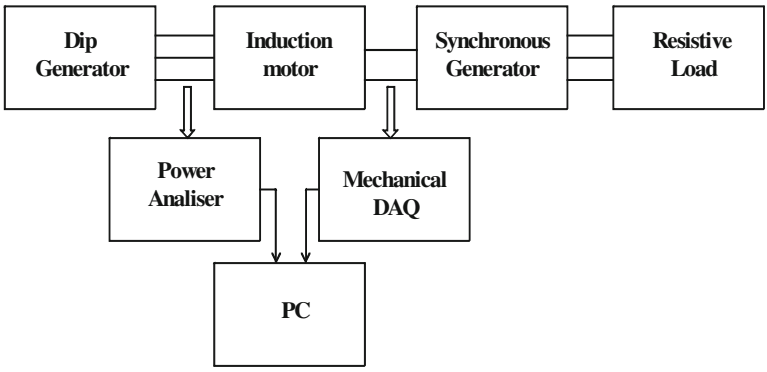

Fig. 4 Bench components for testing three-phase induction motor to voltage dips

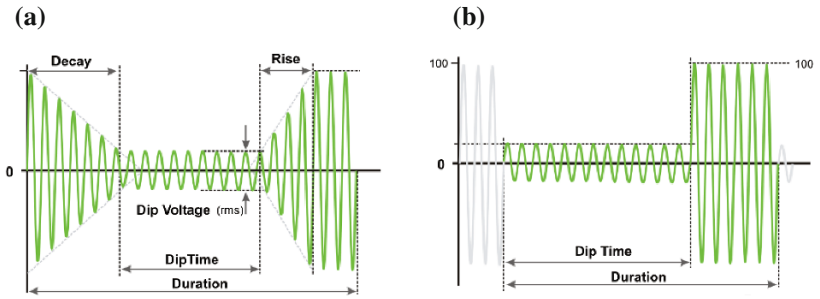

Fig. 5 Voltage dip shaves: **a** gradual; **b** abrupt

3.2 EUT and Voltage Dip Testing Regimes Description

As case study, a squirrel cage induction motor (Fig. 4) is used as equipment under test (EUT), with the following nominal parameters: P_n = 1.5 kW, U_n = 400 V, n = 380 rpm, star connection, I_n = 4.4 A. The motor is connected to a three-phase synchronous generator loaded by the variable resistors.

Two types of dips have been created and applied: with gradual (non-rectangular) shape, and abrupt (rectangular) shape (Fig. 5).

For the non-rectangular gradual voltage dip (Fig. 5a), the RMS voltage is decreased during a decay time t_{dc}, it is maintained constant during the dip time t_d and it is increased during the rise time t_r. The total duration of dip is considered:

$$D_d = t_{dc} + t_d + t_r.$$

In Table 1 the test number identification and the specific time parameters of the gradual and abrupt voltage dips applied on induction motor are presented.

The magnitudes of voltage dips, both for GR and for AB, of 0; 20; 40; 70; 80; 90 % have been considered.

The testing with abrupt three-phase voltage dip is considered more severe.

Table 1 Gradual and abrupt voltage dips time parameters

Gradual voltage dip time					Abrupt voltage dip time	
No. test	t_{dc} (ms)	t_d (ms)	t_r (ms)	D_d (ms)	No. test	t_d (ms)
GR1	50	100	50	200	AB1	200
GR2	100	200	100	400	AB2	400
GR3	500	1,500	500	1,500	AB3	1,500

4 Measurements and Results

With test set-up described above, three sets of tests with gradual dips (GR1, GR2, GR3) and other three sets of tests with abrupt dips (AB1, AB2, AB3) have been applied on the three phase induction motor. The tests are done with different magnitudes of gradual GR and abrupt AB voltage dips for the motor running with 90 % load.

For a measurement time of 20 s, 100 cycle-tests have been registered. Three-phase digital power analyzer registers the RMS values of phase voltages and currents, obtained for averaging on 10 cycles.

For each cycle-test, a set of data have been registered: active phase power *P*, reactive phase power Q, power factor between phase and neutral, harmonic content for voltages and currents. In this paper a comparative analysis regarding the waveform of RMS phase current and the motor active power variation during the voltage dip is done.

4.1 Shape of RMS Current Curves

For each voltage dips test (Table 1), the data corresponding to the 100 test-cycles have been processed and the curves of RMS voltages and currents have been obtained.

Figure 6 shows the shape of RMS voltage dip of type GR3 (magnitudes of 40 and 0 %; dip time 1.5 s), and RMS wave current curve in the supplying line L1 of the motor. For lines L2 and L3, the shape of RMS currents are the same.

Figure 7 shows the shape of RMS voltage dip of type AB3 (magnitudes of 40 and 0 %; dip time 1.5 s), and the shape of RMS current curve in the supplying line L1 of the three-phase induction motor.

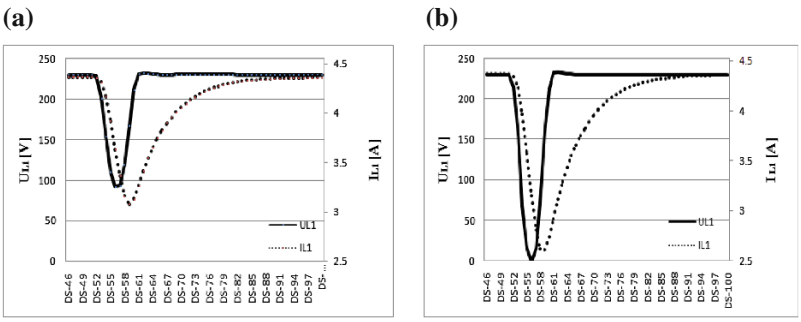

Fig. 6 Comparison between the shape form of RMS current in Line L1 and voltage gradual dip GR3, with dip time 1.5 s and the magnitudes of voltage dips: **a** 92 V (40 %); **b** 0 V (0 %)

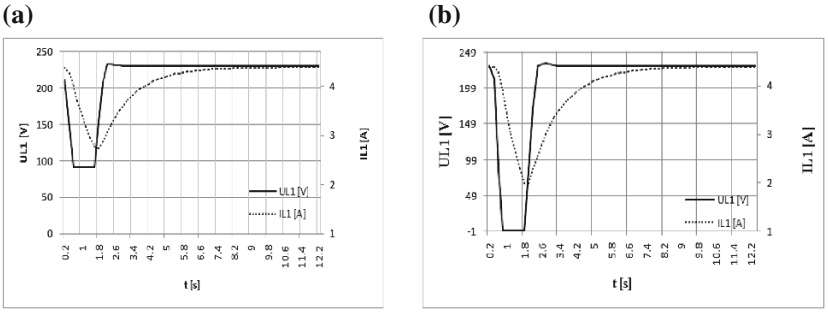

Fig. 7 Comparison between the shape form of RMS current and voltage gradual dip GR3 with dip time 1.5 s and the magnitudes of voltage dips: **a** 92 V (40 %); **b** 0 V (0 %)

An abrupt shape of the dip determines a value of current lower than in the case of a gradual dip. For an abrupt dip, the time of current recovery is longer than for the gradual dip. The graphs indicate an unbalance of the currents on the three phases due to motor structure.

4.2 Variation of Active Power of Induction Motor During the Voltage Dip Test

Figure 8 illustrates the comparison between the shape of RMS gradual voltage dip curve and active power on the phase L1 of the motor, in GR3 test—three phase voltage dip with dip time of 1.5 s and magnitude: 92 V (40 %), and 0 V (0 %).

Figure 9 illustrates the comparison between the shape of RMS abrupt voltage dip curve and active power on the supplying phase L1 of the motor, in AB3 test—three phase voltage dip with dip time of 1.5 s and magnitude: 92 V (40 %), and 0 V (0 %).

Table 2 shows a comparison regarding the active power measured in the voltage dip tests. The significance of the notations is: P_n—nominal power of induction motor (P_n = 1.5 kW); P_d—active power corresponding to t_d duration of voltage dip;

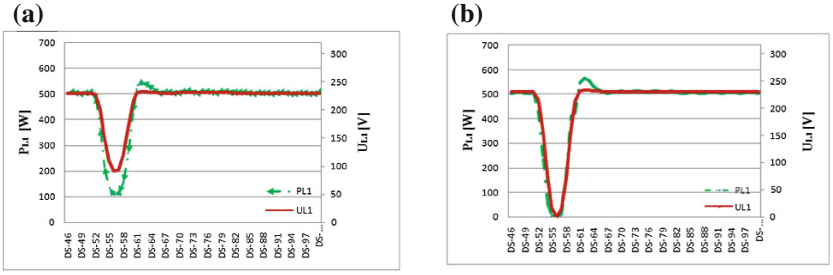

Fig. 8 The shape forms of RMS current and voltage gradual dip GR3 with dip time 1.5 seconds and the magnitudes of voltage dips: **a** 92 V (40 %); **b** 0 V (0 %)

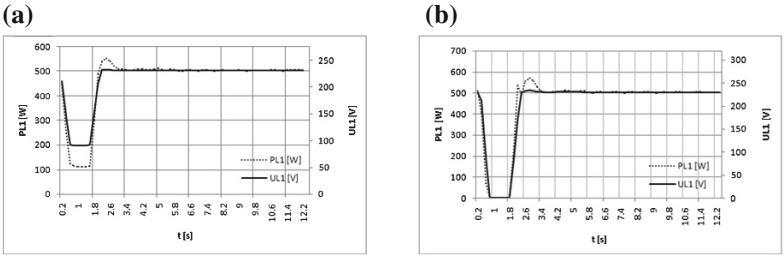

Fig. 9 Comparison between the shape of RMS abrupt voltage dip curve and active power on the phase L1 of the motor, in AB3 test—three phase voltage dip with dip time of 1.5 s and magnitude: **a** 92 V (40 %); **b** 0 V (0 %)

Table 2 Minimum current and power in GR3 and AB3 tests

U_d (%)	Gradual voltage dip GR3 test					Abrupt voltage dip AB3 test				
	I_{min} (A)	P_d (W)	P_d/P_n (%)	$P_{d\text{-}rec}$ (W)	$P_{d\text{-}rec}/P_n$ (%)	I_{min} (A)	P_d (W)	P_d/P_n (%)	$P_{d\text{-}rec}$ (W)	$P_{d\text{-}rec}/P_n$ (%)
0	2.6	603.4	39.7	1403.8	92.3	2.0	418.2	27.9	1,266	84.3
20	2.8	687.3	45.2	1415.5	93.1	2.4	623.7	41.4	1479.9	87.6
40	3.0	787.8	51.8	1430.9	94.1	2.7	671.7	44.7	1329.3	88.5
70	3.6	932.1	61.3	1474.0	96.9	3.3	928.2	61.8	1380.3	91.8
80	3.8	1033.8	68.0	1492.3	98.1	3.6	1072.2	68.4	1411.68	93.9
90	4.0	1184.3	77.9	1514.29	99.62	3.9	1176	78.3	1,464	97.5

$P_{d\text{-}rec}$—active power corresponding to total duration of voltage dip, including the time of recovery for the current; I_{min}–RMS minimum current corresponding to minimum voltage dip.

Power consumption during voltage dip test characterizes the induction motor dynamics: a high induction motor power results in a small variation of torque and speed. Taking into account only the power consumption during the duration of the voltage dip can induce erroneous interpretations of the effect of voltage dip on induction motor.

The active power consumption by the induction motor during the abrupt dip is lower than in the case of gradual dip. This corresponds with smaller values of the torque and speed of motor.

5 Conclusions

This paper analyzes the voltage dip characteristics, the procedure for determining the sensitivity of various types of electrical equipment to the voltage dips, and as case study, the sensitivity of the induction motor to the balanced three-phase

voltage dips is determined and analyzed. A test bench was used which allows to generate the voltage dips with various magnitudes, dip duration, abrupt and gradual shape, of type individual or repetitive, and supplying the induction motors of power between 0.5–30 kW. An abrupt shape of the dip determines a value of current lower than in the case of a gradual dip. For an abrupt dip, the time of current recovery is longer than for the gradual dip. The registered curves of current and power show the displacement of minimum values of RMS current, in correlation with the magnitude of voltage dip. New investigations will be done for non-balanced three-phase voltage dips.

Acknowledgments This paper is supported by the Sectoral Operational Programme Human Resources Development (SOP HRD), ID134378 financed from the European Social Fund and by the Romanian Government.

References

1. Meyar-Naimi, H., & Vaez-Zadeh, S. (2012). Sustainable development based energy policy making frameworks—a critical review. *Energy Policy, 43*, 351–361.
2. Katiraei, F., Iravani, M. R., & Lehn, P. W. (2005). Micro-grid autonomous operation during and subsequent to islanding process. *IEEE Transactions on Power Delivery, 20*(1), 248–257.
3. Moslehi, K., & Kumar, R. (2010). A reliability perspective of the smart grid. *IEEE Transactions on Smart Grid, 1*(1), 57–64.
4. Camilo, L., Cebrian, J. C., Kagan, N., & Matsuo, N. M. (2005, June) Impact of distributed generation units on the sensivity of customers to voltage sags. In *CIRED-18th International Conference on Electricity Distribution Turin*, pp. 1–5.
5. Bollen, M. H. J. (2003). Voltage recovery after unbalanced and balanced voltage dips in three-phase systems. *IEEE Transactions on Power Delivery, 18*(4), 1376–1381.
6. Zhang, L., & Bollen, M. H. J. (2000). Characteristics of voltage dips (sags) in power systems. *IEEE Transactions on Power Delivery, 15*(2), 827–832.
7. Wang, J., Chen, S., & Lie, T. T. (2005). System voltage sag performance estimation. *IEEE Transactions on Power Delivery, 20*(2), 1738–1747.
8. Won, D.-J., Ahn, S.-J., & Moon, S.-I. (2005). A modified sag characterization using voltage tolerance curve for power quality diagnosis. *IEEE Transactions on Power Delivery, 20*(4), 2638–2643.
9. Vatra, F., Postolache, P., & Poida, A. (2013) *Quality of electrical energy* (in Romanian) (Vol. 1, Chap. 4, pp. 157–288). Bucharest: Ed. SIER.
10. Bollen, M. H. J. (1997). Characterization of voltage sag experienced by three-phase adjustable-speed drives. *IEEE Transactions on Power Delivery, 12*(4), 1666–1671.
11. Costa, F., & Driesen, J. (2013). Assessment of voltage sag indices based on scaling and wavelet coefficient energy analysis. *IEEE Transaction On Power Delivery, 28*(1), 336–346.
12. Kanokbannakorn, W., Saengsuwan, T., & Sirisukprasert, S. (2011). The modeling of ac magnetic contactor for immunity studies and voltage sag assessment. In *The 8th Electrical Engineeringl Electronics, Computer, Telecommunications and Information Technology (ECTI) Association of Thailand—Conference 2011*, pp. 621–624.
13. Török, L., & Munk-Nielsen, S. (2012, May). Effect of voltage sags on digitally controlled line connected switched-mode power supplies. In *Proceedings of the 13th International Conference on Optimization of Electrical and Electronic Equipment-OPTIM2012*, ISSN 1842-0133, pp. 770–775.

14. Chilukuri, M. V., Lee, M. Y., & Phang, Y. Y. (2009, June 8–11). Voltage sag sensitivity of home appliances and office equipment. In *Proceedings of the 20th International Conference on Electricity Distribution, Prague*, pp. 1–6.
15. Hosseinian, H., Askarian Abyaneh, H., Shahnia, F., Hatami, H., & Galvani S. (2008, July 6–10). Induction motor behavior at sudden interruptions and voltage sag. In *The International Conference on Electrical Engineering, Okinawa, Japan*, pp. 1–6.
16. Bollen, M. H. J. (1995). The influence of motor reacceleration on voltage sags. *IEEE Transactions on Industry Applications, 31*(4), 667–674.
17. Ojaghi, M., Faiz, J., Shahrouzi, H., & Alimohammadi, S. (2012). Induction motors performance study under various voltage sags using simulation. *Journal of International Conference on Electrical Machines and Systems, 1*(3), 295–302.
18. Golovanov, N., & Lăzăroiu, G. C. (2006). Effects of symmetrical and unsymmetrical sags on induction motors. *U.P.B. Science Bulletin, Series C*, *68*(2), 63–78.
19. Guasch, L., Corcoles, F., & Pedra, J. (2004). Effects of symmetrical and unsymmetrical voltage sags on induction machines. *IEEE Transactions on Power Delivery, 19*(2), 774–782.
20. Pérez, J. J., Cortés, C. A., & Gómez, Á. (2007, October) A study of voltage sags in electric motors. Development of a sag generator. In *The 9th International Conference Electrical Power Quality and Utilization, Barcelona*, pp. 1–4.
21. Helerea, E., Ciobanu, A., & Lepadat, I. (2013, October 11–13) Impact of three-phase voltage dips on the induction motors—an experimental study. In *The 4th International Symposium on Electrical and Electronics Engineering*, Galati, IEEE Catalog Number CFP1393 K-USB. doi: 10.1109/ISEEE.2013.6674381, pp. 1–6.

Effect of the Neutral Interruption on the Unbalanced Three-Single-Phase Consumers

Ionel Lepadat, Elena Helerea, Sorin Abagiu and Daniel Călin

Abstract Phenomena usually associated with neutral conductor interruption are sensitive issues of low voltage electrical networks. These phenomena are now directly related to the power quality, especially in the case of three-phase unbalanced consumers supplied with low balanced/unbalanced three-phase system of voltages. Therefore a detailed analyzes for assessment of the impact of interruption of neutral on the electrical networks and consumers are required. The paper deals with an analytical description of the neutral conductor interruption effect on the unbalanced three single-phase consumers. The simulations for three cases are considered: low voltage supply system with four conductors in normal conditions of operation; the case when the neutral conductor is interrupted in the substation area; the case when the neutral conductor is interrupted in the lines area. It is shown that the neutral displacement voltages and neutral currents depend on the type of fault and on the severity of the three-phase consumer unbalance. The results are useful for appropriate designing of the protection system.

Keywords Unbalance · Low voltage electric network · Three single-phase consumers · Neutral interruption · Simulations

1 Introduction

In the power supply systems of consumers the main protection measure against indirect touching is the linking to neutral and to earth. But, the protection system does not fulfill its function in the case of the unbalanced and nonlinear three-phase consumers.

The presence of deforming and unbalance regimes in low voltages networks has as effects the non-zero neutral voltage displacement and overvoltage on the phases

I. Lepadat · E. Helerea (✉) · S. Abagiu · D. Călin
Transilvania University of Brasov, Brasov, Romania
e-mail: helerea@unitbv.ro

I. Visa (ed.), *Sustainable Energy in the Built Environment - Steps Towards nZEB*,
Springer Proceedings in Energy, DOI 10.1007/978-3-319-09707-7_32

and neutral conductor. The effect is amplified when an accidental interruption of neutral conductor is produced. All of these can cause damages and injuries by touching the equipment masses under voltages [1].

The current researches are done in particular to assess the consequences of the unbalanced regime on the operation of consumers and on the power networks [1–4]. In the low voltage networks with four wires, over voltages caused by interruption of neutral conductor have major effects on the consumers supplying. To prevent these effects, new knowledge of the phenomena which take place should be developed. There are papers, as [4–6], in which the disturbance effects of harmonics and unbalance regarding the neutral conductor loading are analyzed, but there are few papers that study the phenomena associated with accidental interruption of neutral conductor [7–10]. A simplified case of the linear unbalanced three-phase consumer supplied by balanced and sinusoidal three phase voltages is analyzed in [10], where a software application in the LabVIEW 8.1 environment was developed for rapidly calculating the unbalance regime specific indicators.

In this paper there is developed a model able to describe the effect of different types of interruptions of the neutral conductor on the linear unbalanced three single-phase consumer supplied by the low voltage power network with four wires. The model put in evidence the effects when interruptions occur in different locations of the neutral.

2 Three-Phase Network Unbalance in Power Quality Indicator

In three-phase power systems the generated voltages are sinusoidal, with equal magnitude and equal phase angle deviation of 120^{o}. A main cause of voltage unbalance in electrical networks is the uneven distribution of the single-phase load, which usually continuously changes across the three-phase networks. It is the cases of long rural distribution lines, the lighting loads, single-phase traction systems [3].

The effects of the unbalance upon electric equipment of power system are: heating, isolation deterioration, abnormal operation, unwanted driving of the protections. These effects vary in the case of the balanced or unbalanced three-phase consumers, depending on the connection type of transformers (star with working null, star without working null, delta). The current unbalance mainly effects are the supplementary losses, with negative consequences on the energy transfer efficiency.

In order to characterize the unbalance, specific parameters have been introduced by IEC and NEMA. Based on symmetrical component method new unbalance indicators have been defined by the standard IEC 61000-4-30:2003, which take in account the rms values of line/phase voltages and currents, and also the phase angles.

The voltage negative unbalance factor K_{U2} is the ratio between U_2 negative-sequence voltage and U_1 positive sequence voltages [4]:

$$K_{U2} = \frac{U_2}{U_1} \cdot 100\,[\%] \tag{1}$$

Similarly, the current negative unbalance factor K_{I2} is the ratio between I_2 negative-sequence current and I_1 positive-sequence current:

$$K_{I2} = \frac{I_2}{I_1} \cdot 100\,[\%]. \tag{2}$$

The negative-sequence voltage U_2 and current I_2, the positive-sequence voltage U_1 and current I_1, the zero-sequence voltage U_0 and current I_0 are calculated with the symmetrical components method, knowing the rms phase voltages U_{L1}, U_{L2}, U_{L3}, the rms phase currents I_{L1}, I_{L2}, I_{L3} and phase angles. φ_{L1L2}, φ_{L2L3}, φ_{L3L1}. It is worth mentioning that with the zero-sequence component of the current I_0, the value of the current in neutral conductor is obtained, with the relation:

$$I_N = 3 \cdot I_0 \tag{3}$$

According to IEC 61000-4-30:2003, specific compatibility levels are adopted for the low-voltage (LV), medium voltage (MV) and high voltage (HV) networks, shown in Table 1.

The calculations for obtaining the unbalance parameters are laborious. The computation software developed in the LabVIEW environment [10] allows the calculation of the unbalance regime parameters, based on the symmetrical components method.

3 Model of Neutral Interruption in Unbalanced Consumer

It is considered a system of three single-phase consumers, supplied from an electric substation through a long overhead or underground line (LEA/LES). The consumer is linear, unbalanced, with inductive character, supplied by a symmetrical sinusoidal three-phase voltage system with four wires.

The protection scheme is of type TN, in which the neutral of source is connected to the earth and the masses of equipment are connected to the neutral conductor (PEN). This scheme provides guiding the fault current on an imposed current path in order to act the maximal current protection device to isolate the damaged area. The analysis consists on the determination of the voltages and currents in this system when the interruption of neutral is produced in different locations.

Three cases are analyzed:

Case 1—the neutral conductor is not interrupted;

Case 2—the neutral conductor is interrupted in the substation area (Fig. 1, A fault);

Table 1 Voltage negative unbalance factor levels

Voltage level	LV	MV	HV
K_{2U} [%] IEC 61000-4-30	≤2	≤2	≤1

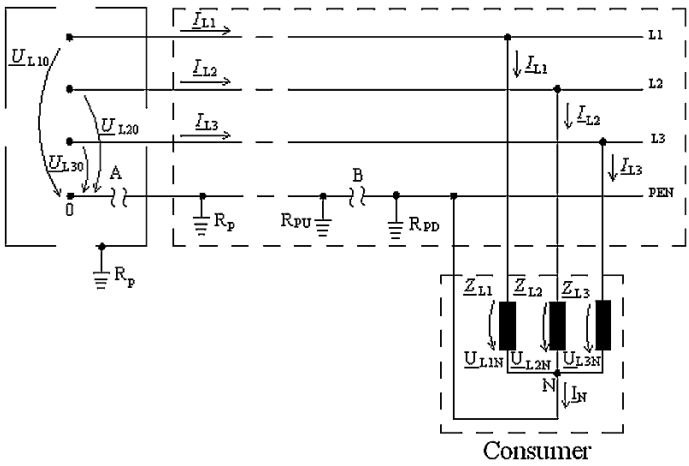

Fig. 1 Electric scheme of the low voltage supply system of a three single-phase consumer in abnormal operation: A fault—the neutral conductor interrupted in the substation area; B fault—the neutral conductor interrupted in the LEA/LES area

Case 3—the neutral conductor is interrupted in the LEA/LES area (Fig. 1, B fault).

A. **The case of the three-phase consumer in normal operation**

The phase voltages and phase currents relative to the consumer are obtained by calculus, knowing the power network and the consumer parameters:

- equivalent impedances consisting of the consumer impedance and electric line impedance on each phase $\underline{Z}_{eL1}, \underline{Z}_{eL2}, \underline{Z}_{eL3}$, respectively, equivalent admittances $\underline{Y}_{eL1}, \underline{Y}_{eL2}, \underline{Y}_{eL3}$;
- impedance of neutral $\underline{Z}_N$, respectively, admittance $\underline{Y}_N$;
- phase voltages of supply system $\underline{U}_{L10}, \underline{U}_{L20}, \underline{U}_{L30}$.

In the case when the neutral conductor is not interrupted, the following quantities are calculated:

- the voltage displacement between the consumer neutral point N and the power system neutral point 0:

$$\underline{U}_{N0} = \frac{\underline{Y}_{eL1} \cdot \underline{U}_{L10} + \underline{Y}_{eL2} \cdot \underline{U}_{L20} + \underline{Y}_{eL3} \cdot \underline{U}_{L30}}{\underline{Y}_{eL1} + \underline{Y}_{eL2} + \underline{Y}_{eL3} + \underline{Y}_{eN}} \tag{4}$$

- the line currents:

$$\begin{aligned} \underline{I}_{L1} &= \underline{Y}_{eL1} \cdot (\underline{U}_{L10} - \underline{U}_{N0}) \\ \underline{I}_{L2} &= \underline{Y}_{eL2} \cdot (\underline{U}_{L20} - \underline{U}_{N0}) \\ \underline{I}_{L3} &= \underline{Y}_{eL3} \cdot (\underline{U}_{L30} - \underline{U}_{N0}) \end{aligned} \tag{5}$$

- the phase voltages at the terminals of consumer:

$$\begin{aligned} \underline{U}_{L1N} &= \underline{Z}_{L1} \cdot \underline{I}_{L1} \\ \underline{U}_{L2N} &= \underline{Z}_{L2} \cdot \underline{I}_{L2} \\ \underline{U}_{L3N} &= \underline{Z}_{L3} \cdot \underline{I}_{L3} \end{aligned} \tag{6}$$

- the neutral current:

$$\underline{I}_{N} = \underline{Y}_{N} \cdot \underline{U}_{N0} \tag{7}$$

Particular cases:

– For balanced case balanced case when equivalent impedances are equal ($\underline{Z}_{eL1} = \underline{Z}_{eL2} = \underline{Z}_{eL3}$), the relation (4) is simplified:

$$\underline{U}_{N0} = \frac{\underline{Y}_{eL1} \cdot (\underline{U}_{L10} + \underline{U}_{L20} + \underline{U}_{L30})}{3 \cdot \underline{Y}_{eL1} + \underline{Y}_{N}} = 0 \tag{8}$$

Only in the case of the balanced, three-phase, linear consumers, the sum of the phase currents at any instant of time is zero, and so there is no neutral current.

– For unbalance case, when two equivalent impedances are equal ($\underline{Z}_{eL1} \neq \underline{Z}_{eL2} = \underline{Z}_{eL3}$), the neutral displacement voltage relation (4) becomes:

$$\underline{U}_{N0} = \frac{\underline{U}_{L10} \cdot (\underline{Y}_{eL1} - \underline{Y}_{eL2})}{\underline{Y}_{eL1} + 2\underline{Y}_{eL2} + \underline{Y}_{N}} \tag{9}$$

The unbalance coefficients for voltage and current are calculated with relations (1), respectively (2).

B. **Case of neutral conductor interrupted in the substation area**

In the case of A fault (Fig. 1), the power network has an abnormal operating mode because the conductor is interrupted on the transformer power station, and consumer phases are connected between neutral conductor (separate from the neutral point of the transformer) and the phase conductors. In this case the neutral current is canceled.

The neutral displacement voltage and phase voltages at the consumer terminals are calculated with the relations (3) and (4).

C. **Case of neutral conductor interrupted in the LEA/LES**

In the case of B fault (Fig. 1), the neutral conductor is interrupted between power supply and neutral of consumer. The neutral current circuit is closed between two earth electrodes, downstream and upstream of the point of interruption, through the dispersion earth resistances which have the same values ($R_{\mathrm{pu}} = R_{\mathrm{pd}}$). For the neutral current calculation the line impedance should be considered, and the distance between the earth electrode downstream l_{Ld} and upstream l_{Lu} of the point of interruption should be known.

The voltage $\underline{U}_{\mathrm{N0}}$ between the neutral point of consumer N and the neutral point of the voltage supply system 0 will be:

$$\underline{U}_{N0} = \frac{\underline{Y}_{eL1} \cdot \underline{U}_{L10} + \underline{Y}_{eL2} \cdot \underline{U}_{L20} + \underline{Y}_{eL3} \cdot \underline{U}_{L30}}{\underline{Y}_{eL1} + \underline{Y}_{eL2} + \underline{Y}_{eL3} + \underline{Y}_{Neud}} \tag{10}$$

where $\underline{Y}_{Neud}$ is equivalent admittance of neutral conductor:

$$\underline{Y}_{Neud} = \frac{1}{\underline{Z}_{Neud}} \tag{11}$$

where $\underline{Z}_{Neud}$ is equivalent impedance, consisting of the impedance from downstream $\underline{Z}_{Neu}$ and upstream $\underline{Z}_{Ned}$ of the interruption point.

$$\underline{Z}_{Neud} = \underline{Z}_{Neu} + \underline{Z}_{Ned} \tag{12}$$

The equivalent impedances from upstream and downstream are:

$$\begin{aligned} \underline{Z}_{Neu} &= (r_N + j \cdot x_N) \cdot l_{Lu}; \\ \underline{Z}_{Nd} &= (r_N + j \cdot x_N) \cdot l_{Ld} \\ \underline{Z}_{Ned} &= \underline{Z}_{Nd} + R_{pd} \end{aligned} \tag{13}$$

where r_N and x_N are the specific resistance and, respectively, inductive reactance of the electric line; $\underline{Z}_{Nd}$ is the impedance of electric line downstream and R_{pd} is the resistance from downstream.

All the calculations are done using MathCAD, and the results are presented as follows.

4 Results and Discussions

The following values of parameters are considered, the same as in paper [10]:

- Line inductivity $L_{L1} = L_{L2} = L_{L3} = L_N = 6\,\text{mH}$ and line resistance $R_{LL1} = R_{LL2} = R_{LL3} = R_N = 0.5\,\Omega$;
- Consumer character is inductive, which for balanced regime has the values of phase impedances: $Z_{L1} = Z_{L2} = Z_{L3} = 10\,\Omega$;
- Three phase voltage supply system is balanced: $U_{L10} = U_{L20} = U_{L30} = 230\,\text{V}$, with mains frequency 50 Hz;
- Dispersion earth resistance of earth electrode is $R_p = 4\,\Omega$.

A. The case of the three-phase consumer in normal operation

For simulations, first in the case of balanced load is considered ($Z_{L1} = Z_{L2} = Z_{L3} = Z_N = 10\,\Omega$) and, then, the cases when the consumer impedance on the phase L1 (Z_{L1}) takes different values.

In Table 2 the results of calculations are done for phase voltages at the terminal of consumer, neutral displacement voltage, voltage unbalance coefficient, and, also for phase currents, neutral current, and current unbalance coefficient. In Fig. 2a and b the dependences of relative values of phase voltages at the terminals of consumer and consumer phase currents are shown in function of relative value of line L1 impedance ($Z_{L1\,ur} = Z_{L1}/Z_0$).

Some observations could be done regarding the displacement voltage and current intensity in the case of consumer operating in unbalance regime.

- The neutral displacement voltage U_{N0} drastically increases when the value of L1 impedance, comparative with L2 and L3 impedances, decreases, corresponding to the increasing the unbalance regime;

Table 2 Results of simulations in the case of balanced/unbalanced consumer without fault, in relative units

Z_{L1} ur	U_{L1N} ur	U_{L2N} ur	U_{L3N} ur	U_{N0} ur	K_{U} [%]	I_{L1} ur	I_{L2} ur	I_{L3} ur	I_{N} ur	K_{I} %
1	1	1	1	0	0	1	1	1	0	0
0.50	1.00	1.00	1.00	0.0000	0.01	2	1	1	1	1.25
0.33	1.00	1.00	1.00	0.0008	0.01	3	1	1	2	2.00
0.25	0.99	1.00	1.00	0.0014	0.02	4	1	1	3	2.50
0.20	0.99	1.00	1.00	0.0022	0.02	4	1	1	3	2.50
0.17	0.99	1.00	1.00	0.0022	0.03	6	1	1	5	3.12
0.14	0.99	1.00	1.00	0.0035	0.03	7	1	1	6	3.33

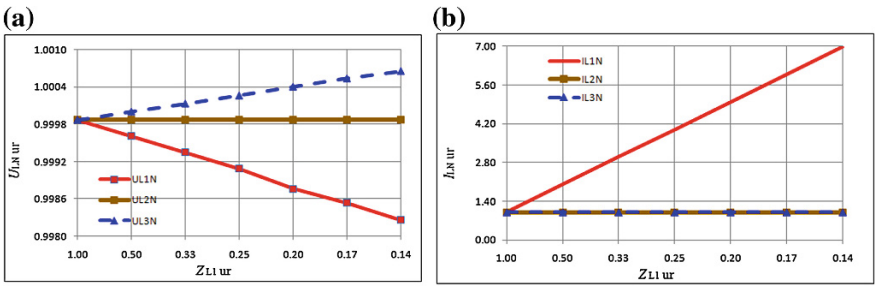

Fig. 2 Effect of variation of phase L1 impedance on the phase voltages at the terminals of consumer (**a**) and on the consumer phase currents (**b**) in the case of non-interruption of neutral conductor

- With increasing the unbalance regime the phase voltage corresponding to the small phase impedance (in this case L1 impedance) not significant decreases, while the phase voltages on the phases L2 and L3, where the values of impedances are higher and constant $(Z_{L1} \neq Z_{L2} = Z_{L3})$, increase;
- With increasing the unbalance regime the neutral current drastically increases;
- The values of phase current increase, the higher value having the phase current on the phase L1.

B. Case of neutral conductor interrupted in the substation area

In Table 3 the results of calculation are done for the case of A fault (Fig. 1). In Fig. 3a, b the dependences of relative values of phase voltages at the terminals of consumer and consumer phase currents are shown in function of relative value of line L1 impedance for A type fault.

Remarks:

- When the neutral conductor is interrupted in substation area the neutral displacement voltage U_{N0} drastically increases, when the value of L1 impedance comparative with L2 and L3 impedance decreases, corresponding to the increasing the unbalance regime;
- With increasing the unbalance regime the phase voltage corresponding to the small phase impedance (in this case L1 impedance) decreases, while the phase voltages on the phases L2 and L3 where the values of impedances are higher and constant $(Z_{L1} \neq Z_{L2} = Z_{L3})$ increase;
- The neutral conductor is interrupted in substation area. the neutral current is cancelled and the values of phase current increase, the higher values having the L1 phase current.

Table 3 Results of simulations in the case of balanced/unbalanced consumer with fault A type fault, in relative units

Z_{L1} ur	U_{L1} ur	U_{L2} ur	U_{L3} ur	U_{N0} ur	K_U [%]	I_{L1} ur	I_{L2} ur	I_{L3} ur	I_N ur	K_I %
1	1	1	1	0.00	0	1.00	1.00	1.00	0	0
0.50	0.75	1.14	1.14	1.15	0	1.50	1.14	1.14	0	20
0.33	0.60	1.24	1.24	1.84	0.01	1.80	1.24	1.24	0	28.5
0.25	0.500	1.32	1.32	2.29	0.01	2.00	1.32	1.32	0	33.3
0.20	0.42	1.37	1.37	2.62	0.01	2.14	1.37	1.37	0	36.3
0.17	0.37	1.41	1.41	2.87	0.01	2.25	1.42	1.42	0	38.4
0.14	0.33	1.45	1.45	3.06	0.01	2.33	1.45	1.45	0	39.9

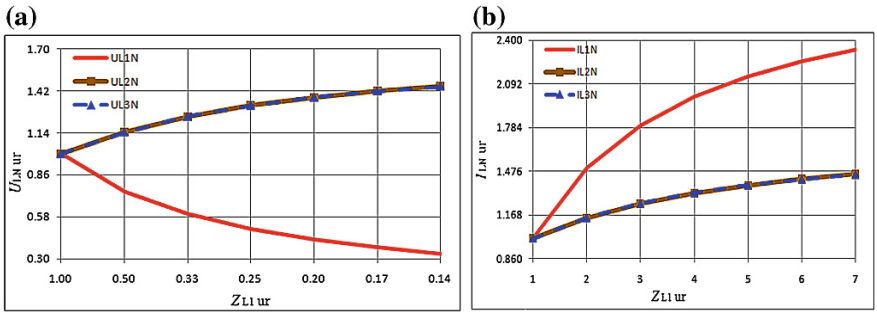

Fig. 3 Effect of variation of phase L1 impedance on the phase voltages at the terminals of consumer (**a**) and on the consumer phase currents (**b**) in the case of neutral interruption to in the substation area (A type fault)

C. Case of neutral conductor interrupted in the LEA/LES area

This case corresponds to the type B fault (Fig. 1), when the neutral current is closed through the dispersion earth resistance of the earth electrode upstream and downstream of the interruption point ($R_{pu} = R_{pd} = 4\ \Omega$). For simulations, first the case of balanced load is considered ($Z_{L1} = Z_{L2} = Z_{L3} = Z_{L0} = 10.43\,\Omega$) and then the cases when the impedance of the line L1 (R_{L1}) take different values.

In Table 4 the results of calculation are done for the case of B fault (Fig. 1). In Fig. 4a, b the dependences of relative values of phase voltages at the terminals of consumer and consumer phase currents are shown in function of relative value of line L1 impedance for B type fault.

In the case of the interruption of neutral conductor in the LEA/LES area, the values of neutral dispersion voltage, the phase voltages at the terminal of consumer and the phase voltages are influenced by the value of earth dispersion resistance of the upstream and downstream of the point in which the fault is produced.

Table 4 Results of simulations in the case of balanced/unbalanced consumer with fault B type fault, in relative units

Z_{L1} ur	U_{L1N} ur	U_{L2N} ur	U_{L3N} ur	U_{N0} ur	K_U [%]	I_{L1} ur	I_{LN} ur	I_{LN} ur	I_N ur	K_I %
1	1	1	1	0	0	1	1	1	0	0
0.50	0.84	1.06	1.11	0.73	0.00	1.68	1.06	1.11	0.39	21.97
0.33	0.73	1.12	1.19	1.26	0.01	2.19	1.12	1.19	0.69	32.76
0.25	0.64	1.17	1.26	1.67	0.01	2.57	1.18	1.26	0.91	39.16
0.20	0.57	1.22	1.31	1.99	0.01	2.87	1.22	1.31	1.08	43.40
0.17	0.51	1.27	1.35	2.25	0.01	3.11	1.27	1.35	1.22	46.42
0.14	0.47	1.30	1.38	2.46	0.01	3.30	1.30	1.38	1.33	48.68

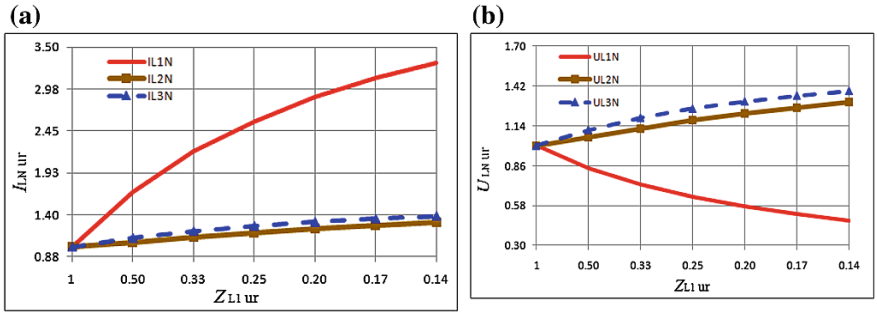

Fig. 4 Effect of variation of phase L1 impedance on the phase voltages at the terminals of consumer (**a**) and on the consumer phase currents (**b**) in the case of neutral interruption to in the substation area (B type fault)

5 Conclusions

In this paper an analytical model is developed and simulations are done to put in evidence the effect of interruption of neutral conductor on the phase voltages and currents of an unbalanced three single-phase consumer supplied with a symmetrical system of three-phase voltages.

It is demonstrated that for the case in which the neutral interruption is in the LEA/LES area, the neutral voltage displacement is higher than that of case 1 and less as that for neutral interruption in the substation area. The phase current also varies for different cases and area when the interruption occurs.

From the analysis made, it appears that further measures are necessary for protection against interruption of neutral conductor for improved security of power supply to the consumer. In the design of low-voltage power networks shall be deemed earth installations can ensure closing the neutral current at the neutral of the transformer in any situation where neutral conductor is interrupted. This ensures limited touch voltages at low values, thus avoiding electric shocks.

References

1. Sufrim, M., Stoica, I., Hristea, V., & Coroiu, N. (2000). *Modern tools for protection against accidental voltages in low voltages electrical installations (in Romanian), ISBN 973-96696-9-7*. Oradea: Ofset.
2. Kim, J. G., Lee, E.W., Lee, D. J., & Lee, J. H. (2005). Comparison of voltage unbalance factor by line and phase voltage, electrical machines and systems, ICEMS 2005. In *Proceedings of the 18 International Conference on Electrical Machines and Systems*, pp. 1998–2001.
3. Olczykowski, Z., & Wasowski, A. (2006). Methods of voltage unbalance estimation in electric power networks. *Electric Power Quality and Utilization Journal, XII*(2), 71–76.
4. Lepădat, I., Mihai, C., & Helerea, E. (2012). Considerations on the Unbalance Regime of the Three-Phase Consumers. In *Proceedings of the 13th International Conference on Optimization of Electrical and Electronic Equipment*, pp. 151–156.
5. Desmet, J. M., Sweertvaegher, I., Vanalme, G., Stockman, K., & Belmans, R. J. M. (2003). Analysis of the neutral conductor current in a three-phase supplied network with nonlinear single-phase loads. *IEEE Transactions on Industry Applications, 39*(3), 587–593.
6. Batrinu, F., Chicco, G., Ciortea, A. O., Porumb, R., Postolache, P., Spertino, F., et al. (2007). *Experimental evaluation of unbalance and distortion indicators in three-phase systems with neutral* (pp. 1486–1491). Lausanne: IEEE Power Tech.
7. Chicco, G., Postolache, P., & Toader, C. (2007). Analysis of three-phase systems with neutral under distorted and unbalanced conditions in the symmetrical component-based framework. *IEEE Transactions on Power Delivery, 2*(1), 674–683.
8. Levey, L. (1991). Computation of fault currents and voltages along a multigrounded neutral power line having multiple phase conductors. *IEEE Transactions on Power Delivery, 6*(4), 1541–1548.
9. Chicco, G., Postolache, P., Scutariu, M., & Toader, C. (2005). low voltage networks operational neutral interruption impact assessment. In *C I R E D 18th International Conference on Electricity Distribution, Turin*, pp. 1–6.
10. Lepădat, I., Helerea, E., & Moaşa, B. (2013). Software application for unbalanced regime analysis in three phase low voltage networks. *Pollack Periodica International Journal for Engineering and Information Sciences, 8*(2), 149–161.

Increasing the Tracking Efficiency of Photovoltaic Systems

Mircea Neagoe, Ion Visa and Bogdan Burduhos

Abstract The total amount of the electrical energy yielded by in-field photovoltaic (PV) modules can be increased by tracking, usually aiming at maximizing the incident direct solar radiation as input of the PV systems. The photovoltaic conversion efficiency is influenced by the PV cell temperature, directly correlated with the ambient temperature and the solar radiation (intensity and spectral distribution, particularly the % of IR); as results, more complex approaches of solar PV tracking can be considered, aiming at maximizing the PV output (electric energy) by optimizing the conversion efficiency based on collected global solar radiation and PV cell temperature. This paper presents a new approach for increasing the PV tracking efficiency; starting with the analysis of the tracking effect on the temperature of silicon photovoltaic modules and based on the specifics of each type of tracking, the paper comparatively discusses different tracking algorithms considering their effect on the input solar radiation. During the past 10 years, the R&D Center of Renewable Energy Systems and Recycling (RES-REC) in the Transilvania University has investigated different tracking systems and algorithms, focusing on optimized solutions tailored to the specific features of the implementation location (e.g. temperate, mountain areas like Brasov, Romania). The research infrastructure includes indoor high quality testing facilities (controlled solar radiation intensity and spectrum, and temperature as variable inputs) and in-field testing rigs (fixed tilted platforms, single-axis and dual-axis tracking systems), on-grid and off-grid connected PV systems. Based on the experimental data collected in the RES-REC Centre, recommendations are formulated on the need for accurate tracked PV system design, avoiding over- or under-estimating the output, thus allowing the implementation of feasible and efficient solutions.

Keywords Photovoltaic systems · Solar radiation · Solar tracking efficiency · Tracking algorithms

M. Neagoe (✉) · I. Visa · B. Burduhos
R&D Center of Renewable Energy Systems and Recycling (RES-REC), Transilvania University of Brasov, Eroilor 29, 500036 Brasov, Romania
e-mail: mneagoe@unitbv.ro

I. Visa (ed.), *Sustainable Energy in the Built Environment - Steps Towards nZEB*, Springer Proceedings in Energy, DOI 10.1007/978-3-319-09707-7_33

1 Introduction

The average power of an in-field fixed PV system usually gets to about 20 % of its maximal power (Watt peak), due to day/night cycles, time-of-day variations in insolation and cloud cover [1]. As results, solar tracking is one of the mostly used solution for increasing the overall output of the solar energy conversion devices [2–5]. A solar tracker is a device that keeps PV modules in an optimal position (mostly perpendicular) towards the solar radiation, during daylight hours. The non-concentrated PV tracking systems are still effective even if they don't follow the sun with high accuracy. If the sunray is off by 10°, the output power can still be 98.5 % of the power obtained during full-continuous tracking. In the worst (cloudiest and haziest) locations, the gain in annual output using trackers can be about 20 %. In sunnier areas, the typical annual gain due to tracking can be on average as high as 30–40 %, but the gain in any given day may vary from almost zero to nearly 100 % [6]. The importance of PV tracking was studied also in the application context of its final benefit ratio: for example, Bione et al. [7] showed that in case of pumping systems driven by fixed and tracked PV systems, the water benefit can be approx. 51 % greater in case of tracked systems (4.9 vs. 7.4 m^3/day).

The main goal of any tracking systems is to increase the amount of direct /beam solar radiation component collected by the PV modules [8–11]. Still, during cloudy /mixed days or in areas with changing climate conditions with significant amount of diffuse radiation (D), this approach neglects this radiation component, which is distributed isotropically [12, 13] and is maximal in the horizontal position (parallel to the ground) [14, 15].

2 Problem Formulation

The most usual purpose of tracked PV systems is increasing the direct solar radiation (B) incident on the PV module surfaces, as B represents the radiation component with the highest impact on the photovoltaic energy conversion. Such tracking systems can use either *seasonally-predefined* (based on solar ray angles modeling for the specific implementation location) or *adaptive* (instantaneously calculated) tracking programs. A predefined program needs a complex control system with time monitoring and able to store the predefined hour—solar angle values; the second type of tracking programs usually need 3 photodiodes equally lighted, to position the PVs towards the sun.

The photovoltaic conversion implies the conversion of a photons stream to electrons flow, thus it uses not only the direct solar radiation but also the diffuse and reflected components, if getting enough energy to excite the photovoltaic diode. Therefore, another type of tracking algorithms can be developed to maximize the incident global solar radiation (G), useful for climate areas where diffuse radiation has a significant contribution to the global radiation. Obviously, a tracking system

could use both types of tracking programs, but this adaptive control requires more complex systems and associated higher costs, as they involve solar radiation sensors able to determine the instantaneous variation of the direct and diffuse solar radiation components and also to compute the optimal instantaneous tracking angles.

One issue of PV tracking addresses the conditions where an output-based PV tracking algorithm becomes effective for maximizing the power output of a PV system, being known that the overall conversion efficiency of PV modules depends on current incident solar radiation and also on photovoltaic cell temperature.

Considering the standard PV module, the maximization of their output power using tracking systems can be modeled starting with the definition of the conversion efficiency:

$$P_{el} = \eta_{PV} \cdot G^*, \tag{1}$$

where P_{el} is the output electric power; G^*—the collected global solar radiation (normal incident solar radiation on the PV surface), depending on the available solar radiation and the current tracking angles (diurnal and elevation angles) of the PV module; $\eta_{PV}(mat_{PV}, T_m)$—instantaneous efficiency of the PV cell module which mainly depends on the photovoltaic material (mat_{PV}) and the PV module temperature $T_m = T_m(T_a, G^*)$, where T_a—outdoor air temperature.

According to Eq. (1) the electrical power P_{el} can be maximized using the following approaches:

(a) Maximization the received global solar radiation G^* by single- or dual-axis mechanical tracking systems; commonly, this method aims mainly at the direct B^* radiation collection without considering the tracking effects on the conversion efficiency.
(b) The η_{PV} efficiency increase during functioning, which mainly requires photovoltaic materials with increased performances (with a η_{STC} reference value experimentally determined by the PV producers in standard testing conditions, STC) and by decreasing the temperature on the photovoltaic module.
(c) The maximization through tracking of the $(\eta_{PV} \cdot G^*)$product, meaning the collection of an optimal quantity of global solar radiation, knowing that the module temperature is directly depending on the G^* parameter, $T_m = T_m(G^*)$ and it directly influences the PV module efficiency. In this case, for a given photovoltaic material, at working T_a ambient temperature, and without cooling, the optimization process can be described using Eq. (2):

$$\begin{aligned} &\max P_{el} \rightarrow \frac{dP_{el}}{dG^*} = 0, \\ &\frac{dP_{el}}{dG^*} = \frac{d[\eta_{PV}(T_m(G^*)) \cdot G^*]}{dG^*} = \frac{\partial \eta_{PV}}{\partial T_m} \cdot \frac{\partial T_m}{\partial G^*} \cdot G^* + \eta_{PV} = 0, \end{aligned} \tag{2}$$

The result of Eq. (2) allows to identify the optimum $G^*_{opt.MP}$ value: up to this value the electrical output power P_{el} increases with the global solar radiation, while for larger values of the received global solar radiation ($G^* > G^*_{opt.MP}$), P_{el} decreases due to the preponderant negative effect of the T_m temperature on the conversion efficiency η_{PV}:

$$G^*_{opt.MP} = -\frac{\eta_{PV}}{\frac{\partial \eta_{PV}}{\partial T_m} \cdot \frac{\partial T_m}{\partial G^*}} (\text{for a given air temperature } T_a). \tag{3}$$

Considering the definition of the power temperature coefficient, c_1, measured in STC [16], the conversion efficiency η_{PV} is:

$$\eta_{PV} = \eta_{STC} \cdot [1 + c_1 \cdot (T_m - T_{STC})], \tag{4}$$

and

$$T_m = T_a + c_2 \cdot G^*, \tag{5}$$

where $c_2 = (NOCT - 20)/800$, $NOCT$—normal operating cell temperature.

Replacing the parameters from Eqs. (4), (5) and their derivatives in Eq (3), the optimal collected global radiation yielding the maximum power MP is obtained:

$$G^*_{opt.MP} = -\frac{1 + c_1(T_a - T_{STC})}{2c_1c_2}, \tag{6}$$

where $\frac{\partial \eta_{PV}}{\partial T_m} = c_1 \cdot \eta_{STC}$; $\frac{\partial T_m}{\partial G^*} = c_2$.

Case study: considering the technical data of a monocrystalline Heliene HEE215 M 260 Wp PV module: c_1 = –0.44 %/°C, c_2 = 0.03125 °C m^2/W for NOCT = 45 °C (with solar radiation 800 W/m^2, outdoor air temperature 20 °C, wind speed 1 m/s), $\eta_{STC} = 15\,\%$ (STC: solar radiation 1,000 W/m^2, module temperature T_{STC} = 25 °C, air mass 1.5), based on Eq. (6), the $G^*_{opt.MP}$ variation with the ambient temperature T_a is represented in Fig. 1.

According to these results, the optimal value $G^*_{opt.MP}$ ranges between 3,700 and 3,200 W/m^2 for an usual ambient temperatures of 20, …, 50 °C. thus, when the available radiation G^* is higher than $G^*_{opt.MP}$, one has to apply inverse tracking to decrease the collected global solar radiation for achieving maximum output power.

The temperatures on the module that correspond to these $G^*_{opt.MP}$ values are high, 135, …,151 °C (larger than the admissible module temperature specified by the producers) and is associated to a significant decrease in the conversion efficiency, down to values lower than 50 % of the η_{STC}. These $G^*_{opt.MP}$values are never reached on non-concentrated PV modules installed on the Earth, where the average extra-terrestrial radiation is 1,367 W/m^2.

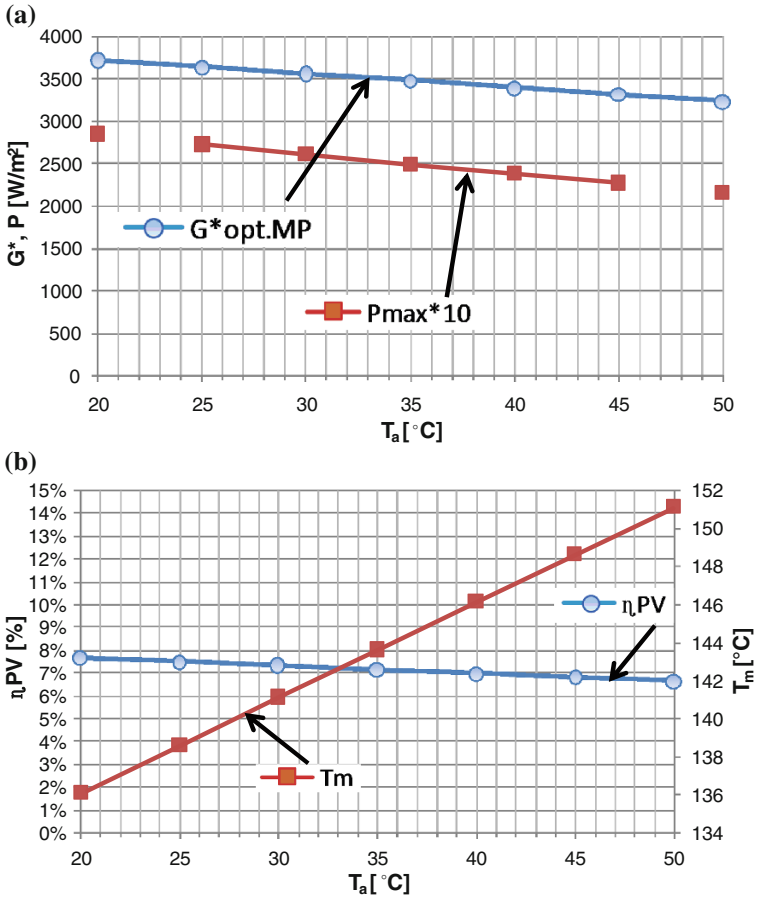

Fig. 1 Variation of the parameters of a m-Si module PV with the ambient temperature: **a** optimal global solar radiation and maximal electrical power generated; **b** conversion efficiency and module temperature

Based on this simulations, following conclusions can be formulated:

(a) Under terrestrial solar radiation conditions, the maximization of the PV output power can be obtained by maximizing the global received G^* radiation; reducing the PV module temperature can also contribute to the increase of the electrical output.

(b) Concentrated photovoltaic modules can receive a larger amount of solar radiation by using concentrating devices and accurate tracking systems, along with cell cooling systems aiming to lower the PV cell temperature. Consequently, this category of tracking systems is used exclusively for aligning the concentrated PV optical axis to the sunrays while small misalignments can drastically reduce or even cease the electrical production of the system.

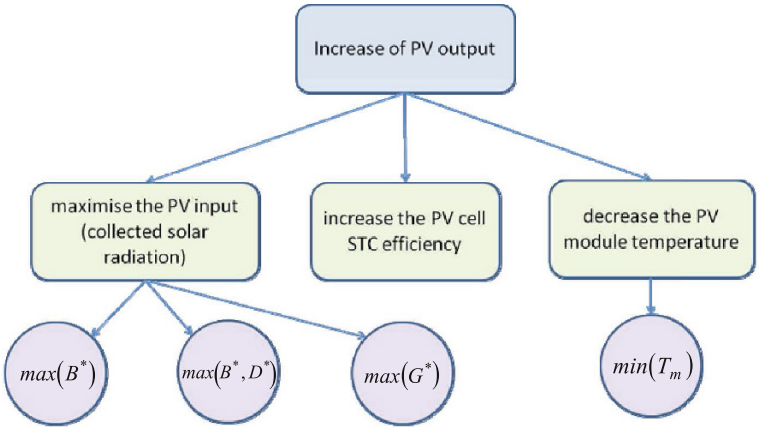

Fig. 2 Increasing the electrical output of non-concentrated photovoltaic modules

Considering these aspects, a systematization of the possible approaches for increasing the electrical output of PV modules without radiation concentration is described in Fig. 2. An obvious increase is related to the use of photovoltaic materials with high conversion efficiency; still this path is limited by the high production costs of the new generations of PV materials. Limiting the temperature of PV modules to a threshold value is another possibility, but involves the existence of high-cost active cooling systems.

The received global solar radiation maximization for non-concentrated PV modules in order to increase the electrical output was approached through optimal tilt (simple construction, insuring the reception of max. 60–80 % of the available radiation) or by using tracking systems (more complex constructive solution, but insuring a collection of more than 80–95 % of the available radiation with a single-axis tracker and over 95 % by dual-axis systems, depending also on the used tracking algorithm).

Further on, the paper outlines the relevant aspects in implementing tracking systems in a specific location: the maximization of the received solar radiation and the optimization of the motion algorithms. The solar angles and the tracker's angles are presented in the first part of the paper, followed by modeling the maximum solar global radiation and tracking algorithms, and finally a comparative analysis on the tracking efficiency of B versus G_{max} stepwise tracking algorithms is developed, using as case study the Brasov, Romania location, for three representative days: a sunny, a mixed and a cloudy day in June 2013.

3 Solar and PV Tracking Angles

Solar tracking is the usual solution for optimizing the electrical output of PV systems due to its capacity to reposition at any moment the PV modules in order to receive the maximal solar radiation with its two main components: a) direct

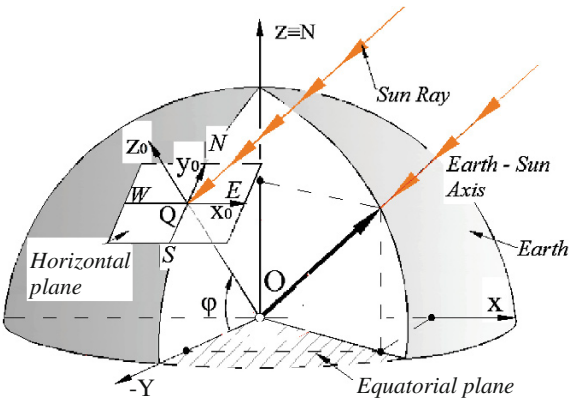

Fig. 3 Reference systems for modeling the sunray angles: global reference system OXYZ and local reference system $QX_0Y_0Z_0$ (φ—latitude of the Q origin point)

radiation (B) having the maximum on the sunray's direction and b) the diffuse radiation (D), maximal in the horizontal plane of the observer.

Generally the global solar radiation profile has B≫D and consequently the design of the solar tracking systems starts with modelling the sunray vector, considering the Q implementation location (Fig. 3) and the solar angles that can be defined in the global reference system of the Earth (OXYZ equatorial system) or in the local observer system ($QX_0Y_0Z_0$) [17]. Thus, angle pairs of azimuth-altitude type (ψ, α) can be defined in the local observer system (Fig. 4a) and the tracking systems associated to them (Fig. 4b, c, d). Similar to the solar angles, each type of tracking system has associated an angle-pair which defines the orientation of the normal vector to the photovoltaic plane, denoted (ψ^*, α^*).

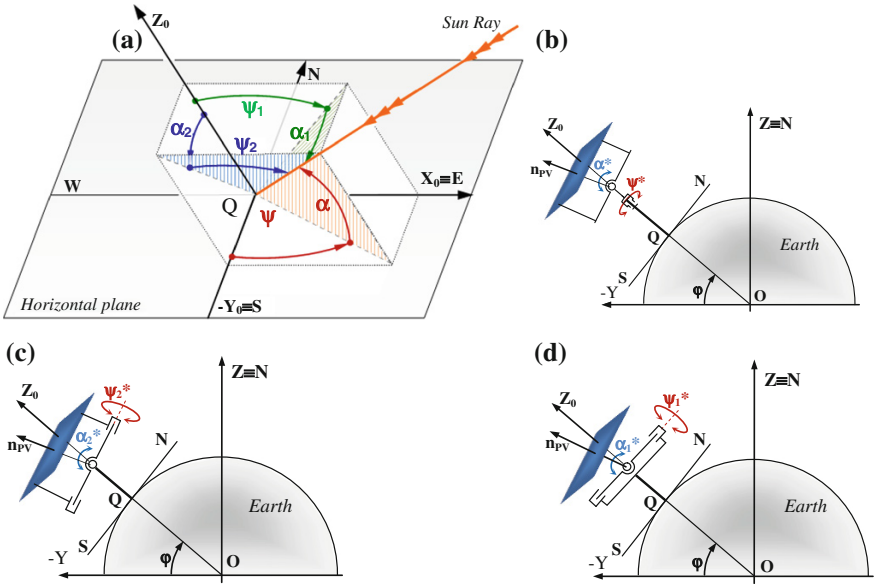

Fig. 4 **a** Azimuth-altitude solar angles and the associated dual-axis tracking systems: **b** (ψ^*, α^*), **c** (ψ_2^*, α_2^*); **d** (ψ_1^*, α_1^*)

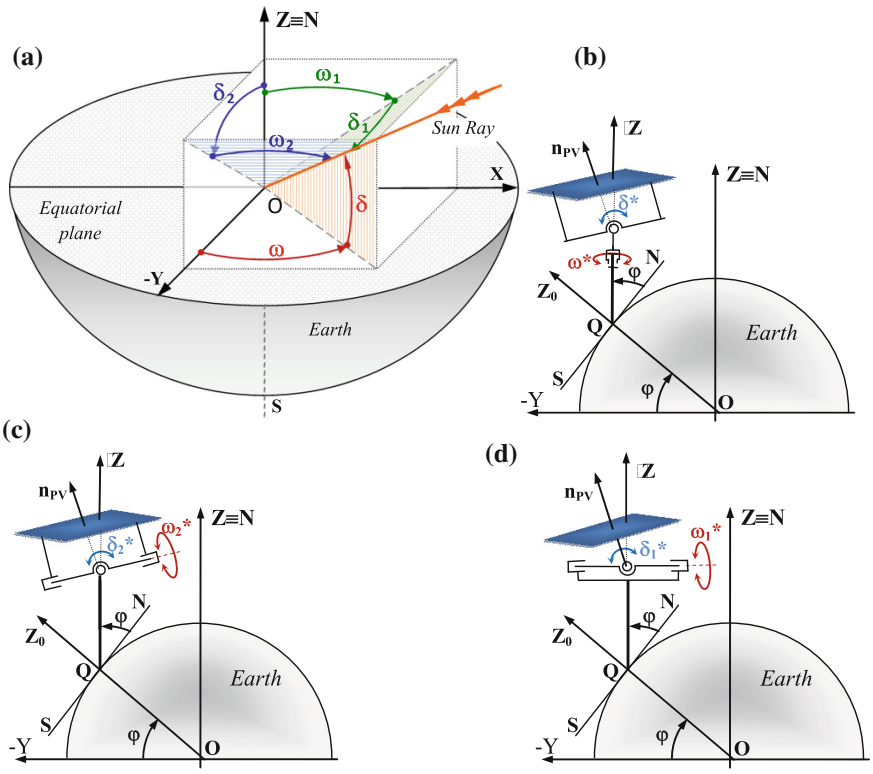

Fig. 5 **a** Hour-declination solar angles and the associated dual-axis tracking systems: **b** (ω^*, δ^*), **c** (ω_2^*, δ_2^*); **d** (ω_1^*, δ_1^*)

Similarly, the solar angles in the equatorial system and their associated tracking systems are presented in Fig. 5.

Six types of dual-axis tracking systems can be thus defined (Figs. 4 and 5), out of which five are distinct solutions: the systems from Figs. 4d and 5d are similar, both having the fixed axes parallel to the X axis ($OX \| QX_0$). As examples, Fig. 6 shows several tracking systems designed and implemented in the RES-REC Center of the Transilvania University of Brasov [18, 19], which correspond to the general schemes presented in Figs. 4b, c, d and 5b.

4 Maximal Global Solar Radiation

As already stated, the global solar radiation G is composed of two main components (B and D) having their maxima on different directions (Fig. 7). As being statistically distributed, the received *diffuse* radiation is maximal if the PV module is

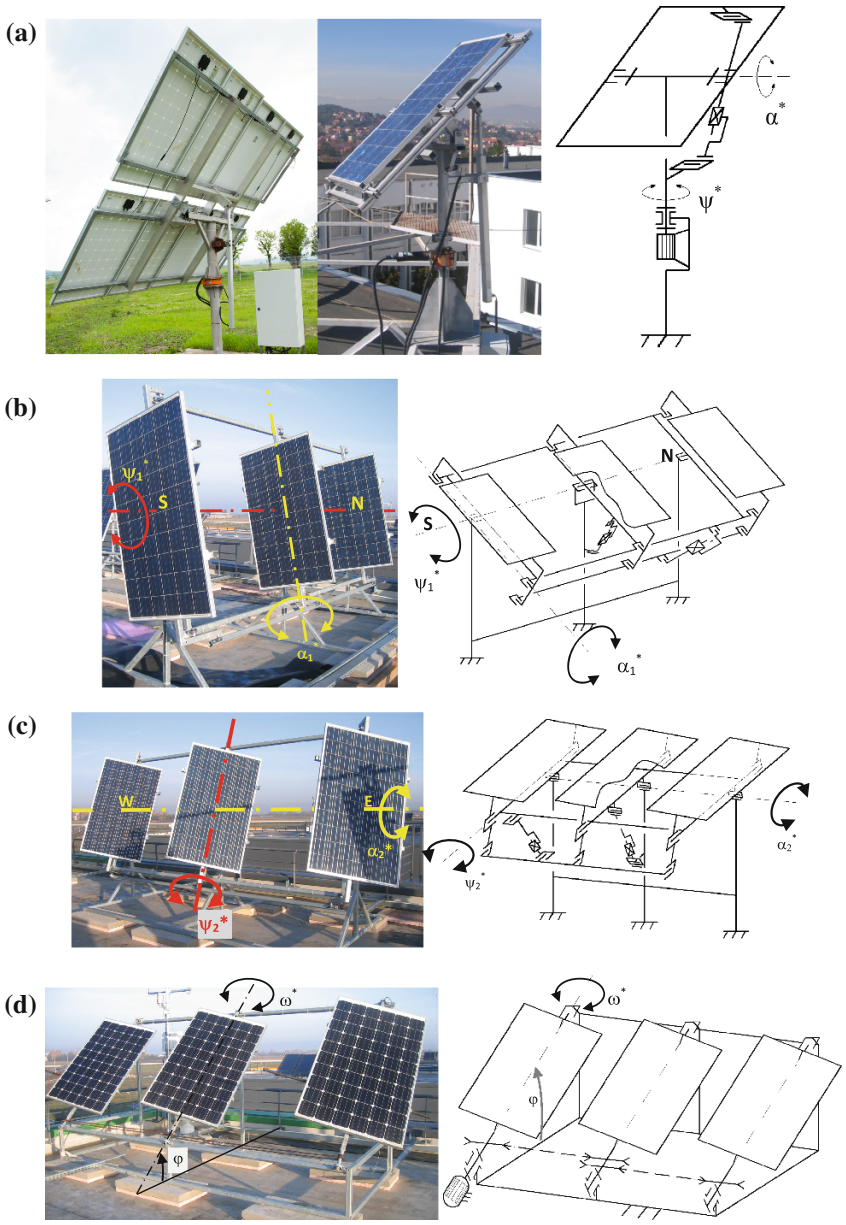

Fig. 6 Experimental rigs of: **a**, **b**, **c** azimuth-altitude type; **d** equatorial type with fixed elevation angle

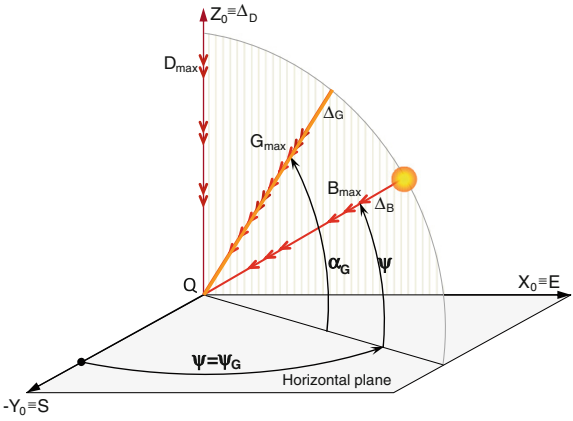

Fig. 7 Modeling the direction Δ_G of the maximal global solar radiation G_{max}

horizontally positioned (parallel to the ground of the observer point—direction $\Delta_D \equiv Z_0$), while the received *direct* radiation is maximal if the PV module is facing to the sun (the solar rays fall perpendicular on the PV surface—direction Δ_B) [20].

Considering an azimuth-altitude type tracking system (see Figs. 4b and 6a), the maximization of the diffuse radiation requires only the adjustment of the elevation angle α to 90°, while maximizing the direct radiation requires the adjustment of both the diurnal (azimuth) ψ and elevation (altitude) α angles.

The two different positions of the maxima allow to identify a third middle-plane (with direction ΔG as normal vector) where the *global* solar radiation is maximal, dependent on the D/B ratio. Due to the influence of the maximal diffuse radiation, with the fixed direction Δ_D, the direction Δ_G is located in the plane defined by Δ_D and Δ_B, and $\alpha_G > \alpha$ (Fig. 7).

The analytical model of the maximal global solar radiation can be thus formulated for identifying both, the instantaneous direction and the quantity of the maximal global solar radiation, given by [21]:

$$\alpha_G = \tan^{-1}\left\{\left[1 + \frac{D_H}{2B_H}\right] \cdot \tan\alpha\right\}; \psi_G = \psi; \tag{7}$$

$$G_{\max} = \frac{B_H \cdot \cos(\alpha_G - \alpha)}{\sin\alpha} + \frac{D_H(1 + \sin\alpha_G)}{2}, \tag{8}$$

where α_G, ψ_G represent the azimuth-altitude angles of the direction of the maximal available global radiation; α, ψ are the current azimuth-altitude angles of the sun ray and B_H, D_H are the direct and respectively diffuse solar radiation measured on the local horizontal plane.

5 PV Tracking Algorithms

A tracking system aiming to maximize the incident solar radiation follows tracking programs which usually consists of correlated values of the motion moments and tracking angles. Ideally the movement should be continuous, but due to economical constraints (high price of actuators able to reach low output angular speed) they are mostly stepwise done.

The input data in the design of a *stepwise tracking algorithm* for a given tracking system are [22–24]:

- The geographical coordinates of the implementation location;
- The local meteorological conditions: database with direct and diffuse radiation, air temperature etc., covering at least one year. Although simulation software exists, the accurate design requires local meteorological data;
- The maximal angular diurnal and elevation strokes which can be achieved by the tracking mechanism;
- The smallest step size (time interval between two movements).

Based on these data, the tracking program contains the following optimized parameters:

- The number of seasons (period of time with the same daily tracking program);
- The step type (constant or variable);
- The minimum number of steps which allow the collection of acceptable amount of solar radiation;
- The parameters of every step (operating hour and step stroke).

According to the capacity of the implemented control system, the algorithm steps can be constant or variable; constant steps require less storage and processing capacity, but slightly reduce the collection of solar radiation as compared to the variable steps. The variable step programs allow more movements during noon hours when solar radiation is peak and fewer movements during the rest of the day. Multiple seasons in a year with different tracking programs according to the day light period are also to be considered. The length of the steps mostly depend on the PV type: concentrated photovoltaics (CPV) require accuracy with movements every few seconds, while for non-concentrated PVs movements every 10–15 min up to one hour are enough.

The optimization of the tracking algorithms aims to maximize the collected direct (B^*), diffuse (D^*) or global (G^*) radiation [25–27].

The optimization towards the direct component B requires only to know the relative position sun-earth at any time, given by a solar angle-pair according to the tracking system type. This algorithm can obtain a high efficiency especially during sunny (clear-sky) days when direct radiation is dominant.

During cloudy days, the diffuse radiation becomes the main component of the global radiation and B optimized tracking algorithms lose their effectiveness. The recommended approach in this case is to horizontally position the PV modules for

collecting the maximal diffuse radiation; this can be done if information on instantaneous D and G radiation values is available and can be used in the PV system controller.

An improved-efficiency tracking algorithm is proposed aiming at maximizing the collected global solar radiation, G^*_{max}. This type of algorithm can be both predefined (based on previous known radiation data) and/or adaptive (depending on the momentary measured radiation data).

In developing a predefined G^*_{max} algorithm, meteorological data in the implementation location are needed over larger periods of time, particularly the direct and diffuse solar radiation. On the other side, for the development of an adaptive G^*_{max}algorithm, a set of two pyranometers or a combined one are needed for providing continuous measurements during the tracker's work, and a more complex control system able to calculate the live-values of the actual optimal angles. These devices can increase the overall cost of the tracking system, cost which becomes acceptable only if the PV installation is large enough.

Based on the previous statements, a general scheme useful in designing optimal tracking algorithms is depicted in Fig. 8: it represents a general overview of the steps needed in the design of PV tracking systems starting with choosing the angle-pair (θ_d—daily angle, θ_e—elevation angle) and ending with the selection of the

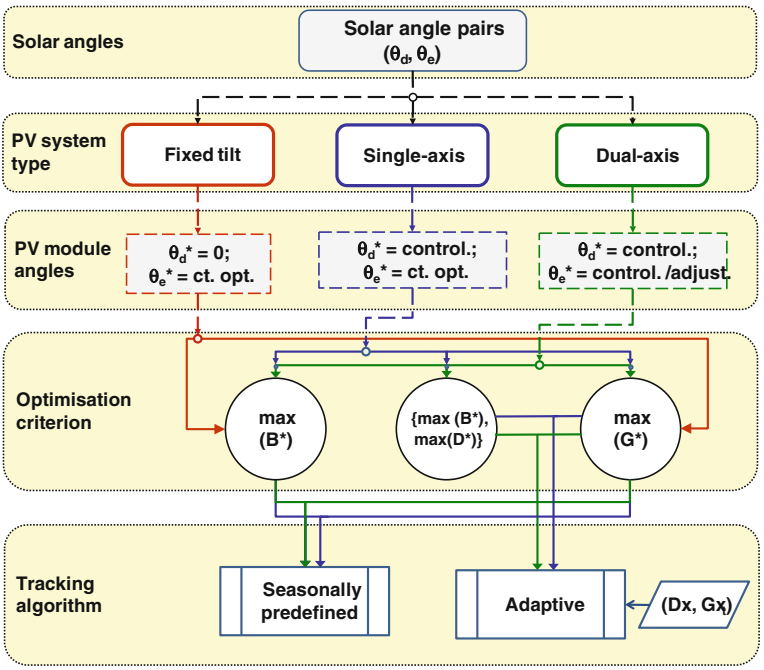

Fig. 8 Systematization of the PV system types and optimization approaches for tracking algorithms

algorithm type, optimized based on a specific criterion: maximization of the collected B, B/D or G radiation. The $\{\max(B^*), \max(D^*)\}$ approach can replace the B algorithm (on sunny periods) with the fixed horizontally position of PV panels (on cloudy periods), based on the live data delivered by the available pyranometers.

6 Case Study: Comparative Analysis of the B Versus G_{max} Tracking Algorithm Efficiency

The tracking efficiency defines the ratio between the collected and the available solar radiation. In this case study, the global radiation is considered in a comparative analysis performed on different four PV planes (fixed and tracked), using in-field meteorological input data from Brasov location (45.65°N, 25.59°E, 600 m above the sea level).

One PV module is continuously following the sun, able to maximize the received direct radiation. The second module continuously follows the direction Δ_G (see Fig. 7) of the maximal global solar radiation. As reference, two fixed planes were also considered: one tilted at 45° and another horizontal.

The comparative study addresses three representative day types in Brasov, from 2013 (18 June—sunny day, 30 June—cloudy day and 20 June—mixed sunny-cloudy day), all of them located in the proximity of the summer solstice when the largest angular strokes are needed and sunny days with a higher level of solar radiation occurs, alternating with cloudy days. The day types were identified based on the E(Dh)/E(Gh) ratios (Fig. 9), calculated based on the data measured in the horizontal plane with a DeltaT SPN1 pyranometer in Brasov, Romania, where E(x) represents the daily energy of the solar radiation x.

Based on the data in Fig. 10, the following statements can be formulated:

- During sunny days there is a very small difference between the available global daily energy on the sunray's B direction and on the direction with G_{max} (E(Gm)/E(Gs) = 100.04 %), indicating that the two algorithms of maximizing B and G radiation are interchangeable. Compared to the fixed modules there is an obvious increase in the available solar energy (E(Gm)/E(Gh) = 145.16 %, respectively E(Gm)/E(G45) = 172.92 %);
- During cloudy days the solar energy difference between the G_{max} and B programs becomes larger (E(Gm)/E(Gs) = 112.31 %). Comparing with the fixed horizontally position, the orientation of a PV module in a cloudy day leads to a small increase in the collected global radiation (E(Gm)/E(Gh) = 101.53 %) or even worsening the G collecting conditions (E(Gs)/E(Gh) = 90.40 %). Hence, the fixed horizontal orientation is recommended in preponderant cloudy days;
- During mixed days the increase in the E(Gm)/E(Gs) ratio can vary between 101–108 %, being E(Gm)/E(Gs) = 103,11 % in this case study.

Close to the summer solstice an interesting result can be observed (Fig. 10a): the fixed horizontal PV module receives more global solar radiation than the fixed tilted one,

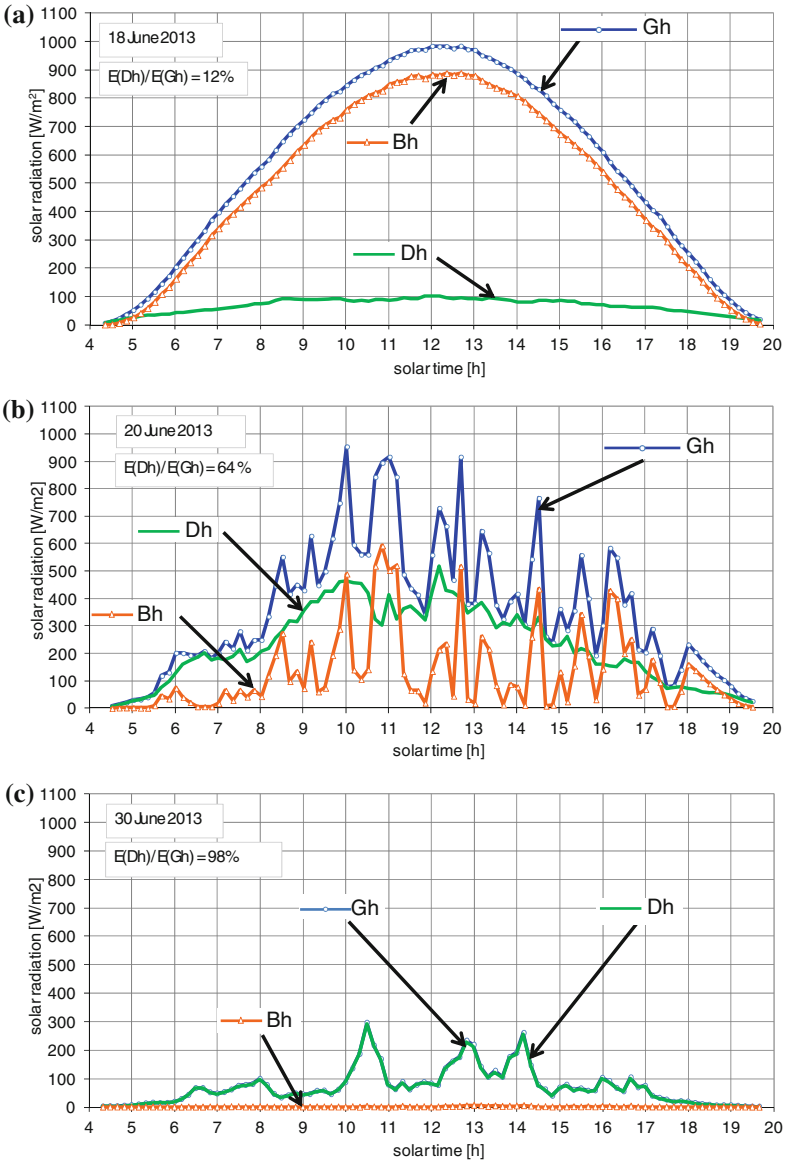

Fig. 9 Variations of the measured solar radiation on the horizontal plane during: **a** sunny day, **b** mixed day, **c** cloudy day

E(Gh) > E(G45). This happens during first and end hours because the sun is positioned behind the PV module (in this case the fixed tilted module receives only diffuse radiation) and at noon because of the fact that the sun is closer to the vertical axis of the

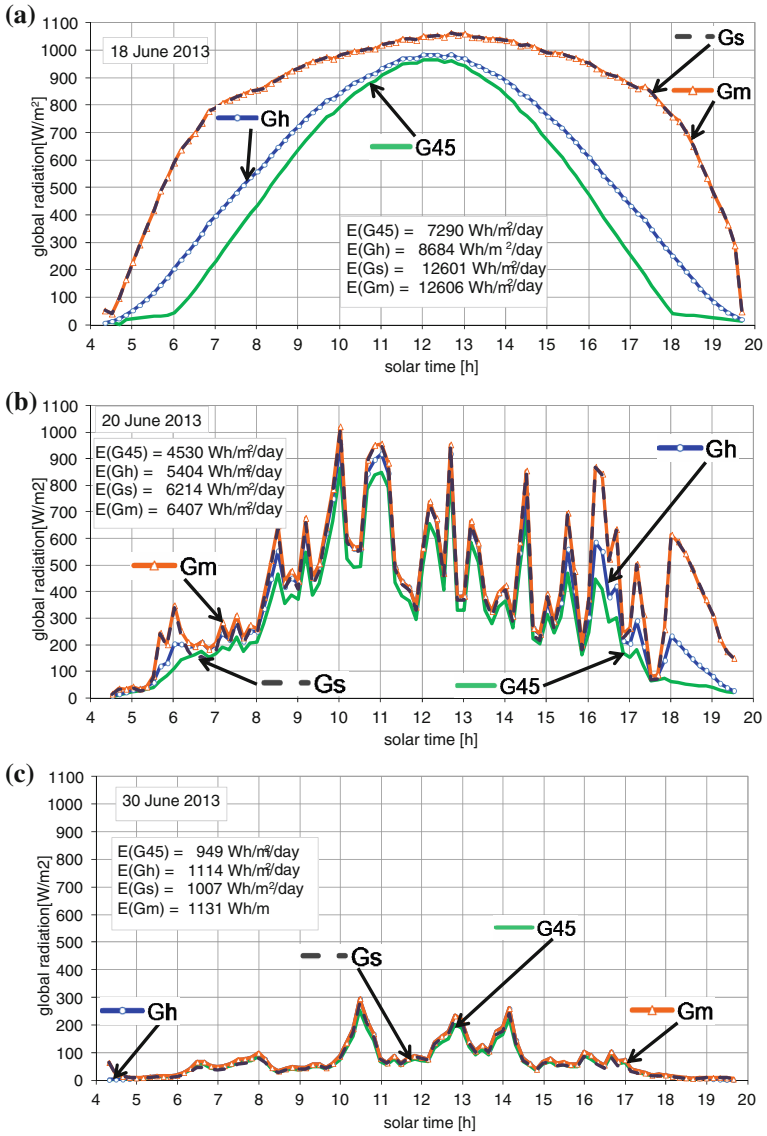

Fig. 10 Variations of the available global solar radiation on the G_{max} (curve Gm) and B (curve Gs) planes versus the fixed horizontal (curve Gh) and fixed 45° tilted (curve G45) planes, in three days: **a** sunny day, **b** mixed day, **c** cloudy day

horizontal PV module than to the axis of the tilted one (in this case the fixed horizontal module received both all the diffuse radiation and most of the direct radiation).

For days far from the summer solstice (e.g. day no. 95 of the year, Fig. 11) the usual expected order of the produced energy is obtained, E(Gh) > E(G45).

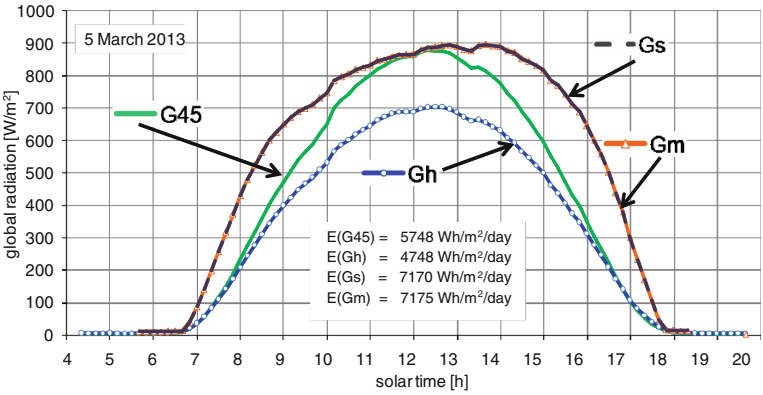

Fig. 11 Variations of the available global solar radiation on the G_{max} (curve Gm) and B (curve Gs) planes versus the fixed horizontal (curve Gh) and fixed 45° tilted (curve G45) planes during 5 March 2013

Further on, based on the 20 June 2013 mixed day data (Figs. 9b and 10b), two predefined orientation programs for optimizing the collection of B and respectively G radiation are applied and compared in terms of their G type tracking efficiency. Both are one hour stepwise programs with the same diurnal displacements, but different hourly variations of the elevation angle: one program uses a step-approximation of the sunray's elevation angle (which assures an optimal reception of the direct radiation B), while the other program uses a stepwise movement of the average elevation which enables the reception of G_{max} radiation. This average elevation value was determined for Brasov location based on measured radiation data for a period of 6 years (Fig. 12).

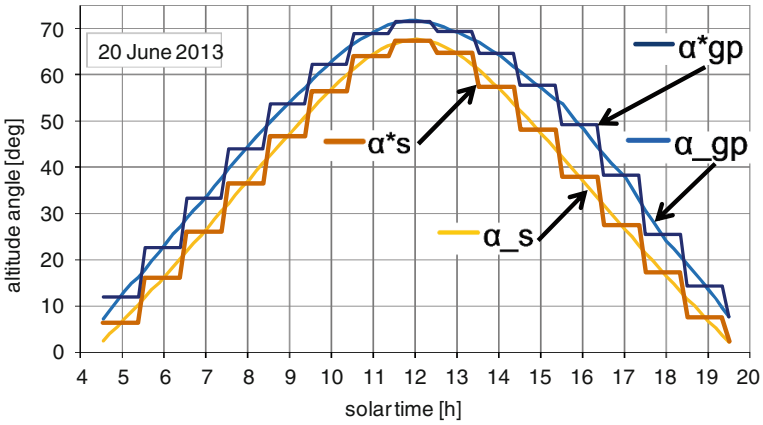

Fig. 12 Predefined hourly stepwise programs of the elevation angle movement following B and average G_{max} radiation

The solar energy ratios calculated based on the four programs of elevation angles (continuous and stepwise) presented in Fig. 12 show that the small increase-improvement of the elevation angle in the average G_{max} approach is ~ 3 % in the case of a continuous orientation (E(Gm)/E(Gs) = 102.72 %) and ~ 1.5 % for stepwise displacements $(E(G^*mp)/E(G^*s) = 101.47\%)$.

7 Conclusions

The main conclusions on the efficiency increase of non-concentrated photovoltaic tracking systems are:

- During sunny days and in preponderant sunny regions a stepwise predefined B tracking algorithm is recommended, according to the relative position of the sun (considering the Δ_B direction—Fig. 7) and considering the insignificant differences between the available global solar energy on sunray and G_{max} directions;
- During cloudy days and in preponderant cloudy regions, horizontally fixed PV modules are recommended for increasing the produced power and minimizing the tracking system stress;
- During mixed sunny-cloudy days an average G_{max} predefined tracking program should be implemented, based on the radiation data measured from the implementation location, to significantly increase the output energy, especially for large scale PV applications, as solar parks.

The previous recommendations can be applied in an adaptive tracking system able to select one of the above three tracking programs according to the solar day type. Identification of the day type implies a tuning research on the limits between sunny/mixed/cloudy periods, defined by the E(Dh)/E(Gh) ratios.

Acknowledgments This work was done in the frame of the Program: Cooperation in Priority Fields - PNII, developed with the support of ANCS, CNDI-UEFISCDI, Romania in the project EST IN URBA, PN-II-PT-PCCA-2011-3.2-051.

References

1. California Institute of Technology (2005). *Report of the basic energy sciences workshop on solar energy utilization*, April 18–21, 2005.
2. Sungur, C. (2007). Sun-tracking system with PLC control for photo-voltaic panels. *International Journal of Green Energy, 4*(6), 635–643.
3. Moldovan, M. D., Visa, I., & Burduhos, B. G. (2011). Energetic Autonomy for a Solar House. *Environmental Engineering and Management Journal, 10*(9), 1283–1290.
4. Abdallah, S. (2004). The effect of using sun tracking systems on the voltage–current characteristics and power generation of flat plate photovoltaics. *Energy Conversion and Management, 45*, 1671–1679.
5. Karimova, Kh S, Saqibb, M. A., Akhterc, P., Ahmedd, M. M., Chatthad, J. A., & Yousafzaid, S. A. (2005). A simple photo-voltaic tracking system. *Solar Energy Materials and Solar Cells, 87*, 49–59.

6. Tracstar. *Should you install a solar tracker?* http://www.helmholz.us/smallpowersystems/.
7. Bione, J., Vilela, O. C., & Fraidenraich, N. (2004). Comparison of the performance of PV water pumping systems driven by fixed, tracking and V-trough generators. *Solar Energy, 76*, 703–711.
8. Abu-Khader, M. M., Badran, O., & Abdallah, S. (2008). Evaluating multi-axes sun tracking system at different modes of operation in Jordan. *Renewable and Sustainable Energy Reviews, 12*(3), 864–873.
9. Singh, B., & Othman, M. Y. (2009). A review on photovoltaic thermal collectors. *Journal of Renewable and Sustainable Energy, 1*(6), 062702.
10. Fahl, P., & Ganapathisubbu, S. (2011). Tracking benefits for solar collectors installed in Bangalore. *Journal of Renewable and Sustainable Energy, 3*(2), 023103.
11. Helwa, N., Bahgat, A., El Shafee, A., & El Shennawy, E. (2000). Maximum collectable solar energy by different solar tracking systems. *Energy Sources, 22*, 23–34.
12. Maatallah, T., El Alimi, S., & Nassrallah, S. B. (2011). Performance modeling and investigation of fixed, single and dual-axis tracking photovoltaic panel in Monastir city. *Tunisia, Renewable and Sustainable Energy Reviews, 15*, 4053–4066.
13. Meek, D. W. (1997). Estimation of maximum possible daily global solar radiation. *Agricultural and Forest Meteorology, 87*, 223–241.
14. Seme, S., & Stumberger, G. (2011). A novel prediction algorithm for solar angles using solar radiation and differential evolution for dual-axis sun tracking purposes. *Solar Energy, 85*(11), 2757–2770.
15. Armstrong, S., & Hurley, W. G. (2010). A new methodology to optimise solar energy extraction under cloudy conditions. *Renewable Energy, 35*, 780–787.
16. Goswami, D. J., Kreith, K., & Kreider, J. F. (1999). *Principles of solar engineering*. Philadelphia: George H. Buchanan Co.
17. Visa I. *Renewable energy systems: case study—solar energy conversion systems*. In The 11th IFToMM International Symposium on Science of Mechanisms and Machines, Mechanisms and Machine Science 18, Springer Pub., 31–49, 2014.
18. Visa, I., Diaconescu, D. V., Saulescu, R. G., Vatasescu, M. M., & Burduhos, B. G. (2011). A new linkage with linear actuator for tracking PV systems with large angular stroke. *Chinese Journal of Mechanical Engineering, 24*(5), 744–751.
19. Neagoe, M., Vatasescu, M., Saulescu, R., & Creanga, N. (2012). On new high performance systems with linear actuators for diurnal orientation of PV platforms. *Applied Mechanics and Materials, 162*, 214–223.
20. Meliss, M. (1997). *Regenerative Energiequellen—Praktikum*. Berlin, Heidelberg: Springer.
21. Burduhos B. G., Visa I., Neagoe M., & Badea M. (2014). *Modeling and optimization of the global solar irradiance collecting efficiency*. International Journal of Green Energy, 2014 (accepted for publication).
22. Burduhos B. G., Visa I., Diaconescu D. V., & Saulescu R. G. (2009). *Novel orientation step-program of a pseudo-equatorially tracked PV panel*. In Proceedings of 24th EU PVSEC: 3835–3843, 2009.
23. Burduhos, B. G., Toma, C., Neagoe, M., & Moldovan, M. D. (2011). Pseudo-equatorial tracking optimization for small photovoltaic platforms from Toronto/Canada. *Environmental Engineering and Management Journal, 10*(8), 1059–1068.
24. Visa, I., Diaconescu, D. V., Popa, V. M., & Burduhos, B. G. (2009). Quantitative estimation of the solar radiation loss in the Brasov area. *Environmental Engineering and Management Journal, 8*(4), 843–847.
25. Kelly, N., & Gibson, T. (2009). Improved photovoltaic energy output for cloudy conditions with a solar tracking system. *Solar Energy, 83*, 2092–2102.
26. Kelly, N., & Gibson, T. (2011). Increasing the solar photovoltaic energy capture on sunny and cloudy days. *Solar Energy, 85*, 111–125.
27. Liu, G. Y., Ren, Y., & Nguang, S. K. (2012). Simulated photovoltaic array systems under a changing environment for temporal performance. *International Journal of Green Energy, 9*(7), 673–684.

Torques on Rotational Axes of PV Azimuthal Sun Tracking Systems

Radu Velicu and Mihai Lates

Abstract Azimuthal tracking systems have two rotational axes: a vertical fixed axis, for azimuthal rotation and a horizontal axis, for the elevation movement. The main loads that must be considering in dimensioning of these systems are the weights and the wind loads. Wind loads depend on wind speed, wind direction, platform geometry, elevation angle. Wind action on buildings is subject of Eurocode 1 Standard which is not fully applicable for tracking systems. A Spanish standard dedicated to wind action on tracking systems is more appropriate. This paper presents loading cases on the platform of a general azimuthal tracking system, considering wind and weight action, depending on specific platform positions and wind direction. Functioning positions but also the safety position are considered. Very important parameters resulting for each loading case are the torques acting along the main rotational axes of the system, used as input data for choosing actuators and design of transmissions.

Keywords Azimuthal tracker · Torques · Actuator

1 Introduction

The solar energy conversion systems are widely used in both domestic and industrial applications. Solar energy is a clean energy source that can be converted into heat [1] or by using the photovoltaic effect (the direct conversion of solar energy into electrical energy) [2, 3].

The efficiency of the devices used for collecting the direct solar energy can be increased by improvement on constructive parameters or by maximizing the solar incident radiation on PV surface by means of tracking systems [4]. Depending on

R. Velicu (✉) · M. Lates
Product Design, Mechatronics and Environment Department, Transilvania University of Brasov, Brasov, Romania
e-mail: rvelicu@unitbv.ro

I. Visa (ed.), *Sustainable Energy in the Built Environment - Steps Towards nZEB*, Springer Proceedings in Energy, DOI 10.1007/978-3-319-09707-7_34

the number of axes of rotation the tracking systems are divided in two categories: single axis systems and dual axis systems. Although the costs of manufacturing and implementation of dual axis tracking systems represents a disadvantage [5], in comparison to single axis system the energy gain is significant [6–9]. Therefore these types of tracking systems are subject for continuous development and implementation.

The dual axes tracking systems are devices that can follow the position of the sun on the sky ensuring this way the perpendicularity of the sun beam on the photovoltaic platform's surface.

The azimuthal tracking system adjusts the position of the PV platform according with the azimuthal and with the altitudinal angles (see Fig. 1). By combining the altitudinal motion α^*, performed around the horizontal axis Ox and the azimuthal motion Ψ^*, performed around the vertical axis Oz, any position of the sun on sky can be followed (see Fig. 1).

Their specific rotation movements are performed using different mechanical transmissions, using linear actuators of screw-nut type, rotational actuators of worm gear type, chain drive systems or various combinations of these. Considering the common aspects of the azimuthal tracking systems, different transmission typologies were identified and presented in [10].

The overall size of the structure and transmission of the tracking system are directly depending on the loads of the photovoltaic platform. From all the loads coming from weight, wind and snow, the main load is caused by the wind action [11, 12].

Due to their specific constructive characteristics, such as high surfaces exposed to wind action, the height above the level of terrain and the orientation, the photovoltaic platforms could be subject to important variable wind loads. The worst

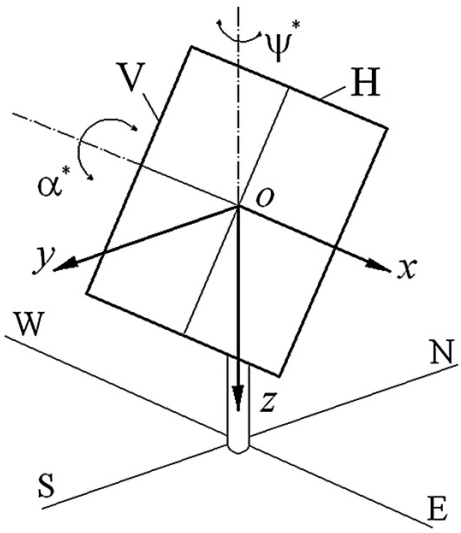

Fig. 1 The specific rotation axes and rotation angles of an azimuthal tracking system

case scenario of wind load must be used to calculate the input parameters for the design of the azimuthal photovoltaic platforms.

The wind action standards are not providing comprehensive guidelines for evaluating the case of wind loads on the platforms. This is the reason for which the specific literature contains many reports of important companies [13], experimental studies [14], numerical simulations resulting from tools such as Computational Fluid Dynamics [15] and computational structural analysis [16].

Based on a comparison between existing standards, compared with results of the experimental study performed and presented in [17], this paper presents the wind load cases, which must be used for calculation of torques on the rotational axes specific to azimuthal tracking systems, input data for dimensioning or checking the transmissions and actuators.

2 Wind Action on Structures

Wind action is evaluated in standards by pressures or by forces; its effect on structures is depending on wind parameters (mean velocity, turbulence characteristics), structure characteristics (shape, size, orientation) and location [18–21].

Standards like Eurocode1 EN 1991-1-4 [18] and ASCE/SEI 7-05 [20] present calculus procedures related to the wind loads determinations. The Spanish Standard NBE-AE 88 [21] presents a model of wind action on tilted open surfaces very similar with the tracking systems for PV platforms. All these standards can be used to determine wind load on tracked PV platforms, even if they are not especially dedicated.

Following, there are presented the most relevant aspects of [18, 20] for determining wind action on open tilted surfaces.

The wind force $\boldsymbol{F_w}$ acting on a structure or a structural component may be determined, according to Eurocode 1, for a height less than 15 m, by using expression

$$F_w = c_f q_p A_{ref}, \tag{1}$$

while the wind pressure relation is

$$p_w = c_p q_p, \tag{2}$$

where: $\boldsymbol{c_f}$ is the force coefficient; $\boldsymbol{q_p}$—velocity pressure; $\boldsymbol{A_{ref}}$—the reference area of the structure or structural element, $\boldsymbol{c_p}$ is the pressure coefficient.

The velocity pressure relation is

$$q_p = \frac{1}{2}\rho v_p^2, \tag{3}$$

where v_p is the peak wind velocity and ρ is the air density, which depends on altitude, temperature and barometric pressure to be expected in the region during wind storms. The general recommended value for ρ is 1.25 kg/m^3.

An analysis of the wind action standards is presented in [22]. The model given in [18] for the buildings roofs is not valid due to the fact that the roof is not considered as an open surface. Models similar with the case of PV platforms are the canopy models —for tilt angle up to 30°, and the signboards model—for vertical positions (90° tilt angle). Romanian standard [19] is similar. Due to the limited range of tilt angle, both standards are not covering all the wind load cases for solar tracking platforms.

The American standard [20] provides model for tilt angles between 0° and 45°, with values of pressure significantly higher than those presented in Eurocode. Smaller values are presented in the model of NASA report [23], for tilt angle range of 20°–60°.

The Spanish Standard NBE-AE 88 [21] presents a model for the whole range of tilt angles 0°–90°, with values close to those from Eurocode, for canopies with tilt angles up to 30°. Values of the pressure coefficients are given for different wind direction (front wind or back wind) and wind angles (see the diagram from Fig. 3 and values from Table 1) [21]. This is covering the entire range of specific cases for tracking systems. Experimental evaluation of wind loads [17] also shows that the Spanish Standard model gives similar values.

In the general case of trapezoidal distribution of pressure, the force coefficient can be calculated based on the limit pressure coefficients c_{p1} and c_{p2} (see Fig. 2) with relation

$$c_f = \frac{(c_{p1} + c_{p2})}{2}. \tag{4}$$

The tilt angle mentioned in all standards is actually the wind angle (angle between wind direction and structure surface) considering the horizontal direction of the wind. Wind angle is not always the tilt angle of the platform since the wind direction follows terrain surface which is not always horizontal. Even for horizontal terrain, there can be consider a deviation of wind direction of ±10° relative to the horizontal direction [13]. It must also be consider the case of lateral wind, when wind angle has nothing to do with the tilt angle of the platform. This is why the angle β from Table 1 is the wind angle and must not be assimilated with the tilt angle or elevation orientation angle α^* of the platform of the tracker (see Fig. 1).

For the general case of trapezoidal distribution of pressure (Fig. 3), a torsional effect appears. It can be evaluated by the resulted torque T_w or the arm e of the resultant force. The width of the surface with pressure distribution is b.

Table 1 c_p values for open platforms [20]

	Wind angle, β						
	0°	10°	20°	30°	40°	50°	60°–90°
c_{p1}	0	0.8	1.2	1.6	1.6	1.4	1.2
c_{p2}	0	0	0.4	0.8	0.8	1.0	1.2

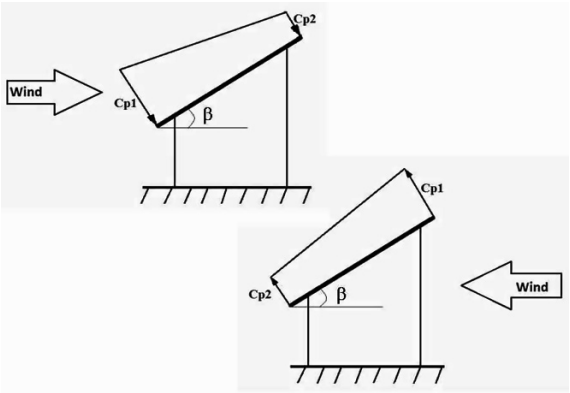

Fig. 2 Pressure coefficients and distribution diagram on PV platforms

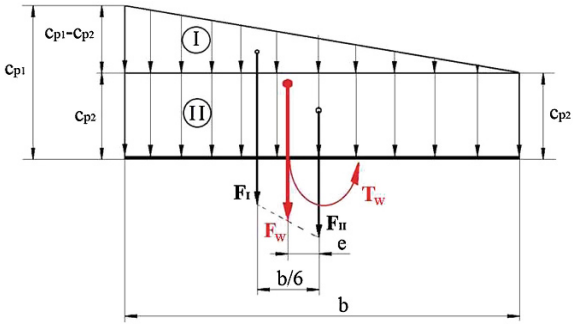

Fig. 3 Wind action torsional effect

The torsional effect is given by the triangular pressure distribution from zone I. The calculated torque is

$$T_w = F_I \frac{b}{6} = \frac{(c_{p1} - c_{p2})}{2} \frac{\rho v_p^2}{2} A_{ref} \frac{b}{6} = \frac{1}{24} (c_{p1} - c_{p2}) \rho v_p^2 A_{ref} b. \tag{5}$$

From the relation between torque and wind force, the arm $\boldsymbol{e}$ of the wind force $\boldsymbol{F_w}$ results as

$$e = \frac{T_w}{F_w} = \frac{(c_{p1} - c_{p2})}{6(c_{p1} + c_{p2})} b. \tag{6}$$

As it can be seen from Eq. 5, besides the dimensions of the rectangular surface, the torque is directly depending on the difference between pressure coefficients and peak wind velocity. A brief analysis of the values of pressure coefficients from Table 1 shows that the higher difference $(c_{p1} - c_{p2}) = 0.8$ is found on wind angles $\boldsymbol{\beta} = \{10°, 30°, 40°\}$, giving maximal values of torques.

3 Wind Load Cases

A tracking system must track the sun for a limited wind velocity v_{lim}. For higher wind velocity, the tracking system must stay in a safety position with horizontal platform. For the safety position, wind load must consider the reference peak wind velocity v_{max} (maximum wind velocity on the specified region over the last 50 years, according to Eurocode 1—Wind actions [18]). Romanian standard [19] gives a reference velocity pressure q_p for each region. If needed, reference peak wind velocity can be calculated from rel. (3). The limited wind velocity v_{lim}, at which the system moves to the safety position, should be around half of the maximum peak wind velocity v_{max} given by standards. The tracking and the safety position case are treated separately.

The case of limited wind velocity v_{lim} is the case of actuators and power transmissions in running, using as input a dynamic torque T_{dyn}. This is a different case than the case of reference peak wind velocity v_{max} when actuators and power transmissions are at rest. In this case, the resulted torque is a static torque T_{st} needed for dimensioning of the break from power transmission or actuator.

Maximal dynamic torque and maximal static torque are used in dimensioning or checking actuators and components of the power transmissions of any sun tracker. Besides the component of the torques, coming from wind action, platform weight G must also be considered. In order to determine the component of torque coming from platform weight, the distance b of center of weight to Ox axis, presented in Fig. 4, must be known. Altitudinal angle of the platform is considered equal with the solar altitudinal angle ($\alpha = \alpha^*$).

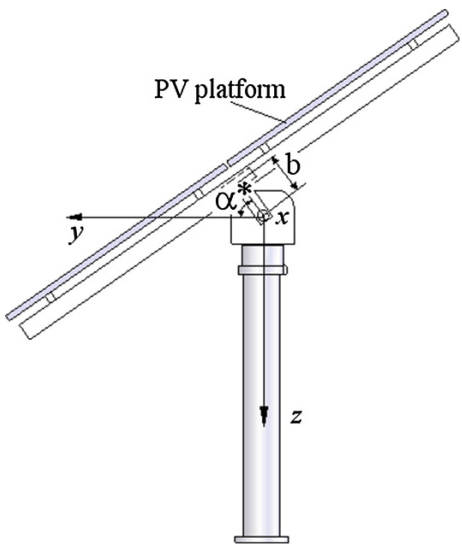

Fig. 4 Altitudinal angle α^* and distance b

Based on an analysis of maximal torques resulted from specific platform positions, wind angle, direction and velocity, the following Load Cases (LC) have been determined for calculus of actuators and elements of transmissions with dynamic torque $\boldsymbol{T_{dyn}}$ on positions of tracking—with limited wind velocity $\boldsymbol{v_{lim}}$ (Fig. 5):

- LC1—trapezoidal distribution along the H dimension of the platform (Fig. 5a);
- LC2—trapezoidal distribution along the V dimension of the platform (Fig. 5b).

Table 2 presents the calculus relations for dynamic torques, considering also the influence of platform weight.

The Load Case 1 (LC1) should consider positions of the platform closed to vertical, with lateral wind $\alpha = 0°–20°$, $\beta = 10°–40°$. For this load case, due to the trapezoidal distribution along H dimension the application point of wind force F_w is moved along Ox axis causing a torque around Oz axis.

For LC2, due to the trapezoidal distribution along V dimension the application point of wind force F_w is moved along Oy axis causing a torque around Ox axis.

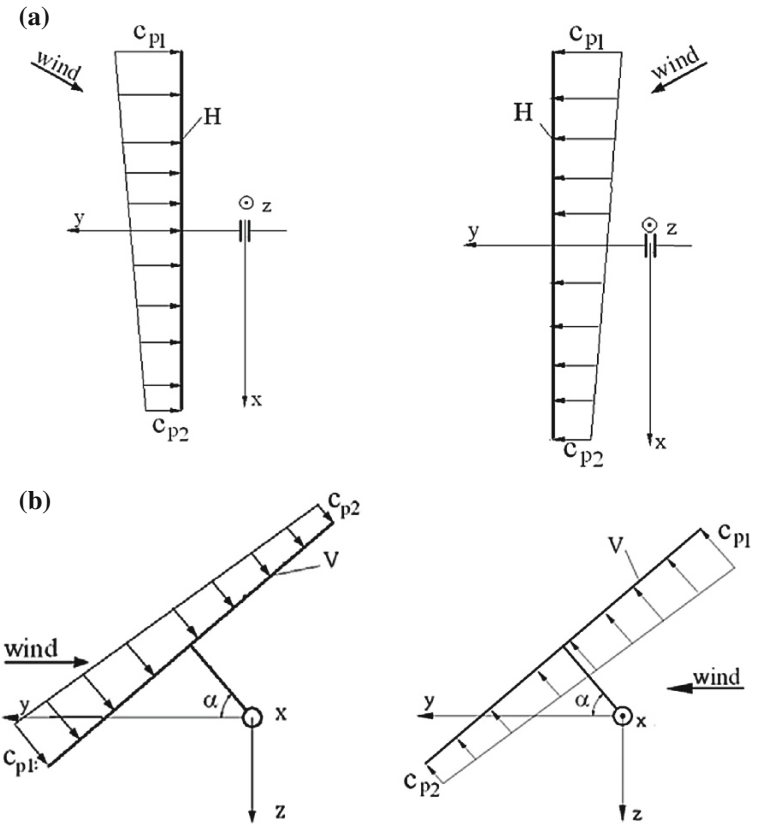

Fig. 5 Wind load cases: **a** LC1; **b** LC2

Table 2 Dynamic torques for Ox and Oz axes

	Load case 1 $\boldsymbol{\alpha}$ = 0°–20°, β = 10°–40°	Load case 2 $\boldsymbol{\alpha}$ = 30°–70°, $\boldsymbol{\beta}$ = 30°–50° ($\boldsymbol{\beta}$ = 90° − $\boldsymbol{\alpha}$ ± 10°)
$T_{x\,dyn}$	$Gb\cos\alpha$, maximum value for $\boldsymbol{\alpha}$ = 0°	$\frac{1}{24}(c_{p1}-c_{p2})\rho v_{\lim}^2 AV\cos\alpha + Gb\cos\alpha$ maximum value for $\boldsymbol{\alpha}$ = 40°, $\boldsymbol{\beta}$ = 40°, back wind
$T_{z\,dyn}$	$\frac{1}{24}(c_{p1}-c_{p2})\rho v_{\lim}^2 AH\cos\alpha$, maximum values for $\boldsymbol{\alpha}$ = 0°, $\boldsymbol{\beta}$ = {10°, 30°, 40°}, front or back wind	**0**

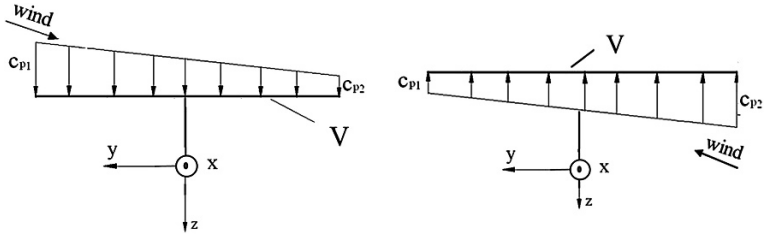

Fig. 6 Load Case 3 (LC3) for the safety position

This case should consider tilted positions of the platform, α = 30°–70°, β = 30°–50° (β = 90° − α ± 10°).

For the safety position case, there is only one Load Case that must be considered for calculus of actuators and elements of transmissions with static torque $\boldsymbol{T_{st}}$—with wind load determined with maximum wind velocity $\boldsymbol{v_{max}}$: LC3—trapezoidal distribution along Oy axis—$\boldsymbol{V}$ dimension of the platform, wind angle $\boldsymbol{\beta}$ = 10° (Fig. 6).

The static torque for the Ox rotational axis results as

$$T_{x\,st} = \frac{1}{24}(c_{p1}-c_{p2})\rho v_{\max}^2 AV. \tag{7}$$

For the actuator and transmission of the azimuthal vertical axis Oz, a static torsion calculus is not needed to be performed, since there is no torsional load on Oz axis during resting in safety position.

4 Conclusions

The load cases previously presented are very few of the possible loading on the components of the tracking system. For strength calculus of components like the platform, other load cases must be considered in calculations and should be selected depending not only on individual maximal values but on resulted maximal stresses.

In conclusion, the following can be drawn:

(a) maximal torques on the rotational axes of the tracking system are mostly depending on wind action;
(b) two types of torques are used in calculus of actuators and components of power transmissions, a dynamic torque and a static torque;
(c) the static torque is depending only on the vertical dimension ***V*** of the platform, this being the reason for which horizontal dimension should always be bigger than vertical dimension of the platform;
(d) elements of transmission and actuator of the vertical axis must only be calculated for dynamic case, where the maximal torque is directly depending on horizontal dimension of the platform.

References

1. Weston, A. H. (2006). Quantifying global energy resources. *Energy, 31*(12), 1685–1702.
2. Goswami, Y. D., Kreith, F., & Kreider, J. F. (1999). *Principles of solar engineering* (2nd ed., pp. 81–172). Philadelphia: Taylor & Francis. (cap.3).
3. Goetzberger, A., & Hoffmann, V. U. (2005). *Photovoltaic solar energy generation* (pp. 1–8). Berlin: Springer. (cap.1).
4. Krauter, S. (2006). *Solar electric power generation-photovoltaic energy systems* (pp. 19–44). Berlin/Heidelberg: Springer.
5. Rizk, J., & Chaiko, Y. (2008). Solar tracking system: more efficient use of solar panels. *Proceedings of World Academy of Science. Engineering and Technology, 31*, 314–316.
6. Verhelst, B. et al. (2010). Technical and business economic study of photovoltaic systems. In: *International Conference on Renewable Energies and Power Quality* (ICREPQ'10), Granada (Spain).
7. Bakos, C. (2006). Design and construction of a two-axis sun tracking system for parabolic trough collector (PTC) efficiency improvement. *Renewable Energy, 31*, 2411–2421.
8. Huld, T., Šuri, M., & Dunlo, D. (2008). Comparison of potential solar electricity output from fixed-inclined and two axis tracking photovoltaic modules in Europe. *Progress in Photovoltaics: Research and Applications, 16*, 47–59.
9. Plesz, B., et al. (2009). Enhancement of solar panel's power generation by the usage of solar tracking. *Proceeding of ECO Pole, 3*(1), 15–22.
10. Butuc, B., & Moldovean, G. (2008). Gears based Azimuthal tracking systems for photovoltaic platforms. *Bulletin of the Transilvania University of Braşov, I*(50), 87–92. (Series I).
11. Ching-Yao, L. (2008). Analysis of structural deformation in a high concentrated photovoltaic system. Available at: http://thesis.lib.ncu.edu.tw.
12. Messenger, R., & Ventre, J. (2004). *Photovoltaic systems engineering* (2nd ed., pp. 179–189). London: CRC Press.
13. Cabanillas, J. The wind and the panacea of the stow position in the solar trackers. www.titantracker.es.
14. Hosoya, N., Peterka, J. A. (2008). Wind Tunnel Tests of Parabolic Trough Solar Collectors. Technical Report No. NREL/SR-550-32282, Ceremak Peterka Petersen, Inc., Fort Collins, CO.
15. Shademan, M., Hangan, H. (2009). Wind loading on solar panels at different inclination angles. In: *Proceedings of 11th Americas Conference on Wind Engineering*, San Juan, Puerto Rico.

16. Velicu, R., Lates, M., Moldovean, G. (2009). Loading cases and forces on azimuthal solar tracking systems with linear actuator. In: *Proceedings of 10th International Symposium on Science of Mechanisms and Machines*, Brasov, Romania.
17. Velicu, R., Moldovean, G., Scaletchi, I., Butuc, B. R. (2010). Wind loads on an azimuthal photovoltaic platform. Experimental study. *Renewable Energies and Power Quality Journal*, No. 8.
18. EN 1991-1-4. (2004). Eurocode 1: Actions on structures. General actions—Part 1–4: Wind Actions.
19. SR EN 1991-1-4: Actions on structures. General actions—Part 1–4: Wind Actions, 2006 (in Romanian).
20. ASCE/SEI 7-05 (2006). Minimum design loads for buildings and other structures. American Society of Civil Engineer.
21. NBE-AE/88, Actions on structures, 1988 (in Spanish).
22. Scaletchi, I., Visa, I., & Velicu, R. (2010). Modeling wind action on solar tracking PV platforms. *Bulletin of the Transilvania University of Brasov, Series I—Engineering Sciences, 3* (52), 115–122.
23. Miller, R. D., Zimmerman, O. K. (1981). Wind loads on flat plate photovoltaic array fields. Boeing Engineering and Construction, pp. 94–97.

Part IV
Sustainable Built Environment Solutions

On the Effect of Injection Moulding Blends of Post-consumer Mixed Polyolefines with Virgin Polyethylene

Laurens Delva, Ludwig Cardon and Kim Ragaert

Abstract Recycling of solid plastic waste composed of postconsumer mixed polyolefines (polypropylene and poly-ethylene) was carried out by injection moulding of secondary material streams. The composition, mechanical and physicochemical properties were characterized. The sink-float technique was used to separate the poly-ethylene fraction, which was then blended with virgin poly-ethylene at different ratios and processed anew. The mechanical and physico-chemical properties were likewise determined. It was found that the different postconsumer mixed polyolefines were of similar quality and had comparable properties. Furthermore, it was demonstrated that the tensile properties of blends consisting of recycled separated poly-ethylene and virgin poly-ethylene follow the law-of-mixtures, while the impact strength does not and is in fact strongly reduced by the presence of different phases within the injection moulded part.

Keywords Blends · Characterization · Injection moulding · Polymer recycling · Post-consumer mixed polyolefins

1 Introduction

Recent yearly plastics demand in Europe is up to 46.4 Mtonne, of which nearly 50 % is made up by the polyolefines (PO) polypropylene PP (19 %), high-density poly-ethylene HDPE (12 %) and low-density polyethylene LDPE (17 %) [1]. There is a steadily growing consumer awareness regarding recycling of materials, which is expressed by a yearly increase in the amount of recycled post-consumer plastics [1, 2]. Of the yearly 24.7 Mtonne post-consumer solid plastic waste (SPW) this now generates, only 24 % is recovered as secondary raw materials through recycling.

L. Delva (✉) · L. Cardon · K. Ragaert
Centre for Polymer and Material Technologies (CPMT), Faculty of Engineering and Architecture, Ghent University, Voskenslaan 362, 9000 Ghent, Belgium
e-mail: Ludwig.Cardon@ugent.be

I. Visa (ed.), *Sustainable Energy in the Built Environment - Steps Towards nZEB*, Springer Proceedings in Energy, DOI 10.1007/978-3-319-09707-7_35

The rest is either burnt for energy recovery (34 %), exported outside the EU or landfilled [1].

Apart from energy recovery by burning, the means of recovering SPW include mechanical (secondary) recycling and chemical (tertiary) recycling [3]. In mechanical recycling polymer materials are recovered through mechanical means such as grinding, washing, separating, drying, re-granulating and compounding. The more advanced techniques of chemical recycling reduce (by chemical degradation) the polymer scrap to smaller molecules, which are suitable for the production of new petrochemicals or polymers. Chemical recycling, however, remains very expensive and is generally not considered on an industrial level [4, 5]. Energy recovery should only be considered a sensible way of waste treatment, when the alternative of material recovery is not economically viable. Yet, the greater part of polymer waste is still recovered in this fashion. What bottlenecks then, prevent the wider use of secondary polymer material streams?

A major technological aspect is that the different polymers which are suitable for mechanical recycling (thermoplastics) remain largely immiscible, leading to inferior mechanical properties for the mixed recycled fractions, when compared to virgin material [4]. Therefore, mechanical recycling of SPW is only feasible for either single polymer streams or mixtures of polymers that can be effectively separated into the individual polymers. Single polymer streams can only realised by a separate collection for each polymer type on the post-consumer level, which is not yet the case in any of the EU27 countries. Some known pilot projects include the collection of PVC building materials and the re-grinding of clean PP crates [4]. Well-defined mixtures currently being collected included PET-PP (bottles and their caps) and PP-PE, the so-called PO fraction from collected packaging materials. PP and PE can be separated from this blend through a gravimetrical method [6].

Even though such recycled fractions are commercially available, European plastics converters (mostly SMEs) remain apprehensive to incorporate these materials in their production (‘as is’ or mixed with virgin materials). A lack of information regarding the purity of the secondary materials stream, the processing related properties and the quantification of (loss of) mechanical properties generally keeps them distrustful of the recycled PO. Therefore, it is our belief that by generating better and more specific technological insights into the possibilities and limitations of working with recycled PO, polymer converting SMEs may come to incorporate recycled PO in their production, which in turn may lead to a reduction in export of SPW outside of the EU and in the longer term, consumer acceptance for recycled polymer products.

Within this research, we consider the mechanical recycling of polyolefine (PO) materials, more specifically blends of polypropylene (PP) and polyethylene (PE). PO blends are commonly mixed into virgin materials at a certain percentage: they can either be used ‘as are’ [7, 8], or one of the composing fractions (PE or PP) may be separated for further use [9–11]. The blends are generally not pure and contain a small fraction of contaminants [8, 9, 12], which are other plastics, solvent residues or one of different possible additives.

Quite often, rheological and mechanical properties are found to follow a simple law-of-mixtures, in which the change in property value is proportional to the amount of recycled polymer which has been added to the virgin material [10, 13, 14]. The molecular weight is generally found to decrease due to the mechanical recycling processing and thermal degradation (chain scission) [13–15]. On the other hand, it has been found that the crystallization and melt temperature of PO do not change significantly with mechanical recycling [15, 16].

Current methods for the improvement of PO blend properties include the use of a compatibilizer to homogenize the composing fractions within the PO blends [8, 12], the addition of stabilizers [9] or reinforcing agents [17].

Within this study, commercially available post-consumer mixed PO streams were characterized in detail regarding their composition and properties. After separating the PE fraction from one of these blends via a float-sink method, different amounts of this recycled PE was blended with virgin PE and test parts were injection moulded. These were tested for various mechanical properties, thus quantifying the impact of the blending on product properties.

2 Materials and Methods

2.1 Mixed Polyolefin Stream

The postconsumer mixed polyolefin (MPO) waste streams used in this work were kindly delivered by two Belgian recycling companies Hallurec NV and Ekol NV. Both materials waste streams consisted mainly of polyethylene (PE) and polypropylene (PP), next to a small rest fraction.

The melt flow index (MFI) was determined according to ISO 1133 with a Zwick Plastometer 4,100 at a temperature of 230 °C and a weight of 2.16 kg. An average of ten measurements was made. The content of volatile components was determined by heating the different samples to 75 °C during 8 h. Different other properties were also measured: ash content (ISO 3451-1), density (DIN 53479), moisture uptake (DIN 53495), VICAT VST temperature (ISO 306—CEAST 6520) and the coefficient of friction (ASTM D1894—Hanatek Advanced Friction Tester).

2.2 Mixtures of Virgin and Recycled Polyolefin Materials

The float-sink technique was used to separate the PE fraction from the other polymer fractions in the mixed PO streams. This technique is based on the difference in density between the PE and the PP content [6]. The PE fraction generally has a density greater than 0.92 g/cm^3, while the PP fraction has one lower than 0.92 g/cm^3 [18]. The separation was done by manually pouring the postconsumer

materials in a alcohol–water fluid with a controlled density of 0.92 g/cm^3. The chosen solvent was isopropanol because of the lower volatility, cost and toxicity compared with other solvents. The apparent density was constantly monitored with a density meter. The disadvantage of this float-sink technique is that the density can differ with fillers and additives [19]. Only the PE fraction at the bottom of the barrel was used because of the uncertain nature of the floating particles.

This separated PE (sPE) fraction was used to prepare different mixtures of recycled PE with a commercially available virgin PE to compare the mechanical properties of the recycled material to these of different mixtures. The selected virgin PE was Purell 2410T from Basell with a MFI of 36 g/10 min (190 °C and 2.16 kg). The influence of the different mix ratios on the injection process and the mechanical properties (identical to the mechanical tests on the MPO stream) was monitored. Mixtures with ratios of virgin material versus recycled material of 100:0, 90:10, 70:30, 50:50 and 0:100 were made.

2.3 Injection Moulding

In this study, an injection moulding machine BOY 22S Dipronic with a universal screw with an L/D of 22 was used to manufacture the test parts for the determination of mechanical properties. A standard test mould with a typical dumbbell shaped tensile bar (ISO 527), flexural bar (ISO 178) and impact test specimen (ISO 180) was used.

The temperature settings from the hopper to nozzle were respectively 180, 200, 220, 220 and 220 °C. An injection pressure of 140 bar and a holding pressure of 120 bar was applied during injection. A cooling time of 20 s with a mould temperature of 30 °C was used.

2.4 Mechanical Properties

Tensile properties (ISO 527) were measured using an Instron 3601 dynamometer, with a load cell of 2 kN at a crosshead speed of 50 mm/min. Flexural properties (ISO 178) were measured using an Instron 5,560 dynamometer. Izod impact properties (ISO 180) were determined using a Zwick 5110-100/00. Mechanical property values reported in this paper represent a mean value from measurements on at least five specimens per compound and the according variations are reported.

Statistical analysis of the results was performed with Minitab 15 through either a one-way ANOVA test, with $p = 0.05$ significance level or an independent sample t-test, with the same $p = 0.05$ significance level.

3 Results

3.1 Mixed Polyolefin Stream Properties

The different physical properties of the MPO streams are presented in Table 1. No large differences between the two delivered mixed PO streams can be detected, which indicates that the two MPO streams have a similar composition.

Table 2 shows the mechanical properties of both MPO streams. Once more, no large differences between the values for the two mixed PO streams can be observed.

3.2 Properties of the Different Blends of Virgin and Recycled PE

Figure 1 shows the tensile (left) and flexural (right) modulus of samples with different virgin/sPE ratios. Comparison of the tensile modulus result groups by one-way ANOVA reveals a significant difference in values of tensile modulus ($p = 0.000$) between the five groups. With the addition of larger fraction of recycled

Table 1 Physical properties of the mixed polyolefin streams. Average values are listed ± standard deviation

Property	MPO Hallurec	MPO Ekol
MFI (g/10 min)	10.3 ± 0.3	7.7 ± 1.1
Volatile components (%)	0.002	0.006
Ash content (%)	1.25	2.52
Density (g/cm^3)	0.821	0.894
Static coefficient of friction (−)	0.45 ± 0.10	0.50 ± 0.02
Dynamic coefficient of friction (−)	0.31 ± 0.03	0.41 ± 0.01
Moisture uptake (%)	0.13	0.12
VICAT temperature (°C)	123.3	114.6

Table 2 Mechanical properties of mixed polyolefin streams

Property	MPO Hallurec		MPO Ekol	
	Mean	Variation (%)	Mean	Variation (%)
Tensile strength (N/mm^2)	17.5	3.5	15.4	5.9
Tensile modulus (MPa)	291.7	9.6	300.8	9.7
Strain at break (%)	21.4	12.6	15.6	15.3
Flexural strength (N/mm^2)	27.8	1.6	26.9	4.2
Flexural modulus (MPa)	251.9	2.6	244.2	6.7
Izod impact strength (kJ/m^2)	3.4	13.0	2.5	6.1

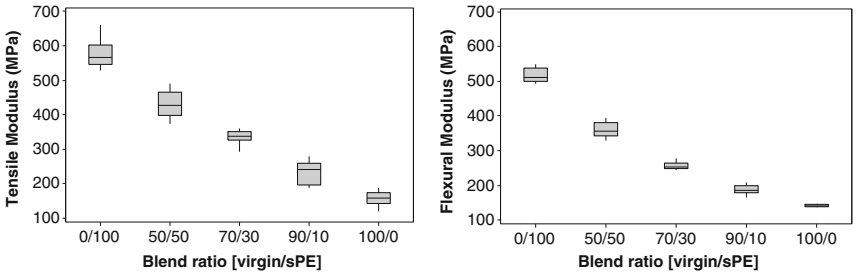

Fig. 1 Tensile (*left*) and flexural (*right*) modulus with different blend ratios virgin/sPE

Table 3 MFI values and volumes of injected moulded parts of the different blend ratios virgin/SPE

Blend ratio (virgin/sPE)	MFI (g/10 min)	V (cm^3)
0/100	0.12 ± 0.02	21.47 ± 0.02
50/50	4.78 ± 0.47	22.18 ± 0.02
70/30	12.51 ± 0.94	22.00 ± 0.02
90/10	24.05 ± 3.52	21.97 ± 0.01
100/0	28.79 ± 4.30	22.07 ± 0.01

sPE, a seemingly linear increase in elastic modulus from that of the virgin PE can be noticed. The same trend is recorded in the corresponding flexural modulus of the different mix ratios. Comparison of these result groups by one-way ANOVA reveals a similar significant difference in values of flexural modulus ($p = 0.000$) between the five groups.

The different MFI's of the mixtures virgin/sPE are shown in Table 3, along with the corresponding volume of the injection moulded parts. The sample with 100 % sPE recycled fraction has a very low MFI of 0.12 g/10 min, which increases with increasing incorporation of virgin material, which has a relatively high MFI of nearly 30 g/10 min.

Finally, Table 4 shows the impact strength of the different mixture ratios. The highest values are recorded for the 100 % virgin and 100 % sPE materials and the impact strength reduces with higher mixture ratios.

Table 4 Izod impact strength with different blend ratios virgin/sPE

Blend ratio (virgin/sPE)	Izod impact (10^{-5} kJ/mm^2)
0/100	2.84 ± 0.25
50/50	0.44 ± 0.03
70/30	0.44 ± 0.05
90/10	2.45 ± 0.42

4 Discussion

The sPE fraction retrieved from the MPO was found to have a remarkably low MFI value, which would make it suitable mostly for extrusion-based processing. Quite likely, the acquired MPO consisted of reground extrusion-based product like foils or bottles. Due to this very viscous flow, the parts injected with 100 % sPE were found to contain somewhat less material than those injected with the blends or virgin PE. The virgin PE used, on the other hand, was chosen specifically for injection moulding and had a quite high MFI, lending a better viscous flow to the blends and permitting a complete filling of the part under holding pressure.

Concerning the mechanical properties of the injection moulded parts, there is no significant difference between the flexural and tensile modulus for the 0/100 ($p = 0.001$), 50/50 ($p = 0.000$), 70/30 ($p = 0.000$) and 90/10 ($p = 0.001$) mixtures. A minor significant difference is noted for the virgin material ($p = 0.073$). This is attributed to the fact that the load is applied transversal to the main polymer chain orientation. It is also noted that the sPE fraction has a significantly higher modulus than the virgin PE and that decrease of this value seems to follow the blending rate between the two polymer fractions. The law of mixtures states that when two substances are mixed, the property of the mixture is a ratio of the properties of each substance, weighted by the proportion of each substance in the mixture. It is mainly used in fibre reinforced composite materials to predict properties at different fibre loadings [20]. This law is given in Eq. 1 with X the property and V the volume fraction of the different materials.

$$X = X_1 V_1 + X_2 V_2 \tag{1}$$

In order to verify whether the virgin/sPE blends follow the law-of-mixtures, the volume fractions of the materials are calculated with the measured densities of the

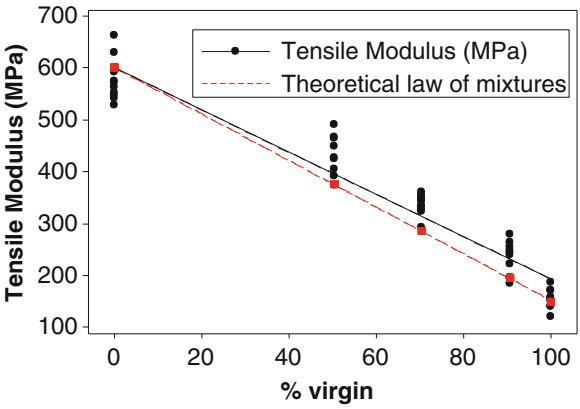

Fig. 2 Comparison between experimental values of the tensile modulus and theoretical values derived from the law-of-mixtures

recylates and a comparison is made in Fig. 2 for the tensile modulus between the experimental results and the theoretical values provided by Eq. 1. It is found that the experimental values correlate very well to those dictated by the law-of-mixtures. The flexural modulus was found to follow the same trend.

The results from the impact testing indicate that the unblended sPE and PE materials have the highest toughness values. A severe reduction of this toughness is noted for the 70/30 and 50/50 blends. This embrittlement is attributed to a phase separation of the composing polymers within the blends. The additional boundaries this induces within the part increase the resistance to plastic deformation and thus reduce the material's ability to absorb the energy from the impact. The effect is less pronounced for the lower blending ratio of 90/10, because the majority of the material matrix remains homogenous PE. This phenomenon is something to be taken into account when designing products for injection moulding with blends containing recycled PO.

As a closing thought, the authors would like to mention that a remaining aspect of recycling PO waste streams is the poor miscibility between the PE and the PP fraction [21]. While this was circumvented in the current study by separating the PE from the MPO, it would mean a significant step for industry if this arduous extraction step could be removed and the recycled MPO could be successfully used 'as is'. Possible solutions include the addition of different compatibilizers such as creating a rubbery interphase while adding EPDM [8, 12], the possibilities of which remain the subject of further study.

5 Conclusions

Two commercially available recycled MPO streams were characterized for their composition and physicochemical properties. It was found that they were of comparable quality. From this MPO stream, the PE fraction was successfully separated by means of a float-sink technique and blended into virgin PE at different ratios. The blends were successfully processed by injection moulding.

It was demonstrated that, while the mechanical properties of blends consisting of recycled sPE and virgin PE follow the law-of-mixtures, the impact strength does not and is strongly affected (reduced) by the presence of different phases within the injection moulded part.

Acknowledgments This study was performed on demand of the Public Waste Agency of Flanders (Openbare Vlaamse Afvalstoffenmaatschappij-OVAM), Belgium. The authors would like to thank Maarten Degroote, Mustafa Erkoç and Marcel Moerman for their assistance with the injection moulding and testing of the materials. An extended version of this manuscript was submitted to the Environmental Engineering and Management Journal.

References

1. PlasticsEurope et al. (2011). Plastics—the Facts 2011. An analysis of European plastics production, demand and recovery for 2010.
2. PlasticsEurope et al. (2010). Plastics—the Facts 2010. An analysis of European plastics production, demand and recovery for 2009.
3. Al-Salem, S. M., Lettieri, P., & Baeyens, J. (2009). Recycling and recovery routes of plastic solid waste (PSW): A review. *Waste Management, 29*(10), 2625–2643.
4. Europe, P.R. (2012). How to boost plastics recycling and increase resource efficiency?
5. Siddique, R., Khatib, J., & Kaur, I. (2008). Use of recycled plastic in concrete: A review. *Waste Management, 28*(10), 1835–1852.
6. OVAM, et al. (2009). Inventarisation separation techniques hard polyolefines in polypropylene (PP) and polyethylene (PE).
7. Bertin, S., & Robin, J. J. (2002). Study and characterization of virgin and recycled LDPE/PP blends. *European Polymer Journal, 38*(11), 2255–2264.
8. Borovanska, I., et al. (2012). Quality assessment of recycled and modified LDPE/PP blends. *Journal of Elastomers and Plastics, 44*(6), 479–497.
9. Brachet, P., et al. (2008). Modification of mechanical properties of recycled polypropylene from post-consumer containers. *Waste Management, 28*(12), 2456–2464.
10. Navarro, R., et al. (2012). Process behavior of compatible polymer blends. *Journal of Applied Polymer Science, 124*(3), 2485–2493.
11. Stangenberg, F., Agren, S., & Karlsson, S. (2004). Quality assessments of recycled plastics by spectroscopy and chromatography. *Chromatographia, 59*(1–2), 101–106.
12. Vilaplana, F., & Karlsson, S. (2008). Quality concepts for the improved use of recycled polymeric materials: A review. *Macromolecular Materials and Engineering, 293*(4), 274–297.
13. Incarnato, L., Scarfato, P., & Acierno, D. (1999). Rheological and mechanical properties of recycled polypropylene. *Polymer Engineering and Science, 39*(4), 749–755.
14. Stromberg, E., & Karlsson, S. (2009). The design of a test protocol to model the degradation of polyolefins during recycling and service life. *Journal of Applied Polymer Science, 112*(3), 1835–1844.
15. Jin, H. Y., et al. (2012). The effect of extensive mechanical recycling on the properties of low density polyethylene. *Polymer Degradation and Stability, 97*(11), 2262–2272.
16. Achilias, D. S., et al. (2008). Recycling techniques of polyolefins from plastic wastes. *Global Nest Journal, 10*(1), 114–122.
17. Jonna, S., & Lyons, J. (2005). Processing and properties of cryogenically milled post-consumer mixed plastic waste. *Polymer Testing, 24*(4), 428–434.
18. White, J. L., & Choi, D. (2004). *Polyolefins: processing, structure development and properties*. Cincinnati: Hanser Gardner Publications.
19. Tall, S. (2000). Recycling of mixed plastic waste: Is separation worthwhile? In: *Institutionen för polymerteknologi*. 2000, Tekniska högskolan i Stockholm: Stockholm, Sweden.
20. Gooch, J. W. (2010). *Encyclopedic dictionary of polymers* (Vol. 2). Berlin: Springer.
21. Sjöqvist, M., & Boldizar, A. (2011). Molecular modification and compatibilization of collected polyethylene. *Journal of Polymers and the Environment, 19*(2), 335–340.

Towards Zero Emissions Furniture

Richard Morris, S. Smith and E. Manzanares

Abstract Staff in the Product Design subject area at the University of Brighton have worked closely with industry over a number of years. One project has required collaboration with business and environment colleagues to look at the role of environmental benchmarking in the furniture industry. The two year project was sponsored by the British Furniture Manufacturers Association and the UK government's Department of Trade and Industry (subsequently the Technology Strategy Board) and involved working with a number of leading UK furniture companies. The project objectives were to undertake an environmental assessment of a range of furniture products, one each for five companies, and to subsequently redesign each item with a view to reducing its energy emissions. The aim was to demonstrate to these, and other companies within the British Furniture Manufacturers Association (BFMA), the purpose and issues in applying environmental benchmarking in their design work. The outcomes were contained in a Brighton project report (Morris et al. in Innovating Domestic and Office Furniture through the application of Environmental Benchmarking. 2009, [5]) and released in a summary dissemination document by the BFMA (Zero Emissions from Office, Contract and Kitchen Furniture. 2009, [6]) which showed that; Significant reductions in emissions could be achieved, that the areas of high environmental impact are however, not always obvious and can be counter intuitive, and that there is no, one formulaic redesign solution. This paper takes the opportunity to release more publicly a fuller explanation of the Brighton outcomes and includes a more recent update of the impact the project has had on the environmental design practice of the partner furniture companies.

Keywords Sustainable design · Product design · Life cycle analysis · Environmental benchmarking

R. Morris (✉) · S. Smith · E. Manzanares
University of Brighton, Brighton, UK
e-mail: R.D.Morris@brighton.ac.uk

I. Visa (ed.), *Sustainable Energy in the Built Environment - Steps Towards nZEB*,
Springer Proceedings in Energy, DOI 10.1007/978-3-319-09707-7_36

1 Introduction

There is widespread and growing acceptance that human activity, especially industrial production, is contributing to a deterioration of the environmental welfare of the planet. Despite this relatively few commercial organisations are implementing the kind of changes that are needed to slow down, halt or even reverse this damage. Many people have attributed this in part to unsustainable lifestyles involving issues of consumerism and an economic system built around perpetual growth. It can however, be difficult for organisations to know exactly how to react within this socio-economic system. Immediate commercial priorities often outweigh longer term environmental considerations whilst unilateral actions can be regarded as a form of commercial suicide.

Environmental benchmarking offers companies the opportunity to undertake a positive course of action by identifying the specific damaging environmental impacts a product or service has which designers can then address. Life Cycle Analysis (or Life Cycle Assessment, LCA) is commonly agreed to be a superior benchmarking technique because its approach is systematic and provides a comprehensive and holistic analysis of impacts and their complex interactions.

There is however, a limited range of case study material available within the product context that provides information on LCA application, role and performance. This article therefore aims to add to the body of knowledge on the use of Life Cycle Analysis and its effects on design and design management. It outlines a project entailing the Life Cycle Analysis and redesign of five furniture products undertaken by the University of Brighton in conjunction with commercial partners. The project was undertaken on behalf of the British Furniture Manufacturers Association (BFMA) and what was at the outset the United Kingdom's Department of Trade and Industry but which subsequently became for the Technology Strategy Board.

2 Life Cycle Analysis

The original project brief proposed an environmental rucksack benchmarking technique which broadly consigns a products accumulated carbon loads into a metaphoric rucksack which it carries throughout its life. The design and manufacture of furniture products however, incorporates a broad spectrum of activity and it is all too easy to make a design change which looks good on paper in one area but which has a deleterious knock on effect at another stage. The project team therefore adopted Life Cycle Analysis (LCA). The original project and reports were completed before the publication of PAS 2050 [1] but the project is consistent with the PAS 2050 methodology, language and references to LCA standards, and conformed to the LCA ISO standard 14040. The methodology adopts four distinct stages:

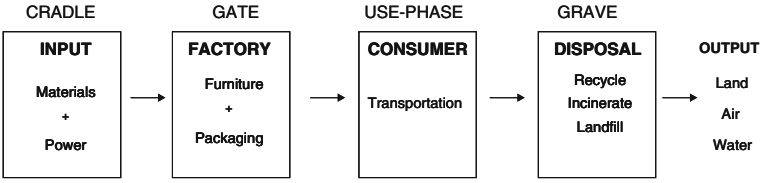

Fig. 1 Boundary subsystem schematic

(i) ISO 14041: Goal and Scope definition and inventory analysis

A Functional Unit and the System Boundary was defined for each product. The functional unit refers to the purpose of the product such as seating, storage or other function. The boundaries are defined as follows (Fig. 1):

Cradle identifies the starting materials for product and packaging and their allocation to production and power (both electricity and gas) for the manufacturing process.

Gate identifies the manufacturing processes of the factory, including packaging and their allocations.

Use-phase or consumer includes transportation. Unlike appliances or electrical goods, there is no further power demand on most furniture and so the use-phase is simplified.

Grave identifies the disposal scenarios for the unit's end-of-life (EOL) and the waste associated with manufacturing (Fig. 1).

The Goal was to identify which materials, processes and disposal methods contribute the largest negative impact so that these can be minimized and, if possible, replaced with more benign alternatives.

ISO 14041: Life cycle Inventory Record

An Inventory Record of environmental and production data was obtained for each of the five selected products. In one case (study iv) the company was using environmental management systems and this data was readily available. In other cases the data had to be ascertained from first hand methods. Generally though only data that was immediately available was used and the LCA boundaries defined accordingly. SimaPro 7 software [2] and its databases, including Ecoinvent, were then used to analyse the Inventory Record for each of the following ten Impact Categories; abiotic depletion, global warming, ozone layer depletion, human toxicity, fresh water aquatic ecotoxicity, marine aquatic ecotoxicity, terrestrial ecotoxicity, photochemical oxidation, acidification and eutrophication.

(ii) ISO 14042: Life cycle impact assessment

SimaPro version 7 software and Ecoinvent database were used to process the data and measure environmental impacts in terms of material use and emissions. The data are allocated on a mass basis based on their contribution to the mass sum of product and co-products produced in manufacturing. This requires much consideration, for example the database is principally European and wherever possible data, inclusive of UK input, was used with energy recovery corrected to reflect UK

electricity mix and emissions compliant with Defra Guidelines [3]. Similar assumptions were required in the assessment of where materials start from, average journeys to customers, fuel types and disposal scenarios. Method CML 2 baseline 2000 was used, an updated method from the Dutch Guide to LCA, published in 1992 by the Centre of Environmental Science (CML). This method is also referred to as "CML 1992", the NOH method or Heijungs et al. [4].

(iii) ISO 14043: Interpretation

After the completion of the calculations, results were normalised, tabularised and graphed in order to aid discussions within the project and design teams. The measure of climate change impact is the global warming potential (GWP) in kg_CO_2_eq. In several environmental impact analyses, a streamlined LCA is considered. This is an analysis based on GWP from the material inventory, production, use-phase and end-of-life disposal. The outcomes of the LCA (and subsequent) redesign work were validated by independent consultants PERA Technology.

3 Re-design

The LCA highlighted those areas where products were causing the greatest environmental damage and this information was then used to guide/inform the development of new design concepts by University of Brighton design staff and partner companies. After the products had been redesigned, their environmental impact was recalculated using the same software and parameters as before. Further analysis and discussion to took place to find those ideas that were most effective and practicable. These findings were reported within the internal project report [5] and summarized within the overall project dissemination report [6] but are outlined in more detail as follows (Figs. 2–5):

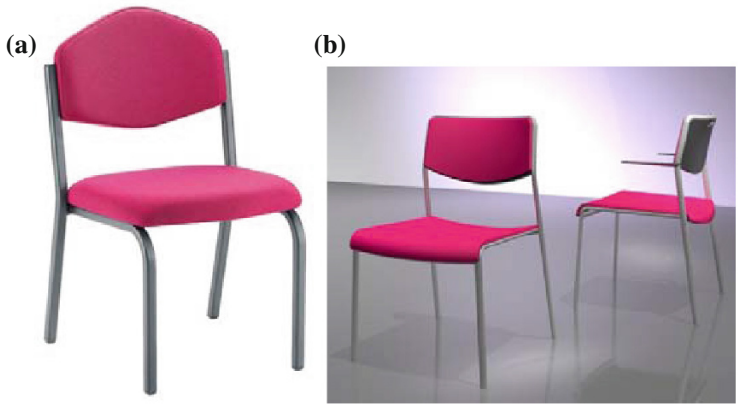

Fig. 2 Stacking chair **a** before re-design **b** after re-design

i. Stacking Chair

The LCA for the stacking chair highlighted the production phase as dominating the products environmental impact through energy consumption. This presented a significant challenge for improvement because the chair examined was otherwise very efficient in its use of materials and processes. The redesign process did not therefore seek to address practical production issues, but focussed instead on its preponderance for 'early retirement' when still fit for purpose.

The new design consequently used similar materials and technology but employed elliptical rather than square tubular steel. Though not as stiff as the square section, this tube has an elegance and softness that the original does not and enhances its emotional appeal. The tube is also bent across the top edge of the back to reduce wear and tear on the cover fabric. The fabric does not need stitching. The redesigned product uses a curved seat board to enhance comfort. The pressed shape added to the strength of the seat board, so a thinner section is possible, reducing materials. Enhanced comfort also means that foam depth can be reduced. Fixings are made in the same way as the original version, but are now covered with moulded plastic shrouds. These add to the financial and environmental cost, but also enhance user appeal—the outer back shroud has a molded handle for lifting and the under-seat molding helps efficient stacking without leaving an imprint in the foam of the chair below (Fig. 2).

The environmental benefits of this redesign cannot be demonstrated numerically, and in fact in fact, the values for the Global Warming Potential of the new chair are slightly higher than the original. The aim however, was to improve the product's aesthetic appeal: its comfort, its visual and tactile qualities; in short: its desirability. If products are more appealing to be with, to use and to own, there is a an increased chance that they will be nurtured and cared for, so extending their useful life and squeezing more value out of the environmental resources that were used when they were made. There is also a greater likelihood that the product will be renovated and reused rather than discarded and dumped.

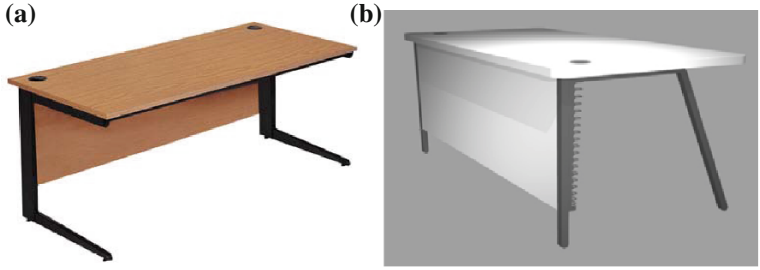

Fig. 3 Office desk **a** before re-design **b** after re-design

ii. **Office Desk**

The desk is part of a much larger range of desking, tables, storage and screen based furniture aimed at the contract office market and call centres. The desk itself is available in a wide variety of surface finishes and colours and can be fitted with optional cable management or storage solutions. The current model has a cantilevered steel end frame with a 25 mm melamine faced chipboard top and 15 mm modesty panel. The panels are edged with an ABS lipping. The LCA noted high levels of waste recycling particularly from heat recovery by burning wood waste. The production process however, included high impact contributions mostly from the degreaser and powder coating components. The contribution from these processes is greater the than energy consumption from gas and electricity.

To reduce this effect the re-design concentrated on the cantilever features that contributed significantly to this effect. Although the cantilever end frame is something of an industry standard it is not structurally efficient as more material is required to resist the downward loads. The revised product consequently stands on four legs. Since most of the load is now transferred directly downwards, it is possible to reduce the weight and section of the frame. There is not a conventional cable management system, but there are two access holes in the top and a moulded 'cable tidy' attached to the inside of the back legs. The leg frame and rails are made from 36 mm square section ERW tubular steel. Each leg frame has one weld and one bend (to reduce energy). The top and front panel are made from Eurolight board by Egger. This is a 38 mm thick board with a honeycomb core made of recycled paper and outer skins of 8 mm chipboard. The edging is extruded from ABS. The revised product weights 31 kg compared to the original design of 48 kg, with a fivefold reduction in global warming potential (Fig. 3).

iii. **Tub Chair**

It was difficult to secure inventory data for the tub chair so the LCA focused particularly on the effects of material production. Whilst these are predominantly natural materials, it was surprising to see the impact effects caused by the processes needed to extract and prepare these materials. As this model is currently selling very

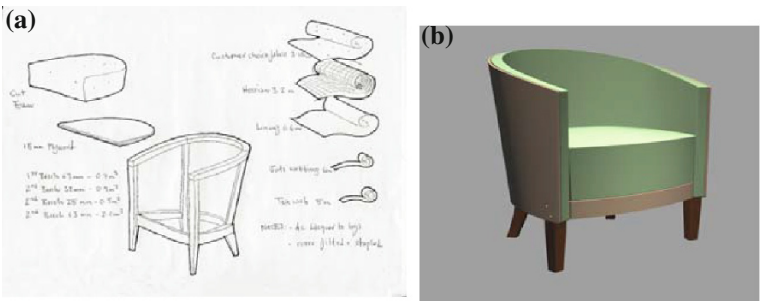

Fig. 4 Tub chair **a** before re-design **b** after re-design

well, the redesign then aimed to improve the environmental profile of the chair without significantly affecting its outward appearance, strength or price. There were consequently substantial alterations to the internal structure of the product. The traditional timber frame has been replaced with a pressed beech shell. Solid show wood legs are fixed to the shell using bolts and T-nuts. The seat board is pressed from timber chips, which are made from harvested forest thinnings. The seat foam is moulded rather than cut from slab foam, so there is no waste in production. A wax finish to the legs is used to avoid the waste due to over-spray and cleaning out spray guns. The fabric is by Design Tex, which has a lower environmental footprint than conventional fabrics. It can be removed by the customer for washing, repair or replacement. Not only does this feature lengthen the product's life, it also adds to its appeal, so it might contribute to additional sales.

The redesigned chair looks, feels and 'sits' just like the existing model. It also offers similar performance levels in terms of strength, stability and durability, so the proposed changes should not have any detrimental effect on sales. The new version offers a number of environmental gains over the existing model: it is lighter and uses less material: the new frame uses 0.0224 m^3 as opposed to 0.042 m^3 in the original—a saving of 0.0196 m^3 per chair. There is no waste of foam or finishing material and it can be easily repaired and serviced during use. The new model will be supplied with two sets of removable covers, enabling customers to clean and replace at regular intervals. It will also mean that customers can renew covers (say, if the décor of the room is changed) without having to send the product back to the factory. This will hopefully extend the product's useful life. All of the components are fixed to one another, rather than glued, so making it easier to dismantle and recycle them when the chair is finally discarded. It will also be easier to repair if damaged (e.g. if a leg is broken, it could be unbolted and replaced.) These changes effect improvement in all of the impact categories with a threefold saving in global warming potential (Fig. 4).

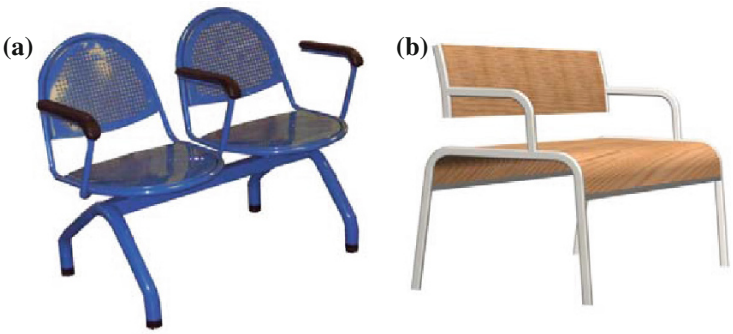

Fig. 5 Public seating **a** before re-design **b** after re-design

iv. **Public Seating**

This public seat comprises of individual seat and back units which are fixed to beams that vary in length to accommodate two, three or four seats (Fig. 5). The seats can be interspersed with tables and optional armrests are also available on request. The units can either be freestanding or fixed to the floor. The structural elements of the seat and back are made from round ERW tubular steel. Beams are either round or triangular steel tube. They are available with either a powder coated or polished chrome finish. The seat and back units can be supplied in one of three alternative materials: upholstered with foam and fabric, polished plywood or perforated steel mesh for a more durable application. Tables are 25 mm MDF with a laminated surface. The soft-topped arm is moulded in polyurethane. The LCA highlighted the effects from the metals for cutting, welding, degreasing and powder coating which will incur around 9 kg_CO_2_eq. Whilst there is some recycling, there was clear scope to reduce the environmental impact through a change and reduction in material type.

The new design is a linear bench, rather than individual seat units. The bench can be offered in a variety of lengths. The seat and back are pressed from constructional beech veneers, faced with a choice of face veneers. These panels can also be upholstered with foam and fabric if required. The end frames are fabricated from flat-sided oval tube 25 × 15 mm. The tubes are bent, welded and dressed before being finished with either powder coated polyester or chrome (Fig. 5).

This redesign project demonstrates the benefit of starting with a clean slate as opposed to modifying an existing product. The company have used this opportunity to develop a new product that is not only environmentally sounder (a 45-fold improvement), it is also sleeker, more user friendly and cheaper. It is better for the environment (reduced emissions), better for the company (improved sales) and better for the user (a more comfortable, versatile and attractive product). This has all been made possible by breaking with the convention of 'beam seating' that has been an industry standard for the last 30 years or so. Beam seating is however, 'over' designed for maximum occupancy. By contrast, the new design is slender and structurally efficient. The shapes that have been pressed into the laminated seat and back maximise stiffness with the minimum material thickness. Using timber for these structural components also helps reduce the product's carbon footprint as timber is renewable and steel is not. The oval section of the end frame has been specified to achieve the greatest possible strength whilst presenting the slimmest possible profile from the front view.

v. **Kitchen unit**

The company is a major supplier of kitchens to the new build housing market and sells directly to the builder. The functional unit is a kitchen cabinet carcass that forms part of a layout of 13 units (exclusive of appliances). The layout consist of a base corner, base, corner sink, base unit, base oven, cornice, flyend, and 5 items for wall and boiler. The weight of these units varies from 20 to 40 kg, but combined the 13 unit's kitchen layout weight is ∼340 kg. The functional unit is comprised of 98 % wood, and a typical composition of material is shown in Table 1.

Table 1 Typical kitchen unit composition

Material	Amount	Unit
Wood	328.8	kg
Steel	5.5	kg
Plastic	0.6	kg
Others	0.1	kg
Electricity	120	kWh

Units are assembled in the company and then wrapped in PE film and each unit separated for stacking using cardboard. They are then transported by road to the customer and in this case, the key to reducing emissions is to redesign the kitchen units for flat pack assembly. It is estimated that transport can be reduced by five times, a savings in both emission and transport cost which will potentially reduce the emission from 29 to 6 kg_CO^2_eq. The use of KD fixings (CAM: Minifix 15 mm housing, Hafele reference 262.26.073, BOLT: Minifix 24 mm connecting bolt, Hafele reference 262.27.010) has been identified as the necessary design changes.

4 Conclusions

All of the products selected were considered well designed, efficient and fit for purpose having often evolved over many years and this emphasised the challenges designers face. Improvements were not immediately obvious and environmental benchmarking was essential in revealing the areas driving environment damage.

Good environmental management systems combined with 3D CAD were pivotal in allowing data for the LCA to be collected and manipulated relatively easily. Once collated the information provided a focus for the design teams. It was also pivotal in giving the designers the confidence to act as the solutions were sometimes counter intuitive. For example, wood is carbon neutral and reducing its content from a product can make the products environmental impact worse. A re-working of the benchmarking technique was then essential to qualify the design changes. All of this required good communication between parties that included environmental and materials scientists, designers, information systems staff and supply chain experts.

It was not possible to identify ‘standard’ design solutions for reducing environmental impact because each of the five furniture products assessed required its own, unique re-design. However, some general issues emerged that might help within the thinking process; minimising weight, using recycled materials, using wood instead of metal, minimising waste. Whilst these might seem obvious, under the microscope of an LCA they seemed to become acutely more important and relevant.

There has been a similar mixed legacy to the project within each company:

The company making the stacking chair (study i) has adopted an overarching environmental policy utilizing ISO14001 and EMS teams to make company-wide changes in fastening and cutting processes that have reduced toxicity, energy and materials. Benchmarking per product is however, considered to be problematic because of the diversity of customers bases (making EOL data difficult) and because industry standard comparisons are skewed by the nature and geography of each company. They await an industry wide formula.

The desking company (study ii) no longer trades but its range has been bought out by another company where no current environmental product benchmarking is reported.

The company making the public seating (study iv) cites the project as having raised the profile of the environment amongst its designers and helped them to win an industry award and new business. Benchmarking has however, not become a routine practice within the company as it is seen as being an expensive activity and there is no LCA undertaken. Environmental consideration is more associated with recycling as a cost saving activity rather than an environmental practice.

The kitchen furniture company (study v) set up a further 2 year project under a UK government sponsored Knowledge Transfer Partnership (KTP) scheme to try and apply the outcomes of the project to the full range of company products. There were however, mixed outcomes and the project was not completed.

The conclusions from this company review are, inevitably, that whilst LCA and benchmarking offers tangible and visible benefits to both economic and environmental baselines, there remains much work to have this practice adopted widely within industry.

Acknowledgments Thanks to Jeff Readman at the University of Brighton Centre for Research into Innovation Management who initiated and contributed to the project and the research, and to Professor Marie Harder of the University of Brighton Waste Energy Research Group who also supported the project. The university of Brighton project team are grateful to the industrial partners for their co-operation by providing the information, time, resources, ideas and images required to support the project. The support of the British Furniture Manufacturers Association and the DTI/TSB are also acknowledged.

References

1. PAS2050. (2008). *Specification for the assessment of the life cycle greenhouse gas emissions of goods and services*. British Standards Institution.
2. SimaPro 7. (2004). http://www.pre.nl/lcasearch. *SimaPro database manual, methods library*. Written by PRé Consultants: Mark Goedkoop, Michiel Oele, Suzanne Effting. Report version: 2.0, June 2004.
3. DEFRA. (2005). *Guidelines for company reporting on greenhouse gas emissions*. Defra Guidelines July 2005 at http://www.defra.gov.uk/environment/business/envrp/pdf/envrpgas-annexes.pdf

4. Heijungs, R., et al. (1992). Environmental life cycle assessment of products, Guide, October 1992 CML, Leiden, The Netherlands, NOH report 9266. The new CML 2 baseline method elaborates the problem-oriented (midpoint) approach. The method in SimaPro 5 is based on the spreadsheet (version 2.02) as published on the CML web site.
5. Morris, R., Taylor, E., Readman, J., Smith, S., Harder, M. (2009). *Innovating domestic and office furniture through the application of environmental benchmarking*. University of Brighton Project final report, 20 March 2009.
6. Zero Emissions from Office, Contract and Kitchen Furniture. (2009). *The British furniture manufacturers trade association*. (http://www.bfm.org.uk/trade/news/projects/projects.html and at http://www.abromhead.co.uk/userfiles/Final%20project%20report%20-%20BFM%20ZEEE8.pdf)

Ecodesign Education—A Necessity Towards Sustainable Products

Lucian Bârsan and Anca Bârsan

Abstract Ecodesigning a product means a "rethinking" of the product, in order to diminish its environmental impact, but preserving, at least, its quality and cost. The product environmental impact has to be assessed during its entire lifecycle (raw materials, manufacturing, transport and distribution, use, end of life), this assessment offering to the design team some information about the design requirements for their product, in order to become a more environmental friendly one. The paper presents the importance and efficiency of the integrative/preventive measures embodied in a product, as part of the ecodesign action compared to the additive/curative measures that are usually considered by the companies. The paper presents also, shortly, a module of Ecodesign, introduced in the engineering curricula at Transilvania University of Brasov, as a response the new requirements of the labour market due to the environment legislation with impact on product design.

Keywords Lifecycle of a product · Ecodesign · Design for disassembly · Design for recycling · Product design

1 Introduction

In the early 90s, the concepts of sustainability and sustainable development became of a great interest and, related to it, the necessity of evaluating the product and the product effects/impacts on the environment over a long period of time. This period of time expends from the early stage of raw material extraction continuing with the production, distribution, use, and disposal stages. This sequence of stages was named "life of a product" and reflects the fact that any product is being born (designed and produced), have a life (use/consumption) and finally ends its life (being disposed).

L. Bârsan · A. Bârsan (✉)
Transilvania University of Brasov, Eroilor 29, 500036 Brasov, Romania
e-mail: abarsan@unitbv.ro

L. Bârsan
e-mail: lbarsan@unitbv.ro

I. Visa (ed.), *Sustainable Energy in the Built Environment - Steps Towards nZEB*,
Springer Proceedings in Energy, DOI 10.1007/978-3-319-09707-7_37

The possibilities of reusing, reconditioning or upgrading the product and recycling the raw materials from a product's parts or incinerating the product with energy recovery created the possibility of extending the life of the product, creating the concept of "life cycle of a product" [1, 2].

At the end of life of a product, the success of the recovery and reprocessing of components and materials, both on technical and economical levels, is not only dependent on the applied recycling technology but also on the design of a product.

The year 2014 marks the end of the United Nations Decade of Education for Sustainable Development (2005–2014, DESD). The goal of this decade, for which UNESCO is the lead agency, was "to integrate the principles, values, and practices of sustainable development into all aspects of education and learning. This educational effort will encourage changes in behavior that will create a more sustainable future in terms of environmental integrity, economic viability, and a just society for present and future generations" [3].

Transilvania University of Brasov celebrates this decade by introducing in engineering courses several modules related to sustainable development, fulfilling the UNESCO decade goals and contributing to enlarge the number of educated graduates in this field. Ecodesign, one of the subjects recently introduced in engineering curricula from Transilvania University of Brasov, intends to facilitate the acquiring of different competencies and knowledge by the students, in the field of designing environmental friendly products. Considering the requirements on product design developed in the last decades by the European Commission, it can be estimated that there will be an increasing demand of engineers educated in the approach of ecodesign in the future. These students, trained in the field of ecodesign, as future engineers, will face better to the labor market requirements, facilitating industries to meet the standards required by this new legislation.

The paper presents the importance of a good "ecodesign" of a product, when some efficient integrated measured are developed related to a new product, and its benefits compared to the case in which just a few curative measures for the same product are considered, and starting from this point forward, the necessary content of en ecodesign model taught in engineering courses of Industrial Design from Transilvania University of Brasov.

2 Ecodesigning a Product

Each stage of a product lifecycle (raw materials, manufacturing, transport and distribution, use, end of life) in order to be fulfilled, requires material and energy resources. During and after the development of the specific activities of the stage, beside the product at the level according the lifecycle stage, wastes are disposed and emissions are released in the environment.

Most manufacturing companies are usually concerned with the products environmental impact, but they are primarily focused on manufacturing operations and the operating life of a product, considered that some additive/curative measures

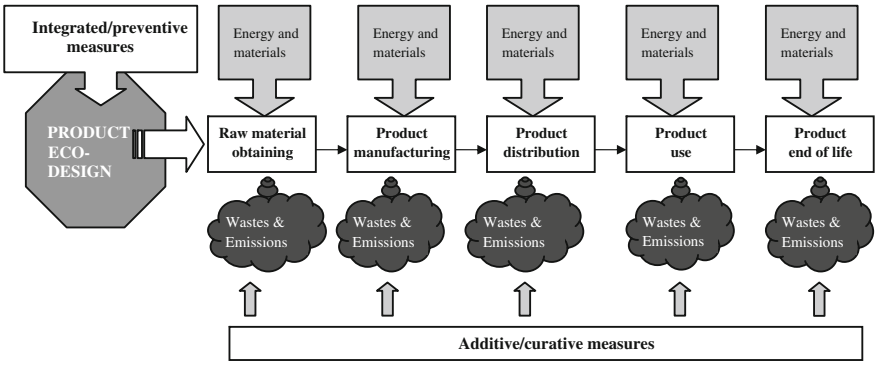

Fig. 1 The lifecycle of a product

(recycling, reclaiming, waste disposal, decreasing of emissions) are sufficient for obtaining a more environmental friendly product.

Better results could be achieved by the company with respect to the environment, but also on economical level, by developing a new design for the product they are manufacturing, in order to use less material and energy resources, this new design having also at its basis the design for reuse, design for recycling and the design for durability. These tools are considered integrated/preventive measures (see Fig. 1). The impact of these measures, considered in the product design process, would be usually significant, with direct benefits on the materials and energy needed for the product, during its entire lifecycle (see Fig. 2). Implicitly, the waste and emissions would be also reduced by implementing the integrated measures in

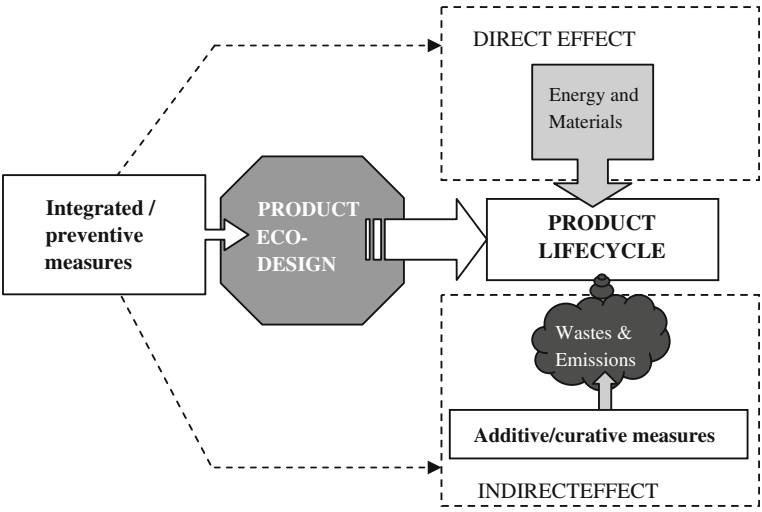

Fig. 2 The effects of the integrated/preventive measures in ecodesign

the design process. Unfortunately, usually, the designing stage of a product rarely involves a crucial dimension for reuse, recycling or increasing the durability of a product [4]. Designing a product to facilitate reusing, recycling or increasing its usage stage represents an important way to reduce the product impact on the environment, significant amounts of material and energy being saved and, in the same time, wastes and emissions being reduced.

All products, be they refrigerators, beverage containers, office chairs or telephones, contribute to a range of environmental problems, like air, water and land pollution and resource depletion with their consequences, global warming, ozone layer depletion, land degradation, reduced biodiversity, acidification, solid waste. Ecodesign is an approach to 'designing-out' as many environmental problems as possible, whilst still producing a high quality, cost effective product. It represents, in fact, the whole of the integrated/preventive measures which can be used in the design process to obtain a more environmental friendly product. Also, it is necessary to underline that ecodesign facilitates the implementing of the additive/curative measures as recycling, reclaiming, waste disposal and emission reducing.

Considering the large range of environmental problems created by products there is also a large variety of strategies for ecodesign, like:

- Minimising the material resources for a product (material content, scraps and discarded material, operational material, package);
- Minimising the energy resources for a product;
- Selecting low impact resources and processes (non-toxic and harmless resources, renewable and bio-compatible resources);
- Product lifetime optimisation (useful lifetime facilitating maintenance, re-use, repair, remanufacturing, up-grading, adaptability);
- Increasing the lifespan of materials;
- Facilitating disassembling (reducing and facilitating operations of disassembly and separation, reversible joining systems, engaging permanent joining systems that can be easily opened).

A product ecodesign is a complex process coming as an answer to the market new requirements regarding the environment protection. Its goal is—that after a product analyse of the environmental impact, using the impact assessment matrix (MET), the EcoReDesign strategy wheel, or a LCA report—to provide the engineer some creative answers to those impacts.

This complex process is expected to be carried on by educated in the field engineers, therefore—the necessity of enrichment of the engineering curricula from universities with an Ecodesign module. In Transilvania University of Brasov, this module was developed at European level in an Erasmus curriculum development project and is taught starting with 2007, trying to be improved and updated year by year, according to the new introduced pieces of legislation affecting the product design, or to new research in the field of materials, technology, energy.

3 The Ecodesign Module Description

After analysing the study of ecodesign in the high education institutions in Europe some conclusions resulted:

- Ecodesign is mainly taught in universities at postgraduate level (e.g., Belgium, Spain, Germany, Italy).
- There are only few countries (Austria, UK, The Netherlands, France, Sweden), where there are modules of ecodesign included in the undergraduate level curricula and only in one or two of these (e.g., The Netherlands), a reasonable percentage (50 % or more) of the students at educational institutes for designers were taught basic ecodesign.
- In almost all the European countries, students who follow other educational trajectories (e.g. engineering) and who well end up in design jobs in industry may never get any training in ecodesign.

Summarizing, it must be concluded that students in technical educational trajectories (who in their future career may be involved in taking design decisions) receive no ecodesign education.

Considering this situation of the ecodesign study in undergraduate technical curricula in the European high education institutions and the labour market needs for engineers and designers with a wide eco-perspective, in Transilvania University of Brasov, Romania, was made the decision to start the enrichment of the engineering courses curricula with a module of ecodesign.

The Ecodesign module is taught in the final year of undergraduate engineering study, as lecture and a project development. The main objective of the module consists in teaching of design principles considering the environment constrains [2]. The students will be taught to model the life cycle of a product, to evaluate it by using appropriate software (EcoIt 99, SimaPro 7) and to give some solutions for the product design in order to become more environmentally friendly. The content of the Ecodesign module is briefly presented in Table 1.

By attending the Ecodesign module, the students acquire different competencies like: cognitive competencies (ecodesign, sustainable development, life cycle of a product ecodesign principles, related legislation), practical competencies (to use an appropriate software in order to evaluate a product impact on the environment, to interpret the results of the evaluation and to adopt the right improvement strategy) and communication and relationship competencies (to use correctly the specific terms and to get used with the work in teams).

4 Results of Ecodesign Module Implementing

a. In Romania, pro-environmental behavior has been a minor subject of concerns for the society and especially for companies due to the fact that environmental problems are still not widely spread.

Table 1 The content of the ecodesign module

Ecodesign module	
Lecture content	Project content
Why ecodesign? (ecodesign motivation, some definitions) **Environment in product life cycle** (the environmental impact of human activities, the environmental impact of a product) **Eco-alternatives in product life cycle** (renewable energy sources, raw materials, manufacturing, transport, product use, product end of life options) **Designing eco-products** (design to minimize material usage, design for disassembly, design for remanufacture, design for waste minimisation, design to minimize hazardous materials, design for energy efficiency) **Eco-product management** (legislation supporting eco-products, managing eco-product development, eco-labeling) **Ecodesign perspectives**	The students choose a product for which they will model and assess the lifecycle. After analyzing and interpreting the results of product lifecycle assessment, they will recommend solutions to improve its design in order to become a more environmental friendly product The project activities are developed as it follows: 1. Product introducing and analyzing; 2. Modeling the lifecycle of the chosen product 3. Evaluating the environmental impact of the chosen product 4. Identifying the suitable strategies to improve the product environmental impact 5. EcoReDesign of the chosen product

In 2012, after the Ecodesign module implementing for the engineering courses of Industrial Design, in Transilvania University of Brasov, an exploratory and comparative research was developed [5]. The aim of this research was to study the pro-environmental attitudes and behavior of the students who had had in the curriculum the Ecodesign module compared with the students who hadn't. The study was carried on 112 students and the conclusion was that the students that acquire environmental knowledge during their university studies are more aware of the threats towards the environment. It was just a first step, a survey regarding our graduates activity in companies, regarding their ecodesign knowledge and skills, has to follow.

b. After studying the Ecodesign module, the engineering students proved a better understanding about the relationship between their design for a product and its effect on the environment. They are apprised about the necessity of evaluating this effect on the entire lifecycle of their product, the tools to evaluate it and about the possible solution to be taken in the design process and their benefits upon the product impact on the environment. In the last years, in most of the final projects of our graduates, aspects regarding measures to decrease the environmental impact of the products they are designing are considered.
c. By implementing the ecodesign principles, the small or larger companies will be able to improve continuously the processes in relation to product development and meantime to achieve the legal requirements regarding the environment.

This improvement can be obtained by the companies, by using the appropriate human resources. These human resources might come from the graduates, beneficiaries of an ecodesign education. They are expected to have knowledge and a new

portfolio of skills in the field of ecodesign as part of sustainable development, facing much better the demands of the companies, implementing an environmental product policy.

References

1. European Commission. (2010). *EUROPE 2020. A strategy for smart, sustainable and inclusive growth.* Brussels.
2. Bârsan, A., Bârsan, L. (2007). *Ecodesign for sustainable development. Volume 1. Fundamentals*. Brasov, Romania: Transilvania University of Brasov Press, ISBN 978-973-598-104-4.
3. http://www.unesco.org/new/en/education/themes/leading-the-international-agenda/education-for-sustainable-development/. Accessed March, 2014.
4. Reid, A., Miedzinski, M. (2008). *Eco-innovation. Final report for sectoral innovation watch*. www.technopolis-group.com. May, 2008. Accessed March, 2014.
5. Pavalache, M., Bârsan, A., Truța, C. (2012). The locus of control as a psycho-social determinant of pro-environmental behaviour. In *World Conference on Psychology, Counselling and Guidance, Izmir*, 09–12 May 2012, Elsevier Ltd. ISSN 1877-0428.

Novel Rubber—Plastics Composites Fully Based on Recycled Materials

Cristina Cazan, Mihaela Cosnita, Maria Visa and Anca Duta

Abstract The paper presents novel composite materials fully based on recycled materials: tire rubber, plastics (polyethylene terephthalate—PET, high-density polyethylene—HDPE), fly ash and wood sawdust. A study on the components' compatibility and interface adhesion is presented. The optimized composites have recorded good mechanical properties (tensile strength and compression strength) and dimensionally stability in various working environments. Materials suitable for indoor or/and out-door applications can be designed and obtained by an optimal choice of the composition and processing parameters, giving use to wastes and reducing the environmental burden.

Keywords Recycling · PET · Rubber · Wood · Composite

1 Introduction

The main problem associated with waste rubber recycling (especially tire powder) and plastic waste is the uneven degradation undergone by the polymeric components during their lifetime, resulting in quite various compositions. Consequently, new strategies have to be developed to use wastes as second raw materials for novel products, with good and controlled characteristics. Blending recycled rubber with plastic materials represents thus an attractive alternative to obtain composites with optimized properties.

In current processing, plastic/rubber composites are reinforced by the addition of filler materials to improve the physical-chemical and mechanical properties, while reducing their cost. Different types of organic/inorganic fillers were reported, such as polymers or metallic oxides. The insertion of metallic oxides as reinforcing agent

C. Cazan (✉) · M. Cosnita · M. Visa · A. Duta
Renewable Energy Systems and Recycling R&D Centre, RES-REC, Transilvania University of Brasov, Eroilor 29, 500036 Brasov, Romania
e-mail: c.vladuta@unitbv.ro

I. Visa (ed.), *Sustainable Energy in the Built Environment - Steps Towards nZEB*, Springer Proceedings in Energy, DOI 10.1007/978-3-319-09707-7_38

represents a new sustainable trend to improve the mechanical performance of the polymeric composites [1].

A series of studies showed that by inserting inorganic filler (SiO_2, TiO_2, CaO, ZnO), inorganic/organic interfaces are formed, which finally led to a complex optimization of the composites' properties such as strength and Young s modulus, dimensional stability, heat resistance [2, 3]. Chen et al. have reported an increase of the glass temperature transition corresponding to the polymeric matrix, when inorganic nanoparticles are introduced in polymeric blends. This is a consequence of the interactions between nanoparticles and the macromolecular chains when a reduced mobility of the polymeric chains around the nanoparticles is obtained [4, 5]. Many reports are on silica nanoparticles addition: composites with SiO_2 inserted in the polymeric matrix were reported as having a slight decrease in the elongation at break and a significant increase of the Young modulus (27 % upon 6 wt% SiO_2 addition) [6]; silica nanoparticles (1 wt%) were alsoo used as filler in composites with polypropylene (PP). The surface activation of the silica nanoparticles was done with sodium hydroxide (NaOH) solution. The tensile strength, tensile modulus and impact strength of the nanosilica/PP composites were improved by activating the filler's surface [7]. These additives will be further found in the wastes; supplementary addition of fillers could also be a path for controlling the properties of the wastes-based composites.

When targeting the development of novel composites fully based on wastes, also these additives should fall in the same category. Fly ash (FA) is a waste produced in huge amounts in combined heat and power plants (CHP) by burning coal. Currently, FA is used by the cement and concrete industries (about 7 % from the annual world production of fly ash). In terms of composition, FA includes in substantial amounts silicon dioxide (SiO_2) (above 50 %, both amorphous and crystalline), alumina and iron oxides, along with calcium oxide, thus it could be used as filler in composite materials for improving the mechanical properties. By incorporating FA in innovative composite materials is an exceptional way to "Build Green", without compromising quality or cost. Several studies describe the possibility to obtain materials using waste plastic materials and fly ash as filler. Fly ash can be valuable reinforcing filler for HDPE, especially when its size is reduced to a nano level [8, 9]. Test results show that unmodified ultra-fine FA is homodipersed in HDPE matrix without aggregation and the tensile strength is slightly reduced (from 21.76 to 19.65 MPa), while the notched impact strength increases from original (27.64 to 60.54 J/m^2).

However, fly ash composition is highly variable, depending on the coal type, the processing parameters, the burner, etc., thus untreated fly ash can have various and unpredictable effects in composites [10, 11]. Several surface modification technologies, involving the addition of coupling-agents or surfactants followed by mechanical mixing, have been reported to modify (and control) the surface properties of fly ash. Changes in the surface morphology and the surface area of fly ash can be obtained controlled surface dissolution/re-precipitation with NaOH, NaOH/NH_4HCO_3, EDTA and HCl [12]. Chemical modifications can improve to a certain degree the interfacial properties between fly ash and rubber/plastic. As result of its ionic and charged surface, it was shown that fly ash has a higher affinity and

adhesion to the rubber phase compared to the plastic phase [13]. Fly ash modification with silane coupling agent leads to improved interfacial bond between the fly ash and HDPE, hence the mechanical properties [14].

Prabhu et al. have used recycled-PET reinforced with fly ash cenospheres (FAC) to obtain composites materials by compression molding. The samples with 5.4–7 % FAC content developed using a pressure of 11.6–14.4 MPa have optimum flexural strength and wear resistance for a possible use as plastic gears in low-tech applications like toys [15]. Recycled PET can be mixed with fly ash waste to produce polyester concrete (PC) [16] and to produce polyester mortar (PM) [17] with high strength, good durability properties and low cost. The material may effectively be used in many construction applications. The fly ash served as a heat conductor, decomposition inhibitor and lubricating agent, allowing homogeneous melting, when 10 and 50 % fly ash was added in PET matrix [18].

Another waste which can be integrated in polymeric composites is wood flour. Marathe et al. have developed composites with polyvinyl chloride as major matrix constituent, ethylene vinyl acetate as polymeric plasticizer, and fly ash and wood flour as fillers [19]. The results showed that wood contributes to an increase of the glass transition temperature and of the Young module, while the FA content has an insignificant effect on these particular properties.

As rubber and PET are common wastes (in abundant amounts), developing a composite using these represents a task that would allow developing low-cost materials, with stability and mechanical properties tuned by FA addition. Among all fiber reinforcing materials, PET has good mechanical properties, particularly in high-modulus and low shrinkage. However, PET fiber is a relatively inert polymer; thus, the major problem is related to the well-known lack of compatibility between PET and rubber, and this could be solved by adding a compatibility agent (e.g. waste HDPE) and other components/additives as wood sawdust. This paper presents the steps followed in developing groups of composites, fully obtained using wastes, with tuned properties targeting indoor or outdoor applications. The role of interfacial control and the path to reach this is outlined for composites rubber—PET composites, with small amounts of HDPE, FA or wood flour.

2 Experimental

2.1 Materials

The materials used for obtaining the composites were:

- tire rubber as matrix (which consists in four different types of rubber: natural-, styrene-butadiene-, polybutadiene- and butyl-rubber)
- polyethylene terephthalate (PET) from soft drinks bottles
- high density polyethylene (HDPE) from bottles (Teli Company)

- wood flour (oak) from the university workshop, with a natural moisture content of 5.28 %.
- Fly ash powder, collected from the electrofilters of the CPH plant Brasov, Romania. The main components are SiO_2 (53 %), Al_2O_3 (22 %) and Fe_2O_3 (9 %), therefore according to the ASTM standards the fly ash is of F type and has the tendency to aggregate when mixing with CaO, but not with water. The minority components are unburned carbon (3.8 %) and various oxides as: CaO (3.6 %), MgO (2.4 %), K_2O (2.2 %).

Before use, the ash was washed with ultrapure water under continuous stirring (50 rpm) at room temperature for 48 h to remove the soluble compounds. The ash was chemically modified by alkali treatment (48 h in 2N NaOH). Then, the fly ash was dried and rinsed in ultrapure water 48 h until constant pH, and then dried again, at 120 °C for 2 h. The XRD and AFM analyses show that the ash was chemically changed, some oxides (CaO, Al_2O_3, MgO and partially SiO_2) were affected by NaOH dissolution and the resulted conglomerates show micro-pores [12].

2.2 Samples Preparation

A series of composites were obtained via compression moulding in an oven thermostat (type ECv 200–300), using second raw materials. The components were thermally processed for 60 min at different temperatures (150–260 °C), depending on the components' degradation temperatures.

To test their application range, the composites were tested at long term immersion in water (for sample type S—500 h and type P—120 h). The samples codes and their composition are presented in Table 1.

The first step in valorizing the polymeric waste was made by blending PET and rubber with/without fillers. Because the interactions between the polymer matrix and the fillers lead to a more rigid structure (by decreasing the degree of freedom for

Table 1 The samples code and the composition of the composites materials

Samples code	Composition	T_{curing}[°C]
S	Rubber:PET:HDPE = 60:35:5	240
S-H_2O	Rubber:PET:HDPE = 60:35:5 immersed in water	240
S-FA	Rubber:PET:HDPE:fly ash = 59.75:35:5:0.25	240
S-FA-H_2O	Rubber:PET:HDPE:fly ash = 59.75:35:5:0.25 immersed in water	240
P-W	Rubber:PET:HDPE:wood = 80:10:5:5	150
P-W-H_2O	Rubber:PET:HDPE:wood = 80:10:5:5 immersed in water	150
P-W-FA	Rubber:PET:HDPE:wood:fly ash = 79:10:5:5:1	150
P-W-FA-H_2O	Rubber:PET:HDPE:wood:fly ash = 79:10:5:5:1 immersed in water	150

the macromolecules), coupling agents such as TiO_2, HDPE, LDPE were inserted into the composites, and the preliminary results showed that HDPE ensures the best compatibility of rubber and PET.

Further, the curing temperature was optimized. Considering the thermal properties of the components (T_g, flowing and decomposition temperatures), composites were obtained in a temperature range of 150–260 °C. The best mechanical performance was achieved at 240 °C.

Then, composites with inorganic filler (up to 2 %) were prepared starting from these previously optimized compositions. The percentage of metal oxide (x) used as filler in the composites obtained from rubber: PET HDPE: metal oxides = (60 − x): 35: 5: (x < 2), was optimized to x = 0.25 %.

By adding small amounts of wood sawdust to polymeric blends of rubber-HDPE-PET, an increase of the mechanical performance was observed. Experiments showed that by decreasing the curing temperature of polymeric blends, the mechanical strength was increased. The best mechanical properties were obtained when the temperature was 150 °C. This effect is the consequence of the compatibility role of woody components, but it was registered only up to a maximum temperature of 200 °C. Obviously, at micro-level, this compatibility is the result of new interfaces/bonds between the composite components.

Further, because the main target of our work is to obtain composite materials with good mechanical performance fully based on wastes, fly ash was added as filler (as a substitute of metal oxides), for the both series of composites (with/without wood). It was found that fly ash visibly improves the mechanical properties of the composite. These composite materials can be used for indoor/outdoor applications; therefore the water stability was also investigated. The results are presented below.

2.3 Characterisation

Mechanical tests: Tensile strength (σ_{tr}) was evaluated according to SR EN ISO 527-4:2000 using a Zwick/Roell instrument (Z020), at a traction speed of 100 mm/min. The compression resistance (R_C) was tested on the same mechanical testing equipment, according to SR EN ISO 527-4:2000. Each measurement was performed on three samples and the mean values are reported.

FTIR analysis: The chemical structure of the composites and the interface bonds were outlined by recording their IR spectra. Fourier Transform Infrared Spectroscopy (FTIR) analysis using a spectrophotometer (Vertex V70, Bruker) was used to record the reflectance spectra, in the 600–4,500 cm^{-1} range, after 16 scans, with 4 cm^{-1} resolutions.

SEM and EDX Analysis: Micrographs were obtained using SEM, Hitachi, S3400 N, type II, and quantitative elemental analysis of the samples was performed using EDX (Thermo, Ultra Dry, Noran System 7, NSS Model, 2,000,000 counts/s), with the sensitivity down to a few atomic percent.

Atomic force microscopy: The morphology of the nanocomposite surface was investigated by atomic force microscopy (AFM NT-MDT model NTEGRA PRIMA EC). The images were taken in semi-contact mode with "GOLDEN" silicon cantilever (NCSG10, force constant 0.15 N/m, tip radius 10 nm).

X-ray analysis: The X-ray diffraction measurements were used to evaluate the effect of fly ash nanoparticle on the interfaces and composites crystalline structure. Data were collected with Bruker D8 advance Diffractometer CuKα radiation of λ = 1.54016 Å, over the range 2θ = 5 ∼ 60° in the fixed time mode with a step interval of 0.01°, at 25 °C temperature. The variations in the composites crystallinity were evaluated from the ratio of the diffraction peak areas.

Contact angle measurements: The surface energy and the interfacial tension between the composite surface and the liquid were evaluated using contact angle measurements with OCA-20 System (DataPhysics Instruments) at room temperature.

The sessile drop method was used, with distilled water and NaCl 3.5 % as testing liquids to calculate the surface energy and its polar and dispersive components. The surface energy was calculated according to the OWRK method [20] from the contact angle values and the contributions of the water /NaCl solution. Following values were used: for water σ = 72.10 mN/m (σ^p = 52.20 mN/m; σ^d = 19.90 mN/m), and for NaCl 3.5 % σ = 73.76 mN/m (σ^p = 22.20 mN/m; σ^d = 51.56 mN/m) [21]. The interfacial tension between the composite surface and the liquids was calculated with Eq. (1) [20]:

$$\sigma_{SL} = \left[\sqrt{\sigma_{LV}^{p}} - \sqrt{\sigma_{SV}^{p}}\right]^2 + \left[\sqrt{\sigma_{LV}^{d}} - \sqrt{\sigma_{SV}^{d}}\right]^2 \quad (1)$$

where: $\sigma_{LV}^{p}, \sigma_{LV}^{d}, \sigma_{SV}^{p}$ and σ_{SV}^{d} are the polar and disperse components of the surface energy.

3 Results and Discussions

3.1 Mechanical Tests

In a composite, the mechanical strength is mainly influenced by the interface type and interfacial bonds, which in turn significantly depend on the processing temperature and duration, and the initial composition (hereby: the amount of rubber, PET, HDPE, fly ash, and wood).

While rubber has many recycling path, PET is more seldom recycled as second raw material and is mostly used to recuperate the embedded energy (by burning); therefore, one aim in developing novel composites based on wastes would be to reach stable composites (in the working conditions), which have the PET percentage as high as possible.

Table 2 The mechanical properties of the composites

Type of composites	σ [N/mm^2]	E [N/mm^2]	R_c [N]
S	1.57	2.56	69.66
S-H_2O	1.41	1.23	52.01
S-FA	1.29	25.75	82.67
S-FA-H_2O	1.44	7.77	52.97
P-W	1.89	2.86	61.70
P-W-H_2O	1.69	2.17	42.12
P-W-FA	1.51	1.73	50.34
P-W-FA-H_2O	1.52	2.13	62.80

By a careful optimization of the components (particularly the compatibility agent HDPE and the fillers), and of the processing conditions, composites with 35 % PET content could be obtained, having very good mechanical properties, as outlined in Table 1 (samples S, S-FA and their counterparts after long term water immersion); wood addition allow significantly decreasing the processing temperature but this was corroborated with a lower amount of PET that could be embedded in stable composites (samples P-W, P-W-FA and the water immersed ones, Table 1).

The specific characteristics recorded during mechanical tests highlighted the tensile strength of the composites, Table 2. Sample **S-FA** have the highest elongation to maximum force (compression force is 8267 N) and the modulus of elasticity of 25.75 N/mm^2. Knowing the work of fracture and cross-sectional area of the specimen, the tensile stiffness was calculated. High tensile strength of 1.89 N/mm^2 was obtained for sample **P-W**, followed by sample **P-W-FA** (1.69 N/mm^2) and with a lower stiffness for sample with **S-FA** (1.29 N/mm^2). A decrease in the elastic range is observed, due to possible cross-links made by HDPE.

The mechanical strength of the samples S and SW decreases when they are immersed in water. For composites S, the water molecules may cause creep phenomena and possible rearrangements of the macromolecules which lead to lower tensile forces. In the case of wood composites (SW), water is absorbed by the hydrophilic component (W), causing an expansion, thus the samples have a lower tensile strength. Moreover, plasticization and changes of the matrix due to water absorption may occur, changing the properties of the interface.

The strength increases for samples with FA and immersed in water (samples S-FA-H_2O and P-W-FA-H_2O). This may be explained by the FA surface properties. After fly ash treatment with NaOH, surface voids are obtained which promotes the formation of an interface with the rubber macromolecular chains. This is less likely to happen with the PET molecules, which are more rigid and bulky. By increasing the fly ash content in the composite, more macromolecular chains are expected to attach on the filler's surface. However, when increasing the temperature, the free volume of polymer increases, leading to the relaxation of the polymeric chains, thereby increasing the elastic modulus, [22]. The main component from the FA

(SiO_2) improves the interaction between PET/HDPE and fly ash, and thus the compressive strength [23, 24].

At the same time, the compressive strength is increasing for the samples S-FA versus the S composites with approximately 15 %, while a decrease of 18 % for the samples PW-FA compared to PW samples was registered, as FA may interact with wood creating a weaker interface.

The tensile strength of the samples containing wood (**P-W**) increases with the processing temperature, while the fly ash amount is causing a proportional decrease. This behavior could be caused by the agglomeration of inorganic nanoparticles, at higher temperatures when the (pseudo-)plastic state may characterize at least on component in the composite; these clusters may act as a barrier for stress transmission from the polymeric matrix to the wood fibers, thus reducing the mechanical properties. For all immersed composites, an improvement of the tensile strength was observed, as a result of bonded water, which acts as plasticizer.

These results reflected the synergistic effect of wood, FA and water on the composites properties. It may be concluded that:

- wood addition to rubber-PET-HDPE blends improves the mechanical performance of the composite, and meanwhile, an economic benefit was achieved (considering the lower curing temperatures);
- inorganic filler in proper amount may lead to a good dimensional stability for wood-containing composites

Thus, considering these results, one may recommend PW for indoor and PW-FA for outdoor applications.

3.2 FTIR Analysis

The IR spectra contain bands specific to the components, and new bands due to macromolecular chain divisions that occur in rubber and due to possible phase transitions, in bulk and at the interfaces. These bands are presented in Table 2. The thermal processing of the polymeric blends with inorganic filler may lead, beside mechanical adhesion, to physical or chemical bonds between the composite components. These are the consequences of oxidative processes or/and due to the reciprocal affinity.

The IR spectrum of fly ash shows that the wave number 1,085 cm^{-1} corresponds to SiO_4 tetrahedral structure, particularly to the internal Si-O-Si links. The bands at 1,010–1,090 cm^{-1} of the treated ash samples correspond to the cyclic structure based on Si-O-Si.

When FA is added, some bands are no longer evidenced, as compared to the reference (without FA): 1,715 cm^{-1} (−C = O), 1,447 cm^{-1} (specific to C = C from rubber and HDPE, $-CH_2$ from PET and −CH wood), 1,267 cm^{-1} (C-O-C from PET and wood) and a new band is formed at 1,640 cm^{-1}. Newly formed band (1,640 cm^{-1}) may belong to the vibrations of H-O and H-OH—hidroalumino-silicate reaction

products. At the same time it can be a shift of the main band at 1,075 cm^{-1} (attributed to asymmetric vibrations of Si-O bonds and Al-O [25]), suggesting processes of solubilization and polycondensation with the partial substitution of groups $SiO4^{4-}$ with $AlO4^{5-}$ in the composite materials. These support the assumption of newly formed physicochemical interfaces between the components.

After immersion in water, (samples S-H_2O and S-FA-H_2O), the degradation of −CH = occurs which is indicated by the missing wavelength band 2,840 cm^{-1}. The characteristic band of the −OH groups (3,686 cm^{-1}) disappears as result of a possible development of physical-chemical interfaces (hydrogen/dipol-dipol bonds) between the water molecules and the composites components.

Although the samples were designed with/without wood (the samples type S and P-W), the shape of the spectral bands in the IR spectra is similar, with the formation of two bands at 1,601 and 717 cm^{-1} which correspond to the degradation of C = C bonds and the vibration of −CH groups. This confirms the higher tensile strength of the sample P-W.

Adding fly ash to the S-P composites led to significant changes in the FTIR spectra. It was observed that the band attributed to C = C group from rubber is missing, along with the deformation vibration of water in wood (at 1,610 cm^{-1}) and formation of two bands at 1,586 and 1,531 cm^{-1}. First one (1,586 cm^{-1}) being assigned to lignin, and second one to carboxylate groups ($-COO^-$), or to C = C group from rubber, thus showing possible chemical interactions among the components (rubber, wood and fly ash). The wavelength range 1,200–1,500 cm^{-1} contains a series of distinct bands corresponding to the primary alcoholic group CH_2OH (1,430, 1,355, 1,215 cm^{-1} vibration deformation). Here are summarized and deformation vibrations of C-O bonds and C-H. Rich metallic oxides of fly ash may lead to the formation of water insoluble compounds in the composite (e.g. calcium carboxylate). After fly ash addition, a shift to lower wave numbers was observed for the bands from 1,458 cm^{-1} (C = C from rubber) and 1,245 cm^{-1} (C-O-C from PET or wood) to 1,428, respectively to 1,215 cm^{-1}, Fig. 1. A new band appeared between them, at 1,355 cm^{-1} corresponding to the wood components ($-CH_3$ of lignin or hemicellulose. or −OH from polyzaharide), revealing chemical

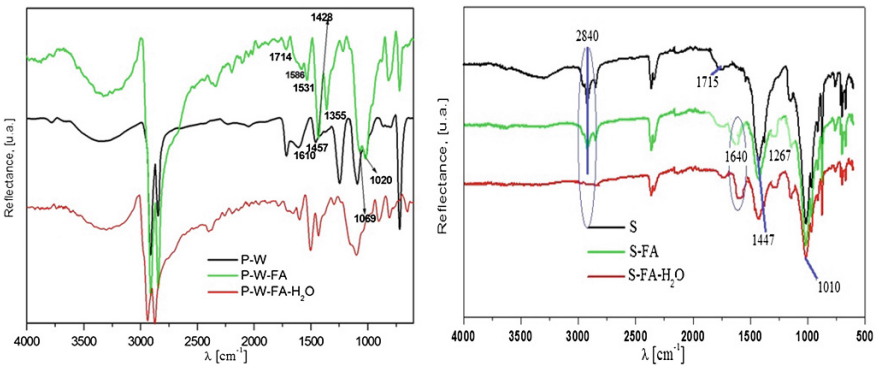

Fig. 1 FTIR spectra for samples type S and type P

interactions of rubber, PET, HDPE, wood with components of fly ash, resulting in an increase of interface flexibilization.

Further, water immersion of this composite bring other set of changes in its spectrum, as the group of bands (2,842, 1,722, 1,369, 1,219, 719 cm^{-1}) shifted to higher wave numbers. This change indicates an increase in the rigidity degree of the composite, confirming the mechanical tests results, which showed higher compression strength after water immersion. The bands corresponding to: 1,069, 1,020 and 874 cm^{-1} after water immersion, are transformed in a wider band at about 1,019 cm^{-1}, supporting the assumption of physical-chemical interactions of PET and wood with fly ash, which led to an increase in the interfacial adhesion and consequently in the mechanical performance of the composite.

3.3 Contact Angle Measurements

Considering the possible outdoor applications of the composites, the behavior of the optimized materials in contact with different liquids was studied using contact angle measurements. Also, contact angle measurements were performed to evaluate the surface energy of the composites. The higher the contact angle is, the lower is the surface energy of the composites, which is a desirable property considering the outdoor applications (non-wetting). Contact angle depends on the interaction between the sample's surface charge and the testing liquid. The nature of the sample, of the test liquid and the porosity of the samples determines different values of the contact angles.

Adsorption/absorption of aqueous solutions of electrolytes, respectively water, was carried out from the first contact moment of the drop with the surface. The polar and dispersive contributions of the surface energies were calculated based on the initial contact angle values, Table 3.

Table 3 Surface energy values for the composites disscused

Composites	Surface energy, (mN/m)	Dispersive component (mN/m)	Polar component (mN/m)
S	17.87	1.85	16.02
S-H_2O	66.28	65.32	0.95
S-FA	45.91	45.80	0.11
S-FA-H_2O	28.65	8.46	20.19
P-W	81.27	11.43	68.83
P-W-H_2O	18.80	14.56	4.24
P-W-FA	181.30	57.80	123.5
P-W-FA-H_2O	125.28	27.87	97.41

The highest value of the contact angle was recorded for the sample S-FA (97.24°), and the highest surface energy was found for the sample P-W-FA (181.3 mN/m with predominant polar component). In consequence, the sample with fly ash shows predominantly hydrophobic properties, but it can be wetted by NaCl solutions, confirming the presence of polar compounds (weak) at the surface.

Lower values of the contact angle were recorded for the samples P-W and P-W-FA than for samples S and S-FA. This results is due to water from wood (bound water and free water), and could also be related to the presence of polar compounds from the degradation of the polymers. Contact angle values ($\Theta < 78°$) decrease when the type S samples are immersed in water. A stronger interface is created and a low wetting capacity is obtained.

For the composites type S-FA/S-FA-H_2O and P-W-FA/P-W-FA-H_2O a decrease in surface energy was registered: about 37 % for S samples and 31 % for the P type. This decrease of surface tension has an influence on the mechanical properties: the tensile strength is increasing for the samples immersed in water, Table 1. The presence of water molecules lead to a higher polar component of the surface energy, having a positive influence on the tensile strength of composites. The addition the wood in the composites brings a significant contribution to the surface tension and tensile strength. This could be the result of new physico-chemical interfaces formed between wood and the composite's components as already indicated by the FTIR analysis. Moreover, the surface morphology and/or the presence of a high concentration of polar compounds on the composite surface may have an influence.

It is also to notice that water immersion significantly changes the ratio between the polar and the dispersive components, confirming the capillary irreversible adsorption. This effect is stronger for the composites that had an initial high polar component as result of the oxidation degradation of the polymers, with poor consequences on the interfaces. Contact angle values can be changed in this case also as result of the roughness value. This effect is more likely in the FA-containing composites.

The wetting behavior is directly correlated with the surface energy and is affected by at least two factors:

- Surface composition: the oxides at the surface lead to a higher surface energy and better wetting phenomena, while the migration/agglomeration of the oxide particles in the composites volume leaves a hydrophobic surface area with low energy.
- Surface roughness: a rough surface, with edges and corners has a higher surface energy and is more hydrophilic/less hydrophobic compared to a smooth surface.

For the composites containing fly ash, a charge at the surface was obtained, as a result of possible interactions between the active centers of ash and the other components.

3.4 X-ray Diffraction

X-ray diffraction measurements were carried out to evaluate the effect of fly ash nanoparticles and of wood sawdust at the interface and to determine the crystalline structure of the composites. In all diffractograms, an amorphous phase due to the polymeric component of composites (in specially rubber) is observed. Some components of the composite contain crystalline phase(s), such as PET, HDPE (polymer with a higher crystallinity). The crystallinity increases when organic/inorganic fillers (wood/fly ash) are added in the composite, as these may act as nucleation centers at the moulding temperature. The X-Ray diffractogram for the fly ash based composites indicates predominant amorphous phases also for silica and alumina [26, 27] along with quartz. For wood, a low crystallinity percent is observed from the diffractogram. This confirms the IR data of wood, where low intensity bands characteristic to crystalline and amorphous domains were observed (approximately: 1,355, 1,428 cm^{-1} and 874, 2,900 cm^{-1}) [28]. As in the case of FA, wood raises the crystallinity degree of the samples. Corroborating the contact angle measurements and XRD, we may conclude that both, the composition and the cristallinity are responsible for surface and/or interface interactions with testing liquids and/or immersed water, Fig. 2.

Comparing the samples S and P-W, a higher crystallinity degree is observed for sample P-W, which has an organic/polymeric structure, closer to the polymeric main components in the composite. The XRD data has shown an increase of the crystallinity degree for both, the S and P-W, after their water immersion (35% respectively 20 %). Water molecules entering the polymeric composite structure are creating a higher ordered structure due to the re-arrangement of the macromolecular chains. The washing out process of the amorphous compounds may be also reflected in the increased crystallinity degree.

It is interesting to notice that, the higher crystallinity degree of water immersed samples S and P-W do not compulsory lead to an increase in mechanical performance, as the mechanical tests show.

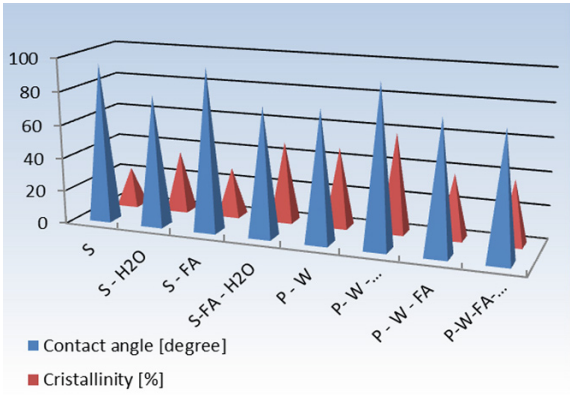

Fig. 2 The contact angle values and the crystallinity for the composites

The samples **S-FA** recorded an increase of crystallinity degree, as a result of composite densification, as the mechanical tests results indicated a higher compression resistance, fact also sustained by the remarkable Young moduli value (25.75 N/mm^2). At the opposite side, fly ash addition to P-W sample has lowered the crystallinity, as the mechanical tests has already confirmed, showing a decrease in the mechanical strength. The contact angle measurements also revealed this behavior registering a higher surface energy of P-W-FA compared with sample without fly ash.

Water immersion of composites with fly ash leads to significant changes. S-FA-H_2O sample recorded a considerable crystallinity increase (with 39%), compared with S-FA, but—at the same time, a drastic decrease in compression strength as mechanical tests confirmed (with 36%). Contrary, the P-W-FA sample showed a merely behavior regarding crystallinity, Fig. 2, but an unexpected increase in compression strength as mechanical tests showed. This confirms that fly ash addition to P-W leads to a more micro-porous structure. In this context, the positive effect of water which is retained in the micro-pores and acts as plasticizer is higher, supporting the results of FTIR analysis, mechanical tests.

3.5 AFM Analysis

The atomic force microscopy analysis was performed to investigate the influence of inorganic and organic additives on the surface morphology of composites.

The root mean square (RMS) roughness of the composites and AFM images are presented in Figs. 3, 4, 5, 6. Physical changes on the surface, such as the formation of micro-porosity and micro-roughness were simultaneously recorded with the changes due to partial degradation of rubber HDPE and respectively PET at the

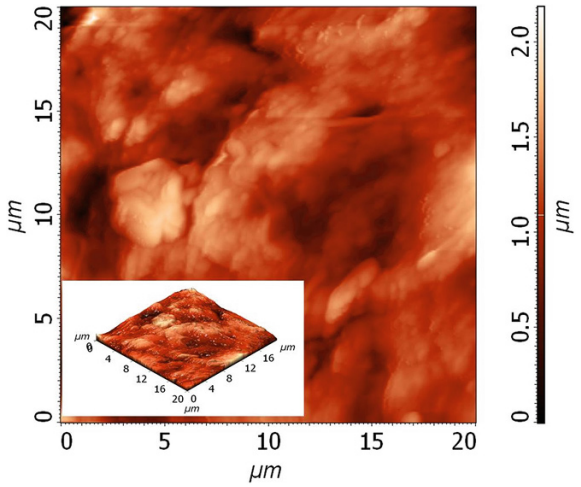

Fig. 3 AFM images for **S** sample, RMG = 253.6 nm

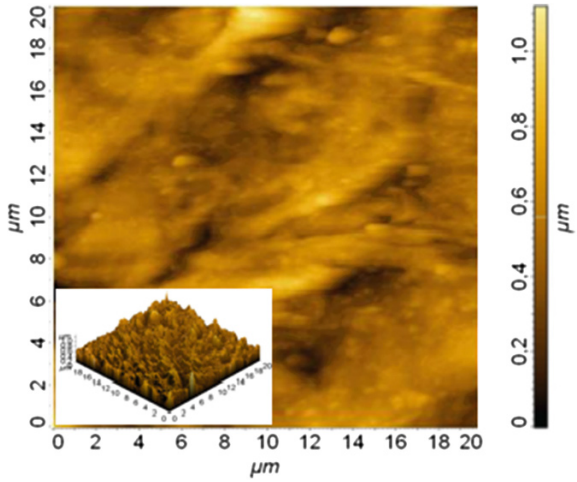

Fig. 4 AFM images for **P-W** sample, RMG = 127.0 nm

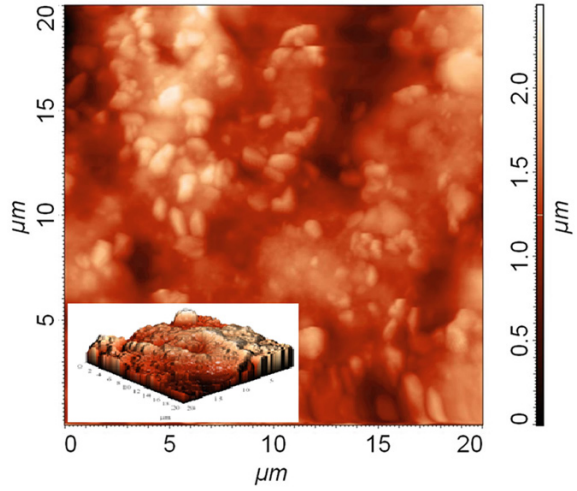

Fig. 5 AFM images for **S-FA** sample, RMG = 245.5 nm

surface, as partial oxidation occurs in the outer layers of nanocomposites at contact with the air and, most likely due to defects in the matrix interface.

The roughness increases with the addition of organic and inorganic fillers. The fly ash and wood particles are well encapsulated in the PET and rubber bulk, therefore a smooth surface is formed, as in the P-W-FA composite (RMG = 106.3 nm), Fig. 6. The composite type P-W-H_2O has the highest roughness (355 nm). Water penetration in the composites leads to low ordered rearrangements of the macromolecular chain, in good agreement with XRD analysis results (a higher crystallinity 59.8 %) and the lower compression resistance. The composite type P-W-FA with a compact structure (50.34 N/mm^2) has the lowest

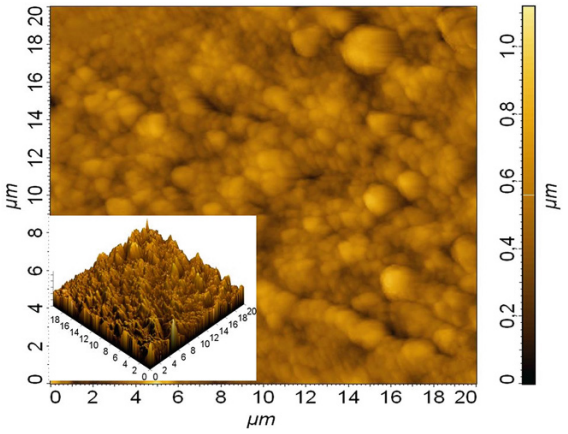

Fig. 6 AFM images for **P-W-FA** sample, RMG = 106.3 nm

surface roughness. This is probably due to the offensive effect of the wood degradation products on the polymeric composites that leads to surface chemical oxidation that mainly attacks edges and corners.

4 Conclusions

Polymeric composites based on rubber-PET with/without organic filler and with/without inorganic filler are reported. Wood addition to polymeric composites based on recyclable rubber, PET and HDPE reduces the curing temperatures, which is an economic advantage. As FTIR data reported, wood proved to be a good compatibility agent in rubber-PET-HDPE based composites. The complex inorganic FA (rich in metallic oxides) brings improvements in the mechanical response of composites containing wood.

Water seems to act as a plasticizer agent in wood based composites, and moreover it was proved the synergistic positive effect of water, wood and proper amount of fly ash on output properties of composites.

The best composite in terms of dimensional stability with mechanical performance for outdoor applications was found to be that with composite rubber-PET-HDPE-wood-fly ash (P-W-FA-H_2O) while for indoor application the composite rubber-PET-HDPE-wood (P-W) is recommended.

Acknowledgments This paper is supported by the Sectoral Operational Programme Human Resources Development (SOP HRD), financed from the European Social Fund and by the Romanian Government under the project number POSDRU/159/1.5/S/134378.

References

1. Cazan, C., Cosnita, M., & Duta, A. (2013). Polymeric wastes from automotives as second raw materials for large scale products. *Environmental Engineering and Management Journal 12*, 1649–1655.
2. Bhat, G., Hegde, R. R., Kamath, M. G., & Deshpande, B. (2008). Nanoclay reinforced fibers and nonwovens. *Journal of Engineered Fibers and Fabrics 3*, 22–34.
3. Uddin, N. (2013). Developments in fiber-reinforced polymer (FRP) composites for civil engineering, *Woodhead Publishing Series in Civil and Structural Engineering 45*, Alabama, USA.
4. Chen, K., Wilkie, C. A., & Vyazovkin, S. (2007). Nanoconfinement revealed in degradation and relaxation studies of two structurally different polystyrene–clay systems. *The Journal of Physical Chemistry B 111*, 12685–12692.
5. Chrissafis, K., Paraskevopoulos, K. M., Papageorgiou, G. Z., & Bikiaris, D.N. (2008). Thermal and dynamic mechanical behavior of bionanocomposites: Fumed silica nanoparticles dispersed in poly(vinyl pyrrolidone), chitosan, and poly(vinyl alcohol). *Journal of Applied Polymer Science 110*, 1739–1749.
6. Aso, O., Eguiazábal, J. I., & Nazábal, J. (2007). The influence of surface modification on the structure and properties of a nanosilica filled thermoplastic elastomer. *Composites Science and Technology 67*, 2854–2863.
7. Lin, O. H., Akil, H. M., & Ishak, Z. A. M. (2009). Characterization and properties of activated nanosilica/polypropylene composites with coupling agents. *Polymer Composites 30*, 1693–1700.
8. Stapathy, S., Nando, G. B., Nag, A., Nag, A., & Raju, A. (2013). HDPE-fly ash/nano fly ash composites. *Journal of Applied Polymer Science, 130*, 4558–4567.
9. Guo, D., Xue, B., & Bao, J. (2013). Preparation and properties of high-density polyethylene composite filled with ultrafine fly ash. *Gaofenzi Cailiao Kexue Yu Gongcheng/Polymeric Materials Science and Engineering*, *29*, 149–152.
10. Cokca, E., & Yilmaz, Z. (2007). Use of rubber and betonite added fly ash as a liner material. *Waste Management 24*, 153–164.
11. Fan, Y. M., Yin, S. H., Wen, Z. Y., & Zhong, J. Y. (1999). Activation of fly ash and its effects on cement properties. *Cement and* Concrete Research *29*, 467–472.
12. Visa, M., & Duta, A. (2010). Adsorption behavior of Cd^{2+} and Cu^{2+} on a mixture FA: TiO2. *Revue Roumaine de Chimie, 55*, 167–173.
13. Sridhar, V., Xiu, Z. Z., Xu, D., Lee, S. H., Kim, J. K., Kang, D. J., et al. (2009). Fly ash reinforced thermoplastic vulcanizates obtained from waste tire powder. *Waste Management, 29*, 1058–1066.
14. Atikler, U., Basalp, D., & Tihminlioglu, F. (2006). Mechanical and morphological properties of recycled high-density polyethylene, filled with calcium carbonate and fly ash. *Journal of Applied Polymer Science*, *102*, 4460–4467.
15. Prabhu, K. B., Chomal, G. J., & Kulkarni, S. M. (2013). Investigation on effect of processing parameters on properties of recycled-pet composites using taguchi method. *International SAMPE Technical Conference* (pp. 1256–1270).
16. Rebeiz, K.S. (1996). Strength and durability properties of polyester concrete using pet and fly ash wastes. *Advanced Performance Materials, 3*, 205–214.
17. Rebeiz, K., Rosett, J., & Craft, A. (1996). Strength Propertie of Polyester Mortar Using PET and Fly Ash Waste. *Journal Energy Engeneering, 122*, 10–20.
18. Li, Y., White, D. J., & Lee Peyton, R. (1998). Composite material from fly ash and post-consumer PET. *Resources, Conservation and Recycling 24*, 87–93.
19. Marathe, D. S., & Joshi, P. S. (2010). Characterization of highly filled wood flour-polyvinyl chloride composites: Dynamic mechanical and dielectric analysis. *Polymer Engineering and Science, 50*, 1253–1260.
20. Fowkes, F. M. (1967). *Treatise on adhesion and adhesives*. New York: Marcel Dekker.

21. Busscher, H. J. (1984). The effect of surface roughening of polymers on measured contact angles of liquids. *Colloids and Surfaces, 9*, 319–331.
22. Sridhar, V., Chaudhary, R. N. P., & Tripathy, D. K. (2006). Effect of carbon blacks on the relaxation phenomenon în chlorobutyl vulcanizates. *Journal of Applied Polymer Science, 102*, 1809–1820.
23. Cosnita, M., Cazan, C., & Duta, A. (2013). The influence of CaO addition and processing temperature on the mechanical properties of recycled rubber, PET and wood based composites. *Materials Science and Engineering B* (submitted for publication).
24. Ton-That, M. T., Denault, J., Perrin, F., Leelapornpisit, W., Hu, W., & Cole, K. C. (2009). *New High Performance Natural Fiber Composites, Composites & Polycon*. Tampa, FL USA: American Composites Manufacturers Association, January 15–17 2009.
25. Khale, D., & Chandhary, R. (2007). Mechanism of geopolymerisation and factors influencing its development, a review. *Journal of Materials Science, 43*, 720–735.
26. Lin, R. B., & Shih, S. M. (2003). Characterization of Ca(OH)2/fly ash sorbents for flue gas desulfurization. *Powder Technology, 131*, 212–222.
27. Lin, R. B., Shih, S. M., & Liu, C. F. (2003). Characteristics and reactivities of Ca(OH)2/silica fume sorbents for low-temperature flue gas desulfurization. *Chemical Engineering Science, 58*, 3659–3668.
28. Malutan, Th., Pui, A., & Obrocea, P. P. (2012). *IR A pulps obtained by the sulfur additives*. PhD thesis.

Thin Film Vis-Active Photocatalysts for Up-scaled Wastewater Treatment

Anca Duta, Alexandru Enesca, Luminita Isac, Dana Perniu, Luminita Andronic and Cristina Bogatu

Abstract One main reason that limits their large scale application is the cost of the photocatalytic processes, mainly related to the costs of the UV radiation that activates most of the highly efficient photocatalytic materials and therefore, VIS-active photocatalysts are intensively studied; additionally, in industrial processes, fine powders are to be avoided although they have the advantage of larger specific areas, thus potential larger activity. This paper presents a review of the results obtained in the research group in optimizing photocatalysts used as thin films; doctor blade and spray pyrolysis deposition are comparatively analyzed. In situ doping using templating agents (surfactants) represented a viable path to extend the optoelectronic response towards VIS in wide band gap semiconductors. An additional advantage is morphology control reached when using surfactants. By associating two semiconductor photocatalysts as *n-n* tandems or *n-p* diode type materials, VIS-activated thin films can be obtained and the step-wise development of a novel family of VIS-active photocatalysts is presented for composite materials containing two or three components from the group of TiO_2, WO_3, SnO_2, ZnO, Cu_xS.

Keywords Heterogeneous photocatalysis · Composite photocatalyst · VIS-active photocatalyst · Wastewater treatment

1 Introduction

The pioneering work of Giacomo Ciamician in the end of the XIXth century outlined that solar radiation can be used to obtain fuels by artificial photochemical reactions, [1]. It took almost one century to experimentally prove that hydrogen can be produced in photocatalytic processes based on wide band gap semiconductors,

A. Duta (✉) · A. Enesca · L. Isac · D. Perniu · L. Andronic · C. Bogatu
Renewable Energy Systems and Recycling R&D Centre (RES-REC), Transilvania University of Brasov, Eroilor 29, 500036 Brasov, Romania
e-mail: a.duta@unitbv.ro

I. Visa (ed.), *Sustainable Energy in the Built Environment - Steps Towards nZEB*, Springer Proceedings in Energy, DOI 10.1007/978-3-319-09707-7_39

[2] and this was the beginning of an intensive work, all over the world, for improving heterogeneous photocatalysis and extending its applications towards very many domains. Now-a-days photocatalytic decomposition of organic compounds (oxidation) or photocatalytic neutralization of toxic species by reduction has been proved efficient at laboratory scale for various applications, ranging from health (cancer therapy, [3]) to automotive industry (self-cleaning, anti-corrosive and anti-microbial coatings, [4, 5]). Still, most of the applications are expected in environmental technologies for atmospheric, water and soil remediation, [6]. For atmospheric depollution several solutions are already on the market (as the photocatalytic coatings on the tiles in surgery rooms, for sterilization and the NOx removal from average loaded gas streams), but up-scalable solutions for wastewater treatment are developed only at pilot scale.

The use of heterogeneous photocatalysis in wastewater treatment is mainly reported as promising for decreasing the BOD, [7] and/or for removing taste and odor, [8] (thus focusing on wastewaters resulted from residential use, agriculture, pharma, food industry, etc.) but most of the investigations are concentrated on industrial wastewaters, particularly on those loaded with pollutant and toxic organic compounds (phenols, chloro-phenols, organic acids) as these are difficult to degrade in conventional processes, down to the discharge limits.

Additionally, the need for sustainability has focused the research on novel, efficient and affordable solutions for water reuse (with quality thresholds more severe than those of water discharge), thus photocatalysis is likely to occupy a significant role in the future wastewater treatment, to remove the pollutants by mineralization and/or to prepare water for conventional re-treatment processes.

One largely investigated application is on wastewaters resulted from the textile industry. Thousands of papers published in the past decade are reporting on various photocatalysts, efficient in different dyes degradation. As from the very beginning, TiO_2 is still reported as the most efficient wide band gap semiconductor in wastewater photocatalytic treatment and is highly investigated also due to its water-stability and lack of toxicity. Still, TiO_2 has a major disadvantage which comes from its intrinsic nature: it has a wide band gap (i.e. 3.1–3.2 eV) that makes it active only under UV radiation. In terms of up-scaling this is a huge disadvantage that makes it un-competitive in terms of operation costs, [9]. Therefore, alternatives were investigated, using narrow band gap semiconductors as photocatalysts (e.g. sulfides) which proved to be effective under VIS irradiation (as expected) but have the problems of water-stability and toxicity of the leachate. Doping the wide band gap semiconductors improved the VIS response but cation doping is actually detrimental to the photocatalytic efficiency and anion doping needs a very careful control, [10].

New concepts emerged, as coupling n-p semiconductors or developing metal-semiconductor interfaces (thus developing active junctions, with clear charge segregation), [11, 12] and the results are interesting as meeting all the targets: the shift to the VIS response, water stability and lack of toxicity. Further on it was proved that a significant shift to VIS can be obtained even when coupling two n-type semiconductors if the energy bands are suitably aligned, [13, 14].

Obviously, photocatalytic powders are more effective as they have a larger interfacial area exposed to the pollutants and are mobile; these are advantages in experimental tests but for industrial applications the use of suspensions involves a limited flow operation range and requires additional steps for the photocatalyst separation and recovery. Therefore, immobilized photocatalysts are investigated as thin films deposited on different substrates, on ceramic tiles, glass or metal plates, rashig rings, [15]. A novel approach is to cover fabrics or the walls of the photocatalytic reactor by using photocatalytic inks, similarly obtained like the regular ink-jet printers suspensions/emulsions, by using nano-sized grains of photocatalytic materials, [16, 17].

2 Photocatalysts Efficiency

As already mentioned, a huge amount of papers report on novel photocatalysts and most of them outline good or very good results in degrading a broad variety of pollutants. But, as in any photo-catalytic process, the results depend on several factors, among which the most important are (1) the amount of catalyst for a given amount of pollutant and wastewater and (2) the amount of energy used for degrading the photocatalysts, i.e. the radiation intensity and spectral range (wavelengths). Thus, efforts for standardization are done for almost one decade and cover the following aspects:

(a) *The photocatalytic process yield* is usually defined as "the ratio of the rate of a photocatalytic transformation to the rate of incident photons impinging on the (external) reactor walls", [18, 19]; this definition is not fully applicable as it involves the total incident radiation (including the scattered part) and not the radiation actually used by the material. Therefore one proposal is to use the relative photonic efficiency, representing the ratio of the quantum yield for the particular investigated process to the quantum yield in degrading phenol (used as reference). In the practical evaluation of advanced oxidation processes one figure of merit is EEO (the electrical energy per order), defined as the number of kilowatt hours necessary to degrade a given pollutant by one order of magnitude (factor of 10) in one cubic meter of water.

(b) *The reference pollutant*: as already outlined, for quantum yield calculations, phenol is proposed as reference pollutant; so far, to test the photocatalytic activity and its versatility, three tests seems to get recognition: the stearic acid test, the methylene blue test and the resazurin ink test, respectively, [20]. It is also to mention that in testing photocatalysts for dyes oxidation another reference material could be recommended, methyl orange as this is more stable than methylene blue, thus the performance of the catalytic materials could be better judged.

(c) *The reactor type*: according to the reactor type (fixed bed, fluidized bed, stirred tank, etc.) the efficiency can vary as result of the diffusion limited steps.

These are important aspects that should be unitarly adopted when reporting on novel materials but particularly when proposing these materials for up-scaling in industrial/environmental processes.

3 Up-scaling Heterogeneous Photocatalysis

In 1993, advanced oxidation processes based on heterogeneous photocatalysis were described as emerging (and promising) technologies for wastewater treatment, [21]. After 20 years, the progress is significant in terms of materials but the spread of heterogeneous photocatalysis at industrial scale is still not reached. The main issues limiting the large scale replication are:

(a) *The photocatalyst sensitivity/stability in the working environment*: except TiO_2, most of the photocatalytic materials are developing surface chemical reactions at extreme pH values. Additionally, the point of zero charge (pzc) of the photocatalytic material should be measured and the working pH should be selected according to this value and to the pzc of the pollutant(s), by identifying the pH window where opposite charges are registered and the material is innert. This is important because in efficient photocatalysis, electrostatic attractions photocatalyst–pollutant represent a must.

(b) *The photocatalytic process*: for large amounts of wastewaters (as in municipality plants) the only viable option is represented by the continuous flow processes and the pilot plants based on heterogeneous photocatalysts seem not to be prepared for this yet; therefore, in an initial estimation, photocatalysis could represent a viable option for the treatment of waters that, without being in huge amounts, are loaded with toxic pollutants very difficult to degrade in conventional processes, thus in pre- or post-treatment plants in companies, hospitals, etc. To be efficient, these plants should be designed for water re-use and mineralization is the primary target in process optimization. The decomposition of organics into inorganic (gaseous) compounds can be primarily observed by the decrease in the Total Organic Carbon (TOC), Total Nitrogen (TN), along with other quality indicators (BOD, COD, etc.).

(c) *The costs*: the use of UV radiation makes heterogeneous photocatalysis the less competitive wastewater treatment, by now. Therefore, for upscaling, efforts should be focused on VIS activated processes and particularly solar-activated processes (a combination of VIS and UV) when the costs with the irradiation energy are much lowered. Additionally, the costs of the photocatalytic materials per unit of treated pollutant in a m^3 of water should be lowered. This implies: photocatalytic materials obtained from low cost precursors (inorganic), and restricted use of PGM (although Pt, Au and Ag loaded photocatalysts are more active). This also implies photocatalytic materials active in small amounts per volume unit of treated water (e.g. very thin films), able to stand for many oxidation cycles.

The transition from the conventional wastewater treatment processes to the advanced oxidation processes implies also the development of combined alternatives. One promising route is to match homogeneous and heterogeneous photocatalysis by adding oxidant species (hydrogen peroxide, ozone, Fenton systems), [22]. The ozone addition was reported to increase by ten folds the quantum yield in methanol decomposition on TiO_2, [23], and the reason is obviously the increased amount of $HO^{\cdot}$ active species (homogeneous photocatalysis) but also the decrease in recombination, an effect that is also common to H_2O_2.

Another possible route (yet at laboratory scale) for decreasing the costs by giving full use of the incident energy would be the combined photocatalysis and hydrogen production as these are valorizing the anodic (oxidation—photocatalysis) and cathodic (reduction—hydrogen production) half-reactions that could be expected by the simultaneous generation of holes and electrons, [24].

Considering this state of the art, our group developed research on photocatalytic processes, targeting the increase in the efficiency and the transferability towards industrial applications of the newly developed solutions. The results obtained in developing thin films of VIS-active photocatalysts are comparatively analyzed.

4 Thin Film Photocatalysts

Basically, thin films can be developed starting from powders or directly from a precursor system, as Fig. 1 shows.

Most commonly, powders are obtained by wet chemical techniques, like sol-gel (SG), chemical bath deposition (CBD) or hydrothermal synthesis (HT). Due to the properties of the organo-metallic compounds and there fast reactivity with water they represented the first choice for powders preparation; usually metal-precursor alkoxides (ethoxides, iso-propoxides) are used, along with morphology and grain-size controlling agents (e.g. acetylacetone). When using the powders as such, annealing is done for allowing the synthesis reaction to reach its maximum conversion, extending the crystallinity degree, removing unnecessary by-products, sintering, etc. According to the final product, the annealing temperature is chosen to allow the targeted transformations without losing active material (at temperatures below sublimation, melting or oxidation).

To prepare thin films, the powders should be deposited in thin, homogeneous, and free- of cracks layers. Most common techniques are doctor blade and its varieties as print screening using fluid pasts, while for much more diluted suspensions dipping or spraying can be employed.

The parameters that should be controlled for obtaining an optimal paste are the powder to solvent ratio, the surfactant(s), the mixing speed, etc.

The paste deposited as thin films is further subject of drying (if the initial powders were annealed) or of annealing (if the powders were not annealed). Smooth surfaces are obtained if the solvent is slowly released from the films, therefore a combination of drying (at 40–80 °C), followed by annealing is

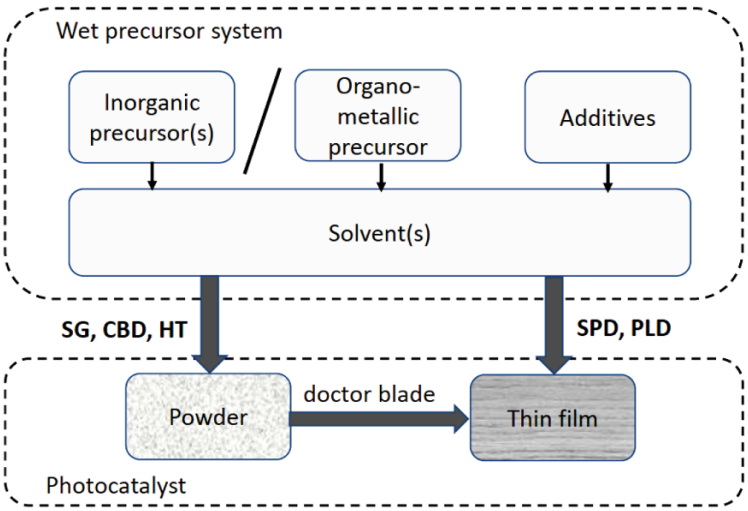

Fig. 1 Routes to obtain photocatalytic thin films

recommended, even for previously annealed powders, to further promote sintering in the thin films; this is a pre-requisite for the surface opto-electronic properties required during photocatalysis, when the electron-hole pair formed during irradiation needs to effectively split for following different reaction paths (reduction/oxidation). A continuous charge flow will thus support the reduced recombination and this is insured at nano-level by extended crystallite sizes and at micro-level by the lack of pinholes and cracks. This mechanism is less important if the crystallites are at quantum dots size, when quantum confinement dominates but this dimensional level should be reached in powder synthesis; in this case annealing is not recommended as it increases the crystallite sizes out of the quantum dots range.

For benchmarking, almost any newly developed photocatalyst uses TiO_2 Degussa P25 as reference. This product is a combination of anatase and rutile polymorphs (20–25 % rutile and 80–75 % anatase), with a highly suitable grain size (30–35 nm), [25] and a BET surface area of 55 ± 15 m^2/g; this combination makes Degussa P25 one of the most performant powder photocatalyst. There are thousands of papers reporting on dyes photodegradation on TiO_2 and recent reviews outline the need for a careful design of the photocatalyst, according to the targeted applications, [26].

Thus, although efficient, Degussa P25 can be surpassed in at least two ways: (1) increasing the efficiency in organic pollutants degradation (towards mineralization) and (2) extending the photocatalytic response towards the VIS range. This can be reached by doping (with metal cations or non-metal anions), by tuning the anatase: rutile ratio, by developing composite systems, by developing Schotky-type systems (semiconductor-metal interfaces), etc. Our group particularly focused on cation doping and on developing composite systems.

4.1 Photocatalytic Efficiency of Thin Films Obtained by Doctor Blade Technique

By using doctor blade, thin films were prepared and used in the photocatalytic degradation of methyl-orange (MO) and methylene blue (MB). These dyes were chosen because of their rather different structure (and flexibility); additionally, MO is recognized as being highly stable in photodegradation, thus most of the commercial dyes are supposed to lead to higher degradation/mineralization efficiencies.

Using TiO_2 Degussa P25, a broad variety of thin layered photocatalysts were prepared and the photocatalytic conditions were optimized (pH, process duration, dyes concentration). The steps followed in optimization were previously presented and the best process conditions are presented in Table 1.

The efficiencies in MO and MB photo-bleaching on mono-component photocatalysts are presented in Fig. 2.

Cadmium doping was chosen for investigating a concurrent process that might occur when treating industrial wastewaters, where dyes and metal cations are competing for the same reactions sites, that are slowly blocked by the metal irreversible adsorption (in the working conditions). Thus surface doping was done by immersing the thin film in a Cd^{2+} solutions, reaching a surface cation concentration of about 0.1 %. The results show the "poisoning" effect of cadmium with a consequent reduction in efficiency.

On the other hand, mixing the nano-sized Degussa P25 with the micro-sized anatase powder (Aldrich) thin films with MO removal efficiency similar to pristine Degussa were obtained, with the advantage of an easily processing of the paste and film. Further on, powders with various anatase:rutile ratio were prepared by sol-gel and mixtures was developed respecting the same nano-micro composite concept. The finely tuned anatas:rutile ratio allowed obtaining slightly higher efficiencies both in MO and in MB photo-bleaching, as compared to the reference.

A significant increase in the photodegradation efficiency was obtained when using a thin film containing copper sulfides ($Cu_{x=1\ldots2}S$), with efficiencies that largely exceed those obtained when using TiO_2. This is not surprising, considering that copper sulfide as bulk material shows both an indirect band gap between 1.05 and 1.21 eV and a direct band gap between 2.4 and 2.36 eV [34]. Micro-sized grains were used to prepare the thin films but, the long term stability of copper sulfides in water represents an issue that limits their application in industrial processes.

Industrial wastewaters rarely are loaded with a single pollutant. Particularly wastewaters from textile industry are loaded with mixtures of dyes, therefore further tests were done, using the reference TiO_2 Degussa P25. Wastewaters collected from a polyamide dyeing company contains three dyes: the acid dyes Bemacid Gelb, BG, (CAS EINECS: 235-406-9, $C_{25}H_{19}N_4NaO_8S_2$, M = 590.56 g/mol), Bemacid Rot, BR, (CAS EINECS: 276-115-7, $C_{24}H_{20}ClN_4NaO_6S_2$, M = 583.0 g/mol) and Bemacid Blue, BB, (CAS EINECS: 267-224-0, $C_{31}H_{28}N_3NaO_6S$, M = 593.63 g/mol). Mixtures of two dyes were tested and the results are presented in Fig. 3.

Table 1 Optimized photocatalytic processes on thin films obtained by doctor blade technique

Photo-catalyst	Dye	Radiation	Contact time, (min)	Optimised conditions	References
TiO_2 Degussa	MO	UV	360	MO: 0.0125 mM,	[27]
	MB			MB: 0.0125 mM,	
				H_2O_2 addition	
TiO_2 Degussa: 0.1 % Cd	MO	UV	360	MO: 0.00625 mM,	[28]
	MB			MB: 0.00625 mM,	
TiO_2 Degussa:TiO_2 Aldrich = 1:1	MO	UV	360	MO: 0.0125 mM,	[29]
	MB			MB: 0.0125 mM,	
				H_2O_2 addition	
TiO_2 Degussa:TiO_2 Sol-gel = 1:1	MO	UV	360	MO: 0.0125 mM,	[29]
	MB			MB: 0.0125 mM,	
				H_2O_2 addition	
Cu_xS	MO	UV	360	MO: 0,0125 mM,	[30]
	MB			MB: 0,0125 mM,	
				H_2O_2 addition	
TiO_2 Degussa	BG-BR	UV	360	Overall: 20 mg/L (BG + BR)	[31]
TiO_2 Degussa	BG-BB	UV	360	Overall: 20 mg/L (BG + BB)	[31]
TiO_2 Degussa	BR-BB	UV	360	Overall: 20 mg/L (BR + BB)	[31]
TiO_2 Degussa: WO_3 = 1:1	MO	UV	240	MO: 0,0125 mM, H_2O_2 addition	[32]
TiO_2 Degussa: WO_3 = 1:1	MO	UV	360	MO: 0,0125 mM,	[33]
				H_2O_2 addition	
Cu_xS:TiO_2 Degussa = 3:7	MO	UV	180	MO: 0,0125 mM,	[30]
	MB		300	MB: 0,0125 mM,	
				H_2O_2 addition	
Cu_xS:TiO_2 Degussa = 3:7	MO	VIS	180	MO: 0,0125 mM,	[30]
	MB		300	MB: 0,0125 mM,	
				H_2O_2 addition	
Cu_xS:TiO_2 Degussa = 1:1	MO	VIS	240	MO: 0,0125 mM,	[30]
	MB		300	MB: 0,0125 mM,	
				H_2O_2 addition	

Regardless the combination, the photodegradation efficiency of each individual dye is almost constant, proving that there is little reciprocal interaction between the dyes in solution and each is degraded according to a specific mechanism. The quinone-dye BB shows the lowest stability (highest degradation efficiency), while the azo-dyes BG and BR are more stable (as also MO is). The core molecule of BR is actually MO and on the two heads, two further aromatic nuclei are grafted with σ

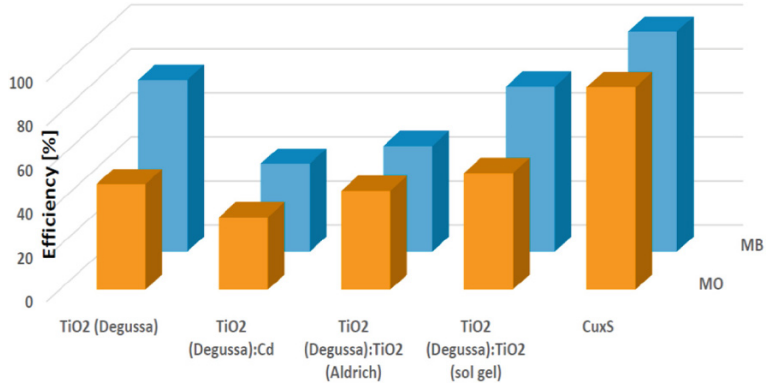

Fig. 2 Methyl orange and methylene blue photodegradation efficiencies on TiO_2 and Cu_xS

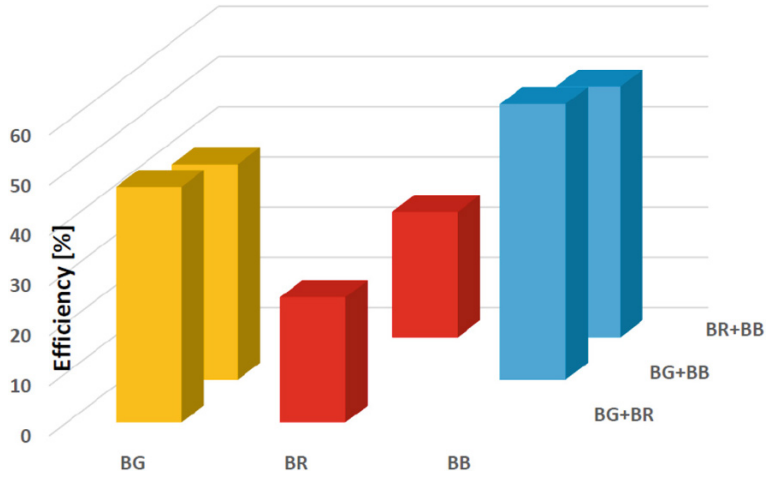

Fig. 3 Photo-bleaching efficiency of commercial dyes on TiO_2 thin films

bonds. Thus, the more flexible the dye molecule is, the more difficult is to degrade it. This conclusion is supported by the structural features of the dyes containing aromatic rests of antracen (BB), naphthaline (BG), and benzene (BR).

As already outlined, highly stable TiO_2 is UV active (E_g = 3.2 eV), while possible VIS-active Cu_xS is less stable in water. Thus, a combination of these could represent a solution; various ratios of TiO_2:Cu_xS were investigated as photocatalytic composites for MO and MB removal and the results for the optimized ratios are presented in Fig. 4.

A first unexpected result was that, under UV irradiation, the efficiency for both dyes degradation was higher (99 %) than any of the components (TiO_2 or Cu_xS), thus a synergistic effect was developed. This can be explained when considering

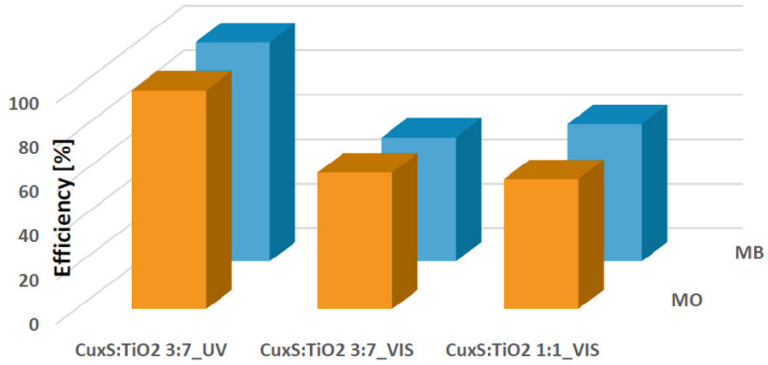

Fig. 4 Photocatalytic efficiency in MO and MB removal on composite substrates

that TiO_2 is an n-type semiconductor, while Cu_xS is of p-type, thus in situ developing n-p junctions that allow charge segregation, consequently efficient and fast formation of charge carriers. Following the concepts developed for the photovoltaic cells of the 3rd and 4th generation, this junctions should be active also under VIS irradiation and this was confirmed by performant efficiencies (above 60 %) in MO and MB bleaching.

The composites could contain also similar types of semiconductors (n-n) in tandem systems, as the TiO_2-WO_3 nano-micro sized grains. This combination was also effective but the WO_3 pH sensitivity raises operation issues and needs to be carefully controlled.

Technological speaking, to prepare thin films starting from powders is an easy up-scalable process but, considering the entire production cycle (including powders production), the energy consumption and the environmental burden can lead to a less sustainable process. Therefore, direct production of thin films represents recommendable solutions, also considering that lower amounts of material are required because much thinner films can be used, as their adherence and coherence is better.

4.2 Photocatalytic Efficiency of Thin Films Obtained by Spray Pyrolysis Deposition

There are many thin films deposition alternatives but, considering that photocatalytic applications require large covered areas, only few techniques can be depicted as industrial-acceptable. Basically, these techniques should be low energy consuming (thus avoiding vacuum), based on low cost precursors, able to be implemented on equipment that is not limited at cm^2 deposition areas (thus excluding furnaces) and, on the other hand, should allow fine tuning the main materials properties (crystallinity, polymorphism, morphology, surface charge) by simply modifying the deposition parameters. One technique that meets all these requirements is Spray Pyrolysis

Deposition (SPD), where an aerosol cone, prepared from the precursor solution with a carrier gas, is directed on the heated substrate where the pyrolysis reaction occurs and forms the thin film. The parameters that can be tuned are presented in Fig. 5.

The system compulsory consist of the precursor metal compound (inorganic salt or organo-metallic compound) and the solvent (according to the precursor, this can be water, alcohol/ethanol or a mixture of these). The precursor is subject of solvation and the solvated cation has a given reactivity (in the deposition conditions), that can be influenced by the type of solvent(s). To further tailor the reactivity in the pyrolysis reaction, the cation can be involved in structures of average stability, formed with complexing agents that will partially or totally replace the solvent in the first solvation sphere.

A specific control could be reached by using surfactants, bellow and above the critical micelle concentration (CMC) when the templating effect can be controlled by choosing the charge of the head and the length of the surfactant's tail. A detailed discussion is presented elsewhere, [35].

The use of various solvents and additives has little influence on crystallinity but can strongly change the morphology. For example, in ZnO deposition the morphology can totally be changed when using the anionic surfactant sodium dodecyl-sulfate (SDS), the cationic dodecyl-trimethyl-ammonium bromide (DTAB) or the nonionic dodecanol (DD). These surfactants have identic C_{12} linear tail but the interactions developed between the ionic or polar heads and the zinc cation are different, in terms of electrostatic forces (attraction/repulsion) and in terms of location (close to the surface, bellow the CMC of the surfactants and additionally on/in the micelles for concentrations higher than CMC). The templating effect of the surfactants, leading to more ordered arrangements allow the formation of macro-smooth layers, with roughness bellow 50 nm, Figs. 6, 7, and 8. Morphology control is essential especially when multi-layered structures are targeted, as in composite photocatalytic films.

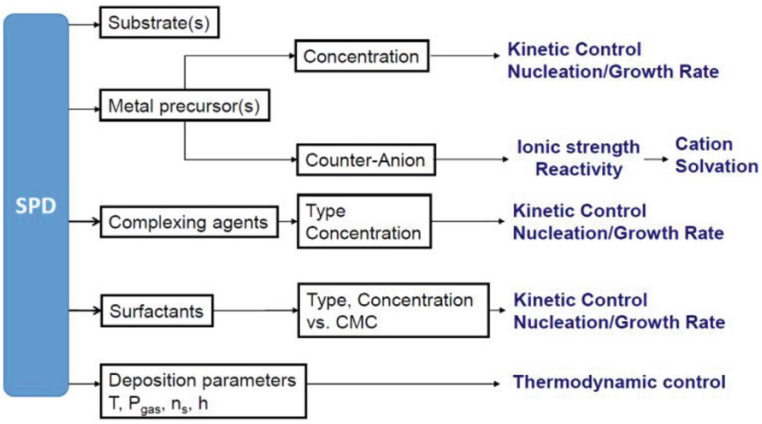

Fig. 5 Parameters that can control the thin films morphology in SPD

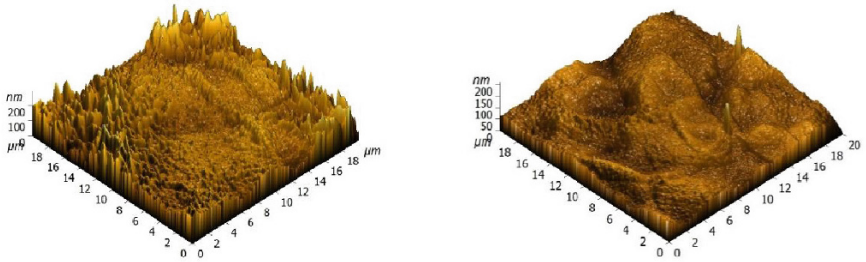

SDS, 50 ppm < CCM (= 96ppm) SDS, 150 ppm > CCM

Fig. 6 AFM images of ZnO thin films obtained using SDS

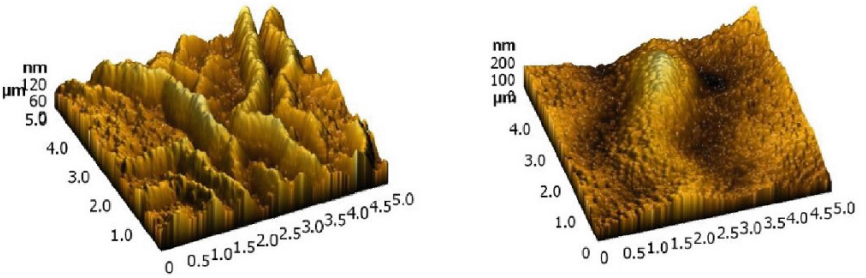

DTAB, 200 ppm < CCM (= 362 ppm) DTAB, 600 ppm > CCM

Fig. 7 AFM images of ZnO thin films obtained using DTAB

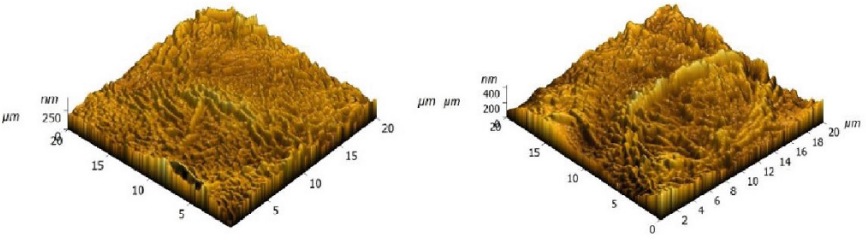

DD, 500 ppm < CCM (= 820 ppm) DD, 1000 ppm > CCM

Fig. 8 AFM images of ZnO thin films obtained using DD

The technique as such allows changing the carrier gas pressure, thus the droplet sizes in the aerosols, and therefore at very high pressures powders can be obtained in SPD. By correlating the substrate temperature, the carrier gas pressure and the distance between the nozzle and the substrate (h), the film density can be controlled,

while by increasing the number of spraying sequences (n_s), the film thickness can be increased. There never is a linear correlation between the film thickness and n_s, because of densification processes and the in situ annealing that starts during the residence of the film on the heated substrate.

The SPD deposited films are usually annealed, for increasing the crystallinity, for sintering and for releasing the by-products that are trapped in the film. Annealing in controlled atmosphere is also possible, particularly when sulfides are targeted (by sulfurization). Steps followed in developing efficient, optimized complex photocatalytic films by SPD are synthesized in Table 2.

The results show similar values (slightly higher) for the much thinner SPD films as compared to the doctor blade ones. In both situations the addition of hydrogen peroxide significantly increases the efficiencies, as result of the electrons trapping effect, thus reducing recombination.

As the method proved to be highly suitable for large area thin films deposition and the properties could be well controlled, SPD was used to extend the variety of photocatalysts, aiming at increasing the efficiency (including the VIS range), reducing costs and mitigating the dependence on critical materials, by replacing TiO_2 or by involving it in composite structures. The results also indicate a direct correlation between the band gap values and the photocatalytic efficiency in MO and MB bleaching: $E_{g,CuxS}$ (1.6–2.2 eV) < $E_{g,TiO2}$ (3.1–3.4 eV) < $E_{g,ZnO}$ (3.4–3.7 eV) < $E_{g,SnO2}$ (3.45–3.85 eV); the quite large deviation from the theoretical values is mainly the result of trapped by-products (particularly carbon from acetylacetone which was used as complexing agent in all syntheses) and of the polycrystalline structures that are developed, with crystallites' sizes of 15–30 nm. Thus, higher efficiencies are registered where a larger amount of charge carriers can be generated, in the semiconductors with lower band gaps.

The research in the past years focused on VIS-active photocatalysts. This implies a band gap that allows the use of radiation with wavelength above 300 nm, or developing engineered band gap interfaces, that through the charge flow (holes and/or electrons) allow charge segregation and/or suppress recombination. The first alternative was tested for Cu_xS and ZnO and the surfactants addition lead to increased VIS-efficiency.

The target of using solar radiation supports our experiments under UV + VIS irradiation. Stacked layers composites combining two or three layers of TiO_2, Cu_xS-Cu_xO and SnO_2 proved to be highly efficient in MB degradation; for water reuse, mineralization is compulsory thus the efficiency was investigated considering the TOC and TN decrease; impressing values above 75 % for TOC and 50 % for TN were reached, outlining that this newly developed types of photocatalysts represents a path that needs to be extended and optimized. The results also show that the mechanisms are complex and that nitrogen removal from wastewater is the challenging task for the near future.

Table 2 Optimized photocatalytic processes on thin films obtained by spray pyrolysis deposition

No.	Photo-catalyst	Dye	Radiation	Time [min]	Optimised conditions	η [%]	References
1	TiO_2	MO	UV	360	MO: 7.18 mg/L	76	[36]
		MB			MB: 7.18 mg/L	78	
2	TiO_2: 0.1 % Cd	MB	UV	360	MB: 0.003125 mM	36	[37]
3	ZnO, SDS	MO	UV	360	MO: 0.0125 mM	45	[38]
			VIS	360	H_2O_2 addition	20	
4	ZnO, DTAB	MO	UV	360	MO: 0.0125 mM	52	[38]
			VIS	360	H_2O_2 addition	16	
5	SnO_2	MB	UV	360	MB: 0.0125 mM	38	[39]
6	SnO_2	MB	UV	240	MB: 0.0125 mM	15	[40]
7	SnO_2	MB	UV	360	MB: 0.0125 mM	57	[41]
					H_2O_2 addition		
8	SnO_2: 0.5 % W	MB	UV	360	MB: 0.0125 mM	28	[42]
					H_2O_2 addition		
9	SnO_2: 0.25 % Zn	MB	UV	360	MB: 0.0125 mM	30	[42]
10	Cu_xS	MB	VIS	240	MB: 0.0125 mM	93	[43]
					H_2O_2 addition		
11	Cu_xS	MB	VIS	1080	MB: 0.0125 mM	80	[43]
					H_2O_2 addition		
12	SnO_2/TiO_2	MO	UV	360	MB: 0.0125 mM	69	[44]
					H_2O_2 addition		
13	SnO_2/TiO_2	MB	UV + VIS	360	MB: 0.0125 mM	TOC: 91	[13]
						TN: 72	
14	SnO_2/Cu_xS	MB	UV + VIS	360	MB: 0.0125 mM	TOC: 75	
						TN: 54	

(continued)

Table 2 (continued)

No.	Photo-catalyst	Dye	Radiation	Time [min]	Optimised conditions	η [%]	References
15	$SnO_2/TiO_2/WO_3$	MO	UV	360	MB: 0.0125 mM	63	[44]
					H_2O_2 addition		
16	$SnO_2/ZnO/Cu_2S$	MO	UV	360	MO: 0.0125 mM	25	[11]
		MB			MB: 0.0125 mM	31	
17	$SnO_2/ZnO/Cu_2S$	MO	UV	360	MO: 0.0125 mM	26	[11]
		MB			MB: 0.0125 mM	42	
					H_2O_2 addition		
18	SnO_2/Cu_x, Cu_xO/TiO_2	MB	UV + VIS	360	MB: 0.0125 mM	TOC: 78	
						TN: 60	

5 Conclusions

Since almost 40 years, heterogeneous photocatalysis was intensively studied in terms of materials, process and lately, in terms of costs. There are already market applications, ranging from self-cleaning, anti-fogging and anti- corrosive coatings up to indoor air sterilization but the large-scale environment photocatalytic processes are still seldom. The paper presents a review on the latest developments and trends, particularly focusing on wastewater treatment, aiming at water recycling. The results obtained in the RES-REC group were step-wise developed to obtain thin photocatalytic films, active under VIS and solar radiation, efficient in dyes mineralization. The concept of nano-micro composites of diode or tandem type developed in our group, is detailed presented and proves a viable path for further optimization.

Acknowledgments We hereby acknowledge the structural founds project PRO-DD (POS-CCE, O.2.2.1, ID 123, SMIS 2637, No 11/2009) for providing the infrastructure used in this work and the PNII-Cooperation project NANOVISMAT, contract no. 162/2012 financed by UEFISCDI which supported the latest research hereby presented.

References

1. Venturi, M., Balzani, V.,& Gandolfi, M. T. (2005). Fuels from solar energy. A dream of giacomo ciamician, the father of photochemistry, *Proceedings of the 2005 Solar World Congress Orlando*, Florida, USA. August 6–12, 2005.

2. Fujishima, A., & Honda, K. (1972). Electrochemical photolysis of water at a semiconductor electrode. *Nature, 238*, 37–38.
3. Fujishima, A., Rao, T. N., & Tryk, D. A. (2000). Titanium dioxide photocatalysis. *Journal of Photochemistry and Photobiology C: Photochemistry Reviews, 1*, 1–21.
4. Yao, L., & He, J. (2014). Recent progress in antireflection and self-cleaning technology—from surface engineering to functional surfaces. *Progress in Materials Science, 61*, 94–143.
5. Ortelli, S., Blosi, M., Albonetti, S., Vaccari, A., Dondi, M., & Costa, A. L. (2013). TiO_2 based nano-photocatalysis immobilized on cellulose substrates. *Journal of Photochemistry and Photobiology A: Chemistry, 276*, 58–64.
6. Primo, A., & García, H. (2013). Solar photocatalysis for environment remediation (Chap. 6). In S. L. Suib (Ed.), *New and future developments in catalysis* (pp. 145–165). Elsevier: Amsterdam.
7. Malato, S., Fernández-Ibáñez, P., Maldonado, M. I., Blanco, J., & Gernjak, W. (2009). Decontamination and disinfection of water by solar photocatalysis: Recent overview and trends. *Catalysis Today, 147*, 1–59.
8. Antonopoulou, M., Evgenidou, E., Lambropoulou, D., & Konstantinou, I. (2014). A review on advanced oxidation processes for the removal of taste and odor compounds from aqueous media. *Water Research, 53*, 215–234.
9. Bolton, J. R., Bircher, K. G., Tumas, W., & Tolman, C. A. (2001). Figures-of-merit for the technical development and application of advanced oxidation technologies for both electric- and solar-driven systems. *Pure and Applied Chemistry, 73*(4), 627–637. IUPAC.
10. Herrmann, J.-M. (2010). Fundamentals and misconceptions in photocatalysis. *Journal of Photochemistry and Photobiology A: Chemistry, 216*, 85–93.
11. Enesca, A., Isac, L., & Duta, A. (2013). Hybrid structure comprised of SnO_2, ZnO and Cu_2S thin film semiconductors with controlled optoelectric and photocatalytic properties. *Thin Solid Films, 542*, 31–37.
12. Ayati, A., Ahmadpour, A., Bamoharram, F. F., Tanhaei, B., Mänttäri, M., & Sillanpää, M. (2014). A review on catalytic applications of Au/TiO_2 nanoparticles in the removal of water pollutant, Chemosphere, Available online February 18, 2014.
13. Enesca, A., Isac, L., Andronic, L., Perniu, D., & Duta, A. (2014). Tuning SnO_2–TiO_2 tandem systems for dyes mineralization. *Applied Catalysis B: Environmental, 147*, 175–184.
14. Hamrouni, A., Lachheb, H., & Houas, A. (2013). Synthesis, characterization and photocatalytic activity of ZnO-SnO_2 nanocomposites. *Materials Science and Engineering: B, 178*, 1371–1379.
15. Sampaio, M. J., Silva, C. G., Silva, A. M. T., Vilar, V. J. P., Boaventura, R. A. R., & Faria, J. L. (2013). Photocatalytic activity of TiO_2-coated glass raschig rings on the degradation of phenolic derivatives under simulated solar light irradiation. *Chemical Engineering Journal, 224*, 32–38.
16. Hosseini Zori, M., & Soleimani-Gorgani, A. (2012). Ink-jet printing of micro-emulsion TiO_2 nano-particles ink on the surface of glass. *Journal of the European Ceramic Society, 32*, 4271–4277.
17. Kralova, M., Dzik, P., Vesely, M., & Cihlar, J. (2014). Preparation and characterization of doped titanium dioxide printed layers. *Catalysis Today, 230*, 188–196.
18. Serpone, N. (1997). Relative photonic efficiencies and quantum yields in heterogeneous photocatalysis. *Journal of Photochemistry and Photobiology A: Chemistry, 104*, 1–12.
19. Serpone, N., Sauvé, G., Koch, R., Tahiri, H., Pichat, P., Piccinini, P., et al. (1996). Standardization protocol of process efficiencies and activation parameters in heterogeneous photocatalysis: Relative photonic efficiencies ζr. *Journal of Photochemistry and Photobiology A: Chemistry, 94*, 191–203.
20. Mills, A., & McFarlane, M. (2007). Current and possible future methods of assessing the activities of photocatalyst films. *Catalysis Today, 129*, 22–28.
21. Herrmann, J.-M., Guillard, C., & Pichat, P. (1993). Heterogeneous photocatalysis: an emerging technology for water treatment. *Catalysis Today, 17*, 7–20.

22. Santiago-Morales, J., Gómez, M. J., Herrera-López, S., Fernández-Alba, A. R., García-Calvo, E., & Rosal, R. (2013). Energy efficiency for the removal of non-polar pollutants during ultraviolet irradiation, visible light photocatalysis and ozonation of a wastewater effluent. *Water Research, 47*, 5546–5556.
23. Mena, E., Rey, A., Acedo, B., Beltrán, F. J., & Malato, S. (2012). On ozone-photocatalysis synergism in black-light induced reactions: Oxidizing species production in photocatalytic ozonation versus heterogeneous photocatalysis. *Chemical Engineering Journal, 204–206*, 131–140.
24. Zhang, W., Li, Y., Wang, C., Wang, P., & Wang, Q. (2013). Energy recovery during advanced wastewater treatment: Simultaneous estrogenic activity removal and hydrogen production through solar photocatalysis. *Water Research, 47*, 1480–1490.
25. Almquist, C. B., & Biswas, P. (2002). Role of synthesis method and particle size of nanostructured TiO_2 on its photoactivity. *Journal of Catalysis, 212*, 145–156.
26. Nakata, K., & Fujishima, A. (2012). TiO_2 photocatalysis: Design and applications. *Journal of Photochemistry and Photobiology C, 13*, 169–189.
27. Andronic, L., & Duta, A. (2008). Influence of pH And H_2O_2 On Dyes Photodegradation. *Physica Status Solidi C—Current Topics in Solid State Physics, 5*, 3332–3337.
28. Andronic, L. A., Enesca, A., Vladuta, C., & Duta, A. (2009). Photocatalytic activity of cadmium doped TiO_2 films for photocatalytic degradation of dyes. *Chemical Engineering Journal, 152*, 64–71.
29. Andronic, L., Andrasi, D., Enesca, A., Visa, M., & Duta, A. (2011). The influence of titanium dioxide phase composition on dyes photocatalysis. *J Sol-Gel Science and Technology, 58*(1), 201–208.
30. Andronic, L., Isac, L., & Duta, A. (2011). Photochemical synthesis of copper sulphide/titanium oxide photocatalyst. *Journal of Photochemistry and Photobiology A: Chemistry, 221*, 30–37.
31. Andronic, L., & Duta, A. (2012). Photodegradation processes in two-dyes systems—simultaneous analysis by first-order spectra derivative method. *Chemical Engineering Journal, 198–199*, 468–475.
32. Carcel, R. A., Andronic, L., & Duta, A. (2011). Photocatalytic degradation of methylorange using TiO_2, WO_3 and mixed thin films under controlled pH and H_2O_2. *Journal of Nanoscience and Nanotechnology, 11*, 1–7.
33. Carcel, R. A., Andronic, L., & Duta, A. (2012). Photocatalytic activity and stability of TiO_2 and WO_3 thin films. *Materials Characterization, 70*, 68–73.
34. Gadave, K. M., & Lokhande, C. D. (1993). Formation of Cu_xS films through a chemical bath deposition process-letter. *Thin Solid Films, 229*, 1–4.
35. Duta, A., Andronic, L., Perniu, D., Manceriu, L., & Enesca, A. (2014). Crystalline wide band gap semiconductors with opto-electronic proeprties. In *Handbook of nanofunctional materials* (pp. 157–176). Hauppauge: Nova Science Publishers.
36. Andronic, L., & Duta, A. (2007). TiO_2 thin films for dyes photodegradation. *Thin Solid Films, 515*, 6294–6297.
37. Andronic, L., & Duta, A. (2011). The influence of precursor's composition and concentration on cadmium doped TiO(2) film. *Central European Journal of Chemistry, 10*, 85–90.
38. Duta, M., Perniu, D., & Duta, A. (2014). Photocatalytic zinc oxide thin films obtained by surfactant assisted spray pyrolysis deposition. *Applied Surface and Science*, *316*, 80–88.
39. Enesca, A., & Duta, A. (2010). Influence of the precursors' composition on the properties of SnO_2 thin films. *Thin Solid Films, 519*, 568–572.
40. Enesca, A., & Duta, A. (2011). The influence of organic additives on the morphologic and crystalline properties of SnO_2 obtained by spray pyrolysis deposition. *Thin Solid Films, 519*, 5780–5786.
41. Enesca, A., Bogatu, C., Voinea, M., & Duta, A. (2010). Opto-electronic properties Of SnO_2 layers obtained by SPD and ECD techniques. *Thin Solid Films, 519*, 563–567.

42. Enesca, A., Andronic, L., & Duta, A. (2012). Optimization of opto-electrical and photocatalytic properties of SnO2 thin films using Zn2+ and W6+ dopant ions. *Catalysis Letters, 142*, 224–230.
43. Isac, L., Andronic, L., Enesca, A., & Duta, A. (2013). Copper sulfide films obtained by spray pyrolysis for dyes photodegradation under visible light irradiation. *Journal of Photochemistry and Photobiology A: Chemistry, 252*, 53–59.
44. Enesca, A., Andronic, L., & Duta, A. (2012). The influence of surfactants on the crystalline structure, electrical and photocatalytic properties of hybrid multi-structured (SnO_2, TiO_2 and WO_3) thin films. *Applied Surface and Science, 258*, 4339–4346.

Fly Ash Based Substrates for Advanced Wastewater Treatment

Maria Visa, Cristina Cazan and Luminita Andronic

Abstract From coal combustion millions of tons of ash are being generated every year and this leads to huge environmental problems. Nowadays the annual ash production is about 600 million tons per year from which 75–80 % is fly ash. One solutions for solving this problem would be wastes reuse (fly ash in this case) as second raw material to obtain new materials, such as zeolites, which can be further used as adsorbents/photocatalysts in wastewater treatment for heavy metals, dyes, etc. removal. Fly ash has a suitable composition (amorphous aluminosilicate glass being the prevalent reactive phase) that could allow zeolites production and has the advantage of low cost. Therefore, alkali processing of fly ash, at increased temperature and pressure can be a viable path (e.g. by hydrothermal treatment). Heavy metals are excessively released into the environment due to high urbanization and industrialization. These pollutants do not degrade into harmless end products as the organic pollutants do. They can affect life forms even at low concentrations because of their increased toxicity. For their removal many techniques are used among which adsorption is one representative choice in terms of efficiency and selectivity. This paper presents a synthesis of the results obtained in developing highly efficient fly-ash based substrates for heavy metals removal in advanced wastewater treatment processes. The influence of the fly ash composition (collected from CHP Plants from Romania) is discussed in correlation with the adsorption efficiency of heavy metals and dyes from one, two or three pollutants systems. Further on the efficiency is correlated with the substrates' properties and hydrothermal processing conditions; the XRD diffractograms confirm the crystalline structure and shows that the main components of modified fly ash are: different mixed compounds of SiO_2 and Al_2O_3, albite, γ oxide Fe_2O_3. These crystalline components have uniform microporous structures, shown by SEM that supports *ionic or highly polar interactions, due to their negatively charged surface.*

Keywords Adsorption · Wastewater treatment · Fly ash · Heavy metals · Dyes

M. Visa (✉) · C. Cazan · L. Andronic
Renewable Energy Systems and Recycling R&D Centre, Romania,
Transilvania University of Brasov, Eroilor 29, 500036 Brasov, Romania
e-mail: maria.visa@unitbv.ro

I. Visa (ed.), *Sustainable Energy in the Built Environment - Steps Towards nZEB*,
Springer Proceedings in Energy, DOI 10.1007/978-3-319-09707-7_40

1 Introduction

Water is a necessary environmental factor of life, while being an important raw material for the industry, as most chemical reactions occur in aqueous medium. Saving water to save the planet and to make the future of mankind safe is what we need now. Most often pollution of surface water is the result of human activity (anthropogenic pollution), with major consequences on the eco-systems and, eventually on the global water resources. The result is now-a days the water stress and the forecast is dim if not suitable and concerted actions are planned and implemented all over the world.

Polluted water may be loaded with different pollutants, as water is a very good host for multiple substances depending of the source, for example: the polluted waters from agriculture will contain mostly pesticides, nitrogen fertilizers (phosphate) and salts; sewage water will contain remnants of household (detergents, fats, manure etc.) and industrial wastewaters contain a broad range of organic and inorganic chemicals.

The main dangerous pollutants in wastewater resulted from metal finishing, dyes manufacturing and textile industry and food processing are: heavy metals dyes and surfactants.

The largest amount of heavy metals (HM) from industry are discharged directly into rivers; in Europe, in 2001 huge amounts of HM were discharged: 864 t/year chromium, 71.5 t/year nickel, 45.8 t/year copper, 41.7 t/year lead, 8.1 t/year cadmium, 5.1 t/year arsenic and 0.5 t/year mercury [1].

There are over 10,000 commercial dyes available today and yearly there are produced 7 × 105 tons of dyes [2] with complex chemical structure (with aromatic rings); on average 2 % of these are exhausted in aqueous effluents, while 10 % of dyes are lost during the dyeing process [3] and remain in the environment for a long time. The main indicator of water pollution is color, which in addition to unsightly problem (even at concentration below 0.005 mg/L) also brings other problems such as inhibition of photosynthesis because many dyes are toxic and eutrophication thus affecting aquatic organisms; many dyes are carcinogenic, mutagenic and can harm the kidneys, the liver, reproductive system, brain and central nervous system [4]. Also traces of toxic metals are expected from organo-metallic dyes and additives.

Textile industry followed by the food industry are the largest consumers of water for processing, while the chemical industry uses a large amounts of water for cooling the obtained products and the installations, Fig. 1.

Nature has its own mechanisms to neutralize the pollutants but, if discharged wastewater flows are high and in too large concentrations, nature can no longer meet this task because each water has a limited self-purification capacity. Water self-purification is a natural process involving physical, chemical, biological and bacteriological factors. If that limit is exceeded, sudden and irreversible changes may occur in its flora and fauna that might even turn it into dead water (fish dies and become infection sources, both for the natural ecosystem and for public health).

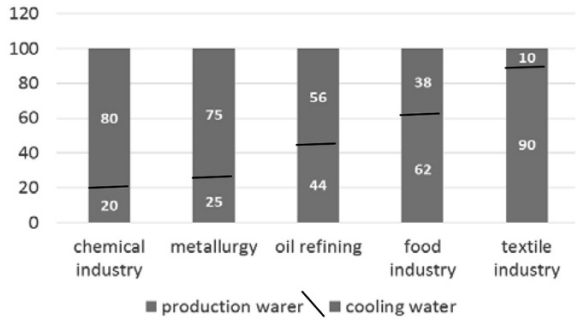

Fig. 1 Distribution of water consumption for different industries [5]

Wastewater treatment involves a combination of physical, chemical, biological and bacteriological processes, designed to reducing the organic, inorganic and bacteriological pollutants in order to protect the environment for obtaining the clean water. The degree of treatment depends on the technologies and the equipment employed to remove a mix of substances (sludge) which in turn must be disposed of, as not to cause any harm to the environment. The non-biodegradable pollutants involve complex processes, expensive equipment and can be satisfied by employing advanced methods of treatment (AMT). The current trend is to use low cost materials, including wastes, and innovative technologies. The pollution or toxic effect of a substance depends on its structure and concentration.

Usually, heavy metals in high concentration can be removed in wastewater in two steps:

1. *Chemical precipitation*—adding reagents to form low-soluble heavy metals compounds (hydroxides, sulfides, carbonates).
2. *Coagulation and flocculation*—adding specific reagents.

Depending on the initial composition, many alternatives for advanced wastewater treatment are proposed:

- adsorption: regular adsorption, ion exchange [6], complexing followed by adsorption of the metal complex;
- reduction reactions and electrochemical processes [7];
- membrane processes: microfiltration (MF); ultrafiltration (UF) [8]; nanofiltration (NF) [9]; electrodialysis (ED); reverse osmosis [10].

Among these, adsorption technologies have several advantages: easy operation and well known technology, inexpensive equipment, less sludge, adsorbents' reuse after desorption.

Wastewater containing dyes are hard to treat because the organic molecules are persistent to aerobic digestion and are designed to have good resistance to light. Synthetic dyes cannot be easily and efficiently removed from wastewater by traditional methods at affordable costs. The methods of dyes removal can be divided in

three classes: biological [11, 12], chemical and physical [13] methods and are presented in Table 1.

These methods have advantages and disadvantages, depending on the load in wastewaters and on the cost.

Adsorption is present in many natural, physical, biological, and chemical systems, and is widely used in industrial applications. However to develop an adsorption process at industrial and commercial scale requires the availability of a suitable adsorbent in large quantities at feasible cost. This has stimulated fundamental researcher in adsorption and led to the development of new adsorbents. A large application of adsorption as a separation process was extended by the development of molecular sieves adsorbents and especially the synthetic zeolites.

Therefore many studies are focusing on low-cost, highly efficient adsorbents. The low cost adsorbent materials can be natural compounds (clays, bentonite [14] diatomite pillared layer [15], kaolinite, smectites, vermiculites, palygorskites), volcanic tuff, zeolites [16], cellulose, chitin [17], red mud resulted from the aluminum processing [18], agricultural by-products [19] (apple, pomace [20], wheat straw, wheat bran, coir pith [21] corncobs or barley husks [22], rice husk [23], peanut hulls [24], orange peel [25]), different types of sawdust [26], powder of different leaves [27], organic artificial or synthetic waste (bone char [28], scrap rubber, humus, or bituminous coal [29]), wood based biosorbents (pine sawdust [30], maple sawdust [31], cedar sawdust [32], straw, seeds hulls [33], wheat bran, sawdust oak [34], wood fiber [35], treated cotton [36], peat [37], sugar beet pulp [38], marine alga Padina [39]) or, activated sewage sludge [40].

Ash, resulting from burning coal or biomass is a mixture of oxides with unburned carbon and other minority inorganic compounds thus has a predominant negative surface charge and represents a promising adsorbent.

The use of fly ash for heavy metals removal from wastewater was reported as early as 1975 (Gangoli et al.). Since then, many research groups focused on

Table 1 Methods for dyes removal from wastewater biological methods chemical methods

Biological methods	Chemical methods	Physical methods
• Bleaching in the presence of fungicides • Adsorption on microbial biomass • Aerobic and anaerobic degradation • Bioremediation • Nitrification, denitrification, • Fermentation reactors, • Activated sludge tanks	*Oxidative processes* • Photochemical oxidation (Fenton reactions), • Heterogeneous photo-catalysis • Ozonation • Oxidation with NaOCl • Electrochemical oxidation • *Coagulation* • *Flocculation combined with flotation* • *Precipitation-Flocculation with* Fe(II)/$Ca(OH)_2$ • *Electrocoagulation* • *Ion exchange*	• Physical Adsorption • Irradiation • Membrane processes (microfiltration, ultrafiltration, nano-filtration, • Reverse osmoses)

optimizing the efficiency of fly ash-based adsorption processes. Lately, dyes removal from industrial wastewaters by adsorption on different waste materials was investigated. Many research groups tested the fly ash in adsorption of methyl orange, methylene blue [41, 42].

The use of wood ash is mostly reported for heavy metals adsorption [43, 44] and also for industrial wastewater resulted from dyes manufacturing and textile industry [45]. Experiments using methylene blue as testing dye are reported on rice husk ash [46] and other ash types, being explained by the significant amount of unburned carbon [47].

Fly ash, the lightest fraction resulted in coal burning is also largely investigated for heavy metals and dyes adsorption [48] because the priority compounds from fly ash favor the heavy metals adsorption and are active sites in dyes' immobilization.

2 Materials and Methods

Brasov City has a CPH plant which works with two boilers (420 t/h capacity) and two turbo-aggregates generating 50 MW each. Every year 6×10^5 tons of coal are burned and the fly ash resulted amounts 2×10^5 tons/year, out of which only 1/3 is reused as a cement additive. One possible application is to develop alternative processes (like wastewater treatment), involving the use of this waste.

The major oxide components in fly ash, with a certain influence in heavy metals and dyes removal are presented in Table 2. Using emission spectrometry other metals were also identified in small amounts (Ba, Cu, Sn, Pb, Cr, Ni, V, Zn, Ti). According to the ASTM standards, the raw FA pertains of class F because the sum of the SiO_2, Al_2O_3 and Fe_2O_3 is above 70 %.

The raw fly ash was supplied by the CHP Plant Brasov, Romania directly from the electro-filters, having a grain diameter between 40 and 100 μm, but can vary form 1 μm at over 200 μm, with various grain size distribution curves Fig. 2.

Some deviation may exist for these values due to smaller particles agglomeration. More and more are now investigated the optimized fly ash compositions to obtain an efficient adsorbent able to remove heavy metals and dyes from wastewaters with complex composition.

The fly ash crystalline structure was evaluated by XRD (Advanced D8 Discover Bruker diffractometer, $Cu_{K\alpha 1}$ = 1.5406 Å, 40 kW, 20 mA, 2θ range 10°–70°, scanning step 0.02°, scan speed 2 s/step) and complementary data were obtained by FTIR spectroscopy (Spectrum BX Perkin Elmer BX II 75548, λ = 400–4,000 nm).

Table 2 The fly ash composition

FA composition (%)									
SiO_2	Al_2O_3	Fe_2O_3	CaO	MgO	K_2O	Na_2O	TiO_2	MnO	LOI*
53.32	22.05	8.97	5.24	2.44	2.66	0.63	1.07	0.08	1.58

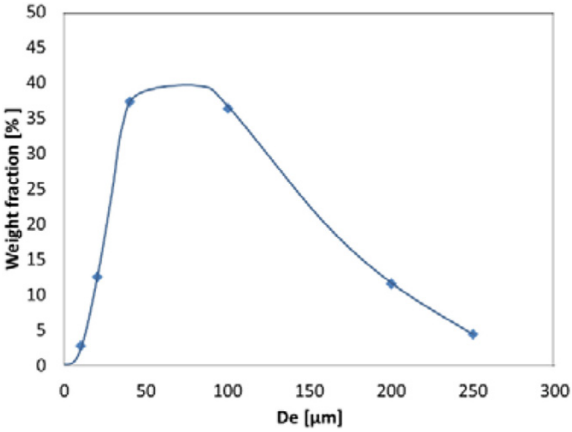

Fig. 2 Particle size distribution of the fly ash

The X-ray diffraction (XRD), Fig. 3 show that predominant mineral phases are crystalline and the major components are: SiO_2 (as αSiO_2 quartz, quartz syn and tetragonal and orthorombic SiO_2) combined with Al_2O_3 (as rhombo H, mullite $3Al_2O_3 \cdot 2SiO_5$ and γ-Al_2O_3), iron oxides (hematite Fe_2O_3 and magnetite Fe_3O_4), the less MnO_2, lime (CaO) and gypsum $CaSO_4 \cdot 2H_2O$. The particle size of mullite produced by the decomposition of kaolinite may be as small as 0.01.

The unburned carbon graphite and carbon hexagonal (chaoite), along with compounds as micro-sized crystallites represents a significant part of the substrate and can explain the versatility of this material in adsorption processes of heavy metals, organic pollutants, including dyes and surfactants [49]. Based on this type of data the empirical formula can be: $Si_{1.0}Al_{0.45}Ca_{0.51}Na_{0.04}Fe_{0.039}Mg_{0.020}\ K_{0.013}Ti_{0.011}$.

Considering its generic composition, FA can also be used as a low-cost adsorbent, solving two major environmental problems, by recycling and reducing the air and water pollution and by developing novel products. A more recent approach is to

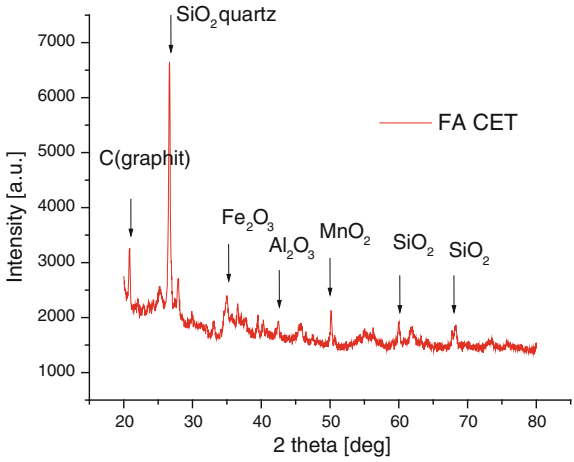

Fig. 3 XRD graph of raw fly ash

use FA as a resource for advanced adsorbent materials used for heavy metals (HM: cadmium, cooper, nickel, iron, lead, zinc) and dyes (methylene blue—MB, and methyl orange—MO) [50–53] removal.

The fly ash surface properties are strongly depending on many factors, including the coal type/composition, the coal- burning process in the power plant and the furnace characteristics. The differences are related to the oxides and carbon composition in the fly ash and recent studies proved that the heavy metal adsorption effectiveness is enhanced by the CaO content [54, 55]. These differences are registered even at the same CHP, from one coal batch to another and raise significant problems when designing a technology aiming at fly ash reuse as novel adsorbent. Therefore, fly ash should be conditioned, for getting a more constant (and reproducible) composition. Obviously, the conditioning process will also target the enhancement of the surface properties, by increasing the amount and affinity of the active sites, for a given group of pollutants.

Conditioning aims at accelerated solubilization of chemically unstable or water-soluble compounds, followed by re-precipitation of low solubility compounds; the development of higher BET specific surfaces represents a complementary aim, along with the control of the surface charge (value and sign). For the removal of heavy metals cations, the surface should be negatively charged, while for organics removal, the charge is depending on the predominant charge of the pollutant. The use of concentrated NaOH solutions for modifying the fly ash (FA) surface is reported, in processes at room temperature [56], and in hydrothermal processes. The chemical reactions on the FA grains surface are complex leading to composition modifications, due to dissolution and precipitation of various compounds, mainly alumina-silicates [56] and rearrangements of the oxide/carbon phases in the FA; crystal dissolution can also appear, increasing the amorphous phase; this treatment can lead (at extreme pH and temperature) to the development of ion exchanging surfaces, of zeolite type. But, the use of highly concentrated NaOH solutions (8 M [57], or pH = 13.95 [58]) can rise environmental problems and increases the complexity of the wastewater treatment technology. Therefore, alternatives must develop: either the use of less concentrated NaOH (0.5, 1, 2N, even 4N) solutions for surface modification and/or the use of other surface modifiers.

Heavy metals are easily reacting with chelating agents such as Complexone III (the sodium salt of the ethylenediamine tetraacetic acid) solution (CIII, Rearal, 99 %, c = 10 %), Eriochrome Blacke T solution (EBT, 96 %, c = 0.5 %) or Pyrocatechol Violet solution (PV, Merck, 98 %, c = 0.5 %) [59]. Following this rational, FA surface was modified, by batch mixing for 48 h, of a 1/10 ratio dispersion of FA with each chemical agents. The XRD peaks in Fig. 4 prove a complex composition, rich in various inorganic components (oxides and salts); graphite is also present in the FA, in almost constant amount in the unmodified and in the modified FA. The data also show crystalline modifications up to 36.83 % that can be attributed to dissolution of tetragonal (t) SiO_2 followed by re-precipitation of orthorhombic (o) SiO_2 forming aggregated particles with diameters less than 5 μm; these develop fractured morphologies, with more edges, consequently a surface with higher roughness, as presented in Fig. 5.

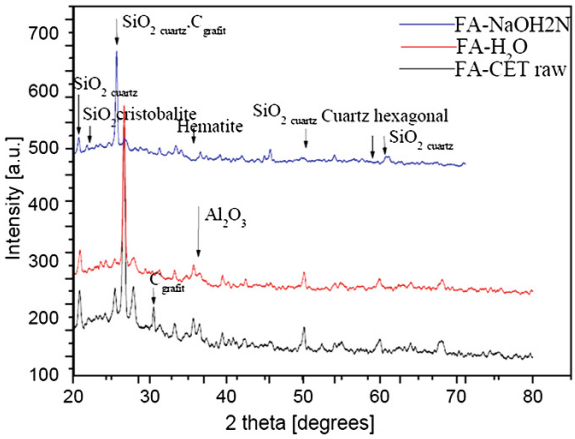

Fig. 4 XRD patterns of FA raw, washed and treated with NaOH 2N, main components

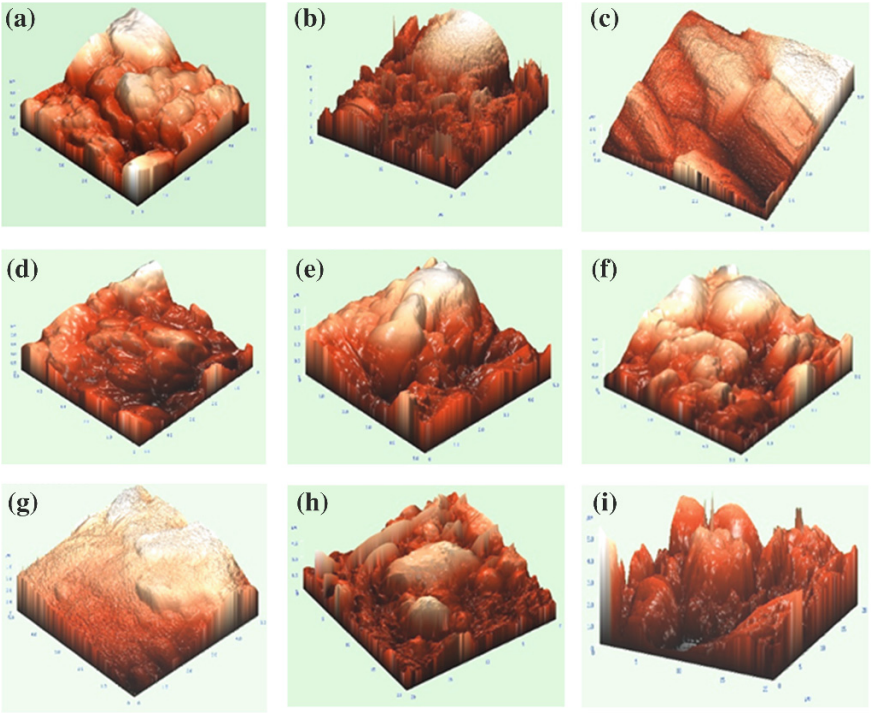

Fig. 5 Surface morphology of: **a** raw FA; **b** washed FA; **c** FA modified with HCl 2N; **d** FA modified with NaOH 1 N; **e** FA modified with NaOH 2N; **f** FA modified with NaOH 4N; **g** FA modified with CIII; **h** FA modified with PV; **i** FA modified with EBT [60]

The surface morphology is changed, Fig. 5c, d. The raw FA consists of conglomerates of spherical particles, with diameters ranging from 1 to 30 μm. The FA modified with NaOH 2N leads to higher specific surface and increased dimension homogeneity that can explain the high efficiencies registered in heavy metals removal even at very short contact times.

2.1 The Adsorption Experiments

To test the efficiency of these substrates, the experimental protocol was designed for heavy metals removal via adsorption.

The experiments were conducted, under mechanical stirring, at room temperature using cadmium and nickel ions from aqueous solutions in a broad concentration range: 10–1,000 mg/L. These two cations were chosen because: (i) cadmium is one of the most toxic cations, quite pH sensitive (at pH > 8.1 it forms the insoluble cadmium hydroxide); (ii) copper is another heavy metal but with lower toxicity, still having a low discharge limit (iii) in water both cations are hydrated as $[Cd(H_2O)_6]^{2+}$ and $[Cu(H_2O)_{4-6}]^{2+}$, thus they have different volume, different mobility and are expected to well test the adsorption limits of the substrates.

Heavy metal concentrations, before and after adsorption were evaluated by atomic adsorption spectroscopy (AAS) (Analytic Jena, ZEEnit 700), at λCd = 228.8 nm, at λNi = 232.0 nm and λCu = 324.75 nm.

The adsorption efficiency, η, and capacity qt were evaluated based on the optimal time and mass balance previously set:

$$\eta = \frac{(c^i_{HM} - c^t_{HM}) \times 100}{c^i_{HM}} \tag{1}$$

$$q_t = \frac{(c^i_{HM} - c^t_{HM}) \times V}{m_{ss}} \tag{2}$$

where: c^i_{HM} and c^t_{HM} represent the initial and momentary equilibrium concentrations of the heavy metal (HM, mg/L), V the solution volume (L) and m_{ss} is the amount of solide substrate (g).

The immobilization efficiency of Cd^{2+} and Ni^{2+} from mono-cation solution metal are discussed in connection with contact time from 5 min up to 60 min, wastewater volume: adsorbent mass ratio (1 g:100 mL) and ions concentration; Langmuir and Freundlich mechanisms were found to describe the adsorption processes. The process follows a pseudo-second order kinetic, for both metals, on the entire concentration range. Highly efficient adsorption, even at very low heavy metals concentrations (20 ppm), is registered for fly ash modified with NaOH. As expected considering their mobility, copper cations adsorb faster and with higher efficiency. Therefore, further investigations focused on cadmium cation adsorption. As reference, adsorption test were done on wet activated carbon powder (Merck), to

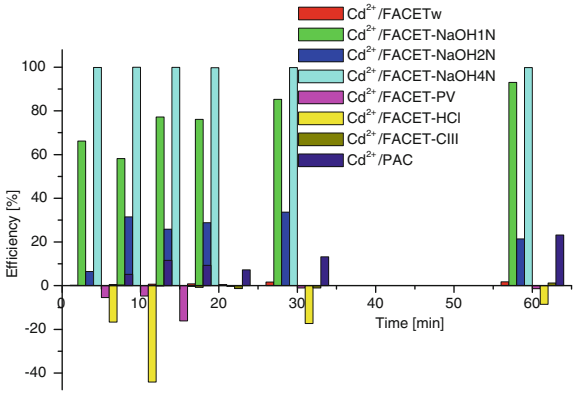

Fig. 6 The efficiencies removal of Cd^{2+}ions from aqueous solutions on substrates-FA-modified [60]

evaluate the contribution of the carbon content in FA on the cadmium removal efficiency. The results proved that the carbon, even activated does not represent the major constituent in the very good FA efficiency. Further modified FA substrates are tested, targeting the increase in the cadmium adsorption efficiency, Fig. 6.

The results showed that the lowest heavy metals adsorption efficiency occurred when the FA was treated with HCl 2N, this effect being caused by a positive surface charge leading to repulsions between the surface ($\equiv SiOH_2^+$) and metal ions. Similar poor efficiencies are registered when using complexion agents (CIII, PV) as FA modifiers and desorption registered on FA modified with PV, Fig. 6, could be the result of the development of very smooth morphologies. By using EBT as modifier the removal efficiencies are good (as result of selective dissolution, responsible for high specific surface morphologies), Fig. 5 (i). Still, the use of EBT is limited by the costs. The cadmium adsorption efficiency on FA modified with NaOH of different concentrations proves that different reactions are developed at different concentrations (1, 2 and 4N) which may increase the adsorption capacity of substrate Fig. 6.

Similar adsorption experiments were further developed for more heavy metals cations: Cd^{2+}, Cu^{2+} and Ni^{2+} from mono-cation solutions. The process follows a pseudo-second order kinetic, for both metals, on the entire concentration range. Highly efficient adsorption, even at very low heavy metals concentrations (20 ppm), is registered for fly ash modified with NaOH.

The cations adsorption efficiency strongly increases when the adsorption substrate is FA washed with NaOH 2N, with very good results for nickel and cadmium cation, Fig. 7.

The experimental data were used for identifying the adsorption mechanisms. The Langmuir model describes the absorption of both metals and the linearization (analogue of the Scatchard plot, [60], was well fitted, Fig. 7; this confirms the preferential adsorption of the heavy metal cations on the oxide FA CET-NaOH surface. The adsorption of nickel ions on FA-CET modified with NaOH 2N

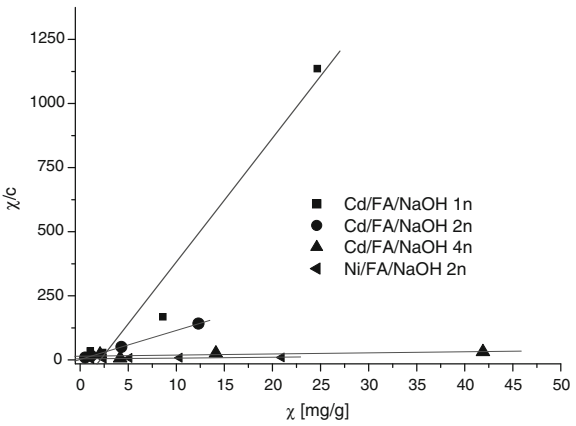

Fig. 7 Linearization of the Langmuir isotherm [59]

solution is well modelled both by the Freundlich isotherm and Langmuir model for all the concentrations between 10 and 250 ppm. The high values of Freundlich k parameter (10.2) show that the nickel ions developed strong bonds with the active adsorbent. The adsorption kinetics gives information on the rate of heavy metal uptake, on the adsorbent surface and supports tailoring the adsorbent surface for the target, in this case—cadmium and nickel adsorption on FA-CET/NaOH 2N (1 g/100 mL) from aqueous solutions. Three kinetic mechanisms are usually reported for adsorption on heterogenous substrates as is the fly ash: pseudo-first order, pseudo-second order and interparticle diffusion, expressed by Eqs. (3)–(5), [61–63]:

$$\log(q_e - q) = \log(q_e) - \frac{k_1}{2{,}303} t \tag{3}$$

$$\frac{t}{q} = \frac{1}{k_2 q_e^2} + \frac{t}{q_e} \tag{4}$$

$$q = k_{id} t^{1/2} + C \tag{5}$$

where q and q_e represent the amount of metal adsorbed at the moment (t) and at equilibrium (mg/g), and k are the reaction constant rates.

Based on the correlation calculations, it could be proved that only the pseudo-second order kinetic can describe the process, with correlation factors, R^2, above 0.930, as presented in Table 3 and Fig. 11 for (a) cadmium and (b) nickel.

This mechanism confirms that the active sites and the metal ion concentration are of equal importance. The higher maximum adsorption capacity for nickel can be related with its ionic volume and the partial loss of hydration water, which differently runs for cadmium and nickel at the natural pH of the test solutions.

A compromise should be reached between the contact time and the amount of substrate in a given volume of pollutant solutions, when targeting the use of the FA substrate modified with NaOH 2N. Therefore, new series of tests were done by

Table 3 The parameters of the pseudo-second order kinetic for Cd^{2+} and Ni^{2+} adsorption on FA/NaOH 2N

Ion	k_2 (g/mg min);	q_e (mg/g)	R^2
Cd^{2+}	0.008	29.58	0.937
Ni^{2+}	4.122	22.03	1.00

adding only 2 g of substrate to 100 mL solution of Cd^{2+}, 0–400 mg/L ($CdCl_2$, Scharlau Chemie) and Cu^{2+}, 0–400 mg/L ($CuCl_2$, Scharlau Chemie). The mixture was stirred up to 90 min at room temperature, then the substrate was removed by vacuum filtration and the supernatant was analyzed.

The results presented in Fig. 8 show good removal efficiencies, both for cadmium and copper.

As already outlined, the FA composition depends on the coal source and burning parameters. To investigate the importance of the FA source, comparative studies need to be done, using FA from different sources. Two types of raw FA were collected from the electro-filters of two CPH plants, from Brasov (FA1) and from Mintia (FA2), Romania. The sum of the SiO_2, Al_2O_3 and Fe_2O_3 is, for both ashes, above 70 % therefore, according to the ASTM standards, both FA are of type F. Consequently, ratio SiO_2/Al_2O_3 in the FA is mainly responsible for the substrate efficiency and the grains are not aggregating, even during long contact with water. The ash was washed in ultrapure water, by stirring (50 rpm), at room temperature, for 48 h, to remove the soluble compounds. The main characteristics of the two FAs are presented in Table 4.

Experiments were done to test the adsorption efficiencies of heavy metals on the FA1 and FA2 substrates and the results show a good adsorption capacity of FA2 NaOH 2N in removing Cd^{2+}, Cu^{2+} or Ni^{2+} from mono-cation solutions, Fig. 9a, b. The results prove that the conditioning processes are different, and are mainly influenced by the silica and alumina content.

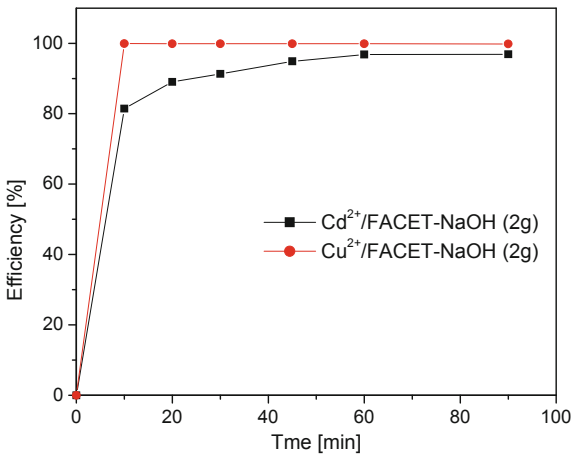

Fig. 8 Adsorption efficiency versus contact time: Cd^{2+}, Cu^{2+}

Table 4 Fly ash characterization

Ash	FA composition (%)										pH*	K* (μS)
	SiO	Al_2O_3	Fe_2O_3	CaO	MgO	K_2O	Na_2O	TiO_2	MnO	LOI		
FA1	53.70	21.60	9.56	3.63	2.39	2.20	0.68	0.76	0.05	3.80	10.45	0.4
FA2	46.05	20.08	9.93	6.07	2.35	2.28	0.83	0.06	0.09	4.45	11.48	0.4

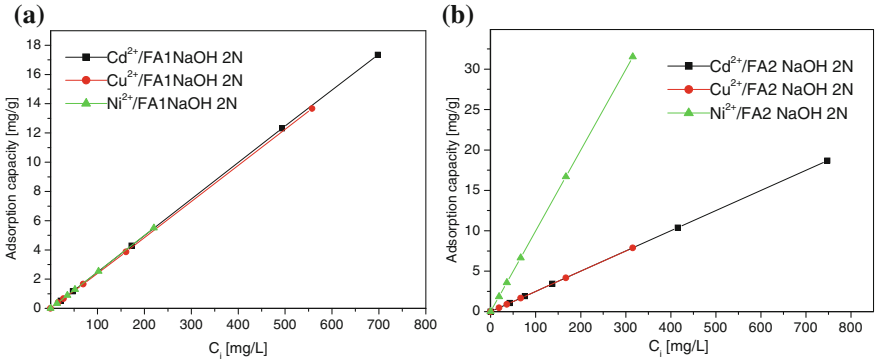

Fig. 9 **a** Adsorption capacity of Cd^{2+}, Cu^{2+}, Ni^{2+} on modified FACET(FA1NaOH 2N); **b** Adsorption capacity of Cd^{2+}, Cu^{2+}, Ni^{2+} on modified FAM(FA2 NaOH 2N)

During alkali conditioning with NaOH 2N for 48 h, several interactions are expected, according to reaction (6), [64]:

$$NaOH_{aq} + FA_s \rightarrow Na_a(AlO_2)_b(SiO_2)_c \cdot NaOH \cdot H_2O \quad (6)$$

when on the FA surface can developed new active site ($\equiv SiO^-$) and ($\equiv AlO^-$) which allows metals to form complexes at the surface (Eqs. 7 and 8), [65–67]:

$$2(\equiv SiO^-) + M^{2+} \rightarrow (\equiv Si - O)_2M \quad (7)$$

$$2(\equiv AlO^-) + M^{2+} \rightarrow (\equiv Al - O)_2M \quad (8)$$

These reactions are different, depending on the type of FA. By dissolution of acidic oxides, the specific surface area is enhanced and activated and the efficiency of heavy metals removal increases. The re-precipitation processes can lead to new polymorphs and provide a large specific surface, suitable for adsorption.

2.2 Alternatives in Conditioning the Fly Ash Substrate

As a separate group of studies showed, dyes also well adsorb on FA, thus they can also act as conditioning compounds. The expected advantage is the development of an uniform mono-layer with predictable charge, that can be tailored according to the pollutant that should be removed.

Therefore, a new set of samples were prepared using washed FA further treated with methyl orange, Merck 0.01 %, under 48 h stirring followed by filtration; this substrate was treated with NaOH 2N under 48 h stirring (FA/MO/NaOH 2N)—to get the required negative charge for cations adsorption, followed by filtration, washing with ultra-pure water and drying, at 105–120 °C for 2 h.

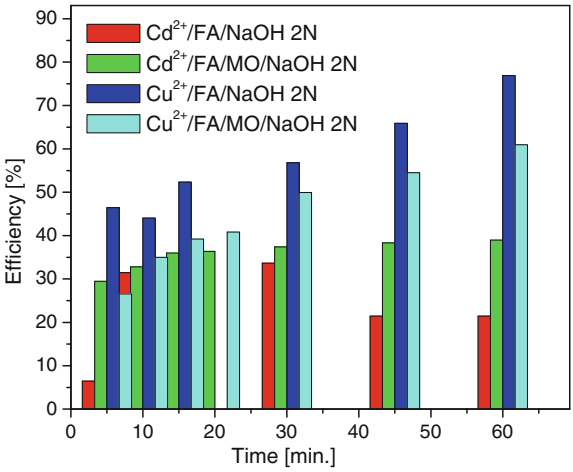

Fig. 10 Heavy metals adsorption efficiency on modified FA: Cd^{2+} and Cu^{2+}

After cadmium and copper cations adsorption, compounds of these metals could be identified in the crystalline structure along with surface morphology modifications, confirming that adsorption is likely to be the result of chemical modifying reactions. The variations in the adsorption efficiency for a 1:100 ratio FA/MO/NaOH 2N: metal solution volume is presented in Fig. 10.

The results allowed setting the optimal contact time at 30 min, a value considered technologically feasible for both substrates and cations. The effect of the adsorbent mass on the adsorption efficiency was investigated; it was proved that good Cd^{2+} adsorption occurs at a dose of 4 g FA for 100 mL solution. The optimized adsorption process for cadmium was then applied for solutions containing copper.

A similar path was followed for optimizing the conditions for Pb^{2+} and Zn^{2+} adsorption from synthetic aqueous solutions. Fly ash was modified in two steps: (1) with NaOH 2N solution followed by (2) a treatment in methyl orange 0.2 mM solution, FA-NaOH-MO, [68]. The dried FA-NaOH was sieved and the 40–100 μm fraction was selected for adsorption experiments. Parallel investigations were conducted on FA modified only through alkali treatment and on the FA-NaOH-MO substrate. Both substrates were characterized using XRD for FA crystalline structure and AFM images were used to investigate the morphology, surface roughness and pore size distribution. The XRD spectra show that the major components of FA/MO/NaOH 2N are: carbon, SiO_2 in various structures (cubic, rhombohedric) and combined with Al_2O_3 as silimanite (Al_2SiO_5), mullite ($3Al_2O_3 \cdot 2SiO_5$), along with γ-Al_2O_3, hematite (Fe_2O_3) and CaO.

The XRD spectra, Fig. 11, show that aluminum silicate and other oxide components vary from one type of substrate to another supporting the assumption of surface modifications.

Two heavy metal cations were selected to test the adsorption efficiency, based on their different polarizability. The Pb^{2+} and Zn^{2+} adsorption efficiency, η, on modified FA was evaluated to optimize the contact time and the amount of substrate for

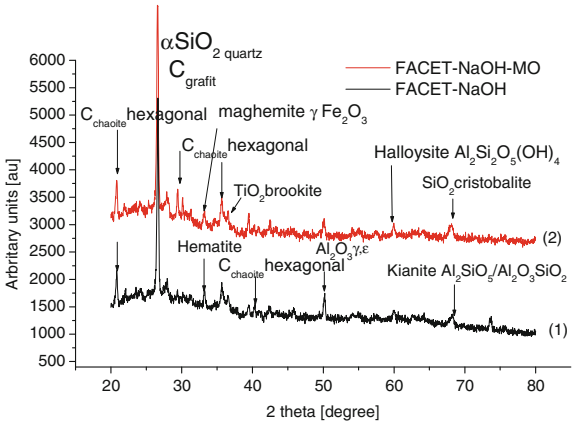

Fig. 11 XRD of FA modified with (*1*) NaOH 2N; (*2*) FA NaOH 2N and MO 0.02 mM [67]

a given volume of pollutant solution. The residual metal concentration from the supernatant were analyzed by AAS, at λ_{Zn} = 213.9 nm and λ_{Pb} = 283.3 nm, after calibration.

The dynamic adsorption results are presented in Fig. 12, for the lead and zinc adsorption on FA-NaOH, compared with the results obtained using FA-NaOH-MO as adsorbents.

The low adsorption efficiency of Pb^{2+} and Zn^{2+} cations on FA-NaOH-MO comparative with the efficiencies on FA-NaOH show that a share of pores are occupied with methyl orange molecules, as also supported by the AFM images and the average roughness values. Increasing the amount of adsorbent from 0.5 g up to 3 g for 50 mL solution the initial pH increases up to 8 (still below the precipitation value) while the adsorption efficiency of the heavy metals increases as result of a larger amount of active centers in the system. The optimal adsorbent amount is found to be 1.5 g for Pb^{2+} cation removal respectively 1.25 g for Zn^{2+}.

So the optimal parameters to remove the metals ions (Pb^{2+}, Zn^{2+}) are:—contact time: 60 min; amount of substrate in 100 mL solution: 1.25–1.5 g.

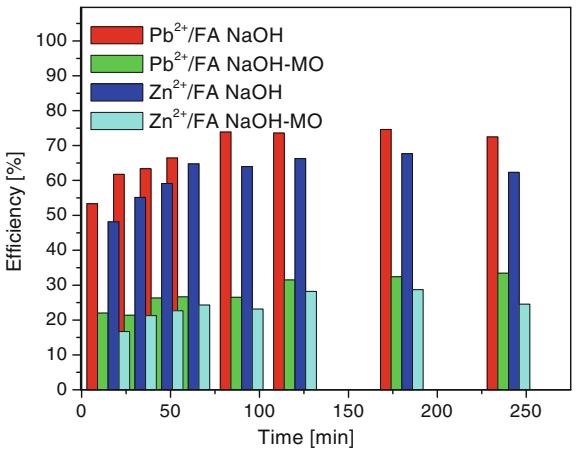

Fig. 12 Lead and zinc immobilization efficiency versus contact time

By comparing these results with those obtained in copper and cadmium removal for the same types of substrate the conclusion that can be formulated is upon the need for preliminary optimization studies for each type of pollutant/wastewater, prior the development of a scalable process.

The pseudo-second order kinetics did well apply to the adsorption processes.

The Pb^{2+}adsorption capacity on the investigated substrates was 94.3 mg Pb^{2+}/g FA-NaOH and 42.2 mg Pb^{2+}/g FA-MO-NaOH, respectively, showing a possible chemical adsorption, involving valence forces (through electrons sharing) between the adsorbent and the adsorbed species.

The lead in aqueous solution may suffer solvation, hydrolysis or polymerization [68], forming many polynuclear species such as: $Pb_2(OH)^{3+}$, $Pb_3(OH)^{4+}$ which can be adsorbed. These larger compounds are more sensitive to the surface porosity, thus explaining the lower adsorption capacity of the MO-modified substrate. The Zn^{2+} cation can interact with the MO molecules, forming stable complexes on the FA surface. Adsorption studies carried out to estimate heavy metal removal from wastewater, using fly ash, showed that the efficiency follows the order: $Pb^2 > Zn^{2+} > Cu^{2+} > Cd^{2+} > Ni^{2+}$ [69].

2.3 *Fly Ash Based Composite with Bentonite for Multi-cation Wastewater Treatment [70]*

The wastewaters resulted from many industrial processes usually contain two, three or more heavy metal along with other pollutants. As their ionic radius and hydration number are different, eventually these cations will have different mobility and polarizability, thus different affinity in adsorption, for specific adsorption sites. Therefore, one alternative was to investigate a combination of substrates, based on fly ash and an abundant natural compound, bentonite or diatomite.

Bentonites are the most abundant argillaceous materials which can be used in wastewater treatment [10]. They are reported as low cost efficient adsorbents for some heavy metals (copper, lead, cadmium and zinc) while modified bentonite was used for removing ^{60}Co radionuclide from radioactive waste solutions. The outstanding adsorption capability is due to main mineral component as montmorillonite, smectite and clay. There is a growing interest in using low cost adsorbents, fly ash, bentonite or their mixtures. If these materials are optimised to remove the heavy metals or dyes, the adsorption process could be a promising technology.

Comparative adsorption studies were done using washed fly ash (FAw), bentonite (B) and their mixtures. Bentonite was provided from the NW Romania area. The major oxide components in fly ash and bentonite, with a certain influence in heavy metals and dyes removal are presented in Table 5. Using emission spectrometry other metals were identified in traces (Ba, Cu, Sn, Pb, Cr, Ni, V, Zn, Ti). According to the ASTM standards, the raw FA pertains of class F as the sum of the SiO_2, Al_2O_3 and Fe_2O_3 is above 70 % [71], while bentonite is of Na type [58].

Table 5 Adsorbent materials composition

FA composition (%)									
Major oxides (%wt)									
SiO_2	Al_2O_3	Fe_2O_3	CaO	MgO	K_2O	Na_2O	TiO_2	MnO	LOI*
53.32	22.05	8.97	5.24	2.44	2.66	0.63	1.07	0.08	1.58
Bentonite composition (%)									
Major oxides (%wt)									
72.11	14.92	2.62	2.31	2.12	1.34	1.91	0.62	0.05	2.06

The crystalline degree of (B) is 79.5 % the rest being represented by amorphous phases. The crystallites size, calculated with the Scherer formula ranges from 171.0 to 653.2 Å.

Part of the oxides in raw FA and bentonite are water soluble. These chemical and structural changes are mirrored in morphology modifications, Fig. 13a, b resulting in large differences in the substrates' affinity for heavy metals.

On phases distributions images there can be seen less agglomerates in new material adsorbent so more mesopores ready for to lodge the cations of heavy metals or dye molecules.

The SEM images (Fig. 14) show significant differences between the substrates: most FAw particles are spherical with diameters between 3.61 and 111 μm. The bentonite particles have a stratified structure with hexagonal large agglomerates, with sizes between 2.23 and 8.08 μm. The surface morphologhy of FAw and bentonite appears as corn flake crystals with fluffy appearance revealing the fine platy structure.

The high global surface energy and a large polar component (polar contribution FA:B = 241.17 mN/m), recommends the material as a good adsorption substrate for heavy metals in batch experiments, under stirring up to 240 min at room temperature (20–22 °C), at the natural pH of the dispersion, Table 6.

Two series of experimental tests were done on mono solution with one pollutant Cd^{2+}(c_{Cd} = 750 mg/L, using $CdCl_2 \cdot 2.5H_2O$, two heavy metals solution (Cd^{2+} and

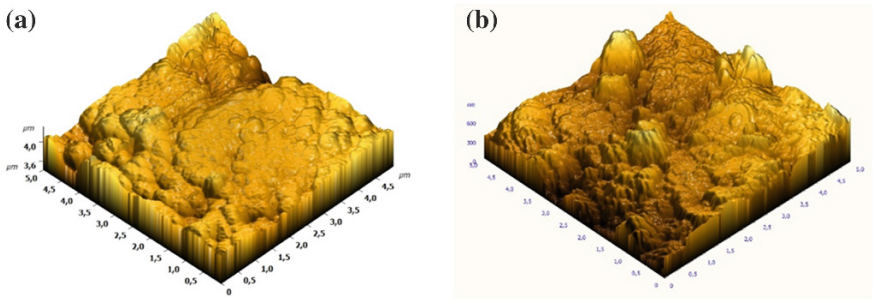

Fig. 13 The AFM topography and phase distribution **a** FAw Average Roughness, 62.6 nm; **b** FAw + B Average Roughness, 148.4 nm

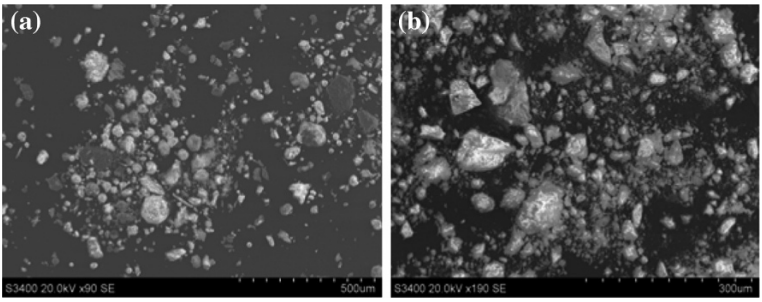

Fig. 14 The SEM images **a** FAw and **b** Bentonite

Table 6 The natural pH values of the solution with adsorbent

FAw:B [g:g]	1:0	0:1	0.25:0.75	0.50:0.50	1.00:1.00	0.5:1.5
pH	7.4	9	6.2	5	5.1	6.5

Cu^{2+}, c_{Cu} = 400 mg/L, using $CuCl_2 \cdot 2H_2O$. The lowest admissible discharge concentrations are, in most national regulations set for cadmium therefore, the optimized adsorption conditions set for cadmium were extended also for copper in multicomponent solutions, in the tests performed using FAw, B and their mixtures, as the Table 7 shows. The optimal adsorbent mass: wastewater volume was evaluated based on cadmium 750 mg/L solutions, using contact duration of 90 min, while the optimal contact time was evaluated on suspensions of 0.5 g FAw in 100 mL multicomponent solutions of Cd^{2+} and Cu^{2+}.

The results proved that the pseudo-second order kinetic well describes the adsorption mechanism for both cations, on bentonite and theirs mixture the investigated substrates. The kinetic parameters are presented in Table 8 for cadmium.

The adsorption equilibrium for cadmium and copper needs 90 min to be settled therefore, this was the set as optimal time in all experiments. Also, for these two ions, higher substrate dosage is required, almost similar removal efficiencies (close to 70 %), being registered at 2 g of FAw:B dispersed in 100 mL of solution. The removal efficiency increases with amount of bentonite in the mixture, proving that adding B to FAw represents a path to fulfil the set target: the use of washed FA in advanced wastewater treatment. The FAw:B substrate is highly efficient (>80 %) for the removal of all cations at concentrations below 100 mg/L, thus for advanced wastewater treatment, another preliminary process (e.g. precipitation)

Table 7 Substrates and pollutant systems experimentally tested

Substrates (g) FAw: B	1:0	0:1	0.25:0.75	0.50:0.50	1.00:1.00 0.50:1.50
Substrate	(FAw)	(B)	(1)	(2)	(3) (4)
Pollutant systems	Cd^{2+}	Cd^{2+}	Cd^{2+}+Cu^{2+}	Cd^{2+}+Cu^{2+}	Cd^{2+}+Cu^{2+}

Table 8 Kinetic parameters of cadmium removal on FAw:B mixed substrate

FAw:B [g:g]	Pseudo first-order kinetics		Pseudo second-order kinetics			Interparticle diffusion		
	K_L (min^{-1})	R^2	k_2 (g/mg min)	q_e (mg/g)	R^2	K_{id} ($mg/gmin^{1/2}$)	C	R^2
Cadmium								
1:0	–	0.413	–	–	0.854	–	–	0.801
0.50:0.50	–	0.627	0.147	31.646	0.998	–	–	0.535
0.25:0.75	–	0.023	0.049	30.395	0.998	–	–	0.409
0:1	–	0.026	0.059	42.553	0.999	–	–	0.446
1:1	0.007	0.954	0.408	19.841	0.997	–	–	0.592
1.5:0.50	–	0.236	0.092	28.011	0.998	–	–	0.454

could be necessary. The experiments also showed that the efficiency follows the order $Cu^{2+} \geq Cd^{2+}$, according to the dimensionless separation factors σ: $\sigma_{Cu^{2+}} = 0.243 > \sigma_{Cd^{2+}} = 0.151$.

Experiments done using cations mixtures showed similar results; using as substrates FA, bentonite (B) and theirs mixture, the simultaneous adsorption process of cadmium and cooper can be well described with the pseudo-second order kinetic equation. The kinetic parameters are presented in Table 9.

The data prove that copper adsorption can follow more parallel mechanisms, which could be expected considering the FAw:B composition and/or the pores distribution with active sites of various energies. The values of the adsorption capacity on FAw:B is found to decrease in the order $Cu^{2+} > Cd^{2+}$ on mixtures 0.5:0.5 and 1:1. Bentonite increases the adsorption capacity of the substrate, as expected considering the differences in the specific surface energy between FAw and B,

Table 9 Kinetic parameters of the simultaneous heavy metal removal on FAw:B

FAW:B [g:g]	Pseudo first-order kinetics		Pseudo second-order kinetics			Interparticle difusion		
	KL (min^{-1})	R^2	k_2 (g/(mg min))	q_e (mg/g)	R^2	K_{id} (mg/$gmin^{1/2}$)	C	R^2
$Cd^{2+}(Cd^{2+}+Cu^{2+})$								
0.50:0.50	–	0.415	1.613	24.752	0.948	1.505	0.851	0.942
1:1	0.022	0.843	0.379	10.341	0.998	–	–	0.547
1.5:0.5	0.013	0.967	7.330	20.877	0.982	–	–	0.867
$Cu^{2+}(Cu^{2+}+Cd^{2+})$								
0.50:0.50	0.016	0.886	1.348	25.839	0.976	1.035	7.456	0.962
1:1	0.026	0.962	0.477	14.771	0.999	0.274	10.603	0.852
1.5:0.5	0.012	0.931	0.092	16.78	0.999	0.092	15.425	0.903

mainly related to the higher aluminosilicates content in B. The Cd^{2+} and Cu^{2+} cations can be adsorbend by the silanol group (Si–OH) of the layers, but theirs numbers is distinctly smaller (Eqs. 9 and 10):

$$Si-OH + Cd^{2+}(H_2O)_n \Leftrightarrow Si-OCd^{+}(H_2O)_{n-x} + H^{+}(H_2O)x \quad (9)$$

$$Si-OH + Cd^{2+}(H_2O) \Leftrightarrow (Si-O)_2Cd(H_2O)_{n-x} + 2H^{+}(H_2O)x \quad (10)$$

2.4 Fly Ash–TiO_2 Photocatalyst Mixed Substrates [51, 73]

Mixed substrates are efficient in adsorption, particularly in heavy metals adsorption. The second major step in the research was to develop mixed substrates, active both in adsorption and photocatalysis.

These substrates can host complex processes, as photocatalysis has as initial step adsorption; additionally, the heavy metals in the system can interact with the photocatalyst with consequences that should be controlled. Therefore, preliminary adsorption studies (in dark) need to be done on these types of substrates.

2.5 Fly Ash CET/NaOH 2N–TiO_2

The contribution of each component should be separately investigated, as in the comparative tests performed using: (i) 1 g FA + CET/NaOH 2N (FA1) in 100 mL cadmium/cooper solutions and: (ii) 1 g TiO_2 (Degussa P25) in 100 mL cadmium/cooper solutions. The results are presented in Fig. 15.

The TiO_2 influence on the adsorption capacity was studies by modifying the ratio FA: TiO_2 (3:1; 2.5:1.5; 2:2; 1.5:2.5; 1:3) and optimizing the contact time

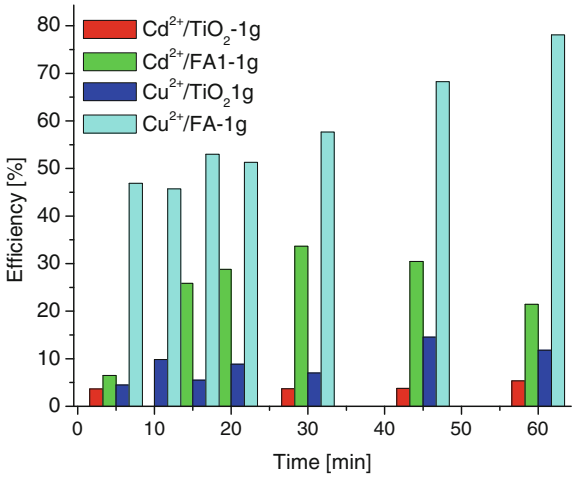

Fig. 15 Cadmium and cooper immobilization efficiency versus contact time [51]

(30 min.). The results presented in Fig. 16, show the best efficiency for cadmium and cooper obtained on two types of substrates: FA: TiO_2 (3:1; 2:2) at optimum ratio of 4:100 g/mL.

Mixed substrates, FA-CET/NaOH 2N, and TiO_2 (FA1-TiO_2) were used in adsorption tests, following the above optimized conditions. For an initial cadmium concentration of 50 ppm, the required efficiency in a one step process able to fulfil the discharge regulations (<0.3 ppm) is 99.4 %. High adsorption efficiencies, even at low cadmium concentrations when diffusion tends to hinder adsorption, are obtained on FA: TiO_2 ratios of 3:1 and 2:2 respectively, Fig. 16b.

Mixing TiO_2 with FA enhances the adsorption efficiency and rate, comparing with the single substrates thus, a synergic effect can be reported; a primary explanation is linked to the alkaline pH, induced by the modified FAs in the dispersion. The HO^- ions, negatively charge the amphoteric TiO_2 (the zero charge point of TiO_2 is 6.2), activate the surface and increase the adsorption affinity for cations.

The pseudo-second order kinetics has the maximum rate constant for cooper (51.5 g/mg min) at a 2:2 ratio of FA:TiO_2. Two parallel kinetic mechanisms could be applied for the majority adsorption processes: pseudo-second order kinetics and interparticle diffusion, confirming the high heterogeneity of the substrates.

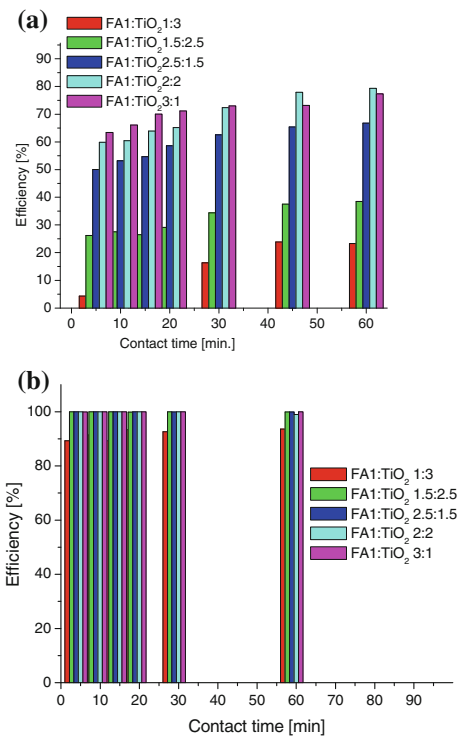

Fig. 16 Adsorption efficiency of **a** Cd^{2+} and **b** Cu^{2+}on mixed substrates (FA-CET-NaOH2N:TiO_2)

The Langmuir model could not describe the cadmium and copper adsorption as result of a highly heterogeneous substrate, except the adsorption on FA:TiO_2 = 1:3, with a surface less heterogeneous, proving that a mono-layer adsorption is possible. The Freundlich isotherm could better describe the adsorption and this is a supplementary prove that heterogeneous substrates are developed by FA modifications. The experimental results show that this can be an up-scalable solution and represent a first stage in investigating the one step process of industrial wastewater treatment.

2.6 Novel Fly Ash-Based Substrates for Multi-cation Wastewater Treatment

The investigations previously detailed proved that conditioning by alkali treatment (1–3 N) can be a viable path for enhancing the adsorption efficiency of heavy metals [65] or multi component systems of heavy metals and dyes [50].

These concentrations are significantly lower compared with the 5–8 N usually reported. For competitive, efficient multi-cation removal, the substrates need to have very good adsorption properties (specific surface, surface charge etc.) and controlled affinity. Additionally, the concurrent processes need to be investigated in multi-cation synthetic systems, used as simplified models for the advanced treatment of industrial (real) wastewaters. Based on these assumptions a new set of experiments were done, including the aim of obtaining novel, zeolite-type substrates.

Class "F" fly ash (FA), collected from the Central Heat and Power (CHP) Plant Brasov (Romania), with oxides composition SiO_2/Al_2O_3 over 2.4 proved good adsorbent properties, and was further used for obtaining a new substrate with good adsorption capacity for heavy metals from multi-cation wastewater treatment.

To activate fly ash, NaOH solution 3 M was used at a 1/10 g/mL ratio between the sample and the activation solution. In the 1,000 mL volumetric flask with reflux condenser, the new adsorbent was obtained from the slurry under stirring for 72 h, at atmospheric pressure and 100 °C, on a thermo-stated heating plate. The new material was noted FA-Z and was comparatively analyzed with the washed fly ash (FA-W).

The XRD analysis show that some crystalline phases of FA-W (quartz and mullite, cristobalite) are mostly absent in the new material (FA-Z), while the new crystalline phases in FA-Z are sodium aluminium silicate ($Na_6[AlSiO_4]_6 \cdot 4H_2O$), sodium aluminium silicate hydrate (phillipsite), ($Na_6Al_6Si_{10}O_{32} \cdot 12H_2O$), sodium aluminum silicate hydroxide hydrate, ($Na_8(AlSiO_4)_6(OH)_2 \cdot 4H_2O$), clinoptilolite $(Na,K,Ca)_5(Al_6Si_{30}O_{72} \cdot 18H_2O)$, tobermonite $(Ca,K,Na,H_3O)(SiAl)O_3 \cdot H_2O$ and other phases of the aluminosilicates. This confirms that chemical restructuring occurs within FA-W. The crystalline degree of FA-Z is estimated at 45.65 %.

The AFM images were used for surface morphology studies, Fig. 17. The average roughness of FA-W is 72.7 nm and for FA-Z average roughness decrease at

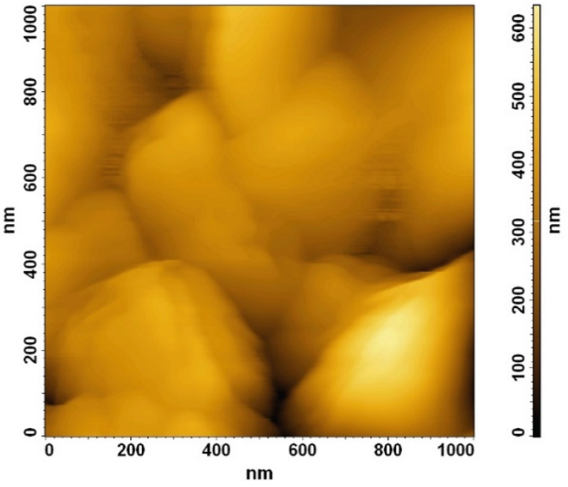

Fig. 17 AFM topography and average roughness of FA-Z

23.4 nm. The dissolution of the soluble compounds in raw FA lead to a new topography resulting in more homogeneous and smooth surfaces. But, the thermal alkali treatment for producing FA-Z is responsible for a significant reorganization at/of the surface as the AFM image in Fig. 17 confirms.

The surface area of the FA-W and FA-Z were analysed and the results show a strong increase in the specific surface from 6.14 at 37.97 [m^2/g], and a decrease in the average pores diameter at 15.4 [nm]; corroborated with the previous surface and structural data, these indicates a new type of organisation in the FA material.

Cation adsorption involves mainly electrostatic forces therefore the surface energy (207.12 mN/m) of the new substrate (FA-Z) can strongly influence the adsorption process.

The new material was tested as adsorbent for simultaneous removal of Pb^{2+}, Cd^{2+} and Zn^{2+} from three-cation solutions. The adsorption experiment tests were run on three-component solutions of Cd^{2+}, 0–700 mg/L, ($CdCl_2$, Scharlau Chemie), Zn^{2+}, 0–350 mg/L, ($ZnCl_2$, Scharlau Chemie), respectively Pb^{2+}, 0–1,350 mg/L using the novel adsorbent (FA–Z).

To evaluate the adsorption efficiency and investigate the adsorption isotherms, the dispersions were stirred up to 240 min at room temperature (20–25 °C), then the substrate was removed by vacuum filtration and the supernatant was analyzed.

The optimal contact time was evaluated on suspensions of 0.5 g FA-Z in 100 mL multicomponent solutions of Cd^{2+} (700 mg/L), Zn^{2+} (350 mg/L) respectively Pb^{2+} (1,350 mg/L). Aliquots were taken each 15, 30, 45, 60, 90, 120 180, 240 min., when stirring was briefly interrupted and the substrate was removed by filtration. The residual metal concentrations in the supernatant were analyzed by AAS, at: λ_{Cd} = 228.8 nm, λ_{Zn} = 213.9 nm and λ_{Pb} = 283.3 nm, based on the calibration curves.

In all cases, the working pH value increased from 5.6 (natural pH value in the three—cations solutions with FA-Z.) to 6.6 involving a slow release of the alkali traces resulted from synthesis.

The process parameters (contact time, substrate's dosage and initial cations' concentration) were optimized considering the maximum removal efficiency of Cd^{2+}, Pb^{2+} and Zn^{2+} ions, η, on FA-Z [71]. The experimental data show a very efficient lead removal, after a very short contact time and on a broad concentration range. The adsorption equilibrium for cadmium and zinc needs 90 min to be settled therefore, this was the set as optimal contact time in all further experiments. Also, for these two ions, higher substrate dosage is required, almost similar removal efficiencies (close to 70 %) being registered at 1.3 g of FA-Z dispersed in 100 mL of solution, while a dosage of 0.5 g/100 mL allows almost complete lead removal.

These data can be linked with the cation's transport rate toward the substrate but can have also other reasons like occupying more active sites with a single large, hydrated cation or the need for supplementary reaction energy if adsorption occurs with dehydration. The data also show that cadmium and zinc have a much lower affinity for the FA-Z substrate, showing an efficiency decrease for contact times longer than 240 min, supporting the assumption of an adsorption process without dehydration.

The adsorption studies carried out to estimate the heavy metal removal from wastewater, using fly ash, showed that the efficiency follows the order $Pb^{2} > Zn^{2+} \geq Cd^{2+}$.

The adsorption efficiency of this new type of substrate was compared with those of C100 micro-porous and C150 macro-porous cation exchangers, in the same experimental conditions and the results are presented in Fig. 18.

As expected considering the participants in the processes, in all cases the adsorption efficiency on the microporous substrate is higher than on the macro-porous. In lead removal, the FA-Z substrate is slightly more effective than the

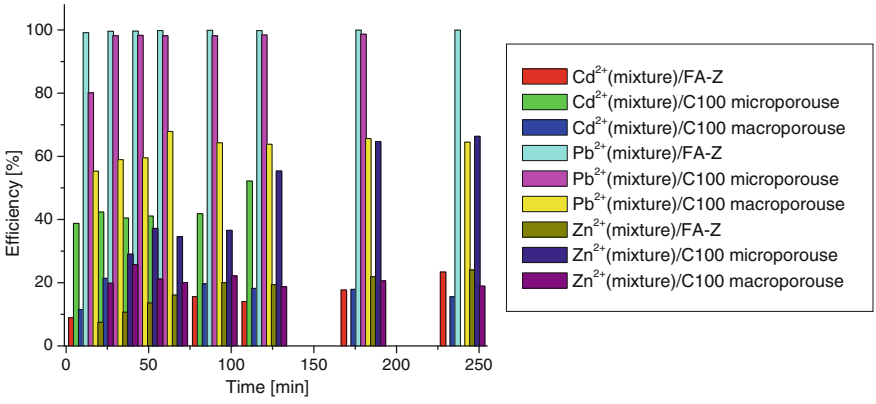

Fig. 18 Cd^{2+}, Pb^{2+}, Zn^{2+}, immobilization efficiency versus contact time

microporous ion exchanger. It is also to notice that for cadmium and zinc removal the macroporous cation exchanger gives almost similar results as FA-Z.

The data recommend thus the FA-Z substrate for lead selective adsorption from complex cation mixtures, being also able to efficiently replace the cations exchanges in current lead removal processes even when mixed with other species.

The pseudo-second order kinetic model is based on the assumption that the rate limiting step may be a chemical adsorption involving the valence forces through sharing or exchange of electrons between the adsorbent and the adsorbate [71, 72]. The model is mentioned in literature for many systems, including Cu^{2+}, Co^{2+}, Zn^{2+}, Mn^{2+} adsorption on zeolites, Pb^{2+} and Cu^{2+} removal on humic acid [73], Cu^{2+}, Ni^{2+}, Cd^{2+} removal on fly ash from single- or double-pollutant solutions [74].

The adsorption results showed that the Langmuir model is well fitting the data. Table 10 presents the adsorption parameters for the heavy metal ions (Cd^{2+}, Zn^{2+} and Pb^{2+}) calculated from the slope of the linearization plot of the isotherm equation.

On the cation exchangers, chemisorption is the representative mechanism, as expected, for all the three cations, with the maximum adsorption capacity having values close to those obtained in the kinetic investigations, for the pseudo-second order mechanism, except lead adsorption on the microporous cation exchanger, where the values are significantly lower than those evaluated based on kinetic studies. Further adsorption-desorption studies will be employed to elucidate this aspect.

Table 10 Adsorption isotherm parameters

Langmuir isotherm			
Parameters	q_{max} (mg/g)	a (L/mg)	R^2
FA-Z			
Cd/(Cd + Pb + Zn)	28.089	0.0006	0.998
Pb/(Pb + Cd + Zn)	–	–	0.462
Zn/(Zn +Cd + Pb)	13.387	0.0016	0.999
CI00 microporous			
Cd/(Cd + Pb + Zn)	59.172	0.0004	0.999
Pb/(Pb + Cd + Zn)	144.927	0.0008	0.999
Zn/(Zn + Cd + Pb)	30.864	0.0005	0.999
C150 macroporous			
Cd/(Cd + Pb + Zn)	42.194	2.37×10^{-5}	0.939
Pb/(Pb + Cd + Zn)	142.857	0.0003	0.997
Zn/(Zn +Cd + Pb)	17.699	0.0059	0.991

3 Conclusions

One way to use fly ash is the development of novel and efficient substrates for advanced wastewater treatment. To increase its efficiency and reproducibility a novel concept was proposed, by developing substrates able to simultaneously remove inorganic and organic pollutants in a "one step" process. The results presented in this work represent a concise synthesis on the research activity on the new adsorbents materials that—besides efficiency, also meet several targets: they are low cost, they can be developed in accessible, up-scalable processes and they can be used in the removal of a wide range of pollutants including heavy metals.

The choice of the chemical reagent to modify and homogenize the fly ash surface is important and must target: (i) the increase in the specific surface (by local dissolution/repreciptiation); (ii) the increase in the crystallinity percentage of the main components (silica, alumina); (iii) tailoring the surface charge according to the use (e.g. negative homogeneous charge when heavy metals adsorption is planned). To allow all the surface reactions to reach equilibrium, this condition step must be developed over a long duration (48 h).

The use of acids (HCl) or solubilizing agents (like Pyrocatechol violet or Complexone III) is not recommended as these will chemically react with the surface edges and corners, leaving very smooth surfaces, with low adsorption efficiencies. Alkali conditioning, with NaOH 1 N, 2N and 4N solutions proved to meet all these targets; according to the adsorption results, the best substrate proved to be that obtained when using NaOH 2N.

Adsorption of heavy metals efficiently runs on fly ash conditioned with NaOH 2N. This substrate proved to be highly efficient in heavy metals (cadmium, copper, nickel) removal even at very low concentrations (50 ppm), recommending this material in the advanced treatment for water discharge/reuse, after a conventional treatment step (precipitation).

Selective adsorption is also possible as it was proved when investigating concurrent heavy metals adsorption: the copper cations are faster adsorbed with higher efficiency having the higher mobility and ionic degree of the copper tetra-hydrated complex, comparing to the hexa-complexes of Cd and Ni.

The alkali treatment raises sustainability issues therefore, the alkali fly ash may replace with washed fly ash (FAw) improved with washed powder bentonite (B), natural adsorbents with a composition almost identical to the fly ash. An important characteristic of the composite FA:B (1.5:0.5) is its large cation adsorption capacity, with convenient efficiencies after 90 min of contact time.

Combination of the substrate alkali modified fly ash (with NaOH 2N) with a photocatalyst (TiO_2) can reach full removal of the heavy metals, with over 90 % efficiency. The results obtained in cadmium and cooper removal on substrates with different FA:TiO_2 ratios, showed the optimal ratios: FA:TiO_2 = 3:1 and 2:2.

The fly ash is a potential candidate for getting substrates with significantly higher specific surface and controlled surface charge, of zeolite type. The usual process is a rough hydrothermal synthesis. The results hereby presented show that

zeolite type materials can be obtained in mild conditions (100 °C and 1 atm). A new adsorbent material, FA-Z, was obtained from fly ash and was investigated as substrate for complex adsorption processes in a tri-pollutant system, containing lead, zinc and cadmium cations. The adsorption studies proved that the novel material FA-Z is highly active in lead removal from mixtures also containing cadmium and zinc, on a broad concentration range and after a short contact time. Lead removal on FA-Z is more efficient when compared also with the highly effective micro-porous cation exchanger. This recommends the new material for replacing the traditional synthetic ion exchanger in cation removal and especially in selective lead adsorption from mixtures containing more cations.

Acknowledgments This paper was supported by a grant of the Romanian National Authority for Scientific Research, CNCS—UEFISCDI, project number PNII-RU-TE-2012-3-0177/2013.

References

1. Inglezakis, V. J., & Poupoulos, S. G. (2006). *Adsorption, ion exachange and catalysis*. Amsterdam: Elsievier.
2. Andini, S., Cioffi, R., Colangelo, F., Montagnaro, F. & Santoro. L. (2008). Adsorption of chlorophenol, chloroaniline and methylene blue on fuel oil fly ash. *Journal of Hazardous Materials*, *157*, 599–604.
3. Babu, B. V., Rana, H. T., Ramakrishna, V., Mahesh S. (2000). C.O.D. reduction of reactive dyeing effluent from cotton textile industry, *Journal of the Institution of Public Health Engineers India*, *4*, 5–11.
4. Chen, S., Zhang, J., Zhang, C., Yue, Q., Yan, L., & Chao L. (2010). Equilibrium and kinetic studies of methyl orange and methyl violet adsorption on activated carbon derived from *Phragmites australis*. *Desalination*, *252*, 149–156.
5. Aridmide, D., Preda, C., Butnaru, R., Dan, D., & Greavu, V. (2002). *Manualul inginerului textil* (Vol. I). Bucureşti: Editura A.G.I.R.
6. Visa, M., & Duta, A. (2007). Adsorption mechanisms of heavy metals on fly ash with modified surface charge. In *AIChE Anual meeting, Salt Lake City, Utah, USA, Conference Proceedings*.
7. Mohammadi, T., Razmi, A., & Sadrzadeh, M. (2004). Effect of operating parameters on Pb^{2+} separation from wastewater using electrodialysis. *Journal of Desalination*, *167*, 379–385.
8. Kowalska, I., Kabsch-Korbutowicz, M., Majewska-Nowak, K., Winnicki, T. (2004). Separation of anionic surfactants on ultrafiltration membranes. *Jounal of Desalination*, *162*, 33–40.
9. Bowen, R. W., & Welfoot, J. S. (2002). Modeling of membrane nanofiltration—pore size distribution effects. *Chemical Engineering Science*, *57*, 1393–1407.
10. Ujang, Z., & Anderson, G. K. (1998). Performance of low pressure reverse osmosis membrana (LPROM) for separating mono-and divalent ions. *Journal of Water and Science Technology*, *38*, 521–533.
11. Pearce, C. I., Lioyd, J. R., & Guthrie, J. T. (2003). The removal of colour from textile wastewater using whole bacterial cells: a review. *Dyes Pigments, 58*, 179–196.
12. Ghoreishi, M., & Haghighi, R. (2003). Chemical catalytic reaction and biological oxidation for treatment of non-biodegradable textile effluent. *Chemical Engineering Journal*, *95*, 163–169.
13. Hatch, K. L. (1984). Chemicals and textiles, Part 1. Dermatological problems related to fiber content and dyes. *Textile Research Journal*, *54*(10), 664–682.

14. Brigatti, M. F., Colonna, S. (2005). Mercury adsorption by montmorillonite and vermiculite: a combined XDR, TG-MS, and EXAFS study. *Journal of Applied Clay Science.*
15. Šljivić, M,. Smičiklas, I, Pejanović, S., & Plećaš, I. (2009) Comparative study of Cu^{2+} adsorption on a zeolite, a clay and a diatomite from Serbia, *Journal of Applied Clay Science*, *43*, 33-40.
16. Min-Gyu, L., Gyeongbeom, Y., Byoung-Joon, A., & Felicity, R. (2000). Coversion of coal fly ash into zeolite and heavy metal removal characteristics of the products. *Korean Journal of Chemical Engineering, 17*(3), 325–331.
17. Zhou, D., Zhang, L., Zhou, J., & Guo, S. (2004). Cellulose/chitin beads for adsorption of heavy metals in aqueous solution. *Water Research, 38*, 2643–2650.
18. Çoruh, S., Ergun, O. N.: Copper adsorption from aqueous solutions by using red mud—An aluminium industry waste. In *Survival and sustainability environmental earth sciences* (pp. 1275–1282). Springer, Berlin.
19. Maiti, S., Purakayastha, S., & Ghosh, B. (2008). Production of low-cost carbon adsorbents from agricultural wastes and their impact on dye adsorption. *Chemical Engineering Communication, 198*, 386–403.
20. Bhushan, S., Kalia, K., Sharma, M., Singh, B., & Ahuja, P. S. (2008). Processing of apple pomace for bioactive molecules. *Critical Reviews in Biotechnology, 4*, 285–296.
21. Joseph, C. G., Bono, A., Krishnaiah, D., Soon, K. O., Kavitha, D., & Namasivayam, C. (2007). Experimental and kinetic studies on methylene blue adsorption by coir pith carbon. *Bioresource Technology, 98*, 14–21.
22. Robinson, T., Chandran, B., & Nigam, P. (2002). Effect of pretreatments of three waste residues, wheat straw, corncobs and barley husks on dye adsorption. *Bioresource Technology, 85*(2), 119–124.
23. Saha, P., Das Mishra, R., & Husk, R. (2012). Adsorption of safranin onto chemically modified rice husk in a upward flow packed bed reactor: artificial neural network modeling, *Biotechnology Advanced*, *44*, 7579–7583.
24. Song, J., Zou, W., Bian, Y., Su, F., & Han, R. (2011). Adsorption characteristics of methylene blue by peanut husk in batch and column modes. *DES, 265*, 119–125.
25. Feng, N., Guo, X., & Liang, S. Adsorption study of copper (II) by chemically modified orange peel. *Journal of Hazardous Materials*, *164*, 1286–1292.
26. Rafatullah, M., Sulaiman, O., Ibrahim, M. H., & Hashim, R. (2009). Scavenging behaviour of meranti sawdustin the removal of methylene blue from aqueous solution. *Journal of Hazardous Materials, 170*, 357–365.
27. Ponnusami, V., Vikram, S., & Srivastava S. N. (2008). Guava (*Psidium guajava*) leaf powder: novel adsorbent for removal of methylene blue from aqueous solutions, *Journal of Hazardous Materials*, *152*, 276–286.
28. Sharma, D. C., & Forster, C. F. (1994). The treatment of chromium waste waters using the sorptive potential of leaf mould. *Bioresource Technology, 49*, 31–40.
29. Yagub, M. T., Tushar Kanti, S., & Ang, H. M. (2012). Equilibrum, kinetics, and thermodynamics of methlene blue adsorption by pine tree leaves. *Water Air and Soil Pollution*, *223*(8), 5267–5282.
30. Cheung, C. W., Porter, J. F., & Mckay, G. (2012). Sorption kinetic analysis for the removal of cadmium ions from effluents using bone char. *Water Research, 35*, 605–612.
31. Taty-Costodes, V. C., Fauduet, H., Porte, C., & Delacroix, A.. (2003). Removal of Cd(II) and Pb(II) ions, from aqueous, by adsorption onto sawdust of *Pinus sylvestris, Journal of Hazardous Materials*, *105*, 121–142.
32. Yu., L. J., Shukla, S. S., Dorris, K. L., & Shukla, B., Margrave J. L. (2003). Adsorption of chromium from aqueous solutions by maple saw dust. *Journal of Hazardous Materials*, *100*, 53–63.
33. Hameed, B. H., & Daud, F. B. M. (2008). Adsorption studies of basic dye on activated carbon derived from agricultural waste: Hevea brasiliensis seed coat. *Chemical Engineering Journal*, *139*, 48–55.

34. Argun, M. E., Dursun, S., Ozdemir, C., & Karatas, M. (2007). Heavy metal adsorption by modified oak sawdust: Thermodynamics and kinetics. *Journal of Hazardous Materials*, *141*, 77–85.
35. Deng, H., Lu, J., Li, G., Zhang, G., & Wang, X. (2011). Adsorption of methylene blue on adsorbent materials produced from cotton stalk. *Chemical Engineering Journal, 172*, 326–334.
36. Bouzaida, I., & Rammah, M. B. (2002). Adsorption of acid dyes on treated cotton in a continuous system. *Journal of Material Science Engineering*, *21*, 151–155.
37. Ho, Y. S., & McKay, G. (2004). Sorption of Cooper (II) from aqueous solution by peat. *Water, Air, and Soil Pollution, 158*, 77–97.
38. Mata, Y. N., Blázquez, M. L., Ballester, A., González, F., Muñoz, J. A. (2009). Sugar beet pulp pectin gels as biosorbent for heavy metals: Preparation and determination of biosorption and desorption characteristics. *Chemical Engineering Journal*, *150*, 289–301.
39. Pairat, K., & Qiming, Y. (2001). Cadmium (II) removal from aqueous solutions by pre-treated biomass of marine alga Padina. *Environmental Pollution, 112*, 209–213.
40. Otero, M., Rozzada, F., Calvo, L. F., Garcia, A. I., & Morán, A. (2003). Elimination of organic water pollutant using adsorbents obtained from sewage sludge. *Journal Dyes Pigments, 57*, 55–56.
41. Tellez, G. T., Nirmalakhandan, N., & Gardea-Torresdey, J. L. (2002). Performance evaluation of an activated sludge system for removing petroleum hydrocarbons from oilfield produced water. *Advance in Environmental Research, 6*(4), 455–470.
42. Hameed, B. H., Ahmad, A. L., & Latiff, K. N. A. (2007). Adsorption of basic dye (methylene blue) onto activated carbon prepared from rattan sawdust. *Dye Pigment, 75*, 143–149.
43. Nomanbhay, S. M., & Palanisamy, K. (2005). Removal of heavy metal from industrial wastewater using chitosan coated oil palm shell charcoal. *Electronic Journal of Biotechnology, 8*(1), 43–53.
44. Yangcheng, L., Jing, H., & Guangsheng, L. (2007). An improved synthesis of chitosan bead for Pb(II) adsorption. *Chemical Engineering Journal, 226*, 271–278.
45. Bulgariu, L., Bulgariu, D., & Macoveanu, M. (2010). Kinetics and equilibrium study of nickel (ii) removal using peat moss. *Environmental Engineering and Management Journal, 9*(5), 667–674.
46. Chandrasekhar, S., & Pramada, P. N. (2006). Rice husk ash as an adsorbent for methylene blue - effect of ashing temperature. *Adsorption, 12*, 27–43.
47. Rongsayamanont, C., & Sopajaree, K. (2007). Modification of synthetic zeolite pellets from lignite fly ash A, The Pelletiyation, WOCA 2007.
48. Li, Q., Su, H., Li, J., & Tan, T. (2007). Studies of adsorption for heavy metal ions and degradation of methyl orange based on surface of ion-imprinted adsorbent. *Process Biochemistry, 42*, 379–383.
49. The scientific report of the project New adsorbents of zeolite type obtained from waste fly ash collected from Romanian Combined Heat and Power Plants. PN-II-RU-TE- 2013-3-0177, coordinator Maria Visa.
50. Visa, M., Carcel, R. A., Andronic, L., & Duta, A. (2009). Advanced treatment of wastewater with methyl orange and heavy metals on TiO_2, fly ash and their mixtures. *Journal of Catalysis Today, 144*(1–2), 137–142.
51. Visa, M., Nacu, M., & Carcel, R. A. (2011) Fly ash substrates for complex wastewater treatment. In: *WOCA Conference*, May 9–12, 2011, Denver, Co. SUA. http.www.flyash.info.
52. Visa, M., Bogatu, C., & Duta, A. (2010). Simultaneous adsorption of dyes and heavy metals from multicomponent solutions using fly ash. *Journal of Applied Surface Science, 256*, 5486–5491.
53. Visa, M., & Duta, A. (2007). Adsorption mechanisms of heavy metals. In *AIChE Conference, Salt Lake City*.
54. Visa, M., & Duta, A. Cadmium and nickel removal from wastewater using modified fly ash—thermodynamic and kinetic study. *Scientific Study & Research*, *8*(40). ISSN 1582-540x.

55. Banerjee, S. S., Jayaram, R. V., & Joshi, M. V. (2003). Removal of Nickel (II) and Zinc (II) from Wastewater Using Fly Ash and Impregnated Fly Ash. *Seperation Science and Technology, 38*, 1015–1032.
56. Wang, S., Li, L., & Zhu, Z. H. (2007). Solid-state conversion of fly ash to effective adsorbents for Cu removal from wastewater. *Journal of Hazardous Materials, 139*, 254–259.
57. Shawabkeh, R., Al-Harahsheh, A., Hami, M., & Khlaifat, A. (2004). Conversion of oil shale ash into zeolite for cadmium and lead removal from wastewater. *Fuel, 83*, 981–985.
58. Lee, W. K. W., & van Deventer, J. S. J. (2002). Structural reorganisation of class F fly ash in alkaline silicate solutions. *Colloids and Surfaces A, 211*, 49–66.
59. Visa, M., & Duta A. (2007). Cadmium and nickel removal from wastewater using modified fly ash—thermodynamic and kinetic study. *Scientific Study & Research*, *8*(40). ISSN 1582-540x.
60. Marczewski, A. W. (2002). *A practical guide to isotherms of adsorption on heterogeneous surfaces*. http://adsorption.org/awm/ads/Ads.htm.
61. Lagergren, S. (1898). About the theory of so-called adsorption of soluble substances. Kungliga Svenska Vetenskapsakademiens. *Handlingar, 24*, 1–39.
62. Ho, Y. S., & Mc Kay, G. (1999). Pseudo-second order model for sorption processes. *Journal of Process Biochemistry, 34*(1999), 51–465.
63. Allen, S. J., McKay, G., & Khader, K. Z. H. (1999). Interparticle diffusion of a basic dye during adsorption onto sphangum peat. *Jouirnal of Environmental Pollution, 56*, 39–50.
64. Visa, M., & Duta, A. (2008). Advanced Cd^{2+} removal on dispersed TiO_2-fly ash. *EEMJ, 7*(4), 373–378.
65. Reyad, S., Al-Harahsheh, A., Hami, M., & Khlaifat, A. (2004). Preparation and determination of pulp pectin gels as biosorbent for heavy metals. *Fuel, 83*(7–8), 981–985.
66. Perić, J., Trgo, M., & Medvidović, N. V. (2004). Removal of zinc, copper and lead by natural zeolite—a comparison of adsorption isotherms. *Water Research, 38*, 1893–1899.
67. Visa, M. (2011). Heavy metals removal on dye—modified fly ash substrates. WOCA 037.
68. Tao, Y., Lianbie, Y., Pan, J., Wang, Y., & Tang, B. (2009). Removal of Pb(II) from aqueous solution on chitosan/TiO_2 hybrid film. *Journal of Hazardous Materials*, *161*, 718–722.
69. Mathur, S. K., Khare, D. C., & Ruoainwar. A. (1989). *Removal of heavy metals from main sewer- water of Varanasi city adsorption on fly ash and blast furnace slag*. *Journal of Industrial Pollution Control*, *5*, 52.
70. Visa, M. (2012). Tailoring fly ash activated with bentonite as adsorbent for complex wastewater treatment. *Journal Applied Surface Science*, *263*, 753–762.
71. Visa, M., Isac, L., & Duta, A. (2009). Fly ash—activated carbon powder composites for dyes and heavy metals removal. In *2nd International Conference on Multi-Functional Materials and Structures, Qingdao*, Multi-Functional Materials and Structures II, 79–82 (pp. 243–246). Trans Tech Publications.
72. Visa, M., & Duta, A. (2010). Adsorption behavior of cadmium and copper compounds on mixture FA:TiO_2. *Revue Roumaine de Chimie, 55*, 167–173.
73. Zahariam, C., Suteu, D. (2012). Textile organic dyes—characteristics, polluting effects and separation/elimination procedures from industrial effluents—A critical overview. Gheorghe Asachi Technical University of Iasi, Faculty of Chemical Engineering and Environmental Protection, Romania.
74. Lesmana, S. O., Novie, F., Soetaredjo, F. E., & Sunarso, J. (2009). Suryadi Ismadji: Studies on potential applications of biomass for the separation of heavy metals from water and wastewater. *Biochemical Engineering Journal, 44*, 19–41.

Part V
Sustainable Human Settlements

European Master in Renewable Energy

Paola Mazzucchelli and Nathalie Richet

Abstract Since 2002, EUREC has been coordinating a European Master in Renewable Energy, which is currently taught in nine universities from around Europe. The aim of the European Master is to train post-graduate students to fill the gap between the growing industry demand for specialised renewable energy expertise and the skills available in the job market. Additional Master courses in the area of sustainable energy are currently under development with the support of EUREC.

Keywords Renewable energies · Master degree · Europe · High qualified employment

1 Introduction

EUREC is the Association of European Renewable Energy Research Centres. Launched in 1991 and located in Brussels, its mission is to promote and support the development of innovative technologies and human resources to enable a prompt transition to a sustainable energy system.

In 2002, five European universities, members of EUREC (the Association of European Renewable Energy Research Centres), decided to join forces in order to create a Master degree dedicated to renewable energy technologies to be taught at European level [1]. The aim of such a course was to train post-graduate students to fill the gap between the growing industry demand for specialised renewable energy expertise and the skills available in the job market. The first Academic Year was launched in 2002–2003, and 19 students registered for it.

P. Mazzucchelli (✉) · N. Richet
EUREC, Brussels, Belgium
e-mail: mazzucchelli.p@eurec.be

N. Richet
e-mail: richet@eurec.be

I. Visa (ed.), *Sustainable Energy in the Built Environment - Steps Towards nZEB*,
Springer Proceedings in Energy, DOI 10.1007/978-3-319-09707-7_41

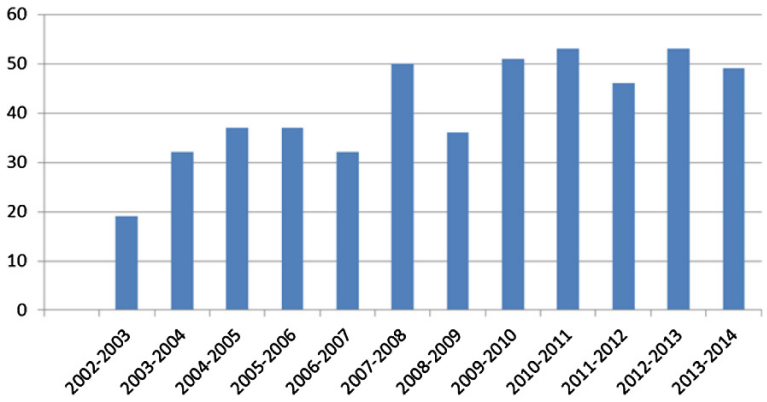

Fig. 1 Evolution of the number of students attending the European master in renewable energy per academic year

Since then, both the number of students and universities has been growing all over the years (Fig. 1).

Today, the European Master in Renewable Energy welcomes around 50 students per Academic Year, and is taught in nine universities around Europe: MINES-ParisTech (FR); Zaragoza University (ES); Loughborough University (UK); Oldenburg University (DE); Hanze University of Applied Sciences (NL); Northumbria University (UK); National Technical University of Athens (GR); Université de Perpignan (FR); IST Lisbon (PT).

2 Master Course Description

The European Master in Renewable Energy is structured around three semesters:

- During the *core semester*, which runs from September/October to January, students acquire a solid foundation in key renewable energy technologies and the socio-economic issues surrounding their deployment. According to the chosen university, the core can be studied in English (in Oldenburg, Loughborough and Hanze), French (in MINES-ParisTech) or Spanish (in Zaragoza). The Core providers all teach these subjects:
  - Core Foundation
  - Core Solar
  - Core Wind
  - Core Biomass
  - Core Water
  - Introduction socio-economics issues

Each University has its own teaching methods—distribution of modules can be organised differently—nevertheless we ensure that at the end of the core semester EUREC students have the same understanding and the same knowledge on renewable energy technologies, enabling them to follow any of the offered specialisations.

- The *specialisation semester*, which runs from February to May, focuses on a particular technology. In-depth theory classes alternate with practical work in laboratories and technical visits. The specialisations currently available are:
  - Wind energy (taught at NTUA, Greece)
  - Photovoltaics (taught at Northumbria University, UK)
  - Solar Thermal (taught at Université de Perpignan, France)
  - Grid Integration (taught at Zaragoza University, Spain)
  - Ocean energy (taught at IST Lisbon, Portugal)
- For the last 6 months, upon completion of the specialisation, students gain practical experience through a *project* undertaken in a company or a research centre. In December, each student comes to Brussels to present the results of the 6-month project.

The balanced mix of theoretical and practical courses, as well as the three-semester structure including a six-month internship, provides the students not only with high level technical and scientific competences, but also with soft skills such as flexibility and adaptability to work in a multicultural environment, which are essential when working in an expanding and global market. The European Master in Renewable Energy students evolve in an international and multicultural environment. Every year, they represent a mix of around 20 different nationalities, from all continents

The students are also requested to study in two different countries, in order to promote mobility and the European dimension of the Master course.

The degree given to successful students at the end of the course is handed out by the respective core university. It has a different name in each country:

- European MSc in Renewable Energy from Loughborough University
- Mastère spécialisé en Energies Renouvelables de MINES-Paristech
- Master Europeo de Energias Renovables de la Universidad de Zaragoza
- European MSc in Renewable Energy from Universität Oldenburg
- European MSc in Renewable Energy from Hanze University

In addition to their diploma from their respective core university, students receive a Certificate of Equivalence from EUREC. This document formally states that the different degrees given by the five core Universities are equivalent in value and contents. The course is assessed with laboratory work, mini-projects, end-of-term exams and a project.

The degree obtained by graduates of the European Master in Renewable Energy at the end of the course is awarded by the respective core university. Degrees awarded by Loughborough University, MINES-Paristech, Universidad de

Zaragoza, Carl von Ossietzky Universität Oldenburg and Hanze University are therefore fully recognised as postgraduate university degrees both in the respective countries (United Kingdom, France, Spain, Germany and the Netherlands) and in the other 28 Members States of the European Union. Non-European students who successfully complete the European Master in Renewable Energy obtain a degree which is supposed to be recognised by the relevant authorities also in their countries of origin. However, the recognition of an educational qualification depends on the competent authorities at national and regional level outside the EU. Students who necessitate an integrative official statement certifying the nature, level, context, content and status of the studies that were successfully completed (therefore similar to the "European Diploma Supplement") can obtain such a declaration upon simple written request to EUREC or to the core university where they first studied.

3 New European Master Courses

Given the success of this format, some of EUREC member universities have been discussing the opportunity to launch additional European Master courses.

Two courses are currently under development:

- One is going to be dedicated to *Sustainable Energy Systems Management* with a view to preparing managers equipped with the necessary competences and skills to facilitate the introduction and widespread use of sustainable energy technologies
- The other one is going to be dedicated to *Sustainable Energy and Society* with a view to preparing change agents and change strategists whose role is to facilitate the transition towards a more sustainable energy system

The starting point to launch additional Master courses at European level is based on an analysis of the current job market for renewable energy jobs, and the need to introduce a high level, innovative and flexible teaching, which can prepare a high qualified workforce to respond to the challenges of an international and globally growing industry.

4 Conclusions

The main features of successful Master courses at European level are:

- Strong partnership of universities -which competences are complementary (or "with complementary competences")
- Teaching modularity: the three-semester course
- Practical exercises in laboratories and hand-on seminars
- Project semester with a direct exposure to the working environment

- Strong partnership with the industry, as main recruiter
- A coordinating organisation, responsible for ensuring quality, homogeneity and consistency of the image of the European Master course
- International recognition of the Master degree

Reference

1. www.master.eurec.be.

Business Development in Renewable Energy

Yoram Krozer

Abstract This paper discusses how to foster development of renewable energy business. Factors that impede or enhance renewable energy in the EU 27 member states in the period 1998–2008 are analyzed. Nine factors are considered: population density, production output and energy sector output to indicate market conditions, public total expenditures, subsidies and environmental protection expenditures to indicate institutional conditions, R&D, share of students in population and venture capital to indicate firm's resources. Scarce space for business development and vested energy interests are the main impediments. R&D and venture capital are main drivers. The US and EU support for R&D and venture capital in renewable energy are compared. The US support is larger and mainly based on R&D grants. It has generated large, innovative enterprises. The EU support is mainly based on price guarantees for renewable energy delivery to grid. It has generated many enterprises. Building capabilities through stakeholders' networks in early phase of business development and clusters in the later phase is recommended.

Keywords Renewable energy · Factors · EU · Clusters · Networks

Highlights

1. Main barriers for renewable energy business are space scarcity and vested energy business, main drivers are research and development and venture capital.
2. More public support for renewable energy in US than in EU invoked larger firms in the US, price guarantees in the EU invoked more enterprises and employment in the EU than in the US.

Y. Krozer (✉)
CSTM-Twente Centre for Studies in Technology and Sustainable Development, University of Twente, Enschede, The Netherlands
e-mail: Krozer@xs4all.nl

Y. Krozer
Sustainable Innovations Academy, Amsterdam, The Netherlands

I. Visa (ed.), *Sustainable Energy in the Built Environment - Steps Towards nZEB*, Springer Proceedings in Energy, DOI 10.1007/978-3-319-09707-7_42

3. Demand for renewable energy, high margins and growing consumption in electricity in the EU has generated €135 billion market that grows €13 billion a year.
4. Renewable energy capability can be developed through the stakeholders' networks entailing specialization in business clusters.

1 Introduction

Business aiming to serve a common good is challenging because people rarely pay for public interests without direct private gains unless social sense of urgency generates public demands [19, 22]. Public demand for good environment is irrefutable, for instance for mitigation of climate change. The reasons why these demands emerge is discussed in other papers with regard to knowledge intensive societies [15, 25, 55]. Given these demands, this paper discusses countries' and regions' possibilities of developing renewable energy business. Herewith, renewable energy is considered a quasi-common good that serves energy for private consumption and energy security, climate change mitigation and others for public interests. The renewable energy business covers production, distribution and consumption of biomass and waste, hydro, geothermal, solar and wind resources, as well as energy efficiency through storage, distribution, co-generation, processing, saving with related management and policymaking.

The renewable energy business is a large and growing business. The global cleaner technologies sales in 2010 were USD 499 billion (euro 372 billion), out of which 45 % was renewable energy, 14 % energy efficiency, 34 % water treatment, 5 % waste treatment and 2 % others (Copenhagen Cleantech Cluster 2012). In comparison, these sales approximate to the total global car sales in the same period. The data are based on the investors' sources. Investments in renewable energy business grew during 2004–2010 on average 30 % a year to euro 211 billion in 2010 though with a large range of 0.4–75 % a year [32]. This average growth rate is higher than the average growth rate in informatics. The growth is expected to continue in the next decades. Global scenarios tend to assume a higher energy growth than income growth due to demands in emerging and low-income economies, and even higher renewable energy growth due to climate change mitigation and resource diversification [38, 43, 47, 51]. The share of renewable energy in the global final energy consumption is expected to be higher than the present 19 % measured in 2011 [42]. The subsequent energy scenarios expect higher shares [52, 56], whereas recent ones envisage the possibility of a fully renewable energy dependent supply in the EU by 2030 [49] and globally by 2050 [4]. These scenarios suggest that the renewable energy business can develop capabilities to satisfy global energy demands.

The renewable energy business generates many innovations. These innovations are studied from various angles. One approach is the managerial view focused on

the firms' resources as presented in Sharma and Vredenburg [44]. Another one is the mainstream (neoclassic) perspective that underpins the roles of prices for signaling and allocation, which is reviewed among others in Ruttan [41]. The institutional perspective addresses decision making with respect to technological, social, ethical and economic issues, which is reviewed in Steger et al. [48]. This paper uses the evolutionary argumentation for discussion about barriers and drivers for the renewable energy business. Herewith, Jacobsson and Johnson [19] presented a framework with factors that pose main barriers: imperfect actors and markets (poorly articulated demand, established technology with increasing returns, local search processes, market control by incumbents), deficient networks (poor connectivity and wrong guidance with respect to future markets) and failing public institutions (legislative failures, failures in the educational system, skewed capital market and underdeveloped organisational and political power of new entrants). Hekkert et al. [17] presented a framework with factors that are main drivers: entrepreneurial activities, knowledge development, knowledge diffusion through networks, guidance of search, market formation, resource mobilization, and creation of legitimacy. Other studies bring in many nuances [12, 29, 35]. In this paper main barriers and drivers are assessed with statistical data in Sect. 2. Experiences with policy support in the US and EU are presented in Sect. 3. Business opportunities in the EU are discussed in Sect. 4. Policies to generate capabilities are addressed in Sect. 5. Conclusions are in Sect. 6.

2 Factors in Renewable Energy Business

What are the barriers and drivers for the renewable energy business? In order to answer this question, an assessment of statistical data in the EU with respect to its macro-economic conditions and international fuel prices is done. Given that the main macro-economic change occurred after the financial crash in 2008 when the economic slow-down entailing a dip in renewable energy investments, the analysis in this paper stops in 2008. The internationally traded fuel prices, so called Free On Board (FOB), fluctuate. High oil prices influence all fossil fuel prices, which makes renewable energy attractive. Regarding the oil prices two periods are specified: 1998–2002 when the annual average real oil prices fluctuated at the level of the 2002 price and 2003–2008 when the real oil prices increased two times followed by fluctuations at the level of the 2008 price. Also the fossil fuel mix prices for electricity generation in the EU is calculated based on the fuel prices corrected for consumed volume in electricity generation. All prices accounted in the real USD 2000 price that is inflated with consumer price index and converted per year into euro.

Nine factors that can impede or foster renewable energy business development are selected with regard to the Jacobsson and Johnson [19] framework and available EU statistical data (Eurostat). The factors are: population density, production output and energy output that refer to the market conditions, public expenditures, subsidies

and environment protection expenditures that refer to the institutional conditions, research and development expenditures (R&D), students' share in population and venture capital that refer to firms' resources. All factors are calculated per capita per year and compiled into the averages during 1998–2002 and 2003–2008. Since the largest renewable energy producing countries are not always the largest consumers the analyses cover all producers and all consumers, as well as ten largest producers and ten largest consumers. The annual average change in each of the factors and the change in renewable energy production and consumers are compared to indicate whether the trend is converging (when correlations are positive), or diverging (when correlations are negative). For consistence in the data used, only the Eurostat is used. Malta is excluded because it does not provide sufficient data. Croatia is excluded because it joined the EU in 2013. Some missing data are linearly extrapolated. Only a few data on the regional renewable energy are found: eight regions in Austria that has produces much renewable energy and seven regions in Hungary that produces little renewable energy. However, these data are insufficient for analyses. Pearson correlations coefficients (R^2) between the factors and renewable energy production and consumption are calculated.[1] Sensitivity analyses cover: correlating per year and compiling into the average correlation coefficient per period and correlating for every renewable energy resource: biomass and waste, hydro, geothermal, solar and wind. Herewith, it can be noted that nearly 50 % of all renewable energy production in the period 2003–2008 is biomass and waste based. For interpretation of results it is assumed that R^2 larger than 0.5 or smaller than −0.5 indicate important factors but not causal relations. The results are summarized in Table 1. Appendix 1 shows the data: annual average per capita MW renewable energy production and consumption, and the factors.

The correlation is formally:

$$R^2(x,y) = \sum (x-\bar{x}) \cdot (y-\bar{y}) \Big/ \sqrt{\sum (x-\bar{x})^2 \cdot \sum (y-\bar{y})^2}$$

Columns show producers and consumers in the EU, ten largest producers and consumers and the annual change in the EU, all these divided into periods 1998–2002 and 2003–2008. The first row presents per capita renewable energy production and consumption. Large differences in the EU exist: ten largest producers are nearly three times larger per capita than the EU average and ten largest consumers are seven times larger per capita than the EU average. The renewable energy production and consumption have grown much faster during increasing oil prices than during low prices: production growth was 6 to 2 % and consumption 4 to 1 %. Other rows present factors. High positive or negative correlations of the factors and renewable energy production and consumption are shown bold. These are the main impediments and drivers.

[1] x is the annual average volume and change and y is the annual average factor volume or factor change.

Table 1 EU cross countries Pearson correlations (R^2) between production and consumption of renewable energy and several business development factors during steady and increasing oil prices (all data based on Eurostat)

Correlation are annual averages of the periods							Renewable energy producing countries		Renewable energy consuming countries			
	All EU		Ten largest		Change		All EU		Ten largest		Change	
	1998–2002	2003–2008	1998–2002	2003–2008	1998–2002	2003–2008	1998–2008	2003–2008	1998–2008	2003–2008	1998–2008	2003–2008
MWh/capita	2.3	3.0	7.4	8.3	2 %	6 %	1.0	1.1	7.0	7.8	1 %	4 %
Market conditions												
Population density	(0.5)	(0.5)	(**0.6**)	(**0.7**)	(0.2)	(0.3)	(0.4)	(0.4)	(0.4)	(0.4)	0.1	(0.0)
Production volume	0.2	0.1	0.5	0.5	0.3	0.2	0.3	0.3	**0.6**	**0.6**	0.1	(0.2)
Energy output	0.3	0.0	(0.4)	(**0.6**)	(0.2)	(0.1)	0.3	(0.2)	0.0	(0.3)	0.0	(0.2)
Public institutions												
Public expenditure	0.3	0.2	0.5	0.4	0.1	0.1	0.5	0.4	**0.6**	**0.6**	0.1	(0.3)
Subsidies volume	0.5	0.3	0.3	0.3	(0.1)	0.3	0.5	0.5	0.5	0.5	0.0	(0.1)
Environment protection	0.3	(0.0)	0.1	0.2	0.0	0.3	(0.0)	(0.0)	0.5	0.5	(0.1)	(0.3)
Firms resources												
R&D expenditures	**0.6**	0.5	**0.7**	**0.7**	0.2	(0.1)	**0.6**	**0.6**	**0.8**	**0.8**	(0.0)	(0.3)
Students share	0.1	0.4	0.5	0.3	0.1	0.1	0.2	0.1	0.2	(0.1)	(0.0)	(0.1)
Venture capital	0.3	**0.7**	**0.8**	**0.7**	**0.6**	0.1	**0.7**	**0.8**	**0.9**	**0.8**		0.1

2.1 Market Conditions

Population density, defined as the number of people per square kilometer, indicates space scarcity for renewable energy. Since the renewable energy resources have lower energy density than fossil fuel resources more space would be needed for the state-of-the-art renewable energy technologies to meet all energy demand in densely populated countries like the United Kingdom [30] and the Netherlands [50]. The factor analysis shows that the limited space is an important impediment for the production, not for the consumption. The sensitivity assessment with correlation per year confirms this finding. In particular, the biomass production is constrained by scarce space.

Production volume is indicated by the Gross Domestic Product in euro per capita. It is observed that environmental technologies and renewable energy production was larger and grew faster in the rich countries than in the emerging and developing economies [27, 37]. The factor analysis confirms these studies only insofar that the largest per capita EU economies are also the largest renewable energy consumers. Sensitivity analysis confirms that the countries' production volume is moderately important for renewable energy production and consumption; it is relevant for solar energy.

Energy output is indicated by the Index Energy Output in euro per capita. Intuitively, it would be expected that large energy producers also produce much renewable energy due to scale advantages. Gross et al. [16], for instance, observed that the renewable energy production growth in the 1990s was associated with decreasing unit costs albeit doubts exist whether scale of the renewable energy production is important compared to other factors [12]. A positive correlation could be expected but the energy output is negatively correlated with the renewable energy production, less negatively with its consumption. The sensitivity analyses per year and per renewable resource confirm this finding. Low renewable energy production is found in the large energy producing countries such as Belgium, Cyprus, Netherlands, Poland and UK. The large energy producers possibly do not care much about renewable energy because other resources are available and vested energy interests could have impeded renewable energy business [9].

2.2 Public Institutions

Public expenditure is indicated by the total government expenditure in euro per capita. It is often argued that high government expenditures for the renewable energy production and consumption are necessary because these are in development phase [18]. Given priority for the renewable energy in many EU countries, one would expect a lot of renewable energy production and consumption in the countries with high public expenditures. An indication of it is the observation that renewable energy in the EU grows twice as fast as in other OECD countries thanks

to government expenditures [3]. High positive correlations would be expected but only moderate correlations are found for the renewable energy production and higher for its consumption. Big public spenders per capita are often small renewable energy producers, for instance Belgium, Ireland, Luxemburg, Netherlands and UK. The sensitivity analysis per year confirms this finding. The analysis per resource shows that the government expenditures are important for the solar energy consumption but hardly for the other renewable energy resources.

Subsidies are indicated by the total subsidy in euro per capita. All subsidies are included, which means the subsidies in favour of the renewable energy business and ones in support of the fossil-fuel businesses. The subsidies in support of fossil fuels were until 2008 much larger than for renewable energy in the EU [11, 26]. Regarding the ambivalent allocation of subsidies one could expect moderate correlations. This analysis confirms this expectation. Nevertheless, the subsidies for hydro and wind production are important.

Environment protection is indicated by the total expenditures on environment protection in euro per capita. High expenditures suggest political interest in renewable energy as a tool of environmental policy next to other instruments, such as emission trading [34]. High correlations could be expected. However, all correlations are low, even somewhat negative for the consumption. The sensitivity analysis and the resource-specific assessments confirm this finding. Environmental policies rarely foster renewable energy but can cause trade-off between renewable energy and environmental performance.

2.3 Firms' Resources

R&D is indicated by the total research and development expenditures per capita. Since high correlation between R&D and total industrial production is found in the EU [46] high R&D could foster renewable energy as well as fossil fuel. Nevertheless, high positive correlations are found between R&D and the renewable energy production. It is even higher for the consumption. This is confirmed in the sensitivity analysis and for consumption of hydro and solar energy. The renewable energy business is apparently highly knowledge intensive.

Students share is the share of students in population. Since it is argued that higher education increases managerial awareness about sustainability [33, 57], high share of students in population could foster renewable energy. High correlations would be expected. However, these are low for the production and negligible, even somewhat negative, for the consumption. The sensitivity analysis and correlations per resource confirm the results. High concentration of students is a negligible factor for the renewable energy business.

Venture capital is the available venture capital in euro per capita. It indicates the investors' equity in firms. Much venture capital could foster renewable energy and fossil fuels. High positive correlation between venture capital and renewable energy production and consumption can be expected. The factor analysis confirms this.

The sensitivity analysis also underpins this result. In particular, the biomass and hydro production and consumption benefit from venture capital.

The main impediments for the renewable energy business are scarce space and large energy output. The main drivers are large R&D and venture capital. Links between these factors are also assessed. Space scarcity is not linked to other factors. It implies that the sparsely populated countries are not necessarily poor ones, with low R&D, or lack venture capital. Energy output is also unlinked. Although public expenditures and subsidies are moderately correlated with renewable energy they are linked with R&D. The public expenditures and subsidies could foster renewable energy through R&D. R&D and venture capital are also linked. The countries in top ten R&D and top ten venture capital per capita produce nearly three times more renewable energy than the EU average, albeit only 6 out of 12 countries are in the top ten countries for both factors.

3 Public Support to Renewable Energy Business

How policies foster R&D and venture capital, two main drivers for renewable energy, is discussed based on the US and EU policy support. These were the largest investors in renewable energy until present.

Options for policy support of R&D and venture capital are explained using the managerial view on innovation process. Figure 1 illustrates this viewpoint. The figure presents the profit as a function of time: horizontal axis is time and vertical axis is profit. Typical phases, investors and usual interest rates are labeled on the figure. Dotted lines indicate options for policy support. When an entrepreneur aims to launch a new product, he or she considers several years of costly R&D to create a saleable novelty (invention), followed by start-up of an enterprise or a project and a pilot for testing its invention before sales (innovation). Profit is negative during all these phases, which implies piling up costs. The costs must be covered by the investors' equity, which means venture capital, because loans for innovations are usually too risky; innovators can seldom cover the costs and their know-how is barely saleable as guarantees. For policy support there are only two options. Policy can reduce the costs through subsidies, for example R&D grants. The subsidies add to equity. Policy can also reduce investors risks, for instance through price guarantees. A guarantee attracts investors and loans.

Many policy instruments are developed based on these two options.

An international study has identified 178 instruments in 2006 [54]. Most instruments are found in the US and Western Europe, less in Asia, Eastern Europe and Latin America, hardly any in Africa. Most of them are grants for R&D and guarantees for expansion (commercialisation), which is for beginning and end of innovation processes. Only a few instruments are found for pilots, hardly any for start-ups. Entrepreneurs know how to use the instruments. For instance, 31 interviewed entrepreneurs used 163 instruments, it means globally on average about 5 per entrepreneur though more than average in Western Europe and US. In-depth

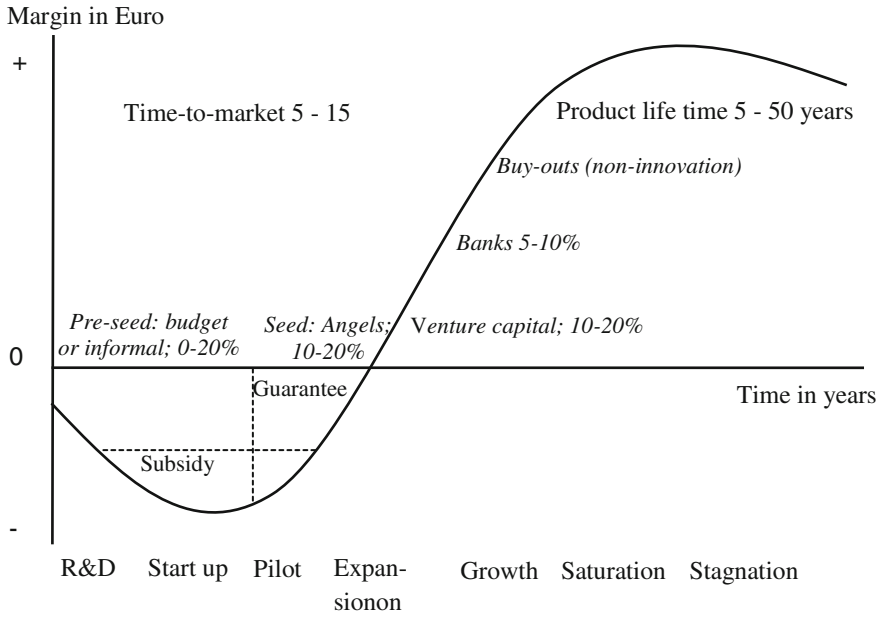

Fig. 1 Options for financing of an innovation process

country's analysis would find more instruments. In the Netherlands, for example, this study has mentioned 6 instruments; a Dutch metal branch study identified 23 instruments [14], web-based information shows many more (Subsidiedatabank.nl) and a consultant has mentioned about 1,900 possibilities [53]. The United Nations Environment Program (UNEP) advocated for more instruments, in particular to attract bankers [31]. This follows the German policy on the feed-in tariffs, which are price guarantees per unit renewable energy delivery to grid imposed by authorities on electricity generators [5]. Meanwhile, many EU countries introduced feed-in tariffs or similar subsidies albeit specifications vary with respect to renewable energy resources, years of guarantee validity, conditions for deliveries to grid and the tariff structure [21]. Many states in the US have introduced the renewable portfolio standards, which are obligatory renewable energy purchases without tariffs and a few states and networks also introduced feed-in tariffs [8]. What options is better is debated.

Several US studies have argued that high private investment in renewable energy in the US has generated its superiority. Herewith, R&D public support is valuable [1, 36, 40, 45]. The US firms were the largest by stock market value in 2008. Their value covered 42 % of the USD 560 billion (418 billion euro) global value. The US firms were also the most innovative ones, though the EU-based firms lead in wind, the Chinese in solar, and the Japanese in energy saving building and equipment. These findings are compiled in Appendix 2. The US business superiority despite the

larger EU total market is attributed to high private R&D, good bankruptcy regulations, risk-taking financiers, venture capital on universities and flexible labour, whereas the EU feed-in tariffs EU would distort electricity prices [10]. However, a US study into the EU feed-in tariffs found no distorting effects [20] and the US scholars advocate more public support for the risk-taking investments [58]. Other scholars argue that the US has generated more risk-taking equity in the renewable energy business compared to the EU that has attracted more total investments but mainly in the risk-avoiding acquisition [22]. However, the arguments could be biased because investors data is scarce.

A larger public support in the US than in the EU, which is largerly based on R&D grants, could also explain the larger and innovative renewable energy firms in the US. Unfortunately, only incidental data underpin this explanation because statistical data on the private and public expenditures in renewable energy are not available. Biermans et al. [2] has found that the total public support envisaged for the renewable energy business in US in 2008 was USD 94.1 billion (euro 70.2 billion) compared to USD 22.8 (euro 17 billion) in the EU. Both were programs for overcoming financial crisis in 2008. The EU expenditures on the feed-in tariffs in 2008 approximated 25 billion euro, calculated with average feed-in tariff of minimum and maximum multiplied by production volume per energy resource [26]. Similar is estimated by the Council of European Energy Regulators [6]. Hence, the projected public support for renewable energy was 70.2 billion Euro in the US and 53.2 billion euro in the EU excluding the US feed-in tariffs because these are unknown. Moreover, the EU provides much more support to the rival fossil fuels business. The OECD data on subsidies during 2005–2008 indicate 25.6 billion euro annual average in the EU and 9.1 billion euro in the US; the EU data is about the minimum because several countries and subsidies are not covered.

The large US public support focused on R&D invoked large and innovative companies, whereas the smaller EU support focused on feed-in tariffs generate more businesses and employment. Table 2 shows the annual average number of enterprises and employees and their growth in energy sector in the US and EU during 2008–2011. This period is after the introduction of the feed-in tariffs in the EU and during the financial crisis. Herewith, it should be noted that not all starting energy companies are based on renewable energy. There are less energy businesses in the US than in the EU, the number hardly grows but they are much larger than in the EU. The EU feed-in tariffs invoked a spectacular business growth by 24 % annual average compared to only 1.9 % in the US. It also gained about 23,000 additional job a year despite an increasing scale per company. For comparison, number of ICT enterprises grew by only 3 % a year in the EU and the jobs decreased in the same period.

It is plausible that the US and EU public support for the renewable energy business matches their aims. It implies that both can be effective but risking high social costs. The US support when aiming at the large, innovative firms can consistently provide R&D grants to strengthen equity of the promising beneficiaries but

Table 2 Number of enterprises (establishments in US), employees and their growth in the EU and US

		Average 2008–2011	Average annual change (%)
US	Number enterprises	12,634	1.9
	Employees	599,114	0.1
	Employees/enterprise	47	−1.8
EU	Number enterprises	85,237	24
	Employees	1,281,465	1.8
	Employees/enterprise	16	−18

risking that the supported firms fail in competition. The EU support when aiming at energy security and climate change mitigation can consistently guarantee non-discriminatory prices that enlarge the renewable energy markets but risk that too high tariffs compared to the market prices cause social costs. No instrument is a golden bullet but a deliberation about social cost—benefits versus social risks within bounded rationality of decision makers.

4 Renewable Energy Opportunities

What kind of energy business is attractive regarding volume and prices in the EU? The total energy consumption volume is hardly an incentive because it is stable. The volume calculated for the EU 27 during 1995–2011 covers the residential and business energy consumption on-site and in transport (more recent data is unavailable). The on-site consumption is based on the Eurostat energy statistical data, the transport consumption is derived from the Eurostat transport statistics using share of passengers and freight mileage in total mileage.[2] About 1.1 billion ton oil equivalent (t.o.e.) a year is consumed, equivalent to 13,000 GWh, out of it: 26 % residential, 43 % business, 25 % in passengers transport and 5 % in freight transport. It is about 2.3 t.o.e. or 27 MWh, per capita; the Central and East European countries consume less than 2 t.o.e., Luxemburg, Finland and Sweden more than 3 t.o.e. per capita. No significant changes occurred: the on-site energy consumptions decreased less than 1 % annually and in transport increased by 1 % a year. Nevertheless, there are several market opportunities for the energy start-ups.

[2] The share of kilometer-passengers for the residents consumption respectively kilometer-ton freight for business consumption in total is accounted per modality based on three years average mileage (2010–2012). For air and ship transport an average travel distance is assumed: 1,440 km for passengers ships and 3,600 freight ships and 2,270 km flight; a kilometer-passenger is assumed equivalent of 0.1 km-ton.

One opportunity is due to consumption growth of the renewable energy resources. It has grown by 6 % a year to cover more than 14 % share in the total energy consumption in 2011, which is still lower than the global 19 % share due to high biomass consumption in the developing countries but even higher share is envisaged by the EU for 2020 and its progress is on track. In particular, the high-tech renewable energy consumption of solar and wind energy grows fast. Other opportunities relate to high gross margins, i.e. sales minus energy resources purchase. The EU 27 gross margins are calculated only for gas and electricity in the on-site energy consumption because transport price data are unavailable, though energy-efficiency in transport is an attractive market regarding high oil prices, duties and taxes. Table 3 shows four indicators for the residential and business gas and electricity consumption. Appendix 3 shows countries data. The first indicator is the share of fossil fuel price in sale price in euro per kilowatt hour, which indicates possible value addition: the smaller this share the larger value can be added. The second indicator is the total gross margin. This shows the market volume for energy business. The third one is the average annual margin increase which indicates the market growth. The last one is the average annual sale price increase, which shows the price factor of the market growth.

The residential electricity consumption generates by far the highest value addition. Various value adding services and products are attractive, such as energy-efficient lightning, electricity monitors and so on. The largest market is in the business electricity consumption. Large energy-efficiency investments can be economic. The electricity markets together cover about 78 % of the total 135 billion euro market for the energy-efficient innovations. For comparison, it is twice larger than the ICT market or similar to the real estate market. Gas is mainly consumed for heat. It is a smaller market with low value addition, albeit gas volume in kWh is larger than in electricity. High value addition in electricity compared to gas can attract new services and products that add value, e.g. co-generation for transforming heat into electric power. Furthermore, the gross margins increased in all cases because volumes have grown, particularly gas consumption has grown due to subsidies in several EU countries and policies aiming at substitution gas for coal

Table 3 Indicators of the gas and electricity market in the EU 28 Member states during 2004–2011

All are annual averages	Euro/kWh	Million euro	Annual increase	
	Fuel to sale price (%)	Gross margin	Gross margin (%)	Sales prices (%)
gas business	75	17,415	50	2
gas residential	23	12,312	8	5
electricity business	26	62,222	4	5
electricity residential	7	43,474	2	1
Total		135,424		

Annual average increase of the FOB gas price is 21 % and fossil fuel mix price is 10 %

and oil. The sales prices of energy products also increased albeit slower than the FOB prices of fossil fuels, which makes local resources attractive. When margins grow faster than sales prices it means that more is consumed despite higher prices, i. e. low or positive price elasticity of demand for energy products. This holds true for all energy sources except the electricity consumption in businesses. The price inelastic demand for energy attracts cost-effective energy management, such as optimization of electricity consumption and better heat utilization.

The high growth of energy enterprises and their success, measured by employment, can be explained by the cumulative effects of growing demand for renewable energy and growing energy consumption despite higher prices. This stimulates innovations in using local resources, in value adding processing of fossil fuels and energy-efficient management. The distributed energy systems emerge, called smart grid.

5 Renewable Energy Capabilities

Regarding opportunities for renewable energy through value adding products how can policies foster the entrepreneurial capabilities? This is discussed with reference to theories on knowledge interactions for innovations, so called knowledge spillover.

In the mainstream train of thought, knowledge spillover occurs due to proximity of specialisms. Specialist clusters would generate know-how entailing innovations. Hence, specialists are pulled to companies (e.g. to Dassault aerospace in Toulouse, France or to Glaxo biotechnology in North Triangle, North Carolina, U.S.) and vice versa, specialist research centres aim to generate industries (e.g. Joint Research Centre on energy near Milano, Italy, or Santa Fe Institute on complex systems in the U.S.). Porter's work on clusters popularized this argumentation for policy making. Many embraced this view for creation of "top-tech" valleys, campuses, incubators, and similar. The renewable energy clusters also multiplied, often called cleantech. The cluster policy promised business development, which attracted billions of euros in public funding. Results, however, are dubious. Statistical studies relating the numbers of patents and innovations to employment and turnover show that clustering has positive effects only within a sector or in a region but not across sectors or regions. This is to say that public funding for strong industries may work, which is tautology. Case studies do not indicate positive effects of clusters on innovations. Studies also suggest that enterprises have too little local interdependencies to justify the clustering policies. Know-how is also mobile. A statistical study on the French cluster policy argued that 1.8 billion euro public funding have not invoked clustering because firms spontaneously spur know-how efficiently. A similar case was found in the Cambridge region that hosts several excellent innovation centers. A case study on a Dutch energy cluster suggests that clusters often impede innovations because vested interests are reinforced due to public funding [23].

Another view focuses on the knowledge and cultural diversity. The argument is that innovation processes involves numerous gradual improvements and interactions that are unpredictable, let alone steerable [39]. Knowledge spillover, therefore, would flourish due to variety of potential customers, suppliers, investors, experts interacting in formalized and tacit manner [28]. This image of diverse interactions that are structured by local and regional stakeholders created a metaphor of learning networks, popularized as "triple helix". Cases suggest that such networks generate innovations, which attracts businesses. Florida (2002) underpinned that statistically for the US. The culturally diversified, urban work and living environments would attract highly educated and skilled professionals who generate knowledge spillovers in networks (Florida 2002), but also large science and arts projects could attract knowledge. A trustful cultural setting would foster risk-taking, which is necessary for innovations. A study on the renewable energy networks in the EU underpinned the diversity of the successful stakeholders' networks, which implies that there many ways to foster the entrepreneurial capabilities [24].

These views do not necessarily exclude each other. The clusters and networks metaphors could address different phases in business development. The networking would apply to the early phases when skills must be generated and innovators scouted for start-ups. The networking, herewith, fosters the starting entrepreneurs and reduces investors' risks. Policies that enable life-long learning, scouting of talents, matchmaking between groups, co-funding of start-ups and pilots and other tools for the experimentation before commercialization would foster the entrepreneurial capabilities. The policy focus on those elements in energy portfolios that match regional socio-economic and natural potential would generate innovations entailing business clusters. The clusters would generate economies of scale that is needed for the commercialization. The policies that attract external businesses and know-how with public and private funds could be justifies when competitive businesses are established.

6 Conclusions

The renewable energy business is relevant to economic development not only to meet global energy demand but also to generate income while mitigating climate change. The question about how public policies can foster renewable energy business has been discussed based on the factor analysis of renewable energy production and consumption with the EU statistical data during 1998–2008. Among nine factors analyzed, which are population density, production output, energy sector, public expenditures, subsidies, environment protection, R&D, share of students and venture capital, the main impediments for the EU renewable energy business are limited space and strong fossil fuel interests and the main drivers are large R&D and available venture capital. Public support for the R&D and policies that foster venture capital are instrumental. Comparison of the US and EU policy support indicates that the US attained a larger and more innovative renewable

energy business mainly due to much larger public support for its R&D. The EU, however, has generated many new enterprises and jobs mainly due to its policy of price guarantees called feed-in tariffs. The energy market generates many opportunities for highly valued services and products. In addition to renewable energy for fossil fuel substitution opportunities are due to high and growing margins in energy consumption. Value adding services and products for the residential electricity consumption are, such as energy-efficient lightning, electricity monitors and so on. Energy-efficiency increase in the business electricity consumption is often economic. Co-generation for transforming heat into electric power and reuse of heat waste can be net beneficial. Low price elasticity of energy demand makes energy management attractive. Development of capabilities in renewable energy largely depends on the knowledge spillovers. When such energy are in the early development phase capabilities can be developed through stakeholders networks. Public support to attract skills and innovators is needed. The propositions to generate clusters can be attractive in situations with the developed renewable energy business aiming at commercialization. The renewable energy business is sufficiently large and fast growing to justify public efforts in its development for the sake of income, jobs and good environment.

Acknowledgments With kind permission of the publisher to be included in Krozer [26]. Theory and Practices on Innovating for Sustainable Development, Springer, London (forthcoming). I am grateful for comments to Diana Kakwera.

Appendix 1

See Tables 4, 5a, 5b and 5c.

Appendix 2

See Table 6.

Table 4 Per capital renewable energy production, consumption and growth, the largest ten producers and consumers are underlined, the fastest ten growers are bold

42 GJ = 11.6 MWh	Production renewable energy		Production growth		Consumption electricity generation		Consumption growth	
	1998–2002	2003–2008	1998–2002 (%)	2003–2008 (%)	1998–2002	2003–2008	1998–2002 (%)	2003–2008 (%)
EU (27)	2.34	2.98	1.8	6.4	1.0	1.1	1.3	4.4
Belgium	0.61	1.07	5.2	**16.2**	0.2	0.3	3.8	**10.7**
Bulgaria	1.04	1.56	11.3	4.1	0.4	0.6	3.8	**6.0**
Czech Rep.	1.62	2.35	5.4	**6.9**	0.3	0.5	6.4	**8.2**
Denmark	3.85	5.52	6.1	5.5	1.2	1.8	12.7	**5.5**
Germany	1.29	2.91	9.6	**17.5**	0.5	1.0	11.2	**11.7**
Estonia	4.51	6.01	−0.1	5.5	0.5	0.8	0.5	**7.6**
Ireland	0.72	1.06	6.6	**11.5**	0.4	0.7	10.0	**12.4**
Greece	1.46	1.72	−0.1	2.7	0.5	0.7	1.1	**7.6**
Spain	2.02	2.49	0.2	5.5	1.1	1.4	2.1	**9.0**
France	3.07	3.00	−2.5	2.9	1.5	1.3	−0.5	*1.8*
Croatia								
Italy	1.91	2.25	2.5	4.9	0.9	0.9	1.3	2.4
Cyprus	0.74	0.85	−0.4	**7.2**	0.0	0.0	1.0	**16.6**
Latvia	7.59	9.11	4.1	2.7	2.0	2.2	1.0	4.2
Lithuania	2.27	3.13	7.1	5.9	0.5	0.6	3.9	**5.7**
Luxembourg	1.01	1.68	3.0	**14.2**	2.3	2.3	1.7	−0.4
Hungary	0.96	1.39	0.6	**11.2**	0.1	0.2	14.4	**12.5**

(continued)

Table 4 (continued)

42 GJ = 11.6 MWh	Production renewable energy		Production growth		Consumption electricity generation		Consumption growth	
	1998–2002	2003–2008	1998–2002 (%)	2003–2008 (%)	1998–2002	2003–2008	1998–2002 (%)	2003–2008 (%)
Malta								
Netherlands	0.99	1.41	8.4	**6.8**	0.2	0.4	8.2	**12.2**
Austria	9.40	10.12	1.8	3.8	5.7	5.6	2.3	0.8
Poland	1.19	1.42	1.3	4.6	0.2	0.3	1.3	2.4
Portugal	4.18	4.52	−1.2	3.7	1.5	1.6	−2.2	**11.5**
Romania	2.10	2.54	1.1	**6.5**	0.9	1.0	−2.2	4.2
Slovenia	3.92	4.48	5.7	2.9	2.1	2.1	3.1	4.2
Slovakia	1.25	1.84	10.7	6.0	1.0	0.9	5.5	−0.7
Finland	16.86	18.93	3.9	2.5	4.3	4.6	0.5	**5.9**
Sweden	18.17	18.30	1.9	2.6	9.6	8.6	−0.4	1.8
Un. Kingdom	0.45	0.70	6.0	**9.8**	0.2	0.3	6.8	**10.3**

Table 5a Factors per capita: market conditions

	Population density person per km^2		Gross domestic product in euro		Energy production index in euro	
	1998–2002	2003–2008	1998–2002	2003–2008	1998–2002	2003–2008
EU (27)	112	115	18,837	23,142	95	96
Belgium	334	342	24,319	29,710	55	96
Bulgaria	73	70	1,710	3,337	54	110
Czech Rep.	130	130	6,381	11,120	89	102
Denmark	124	127	32,100	39,143	67	92
Germany	230	231	24,979	27,873	94	98
Estonia	32	31	4,534	9,330	88	110
Ireland	54	59	27,543	39,998	–	
Greece	91	92	750	18,225	88	96
Spain	81	88	15,693	21,668	83	90
France	110	115	23,623	27,982	92	93
Croatia						
Italy	189	194	20,942	25,039	86	95
Cyprus	75	82	14,344	18,831	76	91
Latvia	37	36	3,403	6,822	85	110
Lithuania	54	53	3,496	6,902	71	98
Luxembourg	167	179	48,739	69,364	82	90
Hungary	110	108	5,280	8,910	87	104
Malta	1,216	1,278	10,467	12,470		62
Netherlands	425	437	26,145	32,568	55	95
Austria	95	98	25,697	30,825	84	102
Poland	123	122	4,774	6,929	99	104
Portugal	115	119	12,062	15,013	94	91
Romania	94	91	1,840	4,284	79	103
Slovenia	98	99	10,956	15,365	85	95
Slovakia	110	110	4,108	8,215	93	98
Finland	15	16	25,298	31,305		
Sweden	20	20	28,240	34,221	101	92
Un. Kingdom	241	247	26,043	30,649	113	96

Table 5b Factors per capita: institutional conditions

	Total expenditure in euro		Subsidies in euro		Environment protection expenditure in euro	
	1998–2002	2003–2008	1998–2002	2003–2008	1998–2002	2003–2008
EU (27)	8,713	10,760	246	265	131	146
Belgium	12,549	15,291	295	492	143	156
Bulgaria	777	1,427	21	31	6	17
Czech Rep.	3,184	5,085	168	202	35	57
Denmark	18,123	21,264	784	873	269	252
Germany	12,028	12,996	409	316	170	163
Estonia	1,847	3,684	50	80	6	33
Ireland	9,970	15,123	208	200	221	383
Greece	6,152	9,143	18	18	79	120
Spain	6,482	8,989	171	222	40	75
France	12,743	15,330	359	403	128	158
Croatia						
Italy	10,325	12,298	254	253	183	208
Cyprus	5,874	8,409	163	132	31	56
Latvia	1,380	2,889	32	56	3	25
Lithuania	1,415	2,701	31	51	4	43
Luxembourg	20,560	28,490	756	1,086	303	321
Hungary	2,897	4,651	92	124	17	47
Malta	4,684	5,667	189	259	41	182
Netherlands	12,530	15,565	380	411	431	498
Austria	13,708	15,983	850	1,051	180	232
Poland	2,169	3,228	23	40	33	26
Portugal	5,526	7,059	150	135	75	86
Romania	721	1,803	28	56	5	19
Slovenia	5,396	7,263	206	257	57	125
Slovakia	2,032	3,425	93	122	15	28
Finland	13,022	16,122	383	416	153	170
Sweden	16,416	18,105	483	489	73	121
Un. Kingdom	10,799	13,702	118	189	137	176

Table 5c Factors: business resources per capita

	R&D total expenditure in euro		Students in total population		Venture capital investment in euro	
	1998–2002	2003–2008	1998–2002 (%)	2003–2008 (%)	1998–2002	2003–2008
EU (27)	308	414	3.2	3.7	78	154
Belgium	432	537	1.4	3.7	50	44
Bulgaria	7	14	3.1	3.1		
Czech Rep	62	134	2.3	3.1	4	6
Denmark	627	948	3.5	4.0	56	38
Germany	545	685	2.5	2.7	34	41
Estonia	27	78	3.5	4.9		
Ireland	275	470	4.0	4.5	346	34
Greece	55	103	3.7	5.4	7	8
Spain	118	232	4.5	4.3	29	22
France	460	581	3.4	3.4	74	62
Croatia						
Italy	191	273	3.2	3.4	64	37
Cyprus	33	69		2.6		
Latvia	11	32	3.4	5.4		
Lithuania	16	45	3.1	5.3		
Luxembourg	839	1,080	0.5	0.0	1,026	117
Hungary	33	80	2.7	4.1	145	162
Malta		57		2.2		
Netherlands	442	591	3.0	3.4	7	7
Austria	487	696	3.2	3.0	74	19
Poland	26	35	3.6	5.4	4	3
Portugal	71	126	3.6	3.7	19	2
Romania	7	16	1.8	3.4	14	14
Slovenia	131	205	3.8	5.4		
Slovakia	27	36	2.3	3.3		
Finland	705	1,037	5.0	5.7	305	282
Sweden	939	1,216	3.5	4.6	1,498	1,105
Un. Kingdom	412	532	3.4	3.8	13	4

Table 6 The main renewable energy markets innovators in the US, EU and Other countries

Businesses	Resources (input)	Products (output)	Firms stock market value by 27-6-2008, USD billion [40]			Innovators (Firms to watch, [36]		
			US	EU	Other	US	EU	Other
Biofuels	Oils	Biodiesel	N. A.	N. A.	N.A.	7	3	0
	Sugars	Ethanol						
	Waste	Biogas						
Hydropower	Inland	Electric storage	–	–	–	–	–	–
	Waves and Tide							
Geothermal	Groundwater	Heat pumps	2.2	0.5	1.1	–	–	–
	Deep							
Wind power[a]	On shore	Electric	29[b]	153	9	5	4	1
	Off shore							
Solar power	PV	Electric heat	31	27	80	6	1	3
	Thermal (CSP)							
Green buildings	Architecture	Storage certification	39[c]	1	49	7	0	3
	Lighting							
	Micro-generators							
Personal transport	Hybrid (electric)	Batteries	111	0.3	0	6	0	4
	Electric	Fuel cell						
	Hydrogen	Flywheels						
	Hybrid (air)	Compression						
Smart grid	Monitoring	Meters	24[d]	0.1	0	10		
	Point of use	Storage						
	Networks	Smart grid						
	Co-generator	Heat reuse						
Appliances (mobile)	Cells	Embedded systems				7	2	1
	PV							
Carbon trading	CO2 emissions	Trading houses	0	2	0			
Total			237	184	139	48	10	12

[a] Excluding sails and kytes for motion
[b] Assumed 10 % of the total General Electric stock value USD 261,000 million
[c] Assumed 10 % of the Procter & Gamble (Duracell) USD 184,650 million
[d] Assumed 10 % of the IBM USD 164,900 million
Based on [1, 36, 40, 45]

Appendix 3

Fuel prices and energy sales prices in EU countries 2004–2011

	€/kWh	€ million	Growth		€/kWh	€ million	Growth	
	Fuel to sale price €/kWh	Gross margin	Sale price	Gross margin	Fuel to sale price €/kWh	Gross margin	Sale price	Gross margin
	Gas consumption business				Gas consumption residential			
Belgium	83	565	6	84	23	436	6	6
Bulgaria	127	(11)	9	−576	40	2	5	20
Czech Rep.	85	236	9	88	29	183	11	25
Denmark	91	124	10	86	20	113	9	22
Germany	60	5,567	9	14	21	3,271	3	0
Estonia	133	(6)	12	−99	47	(2)	10	−626
Ireland	132	324	−1	38	22	86	−2	6
Greece	0	(282)	0	29	0	(19)	0	83
Spain	92	929	8	157	22	489	1	4
France	75	1,680	9	37	23	1,773	5	4
Croatia	95	92	8	−58	39	21	3	143
Italy	79	2,812	5	36	24	2,114	4	2
Cyprus	0	–	0	0	0	–	0	0
Latvia	120	4	10	189	46	(0)	13	−503
Lithuania	96	67	11	−430	39	6	8	109
Luxembourg	68	76	8	16	26	22	8	21
Hungary	87	304	3	92	39	117	14	−189
Malta	0	–	0	0	0	–	0	0
Netherlands	78	1,598	3	20	23	978	5	1
Austria	75	420	6	93	23	163	5	8
Poland	86	393	9	−112	32	209	8	145
Portugal	79	212	7	29	19	43	3	12
Romania	166	(233)	5	−240	68	(67)	−1	−1,494
Slovenia	79	41	14	54	25	12	8	14

(continued)

(continued)

	€/kWh	€ million	Growth		€/kWh	€ million	Growth	
	Fuel to sale price €/kWh	Gross margin	Sale price	Gross margin	Fuel to sale price €/kWh	Gross margin	Sale price	Gross margin
Slovakia	85	168	8	41	32	82	7	33
Finland	78	216	4	224	0	(3)	0	22
Sweden	59	103	9	123	18	14	8	14
Un. Kingdom	84	2,516	5	−118	28	2,534	6	30
	Electricity consumption business				Electricity consumption residential			
Belgium	24	2,098	2	3	6	1,227	3	−2
Bulgaria	47	249	2	1	15	169	0	2
Czech Rep.	24	1,416	10	12	8	565	7	7
Denmark	28	644	3	2	7	483	3	2
Germany	23	13,837	1	1	5	8,335	0	−1
Estonia	43	78	1	0	13	38	0	0
Ireland	20	735	4	4	5	494	5	7
Greece	28	999	3	3	10	532	5	6
Spain	25	5,700	8	8	7	3,139	6	10
France	35	6,058	3	2	8	5,645	0	−1
Croatia	31	228	6	9	10	196	3	3
Italy	21	9,412	3	3	5	4,394	−2	−2
Cyprus	18	135	10	13	6	87	8	12
Latvia	41	77	8	10	12	42	6	10
Lithuania	31	153	7	8	11	66	5	8
Luxembourg	24	193	3	2	6	49	0	1
Hungary	27	679	3	3	8	429	4	4
Malta	19	56	15	17	7	27	14	14
Netherlands	24	2,904	0	−1	6	1,313	2	1
Austria	26	1,347	6	7	6	867	4	4
Poland	31	2,238	10	13	8	987	5	6
Portugal	26	1,088	3	3	6	693	−4	−3
Romania	37	620	5	5	13	211	3	8
Slovenia	29	264	3	2	9	110	1	1

(continued)

(continued)

	€/kWh	€ million	Growth		€/kWh	€ million	Growth	
	Fuel to sale price €/kWh	Gross margin	Sale price	Gross margin	Fuel to sale price €/kWh	Gross margin	Sale price	Gross margin
Slovakia	23	696	7	8	7	206	2	1
Finland	34	1,380	2	−1	8	807	2	2
Sweden	31	2,211	7	8	7	1,770	5	3
Un. Kingdom	25	7,031	9	8	7	5,862	5	3

References

1. Asplund, R. W. (2008). *Clean energy* (1st ed.). New Jersey: Wiley.
2. Biermans, M., Grand le, H., Kerste, M., & Weda, J. (2009). *De Kapitaalmarkt voor Duurzame Projecten*. Stichting voor Economisch Onderzoek. Amsterdam: Mimeo.
3. Blok, K. (2006). Renewable energy policies in the European Union. *Energy Policy, 34*, 251–255.
4. Blok, K. (2010). The energy report, World Wildlife Fund, Ecofys, OMA, Gland.
5. Böhme, D., & Dürrschmidt, W. (2007). Renewable energy sources in figures—national and international development: Status 2007, Federal Ministry for the Environment, Nature Conservation and Nuclear Safety, Berlin.
6. CEER, Council of European Energy Regulators (2013). Status review of renewable and energy efficiency support schemes in Europe, Ref: C12-SDE-33-03, Bruxelles.
7. Copenhagen Cleantech Cluster. (2012). The Global Cleantech Report 2012, Danish Industry Foundation
8. Couture T., & Cory, K. (2009). State Clean Energy Policies Analysis (SCEPA) Project: An analysis of renewable energy feed-in tariffs in the United States. Technical Report NREL/TP-6A2-45551. Revised June 2009, Golden, Colorado.
9. de Visser, E, Winkel, T., de Vos, R., Blom, M., & Afman, M. (2011). Overheidsingrepen in energiemarkt. CE en Ecofys.
10. Economist, *Europe's tech entrepreneurs*, June 10, 2010.
11. EEA (2004). Energy subsidies in the European Union. *Technical Report* 1/2004. Copenhagen: Mimeo.
12. Farrell, J. (2014). *Renewable energy economies of scale are bullshit*, Institute for Local Self-Reliance http://www.ilsr.org/renewable-energy-economies-scale-are-bullshit/ (visit March 13, 2014).
13. Foxon, T. J., Gross, R., Chase, A., Howes, J., Arnall, A., & Anderson, D. (2005). UK innovation systems for new and renewable energy technologies: Drivers, barriers and systems failures. *Energy Policy, 33*(16), 2123–2137.
14. Grimbilas P. (2008). *Duurzaamheid: De overheidsinstrumenten voor bedrijven*, FME-CWM, Zoetermeer.

15. Grober, U. (2006). *Sustainability—A cultural history* (1st ed.). Cambridge: Green Books.
16. Gross, R., Leach, M., & Bauen, A. (2003). Progress in renewable energy. *Environment International, 29*, 105–122.
17. Hekkert, M. P., Suurs, R. A. A., Negro, O., Kuhlman, S., & Smits, R. E. H. M. (2007). Functions of innovations system: A new approach for analysing technological change. *Technological Forecasting and Social Change, 74*, 413–432.
18. Jacobsson, S., & Bergek, A. (2004). Transforming the energy sector: The evolution of technological systems in renewable energy technology. *Industrial and Corporate Change, 13* (5), 815–849.
19. Jacobsson, S., & Johnson, A. (2000). The diffusion of renewable energy technology: An analytical framework and key issues for research. *Energy Policy, 28*(9), 625–640.
20. Klein, C. A. (2012). Renewable energy at what cost? Assessing the effect of feed-in tariff policies on consumer electricity prices in the European Union. Thesis published in *The Georgetown Public Policy Review*, *18*(1), 43–62.
21. Klein, A., Pfluger, B., Held, A., Ragwitz, M., Resch, G., & Faber, T. (2008). *Evaluation of different feed-in tariff design options—Best practice paper for the International Feed-In Cooperation*, Fraunhofer Institut, Institut for Systems and Innovation Research.
22. Knight, E. R. W. (2010). *The economic geography of clean tech venture capital*. Working paper, University of Oxford.
23. Krozer, Y. (2010). Do innovation clusters pay off ? In M. J. Arentsen, W. van Rossum & A. E. Steenge (Eds.), *Governance of innovation* (1st ed., pp. 107–124). Cheltenham: Edward Elgar.
24. Krozer, Y. (2012). Renewable energy in European regions. *International Journal on Innovation and Regional Development, 4*(1), 44–59.
25. Krozer, Y., & Brezet J. C. (2012). Sustainable innovations and economic growth. Paper for the global and regional research on sustainable consumption & production systems: Achievements, challenges, and dialogues, June 13–15, 2012, Rio de Janeiro.
26. Krozer, Y. (2014). Smart grid and EU 27 countries policy. Paper at the ESEIA Conference, April 23–25, Enschede.
27. Lanjouw, J. O., & Mody, A. (1996). Innovation and the international diffusion of environmentally responsive technology. *Research Policy, 25*(1996), 549–571.
28. Lawson, C., & Lorenz, E. (1998). Collective learning, tacit knowledge and regional innovative capacity. *Regional Studies, 33*(4), 305–317.
29. Lund, P. D. (2009). Effects of energy policies on industry expansion in renewable energy. *Renewable Energy, 34*(1), 53–64.
30. MacKay, D. (2009). *Energy without hot air*, www.withouthotair.com
31. Makinson, S. (2005). *Public finance mechanism to catalyze sustainable energy sector growth.* United Nations Environmental Programme and Sustainable Energy Finance Initiative, Mimeo.
32. McCrone, A. (2012). *Global trends in renewable energy investments*. Bloomberg new energy finances. Franfurt School.
33. Meek, W. R., Pacheco, D. F., & York, J. G. (2010). The impact of social norms on entrepreneurial action: Evidence from the environmental entrepreneurship context. *Journal of Business Venturing, 25*, 493–509.
34. Menanteau, P., Finon, D., & Lamy, M.-L. (2003). Prices versus quantities: Choosing policies for promoting the development of renewable energy. *Energy Policy, 3*, 799–812.
35. Negro, S., Hekkert, M., & Smits, R. E. (2007). Seven typical system failures that hamper the diffusion of sustainable energy technologies. *Energy Policy, 35*, 925–938.
36. Pernick, R., & Wilder, C. (2008). *The cleantech revolution* (1st ed.). New York: Harper.
37. Popp, D. (1998). *Induced innovation and energy prices*. Kansas University, Mimeo.
38. Resch, G., Held, A., Faber, Th, Panzer, Ch., Toro, F., & Haas, R. (2008). Potentials and prospects for renewable energies at global scale. *Energy Policy, 36*, 4048–4056.
39. Rosenberg, N. (1975). Problems in the economists conceptualization of technological innovation. In N. Rosenberg (Ed.), *Perspectives on technology* (1st ed., pp. 61–84). Cambridge: Cambridge University Press.

40. Rubino, J. (2009). *Clean money, picking the winners in the green-tech room* (1st ed.). New Jersey: Wiley.
41. Ruttan, V. W. (2002). Source of technical change: Induced innovation, evolutionary theory, and path dependency. In A. Grübler, N. Nakicenovic & W. D. Nordhaus (Eds.), *Technological change and the environment* (pp. 9–39). Washington DC: Resources for the Future. International Institute for Applied Systems, Laxenburg.
42. Sawin, J. L. (2013). *Renewables 2013, Global Status Report*. Paris: REN21.
43. Sawin, J. L., & Moomaw, W. R. (2009). *Renewable revolution: Low carbon energy by 2030*. Danvers: Worldwatch Institute.
44. Sharma, S., & Vredenburg, H. (1998). Proactive corporate environmental strategy and development of competitively valuable organizational capabilities. *Strategic Management Journal, Strategic Management Journal, 19*, 729–753.
45. Siegel, J. (2008). *Investing in renewable energy* (1st ed.). New Jersey: Wiley.
46. Smith, K. (2000). What is the 'knowledge economy'? Knowledge intensive industries and distributed knowledge bases. Project "Innovation Policy in a Knowledge-Based Economy", European Commission, Mimeo.
47. Statham, B. A. (2007). Deciding the future. Energy Policy Scenarios till 2050. World Energy Council.
48. Steger, U., Achterberg, W., Blok, K., Bode, H., Frenz, W., Gather, C., Hanekamp, G., Imboden, D., Jahnke, M., Kost, M., Kurz, R., Nutzinger, H. G., & Ziesemer, T. (2005). *Sustainable development and innovation in the energy sector* (pp. 211–222). Berlin, Heidelberg: Springer.
49. Teske, S., & Ties, F. (2008). *Energy [R]evolution*, Greenpeace International Europe, mimeo.
50. van Baal, M. (2011). Kunnen wij overschakelen op duurzame energie. Technisch Weekblad. http://www.technischweekblad.nl/rubrieken/energieserie/kunnen-we-overschakelen-op-duurzame-energie.166168.lynkx (visited November 15, 2013).
51. van der Slot, A., van den Berg, W. (2012). *Clean economy, living planet*. Roland Berger Strategy Consultant.
52. van der Veer, J. (2008). *Shell energy scenario's to 2050*, Shell International BV, mimeo.
53. van Elburg, J. C. (2009). *Het perspectief van de koploper*. Rotterdam: Rebel groep.
54. van Ermen, R. (2007). *Comparison and assessment of funding schemes for development of new activities and investments in environmental technologies*. Fundetec, rapportnr 044370, Brussels.
55. Viñuales, J. E. (2013). The rise and fall of sustainable development. Available at SSRN, http://ssrn.com/abstract=2200083 or http://dx.doi.org/10.2139/ssrn.2200083
56. Virdis, M. R. (2003). *Energy to 2050*. Paris: IEA and OECD.
57. Wagner M. (2009). Eco-entrepreneurship: An empirical perspective based on survey data. In G. D. Libecap (Ed.), *Frontiers in eco-entrepreneurship research* (*Advances in the study of entrepreneurship, innovation & economic growth*, Vol. 20, pp. 127–152). Emerald Group Publishing Limited.
58. Zindler, E., & Locklin, K. (2010). *Crossing the valley of death*, Bloomberg New Energy Finance.

SWOT Analysis of Engineering Education and Renewable Energy Sources. Case Study: University of Ruse Angel Kanchev

Nikolay Mihailov

Abstract This paper describes results from SWOT analysis on the education of students in the field of renewable energy sources. The analysis is made taking into account several important factors typical for Bulgaria.

Keywords Education · Renewable energy sources · Technologies

1 Introduction

One of the main purposes of the strategy "Europe 2020" is connected with the climate changes and energetics. It requires reduced CO_2 emissions with 20 %, electrical consumption with 20 % and the increase of the energy production from the Renewable Energy Sources (RES) with 20 % according to the levels from 1990 (Fig. 1).

According to this document and national law the planning and establishment of RES in Bulgaria is intense (Fig. 2). This is explained by the appropriate climate conditions—high levels of solar radiation, wind and hydro energy potential, large quantity of organic substances with animal or plant origin.

Considering these tendencies, a course in the field of RES was started in the University of Ruse Angel Kanchev in the beginning of the year 2000. The first steps are the including of special lectures in the study programs in various faculties. Currently the master courses "Renewable energy sources and technologies" and "Hybrid and electrical vehicles" are suggested.

Educational, training and research activities are realized using modern laboratory base—measuring instruments from Kipp and Zonen, ANTAGE PRO2, thermovision cameras, etc. The students are able to perform tests at a 2 kW PV plant and electrical vehicle from "Ducati" company.

N. Mihailov (✉)
University of Ruse Angel Kanchev, Ruse, 8, Studentska Street, 7017 Ruse, Bulgaria
e-mail: mihailov@uni-ruse.bg

I. Visa (ed.), *Sustainable Energy in the Built Environment - Steps Towards nZEB*,
Springer Proceedings in Energy, DOI 10.1007/978-3-319-09707-7_43

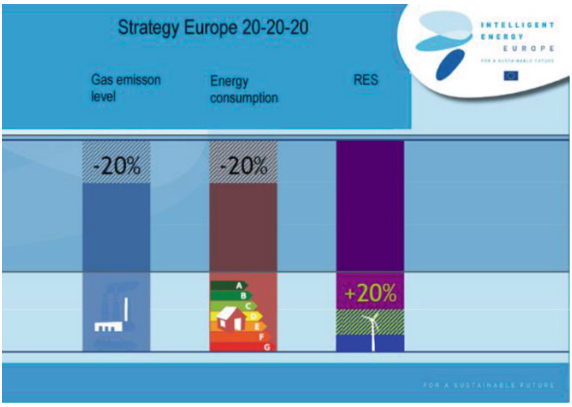

Fig. 1 Elements of the strategy "Europe 2020"

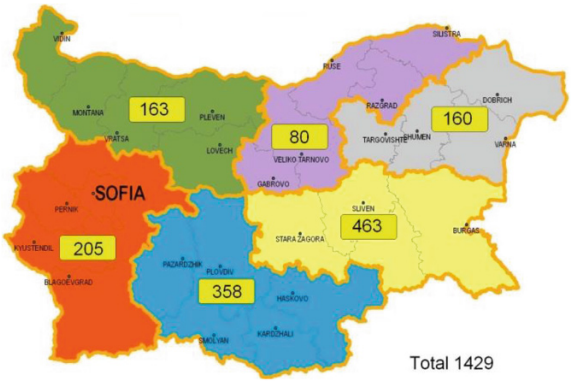

Fig. 2 RES in Bulgarian regions according to Sustainable Energy Development Agency (SEDA)

A lot of European projects help the students to exchange experience with their colleagues from Germany, Austria, Hungary and Romania [1, 2]. In the projects from the programs "Cross border cooperation Romania-Bulgaria 2007–2013", "Intelligent Energy Europe", "Information and Communications Technologies Policy Support Programme" and others there are a lot of students and PhD students involved [3, 4]. The regular 2-year International Scientific Conference Energy Efficiency and Agricultural Engineering attracts a lot of students, PhD student and young researchers working the field of RES.

A SWOT analysis of the RES educational process would help for the improvement of its efficiency.

2 Materials and Methods

Several factors are taken into account during the SWOT analysis.

- Demographic collapse in the country.

Statistical data shows tendency of decline in the population of the country (Table 1). According to the latest research Bulgaria is in 204th place, out of 224 countries, according to the criteria birth rate [5].

During the last 25 years the country's population has decreased with 1.65 million. One of the reasons is the intensive emigration.

Fewer and fewer children are born in the villages, which is a prerequisite for sustaining the development of the branch. At the end of 2012 for the first time the population in villages is under 2,000,000 people. During the observed period 2012, have been abolished 24 villages, and 172 other are desert, i.e. the shown demographic imbalance are turning into a basic obstacle for many systems, including education.

- High rate of unemployment amongst young people.

Due to the closing of almost all big industrial companies, many research institutes of the Bulgarian Academy of Sciences etc., bases for technological development and other have reduced rapidly the opportunities for development of engineers in the above mentioned branch.

Unemployment among young people is very high and is rising during the last years (Fig. 3).

This leads to increase in the search of work abroad.

- Decline in the number of secondary education graduates.

The tendency of permanent decrease in the number of secondary education graduates, including the professional is extremely alarming (Fig. 4).

The above mentioned circumstances have been taken into account during the consideration of the main aspects of training of the electrical engineers in the University of Ruse Angel Kanchev.

Strong Points

(a) Modern laboratory facilities

The faculty of Electrical and Electronic Engineering where the students are educated has a modern laboratory base. In the laboratories latest measurement

Table 1 Demographic collapse of the population of Bulgaria

Year	Birthrate (%)	Mortality (%)	Natural Growth (%)
1970	138,745 people (16.3)	77,095 people (9.1)	61,650 people (+7.2)
2012	69,121 people (9.5)	109,281 people (15.0)	40,160 people (−5.5)

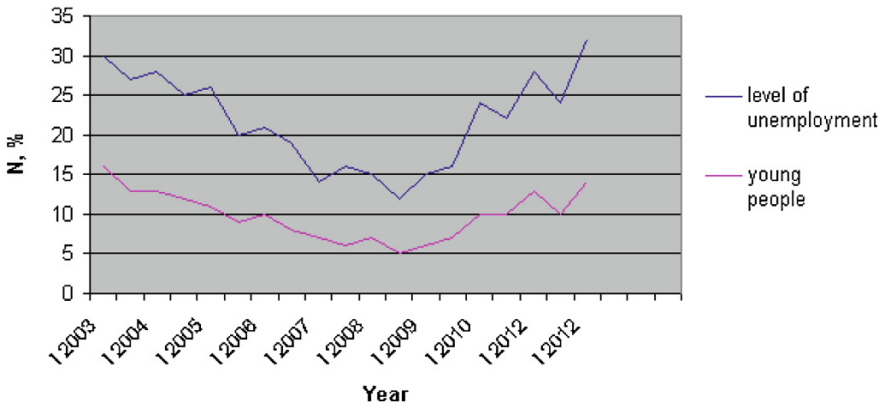

Fig. 3 Tendencies characterizing the youth unemployment

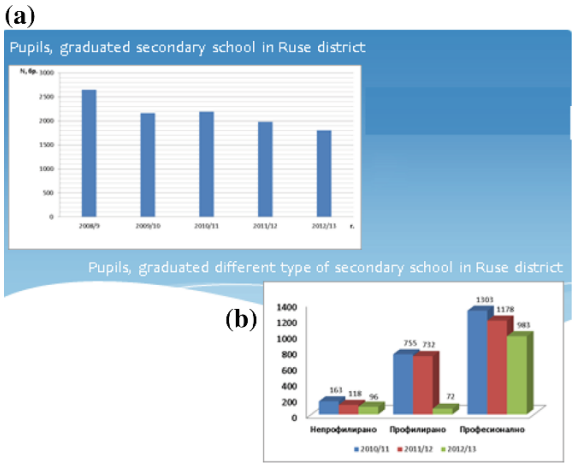

Fig. 4 Number of graduates in district Ruse—total (**a**) and distributed by type of secondary school (**b**)

techniques and computer systems are used. With their help a quality education process is being conducted (Fig. 5).

(b) Modern technical infrastructure for education

All lecture halls have been installed with presentation equipment, computers and interactive boards. The Faculty facilities include video- conference halls, which enable local and foreign leading professors to give lectures to students (Fig. 6).

(c) Modern information services

In the faculty buildings, information panels are placed, from where students gather various information about the study process (timetables and other useful

Fig. 5 View of several laboratories

Fig. 6 View of several lecture halls

information).Students also have access to number of on-line libraries—for example Science Direct, Scopus, Engineering Village, ISI Web of Knowledge, Springer Link etc. (Fig. 7).

(d) Free access to software products

For the purposes of class and diploma work, writing of assignments and other study work, connected with the scientific education, students are given the latest versions of the most commonly used software products (MATLAB, Simulink, Statistica Advanced, CorelDRAW X4, LabVIEW, ABBYY FineReader, Ansys Fluent, SolidWorks Premium, FeatureCAM, AutoCAD Electrical, AutoCAD Mechanical, Autodesk 3ds Max Design, FineHVAC, Acrobat Pro, Photoshop, etc.). Very often leading companies give their products, used in the engineering practice for free or at very low prices.

Fig. 7 Different information systems

(e) Unlimited access to computer halls.

Each student and doctoral student has a free access to unlimited high-speed internet on the territory of the University. Practically each student has access to computer and communication equipment. The University has more than 1,600 PCs. There are 63 access points for WiFi (43 of which belong to Cisco). In internet bandwidth is 1 Gbps for Bulgarian websites and 100 Mbps for international.

(f) Qualified teaching staff.

The Lecturers form the Faculty have high level professional preparation, which ensures the quality of the education process, including to that of the doctoral students (Table 2).

(g) Stable contacts with business organizations.

The Faculty keeps stable contacts with leading international companies—Siemens, Schneider Electric, ABB, etc. (Fig. 8).

Every spring an University exhibition is organized, where prestigious national and international companies participate with modern industrial equipment, technologies, etc. (Fig. 9).

This encourages students from the faculty to seek successful professional realization.

Weak Points

(a) Insufficient practical work.

The crisis in the industrial branch in the country strongly restrict the opportunities for practical education of students. To a certain extent this problem will find a solution trough the project "Student practices", executed with the partnership of 51 universities in the country. More than 60,000 students are planned to participate in the project. The total budget of the project amounts to 56,000,000 BGN and this guarantees the execution of all planned activities.

Table 2 Sustainable academic staff structure

Title	<35 years	(35–45) years	(45–55) years	(55–65) years	>65 years	Total
Professor			1	7.5		8.5
Assoc. Professor		6	15	16	1	38
Principal Assistant, PhD	6	2	6	3		17
Assistant, PhD						0
Principal Assistant		4	6	6		16
Assistant	8					8
Total	14	12	28	32.5	1	87.5

Fig. 8 Fragment of equipment provided by Siemens A/S

Fig. 9 Stands from spring exhibition

(b) Ineffective use of the international programs for student and teacher exchange (ERASMUS, LEONARDO, CEEPUS and others.).

Unfortunately only limited number of students and teachers from the faculty choose to participate in the exchange programs. The reasons for this could be many, but among the important ones is the lack of reciprocity between the partners' relations.

(c) Insufficient language knowledge.

The weak knowledge of students in foreign languages is a serious reason for not participating in the various programs for exchange.

(d) Ineffective participation in scientific projects.

Unfortunately stagnation in industry affects the opportunities for students to participate in scientific projects. At the moment national companies are not interested or do not have enough financial resources for partnerships. In most of the cases they prefer ready technical decisions offered by foreign companies. In this case also partial solution to the problem can be found in the execution of the project "Student scholarships—phase 3". There are scholarships for scientific work. For the summer semester of the academic 2012/2013 have been paid 50 scholarships.

Opportunities for Overcoming the Pointed Weaknesses

The listed weaknesses in engineering education can be overcome by politics, focused on:

- Development of University research center for energy technologies trough the cooperation with leading national and international organizations;
- Enlarging the practice for free language courses, including the continuing education;
- Active governmental participation in the branch, through the development of special programs, oriented towards geographical regions;
- Modernization of education programs according to the new demands—micro-grid systems, energy storage, fuel cells etc.;
- Active participation in international programs for cross-border cooperation, the Operational Programs in the new Programming period, ERASMUS+, Horizon 2020, etc.;
- Attracting of foreign students through the renewing of traditional partnerships or by creating new ones.

Threats

Historical experience of the country shows that the highly developed industry requires a modern education system that is connected with the other systems—social and economic. This is why the threats may emerge:

- Falling behind and restricting of the specialties in the faculty;
- Limited access to the national and international labor market;
- Delay in overcoming the deep economic crisis in the country;
- Continuing high emigration process

These problems are important and have to be solved through coordinated actions of all local and national institutions.

3 Conclusions

It could be concluded that the results from the analysis can be used from the academic management of university to make managing decisions. Of course they have to be taken into account also from the ruling organs on national level, considering the specific place of the electrical engineers in the field of RES among the factors on which the industry of Bulgaria depends on.

Acknowledgments The present paper has been developed with the financial aid of the European social fund. The University of Ruse is solely responsible for the content of this document and it can in no circumstances be viewed as the official position of the European Union or the Ministry of Education and Science. Project:№ BG051PO001-3.3.06-0008 "Aiding the growth of researchers in the engineering field and the information technologies"

References

1. www.ro-bul-ret.eu.
2. 2nd "Green waves" International Autumn Academy Renewable Energy—smart Cities Along the Danube.
3. Grant Agreement No 270981. Balanced European Conservation Approach—ICT services for resource saving in social housing (BECA). http://www.beca-project.eu/home/
4. Grant Agreement No IEE 09/702/SI2.558239. Expert System for an Intelligent Supply of Termal Energy in Industry and other Large—Scale Applications (EINSTEIN II). http://www.einstein-energy.net/
5. Fartunova, M. (2012). Higher education and the labor market: Dilemmas and alternatives. *Sofia, 2012*, 111. Angel Kanchev, University of Ruse. ISBN: 978-954-712-557-5.